ISSN 0289-842X

RIKEN Accelerator Progress Report

1984

vol. 18

理化学研究所
the Institute of Physical and Chemical Research

RIKEN Accelerator Progress Report
January-December 1984

理化学研究所
the Institute of Physical and Chemical Research
Wako-shi, Saitama, 351-01 JAPAN

This volume contains recent information of the accelerators at RIKEN (IPCR), informal reports and abstracts of papers which will be published at scientific meetings or in publications by staff members, guests, and visitors.

CONTENTS

Page

I. INTRODUCTION 1

II. OPERATION OF ACCELERATORS

1. Cyclotron Operation 2
2. RILAC Operation 4
3. TANDETRON-Operation 6
4. Implanter Operation 7

III. RESEARCH ACTIVITIES

1. Nuclear Physics

1. ^{27}Al(d, ^{2}He)^{27}Mg Reaction 8
2. Investigation of Coulomb Excitation for Projectile-Polarization Determination 10
3. Strongly Damped Components in the Reaction of ^{16}O+^{54}Fe System 12
4. Extended TDHF Calculation of the Variance of Mass Distribution in the ^{16}O+^{40}Ca Reaction at E_{Lab}=157.3 MeV 14
5. Low Angular-Momentum Cutoff in Heavy-Ion Fusion Reactions 15
6. Backward Cross Section in the Generalized Exciton Model 18
7. Classical Trajectory Picture of Massive Transfer 20
8. High Spin States in ^{110}Sn 22
9. Lifetime Measurement of the 8^{-} State in ^{110}Sn 24
10. High-Spin States of Ge Isotopes in the Interacting Boson Model 26
11. Ground State Rotational Band in ^{173}Yb Excited by (^{58}Ni, ^{58}Ni') 28
12. In-Beam γ-Ray Study of ^{218}Ra with BGOACS 30
13. In-Beam γ-Ray Study of ^{212}Po Using Radioactive ^{210}Pb Target 32
14. Isomeric Transition of ^{212}Po 35
15. Evaporation-Like Products in ^{14}N+^{238}U Reaction 37
16. High-Lying Single-Proton States of ^{209}Bi Studied by Gamma-Triton Coincidence Measurement in the ^{208}Pb(α, t)^{209}Bi Reaction 39
17. Production and Separation of Neutron-Rich Isotope ^{15}C Using Heavy-Ion Reactions 41

2. Atomic and Solid-State Physics

1. Classical Trajectory Monte Carlo Calculation for Collision Processes of $e^{+}+(e^{-}p)$ and $\mu^{+}+(\mu^{-}p)$ 43

Page

2. Quantum Mechanical Study of the Process $\mu^+ + (\mu^- p) \rightarrow (\mu^+ \mu^-) + p$ 45

3. Transitions of Molecules between High-Angular-Momentum States 47

4. Theoretical Investigation of Molecular Photoionization 49

5. Doubly Differential Cross Sections for Electron-Impact Ionization of Helium 51

6. Potential Energy Curves of Na_2^+, K_2^+, and Na_2 53

7. Electronic Property of Extremely High-Density and High-Temperature Materials 55

8. Electron Stripping Cross Sections from Multiply Charged Ions by Hydrogen and Helium Atoms 57

9. Coupling in Ar-Ti, Ar-Co, and Ar-Zn Systems 59

10. Theory of Radiative Electron Capture I: Nonrelativistic Treatment and Theoretical Paradox 62

11. Theory of Radiative Electron Capture II: Covariant Treatment 64

12. Calculation of the L_{23}-M_1M_1 Auger Energy and the Relative Auger Rates for Ar^{6+} 67

13. Tilted Foil Method Using Thin Carbon Foil 69

14. Beam-Foil Spectroscopy of Highly Ionized Aluminum Atoms 71

15. Intensity Ratio between Kβ and Kα X-Rays from 33 MeV Ar Ions in Solid Targets 73

16. High Resolution Measurement of Cu K X-Rays from Collision Systems of Cu Ions on C Target and C Ions on Cu Target 75

17. REC X-Rays for ^{3}He and ^{4}He Targets 77

18. Production of Highly-Charged Slow Ar Ions Recoiled in 1.05 MeV amu^{-1} Ar^{q+} (q=4, 6, 10–14) Ion Bombardment 78

19. Total Apparent Cross Sections for Ionization of Rare-Gas Atoms by Fully Stripped Projectiles 80

20. Production of Highly-Ionized Recoil Ions in Highly-Ionized, Energetic Ion+Molecule Collisions 82

21. Projectile Dependence of L-MM Auger Electrons Ejected from Ar Target by Heavy-Ion Impact 84

22. Secondary Electrons Emitted from Al under Bombardment with He^+ and He^{++} 86

23. Chemical Bond Effects on Auger Electrons Induced by He^{2+} Ion Bombardment 88

24. Studies of Magnetic Structure of Cobalt Ferrite Surfaces by ^{119}Sb Emission Mössbauer Spectroscopy 90

25. Perturbed Angular Correlation of γ-Rays Emitted from ^{111}Cd ($\leftarrow$ ^{111}In) in α-Fe_2O_3 92

26. TDPAC of γ-Rays Emitted from ^{111}Cd ($\leftarrow$ ^{111}In) in Fe_3O_4 94

Page

27. Perturbed Angular Distributions of Gamma-Rays from Dy under Transient Magnetic Field 96

28. Plasma Wall Interaction 97

29. Origin of Hydrogen in Amorphous Silicon Produced by Glow-Discharge in $Si_2H_6+D_2$ and $Si_2D_6+H_2$ 99

30. Application of Heavy-Ion RBS to the Analysis of Silicon Ohmic Contact Systems 101

31. Depth Profiling of Deuterium in Titanium Carbide by Elastic Recoil Detection Analysis 103

32. Stress-Induced Site Change of H in V Observed by Channeling Experiments 104

33. Lattice Location of Hydrogen in Nb α-Phase as Observed by Channeling Method 106

34. Compositions of Anodized Aluminum with Europium Implantation 108

35. Surface Compositions of Argon-Implanted Kapton Films 109

36. Lamp Annealing of Cd-Implanted GaP 110

37. Helium Bubble Formation in Ni 111

38. Creep Property Improvement of Helium Injected JPCA by Thermomechanical Treatments 113

39. Irradiation Creep of 316 Stainless Steel 115

40. Depth-Dependent Damage Profile in Stainless Steels Irradiated with Ar- and N-Ions 117

41. Effects of Fast Neutron Irradiation on Insulating Materials 119

3. Radiochemistry and Nuclear Chemistry

1. Isotope Production and Labelled Compound Synthesis 121

2. Charged Particle Activation Analysis 123

3. Charged Particle Activation Analysis of Ion-Implanted Oxygen 125

4. Application of PIXE to Environmental Science 126

5. Application of PIXE to Medical Science (II) 128

6. Reliability and Detection Limit for the Elastic Recoil Measurement of Hydrogen 130

7. Measurement of the Impurity Hydrogen Concentrations on the Surfaces of the Neutron Bottle 132

8. High Sensitivity Analysis of Deuterium in Solids by ^{15}N-Induced Nuclear Reactions 134

9. Thermoluminescence from the Ar-Bombarded Silica 137

10. Adsorption Kinetics of $^{119}Sb(V)$ Ions onto α-Fe_2O_3 Surfaces 139

Page

11. *In Situ* Emission Mössbauer Study of $^{119}Sb^{5+}$ ($\rightarrow$ $^{119}Sn^{4+}$) Ions at α-Fe_2O_3-Aqueous Solution Interfaces 141

12. Correlation between Angular Anisotropy of Fission Fragment and Its Mass in System of p+^{232}Th 143

4. Radiation Chemistry and Radiation Biology

1. Electron Scavenger Effects on the Fluorescence Induced by Single High-LET Particle 145

2. Inactivation of Bacterial Spores by a Single Heavy Ion (II) 147

3. DNA Damage in Cultured Human Tumor Cells after Nitrogen-Ion Irradiation 148

4. New Broad Emission Bands from Pressurized Liquid He Impinged by N Ions 150

5. Instrumentation

1. RIKEN BGOACS System 152

2. A Compound Counter System for High-Energy Gamma-Ray Detection 155

3. Liquid Ionization Chamber 156

4. Use of Charge Integrating ADC's with Pulse Shape Discriminators for Neutron-Gamma Discrimination 158

5. Particle Identification with a BaF_2 Scintillator 160

6. Test of MCP and PSD Using X-Rays and Electrons 162

7. One Dimensional Position Sensitive Parallel Plate Avalanche Counter 164

8. Test Machine for Ion Guide Isotope Separator On-Line 166

9. A Coulomb-Excitation Mössbauer Spectrometer 167

IV. NUCLEAR DATA

1. Status Report of the Nuclear Data Group 168

V. ACCELERATOR DEVELOPMENT

1. Present Status of the RIKEN Ring Cyclotron Project 169

2. Sector Magnets for the RIKEN SSC 170

3. Model Study of the RF Resonator for the RIKEN SSC 172

4. RF Power Amplifier for the RIKEN SSC 174

5. A Method of Measuring Two-Dimensional Motion of the Orbit Center Using Three Radial Differential Probes 177

6. Acceleration of Off-Centered Beam in the RIKEN SSC 179

7. Beam Sharing System for RIKEN SSC 181

Page

8. Design of Beam Buncher in the SSC Injection Beam Transport Line 184
9. Control System of the RIKEN SSC 185
10. An Intelligent CAMAC GP-IB Controller Module 187
11. Method of Sealing Vacuum Chambers and Pumping Control System for the SSC 189
12. Performance Test in Cryopump 192
13. Calculation for the Design of a Beam Dump 194
14. Beam Attenuation Device 197
15. Emittance Monitor 199
16. Charge Exchange Technique in the Linac 201
17. Design of a Rebuncher in RILAC 203
18. Production of Highly Charged Ions by Whistler Heating of Plasmas 205
19. Construction of ECR2 207
20. Automatic Control of a Gas Circulation and Gas-Feed System for the Ion Source 209
21. Low-β RFQ Structure-II: High Frequency Model Measurement 211
22. Development of the Medium-β RFQ Structure-III: Study by High Frequency Model 212
23. Development of the Medium-β RFQ Structure IV: Effect of Change of Cell Length, Measurements by Magnetic Analog Models 214
24. Application of the Medium-β RFQ Structure 216

VI. RADIATION MONITORING

1. Leakage-Radiation Measurement in the Underground Passage of the Cyclotron Building 218
2. Routine Monitoring of RIKEN Accelerators 221

VII. LIST OF PUBLICATIONS 223

VIII. LIST OF OUTSIDE USERS AND THEIR THEMES 234

IX. LIST OF SEMINARS 235

X. LIST OF PERSONNEL 236

AUTHOR INDEX

I. INTRODUCTION

H. Kamitsubo

Collaborative research using the 160 cm cyclotron and the variable-frequency heavy-ion linear accelerator (RILAC) has been extensively performed this year. In addition to these two accelerators, an electrostatic accelerator (TANDETRON) of 1 MV and an ion implanter of 250 kV are dedicated to the collaborative research.

During the past one year the cyclotron has been in good condition as before. A new gas feed system with an automatic control device for gas circulation was developed for the cyclotron ion source. The RILAC has also been operated steadily in this period. It should be emphasized that the operation in a full frequency range (17–45 MHz) was realized. Studies of the dynamical behavior of the beam in the RILAC as well as the technical development of the accelerator itself have been performed. A beam attenuation device was developed to reduce beam intensity down to 10^{-4} without deteriorating the beam quality. The RF power can be reduced if ions with higher charge states are accelerated at the RILAC. Test experiments were carried out to promote the ion charge states by putting a stripper foil between resonator cavities. The TANDETRON has been in steady operation in this period.

A variety of studies on the nuclear physics have been carried out mainly by using the 160 cm cyclotron. Nuclear spectroscopy and reaction mechanism for heavy ion collisions were studied experimentally as well as theoretically. Collaborative experiments using the facilities of other institutions such as Institute for Nuclear Study, University of Tokyo, Research Center for Nuclear Physics, Osaka University, and Japan Atomic Energy Research Institute have also been continued.

Instrumental development has been continued for the purpose of building new experimental equipments for the SSC. Construction of a BGO crystal ball was almost completed and used for the test experiment. Development of the ion-guided ion source for an on-line mass separator was started in 1984.

Atomic and solid state physics has been continued in this period. The RILAC is very suitable for the study of atomic collisions because it is capable of accelerating various kinds of ions to a few MeV per nucleon. Experiments were carried out on the beam foil spectroscopy and atomic collisions measuring ultra-violet light, X-rays, Auger electrons, and recoil ions; theoretical work was also performed extensively.

Mössbauer spectroscopy and perturbed angular correlation studies have been continued to investigate the internal fields and structure of the magnetic oxides. Studies on the distribution and lattice location of the impurity atoms in solid materials have been pursued using the channeling and the Rutherford backscattering techniques.

Collaboration with the group of National Research Institute for Metals was continued to study the creep and helium-bubble formation in fusion reactor materials by bombarding with alpha particles as well as protons.

Charged particle activation analysis has been applied routinely to the measurements of the light-element impurities in GaAs, Sb-doped Si, and other semiconductors. Experiments on the radiation chemistry and biology were carried out mainly by using heavy ions.

Construction of the RIKEN Ring Cyclotron (separated sector cyclotron) is in progress. During past one year the construction of the cyclotron vault was completed and four sector magnets together with their power supplies were assembled in it. Fabrication of remaining parts of the cyclotron is now under way.

International collaboration between RIKEN and Cyclotron Laboratory of Texas A&M University has been persued on heavy ion physics. The International Symposium on Heavy Ion Physics coorganized by RIKEN and INS, University of Tokyo, was successfully held last August in Tokyo (Part 1) and at the foot of Mt. Fuji (Part 2).

RIKEN Accel. Progr. Rep. 18 (1984)

II. OPERATION OF ACCELERATORS

1. Cyclotron Operation

K. Ikegami, S. Fujita, K. Ogiwara, H. Takebe,
S. Kohara, T. Kageyama, and I. Kohno

The 160 cm cyclotron was operated on the 24 hr a day basis during the period from October 23, 1983 to November 7, 1984. Statistics of machine operation time is shown in Table 1. Percentage of the net beam time slightly decreased compared with that of the last year. In this period, much effort has been made for fast and easy setting up of the operation parameters for any ions and energies by using a small computer[1] (NEC 9801) equipped to the control system.

Table 1. Cyclotron operation in the period XIX.

	Oscillator	Ion source	Beam
Reading of the time meter on Oct. 23, 1983	81,388.5	85,751.2	49,788.5
Reading of the time meter on Nov. 07, 1984	86,420.1	90,909.0	53,950.1
Difference	5,031.6	5,157.8	4,161.6
Percentage of 382 days	54.9%	56.3%	45.4%
Schedule in this period			
Beam time	240 days		
Overhaul and installation	60		
Periodical inspection and repair	20		
Vacation and holidays	48		
Other scheduled shut down	14		

In January 1984, the newly designed gas circulation and gas-feed systems[2] for the ion source were set up. The gas circulation system is used in order to reuse expensive gases such as ^{3}He and enriched $^{13}CO_2$ and $^{15}N_2$. The gas-feed system is used in order to feed eight kinds of gases; it has two gas-feed lines for mixing gases through two gas flow controllers. These systems can be operated automatically according to the sequence predetermined by a programing controller which consists of an OMRON SYSMAC M5R having an I/O port of max. 256 points.

At the end of March, 1984, the cyclotron was shut down for two weeks. Because a 450 kW motor generator (MG) supplying DC power for the main magnet was broken down. The trouble would have been caused by a reason that some parts of insulators of armature coils were covered with dusts of carbon brushes and destroyed by the flashover between

Table 2. Scheduled beam time and research subjects in the period XIX.

	Subject	Heavy ion	Light ion (hr)	Total
Nucl. Phys.	Nuclear reaction	2,250	838	3,088
	RI production	34	167	201
Fields other than Nucl. Phys.	Nuclear chemistry	0	374	374
	Radiation biology	64	12	76
	Radiation chemistry	216	56	272
	Solid state physics	0	210	210
	Atomic collision	24	0	24
	Radiation damage	69	353	422
Outside users	Radiation damage	46	291	337
	RI production	0	37	37
	Test of track detector	0	11	11
	Single event upset in the LSI memory	116	0	116
	Radiochemical analysis	0	89	89
Total		2,819	2,438	5,257
Percent in total		53.6%	46.4%	100%
Maintenance, operation, and engineering				
Exchange of ion sources			108	
Machine inspection and repair			480	
Total			588	

Table 3. Distribution of beam time among particles accelerated.

Particle	(hr)	(%)	Particle	(hr)	(%)
P	878	16.7	$^{13}C^{4+}$	142	2.7
d	263	5.0	$^{14}N^{4+}$	312	5.9
$^{3}He^{1+}$	230	4.4	$^{14}N^{5+}$	358	6.8
$^{4}He^{2+}$	1,067	20.3	$^{15}N^{4+}$ [a]	120	2.3
Be^{3+}	166	3.2	O^{5+}	960	18.2
$^{12}C^{4+}$	301	5.7	Ne^{6+}	460	8.8
			Total	5257	100

[a] Newly accelerated ion.

commutators. It took three months to repair and overhaul the motor generator. During the three months, a small 250 kW motor generator, which had been used for the 1/3 model magnet, was used temporarily. The maximum energy for heavy ions accelerated was limited owing to the small power of the motor generator.

Table 2 shows the beam time allotment to various research activities in the period XIX. The total scheduled beam time decreased by about 300 hr, as compared with that of the last year. Requirement for heavy ion beams decreased by about 1,000 hr and for light ion beams increased by about 1,000 hr. The use of light ions increased for the studies of nuclear reaction and radiation damage. The 89 hr in the scheduled beam time were alloted to the new study of radiochemical analysis of semiconductor materials by outside users.

Table 3 shows the distribution of the scheduled beam time among particles accelerated. The beam times for proton, deuteron, and alpha increased in contrast to the decrease for heavy ions. $^{15}N^{4+}$ ion was newly accelerated and utilized for performing several experiments such as nuclear reaction. The ion source with sputtering electrode[3] was used to extract high intensity beams of Be^{3+} ions.

References

1) H. Takebe, S. Fujita, and K. Ogiwara: *RIKEN Accel. Progr. Rep.*, **17**, 186 (1983).
2) K. Ikegami, T. Noda, N. Kamiyama, and I. Kohno: Proc. 8th Symp. ISIAT 84, Tokyo, p. 115 (1984).
3) K. Ikegami, T. Kageyama, and I. Kohno: *Jpn. J. Appl. Phys.*, **19**, 1745 (1980).

RIKEN Accel. Progr. Rep. **18** (1984)

II-2. RILAC Operation

Y. Miyazawa, M. Hemmi, T. Inoue, T. Kambara, M. Yanokura, M. Kase, T. Kubo, E. Ikezawa, K. Kihara,* Y. Chiba, and M. Odera

The RIKEN heavy-ion linear accelerator, RILAC, has been in steady operation in this period and various kinds of ion beams were supplied to various targets. Table 1 gives statistics of operation in the period September 1, 1983–August 31, 1984. A beam time shows a decrease of 3.5% compared with that of the previous period, because of machine trouble and shut down for power saving. In this period, the scheduled beam time for 6 days was cancelled by trouble in a motor-generator supplying AC power of 50 kVA to the 500 kV high voltage terminal of the injector. Figure 1 shows statistics of ions used in this period. Most of users preferred to Ar^{4+} ion, and a half of the total beam time was used for this ions. Accelerations of Al, Cu, and He ions were also requested frequently and percentages of their beam times to the total were about 10% for metal ions and 15% for He ion.

Table 1. Statistics of operation in the period of Sep. 1, 1983–Aug. 31, 1984.

	Days	%
Beam time	155	42.3
Frequency change	14	3.8
Overhaul and improvement work	55	15.0
Periodical inspection and repair	27	7.4
Machine trouble	6	1.7
Scheduled shut down	109	29.8
Total	366	100

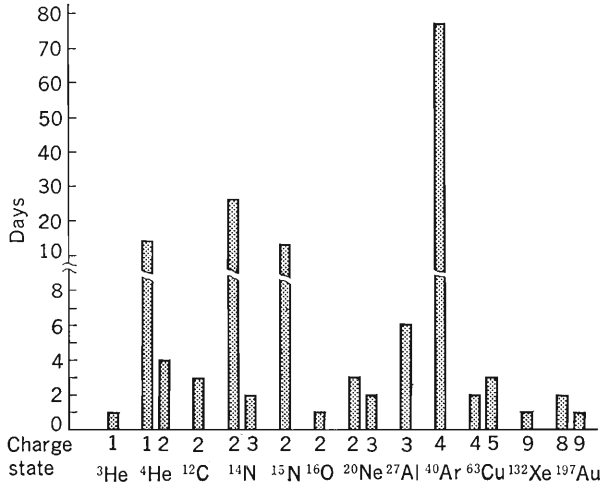

Fig. 1. Statistics of ions used in the period of Sep. 1, 1983–Aug. 31, 1984.

In the spring of 1984, a temporary improvement[1] was made to the driving circuits of the main power amplifiers to get stable operation and to apply higher voltage to accelerating gaps in the resonators in a frequency range of 17 to 40 MHz. By this improvement, the operation of the linac became simpler and easier than before in changing frequency. The use of an automatic frequency setting device,[2] though it is still limited, allows setting of many parameters of the resonators and oscillators feasible. Figure 2 shows the relations among energy per nucleon, frequency, and effective acceleration voltage. The ions having the mass to charge ratios M/q=2–10, such as He^{2+}, N^{3+}, Ne^{3+}, Ne^{4+}, and Al^{3+}, were increased in its maximum energy by the improvement and supplied to the users in the improved

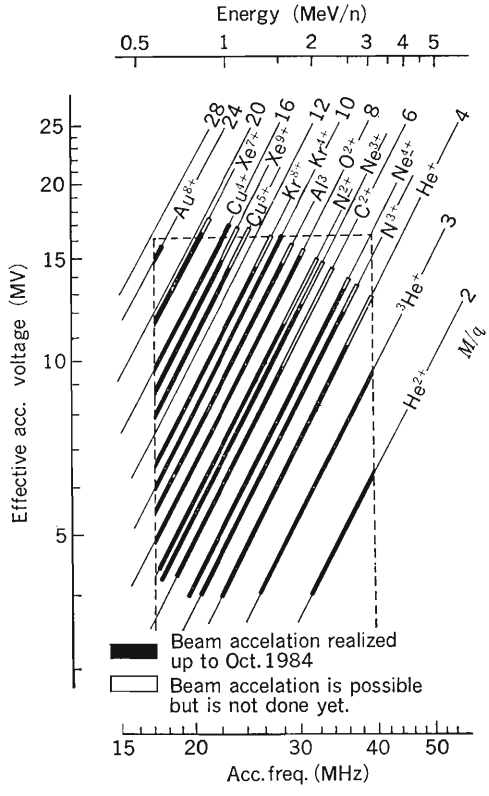

Fig. 2. Relations among energy per nucleon, frequency, and effective acceleration voltage. The number on each line is M/q, the ratio of the mass of ion to the degree of its ionization.

* Sumijyu Examination and Inspection Corporation.

condition. When an Ar^{4+} ion beam is accelerated at frequencies above 28 MHz, the injector voltage and accelerating voltage of each resonator are limited by the maximum ratings of their power supplies. Therefore, in this case it is necessary to use an Ar^{5+} ion beam which has tendency to contain O^{2+} ions.

References

1) Y. Chiba: Private communication.
2) Y. Chiba: *IPCR Cyclotron Progr. Rep.*, **14**, 120 (1980).

RIKEN Accel. Progr. Rep. 18 (1984)

II-3. TANDETRON-Operation

H. Sakairi, T. Kobayashi, E. Yagi, and T. Urai

The machine was operated for 140 days of one year from November, 1983: 110 days for experiments and 30 days for tests. About 100 days were alloted to overhaul, repair, and installation.

Subjects of experimental studies were as follows:

(a) Depth profile of implanted ions
(b) Effect of implantation on surface composition
(c) Laser annealing effects on damage caused by implantation
(d) Lattice location of hydrogen atoms in metals
(e) Microanalysis of oxygen in semiconductors

These studies were performed by the following laboratories:

(1) Inorganic Chemistry Lab. (for (a) and (b))
(2) Deformation Processing Lab. (for (a) and (b))
(3) Friction and Lubrication Lab. (for (a) and (b))
(4) Semiconductors Lab. (for (c))
(5) Metal Physics Lab. (for (d))
(6) Nuclear Chemistry Lab. (for (e))
(7) Cyclotron Lab. (for tests)
(8) Beam Analysis Center (for (a), (b), and (d))

Ions accelerated for these studies were $^4He^{2+}$, $^3He^{2+}$, and B^{2+}. At the exit from the ion source, current intensities of $^4He^-$, $^3He^-$, and BO^- were 1.3 μA, 0.6 μA, and 8μA, respectively. At the exit from the accelerator, current intensities of $^4He^{2+}$, $^3He^{2+}$, and B^{2+} were about a third or a quarter of the above values at the exit from the ion source. The highest acceleration energy was 2.7 MeV for $^4He^{2+}$, and $^3He^{2+}$ ions and 2.1 MeV for B^{2+} ions.

Construction of an additional beam transporting system with an ion optical prism for an electron microscope for the *in situ* observation of damage processes in irradiated materials was almost completed and a test operation is going to start. Other several improvements were carried out satisfactorily in vacuum systems and electronics linking the measuring system with the control system of the accelerator.

Main troubles occurred in the ion sources as in the last period. Deterioration of a lithium boiler of the charge exchanger, coupled to a duoplasmatron, shortened the interval of lithium supply to one third of the normal period. The present boiler has been used for three and a half years. A new boiler is in preparation at the workshop. A cesium gun in the sputtering ion source also broke down because of corrosion and was exchanged with new one. It is the second breakdown and the lifetime of the gun is ascertained to be two years.

RIKEN Accel. Progr. Rep. 18 (1984)

II-4. Implanter Operation

M. Iwaki

The RIKEN 200 kV Low- and High-Current Implanters were described in detail in previous reports.[1),2)] These machines have been utilized in surface-layer modification of materials such as metals, insulators, polymers, and semiconductors. Main subjects under practice are as follows:

(1) Compositions, chemical bonding state, and structure of ion-implanted iron and steel plates
(2) Mechanical and electrochemical properties of ion-implanted iron and steel plates
(3) Compositions, chemical bonding state, and structure of ion-implanted diamonds and glassy carbons
(4) Electrical and electrochemical properties of ion-implanted diamonds and glassy carbons
(5) Compositions, structure, and electrical properties of ion-implanted Kapton and polyacetylene sheets
(6) Preparation of standard samples for secondary-ion mass spectroscopy (SIMS)
(7) Improvement of durability of tools by nitrogen implantation

In order to perform surface-layer modification of tools of various shapes by nitrogen implantation, the third implanter was set up. This implanter, called Z-100, was designed and constructed by Zymet Inc., U.S.A., as shown in Fig. 1. Its implantation system specification and implant characteristics are as follows:

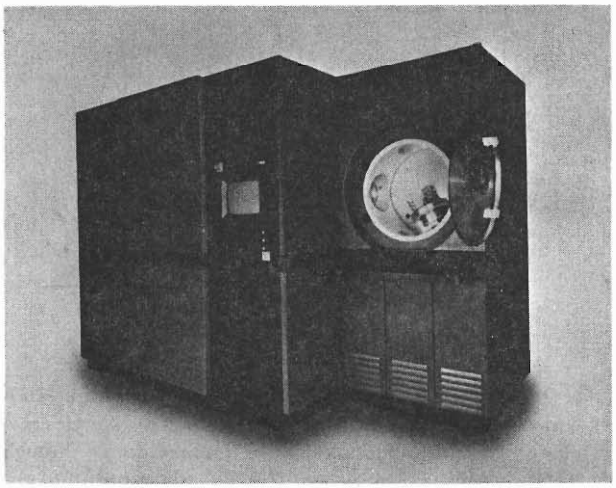

Fig. 1. Implanter Z-100 constructed by Zymet Inc., U.S.A.

(1) Beam energy: 50–100 keV
(2) Ion species: N^+ (~40%)+N_2^+(~60%). In addition to implanting with nitrogen, the machine can also be used to implant all elemental materials which exist in gaseous form simply by attaching an appropriate gas bottle and an evaporation oven: O, Cl, As, Cd, Sb, *etc.*
(3) Ion current: about 5 mA
(4) Ion beam shape: Approx. 3 cm wide×20 cm high at a processing position at maximum voltage
(5) Typical dose: 2×10^{17} ions/cm^2
(6) Implant area: 250 cm^2 (circular)
(7) Ion density: 125 μA/cm^2 (electrical) within a beam spot and 12.5 μA/cm^2 (electrical) average over an implant area
(8) Implant time: <30 min/batch for single surface objects and <90 min/batch for multiple surface objects using disk rotation
(9) Throughput: >1 batch/hr for single surface objects
(10) Implant uniformity: Better than ±10% over 250 cm^2
(11) Implant angle: Variable between 0° and ±90°
(12) Product cooling: Materials to be implanted may be embedded in a water-cooled tray filled with a eutectic alloy or fastened on a water-cooled holder in order to keep the temperature of the treated area from exceeding 200°C
(13) Control system: Microprocessor based system to communicate with stations of subassemblies via a serial optical loop
(14) Vacuum system: Two sets of a 6 inch oil diffusion pump backed with a mechanical rotary pump

The machine has been used for nitrogen implantation in various tools such as injection moulds, PCB drills, and scissors for a barber, and many materials modified by nitrogen implantation are under a practical test in industry and in our institute.

References

1) M. Iwaki: *RIKEN Accel. Progr. Rep.*, **15**, 7 (1981).
2) M. Iwaki: *ibid.*, **17**, 7 (1983).

RIKEN Accel. Progr. Rep. 18 (1984)

III. RESEARCH ACTIVITIES

1. Nuclear Physics

1. ^{27}Al(d, ^{2}He)^{27}Mg Reaction

S. Kohmoto, M. Ishihara, and T. Kubo

[NUCLEAR REACTION ^{27}Al(d, ^{2}He)^{27}Mg and ^{27}Al(d, pp)^{27}Mg, E=24 MeV; measured energy spectra. Spin-flip and/or spin-non-flip reaction mechanism.]

The system of two protons has no bound state; however, simultaneous detection of two protons under small-relative-energy conditions makes it possible to restrict the quantum state of the system to L=0, S=0 and T=1. We call this system ^{2}He. If the relative energy is not small enough, the restriction L=0 is not guaranteed and S=1 component may be involved. Also protons from evaporation process may be observed in such geometry. We designate this system pp.

When compared with other charge-exchange reactions producing neutron-excess nuclei such as (n, p) and (d, pp), the (d, ^{2}He) reaction is characterized by spin-flip (ΔS=1) transition.

On the other hand, (n, p) and (d, pp) reactions may contain both spin-flip and spin-non-flip (ΔS=0) transitions. Because of this peculiarity, we proceeded with a trial study of the (d, ^{2}He) reaction.

Figure 1 shows a schematic diagram of the ^{2}He detection system. Two identical sets of ΔE-E counter telescopes consisting of a 50 μm and a 2,000 μm thick Si detectors were collimated by using 7 mm × 7 mm slits which were separated vertically by 9 mm. At 11 cm away from the target, this system covers an angular interval of θ_{12}=5°–13°. Thin Al foil was used

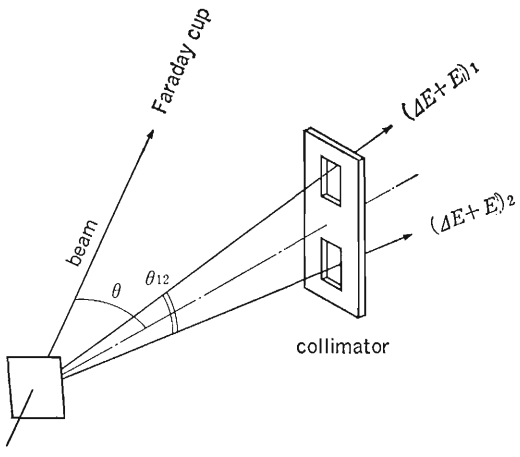

Fig. 1. Schematic diagram of the ^{2}He detection system.

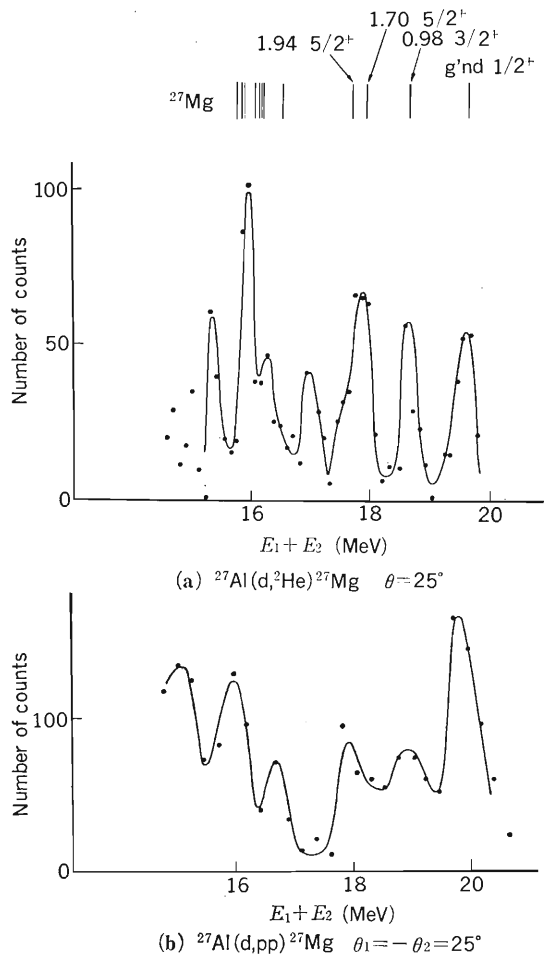

Fig. 2. (a) Energy spectrum of the reaction ^{27}Al(d, ^{2}He)-^{27}Mg at θ=25°, where E_1+E_2 is the sum of the kinetic energies of the two protons. The solid lines are drawn through the data points to guide eye. (b) Energy spectrum of the reaction ^{27}Al(d, pp)^{27}Mg at $\theta_1=-\theta_2$=25°, *i.e.* θ_{12}=50° and θ=0°.

as target. A 24 MeV deuteron beam was furnished by the cyclotron.

Figure 2 displays our preliminary results; Fig. 2(a) is an energy spectrum of the reaction ^{27}Al(d, ^{2}He)^{27}Mg at $\theta=25°$.

The $1/2^+$ ground state, 0.98 MeV $3/2^+$ state, (1.52 MeV $5/2^+$ state+1.70 MeV $5/2^+$ state) and another at about $E_x=3.6$ MeV of ^{27}Mg are relatively well populated. For comparison, we measured a spectrum of the ^{27}Al(d, pp)^{27}Mg reaction at $\theta_1=25°$ and $\theta_2=-25°$, which is shown in Fig. 2(b). Among the low-lying states of the residual nucleus, only the ground state is strongly populated in this reaction. Though it is not possible to compare these spectra rigorously because of the different direction of the recoil nucleus, it is obvious, however, that two reactions proceed in a rather different way. Compound reaction component may not be ignored in the latter reaction. We are preparing measurement of angular distribution of the reaction ^{27}Al(d, ^{2}He)-^{27}Mg to see if the spin-flip (or spin-non-flip) process is the main one to be considered.

RIKEN Accel. Progr. Rep. 18 (1984)

III-1-2. Investigation of Coulomb Excitation for Projectile-Polarization Determination

H. Ohsumi, M. Ishihara, S. Kohmoto, K. Sugimoto,*
T. Tanabe,* and H. Hamagaki*

[NUCLEAR REACTIONS ^{27}Al(^{27}Al, ^{27}Al')^{27}Al*, E=35.5 MeV: measured left-right asymmetry, ^{27}Al-γ coincidence.]

We have been studying nuclear spin polarization (P) of heavy ions produced by means of the tilted foil method.[1] Here we report investigation of a new method[2] for determination of P, which utilizes the left-right asymmetry in the Coulomb excitation. In the Coulomb excitation process, especially in the forward-angle scattering and in the excitation with an adiabaticity parameter $\xi>0.1$, the angular momentum in the direction of $\vec{k}_f\times\vec{k}_i$ is favorably transferred, enhancing the excitation of, for example, $\Delta M=-2$ for a E2 transition (see Fig. 1),[3] where $\vec{k}_f$ and $\vec{k}_i$ are the wave vectors of scattered and incident ions, respectively. In the case of a polarized projectile, the angular distribution is affected by the vector coupling between the polarized projectile-spin and the transferred angular momentum, giving rise to a left-right asymmetry proportional to P. The analyzing power is usually large, and even close to unity when the excitation occurs between states with stretched spin sequences such as $1/2^+\rightarrow 5/2^+$, $5/2^+\rightarrow 1/2^+$. The method is supposed to be particularly useful for ions with relatively high energies, where the cross section for the Coulomb excitation becomes large, while the conventional method using circular polarization of visible light in the decay of excited ions is less efficient because of the reduced cross section for such an atomic excitation process.

In order to study the feasibility of the technique, a preliminary measurement of the Coulomb excitation of ^{27}Al projectile was made using 35.5 MeV ($\sim$1.3 MeV/A) unpolarized beam from RIKEN heavy-ion linear accelerator (RILAC). The ^{27}Al nucleus was chosen, since it can give rise to a stretched-type excitation from the $5/2^+$ g.s. to the $1/2^+$ state (E_X=0.84 MeV), which affords a large analyzing power. The experimental setup is shown in Fig. 2. An ^{27}Al foil target of 200 μg/cm^2 in thickness was used temporarily. Scattered particles were detected by two Si solid-state detectors placed at $\pm 60°$ symmetrically with respect to the beam direction. The detectors of 400 mm^2 were used, subtending a solid angle of 0.15 sr. This angle was chosen by optimizing the balance between a larger cross section for the Coulomb excitation and a larger ratio of the Coulomb excitation to the Rutherford scattering. The latter factor is important for the efficiency of the method since the counting rate is limited primarily by the number of elastic events. The detected particles were registered in coincidence with gamma rays emitted from Coulomb-excited levels. This affords separation of Coulomb excitation events from intense elastic

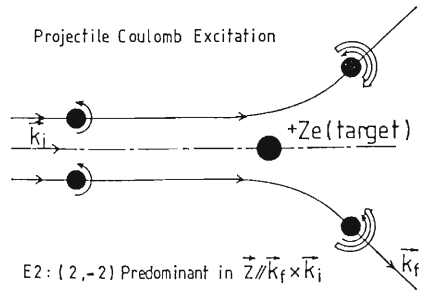

Fig. 1. Schematic figure of an angular momentum transfer in the E2 Coulomb excitation. The angular momentum in the direction of $\vec{k}_f\times\vec{k}_i$ is transferred by the predominant component with the magnetic substate $M=-2$.

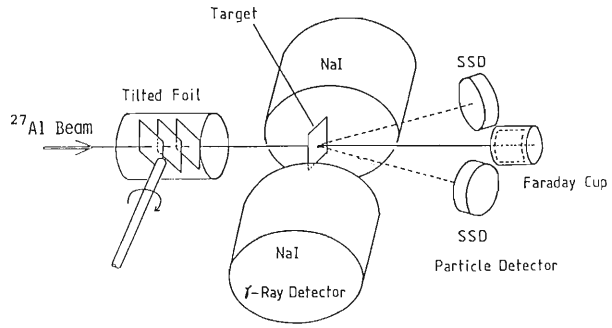

Fig. 2. Schematic figure of the nuclear polarization measurement system installed at C course in RILAC.

* Institute for Nuclear Study, University of Tokyo.

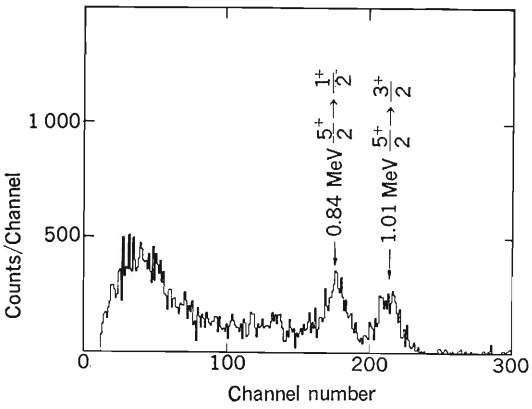

Fig. 3. Gamma-ray spectrum measured in coincidence with scattered ^{27}Al particles. Gamma-rays are emitted from the Coulomb excited-levels.

events and, furthermore, identification of the channel of the Coulomb excitation. The gamma rays were detected with two $3''\phi \times 3''$ NaI detectors placed normal to the reaction plane. Each of them covered a solid angle of 2.2 sr.

Figure 3 shows a gamma-ray spectrum obtained in the coincidence measurement. Two peaks corresponding to the excitations of g.s. $\rightarrow 1/2^+$ (E_X=0.84 MeV) and g.s. $\rightarrow 3/2^+$ (E_X=1.01 MeV) are well separated. A coincidence rate of $\sim$0.3 cps for the g.s. $\rightarrow 5/2^+$ transition was found to be accessible under the present experimental conditions. These results well assure the feasibility of the method to be used for determination of the projectile polarization. Such a measurement could be soon made with the setup as shown in Fig. 2 by placing a tilted-foil in the entrance section of the scattering chamber.

References

1) S. Kohmoto, M. Ishihara, T. Nomura, and Y. Gono: *RIKEN Accel. Progr. Rep.*, **17**, 48 (1983).
2) K. Sugimoto, T. Tanabe, T. Hattori, K. Haga, N. Shikazono, and J. Ichimura: *INS Ann. Rep.*, **1983**, 36.
3) K. Alder and A. Winter: *Rev. Mod. Phys.*, **28**, 432 (1956).

RIKEN Accel. Progr. Rep. 18 (1984)

III-1-3. Strongly Damped Components in the Reaction of $^{16}O+^{54}Fe$ System

K. Sueki, I. Kohno, M. Magara,* Y. Hamajima,**
Y. Hatsukawa,* and H. Nakahara

[NUCLEAR REACTIONS $^{16}O+^{54}Fe$, total reaction cross sections, evaporation-residue cross sections, strongly damped components.]

The strongly damped components in the $^{16}O+^{54}Fe$ reaction, especially, for symmetric mass split products were analyzed on the basis of a diffusion model[1] as well as a rotating liquid drop model[2] for fission. We performed a Goshal-type experiment that has the same compound nucleus with similar excitation energy. We chose the $^{16}O+^{54}Fe$ reaction that has the same compound nucleus as the $^{20}Ne+^{50}Cr$ reaction reported previously.[3]

The systems studied, the conditions for compound-nucleus formation, and its decay by fission are summarized in Table 1.

The experiments were performed using the cyclotron. An enriched self-supporting ^{54}Fe target of 600 $\mu g/cm^2$ in thickness was bombarded with 128 MeV $^{16}O^{5+}$ ions. The reaction products were detected with a ΔE-E counter telescope consisting of a gas proportional ΔE and a 300 μm thickness solid-state E detector.[4] The products with atomic numbers from 5 to 20 could be identified, and the energy spectra and angular and charge distributions of each product were obtained.

The angular distributions of elastic scattering and evaporation residue products in the $^{16}O+^{54}Fe$ reaction at 95 to 128 MeV were measured by a time-of-flight method using cyclotron beam bunching. A start pulse and particle energies were obtained by a silicon surface barrier detector, and the RF trigger pulse was used as a stop pulse. Elastic scattering and evaporation residues were measured to obtain the total reaction cross sections σ_R and the evaporation residue cross sections σ_{ER}, respectively. The results shown in Fig. 1 were also used to determine the grazing angular momentum l_{gr} and the critical angular momentum l_{crit}. In $^{16}O+^{54}Fe$ at 103.5 and 128 MeV, l_{gr} was 50 $\hbar$ and 63 $\hbar$, respectively, and l_{crit} was 41 $\hbar$ and 43 $\hbar$, respectively.

The energy distributions of products with $Z \geq 10$ showed single bell-shaped kinetic energy peaks in the region of the strongly damped components.

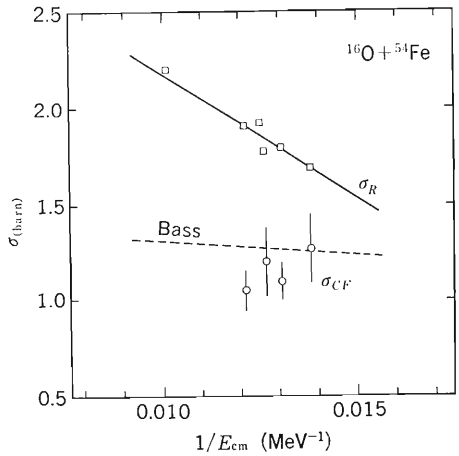

Fig. 1. Measured evaporation residue (fusion) cross sections and total reaction cross sections as a function of $1/E_{cm}$ for $^{16}O+^{54}Fe$. The dashed line represents the values predicted by Bass.[5]

Table 1. Summary of the conditions for compound nucleus formation and its decay by fission.

Reaction	Compound nucleus	Fissility (Z^2/A)	E_{lab} (MeV)	E^*_{CN} (MeV)	$l_{max}(\hbar)$	$l_{crit}(\hbar)$	B_f at l_{crit}
$^{16}O+^{54}Fe$	^{70}Se	16.5	128.	100.	63±2	43±3	12.0
$^{20}Ne+^{50}Cr$			140.	105.	63±2	49±1	5.0

* Faculty of Science, Tokyo Metropolitan University.
** Faculty of Science, Kanazawa University.

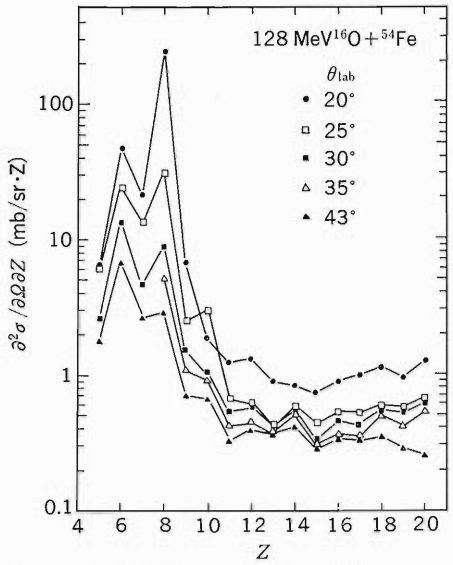

Fig. 2. Charge distributions at various laboratory angles in 128 MeV ^{16}O+^{54}Fe.

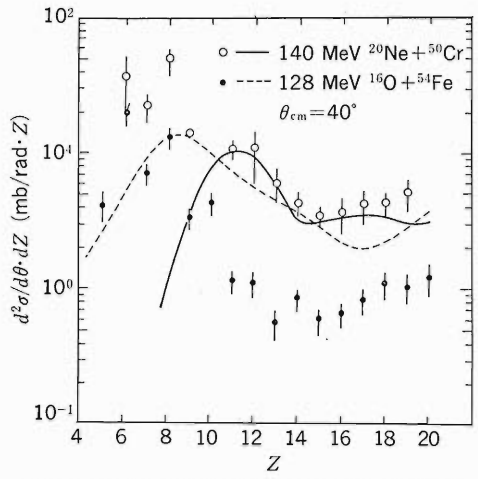

Fig. 3. Charge distributions in two different reaction systems: 140 MeV ^{20}Ne+^{50}Cr and 128 MeV ^{16}O+^{54}Fe. The solid line shows the distributions calculated by the diffusion model[1] in 140 MeV ^{20}Ne+^{50}Cr and the dashed line in 128 MeV ^{16}O+^{54}Fe. The calculations are normalized to the data for Z=13 observed in 140 MeV ^{20}Ne+^{50}Cr.

The angular distributions $d\sigma/d\theta$ for the products with $Z \geqq 13$ showed almost constant in the center-of-mass system. Thus, these products ($Z \geqq 13$) are considered to be either fusion-fission fragments or reaction products emitted after interaction time longer than the time required for one rotation of the composited system. The charge distributions for various angles are shown in Fig. 2. The charge distribution at θ_{cm}=40° is compared with that of the 140 MeV ^{20}Ne+^{50}Cr reaction as shown in Fig. 3. The difference in yields of symmetric fragments ($Z \geqq 13$) is probably explained by the effect of the different critical angular momenta.

We continue similar experiments on 103.5 MeV ^{16}O+^{54}Fe and 120 Mev ^{12}C+^{58}Ni, and analysis of the experimental results are in progress.

References

1) W. Norenbrg: *J. Phys.* C**5**, **37**, 141 (1976).
2) S. Cohen, F. Plasil, and W. J. Sweitecki: *Ann. Phys.* (*N. Y.*), **84**, 557 (1974).
3) Y. Nagame, H. Nakahara, K. Sueki, H. Kudo, I. Kohno, and M. Yanokura: *Z. Phys.*, *A*, **317**, 31 (1984).
4) M. Yanokura, I. Kohno, and H. Nakahara: *Oyo Butsuri*, **49**, 1095 (1980).
5) R. Bass: *Nucl. Phys. A*, **231**, 45 (1974).

RIKEN Accel. Progr. Rep. 18 (1984)

III-1-4. Extended TDHF Calculation of the Variance of Mass Distribution in the $^{16}O+^{40}Ca$ Reaction at $E_{Lab}=157.3$ MeV

S. Yamaji and M. Tohyama

[Extended time-dependent Hartree-Fock theory, Mass distribution, Deep inelastic collision.]

The mass distributions in the $^{16}O+^{40}Ca$ collision at $E_{Lab}=157.3$ MeV were studied in the time-dependent coupled-cluster approximation (TDCCA), which is one of the extended time-dependent Hartree-Fock (TDHF) theories taking the effect of two particle-two hole excitations into account.

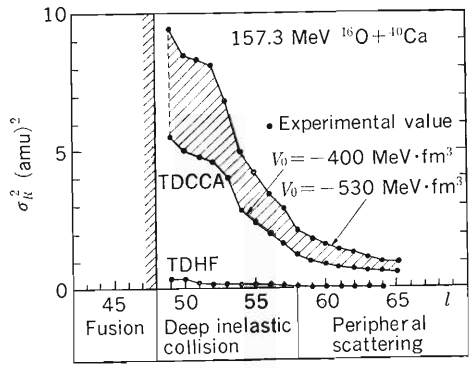

Fig. 1. The variance of mass distributions vs. initial angular momentum l in the $^{16}O+^{40}Ca$ reaction at $E_{Lab}=157.3$ MeV. The shaded area between $V_0=-400$ and -530 MeV·fm^3 shows TDCCA results. V_0 is the strength of the residual interaction of δ-function type. One observed value extracted from the experimental mass distribution[3] is shown by a dot at $l=56\ \hbar$.

We have studied the variance of mass distribution in slab collisions in our previous work.[1] In the present note, we briefly report the results of the realistic three-dimensional calculations, the details of which are given elsewhere.[2]

Figure 1 shows the variances σ_R^2 of mass distribution calculated in TDCCA and TDHF as a function of the initial angular momentum l. It can be seen that the variances σ_R^2 in TDCCA are enhanced by a factor 10~30, as compared to σ_R^2 in TDHF.

Thus, the obtained TDCCA results reproduce the order of magnitude of the large experimental variance of mass distribution, which has not been predicted successfully by the standard TDHF theory.

References

1) M. Tohyama and S. Yamaji: *Phys. Lett. B*, **123**, 16 (1983).
2) S. Yamaji and M. Tohyama: *ibid.*, **147**, 399 (1984).
3) H. Ikezoe, D.G. Kovar, G. Rosner, G. Stephans, E. Ungricht, B. Wilkins, C. Maguire, Z. Kui, W. C. Ma, S. Robinson, D. Watson, G. Word, T. C. Awes, and G. Young: private communication.

RIKEN Accel. Progr. Rep. **18** (1984)

III-1-5. Low Angular-Momentum Cutoff in Heavy-Ion Fusion Reactions

T. Nomura, S. Kohmoto, K. Sueki, K. Morita, T. Kubo,
H. Kudo, M. Adachi,* and H. Kawakami**

NUCLEAR REACTION ^{16}O (^{15}N, xnypz$\alpha\gamma$), E=45–80 MeV; ^{19}F (^{12}C, xnypz$\alpha\gamma$), E=42–80 MeV; ^{27}Al (α, xnypz$\alpha\gamma$), E=25–58 MeV; ^{16}O (^{16}O, xnypz$\alpha\gamma$), E=55–95 MeV; ^{28}Si (α, xnypz$\alpha\gamma$), E=25–58 MeV; enriched ^{28}Si target; measured Eγ, Iγ; deduced excitation functions of some evaporation residues. Evaporation calculation; low-l cutoff in fusion.

High-spin states in a highly excited light nucleus decay preferentially by evaporation of α particles, while low-spin states deexcite mainly by emission of nucleons. Consequently, evaporation residues produced only by nucleon emission in the deexcitation process of a compound nucleus formed in a fusion reaction originate from lowest-spin states of the compound nucleus. Cross sections of such residual nuclei are therefore extremely sensitive to the possible existence of low angular-momentum cutoff in heavy-ion fusion reactions predicted by the time-dependent Hartree-Fock (TDHF) calculations. Figure 1 shows examples of such effects observed in the calculated excitation functions of the ^{16}O(^{16}O, 3p)^{29}Al and ^{16}O(^{15}N, 2pn)^{28}Al reactions. The calculation was performed by the evaporation code GROGI II using the level density parameter $a=A/7.5$+shell correction and similar variable moment of inertia as described in Ref. 1. The shell correction similar to Gilbert and Cameron[2] has been used. It has also been assumed that the low-l cutoff starts to appear at 44 MeV in terms of the excitation energy (E_{CN}) of the compound nucleus for the ^{16}O+^{16}O reaction and at 47 MeV for the ^{16}O+^{15}N reaction as predicted theoretically.[3] A value of lower critical angular momentum ($l_<$) is estimated by

$$l_< = \left\{\frac{2\mu R^2}{\hbar^2}(E_{CN}-E^0_{CN})\right\}^{1/2} \qquad (1)$$

where μ is the reduced mass of the system, R the distance of the two nuclei at the point of contact (R=1.2 ($A_1^{1/3}+A_2^{1/3}$) fm), and E^0_{CN} the critical excitation energy. The sudden decrease in yield indicated by dotted curves in Fig. 1 can be considered as a sensitive signature to probe the possible effect of the low-l cutoff in fusion reactions.

In order to search for the above effect we have measured excitation functions of some evaporation residues by using γ-ray spectroscopy in the reactions of ^{15}N+^{16}O, ^{12}C+^{19}F and α+^{27}Al as well as in the reactions of ^{16}O+^{16}O and α+^{28}Si. The measurement was carried out in the same way as described in Ref. 4. The targets used are LiF, WO_3, $^{28}SiO_2$ (enriched to 99.84%), and metallic Al. Critical energies estimated theoretically are listed

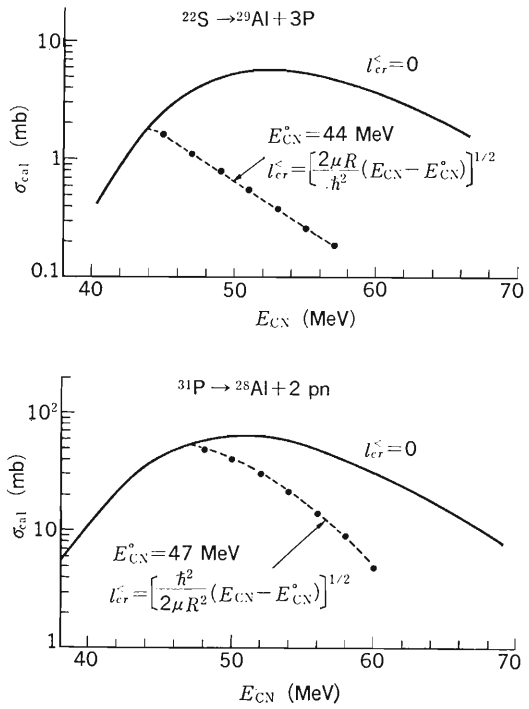

Fig. 1. Excitation functions calculated without low-cutoff (solid curves) and with low-l cutoff (dotted curves) for the ^{32}S → ^{29}Al+3p and ^{31}P → ^{28}Al+2pn channels.

* Department of Applied Physics, Tokyo Institute of Technology.
** Institute for Nuclear Study, University of Tokyo.

Table 1. Critical energies predicted by the TDHF calculations or classical estimate by Wong.[3]

Projectile and target	Q_{CN}[a] (MeV)	E_0 (MeV)[b] TDHF	E_0 (MeV)[b] Eqn. (1)	E^0_{CN}[c] (MeV)
$^{15}N+^{16}O$	19.81	—	27.1	46.9
$^{12}C+^{19}F$	22.95	—	33.2 (B=8 MeV)	56.2
			56.4 (B=12 MeV)	79.4
$\alpha+^{27}Al$	9.67	—	—	—
$^{16}O+^{16}O$	16.54	27	28.4	43.5
$\alpha+^{28}Si$	6.95	—	—	—

a) Q-value for the formation of the compound nucleus.
b) The critical energy for the low-l cutoff in the c.m.s.
c) The critical energy in terms of excitation energy of the compound nucleus.

in Table 1.

The measured thick target yields in the reactions of $^{15}N+^{16}O$ and $^{12}C+^{19}F$ are shown in Fig. 2. The data shown here are normalized on ^{29}Al, which is produced by 2p emission and shows almost a constant yield at high excitation energies. Then, the yields of ^{25}Mg and ^{22}Na produced via αpn and 2αn emission, respectively, are almost the same in both reactions. The yield of ^{23}Na corresponding to 2α emission in the ^{15}N-induced reactions is larger than that in the ^{12}C-induced reaction, suggesting that high spin states are more populated in the $^{15}N+^{16}O$ reaction. The yields of ^{28}Al and ^{27}Mg produced in both reactions respectively by 2pn and 3pn emission are nearly the same at low excitation energies, but show a significantly large difference at high excitation energies. It is important to note that this difference begins to appear around 50 MeV, which is close to E^0_{CN}=47 MeV predicted in the $^{15}N+^{16}O$ reaction.

The average product cross sections for ^{28}Al and ^{27}Mg estimated from the thick target yields are shown in Fig. 3 together with those in the $\alpha+^{27}Al$ reaction. The cross section for ^{28}Al obtained in the α-induced reaction is much larger than that in the HI-induced reaction, presumably due to the significant contribution from the direct reaction like (α, ^{3}He), and therefore cannot be used for comparison. The difference in the yields for ^{28}Al and ^{27}Mg between the two heavy-ion reactions may be ascribed to the existence of the low-l cutoff in the ^{15}N-induced reaction. In fact, the relative behaviour of the calculated excitation functions shown by solid curves agrees well with the data on $^{12}C+^{19}F$, although the absolute cross sections are somewhat larger than the experimental points (we have not yet tried to optimize model parameters in the statistical calculation). The experimental data of ^{28}Al in the $^{15}N+^{16}O$ reaction lie between the dashed curves A and B, which are obtained with the assumption that E^0_{CN}=50 MeV and that $l_<$ is equal to the value estimated from Eqn. (1) (A) or to 70% of that value (B). The data of ^{27}Mg in the ^{15}N-induced reaction agree nearly with the calculated values from the (^{15}N, ^{3}Hep) reaction. This seems

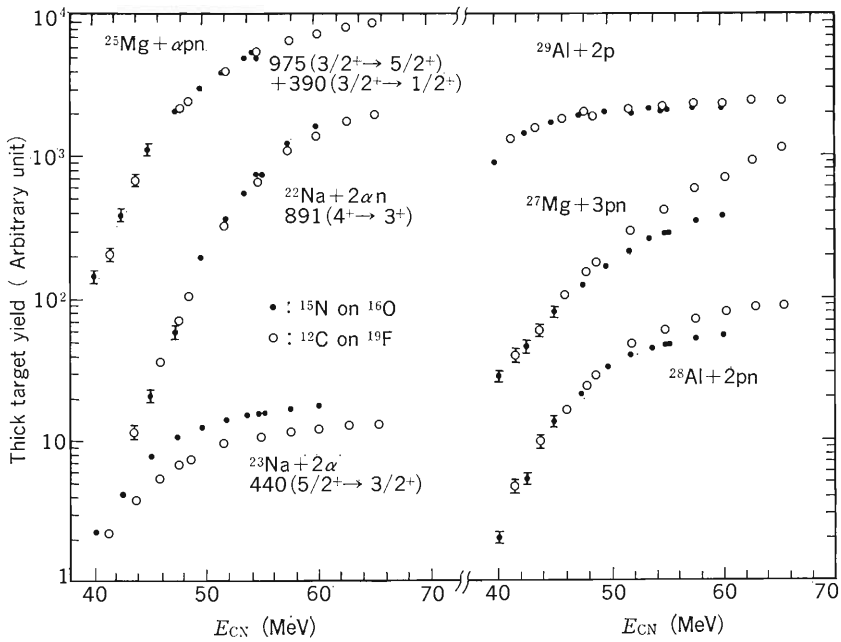

Fig. 2. Thick target yields of some evaporation residues in the $^{15}N+^{16}O$ (black circles) and $^{12}C+^{19}F$ (open circles) reactions given as a function of E_{CN}. The given values are the measured intensities of γ-rays indicated in the figure in units of keV for the nuclei shown in the left-hand side, while they are estimated from the decay of short-life activities for the nuclei given in the right-hand side.

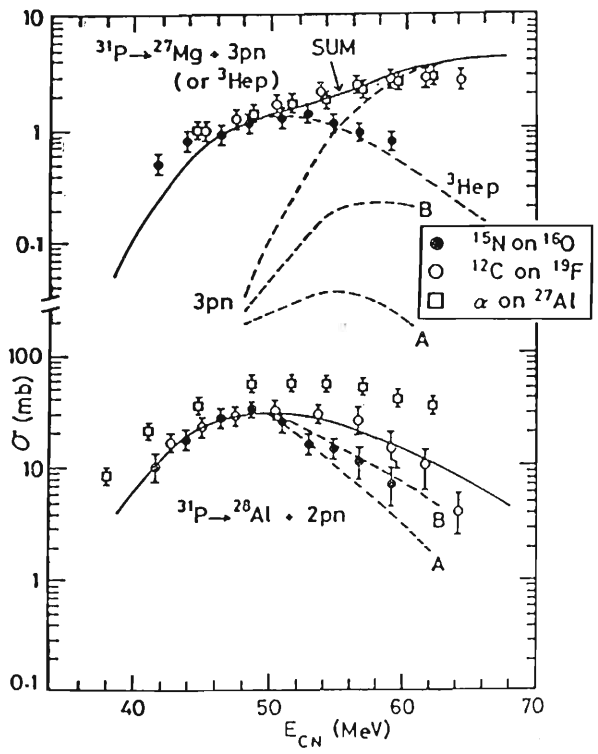

Fig. 3. The measured excitation functions of ^{28}Al and ^{27}Mg together with those calculated by the evaporation code GROGI II. Note that the calculated values are those divided by a factor of two in the case of ^{28}Al and by 1.4 in the case of ^{27}Mg. See the text for the meaning of A and B. Note also that the given experimental values are those multiplied by $\lambda^2(^{15}N)/\lambda^2(^{12}C)$ for the case of $^{12}C+^{19}F$ and by $\lambda^2(^{15}N)/\lambda^2(\alpha)$ for the case of $\alpha+^{27}Al$.

also consistent with the above assumption because the (^{15}N, 3pn) reaction is strongly reduced when the low-l cutoff exists as seen in the figure.

The excitation functions for ^{29}Al measured in the $^{16}O+^{16}O$ and $\alpha+^{28}Si$ reactions turned out to be nearly the same up to $E_{CN}=50$ MeV when the data in the α-induced reaction are multiplied by a factor of $\lambda^2(^{16}O)/\lambda^2(\alpha)$. That is, no signature of the low-l cutoff has been found at 43.5 MeV as predicted from the TDHF calculation (see Table 1). However, the experimental yield of the ^{16}O-(^{16}O, 3p)^{29}Al reaction begins to become considerably smaller than that of the $^{16}O(\alpha, 3p)^{29}Al$ reaction at higher excitation energies. This difference can be reproduced by the statistical model calculation if we assume that $E^0_{CN}=50$ MeV in the ^{16}O-induced reaction and that $l_<$ is equal to 70% of the value obtained from Eqn. (1). The comparison with the data on the $^{20}Ne+^{12}C$ reaction is highly desirable.

References

1) T. Nomura, J. Delaunay, C. Tosello, and N. Bendjaballah: *Nucl. Phys. A*, **305**, 262 (1978).
2) A. Gilbert and A. G. T. Cameron: *Can. J. Phys.*, **43**, 1446 (1965).
3) P. Bonche, S. E. Koonin, and J. W. Negele: *Phys. Rev. C*, **13**, 1226 (1976); J. W. Negele: *Rev. Mod. Phys.*, **54**, 913 (1982) and references therein; C.-Y. Wong: *Phys. Rev. C*, **25**, 1460 (1982).
4) T. Nomura, H. Kudo, S. Kohmoto, K. Sueki, and T. Kubo: *RIKEN Accel. Progr. Rep.*, **17**, 9 (1983).

RIKEN Accel. Progr. Rep. 18 (1984)

III-1-6. Backward Cross Section in the Generalized Exciton Model

K. Sato

[NUCLEAR REACTIONS generalized exciton model, finite size effects, backward cross section, ^{120}Sn (p, p′) at E_p=62 MeV.]

The generalized exciton model[1] has been extensively applied to give preequilibrium angular distributions with the help of useful mathematical reformulation[2),3)] which brings much easier handling of it. Although the model was able to reproduce global characteristics of the preequilibrium angular distributions at incident energies of tens of MeV, it underestimates the angular distribution at backward angles.[4)] Former approaches based on it used the Fermi gas model for target nucleons in evaluating the single nucleon-nucleon scattering kernel $G(\Omega, \Omega')$ between a fast nucleon and a target one which plays a crucial role in determining the angular distribution.[4)] We expect that "the treatment of finite size effects" in the evaluation of the scattering kernel is important to explain the angular distribution at backward angles.

In the present note, we briefly report a study of the preequilibrium angular distribution using the scattering kernel along this line in the framework of the generalized exciton model. We use the single nucleon-nucleon scattering kernel $G(\Omega, \Omega')$ describing the collision process between a fast nucleon N and bound target ones N_t moving in a harmonic oscillator potential. On the simplified assumptions that (1) two nucleons N and N_t interact with each other via the delta-type interaction and (2) the scattering can be treated in the plane-wave Born approximation, we could obtain the scattering kernel in a tractable form utilizing the analytic expressions of the cross section. As averaging over all final nucleon energies discards the important angle-energy correlation,[4)] we average over final nucleon energies only within a small interval of smearing width coming from the finite life of the exciton state (uncertainty principle) in which the collision occurs.

A doubly differential cross section for the emitted nucleon in the early stages of the reaction can be calculated if we put the eigenvalues μ_l (l=0, 1, 2, . . .) of the scattering kernel into a simple closed-form expression.[3)] Considering that our eigenvalues μ_l are dependent on the energy of the fast nucleon before and after collision in every single N-N_t scattering, we make the following replacement

$$\mu_l^{\frac{m+2-m_0}{2}} \rightarrow \mu_l(E_{\text{in}}, E_1)\times\mu_l(E_1, E_2)\times\cdots \times\mu_l(E_{\frac{m-m_0}{2}}, E_{\text{out}}) \qquad (1)$$

in the expansion coefficients ζ_l (m). In Eqn. (1) E_{in} and E_{out} are the incident and the outgoing energies respectively of the fast nucleon, and E_1, E_2, . . . are the mean intermediate energies of the fast nucleon after single collision, after double collision, *etc.* In a simple case that the emitted nucleon comes from the m-exciton state after having lost its initial energy equally in every step of the total $(m+2-m_0)/2$ times collisions, the energies E_i (i=1, 2, . . . $(m-m_0)/2$) take the form

$$E_i=E_{\text{in}}-i\times(E_{\text{in}}-E_{\text{out}})\times\frac{2}{m+2-m_0} \qquad (2)$$

We have analyzed the angular distribution for several (p, p′) reactions with incident energies of 62 MeV. In the calculation, we always put the initial exciton number m_0=3 and other parameters peculiar to the exciton model are the same as those in Ref. 5. The scattering kernel turned out to give the non-negligible backward contribution increasing with energy loss of the fast nucleon N in collision. In Fig. 1 we compare the calculated angular distributions with experimental data[6)] for the reaction ^{120}Sn(p, p′) at E_p=62 MeV for three different outgoing energies. As seen clearly from Fig. 1, agreement is very good except at small angles; especially, agreement in the backward angles is markedly improved. This result suggests the importance of the treatment of finite size effects in the generalized exciton model. The discrepancy at small angles, which is usually the case for every model, is discussed in Refs. 4 and 7. Our calculated results for other targets such as ^{54}Fe, ^{197}Au and ^{209}Bi show nearly similar fitting with the experimental data, although the overestimation of the calculated value becomes a little more than the case of ^{120}Sn target. We have also made calculation using the assumption that the fast nucleon loses its energy

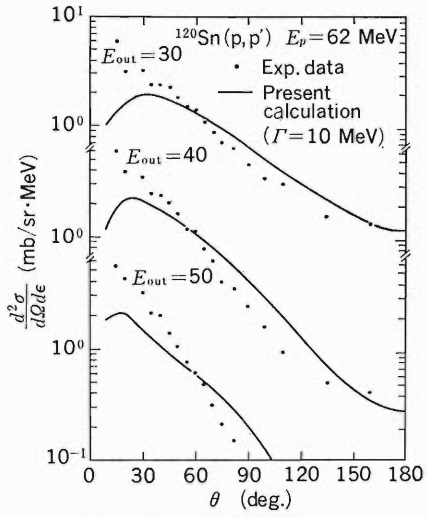

Fig. 1. Comparison of the calculated angular distributions with experimental data for the reaction ^{120}Sn (p, p') at E_p= 62 MeV for outgoing energies 30, 40 and 50 MeV. The solid curves show the calculated results based on Eqns. (1) and (2) with $\hbar\omega=41A^{-1/3}$ and the smearing width $\Gamma=10$ MeV.

randomly in every step of total $(m-m_0+2)/2$ times successive collisions instead of Eqn. (2). This turned out to bring forth only a slight changes of Fig. 1. The decomposition of the cross section at E_{out}=30 MeV into contributions from various exciton states demonstrates that at every angle there is large contribution from the m=3 exciton state (one-step process) in contrast with the rapid falling off of its contribution at backward angles in the results of the Fermi gas model. At backward angles both one- and two-step processes account for about 30% of the total cross section respectively and the remaining 40% comes from the processes of more than two-step ($m>5$). The multi-step direct reaction approach proposed by Tamura *et al.*,[7] which made quantum-mechanical treatment of the finite nucleus, is known to reproduce the preequilibrium angular distribution very well. In their calculation the contribution of the two-step cross section accounts for about 70% (30% one-step contribution) of the total one at backward angles for an ^{27}Al target or about 50% (50% one-step contribution) for ^{209}Bi at this outgoing energy. Comparing the present approach based on the generalized exciton model with those one, we see that the basic physical picture looks quite different. From this point of view, further investigation is necessary to decide which model is plausible.

In conclusion, the use of the scattering kernel including finite size effects greatly improves the backward cross section of preequilibrium nucleon emission induced by a proton of 62 MeV in the framework of the generalized exciton model. In the calculation one- and two-step processes dominate even at backward angles, but those of more than two-step give considerable contribution. Further study to refine the present model and to apply it to the light composite particle emission is desired.

References

1) G. Mantzouranis, D. Aggasi, and H. A. Weidenmüller: *Phys. Lett. B*, **57**, 220 (1975).
2) S. Yoshida: Proc. IPCR Symp. Macroscopic Feature of Heavy-Ion Collision and Preequilibrium Process, Hakone, p. 359 (1977).
3) J. M. Akkermans: *Phys. Lett. B*, **82**, 20 (1977).
4) A. Iwamoto and K. Harada: *Nucl. Phys. A*, **419**, 472 (1984) and references cited therein.
5) K. Sato, A. Iwamoto, and K. Harada: *Phys. Rev. C*, **28**, 1527 (1983).
6) F. E. Bertrand and R. W. Peele: *ibid.*, **8**, 1045 (1973).
7) T. Tamura, T. Udagawa, and H. Lenske: *ibid.*, **26**, 379 (1982).

RIKEN Accel. Progr. Rep. 18 (1984)

III-1-7. Classical Trajectory Picture of Massive Transfer

T. Inamura

[NUCLEAR REACTIONS massive transfer; average l value estimated.]

Massive transfer is a type of heavy-ion reaction in which a massive fragment of the projectile is transferred to the target nucleus, and an energetic light particle such as a proton or an α particle is emitted like a spectator in the forward direction. We first made a very crude approximation to estimate the average orbital angular momentum $<l_i>$ in the incident channel.[1] Here the reaction kinematics given by Siemens *et al.*[2] has been used to estimate $<l_i>$ for the massive-transfer reaction a+A → b+B, B=X+A.

For simplicity, it is assumed that inelastic excitation is negligible in both the incoming and outgoing channels. Since $m_A \gg m_X$ in the present case so that the relative velocities $V_{Bb} \approx V_{Aa}$, the orbital angular momentum of the spectator particle b is given by

$$l_b = \frac{\mu_{Bb}}{\mu_{Aa}} \cdot \frac{R_f}{R_i} \cdot l_i \qquad (1)$$

Similarly, the orbital angular momentum of the massive fragment X in the X+A system is given by

$$l_X = \frac{\mu_{AX}}{\mu_{Aa}} \cdot \frac{R_X}{R_i} \cdot l_i \qquad (2)$$

Here R_i and R_f are the distances between a and A; l_i is the orbital angular momentum in the incident channel. These angular-momentum relations have also been discussed by Ichimura.[3]

The value of l_X should be equal to the average angular momentum $<J_0>$ transferred to the compound system of X+A. The value of $<J_0>$ is experimentally estimated from the average γ multiplicity $<M>$ through the relation

$$<J_0> = <J_R> + \Delta J \qquad (3)$$

where $<J_R>$ is the average spin of the entry-state population and we employed the relation $<J_R> = 2[<M> - 4]$, which is commonly adopted for statistical treatment of γ deexcitation[4]; ΔJ is the average angular momentum carried away by neutrons in the present case. (Empirically, it is known that a single neutron evaporation carries away a unit angular momentum on the average.)

Table 1 summarizes information on angular momenta associated with massive-transfer reactions. Values of angular momenta except for L_{cr} and l_{cr} are experimental ones; the critical angular momenta for fusion, L_{cr} and l_{cr}, for the X+A and a+A systems were estimated using a sharp cutoff formula given by Lefort.[5]

The average orbital angular momentum in the incident channel $<l_i>$ was estimated in such a way that $<l_i> = <l_b> + <J_0>$, where $<J_0>$ was experimentally given by Eqn. (3), and $<l_b>$ was replaced by the classical optimum value given through Eqn. (1). To estimate $<l_b>$, it was assumed that $l_i = l_{cr}$, *i.e.*, $R_i = R_{cr}$, and that R_f is given by the strong absorption radius.[6]

It is interesting to note that the semi-experimental quantity $<l_i>$ has turned out to be equal to l_{cr}, indicating that the assumption $l_i = l_{cr}$ is reasonable in terms of Siemens' kinematics. In this classical model, the value of R_X, which is estimated from Eqn. (2) by substitution $l_X = <J_0>$, becomes somewhat smaller than the critical distance for fusion of X and A.

Table 1. Angular momenta associated with massive transfer: l_{cr} and L_{cr} are critical angular momenta for fusion of projectile and target nuclei, and of massive fragment and target nuclei, respectively; $<J_0>$, which is deduced from the average γ multiplicity $<M>$, the average angular momentum transferred to the compound system of massive fragment and target nuclei; $<l_i>$ the average orbital angular momentum of the incident channel leading to massive transfer. See text for details.

Reaction	E_{lab} (MeV)	$<E_\alpha>$ (MeV)	L_{cr} (ħ)	$<M>$	$<J_X>$ (ħ)	$<J_0<$ (ħ)	$<l_i>$ (ħ)	l_{cr} (ħ)
^{154}Sm(^{12}C, α4n)^{158}Dy	85	29	24	12.1	16.2	20	40	39
^{154}Sm(^{12}C, α4n)^{158}Dy	109	46	26	14.7	21.4	25	49	47
^{159}Tb(^{14}N, α3n)^{166}Yb	95	30	24	14.0[a]	20.0	23	42	42
^{159}Tb(^{14}N, α5n)^{164}Yb	115	30	32	14.9[a]	21.8	27	50	50
^{154}Sm(^{16}O, α6n)^{160}Er	153	45	42	19.8[a]	31.6	38	63	63

[a] See Ref. 1.

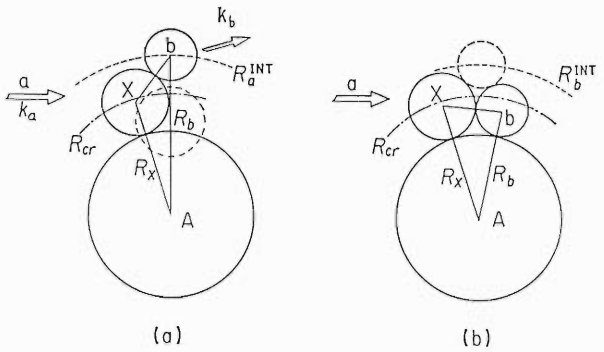

Fig. 1. (a) The instant of massive-transfer reaction a+A → b+(X+A): A is the target, b the spectator particle, and X the massive fragment. R_b is assumed to be equal to the strong absorption radius R_a^{int} of the a+A system. R_{cr} and R_X denote critical distances of the a+A and X+A systems, respectively, where the critical angular momenta are defined. The dotted circle indicates the most probable position for the massive fragment X to be transferred. (b) Preequilibrium emission of the light particle b: R_b^{int} is the strong absorption radius of the b+A system, and R_b the critical distance of the system.

The above argument enables us to visualize the collision process characteristic of massive transfer. Figure 1(a) shows the instant of collision leading to massive transfer, *i.e.*, the spectator particle b to be emitted at R_a^{int} and the massive fragment X to be transferred at R_X. The dotted circle indicates the most probable position for X to be transferred. This presentation may be compared to the statement on massive transfer that is based on the breakup-fusion model[7]: The breakup fusion takes place in the deep peripheral region, which is about 2 fm deeper than the usual peripheral region.

For comparison, in Fig. 1(b) is illustrated the preequilibrium light-particle emission process. A light particle b is at the critical distance for fusion of b and A; and the particle b could be anywhere within the strong absorption radius R_b^{int} as well. In such a case, the collision time should be longer than in the case (a), and the process should be much more energy-dissipative.

References

1) T. Inamura: Proc. Int. School-Seminar of Heavy Ion Physics, Alushta, USSR, Apr. 14–21, p. 298 (1983).
2) P. J. Siemens, J. P. Bondorf, D. H. E. Gross, and F. Dickmann: *Phys. Lett. B*, **36**, 24 (1971).
3) M. Ichimura: Proc. of the Tsukuba Symp. on Heavy Ion Nuclear Physics, Tsukuba, Japan, Mar. 19–21, p. 179 (1981).
4) D. L. Hillis, J. D. Garrett, O. Christensen, B. Fernandez, G. B. Hagemann, B. Herskind, B. B. Back, and F. Folkmann: *Nucl. Phys. A*, **325**, 216 (1979).
5) M. Lefort and C. Ngo: *Ann. Phys.*, **3**, 5 (1978).
6) J. R. Huizenga: Proc. of Symp. on Macroscopic Features of Heavy Ion Collisions, Argonne, ANL/PHY-76-2, p. 1 (1976).
7) T. Udagawa, D. Price, and T. Tamura: *Phys. Lett. B*, **118**, 45 (1982).

RIKEN Accel. Progr. Rep. 18 (1984)

III-1-8. High Spin States in ^{110}Sn

H. Harada, T. Murakami, H. Tachibanaki, K. Yoshida,
J. Kasagi, and T. Inamura

[NUCLEAR REACTIONS ^{98}Mo(^{16}O, 4n), E=76 MeV; measured E_γ, I_γ, $_{\gamma\gamma}(t)$, $\sigma(E_\gamma, \theta)$, DSAM; ^{110}Sn deduced levels.]

The nuclear structure of Sn isotopes has been extensively studied so far. The constancy of the excitation energies of 2^+ states are well explained by the generalized seniority scheme and other low-lying levels are interpreted as neutron two-quasi-particle states. The proton 2 particle-2 hole states are also found to form rotation-like deformed bands in ^{112,114,116,118}Sn.[1] For the isotopes with a mass number less than 110, however, information about high spin states is rather scarce.

We have started a systematic study of the nuclear structure of Sn isotopes with $A \leq 112$, using γ-ray spectroscopic technique with the neutron multiplicity filter.[2] Here we report a result on ^{110}Sn.

The experiment was performed using the ^{98}Mo(^{16}O, 4nγ)^{110}Sn reaction at $E(^{16}O)$=76 MeV. Gamma-ray angular distributions, γ-γ coincidences and Doppler shift attenuations were measured in coincidence with neutrons detected with the neutron multiplicity filter. Identification of γ-rays in ^{110}Sn was made mainly by comparison of the yield of coincidence with more than two neutrons (M_n>2) to that of coincidence with more than one neutron. A ratio of these yields is about 0.14 for 4n channels whereas it is about 0.10 for 3n channels. Figure 1 shows a spectrum which is obtained subtraction of the spectrum of M_n>1 multiplied by a factor of 0.098 from that of M_n>2. As can be seen in the figure, contributions of γ-rays in 3n channels (^{111}Sn and ^{110}In) are completely eliminated. In Fig. 1 also shown is a spectrum obtained in the γ-γ coincidence gated by $2^+ \rightarrow {}^+0$ (1,211 keV), $4^+ \rightarrow 2^+$ (985 keV) and $6^+ \rightarrow 4^+$ (281 keV) transitions in ^{110}Sn.

The 448 keV, 741 keV and 809 keV γ-rays are assigned to those from ^{110}Sn in addition to the previously reported γ-rays.[3] We propose a decay scheme of ^{110}Sn as shown in Fig. 2 on the basis of the γ-γ coincidence measurement. New γ-rays are

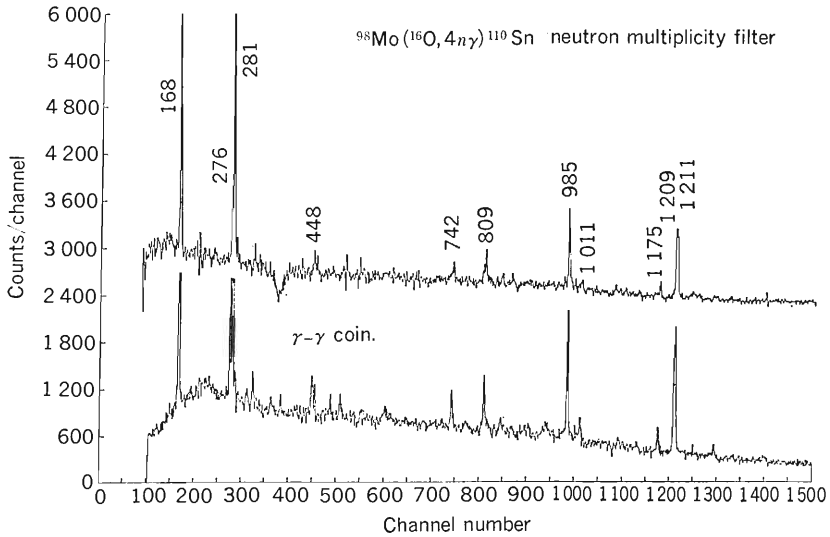

Fig. 1. Gamma-ray spectra obtained in the ^{98}Mo(^{16}O, 4nγ)^{110}Sn reaction. Gamma rays from ^{110}Sn are selected by the neutron multiplicity filter (upper spectrum) and by the γ-γ coincidence gated by 281 keV ($6^+ \rightarrow 4^+$), 985 keV ($4^+ \rightarrow 2^+$) and 1,211 keV ($2^+ \rightarrow 0^+$) γ-rays (lower spectrum).

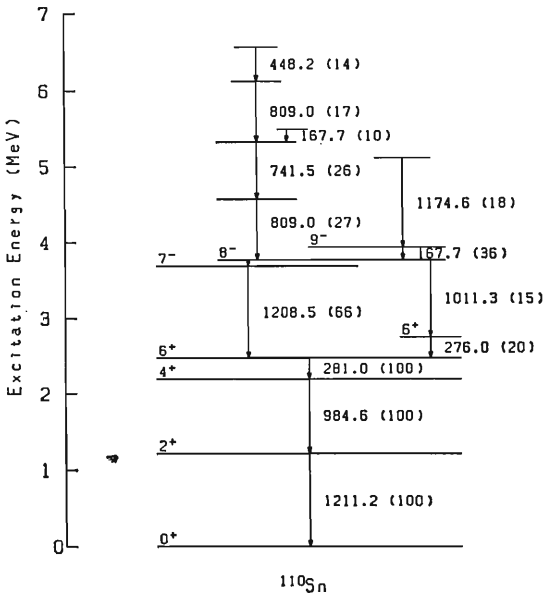

Fig. 2. Proposed decay scheme of ^{110}Sn. Numerical figures in parentheses indicate relative intensities of γ-rays observed in the ^{98}Mo(^{16}O, 4nγ) ^{110}Sn reaction.

assigned as transitions of a sequence of levels above 8^- state at 2,756 keV. These levels can be interpreted as neutron four-quasi-particle excitations, since neutron two-quasi-particle states cannot give high spin states with $J^\pi > 9^-$ and 10^+.

References

1) J. Bron, W. H. A. Hasselink, A. Van Poelgeest, J. J. A. Zalmstra, M. J. Uitzinger, H. Verheul, K. Heyde, M. Waroquier, H. Vincx, and P. Van Isacker: *Nucl. Phys. A*, **318**, 335 (1979).
2) T. Murakami, J. Kasagi, H. Harada, and T. Inamura: *RIKEN Accel. Progr. Rep.*, **17**, 125 (1983).
3) A. Van Poelgeest, J. Bron, W. H. A. Hesselink, K. Allaart, J. J. A. Zalmstra, M. J. Uitzinger, and H. Verheul: *Nucl. Phys. A*, **346**, 70 (1980).

RIKEN Accel. Progr. Rep. **18** (1984)

III-1-9. Lifetime Measurement of the 8^- State in ^{110}Sn

H. Harada, T. Murakami, H. Tachibanaki, K. Yoshida,
J. Kasagi, and T. Inamura

[NUCLEAR REACTIONS ^{98}Mo(^{16}O, 4n), E=76 MeV; measured recoil distance; ^{110}Sn deduced $T_{1/2}$.]

In even tin nuclei, there exist negative parity states at excitation energies of about 3 MeV. They are interpreted as neutron two-quasi-particle states with ($h_{11/2}$, $g_{7/2}$) or ($h_{11/2}$, $d_{5/2}$) configuration. The 8^- state which decays to the 6^+ state is assigned at 3,770 keV in ^{110}Sn.[1] Since the E1 transition is not allowed between two-quasi-particle states with neutrons in valence orbits ($d_{5/2}$, $g_{7/2}$, $h_{11/2}$, $s_{1/2}$, and $d_{3/2}$), this transition gives valuable information on the configuration of these states.

Recoil distance measurement was carried out in the ^{98}Mo(^{16}O, 4n)^{110}Sn reaction at $E(^{16}O)$=76 MeV, using a device which was used for lifetime measurement of levels in ^{49}V.[2] A self-supporting foil of enriched (95%) ^{98}Mo, 0.95 mg/cm^2 thick was used as a target and a thick Ta foil served as a recoil stopper. The relative displacement of the target and the stopper could be adjusted externally and measured by a 1 μm precision micrometer. A Ge(Li) detector was placed at 140° to the beam direction. The measurement was performed with a neutron multiplicity filter as mentioned in Ref. 3.

Figure 1 shows γ-ray spectra obtained for various stopper distances. Arrows in the figure indicate positions of stopped and shifted peaks of γ-rays from ^{110}Sn. Initial velocity distribution of the recoil nuclei is estimated under the assumption that neutrons are emitted isotropically in the center of mass system. The average flight velocity in a vacuum is then calculated by a Monte Carlo program. Although the 1,209 keV γ-ray corresponds to the transition from the 7^- state at 3,692 keV, it turned out that a decay curve of this γ ray is determined by the lifetime of the 8^- state. Thus, we can obtain the lifetime of the 8^- state in good accuracy by analyzing the 1,209 keV γ ray instead of the 1,011 keV γ ray. (The decay scheme of ^{110}Sn is shown in Fig. 2 of Ref. 3.)

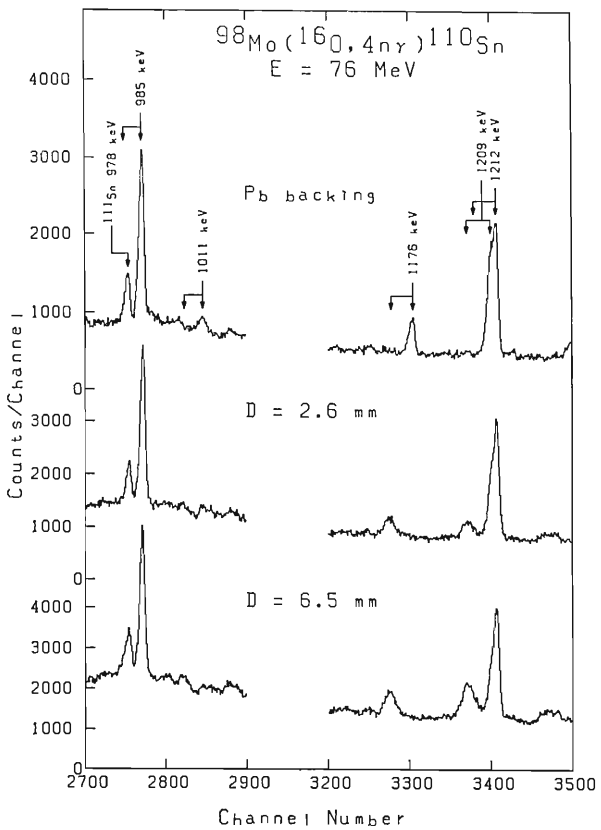

Fig. 1. Gamma-ray spectra obtained in the ^{98}Mo(^{16}O,4n)-^{110}Sn reaction for various stopper distances.

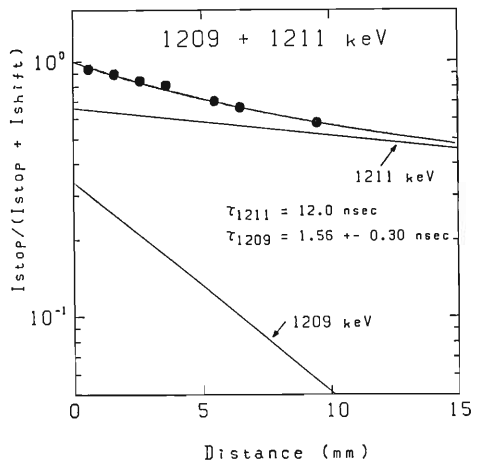

Fig. 2. Plots of the ratio of the yields of the stopped peaks to the total for the 1,209 and 1,211 keV γ rays against stopper distance.

Figure 2 shows the ratio of the yields of the stopped peaks to the total for the 1,209 and 1,211 keV doublet. The decay time of the 1,211 keV transition ($2^+ \rightarrow 0^+$) is known to be 12 ns since it is determined by the lifetime of the 6^+ state at 2,480 keV.[1] A least-squares fit was made with two decay components as shown in Fig. 2. The lifetime of the 8^- state obtained with the average velocity is 1.56 ± 0.30 ns. The reduced B(M2) value of the transition between the 8^- and 6^+ states is therefore 0.23 ± 0.05 W. U., which is consistent with that of the transition between the $11/2^-$ and $7/2^+$ states in ^{111}Sn.[4]

References

1) A. Van Poelgeest, J. Bron, W. H. A. Hesselink, K. Allaart, J. J. A. Zalmstra, M. J. Uitzinger, and H. Verheul: *Nucl. Phys. A*, **346**, 70 (1980).
2) H. Ohnuma and J. Kasagi: *J. Phys. G*, **7**, 1691 (1981).
3) H. Harada, T. Murakami, H. Tachibanaki, K. Yoshida, J. Kasagi, and T. Inamura: p. 22 in this report.
4) R. Brenn, S. K. Bhattacherjee, G. D. Sprouse, and L. E. Young: *Phys. Rev. C*, **10**, 1414 (1974).

RIKEN Accel. Progr. Rep. **18** (1984)

III-1-10. High-Spin States of Ge Isotopes in the Interacting Boson Model

N. Yoshida and A. Arima*

[NUCLEAR STRUCTURE ^{66,68,70,72}Ge; interacting boson model, high-spin states.]

Several high-spin bands have been observed in Ge isotopes.[1),2)] They are interpreted as ground-state bands and particle-aligned bands by comparing with the calculations based on various models.[3),4)] The interacting boson model has been extended so that the aligned bands can be described by allowing some of the bosons to change into pairs of fermions in the high-j orbitals.[5)]

We report a result of calculation, using the extended interacting boson model, of energy levels and B(E2) values of high-spin states in ^{66,68,70,72}Ge. Among particles in the orbitals between magic numbers 28 and 50, we treat the particles in $g_{9/2}$ as fermions explicitly, and assume that particles in other orbitals are represented well by bosons. The hamiltonian is

$$H=H^{B}+H^{F}+V^{BF} \qquad (1)$$

where H^{B} is the IBM hamiltonian, H^{F} is the fermion hamiltonian, and V^{BF} is the interaction between bosons and fermions. As the IBM hamiltonian, we take the proton-neutron interacting boson model (P-N IBM, or IBM2) hamiltonian fitted to low-lying states of the same isotopes. The term H^{F} consists of single-particle energies and two-body interactions. We determine single-particle energies from quasiparticle energies of $g_{9/2}$. As the two-body interaction, we assume the surface delta interaction (SDI), and as the boson-fermion interaction V^{BF}, the quadrupole-quadrupole interaction. The pa-

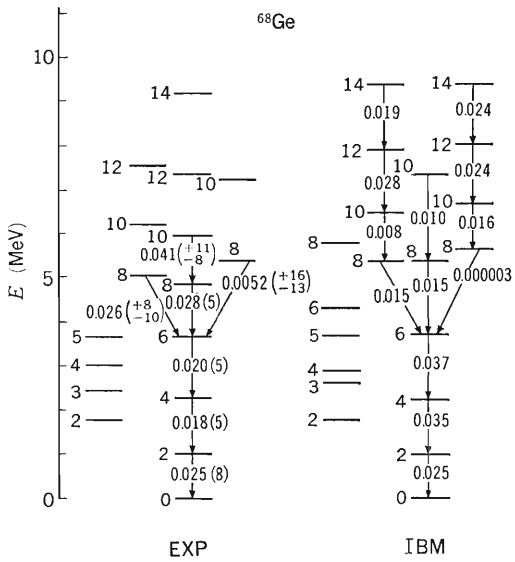

Fig. 1. Comparison between calculated (IBM) and experimental (EXP) energy levels and B(E2) values in ^{68}Ge. Numbers on arrows indicate B(E2) values in units of e^2b^2. Experimental data are taken from Refs. 1–3.

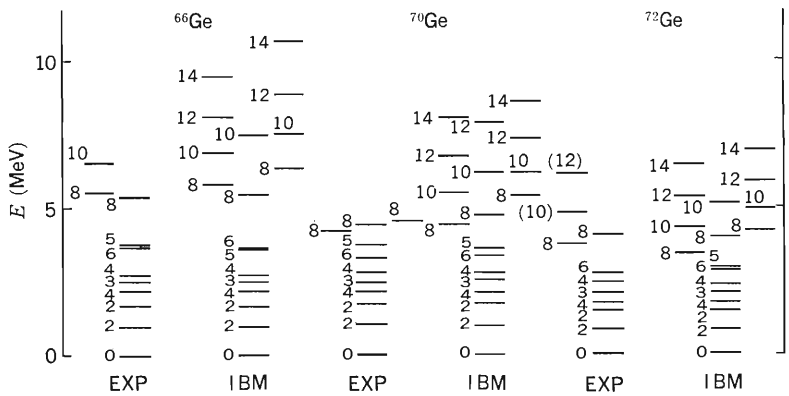

Fig. 2. Comparison between calculated (IBM) and experimental (EXP) energy levels in ^{66,70,72}Ge. Experimental data are taken from Refs. 2 and 3.

* Faculty of Science, The University of Tokyo.

rameters in V^{BF} are varied so as to reproduce the experimental energies and B(E2) values of high-spin states. The hamiltonian is diagonalized in the space consisting of states with bosons only, states with two protons in $g_{9/2}$ and states with two neutrons in $g_{9/2}$. As in the case in our previous work, we do not include fermion pairs coupled to angular momenta 0 and 2.[5] In diagonalization of the hamiltonian, we first diagonalize H^B in the boson space, and choose low-energy eigenvectors as boson basis vectors. They are coupled with fermion pairs to construct the basis in the total system where H is diagonalized.

Figure 1 shows the comparison between calculated and experimental energy levels and B(E2) values of ^{68}Ge. The calculated B(E2) values are normalized to experimental values of the transition from 2_1^+ to O_g^+, although the experimental uncertainty is large for this transition. The yrast levels are fairly well reproduced by the calculation. The calculated location of 10^+ in the ground-state band is higher than that observed, as is often seen in other calculations with rigid cores.[3),4)] The staggering in the γ-band is somewhat exaggerated. The reduction in $B(E2; 4_1^+ \rightarrow 2_1^+)$ has not been explained by calculations so far.[3),4)] Energy levels of other isotopes are shown in Fig. 2; the energy levels are reproduced well by the calculation. However, the calculated B(E2) values sometimes considerably deviate from experimental values. Especially, calculation often gives too small B(E2) values for the states of band-crossing. This feature is common to most calculations of this kind and needs further investigation.[3),4)]

References

1) A. P. de Lima, A. V. Ramayya, J. H. Hamilton, B. Van Nooijen, R. M. Ronningen, H. Kawakami, P. B. Piercey, E. de Lima, R. L. Robinson, H. J. Kim, L. K. Peker, F. A. Rickey, R. Popli, A. J. Caffrey, and J. C. Wells: *Phys. Rev. C*, **23**, 213 (1981).
2) N. J. Ward and F. Kearns: *Nucl. Data Sheets*, **39**, 1 (1983); F. Kearns: *ibid.*, **33**, 481 (1981); F. Kearns and J. N. Mo: *ibid.*, **25**, 1 (1978); **31**, 103 (1980)
3) A. Petrovici and A. Faessler: *Nucl. Phys. A*, **395**, 44 (1983).
4) K. J. Weeks, C. S. Han, and J. P. Draayer: *Nucl. Phys. A*, **371**, 19 (1981).
5) N. Yoshida, A. Arima, and T. Otsuka: *Phys. Lett. B*, **114**, 86 (1982).

RIKEN Accel. Progr. Rep. **18** (1984)

III-1-11. Ground State Rotational Band in ^{173}Yb Excited by (^{58}Ni,^{58}Ni')

A. Hashizume, T. Inamura, M. Ohshima,* E. Minehara,*
S. Kikuchi,* and H. Kumahora**

[NUCLEAR REACTIONS ^{173}Yb (^{58}Ni, ^{58}Ni' γ), E=200 MeV; measured Eγ, Iγ (θ), $\gamma\gamma$-coin, deduced levels, J, π.]

The present experiment is one of the series of studies on the multiple Coulomb excitations of nuclei by heavy ions.[1),2)] The ground state rotational states in ^{173}Yb nuclei are built on $h_{9/2}$-neutron orbital, *i.e.*, 5/2[512]. We have studied the excited states in ^{167}Er; its ground-state rotational band is built on the $i_{13/2}$-neutron orbital and a perturbation effect of rotation on M1 and E2 transitions in the band has been observed.[2)] It is our interest to see if such effect can also be observed on the $h_{9/2}$-orbital.

A metallic ^{173}Yb target evaporated on Ta foil was bombarded with a 200 MeV ^{58}Ni beam from the 20-UR tandem accelerator at Japan Atomic Energy Research Institute. We measured angular distributions of deexcitation γ-rays and γ-γ coincidences. We have also observed Doppler broadened γ-ray lineshapes. The γ-ray singles spectrum was taken with a Compton suppression spectrometer which was placed at 0° to the beam. We have not yet obtained the final results from the shape analysis and have report here the results of γ-γ coincidence and γ-ray angular distributions.

A coincidence spectrum obtained by gating all peaks of γ-ray of intraband transitions are shown in Fig. 1. An example of angular distribution together with theoretical analysis by Winther and de Boer code are shown in Fig. 2. The angular distribution of γ-rays in the band are shown in Table 1 together with mixing ratios. We have established the ground-

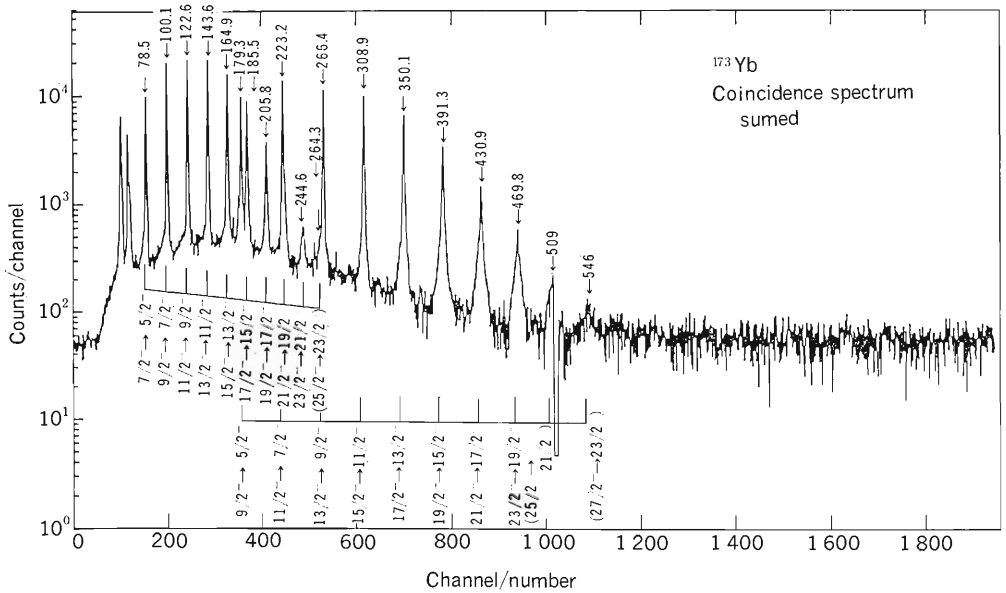

Fig. 1. The coincident γ-ray spectrum obtained by gating on the peaks of γ-rays of intraband transitions.

* Japan Atomic Energy Research Institute, Tokai.
** Department of Physics, Hiroshima University.

state rotation band up to the $23/2^-$ state. It is probable from the coincidence results that the 264, 509, and 546 keV transitions belong to the intraband transitions and that the 1,736 and 2,018 keV states are the members of the ground-state band. The decay scheme is shown in Fig. 3. The states above 610.6 keV ($15/2^-$) were revealed for the first time in the present experiment.

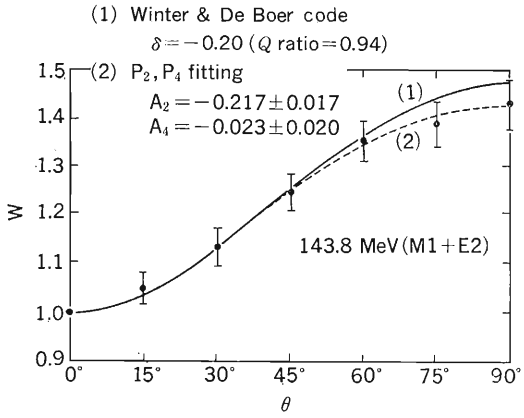

Fig. 2. The angular distribution of 143.8 keV γ-rays.

References

1) T. Inamura, A. Hashizume, M. Ohshima, E. Minehara, S. Kikuchi, and H. Kumahora: *RIKEN Accel. Progr. Rep.* **17**, 26 (1983),
2) M. Ohshima, E. Minehara, M. Ishii, T. Inamura, and, A. Hashizume: *J. Phys. Soc. Jpn.*, **52**, 2959 (1983).

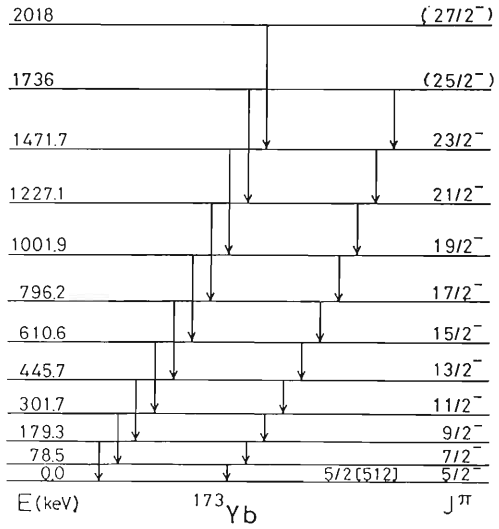

Fig. 3. The Coulomb excited states in ^{173}Yb by ^{58}Ni (E=200 MeV).

Table 1. Results of γ-ray angular distributions. Mixing ratios are shown in the last column. Numbers in parentheses are uncertainties.

Level	E_L(keV)	E_γ(keV)	A_2	A_4	Multi.	δ
$7/2^-$	78.5	78.46	0.003 (15)	0.009 (16)	M1+E2	0.17 (9)
$9/2^-$	179.3	100.55	−0.057 (20)	0.021 (25)	M1+E2	0.14 (8)
		179.31	0.032 (13)	−0.016 (15)	E2	
$11/2^-$	301.7	122.64	−0.180 (22)	0.016 (27)	M1+E2	−0.10 (8)
		223.19	0.035 (12)	0.009 (13)	E2	
$13/2^-$	445.7	143.82	−0.217 (17)	−0.023 (20)	M1+E2	−0.20 (8)
		266.39	0.154 (94)	−0.03 (11)	E2	
$15/2^-$	610.6	164.87	−0.345 (22)	0.043 (28)	M1+E2	−0.39 (13)
		308.87	0.17 (13)	−0.04 (19)	E2	
$17/2^-$	796.7	185.49				
		350.50	0.244 (12)	−0.047 (17)	E2	
$19/2^-$	1001.9	205.75				
		391.26	0.218 (32)	−0.086 (35)	E2	
$21/2^-$	1227.1	225.2				
		430.92	0.220 (26)	−0.102 (28)	E2	
$23/2^-$	1471.9	244.6				
		469.8	0.23 (5)		E2	
(25/2)	1736	264.3				
		509				
(27/2)	2018	—				
		546				

RIKEN Accel. Progr. Rep. 18 (1984)

III-1-12. In-Beam γ-Ray Study of ^{218}Ra with BGOACS

Y. Ishikawa, Y. Gono, M. Sugawara, and M. Fukuda

[NUCLEAR REACTION ^{208}Pb (^{13}C, 3n), E=70 MeV; measured Eγ, Iγ (θ), $\gamma\gamma$-coin, ^{218}Ra deduced levels. 4 sets of Ge(Li) with BGOACS, enriched target.]

Experimental studies of the excited states in ^{218}Ra revealed interesting characteristics of this nucleus such as: (1) the interleaved spin sequence 4^+, 5^-, 6^+, 7^-, ..., 16^+, 17^- and (2) the large B(El)/B(E2) ratios for the deexcitations of the positive and negative parity states.[1)-3)] These phenomena have been tried to be understood based on either IBA[2)] or α-clustering model.[3)] The same characteristics were also found in the neighbouring nuclei. In the case of ^{222}Th (Ref. 4) the calculation based on the coupling of the octupole vibration to the quadrupole deformed core was applied. Experimentally obtained octupole amplitude is somewhat too large compared with that of the theoretical estimation.

The experimental results on ^{218}Ra which were obtained from the experiments made with two Ge(Li) detectors were reported previously.[1)] The experiments were repeated with four sets of the BGOACS systems.[5)] Resulted level scheme is shown in Fig. 1. The negative parity band was extended to the (21^-) state. In addition, five states were found in the side band which starts from the (13^-) state. These states were plotted in the $J(J+1)$ vs. E_X plane (see Fig. 2). The band crossing of the negative parity yrast states can be clearly seen. This phe-

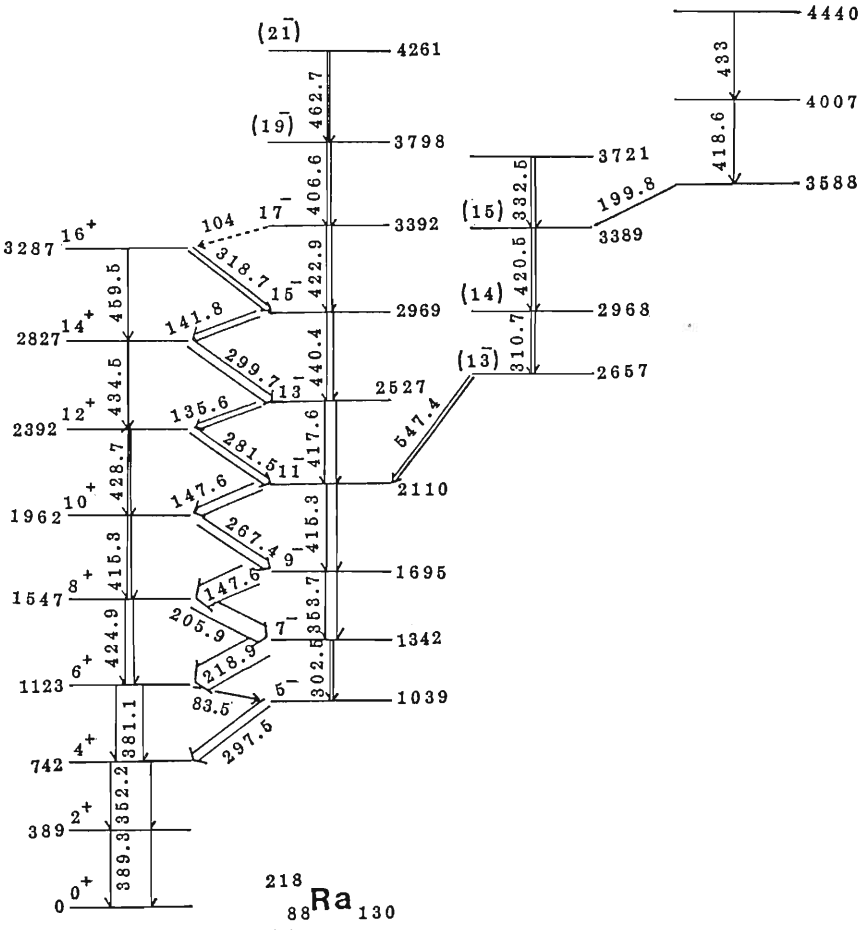

Fig. 1. Level scheme of ^{218}Ra.

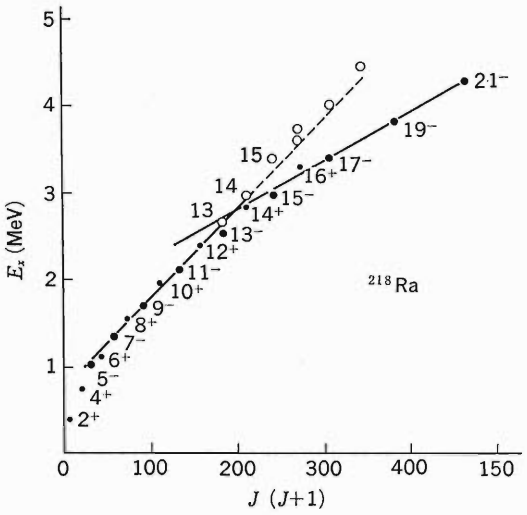

Fig. 2. Plots of the excitation energies of states in ^{218}Ra *vs.* $J(J+1)$ where J is the spin of the states.

nomenon corresponds to the backbending in the plot of the moment of inertia vs. rotational frequency as shown in Fig. 3. The backbending is known to occur when the rotational aligned band crosses the collective rotational band. In the ^{218}Ra nucleus, two possible aligned bands may be considered to cross the negative parity band, *i.e.*, those of the $\pi(i_{13/2}\ h_{9/2})$ and $\nu(j_{15/2}\ g_{9/2})$ orbitals. It may also be worthwhile to point out that the states in the side band locate very close to the extension of the line fitted to the collective negative parity states in

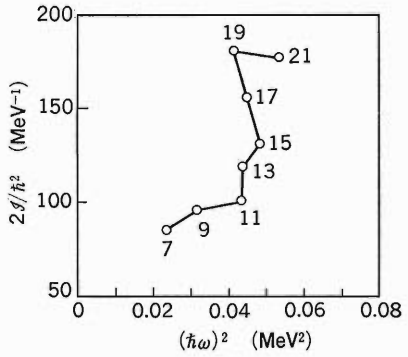

Fig. 3. Backbending plot of the negative parity yrast states in ^{218}Ra.

Fig. 2, when the $\Delta J=1$ characters are assumed for the transitions in the side band.

References

1) Y. Itoh, Y. Gono, M. Sasagase, T. Kubo, M. Sugawara, S. Hayashibe, T. Kohno, and T. Nomura: *RIKEN Accel. Progr. Rep.*, **16**, 48 (1982).
2) J. Fernandez-Niello, H. Puchta, F. Riess, and W. Trautmann: *Nucl. Phys. A*, **391**, 221 (1982).
3) M. Gai, J. F. Ennis, M. Ruscev, E. C. Schloemer, B. Shivakumar, S. M. Sterbenz, N. Tsoupas, and D. A. Bromley: *Phys. Rev. Lett.*, **51**, 646 (1983).
4) D. Ward, G. D. Dracoulis, J. R. Leigh, R. J. Charity, D. J. Hinde, and J. O. Newton: *Nucl. Phys. A*, **406**, 591 (1983).
5) M. Fukuda, Y. Gono, Y. Ishikawa, M. Sugawara, T. Inamura, M. Ishihara, T. Nomura, I. Kohno, H. Kamitsubo, J. Kasagi, and T. Murakami: p. 152 in this report.

RIKEN Accel. Progr. Rep. 18 (1984)

III-1-13. In-Beam γ-Ray Study of ^{212}Po Using Radioactive ^{210}Pb Target

M. Sugawara, Y. Gono, Y. Ishikawa, and M. Fukuda

[NUCLEAR REACTION ^{210}Pb (α, 2n), E=30 MeV, measured $\gamma\gamma$-coin, $\gamma(\theta)$, deduced levels, J.]

The excited states in ^{212}Po were studied by means of in-beam spectroscopic techniques using the radioactive ^{210}Pb target. A preliminary result was already reported.[1] Thereafter the experiments have been made extensively with 30 MeV α-beams. The measurements performed are:

(1) γ-γ Coincidence with a LEPS (Low Energy Photon Spectrometer) and two Ge(Li) detectors which were placed at $-70°$, $-132°$ and 90° with respect to the beam axis

(2) A γ-ray anisotropy obtained from the intensity ratio of those at 90° and 150° with respect to the beam axis

Figure 1 shows a singles γ-ray spectrum taken from the ^{210}Pb+α reaction at 30 MeV. In addition to the known γ-rays originated from ^{212}Po, relatively intense γ-rays were observed. Those stem from a Ni-foil which was used as a backing and impurity materials such as ^{16}O, ^{206}Pb and ^{208}Pb, which were contained in the target. Although there exists a high background, the γ-γ coincidence data provide useful information on the level scheme of ^{212}Po (see Fig. 2).

The level scheme of ^{212}Po could be extended to an excitation energy of 2,884 keV based on the γ-γ coincidence data. Figure 3 shows the proposed level scheme of ^{212}Po. Tentative spin assignments were made using the angular distribution coefficients, A_2/A_0, which were deduced from the γ-ray anisotropies. Furthermore, DCO (Directional Correlation from the Oriented nuclei) ratios were deduced from the coincidence data in order to get complimentary information on the spin assignments. Table 1 lists the angular distribution coefficients and the DCO ratios of the transitions above the 8^+ state. Gamma-rays of 357 and 868 keV have positive A_2/A_0 values and the 577 keV γ-ray has a negative A_2/A_0 value. The spin assignments of the 1,833, 2,409 and 2,701 keV levels could not be given uniquely because of relatively large errors of the A_2/A_0 values and DCO ratios. However, it may be most probable that the spin values of these levels are 10, 11 and 12 using the level systematics of the N=128 isotones (see Fig. 4).

Three shell model calculations have been made on the ^{212}Po nucleus.[2)-4)] The most realistic one among them may be of Strottman.[4] Result of his calculation is shown in Fig. 5. The yrast level sequence is similar to the present experimental result. Comparing the experimental and theoretical level schemes, the 2,884 keV level in Fig. 3 seems to correspond to the spin 14 state in Fig. 5, but this assignment does not conform to the known half-life of 45 s of 2,905 keV isomer because the half-

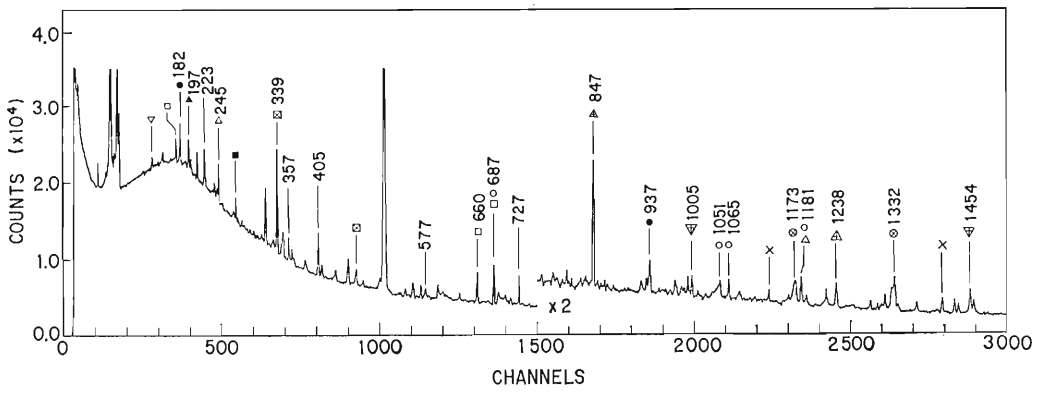

Fig. 1. Singles γ-ray spectrum from the ^{210}Pb+α reaction at 30 MeV. γ-Ray energies indicated in the figure.

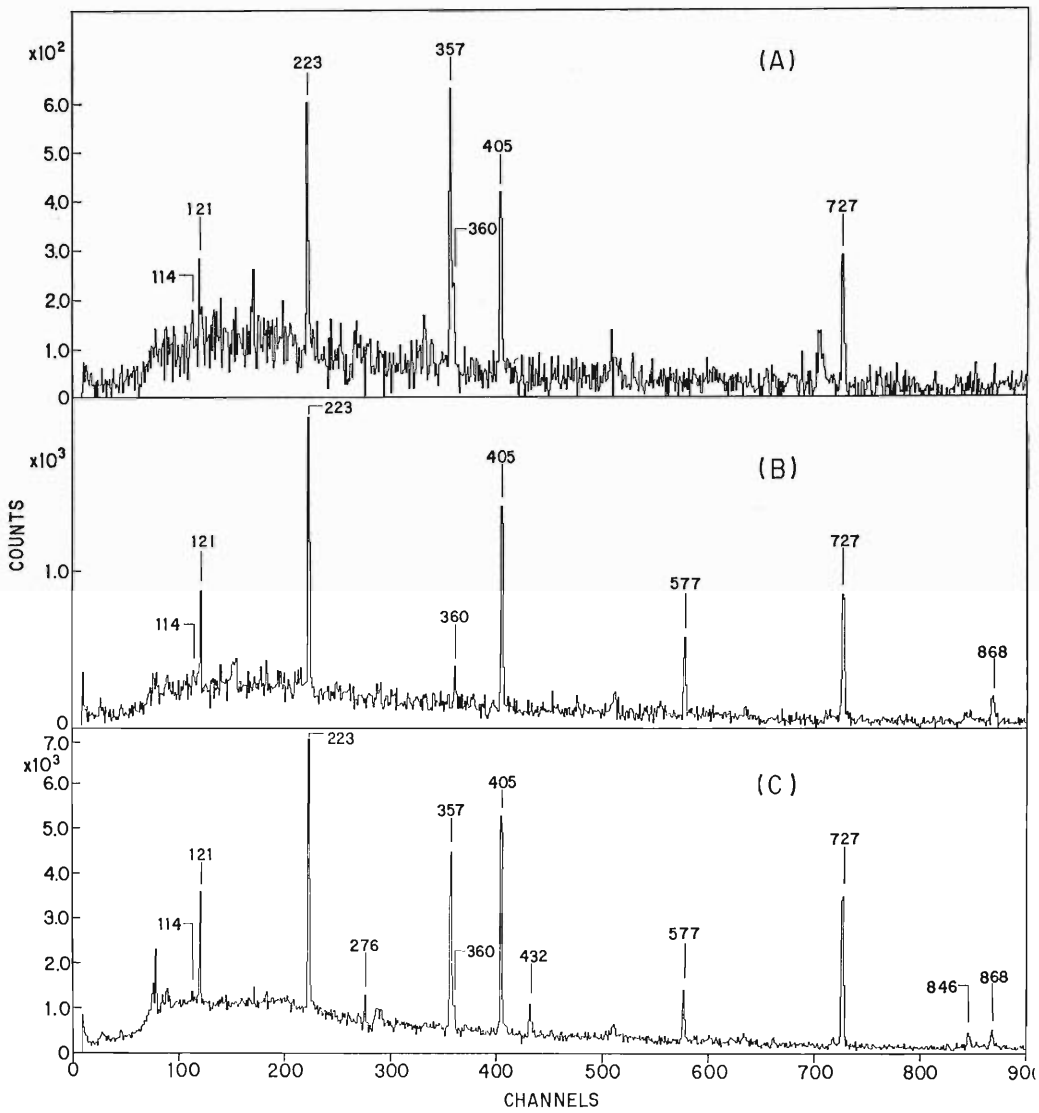

Fig. 2. γ-γ Coincidence spectra. The energies of gated γ-rays are 577 keV (A), 357 keV (B), and 727, 405, 223 keV (C).

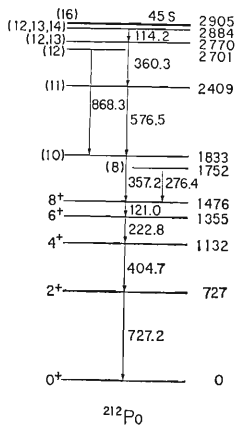

Fig. 3. Proposed level scheme of ^{212}Po.

Table 1. Angular distribution coefficients and DCO ratios (intensity ratios at 70° and 132° in coincidence with 223, 405, 727 keV γ-rays detected by one Ge(Li) placed at 90°) for the transitions above 8^+ level.

$E\gamma$(keV)	A_2/A_0	$W(132°)/W(70°)$
357	0.07 (8)	1.17 (20)
577	−0.41 (8)	0.85 (25)
868	0.40 (10)	1.08 (37)

life of the Weisskopf estimate for the 21 keV E2 transition is 10^{-2} s. However, the level energy of the isomer was determined based on the α-decay data which is usually not accurate enough to discuss on the energy difference less than 20 keV.

Further experiment is necessary to reach the decisive conclusion on this point.

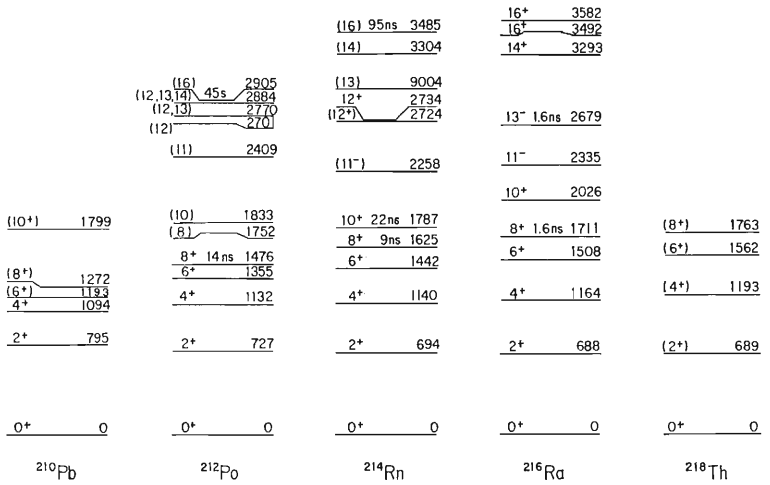

Fig. 4. Level systematics of the $N=128$ isotones.

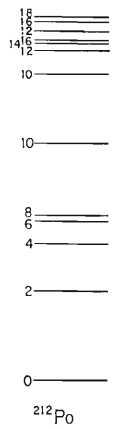

Fig. 5. Shell model calculation by Strottman (Ref. 4).

References

1) Y. Gono, Y. Itoh, M. Sugawara, and I. Fujiwara: *RIKEN Accel. Progr. Rep.*, **17**, 35 (1983)
2) N. Auerbach and I. Talmi: *Phys. Lett.*, **10**, 297 (1964).
3) N. K. Glendenning and K. Harada: *Nucl. Phys.*, **72**, 481 (1965)
4) D. Strottman: *Phys. Rev. C*, **20**, 1150 (1979) and references therein.

RIKEN Accel. Progr. Rep. 18 (1984)

III-1-14. Isomeric Transition of ^{212}Po

H. Kudo, T. Nomura, K. Sueki, and M. Magara*

[NUCLEAR REACTION ^{209}Bi (α, p) ^{212m}Po, $E\alpha$=30–40 MeV, isomeric transition, He-jet transport, α-γ coincidence.]

In ^{212}Po a high spin isomer has been known to exist.[1] An isomeric state in ^{212}Po having a half life of 45 s decays primarily to the ground state of ^{208}Pb by emitting an 11.65 MeV α-particle. The hindrance factor of this α-decay is very large (4×10^{13}), which indicates that the isomer should be in a high-spin state. Some shell model calculations predict the spin-parity of this isomer to be (16^+) or (18^+).[2)-4)] In the calculation by Auerbach and Talmi[2] the spin-parity is (16^+), and in the low-yrast state another possible isomer be in (8^+) state. On the other hand, Glendenning and Harada[4] predicted (18^+) state for the 45 s-isomer and (10^+) isomeric state in the low-yrast state. Chulick and Natowitz[5] suggested the spin-parity state of the 45 s-isomer as (16^+) by DWBA analysis of the angular distribution of this isomer. The lower spin isomeric state of (8^+) with a half-life of 14 ns is ascertained recently by some authors.[6),7)] This evidence seems to support the calculation by Auerbach and Talmi,[2] and therefore, the 45 s-isomer is expected to be in 16^+ state. The partial level scheme of ^{212}Po is shown in Fig. 1 taking into account the situations mentioned above.

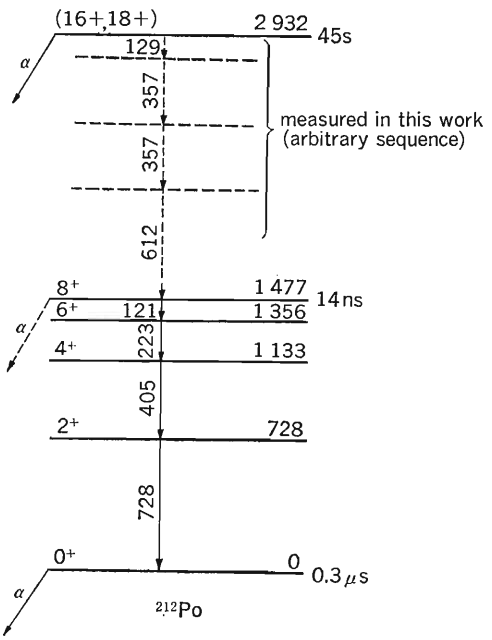

Fig. 1. Partial level scheme of ^{212}Po.

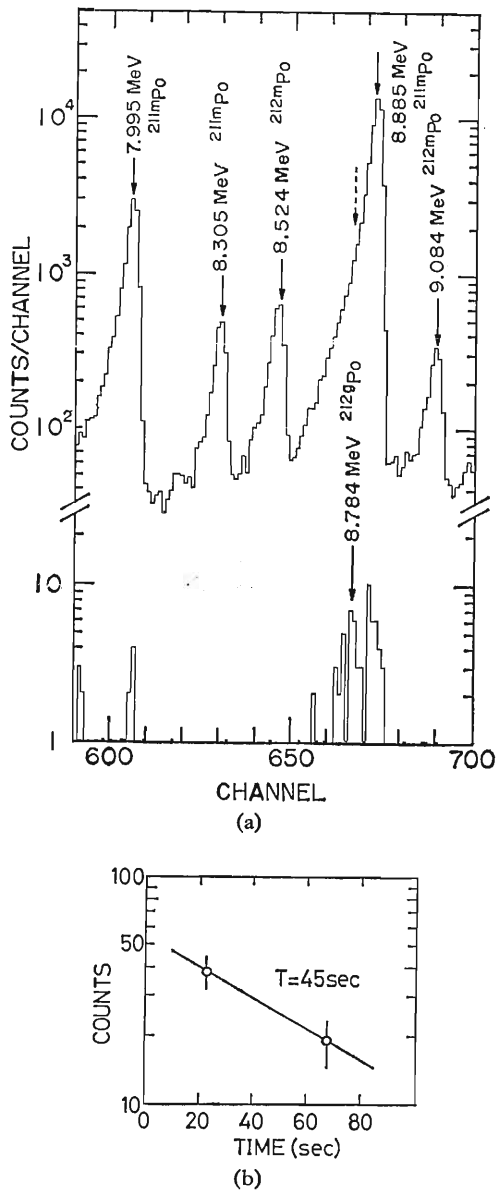

Fig. 2. A part of α-spectra obtained from α-γ coincidence measurement of ^{212m}Po. (a) Singles, (b) 14 to 860 ns delayed spectrum.

* Faculty of Science, Tokyo Metropolitan University.

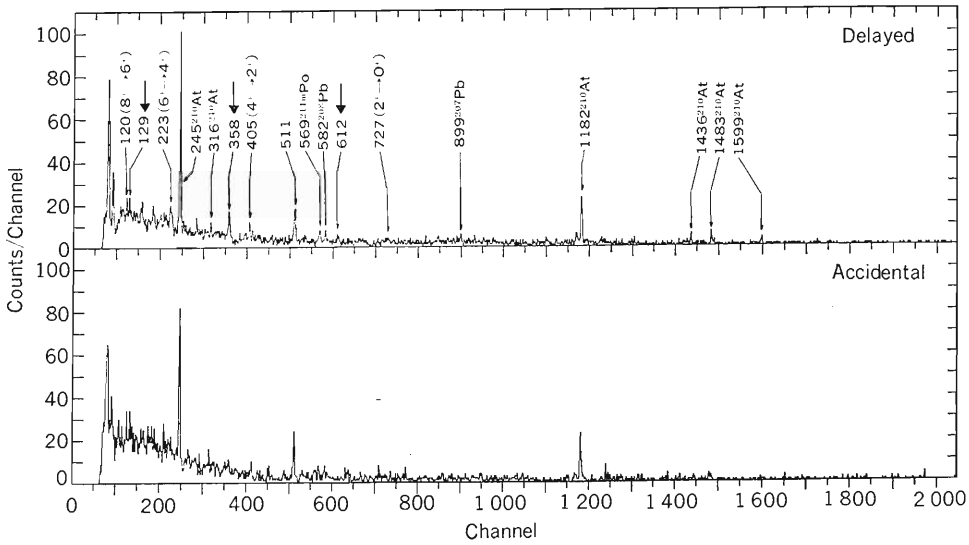

Fig. 3. Gamma-ray spectrum obtained from α-γ coincidence measurement.

However, there is no direct evidence to assign the spin-parity of the 45 s-isomer. In this work, we tried to measure possible γ-decay and to assign the spin-parity of the 45 s-isomer. The ground state of ^{212}Po has a half-life of 0.3 μs and emits an α-particle of 8.784 MeV, which corresponds to the decay to the ground state of ^{208}Pb. So we applied an α-γ coincidence measurement. The reaction ^{209}Bi-(α, p) was used for the production of the nucleus ^{212m}Po. Ten to thirty pieces of ^{209}Bi targets deposited on thin gold foil were irradiated with 40 MeV α-particles from the cyclotron and the reaction products were transported by a helium-jet transport system. The transported products were attached on a collecting tape which was moved by a microcomputer controlled pulse motor to the detection position. A Si(Au) detector of 300 mm^2 in area and 300 μm in thickness and a Ge(Li) detector of a 80 cm^3 active volume were mounted at distances of 3 mm and 4 mm, respectively, from the collecting tape. Coincident signals were stored on a magnetic tape event by event.

The observed α-spectrum in an α-γ coincidence measurement is shown in Fig. 2, where the 8.784 MeV peak is seen in the delayed spectrum. The decay curve of this line measured in coincidence with known γ-rays (223 keV, 405 keV, and 728 keV) is also shown in Fig. 2. A preliminary result in the α-γ coincidence measurement yielded four new γ-rays (129 keV, 357 keV (doublet), and 612 keV) besides the known transitions below the 8^+ state, (see Fig. 3) which yields the branching ratio of the isomeric transition to be $0.070\pm0.020\%$. And the 45 s-isomer seems to be in 18^+ state, assuming the γ-decay is initiated by emitting 129 keV γ-ray and considering the partial half-life of this γ-decay.

References

1) I. Perlman, F. Asaro, A. Ghiorso, A. Larsh, and R. Latimer: *Phys. Rev.*, **127**, 917 (1962).
2) N. Auerbach and I. Talmi: *Phys. Lett.*, **10**, 297 (1964)
3) N. K. Glendenning: *Phys. Rev.*, **127**, 923 (1962).
4) N. K. Glendenning and K. Harada: *Nucl. Phys.*, **72**, 48 (1965).
5) E. T. Chulick and J. B. Natowitz: *Nucl. Phys. A*, **173**, 487 (1971).
6) R. M. Lieder, J. P. D. Didelez, H. Beuscher, D. R. Haenni, M. Muller-Veggian, A. Neskakis, and C. Mayer-Boricke: *Phys. Rev. Lett.*, **41**, 742 (1978).
7) P. Lemmertz, L. J. Alquist, R. Fass, H. Wollnik, D. Hirdes, H. Jungclas, R. Brandt, D. Schardt, and J Zyliez: *Z. Phys. A*, **298**, 311 (1980).

RIKEN Accel. Progr. Rep. 18 (1984)

III-1-15. Evaporation-Like Products in $^{14}N+^{238}U$ Reaction

M. Magara,* K. Sueki, H. Nakahara, H. Kudo,
Y. Hamajima,** and I. Kohno

NUCLEAR REACTION $^{238}U(^{14}N, xn)^{252-x}Es$, $x=5$–7, $E_{lab}=$ 80.4–102.8 MeV; He-jet transport, measured α-spectrum, half-life and excitation function.

The aim of the present work is to understand the reaction mechanism leading to evaporation-like products in heavy-ion induced reactions of heavy nuclei (less than 10 MeV/u). In a heavy reaction system, the fused nuclei are expected to decay both by fission and by light-particle emission, but the competition between the two decay processes in nuclei of high angular momenta is not well understood yet. As a reaction system, we chose $^{14}N+^{238}U$ and einsteinium isotopes with mass numbers of 5–7 neutrons smaller than the mass number of the compound nucleus were investigated.

Light einsteinium isotopes with $A<247$ have been studied by Mikheev *et al.*[1] and Eskola.[2] Mikheev *et al.* first reported in 1967 that by the $^{238}U(^{14}N, xn)$ reaction ^{245}Es, ^{246}Es, and ^{247}Es were synthesized; their alpha-particle energies were 7.70, 7.33, and 7.33 MeV, and their half-lives were 1.33, 7.7, and 5.0 min, respectively.

Later in 1972, by the reaction of $^{241}Am+^{12}C$, Eskola was able to produce and identify $^{245-247}Es$ which decay by electron capture and α emission. He reported that the alpha-particle energies of ^{245}Es, ^{246}Es, and ^{247}Es were 7.73, 7.36, and 7.31 MeV, respectively, and the half-life of ^{247}Es was 4.7 min.

Since there are only a few reports on those isotopes, we first investigated their decay characteristics and then excitation functions.

The target was made by electrodeposition of the purified uranyl nitrate from the ethanol solution onto a 2 μm (3.32 mg/cm^2) Ta foil. The target thickness was 0.53 mg/cm^2 (U equivalent) which was smaller than the recoil ranges of the product nuclei (1.4 mg/cm^2 in uranium) so that almost all the evaporation-like products were expected to recoil out from the target. Beams of ^{14}N ions were provided from the cyclotron and the beam energies were varied from 97.6 to 116.2 MeV. When necessary, thin Al absorbers were used to reduce the beam energy. Northcliffe's[3] range energy curves were used in the latter case to compute the ^{14}N energy at the target position. The reaction products were transferred from the reaction chamber onto a magnetic tape by use of the hellium-jet transport system.[4] The collecting tape was heated at 195° for 10 s to get rid of the oil that would deteriorate the resolution of alpha-spectra. For alpha-particle measurement, we used two Si surface-barrier detectors placed in sequence along the movement of the tape. The irradiation was performed at a regular cycle of 8 min. The measurement was carried out for 8 min at the first detector, and then for 8 min at the second detector. The total detection time was 16 min. This cycle was repeated for about 50 times. Alpha-decay events were recorded together with external clock pulses and stored on a magnetic tape in list mode for data analysis.

One example of the observed α-spectra is shown in Fig. 1, in which the 7.3 and 7.73 MeV peaks are

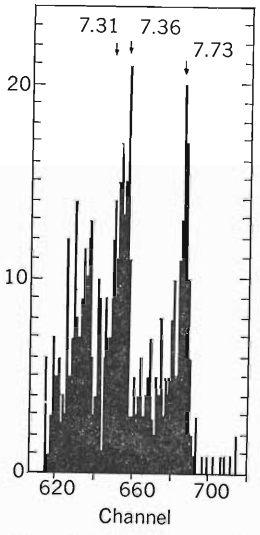

Fig. 1. A part of the alpha-particle spectra observed in repeated bombardment of the 93.1 MeV ^{14}N on a uranium-238 target for 82 times. The events observed in channels less than 640 are mostly due to Cf isotopes.

* Faculty of Science, Tokyo Metropolitan University.
** Faculty of Science, Kanazawa University.

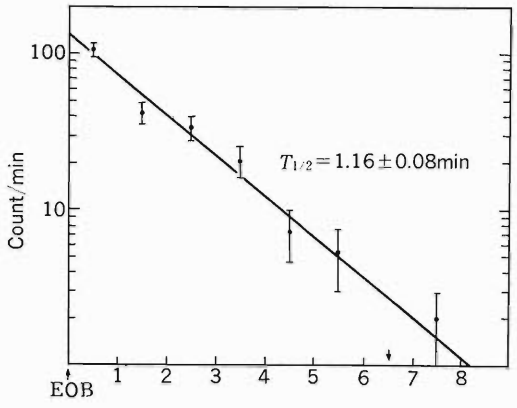

Fig. 2. Decay curve of the 7.73 MeV alpha-particle peak of ^{245}Es observed in repeated bombardment of 90.3–93.1 MeV ^{14}N ions. The error bars indicate one standard deviation.

seen. The energy resolution in terms of FWHM is 37 keV. The 7.73 MeV peak was observable only when the ^{14}N energy was larger than 87.6 MeV and found to decay with a half-life of 1.16 ± 0.08 min, as shown in Fig. 2. It can be assigned to ^{245}Es in agreement with the published data. The 7.3 MeV alpha peak was clearly a complex peak and analyzed into two components from the consideration of its shape and width. Its intensity of the complex peak was found to decay with a half-life of $5.40^{+0.82}_{-0.63}$ min to $5.45^{+0.52}_{-0.52}$ min when the ^{14}N energy was increased from 81.5 MeV to 94.0 MeV. Owing to poor counting statistics, a definite assignment of the two components to ^{246}Es and ^{247}Es was not achieved yet. A tentative excitation function of ^{245}Es is given in Fig. 3 and compared with that reported by Mikheev *et al.* The cross sections were evaluated on

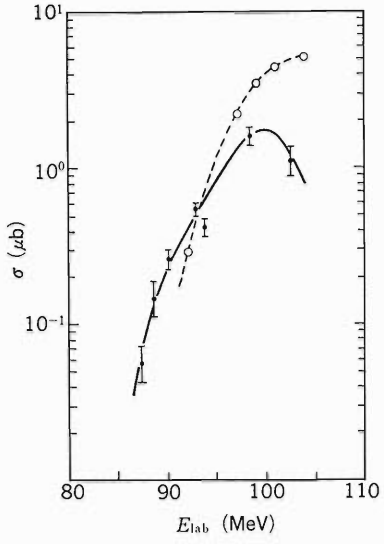

Fig. 3. Excitation function for the reaction ^{238}U(^{14}N, 7n)-^{245}Es plotted *vs.* ^{14}N energy in the laboratory system. Filled circles show the results of present experiments and the solid line is draw through the data points to guide the eye. Open circles show the literature values (Ref. 1).

an assumption that the He-jet transport efficiency was 70% as obtained in previous experiments[5] and data analysis are in progress.

References

1) V. L. Mikheev, V. I. Ilyushchnko, and M. B. Miller: *Sov. J. Nucl. Phys.*, **5**, 35 (1967).
2) P. Eskola: *Phys. Rev. C*, **7**, 280 (1973).
3) L. C. Northcliffe and R. F. Schilling: *Nucl. Data Tables*, **A7**, 233 (1970).
4) H. Kudo, T. Nomura, and J. Fujita: *RIKEN Accel. Progr. Rep.*, **17**, 127 (1983).
5) H. Kudo: private communication.

RIKEN Accel. Progr. Rep. 18 (1984)

III-1-16. High-Lying Single-Proton States of ^{209}Bi Studied by Gamma-Triton Coincidence Measurement in the ^{208}Pb(α,t)^{209}Bi Reaction

M. Ishihara, H. Ohsumi, T. Motobayashi, Y. Nagai,* and T. Shimoda**

[NUCLEAR REACTION ^{208}Pb(α, t)^{209}Bi at E=60 MeV; energy spectra measured at θ=16° in coincidence with gamma rays.]

We have been studying single-particle states at high excitation energies in ^{209}Bi using proton stripping reactions such as (α, t) and (^{12}C, ^{11}B) on ^{208}Pb. Of particular interest is observation of strength distributions of proton states of the 6 $\hbar\omega$ region, which consist of $lj_{15/2}$, $li_{11/2}$, $2g_{7/2, 9/2}$, $3d_{3/2, 5/2}$, and $4s_{1/2}$ states and will appear at 2 $\hbar\omega$ excitation in ^{209}Bi. Such studies of high-lying single particle states have been rare so far[1] while they are complementary to studies of deep-hole states which exist numerously.

Previous results on differential cross sections in the ^{208}Pb(α, t)^{209}Bi reaction at 60 MeV[2] have shown that the reaction is useful in populating those high-lying states with appreciable cross sections. DWBA analyses on the observed angular distributions further indicated that populations of high-spin states are dominant in the continuum region of 4 to 8 MeV excitation, where 50 to 80% of $li_{11/2}$, $lj_{15/2}$ single-particle strengths were observed. There, however, remain considerable uncertainties concerning exact spin assignments and magnitudes of single particle strengths. They primarily arise from ambiguities in the estimate of underlying background tail in the continuum energy spectra and also due to the fact that shapes of angular distributions are too similar among high-spin states to clearly distinguish these states from each other. Supplemental information is certainly desirable in order to remove such uncertainties.

To gain additional information on strength distributions, one can think of coincidence measurements with particles or gamma rays which appear in the decay of excited states of interest. The present report is concerned with such a measurement in which we observed coincidence spectra between tritons and gamma rays in the (α, t) reaction. The measurement of gamma rays particularly suits the case of ^{209}Bi, where neutron and proton separation energies, S_n and S_P, are 7.8 and 3.8 MeV, respectively. Hence, below 7.8 MeV, gamma transitions are supposed to be a dominant de-excitation mode while proton decays will be considerably suppressed even for $E_X > S_P$ because of the large Coulomb barrier. The gamma-ray measurement was further simulated by the expectation that gamma de-excitation of the states at sufficiently high excitation may primarily occur *via* El transitions to low-lying $(n-1)$ $\hbar\omega$ states. Such Δn=1 El transitions will be unhindered except for the effect of giant resonances and well overwhelm possible competitions from Δn=0 M1 and collective E3 transitions. If this is the case, the highly excited initial states of different spins will selectively decay to particular final states according to spin schemes, *e.g.*, $lj_{15/2}^- \rightarrow li_{13/2}^+$, $li_{11/2}^+ \rightarrow lh_{9/2}^-$, $2g_{9/2}^+ \rightarrow 2f_{7/2}^-$, *etc.* Thus one can hope to obtain spin assignments for the initial states by observing high-energy gamma rays and identifying their final states near the ground state, which are well separated from each other in the case of ^{209}Bi.

The experiment was performed using a 60 MeV alpha beam from RCNP cyclotron. Metallic foil of ^{208}Pb with 5.5 mg/cm^2 thickness was used as a target. Two telescopes consisting of 200 μm ΔE and 5 mm E silicon detectors were placed at angles of $\theta = \pm 16°$ to detect outgoing tritons. They subtended solid angles of 30 msr and covered an angular range of $\Delta\theta = \pm 5.5°$. An energy degrader of 1.4 mg/cm^2 Al was placed in front of the telescope to eliminate elastically and inelastically scattered alpha particles. Gamma rays were detected with four units of NaI crystal of a size of $6''\phi \times 6''$. Each of the detectors was located 14 cm apart from the target and had a net photo-peak efficiency of about 2.0% for 1.331 MeV gamma rays. The coincidence events were treated with a CAMAC+MBD11+PDP11/45 system and recorded on magnetic tapes.

* Faculty of Science, Osaka University.
** Faculty of Education, Osaka University.

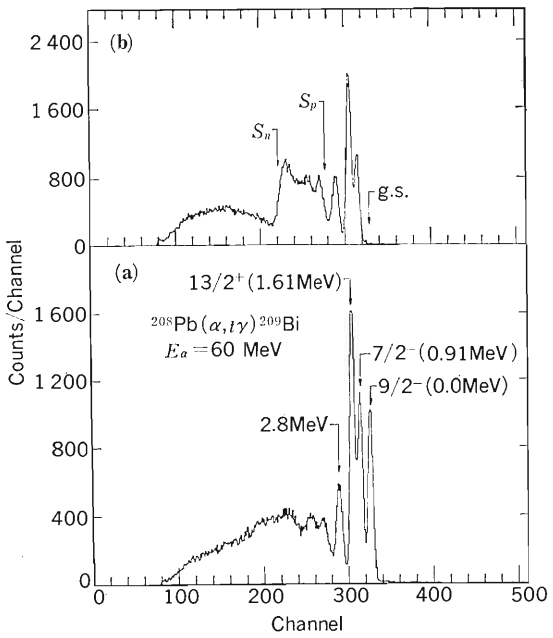

Fig. 1. Energy spectra of tritons observed in the ^{208}Pb(α, t)-^{209}Bi reaction at E_α=60 MeV and θ=16° in singles (a) and in coincidence with gamma rays (b).

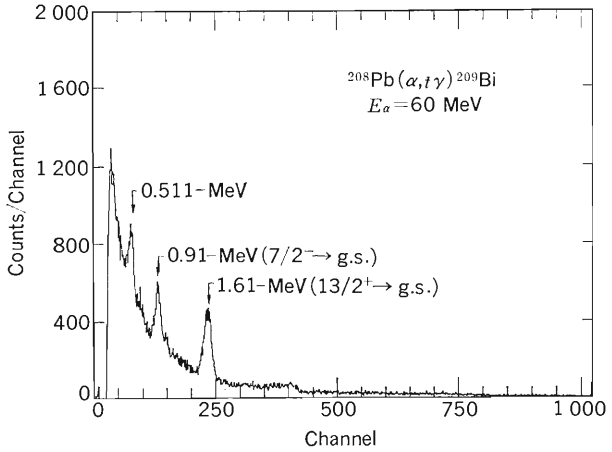

Fig. 2. Energy spectrum of gamma rays taken in coincidence with tritons.

Figure 1 compares singles(a) and coincidence(b) triton spectra. Besides intense discrete lines at low excitation energies, appreciable cross sections are observed in the continuum region above the particle thresholds. In the coincidence spectrum, yields for the region above S_n are strongly suppressed corresponding to opening of a neutron decay mode. On the other hand, yields for the range of $S_P<E_X<S_n$ are enhanced relatively to the lower excitation peaks, indicating that gamma deexcitation is the main decay mode for these states as expected. The

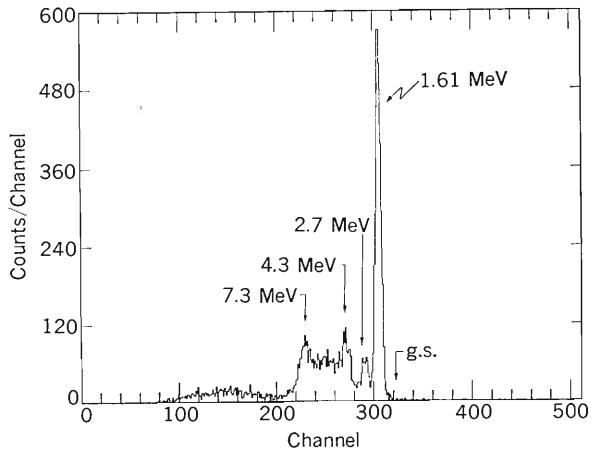

Fig. 3. Energy spectrum of tritons taken in coincidence with the 1.61 MeV gamma transition.

enhancement may imply multiplicity of $M\gamma>1$ of the deexcitation gamma cascades. The coincidence spectrum corresponds to a 10 h run for a single pair of particle and gamma counters and indicates a promising efficiency of the method used. Figure 2 shows a gamma-ray spectrum taken in coincidence with whole tritons. The energy spectrum extends to the region of 8 MeV, indicating the presence of high energy gamma transitions directly feeding low-lying states near the Fermi surface. Two prominent lines of 0.91 MeV ($f_{7/2^-} \rightarrow h_{9/2^-}$) and 1.61 MeV ($i_{3/2^+} \rightarrow h_{9/2^-}$) are present as well as 0.51 MeV annihilation gamma rays. Their intensities are not entirely due to direct excitation of the $f_{7/2}$ and $i_{13/2}$ states but partly due to the population fed from higher states. This situation is indicated in Fig. 3, where a triton spectrum in coincidence with the 1.61 MeV line is shown. Peaks are seen in the region of E_X=4–8 MeV as well as at E_X=1.61 MeV. According to the present scenario, those yields at high E_X can be related to the strengths of $j_{5/2}$ state. Whether the yields are indeed due to single-step transitions to the 1.61 MeV state can be tested by projecting the events on the $E_t+E\gamma$ coordinate. Detailed evaluation of the data including such aspects is in progress.

References

1) M. Ishihara: *Nucl. Phys. A*, **400**, 153c (1983); S. Gales, C. P. Massolo, S. Fortier, E. Gerlic, J. Guillot, E. Hourani, J. M. Maison, J. P. Schapira, B. Zwieglinski, P. Martin, and V. Comparat: *Phys. Rev. Lett.*, **48**, 1593 (1982).
2) E. Takada, M. Ishihara, Y. W. Lui, Y. Mihara, T. Murakami, Y. Toba, and R. E. Tribble: *RIKEN Accel. Progr. Rep.*, **17**, 21 (1983).

RIKEN Accel. Progr. Rep. 18 (1984)

III-1-17. Production and Separation of Neutron-Rich Isotope ^{15}C Using Heavy-Ion Reactions

K. Asahi, M. Ishihara, T. Shimoda,* T. Fukuda,** N. Ikeda,*** C. Konno,*** S. Shimoura,*** K. Katori**, Y. Nojiri,** and T. Minamisono**

{NUCLEAR REACTIONS (^{15}N, ^{15}C), E=119, 158 MeV, (^{18}O, ^{15}C), E=149 MeV; ^{100}Mo, ^{208}Pb, ^{232}Th targets. Measured E- and θ-distributions. Enriched targets.}

The time-like component A_0 of the weak axial-vector current has attracted special attention[1] since Kubodera *et al.* pointed out that the two-body part (mesonic exchange correction) is enhanced in A_0.[2] $J^+ \leftrightarrow J^-$ (J=0, 1/2) β-transitions provide a unique opportunity for such studies, since A_0 is shown to dominate in the rank-zero matrix element for these classes of β-transition.[3] So far evidence for exchange contributions has been looked for in two cases of the J=0 transition.

For the case of J=1/2, in contrast to the J=0 cases, the transition receives contributions not only from the rank-zero but also from the rank-one matrix elements and consequently discrimination between the two contributions is essential for extraction of A_0. This can be achieved by observation of asymmetry[4] in the angular distribution of β-rays in reference to the parent nuclear spin polarization, which would not make sense for J=0 cases.

The present work thus aims at determination of an asymmetry factor for β-decay of ^{15}C ($T_{1/2}$= 2.449 s, Q_β=9.772 MeV). Production of the spin-polarized ^{15}C and preservation of the polarization for longer than the nuclear lifetime are indispensable for the experiment. In the present study, heavy-ion reactions have been chosen as a means to produce ^{15}C for several reasons: (1) light-ion reactions would be extremely difficult to produce such a neutron-rich nucleus unless either radioactive beam or target is used; (2) large recoil energies of products in heavy-ion reactions allow ^{15}C to emerge from a thick target and to be implanted in a selected material appropriate for preservation of spin polarization; and (3) a substantial amount of polarization in reaction products can be expected on the basis of recent observation.[5] It is noted that the use of a double-D type spectrometer facilitates low-background, high-efficiency collection of neutron-rich products for the measurement of β-ray angular distribution.

To this end we performed a preliminary experiment to examine the production of ^{15}C by heavy-ion reactions and to explore the feasibility of isotope separation of neutron-rich products using a spectrometer DUMAS[6] developed at Research Center for Nuclear Physics, Osaka University. Beams of ^{15}N at 119 MeV and 158 MeV and ^{18}O at 149 MeV were obtained from the AVF cyclotron at RCNP. Light fragments emitted from the target were detected by using two sets of ΔE-E SSD telescopes. Signals from the telescopes were recorded in list mode on a magnetic tape. The cross section for the ^{15}C production observed for several targets exhibited broad maximum at angles corresponding roughly to the grazing trajectries, as shown in Fig. 1. A simple estimation of β-ray yields based on these cross section values revealed that at grazing angles sufficient statistics for our asymmetry measurement could be obtained under typical experimental conditions, provided some 5% of polarization is obtained in the reaction. The yields and energy spectra of β-emitting products were investigated to clarify the possibility of isotope separation according to magnetic rigidity. The result shows that possible interfering activities, which have Q_β-values larger than 2 MeV and half-lives in the same range as ^{15}C, can mostly be eliminated through $B\rho$ selection provided by DUMAS without losing main part of ^{15}C yield, as demonstrated in Fig. 2.

In conclusion, we have found that the present method is useful for the detailed study of β-decay and nuclear structures of neutron-rich isotopes such as ^{15}C. Development of the experimental setup along these lines is now under way. The present work also has a particular implication in future experiments which will become possible by using

* College of General Education, Osaka University.
** Faculty of Science, Osaka University.
*** Faculty of Science, Kyoto University.

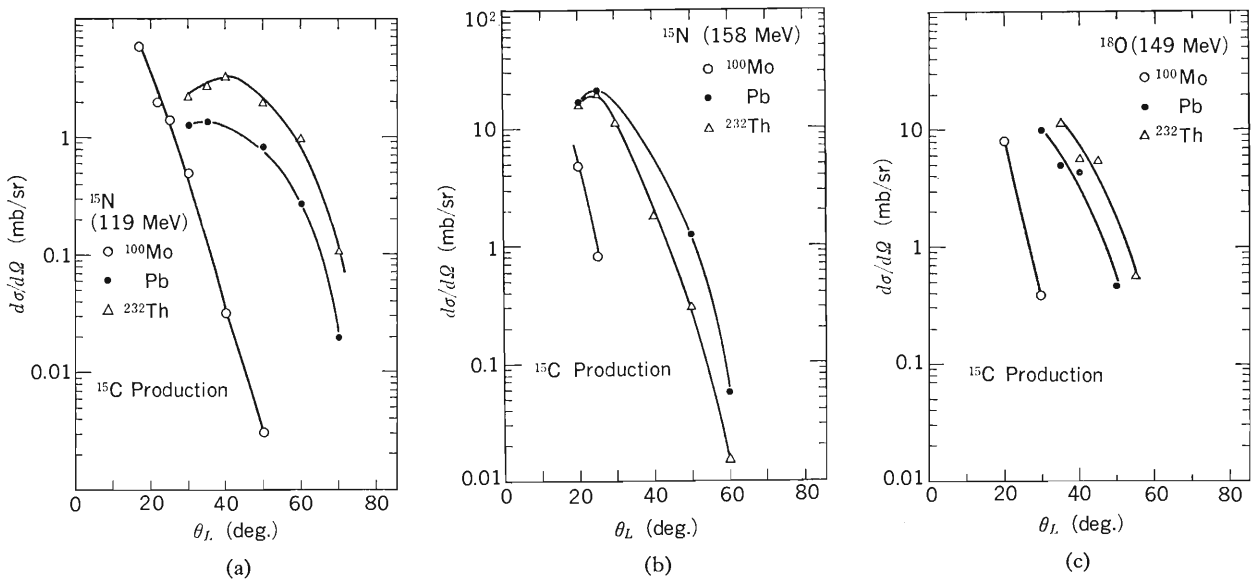

Fig. 1. Angular distributions of ^{15}C in the reactions induced by (a) ^{15}N at 119 MeV, (b) ^{15}N at 158 MeV, and (c) ^{18}O at 149 MeV on the ^{100}Mo (open circles), ^{208}Pb (closed circles), and ^{232}Th (triangles) targets.

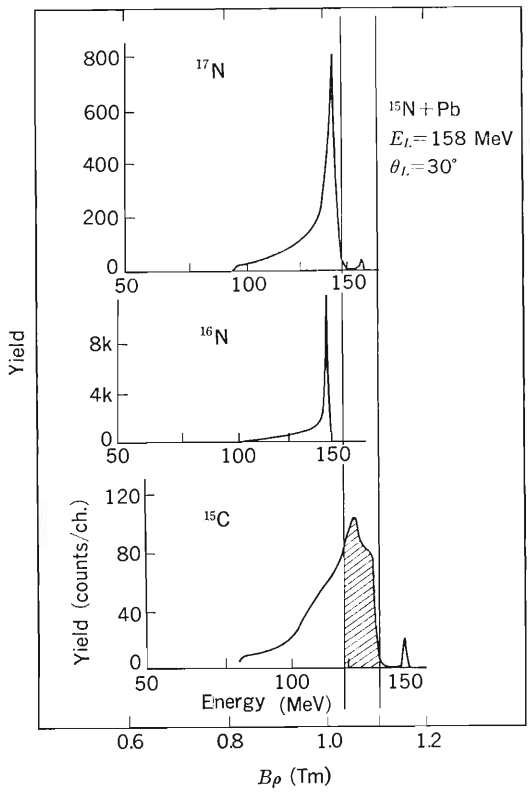

Fig. 2. Schematic illustration of isotope separation using DUMAS, according to the magnetic rigidity $B\rho$. $B\rho$ spectra are shown for the β-emitting products with half-lives ranging from 0.1 s to 100 s. Shaded area represents a possible $B\rho$ window chosen to have largest ^{15}C yield and lowest background contributions.

the new RIKEN accelerator, since the method used here is expected to be extremely powerful when applied to the high-intensity, uniform-velocity fragments obtained in intermediate energy heavy-ion reactions.

References

1) C. A. Gagliardi, G. T. Garvey, J. R. Wrobel, and S. J. Freedman: *Phys. Rev. Lett.*, **48**, 914 (1982); T. Minamisono, K. Takeyama, T. Ishigai, H. Takeshima, Y. Nojiri, and K. Asahi: *Phys. Lett. B*, **130**, 1 (1983).
2) K. Kubodera, J. Delorme, and M. Rho: *Phys. Rev. Lett.*, **40**, 755 (1978).
3) E. K. Warburton, D. E. Alburger, and D. J. Millener: *Phys. Rev. C*, **29**, 2281 (1984).
4) M. Morita: Beta Decay and Muon Capture, W. A. Benjamin Inc., Reading, Massachusetts, p. 173 (1973).
5) K. Asahi, M. Ishihara, H. Kamitsubo, N. Takahashi, Y. Nojiri, T. Minamisono, A. Mizobuchi, and K. Sugimoto: *Nucl. Instrum. Methods*, **220**, 389 (1984).
6) T. Noro, M. Nakamura, H. Sakaguchi, H. Sakamoto, H. Ogawa, M. Yosoi, T. Ichihara, N. Isshiki, M. Ieiri, S. Kobayashi, and H. Ikegami: *RCNP Ann. Rep.*, **1982**, 189 (1983).

RIKEN Accel. Progr. Rep. 18 (1984)

III-2. Atomic and Solid-State Physics

1. Classical Trajectory Monte Carlo Calculation for Collision Processes of $e^+ + (e^-p)$ and $\mu^+ + (\mu^-p)$

A. Ohsaki, T. Watanabe, K. Nakanishi,* and K. Iguchi*

The classical trajectory Monte Carlo (CTMC) method is applied to the pick-up process $A+(BC) \rightarrow (AB)+C$ of a bound light particle by an incident light particle as well as the breakup process $A+(BC) \rightarrow A+B+C$. The calculation has been performed for the cross sections of the processes in the cases of $A=e^+$ and μ^+, $B=e^-$ and $=\mu^-$, and $C=p$.

The three-body problems can always be solved numerically, if we treat them by classical mechanics. An application of classical mechanics, called a classical trajectory Monte Carlo (CTMC) method, has been successful and has been proved to give proper cross sections.[1),2)] The CTMC is a method in which the three-particle motion is solved by Hamilton's canonical equations and the initial quantum states are set statistically using random numbers. The actual physical reason to provide proper cross sections has not been made lucid yet.

In this paper, we calculate the cross sections of

$$e^+ + (e^-p) \rightarrow (e^+e^-) + p \quad (1)$$

$$\rightarrow e^+ + e^- + p \quad (2)$$

and

$$\mu^+ + (\mu^-p) \rightarrow (\mu^+\mu^-) + p \quad (3)$$

$$\rightarrow \mu^+ + \mu^- + p \quad (4)$$

by using the CTMC method. These processes cause a large momentum change between the prior and post channels because the centers of masses of composite particles are largely moved in Processes (1) and (3). For Process (3) the lifetimes of $(\mu^+\mu^-)$ are considered 7×10^{-10}s in the triplet state and 6×10^{-13}s in the singlet state. By comparing the characteristic time of ls orbital of $(\mu^+\mu^-)$, *i.e.*, of the order of 10^{-19}s with the collision time of 1 keV impact, *i.e.*, of the order of 10^{-17}s, the final state of $(\mu^+\mu^-)$ and the collision Process (3) are defined safely.

Comparison with other quantum mechanical calculations[3)-8)] for Processes (1) and (2) and also comparison with recent quantum mechanical calculation[9)] are made and the physical argument for the calculation are also given. The cross sections for positronium formation agree with those obtained by recent quantum mechanical calculations except for low impact velocities. The cross sections for $(\mu^+\mu^-)$ formation are smaller by about 30% in magnitude than those by the quantum mechanical calculations, the first-order Born approximation and the first-order distorted-wave Born approximation. As for practical purpose, there has been some discussion on the feasibility to obtain $(\mu^+\mu^-)$.[10)] If it is successful, this will be much useful for the investigation of quantum electrodynamics. As one of the possible ways to obtain $(\mu^+\mu^-)$, Process (3) is of great interest.

The energy difference between the initial (ground) state and the final (ls) state in Process (1) is 6.80 eV and the threshold energy of Process (2) is 13.6 eV. Processes (1) and (2) are endothermic. Results of calculation for Processes (1) and (2) are shown in Fig. 1. Comparisons with the quantum mechanical calculation are also given there. The CTMC transfer (Process (1)) cross section is a little larger than those by the quantum mechanical calculation except in the energy region less than 25 eV. The general velocity dependence of σ above 30 eV by CTMC is similar to that by the quantum mechanical calculation. The decreasing behavior of transfer cross section is determined by the same physical reason as in charge transfer, *i.e.*, the momentum overlap of the wave functions between the initial and the final bound states. The cross section for breakup process (Process (2)) can be compared with that by the quantum mechanical calculation.

The energy difference in the bound state levels between the initial (ground) state and the final (ls) state in Process (3) is 1.12 keV and threshold energy of Process (4) is 2.52 keV. Both processes (3) and (4) are given in Fig. 2. Comparisons with the recent results by the first-order Born approximation (FBA) and the first-order distorted-wave Born approximation (DWBA)[9)] are also given in Fig. 2. The CTMC

* Department of Chemistry, Waseda University.

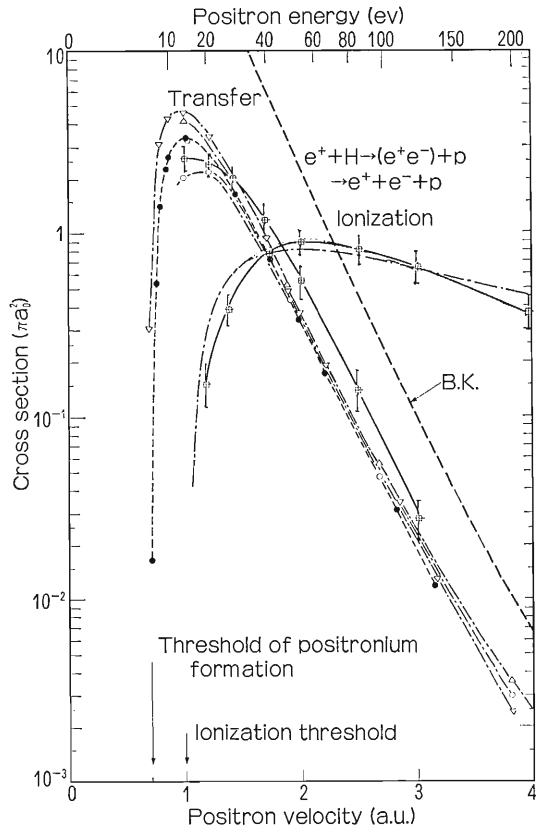

Fig. 1. Positronium formation (transfer, $e^+ + H \rightarrow (e^+e^-) + p$) and breakup (ionization, $e^+ + H \rightarrow e^+ + e^- + p$) cross sections as functions of impact velocity.
Transfer cross section;
—□—: CTMC calculation (present result),
—○—: Partial wave+modified Born approximation by Drachman, McGuire and Omidvar (Ref. 6),
—▽—: First-order Born approximation (Ref. 6),
—△—: Distorted-wave Born approximation without double collision process by Mandel, Guha and Sil (Ref. 4),
—●—: Distorted-wave Born approximation with double collision process by Shakeshaft and Wadehra (Ref. 5),
·····: Brinkman-Kramers method calculation (present result).
Ionization cross section;
—□—: CTMC calculation (present result),
———: Quantum mechanical calculation (Ref. 7).

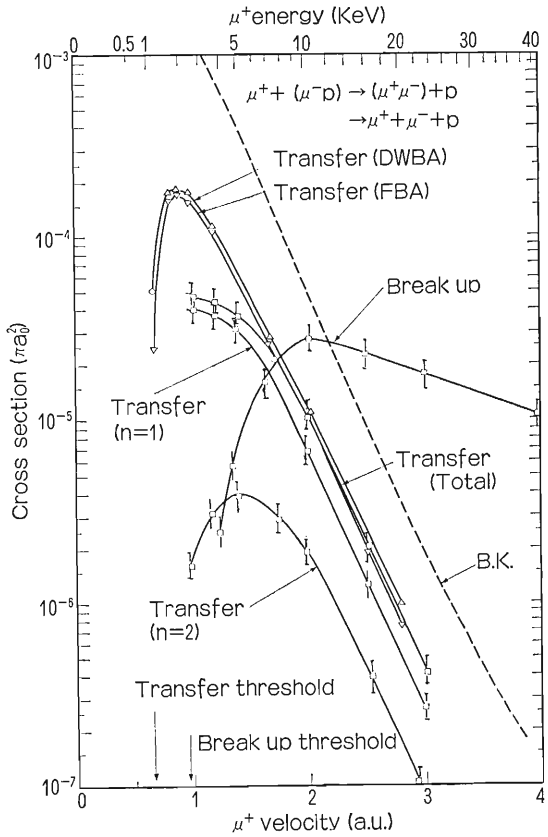

Fig. 2. $(\mu^+\mu^-)$ formation (transfer, $\mu^+ + (\mu^-p) \rightarrow (\mu^+\mu^-) + p$) and breakup ($\mu^+ + (\mu^-p) \rightarrow \mu^+ + \mu^- + p$) cross sections as functions of impact velocity.
Transfer cross section;
—□—: CTMC calculation (present result),
—▽—: First-order Born approximation (Ref. 9),
—△—: The first-order distorted-wave Born approximation by Ma *et al.* (Ref. 9),
·····: Brinkman-Kramers method calculation (present result).
Breakup cross section;
—□—: CTMC calculation (present result).

result is somewhat smaller than those of FBA and DWBA. This feature is different from the positronium formation. In the case of positronium formation, the result by FBA is still smaller than that by CTMC. The rapid decrease in the transfer cross section with impact velocity is due to the same physical reason as that in the cases of positronium formation and charge transfer in ion-atom collision. The breakup cross section can be scaled with that of positron impact.

References

1) R. E. Olson and A. Salop: *Phys. Rev. A*, **16**, 531 (1977).
2) M. Karplus, R. N. Porter, and R. D. Sharma: *J. Chem. Phys.*, **43**, 3259 (1965).
3) A. Rich: *Rev. Mod. Phys.*, **53**, 127 (1981).
4) P. Mandel, S. Guha, and N. C. Sil: *J. Phys. B*, **12**, 2913 (1979).
5) R. Shakeshaft and J. M. Wadehra: *Phys. Rev. A*, **22**, 968 (1980).
6) R. J. Drachman, K. Omidvar, and J. H. McGuire: *ibid.*, **14**, 100 (1976).
7) L. J. Kieffer: *At. Data Nucl. Data Tables*, **1**, 19, 120 (1969).
8) P. W. Bussard, R. Ramuty, and R. J. Drachmann: *Astrophys. J.*, **228**, 928 (1979).
9) Q. Ma, X. Chang, Z. Liu, Y. Liuand, and T. Watanabe: *Phys. Rev.*, submitted.
10) K. Nagamine: Proc. IIIrd LAMPF II Workshops, (eds. J. C. Allred, T. S. Bhatia, K. Rumminer, and B. Talley), LA-9933-C, p. 258 (1983).

RIKEN Accel. Progr. Rep. 18 (1984)

III-2-2. Quantum Mechanical Study of the Process $\mu^+ + (\mu^- p) \longrightarrow (\mu^+ \mu^-) + p$

Q. Ma,* X. Cheng,* Z. Liu,* Y. Liu,* and T. Watanabe

On the occasion when one of the research staff (T. W.) of RIKEN visited Chinese University of Science and Technology (CUST), the theoretical physics group in CUST and the Atomic Physics Laboratory in RIKEN have agreed to make collaborative work in the field of theoretical atomic physics and also in related academic fields. As one of practical projects, we chose the scattering problem of μ^+ on $(\mu^- p)$. This process has been suggested by Nagamine[1] as one of the possible ways to produce $(\mu^+\mu^-)$ atoms from an experimental point of view.

The atomic structures of exotic particles draw much attention from the viewpoint of quantum electrodynamics (QED). They will give us much information concerning QED because the $\mu^+\mu^-$ consists of structureless elementary particles (leptons) and the heavy masses of μ^+ and μ^- enhance various important phenomena related to QED, such as vacuum polarization, Lamb shift, *etc.* As one of the possible ways to produce $(\mu^+\mu^-)$, one can consider the process

$$\mu^+ + (\mu^- p) \rightarrow (\mu^+\mu^-) + p \qquad (1)$$

Here we are formulating and calculating the cross sections for Process (1) by using a quantum mechanical way. Process (1) is characterized by the large mass transfer between the initial and final states and consequently the center of mass of the incident particle is greatly varied. Furthermore, there exists a large endothermic energy difference (1.13 keV) between the initial and final states. In this sense, this is considered to be a typical three-body collision problem. Process (1) has also been investigated by using the classical trajectory Monte Carlo (CTMC) method.[2] The CTMC method treats a three-body problem rigorously in classical mechanics. We can obtain the characteristic features of the three-body problem in the limit of classical mechanics. On the other hand, the quantum mechanical method may show the characteristic features of quantum mechanics. For this reason, if we can obtain similar results for the same process by the first Born approximation or by some improved approximation to those by CTMC, the cross section can be considered reliable.

The first-order Born approximation (FBA) and the first-order distorted-wave approximation (DWBA)[3] have been applied to Process (1). Using the coordinate system illustrated in Fig. 1, the total Hamiltonian of the system can be written as

$$H = -\frac{\hbar^2}{2\mu}\nabla_R^2 - \frac{\hbar^2}{2\nu}\nabla_r^2 - \frac{e^2}{r} + H_i'(\vec{r}, \vec{R})$$

and

$$H = -\frac{\hbar^2}{2\mu'}\nabla_{R'}^2 - \frac{\hbar^2}{2\nu'}\nabla_{r'}^2 - \frac{e^2}{r'} + H_f'(\vec{r'}, \vec{R'})$$

where μ and μ' are reduced masses of the relative motion in the initial and the final states, and ν and ν' are reduced masses of a composite atom in the initial and the final states, respectively. $H_i'(\vec{r}, \vec{R})$ and $H_f'(\vec{r'}, \vec{R'})$ are the interaction Hamiltonians in the initial and the final state.

We approximate the total wave function of the colliding system as

$$\Psi = F_i(\vec{R})\phi_i(\vec{r}) + F_f(\vec{R'})\phi_f(\vec{r'})$$

where $\phi_i(\vec{r})$ and $\phi_i(\vec{r})$ are the ground state eigenfunction of composite particles in the initial and the final state and $F_i(\vec{R})$ and $F_f(\vec{R'})$ the corresponding wave functions of the relative motion.

The equations for $F_f(\vec{R'})$ in FBA and in DWBA are given as

$$\left(-\frac{\hbar^2}{2\mu'}\nabla_{R'}^2 + \varepsilon_f - E\right)F_f^{FBA}(\vec{R'}) + \langle\phi_f(r')|H_i'|F_i^0(R)\phi_i(r)\rangle_{r'} = 0$$

where $F_i^0(\vec{R})$ is a plane wave in the initial state, and

$$\left(-\frac{\hbar^2}{2\mu'}\nabla_{R'}^2 + \varepsilon_f - E\right)F_f^{DW}(\vec{R'}) + \langle\phi_f(\vec{r'})\left|\left(-\frac{\hbar^2}{2\mu}\nabla_R^2 + \varepsilon_i - E\right)\right| \cdot F_i^{DW}(\vec{R})\phi_i(\vec{r})\rangle_{r'} + \langle\phi_f(\vec{r'})|H'_i|F_i^0(R)\phi(\vec{r})\rangle_{r'} = 0$$

From these $F_f^{FBA}(R')$ and $F_f^{DW}(R')$, the scattering amplitude $f(\theta)$ and the total cross section with this $f(\theta)$ can be obtained as

$$\sigma = \frac{v_f}{v_i}\int |f(\theta)|^2 d\Omega$$

* Department of Modern Physics, Chinese University of Science and Technology.

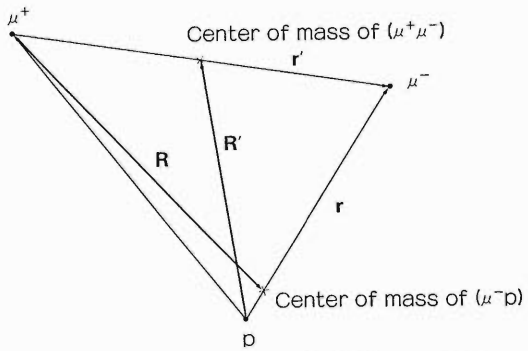

Fig. 1. Coordinate system of colliding particles.

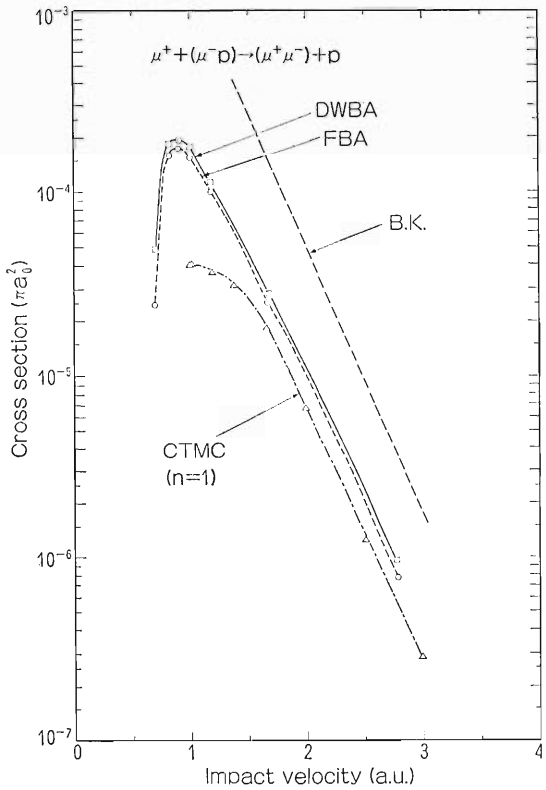

Fig. 2. $(\mu^+\mu^-)$ formation cross section by μ^+ collision on (μ^-p) as a function of impact velocity. ——: the first-order Born approximation (FBA), ·····: the first-order distorted-wave Born approximation (DWBA), –·–△–·–: classical trajectory Monte Carlo method (Ref. 2).

Table 1. $(\mu^+\mu^-)$ formation cross sections by μ^+ impact on (μ^-p).

Impact energy of μ^+	FBA cross section	DWBA cross section
1.13 (keV)	1.29 E-10 (πa_0^2)	1.47 E-10 (πa_0^2)
1.20	2.44 E-05	4.80 E-05
1.70	1.62 E-04	1.79 E-04
2.00	1.77 E-04	1.89 E-04
2.40	1.67 E-04	1.75 E-04
3.60	1.05 E-04	1.09 E-04
7.00	2.54 E-05	2.79 E-05
20.00	7.51 E-07	9.76 E-07
100.00	3.48 E-10	6.02 E-10
1,000.00	7.47 E-16	1.16 E-15

where v_i and v_f are the velocities of the initial and final states, respectively.

Figure 2 and Table 1 show the results of calculation: the cross section for Process (1) as a function of impact velocity in FBA and in DWBA. This shows that the DWBA result is not so much different from the FBA result and these are 30–50% larger than the CTMC results in the impact velocity region of 1.75–3.0 a.u. The BK (Brinkman-Kramers) result is about five times larger than FBA. The CTMC results are considered more reliable than those of FBA and DWBA in the velocity region below 1.7 a.u. From these results we can conclude that the maximum of the cross section lies around 1. a.u. impact velocity (2.0–3.0 keV impact energy) and its magnitude is $3.5\text{–}5.0\times10^{-4}$ a_0^2 (a_0 being the hydrogen Bohr radius) or $2.7\text{–}4.0\times10^{-20}$ cm^2.

References

1) K. Nagamine: Proc. IIIrd LAMPF II Workshop, (eds. J. C. Allred, T. S. Bhatia, K. Ruminer, and B. Talley), LA-9933-C, p. 258 (1983).
2) A. Ohsaki, T. Watanabe, K. Nakanishi, and K. Iguchi: p. 43 in this report.
3) P. Mandal and S. Guha: *J. Phys. B*, **12**, 1603 (1970). FBA and DWBA calculation for $e^+ + H \rightarrow (e^-e^+) + p$

RIKEN Accel. Progr. Rep. **18** (1984)

III-2-3. Transitions of Molecules between High-Angular-Momentum States

I. Shimamura and A. C. Roy

The secondary electrons produced by high-energy charged particles or by ionizing radiation lose their energies, as they penetrate matter, by exciting atoms or molecules. When the energies of the secondary electrons become low ($\lesssim$ a few eV), the main energy-loss mechanism is the rotational excitation of molecules.

The cross section for electron-impact excitation of a molecule from a well-defined rotational state to a well-defined rotational state is difficult to measure directly. This is due to the small rotational level spacings; an electron spectrometer with extremely good energy resolution is required for resolving the rotational lines in the electron energy-loss spectra. On the other hand, reliable theoretical calculations of the cross sections are usually cumbersome.

Molecules in gas at thermal equilibrium are normally distributed among many high rotational states because of small rotational energies. Therefore, transitions from many different rotational states to many different rotational states are taking place in the gas. Calculations of the cross sections for all of these transitions are almost impossible, if separately carried out. Simple relations exist, however, between the cross sections for different transitions $J \to J+\Delta J$ of linear molecules between high-angular-momentum states.[1),2)] A virtue of these relations is that they express the cross sections for the transitions with a fixed ΔJ and with any high J in terms of a single unknown parameter independent of J. We have made an attempt to generalize these relations for symmetric-top molecules, and have reported some results for special cases in the preceding issue of this report.[3)] The following presents the most general results on molecules regarded as symmetric-top rotators.

Symmetric-top rotators are those rigid bodies which have two equal principal moments of inertia. The good quantum numbers of symmetric tops are J for the magnitude of the rotational angular momentum and K and M ($-J \le K \le J$, $-J \le M \le J$) for its projections onto the body-fixed symmetry axis and onto a space-fixed quantization axis. Because the rotational levels are degenerate in M, one may conveniently define the electron-impact excitation cross section $d\sigma(JK \to J'K')/d\omega$ averaged over the initial M and summed over the final M.

Except in very slow collisions ($E \lesssim 10^2$ meV) the molecules hardly rotate during the collision, because the rotational periods of the molecules are much longer than the collision time. Therefore, we may safely employ the adiabatic approximation in which the orientation of the molecular axes is assumed to be fixed during the collision.

The main result obtained in the adiabatic approximation with no further approximations is that

$$d\sigma(JK \to J \pm \Delta J, K+\Delta K)/d\omega = A(|\Delta J|, \Delta K)\,[1 \pm (\Delta J/2J)\{1+(K'^2 - K^2)B(|\Delta J|, \Delta K)\} + O(J^{-2})] \quad (1)$$

with $K'=K+\Delta K$. Both $A(|\Delta J|, \Delta K)$ and $B(|\Delta J|, \Delta K)$ are independent of J and K, and are expressible as linear combinations of the cross sections for $J=K=0$. The two quantities A and B may be calculated theoretically, or may be treated as unknown parameters in analyzing experimental data. Normally, the cross sections are appreciable only for small values of $|\Delta J|$ and $|\Delta K|$, say, smaller than 5 or so. This means that only a small number of independent dynamical quantities determine all the rotational cross sections that play an important part in the energy loss by electrons in a molecular gas. As the initial J becomes large, the cross sections (1) for the $+\Delta J$ and the $-\Delta J$ transitions approach a common limit in a symmetrical way, one from above and the other from below.

In some special cases Eqn. (1) takes even simpler forms:

$$d\sigma(JK \to J \pm \Delta J, K')/d\omega = A(|\Delta J|, \Delta K)\,[1 \pm (\Delta J/2J) + O(J^{-2})] \quad (2)$$

for $|K|=|K'|$, and

$$d\sigma(JK \to JK')/d\omega = A(0, \Delta K)\,[1+O(J^{-2})] \quad (3)$$

for $\Delta J=0$. If the rotator has a plane of symmetry, A and B in Eqn. (1) are independent of the sign of ΔK.

The results reported here are applicable not only to electron-molecule collisions but also to positron-molecule, atom-molecule, and ion-molecule collisions and to photoabsorption and photoionization of molecules, all in the adiabatic approximation. Equations (1)–(3) are useful also in analyzing rota-

tionally unresolved energy-loss spectra of electrons to extract state-to-state rotational transition cross sections.[4)]

References

1) I. Shimamura: *Phys. Rev. A*, **28**, 1357 (1983).
2) I. Shimamura: Chapter II in Electron-Molecule Collisions, (eds. I. Shimamura and K. Takayanagi), Plenum Press, New York p. 89 (1984).
3) I. Shimamura and A. C. Roy: *RIKEN Accel. Progr. Rep.*, **17**, 44 (1983).
4) I. Shimamura: in Wavefunctions and Mechanisms from Electron Scattering Processes, (eds. F. A. Gianturco and G. Stefani), Springer-Verlag, Berlin p. 210 (1984).

RIKEN Accel. Progr. Rep. 18 (1984)

III-2-4. Theoretical Investigation of Molecular Photoionization

S. Hara

Photoionization of molecules is one of the most fundamental problems in the study of interaction of radiation with matter. In this report, photoionization of H_2 is theoretically investigated.

In the present calculation, the final $e+H_2^+$ scattering state has been obtained by taking into account the adiabatic interaction between an electron in the continuum state (photoelectron) and a deformed molecular ion, *i.e.*, by the static exchange approximation with the adiabatic dipole polarization potential added.

The angular distribution of the photoelectron for the transition

$$H_2(X^1\Sigma_g v''=0, J'')+h\nu \rightarrow H_2^+(X^2\Sigma_g v', J')+e$$

has the form[1),2)]

$$I_{v''J''v'J'}(\theta)=\frac{1}{4\pi}\sigma_{v''J''v'J'}[1+\beta_{v''J''v'J'}P_2(\cos\theta)] \quad (1)$$

$$=\sum_j C(J''jJ';000)^2 I_{0j}(\theta) \quad (2)$$

where θ is the angle of an ejected electron measured from the direction of photon-polarization, $\sigma_{v''J''v'J'}$ and $\beta_{v''J''v'J'}$ are the total cross section and asymmetry parameter for the above-mentioned process, J'' and J' are the rotational quantum numbers, and $C(J''jJ';000)$ is the Clebsch-Gordan coefficient. The vibrational quantum numbers v'' and v' are omitted in Eqn. (2) and hereafter. From Eqn. (2), we obtain

$$\sigma_{J''J'}=\sum_j C(J''jJ';000)^2\,\sigma_{0j}$$
$$\sigma_{J''J'}\beta_{J''J'}=\sum_j C(J''jJ';000)^2\sigma_{J''J'}\beta_{J''J'} \quad (3)$$

Vibrationally resolved cross section $\sigma_{v'}$ and asymmetry parameter $\beta_{v'}$ are given by

$$\sigma_{v'}=\sum_{J''J'} g_{J''}\sigma_{J''J'}$$
$$=\sum_{jJ''J'} g_{J''}C(J''jJ';000)^2\sigma_{0j}$$
$$=\sum_j \sigma_{0j},$$
$$\sigma_{v'}\beta_{v'}=\sum_j \sigma_{0j}\beta_{0j} \quad (4)$$

where $g_{J''}$ is the initial rotational distribution with $\sum_{J''} g_{J''}=1$. If the energy of the ejected electron is not so high and the cross section for $\Delta J=J'-J''\geqq 4$ may be neglected, Eqn. (4)

$$\sigma_{v'}=\sigma_{00}+\sigma_{02}$$
$$\beta_{v'}=\left(2.0+\beta_{02}\frac{\sigma_{02}}{\sigma_{00}}\right)\Big/\left(1.0+\frac{\sigma_{02}}{\sigma_{00}}\right) \quad (4')$$

Equation (4') gives a correct value for the photoionization of H_2 by 584 A line, since the cross section for $\Delta J\geqq 4$ is at most 0.3% of that for $\Delta J=0$.[4)]

We now turn to the discussion how we obtain the values of $\beta_{v'}$ from the experimental data of Pollard *et al.*[3)] and Ruf *et al.*[4)] They measured the intensity ratios of the Q and S rotational branches at several angles including 54.7° by using unpolarized radiation. Angular distributions for the Q and S branches in their experiments is given by

$$I_Q(\theta')=\frac{1}{4\pi}\sigma_Q\left[1-\frac{\beta_Q}{2}P_2(\cos\theta')\right]$$
$$I_S(\theta')=\frac{1}{4\pi}\sigma_S\left[1-\frac{\beta_S}{2}P_2(\cos\theta')\right]$$

where

$$\sigma_Q=\sum_{J''} g_{J''}\sigma_{J''J'}, \qquad \sigma_Q\beta_Q=\sum_{J''} g_{J''}\sigma_{J''J'}\beta_{J''J'}$$
$$\sigma_S=\sum_{J''} g_{J''}\sigma_{J''J''+2}, \quad \sigma_S\beta_S=\sum_{J''} g_{J''}\sigma_{J''J''+2}\beta_{J''J''+2} \quad (5)$$

and θ' is the angle between incident radiation and an ejected electron. They used H_2 molecule in which ortho-para ratio is 3 : 1 at very low temperatures (77°K and 140°K). Therefore, for their experiments,

$$g_0=1/4, \quad g_1=3/4, \quad g_{J''}=0\ (J''>2) \quad (6)$$

Substitution of Eqns. (3) and (6) into Eqn. (5) gives

$$\sigma_Q=\sigma_{00}+\frac{3}{10}\sigma_{02}$$
$$\beta_Q=\left(2.0+\frac{3}{10}\beta_{02}\frac{\sigma_{02}}{\sigma_{00}}\right)\Big/\left(1+\frac{3}{10}\frac{\sigma_{02}}{\sigma_{00}}\right)$$
$$\sigma_S=\frac{7}{10}\sigma_{02}, \quad \beta_S=\beta_{02} \quad (5')$$

The ratio of the Q and S branches, $R(\theta')=I_S(\theta')/I_Q(\theta')$ at $\theta'=54.7°$, determines the ratio σ_{02}/σ_{00}

$$R(54.7°)=I_S(54.7°)/I_Q(54.7°)$$
$$=\frac{7}{10}\frac{\sigma_{02}}{\sigma_{00}}\Big/\left(1+\frac{3}{10}\frac{\sigma_{02}}{\sigma_{00}}\right)$$

The measurement of $R(\theta')$ at another angle determines β_{02} since β_{02} is only one unknown parameter left in $R(\theta')$. The asymmetry parameter $\beta_{v'}$ can then be obtained from Eqn. (4').

Table 1. The ratio σ_{02}/σ_{00}, β_{02} and $\beta_{v'}$ for 584 A line.

v'	σ_{02}/σ_{00}	β_{02}	$\beta_{v'}$
0	(a) 0.241	0.749	1.758
	(b) 0.127	0.2	1.797
	(c) 0.103	0.831	1.891
	(d) 0.131 (4)	0.87 (12)	1.868 (14)
	(e) 0.143 (5)	0.89 (15)	1.862 (19)
1	(b) 0.0956	0.2	1.843
	(c) 0.0853	0.782	1.904
	(d) 0.107 (3)	0.75 (11)	1.878 (11)
2	(a) 0.159	0.687	1.820
	(b) 0.0759	0.2	1.873
	(c) 0.0713	0.746	1.917
	(d) 0.088 (2)	0.75 (11)	1.899 (9)
3	(b) 0.0620	0.2	1.895
	(c) 0.0591	0.723	1.929
	(d) 0.075 (2)	0.83 (11)	1.918 (8)
4	(b) 0.0514	0.2	1.912
	(c) 0.0500	0.702	1.938
	(d) 0.062 (2)	0.69 (13)	1.923 (8)
5	(b) 0.0435	0.2	1.925
	(c) 0.0438	0.680	1.945
	(d) 0.054 (2)	0.68 (14)	1.933 (8)

(a) Itikawa,[7] $l=1, 3$; (b) Itikawa *et al.*,[8] $l=1$; (c) Present, $l=1, 3$; (d) Deduced from the data of Ruf *et al.*,[4]; (e) Deduced from the data of Pollard *et al.*[3] Numbers in parentheses are standard deviations. (l is the angular momentum of ejected electron.)

In Table 1, the ratio σ_{02}/σ_{00}, β_{02}, and $\beta_{v'}$ thus deduced from the experimental data are tabulated. The asymmetry parameters $\beta_{v'}$ for small v' are considerably larger than the values obtained by means of relative intensity measurement at several angles.[5),6)] These values are not tabulated. The present results are considered to be reliable more than those of the above experiments since corrections for the reaction volume are not necessary. Table 1 also includes the present and other theoretical values.

References

1) A. D. Buckingham, B. J. Orr, and J. M. Sichel: *Philos. Trans. R. Soc. London, Ser. A*, **268**, 147 (1970).
2) J. M. Sichel: *Mol. Phys.*, **18**, 95 (1970).
3) J. E. Pollard, D. J. Trevor, J. E. Reutt, Y. T. Lee, and D. A. Shirley: *Chem. Phys. Lett.*, **88**, 434 (1982).
4) M-W. Ruf, T. Bregel, and H. Hotop: *J. Phys. B*, **16**, 1549 (1983).
5) J. Kreile and A. Schweig: *J. Electron Spectrosc. Relat. Phenom.*, **20**, 191 (1980).
6) E. D. Poliakoff, J. L. Dehmer, P. M. Dehmer, and A. C. Parr: *Chem. Phys. Lett.*, **96**, 52 (1983).
7) Y. Itikawa: *Chem. Phys.*, **37**, 401 (1979).
8) Y. Itikawa, H. Takagi, H. Nakamura, and H. Sato: *Phys. Rev. A*, **27**, 1319 (1983).

RIKEN Accel. Progr. Rep. **18** (1984)

III-2-5. Doubly Differential Cross Sections for Electron-Impact Ionization of Helium

A. C. Roy and T. Watanabe

When energetic electrons collide with atoms or molecules, one of the important processes that take place is ionization. Ionization cross sections are important quantities in studies of planetary atmospheres, plasma physics, and radiation physics. Detailed knowledge of the process of ionization is also of intrinsic interest because of its fundamental nature, which has not yet been understood completely, however.

When helium atoms, initially in the ground state, are ionized by electron impact, the process with the largest cross section is that in which one electron is ejected and the He^+ ion is left in the ground state

$$e^- + He\ (ls^2\ ^1S) \longrightarrow He^+\ (1s) + 2e^- \qquad (1)$$

The two electrons in the final state are indistinguishable, but it is convenient to refer to the faster electron as the scattered electron and to the slower one as the ejected electron. If the directions of the ejected and scattered electrons are measured in coincidence, together with the energy E_2 of the ejected electron, a triply differential cross section can be defined as

$$\frac{d^3\sigma}{d\hat{k}_1\, d\hat{k}_2\, dE_2} = \sigma(E; E_2, \theta_1\, \theta_2\, \phi_2) \qquad (2)$$

This is a function of the energy of the incident electron E, the energy of the ejected electron E_2, and three angles, namely, the polar angle of scattering of the fast electron θ_1, the polar angle of ejection of the slow electron θ_2 and the azimuthal angle ϕ_2 of the direction of ejection with respect to the plane of scattering.

The doubly differential cross section is given by

$$\frac{d^2\sigma}{d\hat{k}_1\, dE_2} = \int d\hat{k}_2 \frac{d^3\sigma}{d\hat{k}_1\, d\hat{k}_2\, dE_2} \qquad (3)$$

We have obtained the doubly differential cross sections (DDCS) for electron-impact ionization of He in the incident energy range 224.58–2,824.58 eV for the scattering angle of 45°. We have studied only the symmetric case, *i.e.*, the two outgoing electrons have equal energies. The present calculation is based upon the Glauber approximation (GA).[1] The calculation has been performed using the technique of Roy *et al.*[2),3)] that reduces the eight-dimensional Glauber amplitude for the He (e, 2e) He^+ process to a two-dimensional integral.

In the GA, the amplitude for the ionization of He is given by

$$F(\vec{q},\vec{k}_2) = \frac{ik}{2\pi}\int d\vec{b}\, d\vec{r}_1\, d\vec{r}_2\, \phi_f^*(\vec{r}_1, \vec{r}_2) \cdot \Gamma(\vec{b}; \vec{r}_1, \vec{r}_2)\phi_i(\vec{r}_1, \vec{r}_2) e^{i\vec{q}\cdot\vec{b}} \qquad (4)$$

where $\Gamma(\vec{b}; \vec{r}_1, \vec{r}_2) = 1 - \left[\frac{|\vec{b}-\vec{s}|}{b}\right]^{2i\eta}\left[\frac{|\vec{b}-\vec{s}_2|}{b}\right]^{2i\eta}$

$$q = \vec{k} - \vec{k}_1$$

and $\eta = 1/\vec{k}$. Here $\vec{k}$, $\vec{k}_1$, and k_2 are the momenta of the incoming, scattered, and ejected electrons, respectively, and q represents the momentum transfer. $\vec{b}$, $\vec{s}_1$ and $\vec{s}_2$ are the respective projections of the position vectors of the incident particle and the two bound electrons onto the plane perpendicular to the direction of the Glauber path integration. In Eqn. (4), $\vec{q}$, $\vec{b}$, $\vec{s}_1$, and $\vec{s}_2$ are all coplaner and $\phi_i(\vec{r}_1, \vec{r}_2)$ and $\phi_f(\vec{r}_1, \vec{r}_2)$ represent, respectively, the wave functions of the initial and the final states of the target. For the initial state of He we have chosen the following form:

$$\phi_i(\vec{r}, \vec{r}_2) = u(\vec{r}_1)u(\vec{r}_2) \qquad (5)$$

where $$u(\vec{r}) = \lambda^{3/2}\, \pi^{-1/2} e^{-\lambda r} \qquad (6)$$

whereas for the final state of He, we have adopted the following:

$$\phi_f(\vec{r}_1, \vec{r}_2) = 2^{-1/2}\, [\nu(\vec{r}_1)\chi_{\vec{k}_2}^-(\vec{r}_2) + \nu(\vec{r}_2)\chi_{\vec{k}_2}^-(\vec{r}_1)] \qquad (7)$$

where

$$\chi_{\vec{k}_2}^-(\vec{r}) = (2\pi)^{-3/2} e^{\gamma\pi/2}\, \Gamma(1+i\gamma) e^{i\vec{k}_2\cdot\vec{r}_1} F_1(-i\gamma, 1; -i(k_2 r + \vec{k}_2\cdot\vec{r})) \qquad (8)$$

with $$\nu(\vec{r}) = \lambda'^{3/2}\, \pi^{-1/2}\, e^{-\lambda' r} \qquad (9)$$

and $$\gamma = Z/k_2$$

In the present formalism, we have chosen $Z = \lambda$ so that $\phi_i(\vec{r}_1, \vec{r}_2)$ and $\phi_f(\vec{r}_1, \vec{r}_2)$ are orthogonal to each other.

The triply differential cross section is given by

Table 1. Doubly differential cross sections $d^2\sigma/d\hat{k}_1 dE_2$ in units of 10^{-6} a_0^2 Sr^{-1} eV^{-1} in the GA for electron-impact ionization of He for various incident energies E with $E_1=E_2$ and $\theta_1=45°$. $\varepsilon=24.58$ eV.

E-ε(eV)[a]	GA		Experiment[d]
	I[b]	II[c]	
200	317	335	417
300	145	152	195
400	79.8	83.5	107
500	49.4	51.6	65.8
600	33.1	34.5	41.9
800	17.3	18.0	21.0
1,000	10.4	10.7	12.5
1,500	3.99	4.13	4.84
2,000	2.01	2.07	2.36
2,800	0.888	0.981	0.989

a) ε denotes the binding energy defined by E-E_1-E_2.
b) Present Glauber cross sections calculated with the choice 1 wave function for the ground state of He.
c) Present Glauber cross sections calculated with the choice 2 wave function for the ground state of He.
d) Ref. 6.

$$\frac{d^3\sigma}{d\hat{k}_1\, d\hat{k}_2\, dE_2} = \frac{k_1 k_2}{k} |F(\vec{q}, \vec{k}_2)|^2 \qquad (10)$$

The present calculation for DDCS has been performed in two different choices of wave functions for the ground state of He. Choice 1 involves the adoption of the single-parameter product type wave function with a screening parameter $\lambda=1.6875$,[4] whereas choice 2 concerns the use of a similar single-parameter product type wave function with a screening parameter $\lambda=1.618$.[5]

Table 1 presents our GA results for the DDCS along with the corresponding experimental data[6] for the ionization of He by electron impact in the incident energy range 224.58–2,824.58 eV for $E_1=E_2$ and $\theta_1=45°$. We see that the GA cross sections obtained with the choice 1 wave function are always smaller than those obtained with the choice 2 wave function. At an incident energy of 2,824.58 eV the cross section predicted by choice 2 differs from those by choice 1 by 5%, while at an incident energy of 224.58 eV they differ by about 9%. This means that with the decrease in incident energy the difference of cross sections predicted by two choices does not alter substantially. In addition, we notice that in the present case of symmetric geometry the GA cross sections are in reasonably good agreement with experiment. As expected, the agreement decreases at lower energies.

References

1) See, for example, E. Gerjuoy and B. K. Thomas: *Rep. Prog. Phys.*, **37**, 1345 (1974); A. C. Roy and N. C. Sil: *J. Phys. B*, **12**, 497 (1979) and references therein.
2) A. C. Roy, A. K. Das, and N. C. Sil: *Phys. Rev. A*, **23**, 1662 (1981).
3) A. C. Roy, A. K. Das, and N. C. Sil: *ibid.*, **28**, 181 (1983).
4) H. A. Bethe and E. E. Salpeter: Quantum Mechanics of One- and Two-Electron Atoms, Academic, New York p. 147 (1957).
5) See, for example, J. E. Golden and J. H. McGuire: *Phys. Rev. A*, **13**, 1012 (1976).
6) B. van Wingerden, J. T. N. Kimman, M. van Tilburg, and F. J. de Heer: *J. Phys. B*, **14**, 2475 (1981).

RIKEN Accel. Progr. Rep. 18 (1984)

III-2-6. Potential Energy Curves of Na_2^+, K_2^+, and Na_2

H. Sato, M. Kimura,* and R. E. Olson**

The investigation of ion-atom collisions for energies from low to intermediate region (0.1–20 keV/amu) is very active. Recently, several calculations of charge transfer and excitation cross sections by the molecular treatment have been carried out and their results agree well with experimental ones. In this energy range, contribution from valence electrons to the cross sections is dominant and that from core electrons is negligible. Therefore, the methods which replace the effect of core electrons by some analytical potential are very useful to calculate potential energies and wavefunctions of molecular system. The molecular calculation code by the pseudopotential method developed by Bardsley and colleagues[1] was revised to work on FACOM 380 at Computer Center of RIKEN. They adopted a pseudopotential of the Gaussian form given by

$$V(\vec{r})=\sum_{l,m}A_l \exp[-\zeta_l r^2] \mid lm><lm \mid - \frac{\alpha_d}{2(r^2+d^2)^2} - \frac{\alpha_q}{2(r^2+d^2)^3} - \frac{Z_{eff}}{r}$$

where A_l and ζ_l are l-dependent parameters, while α_d, α_q, and d are the dipole and the quadrupole polarizabilities, and the cutoff distance, respectively. Extensive review about the pseudopotential is given by Bardsley.[2] Slater type atomic orbitals (STO's) are used as basis functions. Molecular wavefunction is expressed by a linear combination of the Slater determinants constructed from STO's, not from molecular orbitals.

The potential energy curves of Na_2^+, K_2^+, and Na_2 are calculated by this code. These systems are very interesting and many experimental and theoretical studies have been published. The pseudopotential parameters and the basis functions employed in the calculations are given in Tables 1 and 2. The Na_2^+ molecular ion involves a valence electron. Eighteen STO's are used for σ-state and 8 for π-state, 4 for δ-state. Results are shown in Figs. 1 to 3. It is well known that the pseudopotential method can not be applied to the molecular calculation at a small internuclear distance. As can be seen from

Table 1. Pseudopotential parameters in atomic units.

Na		K	
A_0	10.28195	A_0	9.568369
A_1	2.692467	A_1	2.897295
A_2	−1.452763	A_2	−3.916641
ζ_0	1.294506	ζ_0	0.709742
ζ_1	0.681447	ζ_1	0.363969
ζ_2	1.0	ζ_2	0.748353
α_d	0.945	α_d	5.47
α_q	5.0	α_q	41.5
d	1.1	d	1.5

Table 2. Slater type atomic orbitals employed in the calculation.

Na		K	
Orbital	exponent	Orbital	exponent
2s	0.790	3s	1.135
3s	2.487	3d	0.700
	0.694		0.350
	0.372	4s	1.134
3p	0.721		0.689
	0.558		0.394
3d	1.484	4p	0.820
	0.337		0.556
4s	0.290	5s	0.358

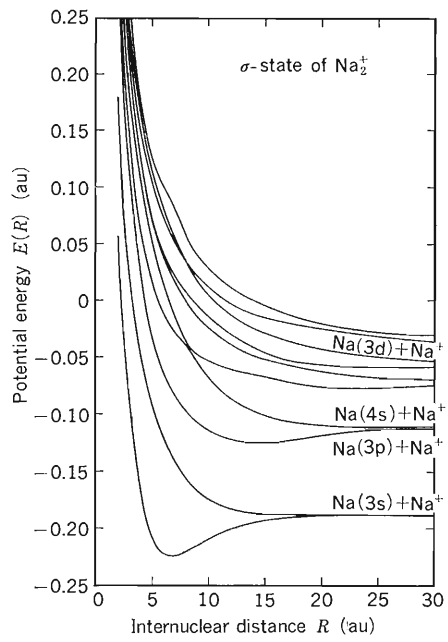

Fig. 1. Potential energy curves of σ-states for Na_2^+.

* JILA, University of Colorado, U.S.A.
** Physics Department, University of Missouri-Rolla, U.S.A.

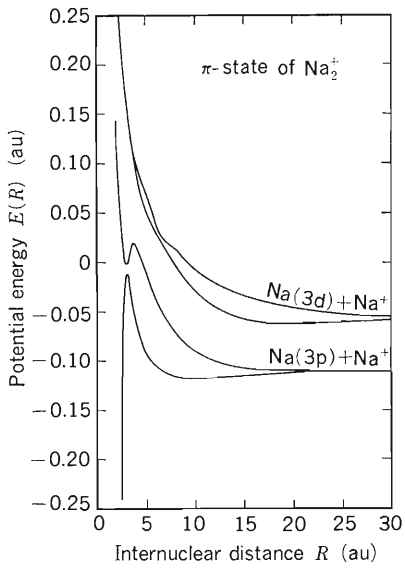

Fig. 2. Potential energy curves of π-states for Na_2^+.

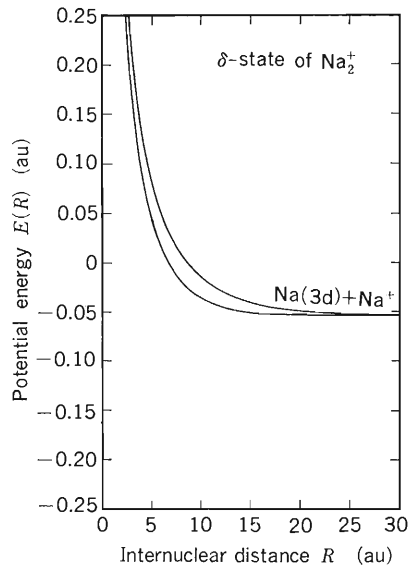

Fig. 3. Potential energy curves of δ-states for Na_2^+.

Figs. 1 to 3, the results for σ- and δ-states are reasonable at all the internuclear distances calculated. On the other hand, the potential energy curves for π-states behave incorrectly in the range of internuclear distance less than 3 atomic units. Fortunately, contribution from the impact parameter less than 3 atomic units to the cross sections is small. Similar results are obtained for the K_2^+ molecular ion. The Na_2 molecule has two valence electrons. Forty two STO's are used as basis functions and 116 configuration functions are constructed for the $^1\Sigma_g^+$ state. The obtained potential energy curves show incorrect behavior similar to those of π-states for Na_2^+ at a small internuclear distance. This comes from the fact that the π^2 configurations are taken into account in the calculations.

References

1) J. N. Bardsley, B. R. Junker, and D. W. Norcross: *Chem. Phys. Lett.*, **37**, 502 (1976).
2) J. N. Bardsley: *Case Stud. At. Phys.*, **4**, 299 (1974).

RIKEN Accel. Progr. Rep. 18 (1984)

III-2-7. Electronic Property of Extremely High-Density and High-Temperature Materials

K. Fujima and T. Watanabe

In inertial-confinement nuclear fusion experiments fuels are compressed to the region of a few hundred times as high as that of usual solid density.[1] During the compression, the fuels are heated as high as thousands of electron volts. Owing to the experimental progress, theoretical investigations on the electronic properties of high-density matters become more than important than ever. The atomic processes in these medium, such as X-ray emission or absorption and a charge stripping process of incident heavy ions, are influenced by these electronic properties. In the study of these problems, there are two difficulties which should be overcome. The first one is how to treat randomly moving and closely existing ions. The second one is the formulation of the electronic states at high temperatures. Many theoretical approaches to these problems have so far been reported using various methods and models.[2] We study the applicability of the DV-X_α calculation to these problems.

Though ions move randomly in mediums, we applied the DV-X_α calculation for the Ne clusters of simple cubic and face-centered cubic at fixed atomic positions (see Fig. 1). The density of Ne is taken to be about one thousand times of the usual solid density and the electron temperature is assumed to be zero for the first step. The physical background of the present cluster model is based on the discussion that the configuration of ions becomes a spacial closest pack at a high-density limit.

In the DV-X_α method, single electron states are calculated on the basis of effective potentials which involves the exchange interaction between electrons in an approximate form of the local potential. The local potential is expressed as being proportional to the cubic root of the local density $\rho(r)$ at each point.[3] The total Hamiltonian of the Ne_8 (simple cubic) or of the Ne_{13} (face-centered cubic) cluster is given by

$$H=-\frac{1}{2}\sum_{j}^{N}\nabla_j^2+U_c+U_{ex}$$

where N is the number of electrons in the cluster and U_c is a Coulomb potential term and U_{ex} represents an exchange interaction term in atomic units. Appropriate boundary conditions for electronic wavefunction are taken as that the charge neutrality can be satisfied within a limited volume considered.

One of our calculation results is given in the Fig. 2, which shows that one electron energies are given as a function of internuclear distance for the face-centered cubic Ne_{13} clusters. For the simple cubic Ne_8 cluster, the energy diagram is not different appreciably from that of Ne_{13}.

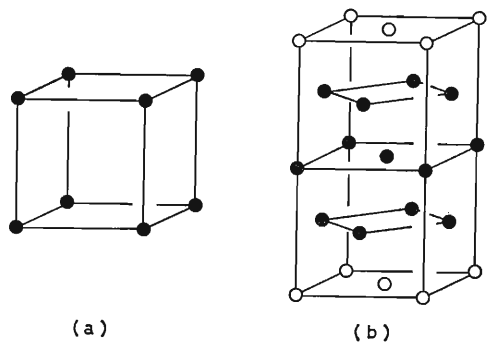

Fig. 1. Model cluster for (a) a simple-cubic Ne_8 cluster and (b) a face-centerd Ne_{13}.

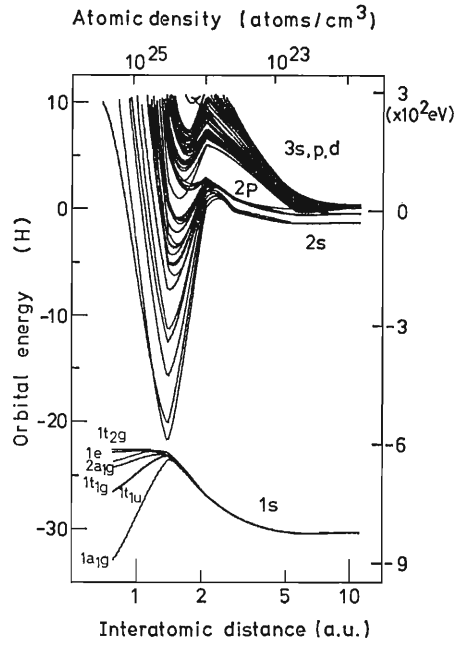

Fig. 2. Orbital energies for a face-centered Ne_{13} cluster as a function of internuclear distance R, or atomic density.

The 2s and 2p orbitals form band-like structure and broaden their energy levels, which can represent the so-called continuum lowering. The core 1s orbital gains energy with decreasing internuclear distance from 10 to 2 a.u., because the screening charge of the nuclear attractive potential increases. At an extremely high density region (higher than 3×10^{23} atoms/cm^3), kinetic energy of electrons rapidly increases because they are confined in a small limited volume. The increase in kinetic energy of outer shell electrons is also seen in the region around 10^{23} atoms/cm^3; this corresponds to the pressure ionization.

We considered the cluster model as each atom is fixed in its minimum position. This model is different from that of high temperature plasma. The motion of ions can be taken into account by considering the deformed clusters which represent their vibrational motion. The effect of high electron temperature can be treated by taking the Fermi-Dirac distribution for electron occupation in their levels. Studies are in progress.

References

1) Ann. Rep. Laser Fusion Program, Institute of Laser Engineering (1980, 1982).
2) J. C. Stewart and K. D. Pyatt, Jr.: *Astrophys. J.*, **144**, 1203 (1965); S. Skupsky: *Phys. Rev. A*, **21**, 1316 (1979); U. Gupta and A. K. Rajagopal: *J. Phys. B*, **12**, L704 (1979).
3) H. Adachi, M. Tsukada, and C. Satoko: *J. Phys. Soc. Jpn.*, **45**, 875 (1976).

RIKEN Accel. Progr. Rep. 18 (1984)

III-2-8. Electron Stripping Cross Sections from Multiply Charged Ions by Hydrogen and Helium Atoms*

S. Karashima, H. Kawagoshi, T. Watanabe, X. Cheng,**
Q. Ma,** Z. Liu,** and Y. Liu**

Recently experimental and theoretical results on the electron loss and capture of ions in matter have become important in the charge equilibrium problems. A few studies have been made in experiments as well as in theoretical calculations[1),2)] for electron loss processes of atomic hydrogen.

In the present paper, we calculate electron stripping cross sections using the binary encounter approximation (BEA). The electron loss process of a multiply charged ion A^{q+} (atomic number Z_1) by collision with a hydrogen or a helium atom B is expressed as

$$A^{q+}+B \rightarrow A^{(q+1)+}+e+B(\Sigma) \qquad (1)$$

After an electron is stripped from the ions, the charge of the ions becomes $(q+1)$ and B does neutral or ionized states, *i.e.*, $B(\Sigma)$ means all electronic states of the atom including ionized states. Our treatment of the electron loss processes is based on BEA, in which the nucleus of B screened by the surrounding electrons collides with electrons in the ion A^{q+}. Here we confine ourselves to the case where the screening effect of the B nucleus by electrons is negligible, *i.e.*, $Z_2 \ll q$ (atomic number Z_2 of B). For the time being we treat $Z_2=1$, 2 and $q \geqq 3$ Z_2. One of the basic approximations in BEA is that the ion interacts with only one electron or nucleus of the target atom at a time.

In the calculation for $Li^{2+}+H$, we have found that BEA will give approximately reliable results of the Process (1).[2),3)] The characteristic feature of this process lies in the large magnitude of momentum transferred to the electrons in the ion A^{q+} on occasions of close collisions with the neutral atom B. Such a collision with large momentum transfer can well be approximated by the classical description. This feature also supports that BEA is considered to be one of the proper methods.

Evaluation of the cross section requires information about the momentum distribution of electrons in the ion. In order to obtain charge stripping cross sections of the ions over the wide range of projectile species, we employ the Thomas-Fermi (TF) statistical method for the calculation of momentum distribution in the ion. In the present paper the momentum distribution $f(p)dp$ and the probability $I_r(p)dp$ of an electron having momentum between p and $p+dp$ at r in the potential $V(r)$ are written by the TF model[4)] as

$$f(p)dp=\int_0^{r(p)} I_r(p)dp\, n(r)\, 4\pi r^2\, dr$$
$$=4\pi \int_0^{E(p)} I_r(p)dp\, n(r) r^2 \left(\frac{dr}{dE}\right) dE \qquad (2)$$

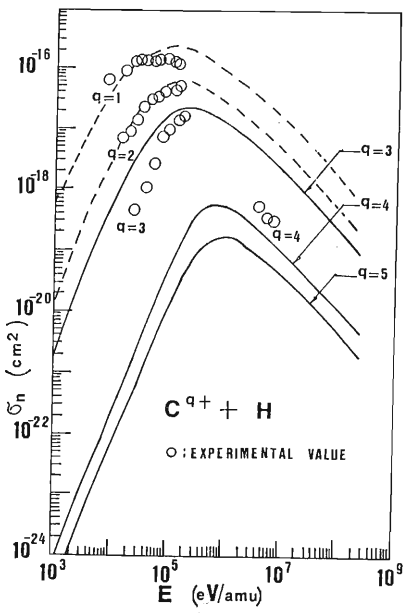

Fig. 1. Electron stripping cross sections for C^{q+} ($q=3$–5) ion by collision with a neutral H atom as functions of impact energy. Dotted lines show the calculated BEA cross sections in the case of target bare nuclear model, *i.e.*, the screening effect of 1s electrons in the hydrogen target is ignored, even when q is not larger than $3Z_2$. The experimental cross section for $C^{q+}+H_2$[7)] is compared directly with our data not multiplied by 2. This is because in the ejection of a tightly bound electrons in the ion the close collision with one of protons in H_2 is required. In this case the other proton lies in a distant position and it is considered to exert a negligible effect on the ejection process of electrons by the first proton.

* Colaborated work of Atomic Processes Laboratory with theoretical physics group at Chinese University of Science and Technology.

** Department of Modern Physics, Chinese University of Science and Technology.

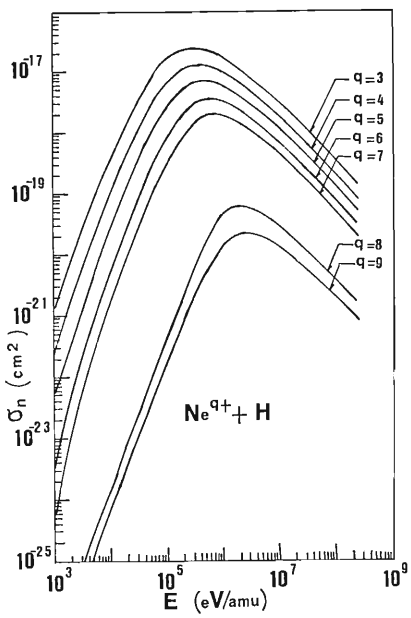

Fig. 2. Electron stripping cross section for Ne^{q+} (q=3–9) ion by collision with neutral H atom as functions of impact energies.

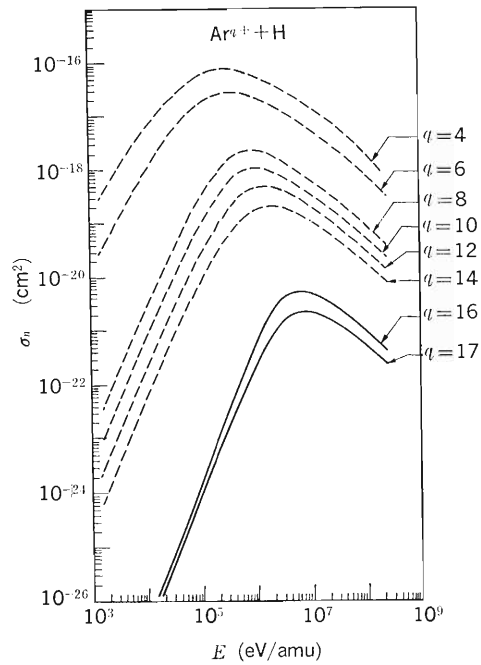

Fig. 3. Electron stripping cross section for Ar^{q+}-ion by collision with neutral H atom. ---- preliminary results.

and

$$I_r(p)dp=\frac{4\pi p^2 dp}{4\pi p_{max}{}^3/3}$$
$$=\frac{3p^2}{p_{max}{}^3}dp \quad \text{for } p\leqq p_{max}$$
$$=0 \quad \text{for } p>p_{max} \qquad (3)$$

where r is considered to be a function of E as $r(E)$ with relation $(p^2/2m)+V(r)=E$ and $n(r)=(8\pi/3h^3)$ $p_{max}{}^3$ (r) is the number of electrons per unit volume at a distance r from a nucleus. The value of the maximum momentum p_{max} is given by the TF equation:

$$\nabla^2 V(r)=-4\pi\, n(r)\, e^2 \qquad (4)$$

$$n(r)=(8\pi/3h^3)\,(2m(V(r)-E_0)^{3/2},$$
$$p_{max}{}^2=V(r)-E_0 \qquad (5)$$

with $V(r)=Z_1e^2/r$ for $r\to 0$, where E_0 is obtained such that $4\pi\int n(r)r^2dr=N$ (N is the number of electrons in the ion).

When we define the ionization cross section, $\sigma_n{}^i(v, w)$, in the laboratory frame for the collision between a nucleus with a velocity v and the atomic electron with a velocity w,[5),6)] the cross section for electron stripping from A^{q+} by collision with the target nucleus $\sigma_n(v)$ is given by

$$\sigma_n(v)=\int_0^\infty \sigma_n{}^i(v, w)\, f(w)\, dw \qquad (6)$$

where $f(w)$, which is determined by the TF model, is a velocity distribution function in Eqn. (2).

Under this background we have made calculations of Process (1) using BEA for C^{q+}, Ne^{q+}, and Ar^{q+} projectile ions (q=3~Z) and a H target atom. Figures 1, 2, and 3 show the preliminary results for electron stripping cross sections. In the case of a He target, the cross section can be expressed by that of H target multiplied by a factor of 4 ($=Z_2{}^2$).

References

1) M. B. Shah and H. B. Gilbody: *J. Phys. B*, **11**, 121 (1978).
2) T. Shirai, K. Iguchi, and T. Watanabe: *J. Phys. Soc. Jpn.*, **42**, 238 (1977).
3) T. Watanabe: Proc. 1984 INS Int. Symp. Heavy Ion Accelerators and Their Application to Inertial Fusion, (eds. Y. Hirao, T. Katayama, and N. Tokuda), Inst. Nuclear Study, Univ. of Tokyo, Tokyo (1984); T. Watanabe: *J. Phys. B*, **18**, L111 (1985).
4) C. A. Coulson and N. H. March: *Proc. Phys. Soc., London, Sect. A*, **63**, 367 (1949).
5) L. Vriens: Case Studies in Atomic Collision Physics I, (eds. E. W. McDaniel and M. R. C. McDowell), North-Holland, Amsterdam, Chap. 6, p. 335 (1969).
6) L. Vriens: *Prcc. Phys. Soc. London, Sect. A*, **90**, 935 (1967).
7) H. Tawara, T. Kato, and Y. Nakai: Electron Capture and Loss Cross Sections for Collisions between Heavy Ions and Hydrogen Molecules, Inst. Plasma Phys., Nagoya Univ., Nagoya, IPPJ-AM-28 (1983).

RIKEN Accel. Progr. Rep. 18 (1984)

III-2-9. Coupling in Ar-Ti, Ar-Co, and Ar-Zn Systems

K. Fujima, T. Watanabe, and Y. Awaya

The target atomic number (Z_2) dependence of simultaneous K-shell and L-shell ionization of Ar ions has been studied by the experimental group of RIKEN.[1),2)] It has been observed that the intensity ratio of Kα hypersatellites to Kα satellites shows oscillatory dependence on Z_2 and it has been suggested that this oscillatory behavior reflects the contribution of $2p_\sigma$–$2p_\pi$ and $3d_\sigma$–$3d_\pi$ rotational coupling electron promotion process to the ionization of K electron of Ar ions in addition to the direct ionization process. The incident energy of Ar ions in lab system was 0.83 MeV/amu, that is $E/\lambda u_k=0.14$, where E is the total energy of Ar ions, λ is the mass of Ar ions in electron mass unit and u_k is the binding energy of K electron of Ar ions (in this estimation, the value for neutral atom is adopted). The purpose of the present work is to estimate this contribution.

The basic idea and the calculation technique have been made by Briggs and Macek[3)] and Watanabe *et al.*[4)] The details of presented calculation are almost the same as those of Watanabe *et al.*[3)] Furthermore, the appropriate extensions have been made in order to treat a hetero-nuclear problem.

The time-dependent wavefunction for Ar(1s) orbitals $\Psi(r, t)$ at the target and projectile distance $\boldsymbol{R}(t)$ with an initial relative velocity of v and impact parameter of b satisfies the time-dependent Schroedinger equation

$$i\hbar\frac{\partial\Psi}{\partial t}=H(r, \boldsymbol{R}(t))\Psi \tag{1}$$

$\Psi(r, t)$ is written as the superposition of $2p_\sigma$ and $2p_\pi$ molecular orbitals with time-dependent coefficients a_1 and a_2 as,

$$\Psi=a_1(t)\phi_{2p\sigma}+a_2(t)\phi_{2p\pi} \tag{2}$$

Substituting Eqn. (2) into Eqn. (1) and omitting the radial coupling term, the coefficient a_1 and a_2 in vector form follow the coupled-equation with the rotational coupling matrix V,

$$i\hbar\frac{d}{dt}A=V(t)A \tag{3}$$

where

$$A=\begin{pmatrix}a_1(t)\\ a_2(t)\end{pmatrix},\quad V=\begin{pmatrix}0 & V_{12}\\ V_{12}^* & 0\end{pmatrix} \tag{4}$$

The matrix element V_{12} is calculated as,

$$V_{12}=\int\phi_{2p\sigma}\frac{vb}{R}L_\zeta\,\phi_{2p\pi}\,d^3x\cdot\exp\left[-i\int(\varepsilon_{2p\sigma}-\varepsilon_{2p\pi})dt/\hbar\right] \tag{5}$$

where L_ζ means rotational operator and $\varepsilon_{2p\pi}$ or $\varepsilon_{2p\sigma}$ stand for one-electron energy and v is the relative velocity of collision system.

The $2p_\sigma$ and $2p_\pi$ molecular orbitals can be written by the anti-bonding and bonding LCAO-MO (molecular orbitals constructed by linear combination of atomic orbitals) of the 1s and 2p orbitals of Ar and those of target atom, *i.e.*, Ti, Co and Zn, with the coefficients C's as,

$$\begin{aligned}\phi_{2p\sigma}&=C_{11}\,\phi_{1s}{}^{Ar}-C_{12}\,\phi_{1s}{}^{T}\\ \phi_{2p\pi}&=C_{21}\,\phi_{2p}{}^{Ar}+C_{22}\,\phi_{2p}{}^{T}\end{aligned} \tag{6}$$

The atomic orbitals ϕ_{1s} and ϕ_{2p} in Eqn. (6) are taken to be the Slater type orbitals with the adjusted orbital exponents ζ_{1s} and ζ_{2p},

$$\begin{aligned}\phi_{1s}&=\sqrt{\frac{\zeta_{1s}{}^3}{\pi}}\,e^{-\zeta_{1s}r}\\ \phi_{2p}&=\sqrt{\frac{\zeta_{2p}{}^5}{\pi}}\,re^{-\zeta_{2p}r}\end{aligned} \tag{7}$$

The orbital exponent $\zeta(R)$ for each atomic orbital is interpolated by the values for isolated and united atom limit using the formula,

$$\frac{\zeta^2(\infty)-\zeta^2(R)}{\zeta^2(\infty)-\zeta^2(0)}=\frac{\varepsilon(\infty)-\varepsilon(R)}{\varepsilon(\infty)-\varepsilon(0)}. \tag{8}$$

The coefficients C's in Eqn. (6) are equal in the homo-nuclear case. In our case C's are derived by minimizing or maximizing the orbital energy $<E>$ of Eqn. (6) with respect to the diatomic Hamiltonian H_d,

Table 1. K-shell ionization probabilities for Ti-Ar, Co-Ar, and Zn-Ar systems.

	$2p_\sigma$–$2p_\pi$ transition probability	Ar 2p component in $2p_\sigma$ state	K-shell ionization probability by BEA (effective charge of projectile)
$Ti+Ar^{+10}$	0.0194 a.u. 0.536×10^{-18} cm^2	0.54	1.5×10^{-18} cm^2 (+14 for Ti)
$Co+Ar^{+10}$	0.0012 a.u. 0.034×10^{-18} cm^2	0.60	1.7×10^{-18} cm^2 (+15 for Co)
$Zn+Ar^{+10}$	0.0010 a.u. 0.028×10^{-18} cm^2	0.32	2.8×10^{-18} cm^2 (+20 for Zn)

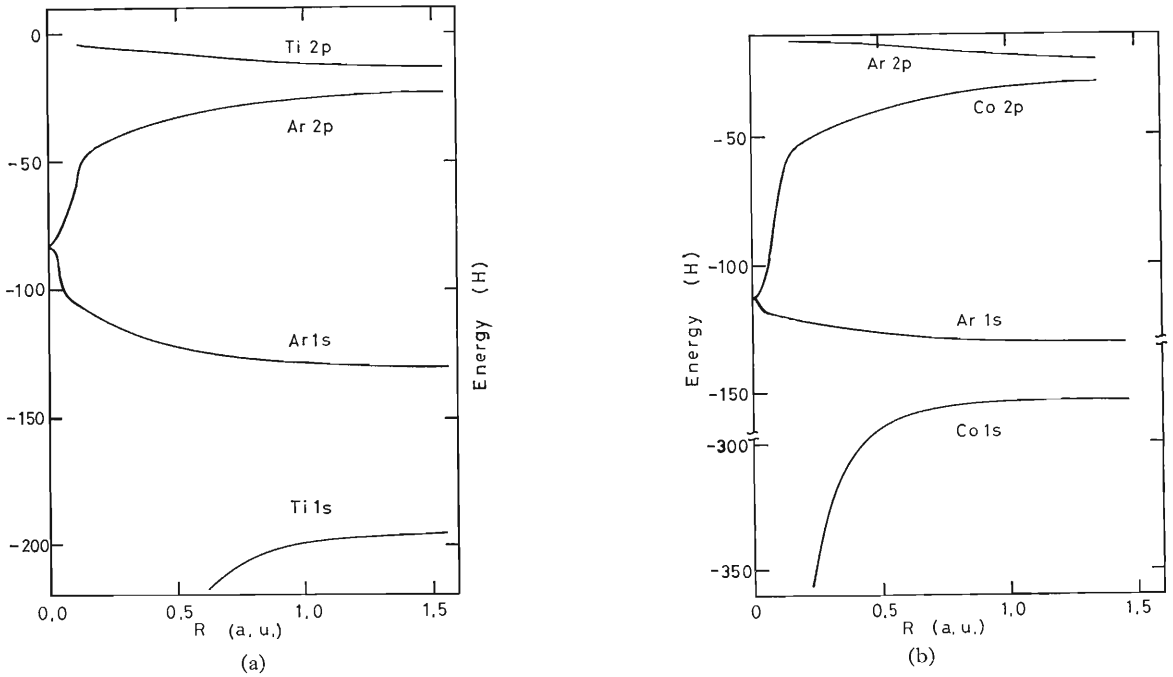

Fig. 1. The correlation diagrams for (a) Ti-Ar and (b) Co-Ar systems.

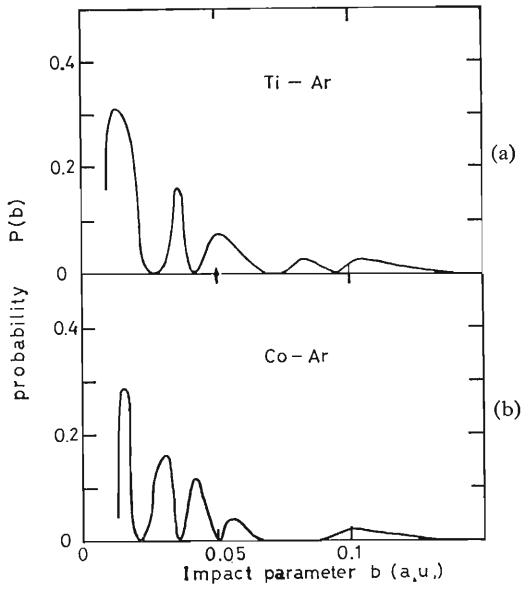

Fig. 2. Dependence of transition probabilities $P(b)$ on impact parameter b at an incident energy of 33 MeV for Ar ion. (a), Ti-Ar; (b), Co-Ar systems.

$$\frac{\partial \langle E \rangle}{\partial t}=0 \tag{9}$$

under the constraint

$$|\phi_{2p\pi}|^2=|\phi_{2p\sigma}|^2=1 \tag{10}$$

where H_d is the summation of the kinetic energy of the electron and the Coulomb attractive potentials from the target Z_1 and projectile atoms Z_2,

$$H_d=-\frac{\hbar^2}{2m}\nabla^2+\frac{Z_1}{r_1}+\frac{Z_2}{r_2} \tag{11}$$

The left hand side of Eqn. (9) and the matrix element of V in Eqn. (4) can be calculated analitically.

$\boldsymbol{R}(t)$ in Eqn. (1) is treated classically and calculated assuming the screened Coulomb scattering potential. The coefficient A is integrated numerically with the initial condition, $C_{1j}=1$ and $C_{2j}=0$ $(j=1, 2)$ for $t=-\infty$.

The transition probability $P(b)$ at the impact parameter b is obtained as,

$$P(b)=|a_2(+\infty)|^2 \tag{12}$$

and the total cross section for K-hole production is given by the integration of $P(b)$ respect to b,

$$\sigma=2\pi\int_0^\infty P(b)\cdot b\cdot db \tag{13}$$

The obtained results are tabulated in Table 1 together with the direct ionization probabilities by calculated binary encounter approximation (BEA).

The obtained K-hole production probabilities by the rotational excitation are large for Ar-Ti and Ti-Co systems and negligibly small for Ar-Zn system. These results can explain the experimental feature qualitatively. However, the calculated cross sections are rather small compared with those by BEA. This may be owing to the over-estimation of BEA probabilities which assume the effective charge for projectiles atoms in somewhat arbitrary way and to neglecting a "the binding effect." The effective charge which is felt by K-electron of Ar ions is estimated by the assumption that the electrons with lower velocities than that of Ar ions can be removed.

Moreover, in the case of the Ar-Co and Ar-Zn systems, the $2p_\pi$ orbitals do not correlate directly to

the atomic 2p orbital for the Ar atom (Fig. 1). Though the transition probabilities between $2p_\pi$ and $3d_\pi$ states by the radial coupling mechanism should be calculated, we took the component of the 2p of the Ar in $2p_\pi$ molecular orbital at $R(0)$ to be a measure for this transition. These values are also tabulated in Table 1.

The difference in the total ionization cross section originate from the difference of energy diagram for Ti, Co, and Zn systems because the coupling matrix elements for V are almost the same in these systems. These features can be visualized in Fig. 2.

References

1) Y. Awaya, T. Kambara, M. Kase, H. Kumagai, J. Urakawa, H. Shibata, T. Masuo, J. Takahashi, and M. Namiki: *RIKEN Accel. Progr. Rep.*, **17**, 49 (1983).
2) Y. Awaya, T. Kambara, M. Kase, H. Shibata, H. Kumagai, K. Fujima, J. Urakawa, T. Masuo, and J. Takahashi: *Nucl. Instrum. Methods*, to be published.
3) J. S. Briggs and J. Macek: *J. Phys. B*, **5**, 579 (1972).
4) T. Watanabe, M. Koike, and F. Minami: *J. Phys. Soc. Jpn.*, **34**, 781 (1973).

RIKEN Accel. Progr. Rep. 18 (1984)

III-2-10. Theory of Radiative Electron Capture I: Nonrelativistic Treatment and Theoretical Paradox

K. Hino, I. Shimamura, N. Toshima, and T. Watanabe

The photon emitting process followed by transfer of an electron from a target to a projectile ion with a high incident velocity

$$A^{q+}+(B^{q'+}+e)\rightarrow(A^{q+}+e)+B^{q'+}+h\nu$$

is called "radiative electron capture (REC)," which is a competitive process with usual non-radiative charge transfer (electron capture (CT)). In high-velocity ionic collisions and also in highly-charged projectile collisions, a role of the REC process becomes essential.[1)]

Shakeshaft and Spruch[2)] investigated a two-body problem in the presence of a radiation field and discussed the so-called "spurious radiation," which was introduced as photon emission based on the motion of a center-of-mass, and they showed the conditions that this spurious radiation term might be deleted. The extension of such conditions to a three-body problem can be easily made. As a result, generally, the only way left to avoid the spurious radiation is to make use of the center-of-mass frame for the three-particle system.

In the formulation of the REC process in the present approach, we take into account nucleus contribution as well as electron contribution to the photon emission. Finally, we have reached a conclusion that the nuclear contribution to the photon emission becomes of the comparable order to the electron contribution. This seems to conflict with our common sense that the intensity of photons originated by the motion of a particle with a mass M and charge q in atomic units is smaller than that of an electron by a factor of q/M.

In our calculation, we assume that one photon is emitted, and that the Coulomb distortion of the wave function of scattered particles is not important, and can be ignored. Furthermore, we use atomic units throughout this report. In accordance with the above assumptions, the transition matrix element for the REC process, T_{fi}, can be written by the first order perturbation (Born) approximation between the initial and final states (χ_i and χ_f) with the interaction H', as

$$T_{fi}=<\chi_f|H'|\chi_i> \tag{1}$$

The asymptotic initial and final states, and, are given in terms of the center-of-mass coordinates r and σ in Fig. 1

$$\chi_i=(2\pi)^{-3}\int d^3\boldsymbol{p}g_i(\boldsymbol{p})\,e^{i\boldsymbol{K}_i\cdot\boldsymbol{\sigma}}e^{i\boldsymbol{p}\cdot\boldsymbol{r}}|0> \tag{2}$$

and

$$\chi_f=(2\pi)^{-3}\int d^3\boldsymbol{q}g_f(\boldsymbol{q})e^{i\left(\frac{a}{\mu}\boldsymbol{K}_f+b\boldsymbol{q}\right)\cdot\boldsymbol{r}}e^{i(a\boldsymbol{K}_f-\boldsymbol{q})\cdot\boldsymbol{\sigma}}|1> \tag{3}$$

where $|0>$ and $|1>$ are the vacuum photon state and the one-photon state, g_i and g_f the initial and final wave functions of bound states in momentum space, respectively, and K_i and K_f the incident and recoil momenta, respectively. Writing the masses of the projectile ion, the target nucleus, and the bound electron as m_1, m_2, and 1, respectively, we will use the notations a, b, and μ as $a=m_1/(m_1+1)$, $b=m_2/(m_2+1)$, and $\mu=m_1(m_2+1)/(m_1+m_2+1)$. H' is taken as the interaction between particles and the radiation field, which is given by

$$H'=-\frac{1}{2}\sum_{i=1}^{3}\frac{Z_i}{m_ic}\boldsymbol{A}(i)\cdot\hat{\boldsymbol{p}}_i \tag{4}$$

where Z_i and $\hat{\boldsymbol{p}}_i$ are the charge and the momentum operator of the i-th particle, respectively, c the velocity of light, and $\boldsymbol{A}$ the vector potential. By the use of dipole interaction in Eqn. (4), the transition matrix element, T_{fi}, is expressed by

$$T_{fi}=-\sqrt{\frac{\pi}{2\omega}}\left[\boldsymbol{e}\cdot\left\{\mu\left(\frac{Z_1}{m_2}-\frac{bZ_2}{m_2}+1-b\right)\boldsymbol{v}-\left(1+\frac{Z_2}{m_2}\right)\boldsymbol{p}_i\right\}\right]g_i(\boldsymbol{p}_i)g_f^*(\boldsymbol{q}_f), \tag{5}$$

where $\boldsymbol{e}$ is the polarization vector of photon, and

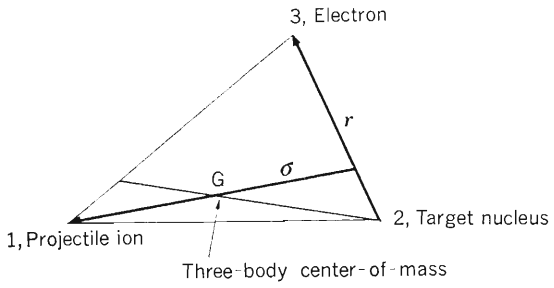

Fig. 1. The independent coordinate set in the center-of-mass system

ω the energy of an emitted photon, $\boldsymbol{p}_i$ and $\boldsymbol{q}_f$ the initial and final momenta of a bound electron given by $\boldsymbol{p}_i=\boldsymbol{K}_f-b\boldsymbol{K}_i$ and $\boldsymbol{q}_f=a(\boldsymbol{p}_i-\boldsymbol{v})$, respectively, where $\boldsymbol{v}=\boldsymbol{K}_i/\mu$. By using the peaking approximation, that is, $g_i(\boldsymbol{p}_i)$ is negligible except for $\boldsymbol{p}_i\sim 0$, the photon distribution cross section is given by

$$\left(\frac{d^2\sigma}{d\omega d\Omega}\right)=\frac{a^3\pi^2\omega}{c^3v}(\boldsymbol{e}\cdot\boldsymbol{v})^2\left[\mu\left(\frac{Z_1}{m_1}-\frac{bZ_2}{m_2}+1-b\right)\right]^2|g_f(-a\boldsymbol{v})|^2\times\int d^3\boldsymbol{p}_i|g_i(\boldsymbol{p}_i)|^2\delta\left(\omega-\frac{1}{2}a\boldsymbol{v}^2+a\boldsymbol{p}_i\cdot\boldsymbol{v}+\epsilon_f-\epsilon_i\right) \quad (6)$$

Where Ω is the solid angle of the emitted photon, ϵ_f and ϵ_i are the initial and final energies of the bound electron, respectively. The term in the square brackets indicates that the intensity of photon emitted from nuclei is of comparable order in magnitude to that from an electron, and hence the radiation intensity of the REC depends on the masses of a target and a projectile ion, respectively, which is here called "isotope effect." For instance, REC intensities $\rho(^4\mathrm{He}/^3\mathrm{He})$ *i.e.*, isotope effect between collision systems, $\mathrm{Ne}^{q+}+{}^3\mathrm{He}$ and $\mathrm{Ne}^{q+}+{}^4\mathrm{He}$, is easily estimated as nearly equal to be two. However such an isotope effect was not observed within seven percent error in measurements by the experimental group of RIKEN with 110 MeV Ne^{10+} and Ne^{q+} bomberdment.[3] This curious and non-selfcontradictory effect cannot be theoretically explained without a three-body fully covariant treatment, which will be indicated in a succeeding report.

References

1) J. S. Briggs and K. Dettmann: *Phys. Rev. Lett.*, **33**, 1123 (1974).
2) R. Shakeshaft and L. Spruch: *ibid.*, **38**, 175 (1977).
3) T. Kambara, Y. Awaya, M. Kase, H. Kumagai, H. Shibata, and T. Tonuma: p. 77 in this report.

RIKEN Accel. Progr. Rep. 18 (1984)

III-2-11. Theory of Radiative Electron Capture II: Covariant Treatment

K. Hino, I. Shimamura, and T. Watanabe

In the preceding report about the nonrelativistic radiative electron capture (REC) process, we described the "isotope effect" based on the photon emission from the nuclei of the three-body system, which was, however, not observed. The present report will show the theoretical explanation of this paradox from the point of fully covariant treatment.

Firstly, the definitions of relativistic notations are introduced. A scaler product of four dimensional vectors, $A=(\boldsymbol{A}, A_0)$ and $B=(\boldsymbol{B}, B_0)$, is represented as $AB=\boldsymbol{AB}-A_0B_0$. Dirac's gamma matrices are defined as $\boldsymbol{\gamma}=-i\beta\boldsymbol{\alpha}$, and $\gamma_4=\beta$, all of which are hermite and satisfy the anti-commutation relation: $\{\gamma_\mu, \gamma_\nu\}=2\delta_{\mu\nu}$, $(\mu, \nu=1\sim4)$. In addition, free propagation functions of half-spin fermion and photon are given as:

$$S_F(x-x')=<0|T[\psi(x), \bar{\psi}(x')]|0> =-\frac{i}{(2\pi)^4}\int d^4p \frac{e^{ip(x-x')}}{ip\gamma+m-i\epsilon} \quad (1)$$

and

$$D_{F,\mu\nu}(x-x')=<0|T[A_\mu(x), A_\nu(x')]|0> =\frac{i}{(2\pi)^4}\int d^4k \frac{\delta_{\mu\nu}e^{ik(x-x')}}{k^2-i\epsilon} \cdot(\text{Feynman gauge}) \quad (2)$$

respectively, where ψ and A_μ are the free field operators of a half-spin fermion and photon, respectively, $\bar{\psi}$ is defined as $\psi^+\gamma_4$, and T is Wick's chronological operator. These two propagation functions should fulfill the following relations:

$$(\gamma\partial_x+m)S_F(x-x')=-i\delta^{(4)}(x-x') \quad (3)$$

and

$$\Box_x D_{F,\mu\nu}(x-x')=-i\delta_{\mu\nu}\delta^{(4)}(x-x') \quad (4)$$

We use the natural units ($\hbar=c=1$) throughout this report, and we consider that fermions always have a half-spin unless otherwise stated.

Some preliminaries for the covariant treatment are introduced below. The interaction Lagrangian density of fermions and photons, L_{int}, is defined as

$$L_{int}=j_\mu A_\mu \quad (5)$$

where j_μ is the electromagnetic current of a fermion, given by $iZ\bar{\psi}\gamma_\mu\psi$, and Z is the charge of the fermion. Here the external c-number source J_μ is introduced in Eqn. (5) as a parameter. Therefore, the interaction Lagrangian density is redefined as

$$L_{int}=j_\mu A_\mu-J_\mu A_\mu \quad (6)$$

By the use of Eqn. (6), S-matrix, $<0|U(\infty,-\infty)|0>$, is given as

$$<0|U(\infty, -\infty)|0> =<0|T\exp\left(i\int d^4x L_{int}(x)\right)|0> \quad (7)$$

and Schwinger's functional derivative[1] about J_μ is defined as

$$\frac{\delta U[J_\mu]}{\delta J_\mu(x)} =\lim_{\epsilon\to0}\frac{U[J_\mu(y)+\epsilon\delta^{(4)}(y-x)]-U[J_\mu(y)]}{\epsilon} \quad (8)$$

The use of Eqn. (8) can lead us to the following convenient relation:

$$i\frac{\delta}{\delta J_\mu(x)}T[U, \alpha, \beta, \ldots] =T[U, A_\mu(x), \alpha, \beta, \ldots] \quad (9)$$

where α and β stand for field operators. Another powerful relation for our purpose is the reduction formula in the interaction representation, given by

$$(\gamma\partial_x+m)T[\psi(x), \ldots] =-i\frac{\delta}{\delta\bar{\psi}(x)}T[\ldots] \quad (10)$$

and

$$\Box_x T[A_\mu(x), \ldots] =i\frac{\delta}{\delta A_\mu(x)}T[\ldots] \quad (11)$$

By the way, it is generally known, the fundamental equation for the nonrelativistic three-body potential scattering is Faddeev's equation, which is expressed after some reformations (Weinberg's equation),

$$\Psi_A^{(+)}=\phi_A+[G_{ca}V_{ca}G_0(V_{ab}+V_{bc}) +(\text{cyclic combination for a, b, and c})]\Psi_A^{(+)} \quad (12)$$

where subscripts a, b, and c are the labels of three particles, that is, projectile ion, target nuclei, and electron, respectively, all of which are denoted in the previous report[2] as 1, 2, and 3. A subscript, A, represents the channel, a+(b+c), ϕ_A and $\Psi_A^{(+)}$

indicate the initial asymptotic wave function and scattering one in channel A, respectively. V_{ij} is the Coulomb potential between particles, i and j. G_0 and G_{ij} stand for the three-body Green functions of free particles and traveling particles with feeling potential V_{ij}, respectively. Now we establish the grand assumption from the viewpoint of Eqn. (12) that the three-body covariant propagator, K_{abc}, may follow the Weinberg-like relativistic equation denoted by:

$$\begin{aligned}K_{abc}(123:456)&=S_{Fa}'(1:4)\,G_{bc}(23:56)\\&+\int\prod_{j=1'}^{12'}d^4x_j[G_{ca}(13:1'3')\,S'_{Fb}(2:2')\,I_{abc}^{\leftarrow}\\&\cdot(1'2'3':4'5'6')\times S'_{F,abc}(4'5'6':7'8'9')\\&\cdot\{I_{abc}^{\leftarrow}(7'8'9':10'11'12')+I_{abc}^{\leftarrow}(7'8'9':\\&\cdot10'11'12')\}+(\text{cyclic combination for a, b, and c})]\,K_{abc}(10'11'12':456)\end{aligned}\tag{13}$$

where S'_{Fa} indicates the one-body propagator of fermion, a, and G_{ac} represents the two-body propagator of fermions, a and c, which follows two-body Bethe-Salpeter (B-S) equation.[3] And the all propagation functions in Eqn. (13) are defined explicitly as:

$$\begin{aligned}S'_{Fa}(x:x')&=<0|T[U\phi_a(x)\\&\cdot\bar{\phi}_a(x')]|0>/<0|U|0>\end{aligned}\tag{14}$$

$$\begin{aligned}S'_{F,abc}(xyz:x'y'z')&=S_{Fa}(x:x')\\&\cdot S'_{Fb}(y:y')\,S'_{Fc}(z:z')\end{aligned}\tag{15}$$

$$\begin{aligned}G_{ac}(xz:x'z')&=<0|T[U\phi_a(x)\,\phi_c(z)\\&\cdot\bar{\phi}_a(x')\,\bar{\phi}_c(z')]|0>/<0|U|0>\end{aligned}\tag{16}$$

$$\begin{aligned}K_{abc}(xyz:x'y'z')&=<0|T[U\phi_a(x)\,\phi_b(y)\\&\cdot\phi_c(z)\,\bar{\phi}_a(x')\,\bar{\phi}_b(y')\,\bar{\phi}_c(z')]|0>/\\&\cdot<0|U|0>\end{aligned}\tag{17}$$

$$\begin{aligned}I_{abc}^{\leftarrow}(xyz:x'y'z')&=i\overleftarrow{D}(x-x')\\&\cdot I_{bc}(yz:y'z')\end{aligned}\tag{18}$$

and so on, where $\overleftarrow{D}_a(x-x')=(\gamma^a\overleftarrow{\partial}_x+m_a)\delta^{(4)}(x-x')+i\Sigma^*(x,x')$, Σ^* is the self-energy of fermion, a, and I_{bc} represents the interaction kernel included in the fermion type B-S (Bethe-Salpeter) equation. Equation (13) can be symbolically rewritten as

$$\begin{aligned}K_{abc}(123:456)&=(1-F_{abc}(123))^{-1}\\&\cdot S'_{Fa}(1:4)\,G_{bc}(23:56)\end{aligned}\tag{19}$$

Now the three-body REC propagator $K_{abc,\mu}$ is defined by the use of Schwinger's functional derivative method, Eqn. (9), as

$$\begin{aligned}K_{abc,\mu}(0;123:456)&=<0|U|0>^{-1}\cdot i\frac{\delta}{\delta J_\mu(0)}\\&\cdot[<0|U|0>K_{abc}(123:456)]\end{aligned}\tag{20}$$

The grand assumption, Eqn. (13), can give us the explicit formal solution of $K_{abc,\mu}$ by using Eqn. (20) as:

$$\begin{aligned}K_{abc,\mu}(0;123:456)&=(1-F_{abc,\mu}(123))^{-1}\\&\cdot F_{abc,\mu}(0;123)\,K_{abc}(123:456)\\&+(\text{propagators which have no contributions to } S\text{-matrix of REC})\end{aligned}\tag{21}$$

where

$$\begin{aligned}F_{abc,\mu}(0;123)&=<0|U|0>^{-1}\cdot i\frac{\delta}{\delta J_\mu(0)}\\&\cdot[<0|U|0>F_{abc}(123)]\end{aligned}\tag{22}$$

S-matrix of REC can be easily obtained from Eqn. (21) by the following procedure: t_0, t_1, t_2, $t_3\rightarrow+\infty$ and t_4, t_5, $t_6\rightarrow-\infty$. The final form of REC S-matrix in the lowest-order in momentum space is reduced to

$$\begin{aligned}S_{fi}&=(2\omega)^{-1/2}\,V^{-5/2}\,(2\pi)^8\\&\times\bar{u}_b(K')\,\bar{\phi}_{ac}(q_f,P')\,Mu_a(K)\\&\cdot\phi_{bc}(q_i,P)\,\delta^{(4)}(K+P-K'-P'-k)\end{aligned}\tag{23}$$

where V is the normalization volume, u_a and $\bar{u}_b$ are the free Dirac spinors, ϕ_{bc} and $\bar{\phi}_{ac}$ are the B-S amplitudes and M represents the lowest-order interaction of REC process, given by

$$\begin{aligned}M&=Z_a(\gamma^a e)(-iK'\gamma^b+m_b)\{-i(P-K')\\&\cdot\gamma^c+m_c\}+(-iK\gamma^a+m_a)\,Z_b(\gamma^b e)\\&\cdot\{-i(P'-K)\gamma^c+m_c\}+(-iK\gamma^a+m_a)\\&\cdot(-iK'\gamma^b+m_b)\,(\gamma^c e)\end{aligned}\tag{24}$$

Here Z_n and m_n are the charge and mass of the n-th particle, and e polarization vector of emitted photon. Vectors, q_i, q_f, K, K', P, P', and k, are ex-

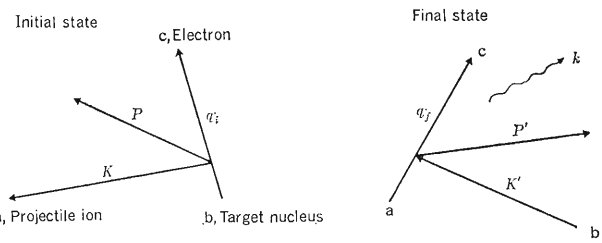

Fig. 1. The explanation of the initial and the final energy-momentum vectors. q_i: relative vector of the composite particle (b-c), q_f: relative vector of the composite particle (a-c), K: incident vector of the particle a, K': recoil vector of the particle b, P: barycentric vector of the composite particle (b-c), P': barycentric vector of the composite particle (a-c), k: emitted photon vector.

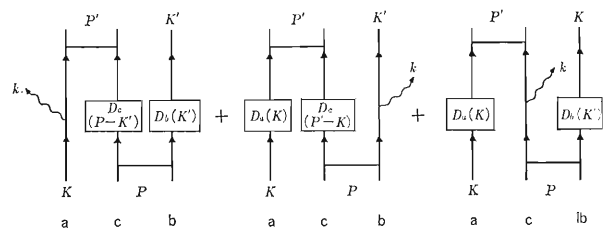

Fig. 2. Feynman diagrams of the lowest-order REC S-matrix $D_k(p)=-ip\gamma^k+m_k$ (k=a, b, and c).

plained in Fig. 1, and the Feynman diagrams are described in Fig. 2. Under the mass-on shell conditions, $\bar{u}_b(K')(iK'\gamma^b+m_b)=0$ and $(iK\gamma^a+m_a)u_a(K)=0$, we take the nonrelativistic limit in Eqn. (24) by the use of the approximations, $<\gamma>\sim-ip/m$ and $<\gamma_4>\sim1$, where $<\gamma>=<u^+\gamma u>$, to reach the following conclusion in the center-of-mass frame, that is, $P+K=P'+K'+k=0$;

$$<M>\sim 4i\left[\frac{m_b m_c}{m_a}Z_a-\frac{m_a m_c}{m_b+m_c}Z_b-\frac{m_a m_b}{m_b+m_c}Z_c\right](e\cdot\mu V) \qquad (25)$$

where the reduced mass μ follows the preceding report, and V is the relative velocity in the lab. frame.

On the other hand, another interaction M' instead of M is defined for the practical purpose as

$$M'=Z_a(\gamma^a e)+Z_b(\gamma^b e)+Z_c(\gamma^c e) \qquad (26)$$

which, as a matter of fact, leads to the following result in the center-of-mass frame:

$$<M'>\sim i\left[\frac{Z_a}{m_a}-\frac{Z_b}{m_b+m_c}-\frac{Z_c}{m_b+m_c}\right](e\cdot\mu V) \qquad (27)$$

This is exactly the same answer with that in the preceding report. Therefore, the interaction, Eqn. (26), cannot avoid to cause the "isotope effect," but we can never arrived at this result from the fully covariant treatment. In such a sense, the "isotope effect" would be interpreted as the incorrect property of non-covariant propagator. The estimations of Eqn. (24) in other frames are straightforward but this will be given somewhere else. The relativistic cross section of REC process is now formulating from Eqn. (24).

References

1) J. Schwinger: *Proc. Natl. Acad. Sci. U.S.A.*, **37**, 452, 455 (1951).
2) K. Hino, I. Shimamura, N. Toshima, and T. Watanabe: p. 62 in this report.
3) E. E. Salpeter and H. Bethe: *Phys. Rev.*, **84**, 1232 (1951).

RIKEN Accel. Progr. Rep. 18 (1984)

III-2-12. Calculation of the L_{23}-M_1M_1 Auger Energy and the Relative Auger Rates for Ar^{6+}

M. Sekiya, T. Noro,* F. Sasaki,* T. Watanabe, and K. Ohno*

Recently there has been considerable interest in the Auger electrons produced by heavy ion atom collisions. Much information can be obtained for energy level of highly ionized atom and ionization mechanism from line positions and Auger rates. Matsuo *et al.*[1] have measured the argon L-shell Auger spectrum by 4.3 MeV Ar^{3+} impact on Ar. They have obtained a spectrum characterized by two sharp peaks located at about 101 eV (A peak) and 111 eV (B peak). Based on the SCF (self consistent field) calculation of Larkins,[3] they identified these two sharp peaks A and B with the L_{23}-M_1M_1 Auger transitions. They further carried out high-resolution experiments[2] for the A and B peaks. These peaks split into two peaks (A_1, A_2 and B_1, B_2), and the B_1 and B_2 peaks have complex structure. Their assignments of the A and B peaks are probably correct, but detailed assignments of the B_1 and B_2 peaks and the Auger rates have not been attempted. We try to classify the nature of the B_1 and B_2 peaks by using the configuration interaction (CI) method and calculate relative Auger rates.

In this work, we consider the Auger process of

$$Ar^{6+}\ (1s^2, 2s^2, 2p^5, 3s^2, 3p;\ {}^1S,\ {}^1P,\ {}^1D,\ {}^3S,\ {}^3P,\ {}^3D) \rightarrow Ar^{7+}\ (1s^2, 2s^2, 2p^6, 3p;\ {}^2P)+e^-$$

corresponding to the B peak, and estimate approximate relative Auger rates for the B lines.

The calculation is performed as follows. All CI calculations are single and double excitation CI (the 1 s orbital is frozen) from a single reference state. The atomic orbitals are obtained by the natural orbital (NO) iteration and two sets of the Slater exponents of the basis functions are optimized for the Ar^{7+} final state and the Ar^{6+} ^3P initial hole state. In the CI calculation of the initial hole states, the configuration state functions (CSF's) for open channels (*e.g.* $Ar^{7+}+e^-$) are not included. The calculated Auger energies are corrected for the spin-orbit effect, whose parameter is obtained from the experimental data of Ar^{7+} L_{23}-M_1M_1 Auger energies.[2]

For the Auger rates, we assume that the continuum wave function of the ejected electron is the Coulomb wave function which is normalized to

$$\cos\ (kr+\delta+(q/k)\ \ln\ 2\,kr-\pi(l+1)/2)$$

as r tends to ∞, where k is the wave number, q is the net charge for the final state, l is the angular momentum for the ejected electron, and δ is the phase shift. The Auger rates is expressed as[4]

$$W_{fi}=(4/k)\ |\ <f\ |\ V\ |\ i>\ |^2$$

where

$$V=\sum_{i=j}1\ /\ r_{ij}$$

and $|f>$ and $|i>$ are the final wave function (including the ejected electron) and the initial wave function, respectively. In this calculation of the Auger rates, $|f>$ and $|i>$ are assumed to be a single configuration, because the initial and the final states wave functions calculated can be expressed almost as a single configuration. Relative Auger rates are calculated, by assuming that the creation probabilities of producing the Ar^{6+} hole states by the collision are the same for all the initial hole states. The numerical integration of the radial wave functions is performed. Results of the Auger energy and the relative Auger rates are shown in Table 1 and Fig. 1, respectively. In Fig. 1, the line positions are adjusted by reducing about 3.0 eV to make the weighted mean values of the present calculation to agree with experiment.[2]

Ar^{6+} L_{23}-M_1M_1 Auger energy in Table 1 shows that the CI results give a better fit to experiment than SCF results (Larkins),[3] but the discrepancy is still large. We consider that the discrepancy is due to the coupling between the continuum and the initial hole states, and the higher order correlation effect. Figure 1 shows that the J value (the total angular momentum) of the initial hole states for the B_1 peak are mostly 2 or 3, and for the B_2 peak, mostly 1. It also shows that the B_1 peak splits into two or three peaks and the B_2 peak, into two. The structure of the B_1 peak is in good agreement with the experiment but the agreement is poor for the B_2 peak.

Much more information on collision mechanism may be obtained from the calculation of more accurate Auger rates. The calculation of the absolute Auger rates is in progress by using CI wave func-

* Faculty of Science, Hokkaido University.

Table 1. Ar^{6+} L_{23}-M_1M_1 Auger energy including the spin-orbit interaction and Auger rates.

J value	Auger energy (eV)	mean*	Relative rates	
$J=1$	111.2		9.7	
$J=3$	112.9	113.5	18.8	59.3
$J=2$	113.5		12.1	
$J=1$	113.8		7.6	
$J=2$	114.2		20.8	
$J=0$	115.6	115.9	1.7	28.5
$J=1$	115.6		22.1	
$J=1$	116.0		2.1	
$J=2$	116.1		2.6	
$J=0$	121.5		2.5	
(weighted mean)		114.2		
Larkins[3]		115.1		
Experiment[2] B_1	110.3	111.3		
B_2	113.2			

* weighted mean energy

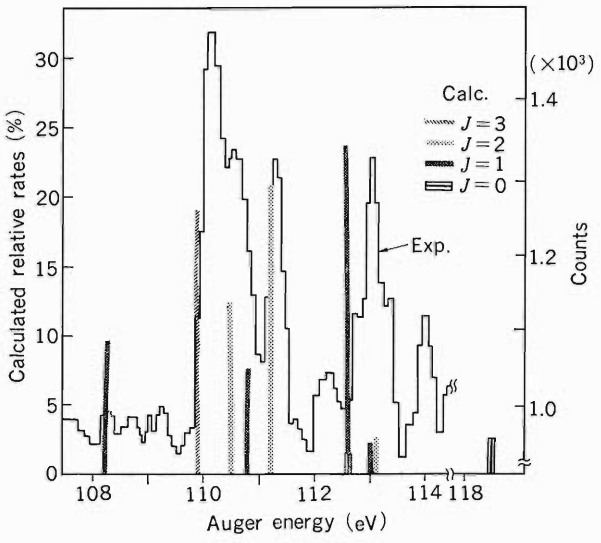

Fig. 1. Calculated relative rates of Ar^{6+} L_{23}-M_1M_1 Auger for the B lines and electron spectrum obtained by 45.7 MeV Ar^{4+} impact.[2]

tions in which coupling to the continuum states is taken into account, and the continuum wave function with an exchange effect for the ejected electron is used.

All the calculations are performed on a HITAC M-280H at the Hokkaido University Computing Center and a FACOM M-380 at the Institute of Physical and Chemical Research (RIKEN).

The results presented here are also reported in contribution from the Research Group on Atoms and Molecular No. 17, Ochanomizu University, Tokyo, Japan (1984).

References

1) T. Matsuo, J. Urakawa, A. Yagishita, Y. Awaya, T. Kambara, M. Kase, and H. Kumagai: *J. Phys. B*, **16**, L239 (1983).
2) A. Yagishita, T. Kambara, M. Kase, T. Tonuma, T. Matsuo, J. Urakawa, J. Takahashi, H. Kumagai, and Y. Awaya: *RIKEN Accel. Progr. Rep.*, **16**, 75, 77, 79 (1982); T. Matsuo, H. Shibata, J. Urakawa, A. Yagishita, Y. Awaya, T. Kambara, M. Kase, H. Kumagai, and J. Takahashi: *ibid.*, **17**, 65 (1983).
3) F. P. Larkins: *J. Phys. B*, **4**, 1 (1971).
4) H. P. Kelly: *Phys. Rev. A*, **11**, 556 (1975); H. P. Kelly and H. S. Kohler: *Phys. Rev. A*, **3**, 1550 (1971).

RIKEN Accel. Progr. Rep. 18 (1984)

III-2-13. Tilted Foil Method Using Thin Carbon Foil

S. Kohmoto, K. Ando, M. Ishihara, and T. Nomura

The tilted foil method (TFM) is very useful for generating an atomic polarized and thereby, through the hyperfine interaction, nuclear polarized beam. With increasing beam energy, however, the degree of atomic polarization generated decreases.[1),2)] Also since at a high energy region, more electrons are stripped from ions than at low energy region, the degree of nuclear polarization should decrease. It is the purpose of our experiments to generate charge-non-equilibrium ions by using thin carbon foils so as to see if it is possible to generate polarized ion beams at the high energy region.

Ion beam ($^{14}N^{2+}$ and $^{14}N^{3+}$) from RILAC was focused on 4 mm×6 mm carbon foil. First of all, it was necessary to search an energy region where charge-non-equilibrium is achieved by using a thin foil. A monochromator was used for scanning wavelength. For this experimental stage, foils were not tilted so as to minimize the foil thickness. No optical elements such as a $\lambda/4$ plate and a linear polarizer were inserted in the optical path to gain the photon numbers.

Figure 1 shows light spectra at three incident energies: E_N=6.25, 11.38, and 28.81 MeV. The spectra of Fig. 1 (a), (c) and, (e) were measured by using thick carbon foil, whereas thin carbon foil of 0.7 or 0.8 μg/cm^2 in thickness was used for those of Fig. 1 (b), (d), and (f). Spectral resolution is, in all cases, about 2 nm. Peak assignment is done according to the wavelengths in literature.

At incident energies E_N=6.25 and 11.38 MeV, the spectra from the foils of different thicknesses

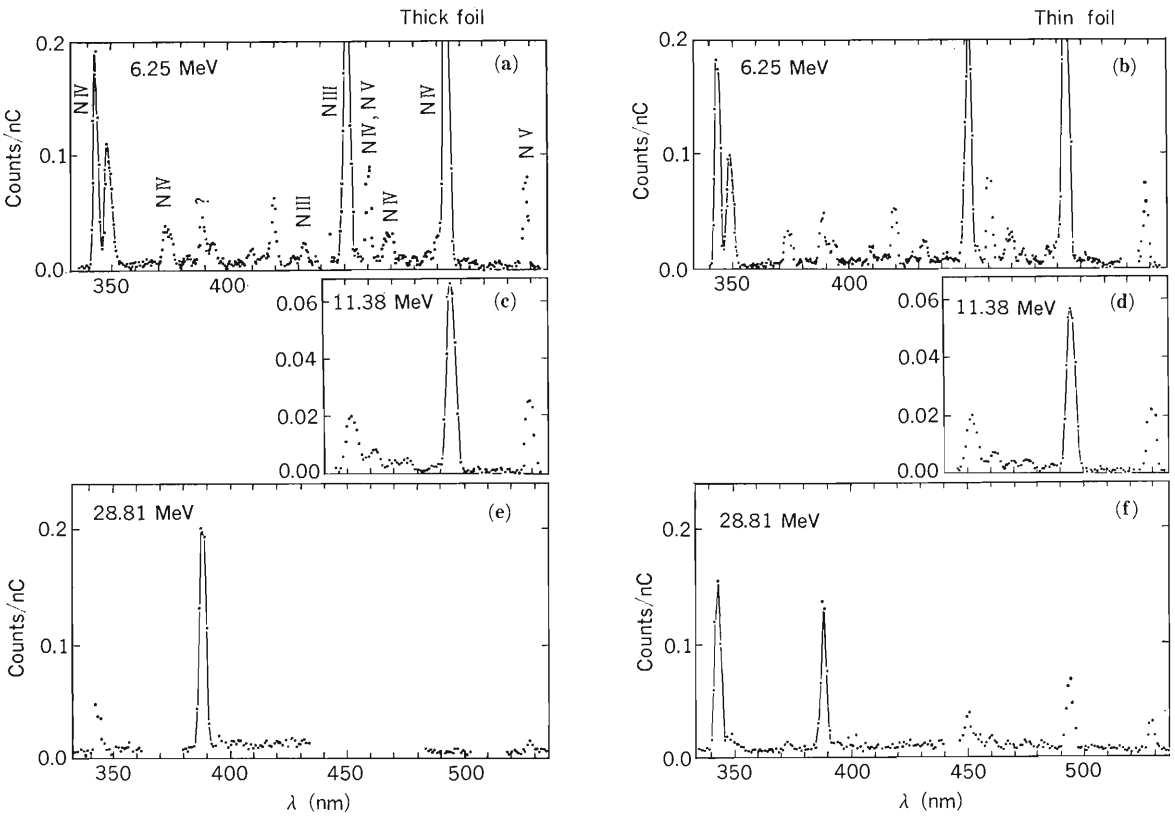

Fig. 1. Light spectra from ^{14}N ions after passing through carbon foil. Photon counts are normalized by integrated current. Normalization of (c) and (d) is different from those of others because of the different foil positions. Spectrum (e) is only partially measured. Beam energies, ion charges and, foil thicknesses are as follows: E_N=6.25 MeV 2^+ ion [(a) 32 μg/cm^2; (b) 0.8 μg/cm^2]. E_N= 11.38 MeV 2^+ ion [(c) 64 μg/cm^2; (d) 0.8 μg/cm^2]. E_N=28.81 MeV 3^+ ion [(e) 32 μg/cm^2; (f) 0.7 μg/cm^2].

coincide exactly. Even with carbon foil of 0.8 μg/cm^2 thickness, ions after passing through the foil arrive at charge-equilibrium-state at these energies. Mean charges at these energies are 4.7 and 5.4, respectively. When the incident energy is increased up to 2 MeV/nucleon, ions reach finally a non-equilibrium state as is shown in Fig. 1 (e) and (f). Peaks observed with thin carbon foil disappear or diminish, with one exception, in the spectrum with thick foil. These lines are believed to belong to N IV or N V. As the mean charge at this energy is about 6.4, the behavior of these peaks is reasonable. The origin of the 390 nm line is not identified.[3)]

A trial experiment was performed to measure the relative Stokes parameter S/I at E_N=28.81 MeV for the line N V (494 nm).

Thin carbon foil of 0.7 μg/cm^2 was tilted by 45°. By using a rotatable $\lambda/4$ plate, a linear-polarizer, and a depolarizer, we measured right- and left-handed circular polarization, from which we estimated the S/I value. Because of the limited beam intensity (about 0.2 μA) only rough estimation was made: $S/I = 2 \pm 6\%$. We plan to measure S/I for the 341 nm line using optical elements of improved transmission in a short wavelength region.

References

1) S. Kohmoto, M. Ishihara, T. Nomura, and Y. Gono: *RIKEN Accel. Progr. Rep.*, **17**, 48 (1983).
2) H. Winter, P. H. Heckmann, and B. Raith: *Hyperfine Interactions*, **8**, 261 (1980).
3) J. Desesquelles: Thèse d'Etat, l'Université de Lyon (1970).

RIKEN Accel. Progr. Rep. 18 (1984)

III-2-14. Beam-Foil Spectroscopy of Highly Ionized Aluminum Atoms

K. Ando, S. Kohmoto, T. Tonuma, H. Kumagai,
Y. Awaya, S. Tsurubuchi, and K. Sato

An experiment of beam-foil spectroscopy was performed to study aluminum spectra, which had been scarecely observed in other facilities.[1),2)]

Aluminum ion Al 3^+ was accelerated up to 38 MeV, and was ionized and excited with a carbon foil of 10 $\mu g/cm^2$. Its average charge was $+10$ and spectra of Al X, XI, and XII were observed. Assignment of spectral lines of each ions of Al X, XI, and XII were made by comparing intensities at different acceleration energies of 35.7, 22.5, and 15.1 MeV, which corresponded to the average charge of 9.9, 8.8, and 7, respectively, after passing through the carbon foil.

A spectrometer used was a grazing incidence type with a 2.2 m diameter Rowland circle and 1,200 grooves/mm grating. Widths of an entrance and exit slit were 0.15 mm which corresponded to the spectral resolution of 0.56 Å. The wavelength was scanned by a stepping motor at 0.0075 inch/step, which corresponded to a wavelength step of 0.12 Å at 100 Å and 0.17 Å at 200 Å.

Figure 1 shows a spectrum observed for aluminum ions of average charge of 9.9 with identified lines. These lines could arise from transitions between $n=3$ and $n=4$ by rough estimation of energy values of levels. Wavelengths of spectral lines were obtained to within an error of ± 0.1 Å from a calibration curve of second order polynomials calculated from known spectral lines of Al X, XI, and XII as references.

For identification of spectral lines, we employed an empirical formula by Edlen[3)] and estimated term values of levels of d and f electrons of Li- and He-like ions. This formula is expressed as a sum of hydrogenic term and polarization correction term.

Term values of other levels of Li- and He-like ions and of Be-like ion were estimated from a hydrogenic formula. Estimated term values are given in Table 1 and the wavelengths calculated from Table 1 for interested transitions are given in Table 2.

Spectral lines due to the transitions of f electron were observed to have strong intensities in this experiment for He- and Li-like ions, so that series of spectra of $n=5$ and 6 for Al XI ^2F and $n=5$ for Al XII ^3F can be easily identified by comparing with the calculated wavelengths. We also tried to

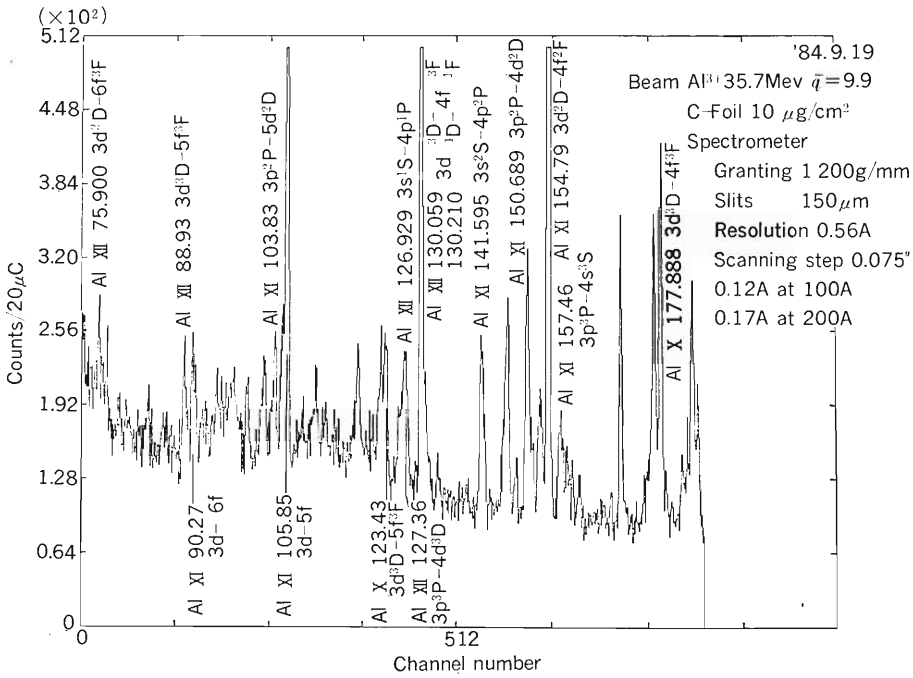

Fig. 1. Beam-foil spectrum of Al.
Al^{3+}, 35.7 MeV; equilibrium charge state, 10^+.

Table 1. Calculated term values.

Al XII	1s4d	15,836,800 cm^{-1}
Al XI	$1s^2$5f	3,033,700 cm^{-1}
	6f	3,196,000 cm^{-1}
	7f	3,293,900 cm^{-1}
Al X	$1s^2$2s5f	2,775,800 cm^{-1}
	6f	2,909,900 cm^{-1}
	$1s^2$2p4f	2,704,800 cm^{-1}
	5f	2,951,700 cm^{-1}

Table 2. Estimated wavelengths in Å.

Al XII	3p ^{3}P – 4d	127.3
	3p ^{1}P – 4d	130.8
Al XI	3d ^{2}D – 5f ^{2}F	105.8
	6f ^{2}F	90.3
Al X	2s3d ^{3}D – 2s5f	123.4
	6f	105.9
	2s3d ^{1}D – 2s5f	127.6
	6f	109.0
	2p3d ^{3}D – 2p4f	183.7
	5f	126.4
	2p3d ^{3}P – 2p4f	187.0
	5f	127.9

Table 3. Identified lines and energy values.

	Identification	Wave-length (Å)	Level	Energy value (cm^{-1})
Al XII	3p ^{3}P – 4d ^{3}D	127.4	4d $^3D_{3,2}$	15,836,700
	3p ^{1}P – 4d ^{1}D	130.9	4d $^1D_2$	15,836,400
Al XI	3p ^{2}P – 5d ^{2}D	103.8		
	3d ^{2}D – 5f ^{2}F	105.8	5f $^2F_{2.5,3.5}$	3,033,000
	3d ^{2}D – 6f ^{2}F	90.3	6f $^2F_{2.5,3.5}$	3,196,000
Al X	3d ^{3}D – 5f ^{3}F	123.4	5f $^3F_{4,3,2}$	2,776,300

identify the spectral lines from 4d ^{3}D and ^{1}D of Al XII. The estimated term value of level of 4d electron is an average of the term values of the ^{3}D and ^{1}D states, but it is close to that of the ^{3}D states because a weight of the ^{3}D state is larger than that of the ^{1}D. We can identified the spectral line from ^{3}D state. We tried to identify a singlet state of the same transition by applying a theoretical term energy expression,

$$E = E_{av} + A * G^1(1s, 4d)$$

where G^1 is the Slater integral calculated by the Hartree-Fock method and A is an angular momentum term, which is 0.3 for ^{3}D and 0.1 for ^{1}D. From the measured ^{3}D energy values, E_{av} was calculated and E for ^{1}D state was 130.9 Å. This line was observed by the side of a strong line of Al XII at 130.6 Å. The identification of these spectral lines were confirmed from an iso-electronic sequence plot of wavenumbers of these transitions against the net charge of various ions.

The strong spectral line from 5f ^{3}F to 3d ^{3}D of Al X was identified. The line from the transition of the singlet term may have strong intensity, because the line from ^{3}F state has strong intensity. We tried to estimate a wavelength of the singlet transition from 5f ^{1}F to 3d ^{1}D by using the theoretical term energy formula as mentioned above. It was estimated as 187.0 Å, but it was beyond the present measurement range.

Newly identified spectral lines and energy values of classified levels are given in Table 3.

As seen from Fig. 1, many strong spectral lines still remain unidentified. These spectral lines may arise from doubly excited states of Al XI (Li-like) and Al X (Be-Like). The transition energies from these highly ionized atoms have not been calculated theoretically so far.

References

1) B. Denne, D. J. Pegg, K. Ishii, E. Alvarez, R. Hallin, J. Pihl, and R. Sjödin: *J. Phys.* (*Paris*), **40**, Coll. 1, 183 (1979).
2) B. Denne, S. Huldt, J. Pihl, and R. Hallin: *Phys. Scr.*, **22**, 45 (1980).
3) B. Edlen: Encyclopedia of Physics, (ed. by S. Flugge), Springer-Verlag, Berlin, Vol. XXVII, p. 125 (1964).

RIKEN Accel. Progr. Rep. 18 (1984)

III-2-15. Intensity Ratio between K_β and K_α X-Rays from 33 MeV Ar Ions in Solid Targets

T. Kambara, Y. Awaya, M. Kase, H. Shibata, and H. Kumagai

We have been measuring K X-rays from Ar ions passing through various solid targets with high resolution to study target atomic number (Z_2) dependence of multiple inner-shell ionization process. We have reported that the L-shell ionization probability of the Ar ions (P_L) at the time of the K_α transition and the hypersatellite to satellite intensity ratio of the K_α X-rays depend on the target atomic number (Z_2) systematically.[1),2)] In the present report, we present the result of measurement of the relative intensity of the K_β X-rays to the K_α X-rays as a function of Z_2. Although preliminary data were presented in the last issue of this report,[3)] we have made measurements for more sorts of target species and found that the ratio has a dependence similar to that of P_L. This implies that the electronic transition from the outer shell is affected by the ionization in the L-shell.

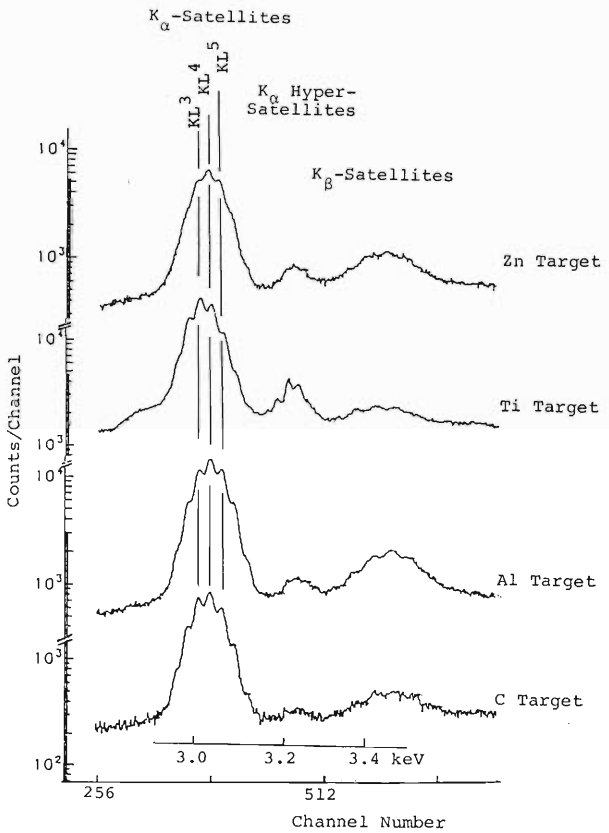

Fig. 1. Examples of K X-ray spectra from 33 MeV Ar ions passing through various targets.

The experimental set up is the same as that reported previously[1)]; the energy of the incident Ar ions from the linac is about 33 MeV and the X-rays are measured by a broad range crystal spectrometer. The target species are Be, C, Mg, Al, Ca, Ti, Cr, V, Fe, Co, Ni, Cu, Zn, Y, Nb, Tb, Ta, and Au. Some examples of the X-ray spectra are shown in Fig. 1. In the spectra, the K_α satellites, the K_α hypersatellites and the K_β satellites are observed from the left- to right-hand side. In order to assign the L-shell hole numbers for the K_β satellite peaks, the result of energy calibration using fluorescent L X-rays of In and Sn is compared with the estimated values of K transition energies.

The L-shell ionization probability at the time of K_α transition is deduced from the intensity distribution of the K_α satellites, as reported previously,[1),2)] and it shows oscillatory dependence on Z_2 with the first minimum at $Z_2=22$ and the second one at $Z_2=45$. This dependence is shown in Fig. 2 (a), where the ionization probability is denoted by P_L (K_α). This fact is described as a result of level matching between the L-shell of Ar ion and the L-

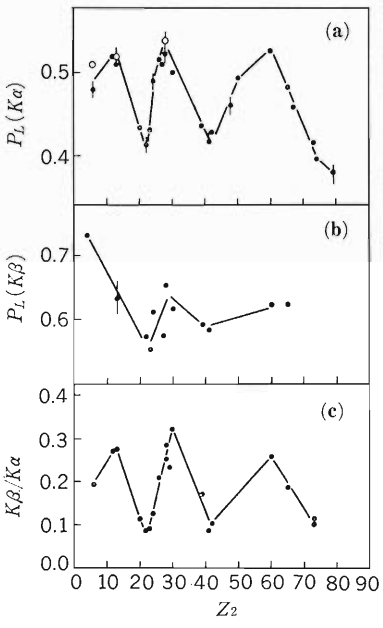

Fig. 2. The target atomic number Z_2 dependence of (a) probability of L-shell holes at the K_α X-ray emission, (b) probability of L-shell holes at the K_β X-ray emission, and (c) intensity ratio between Ar K_β X-rays and K_α X-rays.

and M-shell of target atoms. The ionization probability at the time of K_β transition, P_L (K_β), estimated from the average energy of the K_β satellites, is shown in Fig. 2 (b). It has the same dependence as that of the P_L (K_α) on Z_2 at small Z_2's but the dependence is not clear at large Z_2's. The first minimum is seen in both K_α and K_β transitions but the second one is not clear for K_β one.

The intensity ratio among the K_α satellites, K_α hypersatellites, and K_β satellites is strongly dependent on the target species. The Z_2 dependence of the intensity ratio between K_α satellites and the K_α hypersatellites has been discussed previously.[1),2)] The Z_2 dependence of the intensity ratio between the K_β and K_α X-rays, shown in Fig. 2 (c), is similar to the Z_2 dependence of the ionization probability P_L (K_α) shown in Fig. 2 (a). This may be explained as a result of the increase in electron capture cross section to M-shell according to the level matching and increase in the transition probability of the K_β transitions for ions with more L-shell holes if the number of electrons in the M-shell is independent of the number of L-electrons. Further analysis is in progress.

References

1) Y. Awaya, T. Kambara, M. Kase, H. Kumagai, J. Urakawa, H. Shibata, T. Matsuo, J. Takahashi, and M. Namiki: *RIKEN Accel. Progr. Rep.*, **17**, 49 (1983).
2) Y. Awaya, T. Kambara, M. Kase, H. Shibata, H. Kumagai, K. Fujima, J. Urakawa, T. Matsuo, and J. Takahashi: *Nucl. Instrum. Methods*, **B10**, 53 (1985).
3) T. Kambara, Y. Awaya, M. Kase, H. Kumagai, S. M. Shafroth, H. Shibata, and T. Tonuma: *RIKEN Accel. Progr. Rep.*, **17**, 51 (1983).

RIKEN Accel. Progr. Rep. **18** (1984)

III-2-16. High Resolution Measurement of Cu K X-Rays from Collision Systems of Cu Ions on C Target and C Ions on Cu Target

Y. Awaya, T. Kambara, M. Kase, H. Shibata,
H. Kumagai, M. Nishida, and K. Shima

We have studied target atomic number Z_2 dependence of an average L-vacancy fraction P_L, that of the intensity ratio of K_α hypersatellites and K_α satellites $I(K^h_\alpha)/I(K_\alpha)$ and that of K_β and K_α X-rays $I(K_\beta)/I(K_\alpha)$ as to the K X-rays from Ar ions passing through various kinds of target foil.[1)-4)] The Z_2 dependence of P_L has been discussed and explained from the viewpoints of electron capture and loss processes during creation and filling of the K vacancy of Ar ions accompanying multiple L-shell vacancies and that of $I(K^h_\alpha)/I(K_\alpha)$ from the rotational coupling of $2p\pi$–$2p\sigma$ and $3d\pi$–$3d\sigma$ of molecular orbitals formed by collision partners.

In order to study the difference in ionized states between target atoms and projectile ions, we have measured the K X-rays from the Cu ions passing through C foil and that from Cu target atoms excited by C ions under the conditions that the target atoms and the projectiles have the same relative velocity.

The 0.83 MeV/amu Cu^{4+} and C^{2+} ions were accelerated by the linac and momentum analyzed. Targets used were 80 $\mu g/cm^2$ carbon foil for Cu ions and 0.2 mg/cm^2 Cu foil for C ions. The Cu K X-rays were measured by using a broad range X-ray crystal

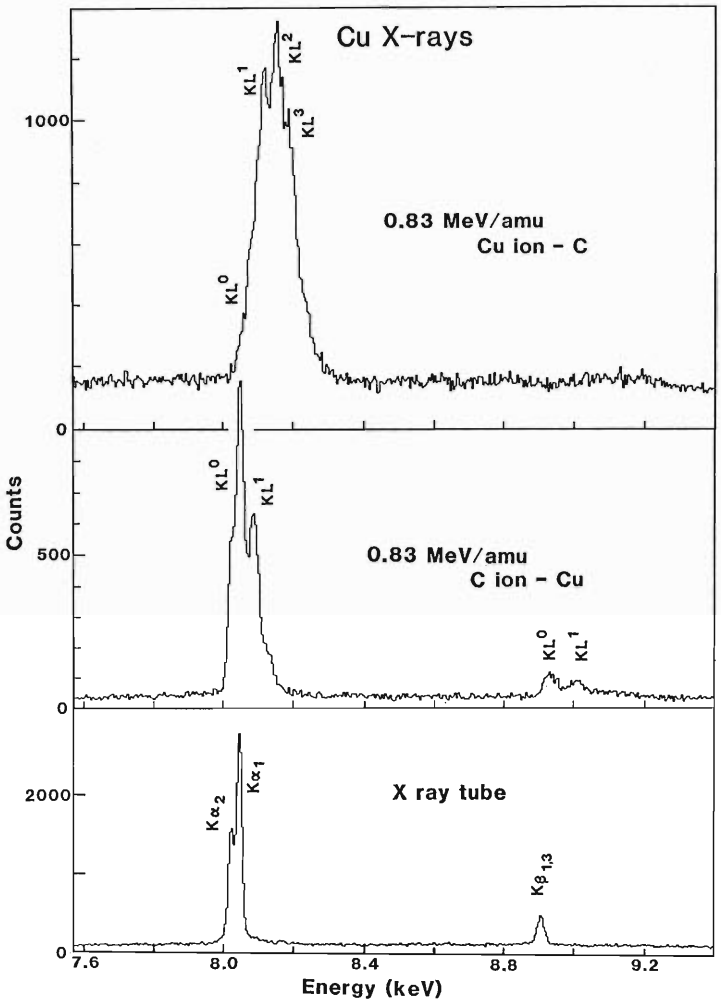

Fig. 1. Spectra of Cu K X-rays from projectile Cu ions passing through C foil and from target Cu foil induced by C-ion bombardment. Fluorescent Cu X-rays are also shown for comparison. The incident energy of Cu ions and C ions is 0.83 MeV/amu.

spectrometer[5] with a crystal of LiF (220) ($2d$= 2.848 Å).

An estimated value of the average charge of incident Cu ions is 17.3+[6] and Cu ions are considered to reach a charge equilibrium state after they traverse the carbon target of a few $\mu g/cm^2$. This means that if a Cu ion loses their electrons successively from low to high binding energies, the ion does not bear L vacancies when it collides with a target C atom. Therefore, the configurations of L and K shells are considered to be nearly the same for the projectile Cu ion and the target Cu atom. On the other hand, the effective charges felt by a projectile Cu ion from a target C atom and that felt by a target Cu atom from a projectile C ion is deemed to be 6+ when a K electron of Cu ion/atom is ionized. The difference between the spectra of Cu K X-rays from the projectile Cu ions and that of the target Cu atoms reflects mainly the density effect in collision system.

The Cu K X-ray spectra obtained from Cu ions and the Cu target are shown in Fig. 1 in comparison with the fluorescent Cu X-rays. KL^n denotes the initial state vacancy configuration with single K and n-multiple L holes. Figure 1 shows that a Cu ion has about two more L vacancies than a target Cu atom when K X-rays are emitted. This is because a Cu ion collides successively with target C atoms whereas a target Cu atom interacts once with a projectile C ion during the K vacancy exists. When a projectile loses one K electron and multiple L electrons in a collision with a small impact parameter, then it can collide with other target atoms with larger impact parameters and captures or loses outer shell electrons before K X-rays are emitted.

Further measurements of Cu K X-rays from both the projectile Cu ions and the target Cu atom excited by carbon at the different collision energies will provide more information about the collision process or the state of the Cu projectile and the atom; studies are in progress.

References

1) Y. Awaya, T. Kambara, M. Kase, H. Kumagai, J. Urakawa, H. Shibata, T. Matsuo, J. Takahashi, and M. Namiki: *RIKEN Accel. Progr. Rep.*, **17**, 49 (1983).
2) T. Kambara, Y. Awaya, M. Kase, H. Kumagai, S. M. Shafroth, H. Shibata, and T. Tonuma: *ibid.*, p. 51
3) T. Kambara, Y. Awaya, M. Kase, H. Shibata, and H. Kumagai: p. 73 in this report.
4) Y. Awaya, T. Kambara, M. Kase, H. Shibata, H. Kumagai, K. Fujima, J. Urakawa, T. Matsuo, and J. Takahashi: *Nucl. Instrum. Methods*, **B10**, 53 (1985).
5) A. Hitachi, H. Kumagai, and Y. Awaya: *ibid.*, **195**, 631 (1982).
6) K. Shima, T. Ishihara, and T. Mikumo: *ibid.*, **200**, 605 (1982).

RIKEN Accel. Progr. Rep. 18 (1984)

III-2-17. REC X-Rays for ^{3}He and ^{4}He Targets

T. Kambara, Y. Awaya, M. Kase, H. Kumagai,
H. Shibata, and T. Tonuma

In order to study target isotope dependence of the cross section of radiative electron capture (REC), we have measured energy spectra and yields of X-rays from the REC process induced by 110 MeV Ne-ions incident on target of ^{3}He and ^{4}He isotopes. Theoretical features of the isotope dependence are discussed in this report.[1,2]

The experimental set-up was almost the same as that reported elsewhere.[3] A beam of 120 MeV Ne^{6+}-ions from the cyclotron passed through a gas cell after it was defined by a 1 mm-wide slit, and then reached a Faraday cup. The target He gas was contained in the gas cell at pressures up to 240 Torr. The pressure was measured by a baratron gauge and set to the same value for the two isotopes. The energy of the Ne-ions are estimated to be about 110 MeV in the gas cell and most of them are considered to be bare (10+) or H-like (9+); therefore the electrons of the target gas can transfer to a K-shell vacancy of the Ne-ion through the REC process. The X-rays emitted from the collision volume passed through a 4 μm-thick Mylar window of the gas cell and were detected by a Si (Li) detector placed at 90° to the beam direction. The X-ray path between the gas cell and the detector was evacuated in order to minimize the absorption of the X-rays.

Examples of the observed X-ray spectra for the both isotopes are shown in Fig. 1. Both spectra were obtained at the same target gas pressure of 240 Torr and with the same amount of the integrated beam current. In the spectra, the peaks at about 1 keV correspond to the characteristic K X-rays from the Ne-ions and one at about 4 keV to the REC X-rays. No difference was observed between the X-ray spectra and REC X-ray yield for the two isotopes. It was concluded that the difference in the REC cross section between the two targets should be within 7%.

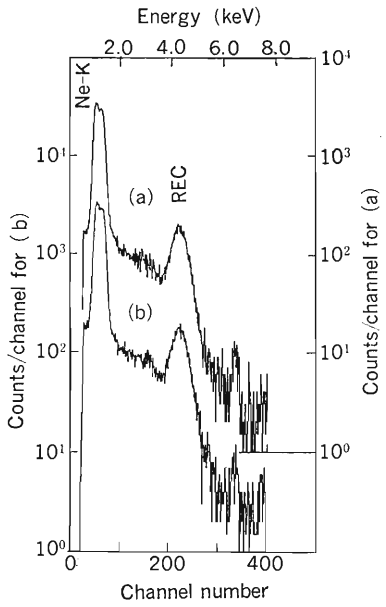

Fig. 1. Energy spectra of X-rays from collisions between 110 MeV Ne-ions and He gas targets at about 240 Torr: (a) for the ^{4}He and (b) for the ^{3}He. Peaks at about 1 keV are Ne K X-rays and one at about 4 keV is REC X-rays to a Ne K-shell vacancy.

References

1) K. Hino, I. Shimamura, N. Toshima, and T. Watanabe: p. 62 in this report.
2) K. Hino, I. Shimamura, and T. Watanabe: p. 64 in this report.
3) T. Kambara, Y. Awaya, A. Hitachi, M. Kase, I. Kohno, and T. Tonuma: *J. Phys. B*, **15**, 3759 (1982).

RIKEN Accel. Progr. Rep. **18** (1984)

III-2-18. Production of Highly-Charged Slow Ar Ions Recoiled in 1.05 MeV amu^{-1} Ar^{q+} ($q=4$, 6, 10–14) Ion Bombardment

T. Tonuma, H. Shibata, S. H. Be, H. Kumagai,
M. Kase, T. Kambara, I. Kohno, and H. Tawara

The charge-state distribution of slow recoil ions produced in collisions of 1.05 MeV amu^{-1} Ar^{q+} (q=4, 6, 10–14) ions with Ar target atoms has been measured. Combining these charge-state distribution data with absolute values of total ionization cross sections measured through a parallel-plate method,[1] we determine the absolute partial cross sections for the production of recoil Ar^{i+} ions.

In Fig. 1 the total apparent cross section ($\Sigma i\sigma_i$) and the partial cross sections (σ_i) for production of recoil Ar^{i+} ions produced in Ar^{q+} ion impact are plotted against the projectile charge state q. Generally speaking, the total cross sections for production of the recoil ions and also the yields of each charge state of recoil ions increase with increasing charge of projectile ions q.[2] In particular, the highly charged recoil ion production is enhanced significantly in high charge projectile ion impact. Olson[3] calculated the cross section σ_i for ejecting i electrons in the M-shell based upon the classical trajectory Monte Carlo (CTMC) method. Dotted lines in Fig. 1 represent his results of calculation for projectile energy of 1 MeV amu^{-1}. The values of the total ionization cross sections ($\Sigma\sigma_i$) calculated by the CTMC method are in agreement with the present results. The present measurements and calculations of the total apparent ionization cross sections ($\Sigma i\sigma_i$) are in accord with each other to within a factor of 2 for a wide variety of projectile charge states though the dependence of the cross sections on the projectile charge q is slightly different from each other. The theoretical partial ionization cross section, however, is underestimated for small i and overestimated for large i.

The partial ionization cross sections σ_i with i higher than 8, where the L-shell electrons are to be ionized, increase with the projectile charge stage q. The partial ionization cross sections σ_i ($i\geq 9$) are analyzed in terms of the ionization probability based upon the independent electron model. The probability P_{m+l} for ionization of m electrons in the M-shell and simultaneously l electrons in the L-shell among 8 electrons in each shell of Ar atom, corresponding to $i=m+l$, in collisions with an impact parameter b, is given by:

$$P_{m+l}(b)=P_m(b)\,P_l(b)$$

where

$$P_m(b)=\binom{8}{m}(p_{\mathrm{M}}(b))^m(1-p_{\mathrm{M}}(b))^{8-m}$$

$$P_l(b)=\binom{8}{l}(p_{\mathrm{L}}(b))^l(1-p_{\mathrm{L}}(b))^{8-l}$$

and $\binom{8}{m}$ and $\binom{8}{l}$ are the binomial coefficients and $p_{\mathrm{M}}(b)$ and $p_{\mathrm{L}}(b)$ represent the ionisation probabilities of a single electron in the M- and L-shells, respectively. In the simplest case, $p_{\mathrm{M}}(b)$ and $p_{\mathrm{L}}(b)$ can be assumed to be constant within the critical impact parameters. As far as the production of slow recoil ions with $i\geq 9$ is concerned, all eight electrons in the M-shell can be assumed to be ionized in the present Ar^{q+}+Ar collisions, that is, P_m is independent of the ionization of the target L-shell electrons. Then, the dependence of the relative values of P_{8+l} on the charge state of the projectile ions is represented only

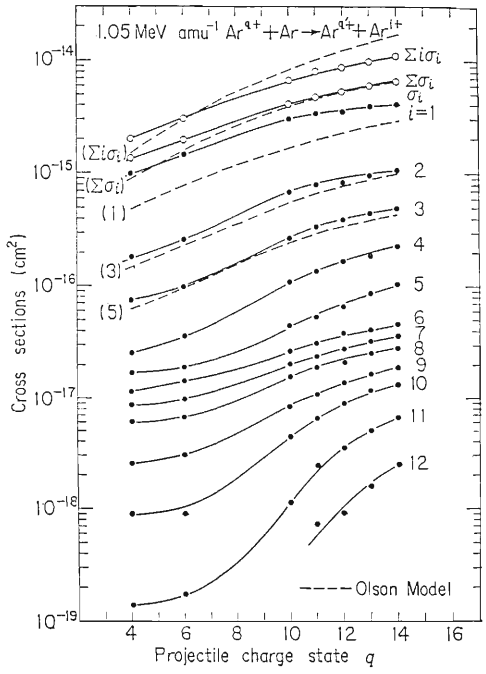

Fig. 1. Total apparent cross section $\sum i\sigma_i$, total cross section $\sum\sigma_i$, and partial cross section σ_i for production of the recoil Ar^{i+} ions as a function of the projectile charge q of 1.05 MeV amu^{-1} Ar^{q+}. Dotted lines represent the results calculated by Olson for the projectile energy of 1 MeV amu^{-1}.

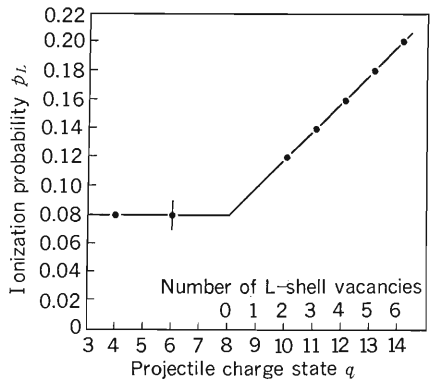

Fig. 2. Ionization probability p_L of the L-shell electrons of Ar atoms plotted against the projectile charge state q in 1.05 MeV amu^{-1} Ar^{q+}+Ar collisions.

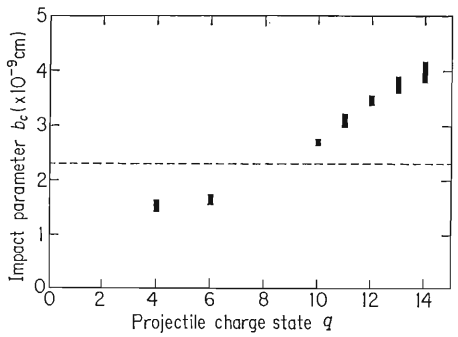

Fig. 3. Critical impact parameter b_c of the L-shell of Ar atoms plotted against the projectile charge state q in 1.05 MeV amu^{-1} Ar^{q+}+Ar collisions. The dotted line represents expected values for the orbital radius of the L electron shell of Ar target.

by P_l, which can be determined by a least-squares fitting to the experimental data.[4] Figure 2 displays a plot of the obtained probabilities p_L against the projectile charge state q. It is found from Fig. 2 that the probabilities p_L for impact of projectiles with charges q=4–6 are independent of the charge state q, but increase significantly for higher projectile charge state q=10–14, which corresponds to the projectiles with two to six L-shell vacancies. By interpolating these results, it is concluded that the ionization is strongly enhanced once the projectile L-shell vacancies are brought into collisions. This enhancement is believed to be due to electron transfer from target atoms into the L-shell vacancies of projectiles. The inner-shell electron transfer of the target atoms contributes significantly to the production of slow, highly charged recoil ions in the high-energy heavy ion impact.

The ionization probability p_L can be assumed to be constant within the critical impact parameter b_c and zero otherwise, that is, p_L is a step function. Therefore, the partial ionization cross section, σ_{8+l}, of the recoil ions is given by $\sigma_{8+l}=\int_0^{b_c} P_l(b)\, 2\pi\, b\, db$. The critical impact parameter b_c can be determined from the experimental data of σ_{8+l} and the estimated values of p_L in Fig. 2. In Fig. 3 b_c values thus determined are plotted as a function of the projectile charge state q. Figure 3 shows that the values of b_c for projectiles with q=4–6 increase slightly with q and are smaller than 2.3×10^{-9} cm expected from the orbital radius of the L-shell electron of the Ar target. The orbital radius is given by $a_L=a_0n^2/Z$, where $a_0=0.529\times10^{-8}$ cm, n designates the principal quantum number of the electron shell, and Z is the effective nuclear charge at that shell. On the other hand, b_c increases significantly for high projectile charge state of q=10–14 and is much larger than the expected value of a_L. It is found that the critical impact parameter for the L electron shell increases significantly once the projectile L-shell vacancies are brought into collision, resulting in a similar trend to the ionization probabilities described above. This result shows that, in the 1.05 MeV amu^{-1} Ar^{q+} ($q\leq6$) ion impact the production of recoil Ar^{i+} ($i\geq8$) ions occurs at distances slightly shorter than the radius whereas, in the Ar^{q+} ($q\geq9$) ion impact at fairly large distances which increase with the projectile charge, indicating that the ionization mechanisms in Ar^{q+} ($q\leq8$) and Ar^{q+} ($q\geq9$) ion impact are quite different from each other. A similar increase in the critical impact parameter in the ionization processes in impact of high q ions with the innershell vacancies has already been reported by Hagmann *et al.*,[5] suggesting that the electron capture into projectiles (L-shell) from a target atom (L-shell) plays a role in the production of highly charged recoil ions in the present work.

References

1) S. H. Be, T. Tonuma, H. Kumagai, H. Shibata, M. Kase, T. Kambara, I. Kohno, and H. Tawara: p. 80, in this report.
2) C. L. Cocke: *Phys. Rev. A*, **20**, 749 (1979).
3) R. E. Olson: *J. Phys. B: At. Mol. Phys.*, **12**, 1843 (1979).
4) T. Tonuma, M. Kase, T. Kambara, H. Kumagai, T. Matsuo, J. Urakawa, H. Shibata, J. Takahashi, S. Özkök, S. H. Be, I. Kohno, and H. Tawara, *J. Phys. B: At. Mol. Phys.*, **17**, L317 (1984).
5) S. Hagmann, C. L. Cocke, J. R. Macdonald, P. Richard, H. Schmidt-Böcking, and R. Schuch: *Phys. Rev. A*, **25**, 1918 (1982).

RIKEN Accel. Progr. Rep. 18 (1984)

III-2-19. Total Apparent Cross Sections for Ionization of Rare-Gas Atoms by Fully Stripped Projectiles

S. H. Be, T. Tonuma, H. Kumagai, H. Shibata,
M. Kase, T. Kambara, I. Kohno, and H. Tawara

In this report we present the results of the total apparent cross sections for ionization of rare-gas atoms by fully stripped projectiles. Further, the results are discussed in connection with the calculation of Olson[1] based on the classical trajectory Monte Carlo (CTMC) method with special emphasis on dependence on Z.

Experimental results for total apparent cross sections for ionization of He, Ne, and Ar targets by 1.05 MeV/amu fully stripped He^{2+}, O^{6+}, O^{8+}, and Ne^{10+} projectiles are given in Table 1. Figure 1 shows plots of measured cross sections versus the atomic number of fully stripped projectiles. Target atom is indicated on each curve. The solid lines show a least-squares fit of the present experimental cross sections including those of Rudd *et al.*[2] to a function $\sigma_+=\sigma_0 Z^\alpha$, where $\alpha=1.84$ and $\sigma_0=0.23\times10^{-16}$ for He target, $\alpha=1.69$ and $\alpha_0=0.61\times10^{-16}$ for Ne, and $\alpha=1.68$ and $\sigma_0=1.52\times10^{-16}$ for Ar. The results of Schlachter *et al.*,[3] Hvelplund *et al.*,[4] and Knudsen *et al.*[5] for the cross sections are also included in this figure. The results of Schlachter *et al.* are for ionization of He, Ne, and Ar targets by C^{6+} projectile of 1.14 MeV/amu, and those of Rudd *et al.* are for H^+ incident on He, Ne, and Ar targets at 1 MeV/amu. The results of Hvelplund *et al.* for O^{8+} incident on He target at 1 MeV/amu represent the sum of the single- and double-electron ionization cross sections, which is the sum of the number of electrons ejected during collision weighted by the individual cross section for each event. The results of Knudsen *et al.* are for H^+, He^{2+}, Li^{3+}, B^{5+}, C^{6+} and O^{8+} incident on He target. These plotted points of Knudsen *et al.* were obtained by extrapolating the curve of the cross sections as a function of projectile energy and are the sum of the single- and double-electron ionization cross sections. As seen from Fig. 1 these experimental data obtained by other groups fall nicely on our experimental curve and are in excellent agreement with our results except the cross section of Schlachter *et al.* for ionization of Ne target by C^{6+} projectiles. Even for this case, the results agree

Table 1. Total apparent ionization cross sections, σ^+, in units of 10^{-16} cm^2. Projectile ion energy is 1.05 MeV/amu.

Projectile	Target		
	He	Ne	Ar
He^{2+}	$0.83^{+0.06}_{-0.04}$	$2.0^{+0.2}_{-0.1}$	$5.0^{+0.4}_{-0.2}$
C^{6+}	$7.2^{+0.6}_{-0.3}$	$13.2^{+1.0}_{-0.6}$	32^{+3}_{-1}
O^{8+}	$10.0^{+0.8}_{-0.4}$	20^{+2}_{-1}	51^{+4}_{-2}
Ne^{10+}	$14.4^{+1.0}_{-0.6}$	$29^{+2.3}_{-1.3}$	71^{+6}_{-3}

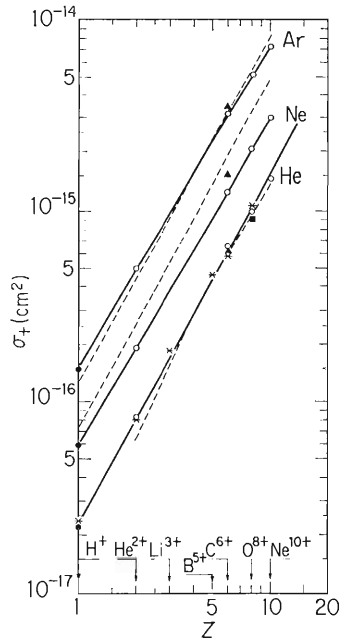

Fig. 1. Total apparent cross sections for ionization of targets by the fully stripped projectiles. The open circles are the present experimental results for He^{2+} ($Z=2$), C^{6+} ($Z=6$), O^{8+} ($Z=8$), and Ne^{10+} ($Z=10$) projectiles of 1.05 MeV/amu; the closed circles are experimental results of Rudd *et al.* (Ref. 2) for H^+ projectiles of 1 MeV; the closed triangles represents experimental results of Schlachter *et al.* (Ref. 3) for 1.14 MeV/amu C^{6+} projectiles; the closed squares shows experimental results of Hvelplund *et al.* (Ref. 4) for 1 MeV/amu O^{8+} projectiles; the asterisks are experimental results of Knudsen *et al.* (Ref. 5) for H^+, He^{2+}, Li^{3+} B^{5+}, C^{6+} and O^{8+} projectiles of 1 MeV/amu; the solid lines show a least-square fit of the present experimental cross sections to a function $\sigma_+=\sigma_0 Z^\alpha$, where Z is the atomic number of fully stripped projectiles; the dotted lines represent the CTMC calculation of Olson (Ref. 1).

with our data within 20%.

It is interesting to compare our experimental data with the CTMC calculation (dotted lines in Fig. 1) by Olson. Generally, the calculation is in agreement with the present results except for those of Ne target. Even for the case of the Ne target, the agreement is not too bad if the overall accuracy of $\pm 50\%$ for ionization of the Ne target, given by Olson is taken into account.

However, there exists a clear difference in the Z-dependence of the cross sections; the calculated cross sections tend to increase approximately with the square of the charge state of the projectile ($\alpha=2$), with a slightly lower dependence at high Z, while in our case $\alpha=1.7$ for Ne and Ar targets, and $\alpha=1.84$ for He target. Although our best fit parameter α for the cross sections with the Z are slightly different from the calculation by Olson, our results agree well with the Z-dependence for Bohr parameter $K>1$ as discussed by Knudsen *et al.* who pointed out that for the perturbation region ($K>1$) the cross section is proportional to Z^2, in agreement with perturbation theory, but for $K>1$ corresponding to our case, namely, in the strong-interaction region the dependence on Z becomes weaker. Here $K=2Zv_0/v_i$, where v_0 is the Bohr velocity and v_i is the projectile velocity.

In conclusion, our results are generally in agreement with the calculation of Olson except for that of Ne target, but our scaling laws for the cross sections with the charge state are found not to follow the Z^2 law predicted by the calculation. However, our results agree well with experimental Z dependence by Knudsen *et al.*

References

1) R. E. Olson: *J. Phys. B*, **12**, 1843 (1979).
2) M. E. Rudd, R. D. DuBois, L. H. Toburen, C. A. Ratcliffe, and T. V. Goffe: *Phys. Rev. A*, **28**, 3244 (1983).
3) A. S. Schlachter, K. H. Berkner, W. G. Graham, R. V. Ryle, P. J. Schneider, K. R. Stalder, J. W. Stearns, J. A. Tanis, and R. E. Olson: *Phys. Rev. A*, **23**, 2331 (1981).
4) P. Hvelplund, H. K. Haugen, and H. Knudsen: *Phys. Rev. A*, **22**, 1930 (1980).
5) H. Knudsen, L. H. Anderson, P. Hvelplund, G. Astner, H. Cederquist, H. Danared, L. Liljeby, and K-G. Rensfelt: *J. Phys. B*, **17**, 3545 (1984).

RIKEN Accel. Progr. Rep. **18** (1984)

III-2-20. Production of Highly-Ionized Recoil Ions in Highly-Ionized, Energetic Ion + Molecule Collisions

H. Tawara, T. Tonuma, S. H. Be, H. Shibata,
H. Kumagai, M. Kase, T. Kambara, and I. Kohno

In the course of investigations on the production mechanism of highly-ionized recoil ions in highly-ionized heavy ion impact, we have already described some of recent results which indicate the significant contribution of electron capture processes to the production of such recoil ions when the innershell vacancies of the projectiles are brought into collisions.[1] We have also measured the production cross sections of highly-ionized recoil Ar^{i+} ions in Ar^{q+} (q=4, 6, 10–14) ion impact.[2]

In the present experiment is used an apparatus similar to that previously described[2] with some modification. To reduce the energy spread of recoil ions due to the extraction field, we used relatively weak extraction field of 40 V applied to two parallel plates apart 1 cm and then accelerated the ions at 1.5 kV. Typical charge spectra of recoil ions from N_2 molecules in 1.05 MeV/amu Ar^{q+} (q=4, 12) ion impact are shown in Fig. 1. In these spectra, in addition to dominant singly-ionized molecular ions N_2^+ which are produced in soft collisions with large impact parameters, we can see a number of peaks corresponding to highly-ionized nitrogen ions (N^{i+}) with a weak trace of N^{6+} ions. As we used $^{14}N_2$ gas molecules, we could not distinguish N^{7+} ions from H_2^+ ions because both have the same m/i (mass to charge ratio) values. It is clearly seen from these spectra that, with increasing the projectile charge q, the production of highly-ionized recoil ions such as N^{4+}, N^{5+}, and N^{6+} ions are significantly enhanced.

It is interesting to compare these data with those in electron impact. However, very few measurements of the cross sections of production of highly-ionized recoil ions from molecular targets by electron impact have been reported. Up to now, N^{3+} ions are the highest charge state directly observed in electron impact whose production cross sections have been reported to be of the order of 10^{-23} cm^2 at 240 eV.[3] Ratios of ions with different charge state in 240 eV electron impact and 1.05 MeV/amu Ar^{12+} ion impact are as follows:

	N_2^+	N_2^{2+}	N^+	N^{2+}	N^{3+}	N^{4+}	N^{5+}	N^{6+}
electron	1.0	1.7×10^{-2}	2.6×10^{-1}	1.2×10^{-2}	1.3×10^{-7}			
Ar^{12+}	1.0	3.1×10^{-1}		4.4×10^{-2}	9.0×10^{-3}	1.5×10^{-3}	5.3×10^{-4}	some

In a comparison of these data, the production cross sections of N^{3+} ions in electron impact reported by Daly and Powell seem to be too small, even if there seems a significant difference in production of highly-ionized recoil ions in electron and ion impact. Production of N_2^+ and N_2^{2+} (which is not separated from N^+ ion in the present work) ions is due to distant collisions with small momentum transfer and is apparently similar to that in single atom ionization. Mechanisms responsible for production of highly-ionized atomic recoil ions from molecular targets is expected to be different from those in single atom targets. The question is whether these highly-ionized atomic recoil ions from molecular targets are produced in ionization processes followed by dissociation or dissociation processes followed by ionization. The collision time in the present system (projectile velocity$\cong1.4\times10^9$ cm/s, molecular bond length$\cong$1Å) is estimated to be of the order of 10^{-17} s, which is much smaller than the dissociation time of molecules ($\cong10^{-14}$–10^{-15} s), though no direct measurement of the dissociation time of nitrogen molecules N_2 has been reported yet. Therefore, these highly-ionized atomic recoil ions are believed to be produced through highly-ionized molecular ions followed by dissociation into two (or more) highly-ionized atomic ions. In electron impact, only singly- and doubly-ionized molecular ions (N_2^+ and N_2^{2+}) have been observed but no molecular ions with higher charge. Even in the present work there is no trace of triply-ionized molecular ions (N_2^{3+}) with m/i=9.33 observed. This may be due to the fact that these highly-ionized molecular ions, probably in highly excited states, are not detected because their life time are too short even if they are produced in collisions. In fact, the intensities of N_2^{2+} ions in electron impact are only 1–2% of those of N_2^+ ions. This is quite in contrast with the fact that the intensities of doubly-ionized Ar^{2+} ions (which have similar binding

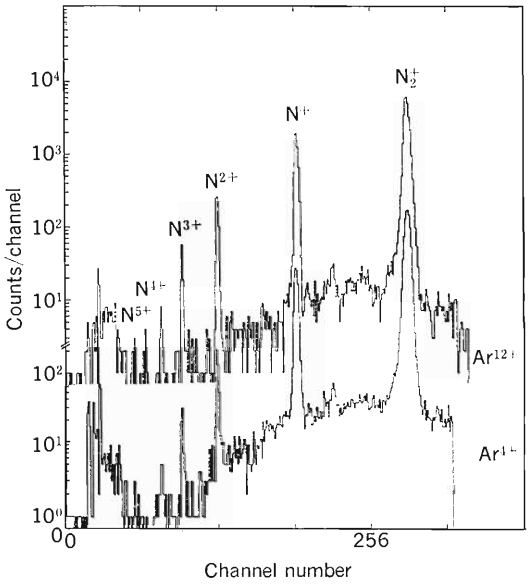

Fig. 1. Typical charge spectra of nitrogen ions produced in 1.05 MeV/amu Ar^{q+} (q=4, 12) ion impact on molecular nitrogen N_2.

energy as of N_2 molecules) is as much as 5–6% of Ar^+ ions. Therefore, such highly-ionized molecular ions are easily dissociated into highly-ionized atomic ions. These highly-ionized molecular ions are assumed to be less likely to dissociate into ions with very asymmetric charge but much likely to do into ions with relatively symmetric charge distribution. Also it is unlikely that low charge state molecular ions dissociate into highly-ionized atomic ions. Therefore, the highly-ionized atomic ions, for example N^{5+} ions, are probably produced via highly-ionized molecular ions through the following pure dissociation processes (for example):

$$N_2^{9+} \rightarrow N^{5+}+N^{4+}$$
$$N_2^{10+} \rightarrow N^{5+}+N^{5+}$$
$$N_2^{11+} \rightarrow N^{5+}+N^{6+}$$

or the dissociation into highly excited atomic states followed by electron emission:

$$N_2^{8+} \rightarrow (N^{4+})^*+N^{4+} \rightarrow N^{5+}+e+N^{4+}$$

These processes are a few examples of the possible dissociation processes.

If the production of highly-ionized atomic recoil ions are assumed to be due to the dissociation (Coulomb explosion) of highly-ionized molecular ions, as discussed above, the product atomic ions should have some kinetic energies due to the Coulomb force between the dissociated atomic ions (the ions with higher charge have higher kinetic energy), compared with those molecular ions such as N_2^+ and N_2^{2+}. These highly-ionized product ions could be assumed to be isotropically distributed with respect of the incident ion direction at the present impact energy. Then, the 100% collection of these product ions through a hole in the parallel plates and acceleration system should be quite difficult. Therefore, when a comparison is made of relative yields of different ions produced in molecular targets, care should be exercised for overall collection efficiency of these ions.

Information such as the energy levels and their lifetimes of highly ionized molecular ions, for example N_2^{10+} ions, as well as accumulation of experimental data could be relevant to further understanding the production mechanism of highly ionized ions from molecular targets.

References

1) T. Tonuma, M. Kase, T. Kambara, H. Kumagai, T. Matsuo, J. Urakawa, H. Shibata, J. Takahashi, S. Özkök, S. H. Be, I. Kohno, and H. Tawara: *J. Phys. B*, **17**, L317 (1984).
2) T. Tonuma, H. Shibata, S. H. Be, H. Kumagai, M. Kase, T. Kambara, I. Kohno, and H. Tawara: unpublished (1985).
3) N. R. Daly and R. E. Powell: *Proc. Phys. Soc.*, **89**, 273 (1966).

RIKEN Accel. Progr. Rep. **18** (1984)

III-2-21. Projectile Dependence of L–MM Auger Electrons Ejected from Ar Target by Heavy-Ion Impact

H. Shibata, T. Matsuo, Y. Awaya, T. Kambara,
M. Kase, H. Kumagai, and N. Tokoro

We have measured the energy distributions of ejected electrons in $Ar^{3,4+}$+Ar collisions with a high energy resolution in order to study the ionization mechanism in heavy-ion atom collisions and the energy levels of highly ionized atoms. L_{23}–M_1M_1 Auger electrons from highly ionized target argon atoms, such as Ar^{7+}, Ar^{6+}, and Ar^{5+}, have been observed, which appears when 3p ionization occurs simultaneously with 2p ionization.[1)]

In the present report, we present preliminary results of the projectile and charge state dependences of the L_{23}–MM Auger transitions of Ar. Though it is known that the normal L_{23}–MM Auger lines appear strongly in the electron or proton impact (see Fig. 1), very few experiments have been made in the heavy-ion impact to study how the degree of the ionization increases as the atomic number of projectile increases. The spectra of the L_{23}–MM Auger electrons ejected from an Ar target by about 1 MeV/amu He, C, N, and Ar ion bombardments have been measured at an ejected angle of 135° with respect to the beam direction. He^+, C^{2+}, N^{2+}, and Ar^{4+} ions were accelerated by the RILAC and He^{2+}, C^{5+}, and N^{6+} ions were produced by passing ions through a carbon foil stripper. The other experimental conditions and apparatus were described elsewhere.[2)]

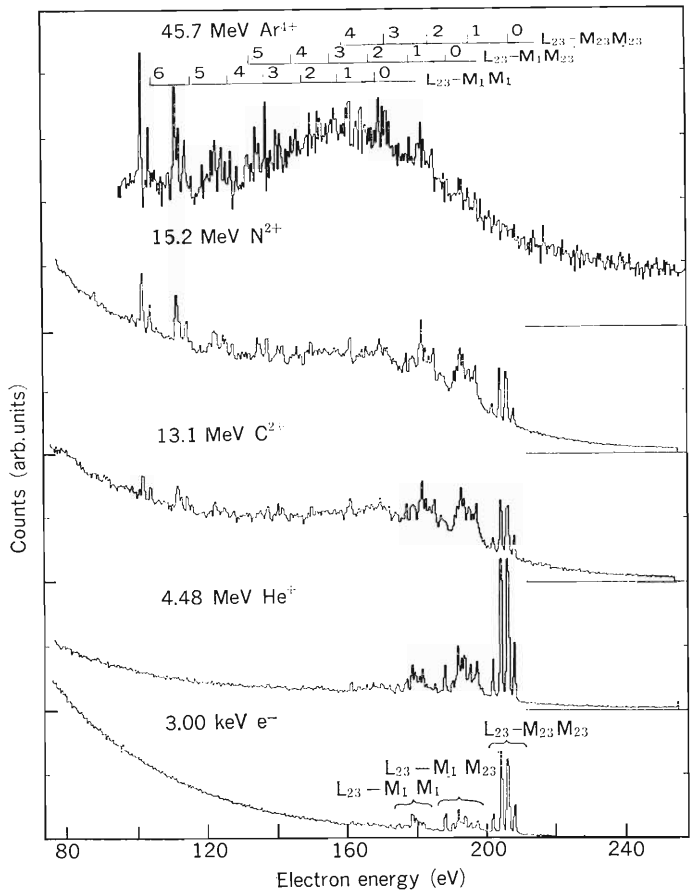

Fig. 1. Energy spectra of electrons ejected from target argon atoms at 135° from the beam direction by about 1 MeV/amu He^+, C^{2+}, N^{2+}, and Ar^{4+} ion impacts and that by electron impact. The lines above the spectra indicate the calculated energy values for the corresponding transitions denoted on their right hand side. The number of each line shows the number of 3p vacancies in the initial state of Auger transition.

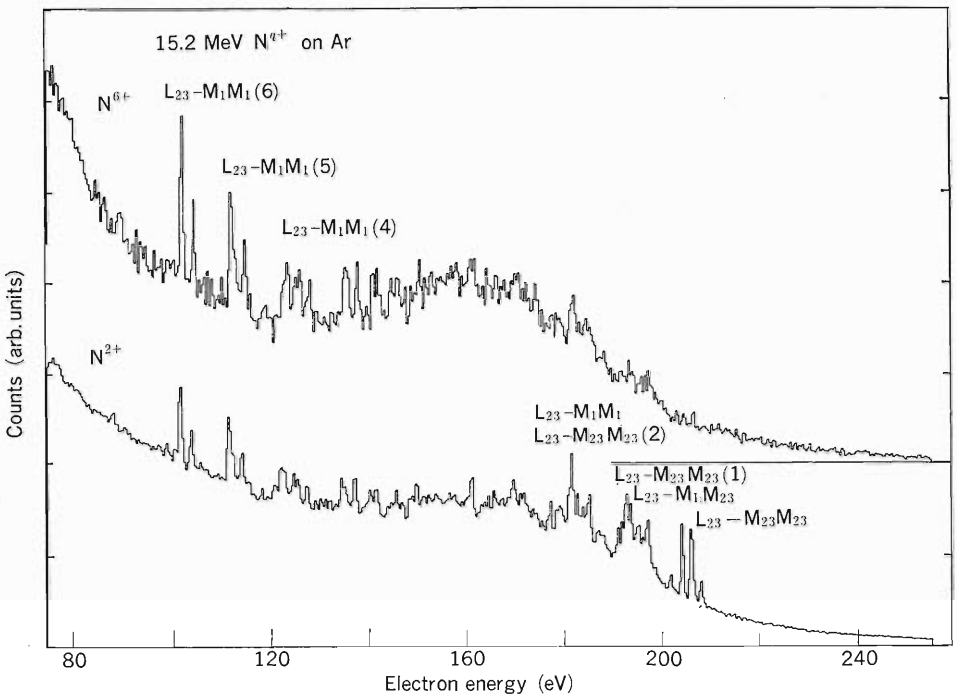

Fig. 2. Energy spectra of electrons from target argon atoms produced by 15.2 MeV N^{2+} and N^{6+} bombardments. The number in the parenthesis of L–MM notation indicates M_{23}-shell (3p) vacancies in the initial state of the Auger transition.

The ejected electron spectra obtained by He^+, C^{2+}, N^{2+}, and Ar^{4+} impacts are shown in Fig. 1 together with a 3.0 keV electron impact data for the comparison. The energy range of electrons was from 80 to 250 eV. The lines above spectra in Fig. 1 indicate L_{23}–MM Auger electron energies calculated by Larkins[3] using the adiabatic model. The number of each line indicates the number of 3p vacancies in the initial state of Auger transition. We have compared the spectra with the theoretical calculations and obtained the following results. In the case of He^+ impact, the normal Auger lines, L_{23}–$M_{23}M_{23}$, L_{23}–M_1M_{23}, and L_{23}–M_1M_1, appeared strongly and they are very similar to the case of electron impact. However, as the atomic number Z of the projectiles increases, the normal Auger lines weakened and the intensities of satellite lines enhanced. Namely, for Ar impact the normal Auger lines disappeared completely and the intensities of the Auger lines from the charge states of 7+, 6+ and 5+ of Ar increased.

Figure 2 shows an example of the charge state dependence of the projectiles having the same velocity. A drastic change is seen between N^{2+} and N^{6+} ion bombardments. For N^{2+} impact the normal Auger transitions were clearly observed; on the other hand, for the case of N^{6+} the normal transitions diminished and satellite lines from the highly ionized atoms enhanced. This may be attributed to the 3p electron transfer from target to projectile, because the one-electron transfer cross section from the target to N^{6+} ion has about two orders of magnitude larger than that for the case of N^{2+} ion.[4]

Further systematic measurements and analysis are in progress.

References

1) T. Matsuo, H. Shibata, J. Urakawa, A. Yagishita, Y. Awaya, T. Kambara, M. Kase, H. Kumagai, and J. Takahashi: *RIKEN Accel. Progr. Rep.*, **17**, 65 (1983).
2) T. Matsuo, J. Urakawa, A. Yagishita, Y. Awaya, T. Kambara, M. Kase, and H. Kumagai: *J. Phys. B*, **16**, L239 (1983).
3) F. P. Larkins: *ibid.*, **4**, 1 (1971).
4) V. S. Nikolaev, L. N. Fateeva, I. S. Dmitriev, and Ya A. Teplova: *Sov. Phys.-JETP*, **13**, 695 (1961).

RIKEN Accel. Progr. Rep. 18 (1984)

III-2-22. Secondary Electrons Emitted from Al under Bombardment with He^+ and He^{++}

A. Koyama, Y. Sasa, and M. Uda

Total yields, γ, of secondary electrons (SE) emitted from metals under bombardment of high-energy light ions are proportional to the stopping power of projectiles, S, over a wide energy range. However, in the case of heavy ion impact, γ/S decreases with increasing S, even in the high energy region where projectiles lose their energy mainly through binary collisions with target electrons (direct Coulomb interactions) and through collective electron excitations; the energy loss by electron capture can be neglected. Then the number of SE created in the surface region should be proportional to S, as in the case of light ion impact. Nevertheless γ/S decreases with S. Therefore the emission probability of SE from the surface might be depressed in the case of heavy ion bombardment.[1)]

In order to elucidate this depression effect on the emission probability, it is indispensable to compare energy spectra of SE induced by heavy-ion impact with those induced by light-ion impact. In this report energy spectra of SE from Al induced by He^+ and He^{++} bombardment are compared to study their projectile charge dependence.

Aluminum was *in situ* vacuum deposited on a substrate of stainless steel at 10^{-9} Torr. The target was transferred to the target chamber at $2\text{–}3\times10^{-10}$ Torr. The angle of an incident beam to the normal of the target surface is 53°. During bombardment, the pressure of the chamber was kept as low as 5×10^{-10} Torr or less. Surface contamination could not be found with Auger analysis using 3 keV electron probe. The optical axis of the electron energy analyzer was set perpendicular to the target surface. Thus only those SE emitted in the normal direction from the surface of the target entered the analyzer and detected. Their emission angle was 127° relative to the incident beam direction. A potential of –9 V was applied to the target, and then SE were accelerated to the analyzer inlet.

Figure 1 (a) shows the energy spectrum of SE induced by He^+ bombardment. Figure 1 (b) is for He^{++} bombardment. Incident energies were 1.1 MeV/amu in both cases. The energy spectrum of SE for incident electrons of 500 eV is also shown for comparison in Fig. 1 (a). Peaks are those of SE (1 eV) and Al L-VV Auger electrons (65 eV), and hyper-satellites (HS) due to two L-shell vacancies (82 eV).

Both spectra induced by He^+ and He^{++} are almost

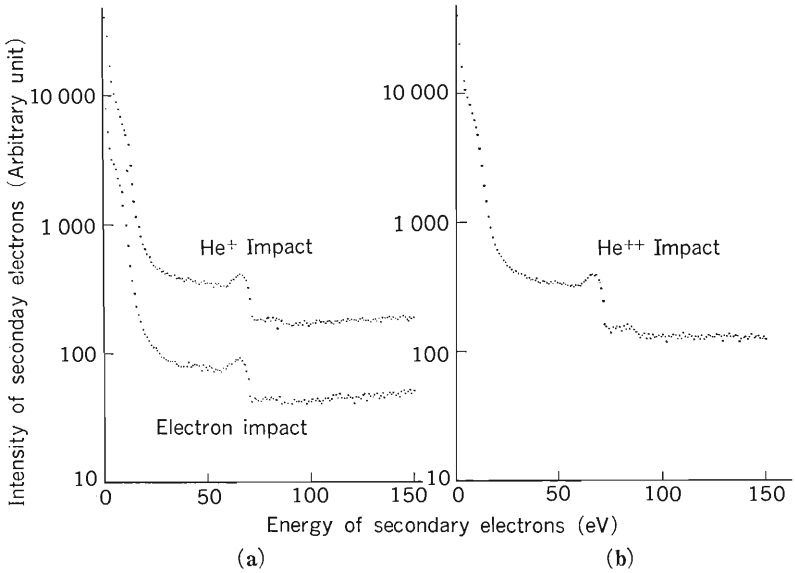

Fig. 1. Energy spectra of secondary electrons from Al induced by He^+ and He^{++} ion bombardment. Incident energy is 1.1 MeV/amu for both projectiles. (a) for He^+. An energy spectrum of secondary electrons for incident electrons of 500 eV is also shown for comparison. (b) for He^{++}.

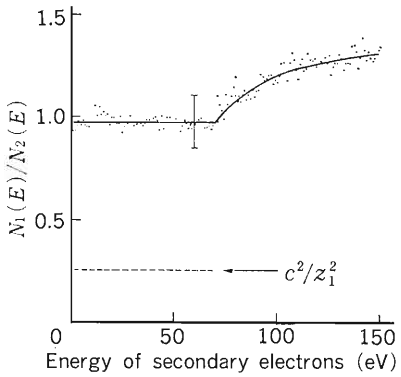

Fig. 2. Ratio of intensities of secondary electrons from Al for incident He^+ to those for incident He^{++} of equal energy of 1.1 MeV/amu. The solid curve is to guide the eye. c^2/z_1^2 is a ratio of square of charge of He^+ to that of He^{++}.

the same in shape, except in the high-energy region above 70 eV. In order to examine this trend more precisely, $R(E)=N_1(E)/N_2(E)$ is shown in Fig. 2. where $N_1(E)$ and $N_2(E)$ are intensities of SE induced by He^+ and He^{++} bombardment, respectively. $R(E)$ is almost constant and equal to unity in the lower energy region from 1–70 eV, and then increases with increasing energy. The increase in intensity of the high energy SE induced by He^+ bombardment is due to backscattering of electrons which are bound initially to He^+ ions but ionized through the electron loss process in the target. In fact, the energy dependence of the spectrum for He^+ impact is similar, in the high energy region above 90 eV, to that for electron impact, as shown in Fig. 1 (a). Since low energy electrons are excited primarily through distant collisions, their excitation probability should be proportional to the square of charge of ions. If it is the case, $R(E)$ should be equal to 0.25 ($=1^2/2^2$) at energies below several eV; however such reduction in $R(E)$ could not be found. It may be caused by the fact that transport processes diminish the character of the primary excitation, or the mean free path of the electron loss for He^+ is short enough compared with the escaping depth of SE. Analysis of this result is now in progress.

Table 1. Intensities of Al L-VV Auger (A) and its hypersatellite peaks (HS) relative to the peak of secondary electrons (SE) and the background (B) at 90 eV.

Projectile	A/SE	A−B/SE	HS−B/SE	A−B/B	HS−B/B
He^+	1.00×10^{-2}	6.1×10^{-3}	6×10^{-4}	1.5	0.15
He^{++}	0.97×10^{-2}	6.5×10^{-3}	7×10^{-4}	2.0	0.23

In Table 1 heights of SE (1 eV), Al L-VV Auger (65 eV), and its hypersatellite (82 eV) peaks are compared for He^+ and He^{++} impact. The mark B means the background for the Auger and hypersatellite peaks. The intensity of SE at 90 eV was adopted as B, because the hypersatellite peaks have no contribution to the background at the energy. Heights of Auger and hypersatellite peaks relative to those of SE (1 eV) are almost the same for both projectiles. Their heights relative to the background are larger by 30–50% for He^{++} than for He^+. This is due to the smaller value of the background for He^{++} bombardment.

Reference

1) A. Koyama, T. Shikata, H. Sakairi, and E. Yagi: *Jpn. J. Appl. Phys.*, **20**, 1216 (1982).

RIKEN Accel. Progr. Rep. 18 (1984)

III-2-23. Chemical Bond Effects on Auger Electrons Induced by He^{2+} Ion Bombardment

M. Uda, A. Koyama, and Y. Sasa

Significant chemical bond effects have been reflected in X-ray satellite structures induced by ion bombardment.[1)-8)] Then it is expected to see similar chemical effects also in Auger spectra. However, no Auger spectra in view of chemical effects, which are excited with fast ions, have been reported yet. By the use of an electron spectrometer operated in an ultra high vacuum ($\sim 2\times 10^{-10}$ Torr)[9)] F KLL or KVV Auger spectra (V: valence band) which were induced by He^{2+} ions accelerated by RILAC were recorded for a series of fluorides.

In situ vacuum deposition of NaF, AlF_3, and Teflon ($(CF_2)_n$) was performed under a standard pressure of 1×10^{-9} Torr. Thickness of the targets thus prepared on stainless steel (SUS 310) backing was about 50Å. The surface of the targets was pre-examined by Auger electron analysis where 2 keV electrons were used as an excitation source to confirm its cleanness. He^{2+} ions with 1.14 MeV/amu were obtained by stripping He^{+} ions having the same velocity through carbon foil.

He^{2+}-induced Auger electron spectra for NaF, AlF_3, and Teflon are shown in Fig. 1. For reference X-ray-induced Auger spectra for these chemical compounds[10)] are also shown in Fig. 2, where A=$2s^22p^4(^1D)+2s^22p^4(^1S)$, C=$2s^12p^5(^3P)$, D=$2s^12p^5(^1P)$, and E=$2s^02p^6(^1S)$, expressed in terms of final state. Here the initial states for these transitions are the same, *i.e.* singly ionized states, $1s^12s^22p^6(^2S)$. The peak B is originated from a doubly ionized initial state[10)] where the initial state has one vacancy each in K and valence band or $L_{2,3}$ shells. Then the peak B is due to or ascribed to the transition $1s^12s^22p^5$ (^3P, ^1P)$\rightarrow 1s^22s^22p^3(^4S, ^2D, ^2P)$ or $KL_{2,3}(^3P, ^1P)\rightarrow L^3_{2,3}(^4S, ^2D, ^2P)$. As can be seen from Fig. 1, the peak B for NaF induced by He^{2+} ion bombardment is much more enhanced than that induced by X-ray. This means that a probability to produce double vacancies on F atoms is much higher in He^{2+} ion excitation than in X-ray excitation. Then a relaxation process on the F L vacancy prior to F KLL or KVV Auger emission can clearly be seen in the intensity distribution of the Auger spectra induced by He^{2+} ion bombardment. The intensity of the peak B decreased with the increase in the covalency of fluorides in order of NaF, AlF_3, and Teflon. Such a tendency is more stressed in the ion induced Auger spectra than in those excited with X-rays. In addition, a shift of the peak D to a low energy side and line broadening can also be seen in the F KVV Auger spectra of these fluorides, which were excited with He^{2+} ions. This is, at least in part, caused by

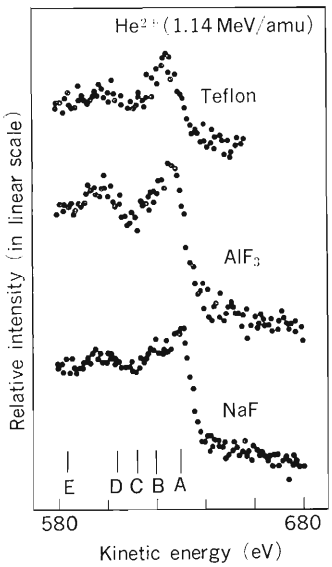

Fig. 1. Auger electron spectra of F KVV or KLL for NaF, AlF_3 and Teflon induced by He^{2+} ions with 1.14 MeV/amu.

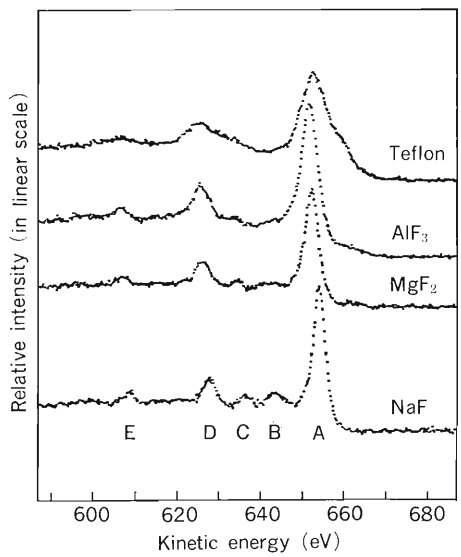

Fig. 2. Auger electron spectra of F KVV or KLL of several fluorides induced by Al K_α X-ray.[10)]

the overlap of several weak peaks originated from doubly ionized initial states. In addition, an intense background at the low energy side of F KVV for the ion induced Auger spectra comes from a shoulder of a broad binary peak centered at about 610 eV. Further analysis is in progress.

References

1) P. G. Burkhalter, A. R. Knudson, D. J. Nagel, and K. L. Dunning: *Phys. Rev. A*, **6**, 2093 (1972).
2) M. Uda, H. Endo, K. Maeda, Y. Awaya, M. Kobayashi, Y. Sasa, H. Kumagai, and T. Tonuma: *Phys. Rev. Lett.*, **42**, 1257 (1979).
3) H. Endo, M. Uda, and K. Maeda: *Phys. Rev. A*, **22**, 1436 (1980).
4) M. Uda, H. Endo, K. Maeda, Y. Sasa, and M. Kobayashi: *Z. Phys. A*, **300**, 1 (1981).
5) M. Uda, K. Maeda, H. Endo, Y. Sasa, and M. Kobayashi: Inner-Shell and X-Ray Physics of Atoms and Solids, (eds D. J. Fabian, H. Kleinpoppen, and L. M. Watson), Plenum, New York, p. 205 (1981).
6) H. Endo and M. Uda: *Z. Phys. A*, **306**, 187 (1982).
7) R. L. Watson, F. E. Jensen, and T. Chiao: *Phys. Rev. A*, **10**, 1230 (1974).
8) O. Benka, R. L. Watson, and R. A. Kenefick: *Phys. Rev. Lett.*, **47**, 1202 (1981).
9) A. Koyama, Y. Sasa, Y. Ishibe, A. Shiraishi, T. Shiga, H. Omori, K. Nishi, M. Fuse and M. Uda: *RIKEN Accel. Progr. Rep.*, **17**, 122 (1983).
10) M. Uda, K. Maeda, A. Koyama, and Y. Sasa: *Phys. Rev. A*, **29**, 1258 (1984).

RIKEN Accel. Progr. Rep. 18 (1984)

III-2-24. Studies of Magnetic Structure of Cobalt Ferrite Surfaces by ^{119}Sb Emission Mössbauer Spectroscopy

T. Okada, F. Ambe, S. Ambe, and H. Sekizawa

A part of the present investigation has been reported.[1] The present report is concerned with the results of subsequent detailed research. The magnetic properties and the chemical states of dilute Sn (←Sb) ions on the surfaces of $CoFe_2O_4$ has been investigated by means of ^{119}Sb emission Mössbauer spectroscopy. Since the origin of the hyperfine magnetic fields H_{hf} at the nuclei of ^{119}Sn (←^{119}Sb) is the electron-spin polarization induced by the surrounding magnetic ions through oxygen ions, the investigation of the fields supplies important information on the exchange interactions between magnetic ions near the surfaces.

Experimental procedures have been reported in previous reports.[1),2)] A tin plate was irradiated with about 1C of 38-MeV α particles accelerated by the cyclotron. The desired nuclide ^{119}Sb remaining in solution was purified by various chemical separations. Carrier-non-added ^{119}Sb (→^{119}Sn) ions were absorbed hydrolytically on the surfaces of the ferrimagnetic oxide powders of $CoFe_2O_4$, the Néel temperature of which was about 520°C. Emission Mössbauer analysis was made on ^{119}Sn arising from ^{119}Sb on the surfaces of $CoFe_2O_4$ by means of a conventional spectrometer in absorber-drive mode.

Emission Mössbauer spectra of the "as adsorbed" $CoFe_2O_4$—^{119}Sb at 297 K (A), 77 K (B), 5 K (C), and 5 K with an external magnetic field H_{ext} (D) are shown in Fig. 1. The field H_{ext} of 35 kOe was applied parallel to the γ-rays. It can be seen from Fig. 1 that emission lines at 297 K (A) and 77 K (B) are considerably broadened compared with that of diamagnetic $^{119}Sn^{4+}$ ions in nonmagnetic material, and that the lines at 5 K (C) and (D) are split into two wide peaks through the supertransferred hyperfine interaction. From the values of isomer shift (+0.2 mm·s^{-1} relative to $BaSnO_3$), it is certain that the ^{119}Sn ions resulting from $^{119}Sb^{5+}$

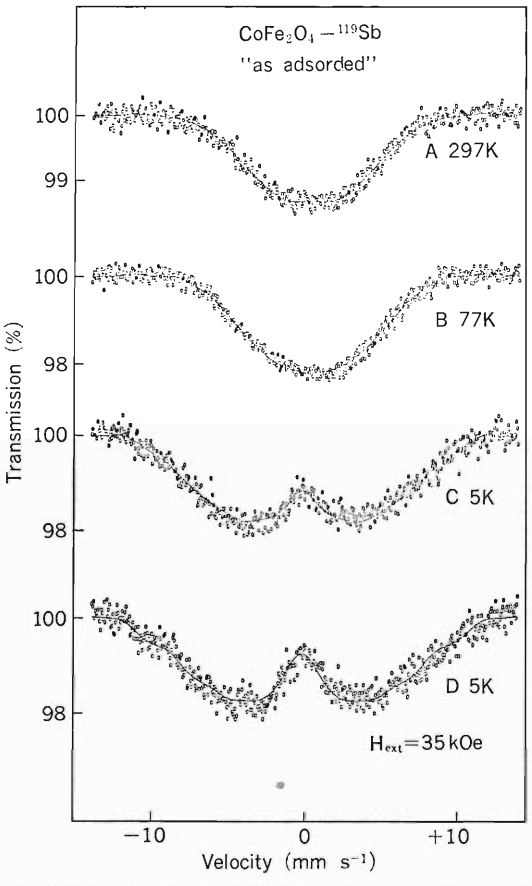

Fig. 1. Mössbauer spectra of "as adsorbed" $CoFe_2O_4$—^{119}Sb.

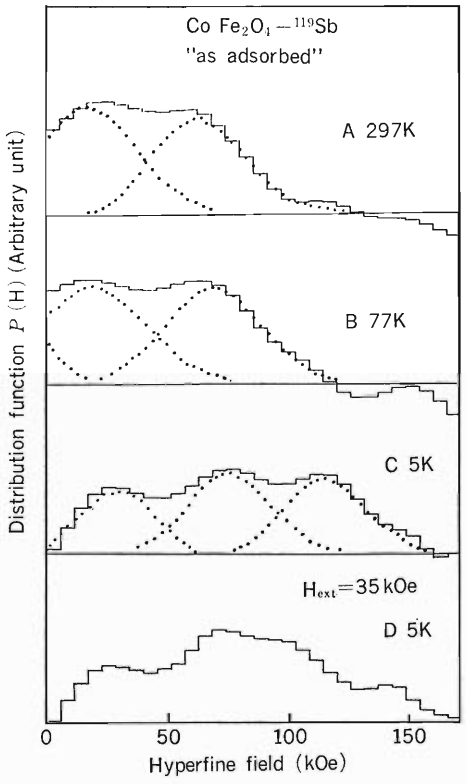

Fig. 2. Distribution function $P(H)$ of the hyperfine magnetic fields of "as adsorbed" $CoFe_2O_4$—^{119}Sb.

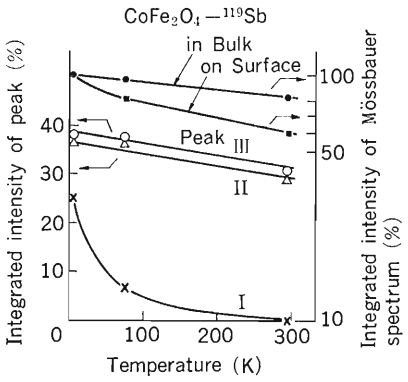

Fig. 3. Integrated intensities of peak I, II, and III and of Mössbauer spectra of "as adsorbed" and bulk $CoFe_2O_4$—^{119}Sb.

ions are tetravalent. Integrated intensities of the Mössbauer spectra of specimens (A), (B), (C), and (D) in Fig. 1 are in a ratio of 0.6: 0.8: 1.0: 1.0 (see Fig. 3). From this ratio, it seems that the ^{119}Sb ions adsorbed on one or two layers above the surfaces are bonded with oxygen ions more weakly than the ^{119}Sb ions in the bulk. Mössbauer spectra were analyzed by the Hesse-Rübartsch method, and the obtained distribution function $P(H)$ of the hyperfine magnetic field H_{hf} is shown in Fig. 2. Figure 2 shows that $P(H)$ at 297 K (A) and 77 K (B) consist of two main parts and a small one and that $P(H)$ of (C) is apparently made up of three parts. These $P(H)$ are preliminarily analyzed by means of fitting with Gaussians, and divided into three peaks (called peak I, II, and III in order of magnitude).

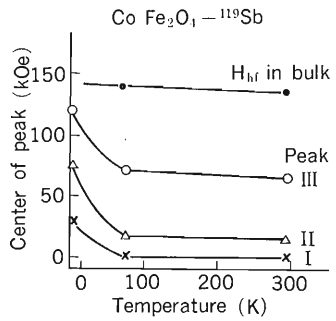

Fig. 4. Center of peak I, II, and III and H_{hf} in the bulk $CoFe_2O_4$—^{119}Sb.

The results of fitting are shown by the dotted lines in Fig. 2. The peak I in (A) and (B) are very small but suddenly grow at low temperature in (C) and (D). From Fig. 3 it seems that (1) $^{119}Sb^{5+}$ ions adsorbed to give peak I are very loosely connected with oxygen ions in the matrix because integrated intensity of peak I is very small in (A) and (B), and (2) magnetic property of ^{119}Sb ions giving rise to peak I is superparamagnetic because the values of H_{hf} are almost zero in (A) and (B) and about 30 kOe in (C) and (D), as seen in Fig. 4. These results indicate that a part of the magnetic ions near the surface layers are superparamagnetic.

References

1) T. Okada, S. Ambe, F. Ambe, and H. Sekizawa: *RIKEN Accel. Progr. Rep.*, **17**, 74 (1983).
2) T. Okada, F. Ambe, S. Ambe, and H. Sekizawa: *Phys. Chem.*, **86**, 4726 (1982).

RIKEN Accel. Progr. Rep. **18** (1984)

III-2-25. Perturbed Angular Correlation of γ-Rays Emitted from ^{111}Cd ($\leftarrow{}^{111}$In) in α-Fe_2O_3

K. Asai, F. Ambe, S. Ambe, T. Okada, and H. Sekizawa

Time differential perturbed angular correlation (TDPAC) of γ-rays is a valuable tool not only in the field of nuclear physics but also in the fields of solid state physics and chemistry. The nuclide ^{111}Cd ($\leftarrow{}^{111}$In) is one of the most popular ones used in this type of measurement. It emits 171–245 keV cascade γ-rays through the 5/2+ intermediate state which has a half life of 85 ns. It has been reported that hyperfine frequencies at ^{111}Cd are widely distributed in insulators[1),2)] due to the after-effects of the preceding electron capture (EC) decay of ^{111}In. Because these distributions were large enough to smear out the hyperfine interactions inherent in the host materials, it is widely believed that TDAPC using a nuclide after EC decay is not useful in studying insulators.[3),4)]

Salomon,[5)] in 1964, made TDPAC measurement on In_2O_3 at 280°C and found that the after-effects were considerably reduced at this temperature. This finding suggests that a nuclide after EC decay is also useful in studying insulators by making a high temperature measurement, but this fact seems to remain unnoticed. It can be also said that the after-effects themselves should be investigated further because they provide valuable information on the electronic excited states of the ions concerned.

We measured TDPAC of γ-rays emitted from ^{111}Cd ($\leftarrow{}^{111}$In) in a typical antiferromagnetic oxide α-Fe_2O_3 (T_N=680°C) in a wide temperature range from 20°C to 714°C to establish the utility of a high temperature measurement and to study the features of the after-effects in magnetic insulators observed around room temperature. In this report, we present some of the results obtained in the present study. The detailed description of the experimental procedures such as sample preparation, data taking and processing, and analysis are given in Ref. 6.

Some representative spectra of $A_{22}\cdot G_{22}(t)$ obtained in the experiment are shown in Fig. 1. In α-Fe_2O_3, it is expected that $^{111}In^{3+}$ ions replace Fe^{3+} ions, and the daughter ^{111}Cd nuclei feel both the hyperfine magnetic field H_{hf}, supertransferred from Fe^{3+} ions, and the electric field gradient (EFG). If there is no disturbance around ^{111}Cd such as the after-effects of the EC decay, it is reasonably assumed that (1) both H_{hf} and EFG are unique, (2) the EFG is axially symmetric, and (3) the angle θ between the direction of H_{hf} and the z-axis of EFG is 90°.

First, we analyzed the observed spectra based on the above assumptions. The values of the Larmor angular frequency ω_L and the quadrupolar angular frequency ω_Q were obtained by a least-squares fitting of the data with a semi-empirical formula $A_{22}\cdot G_{22}(t) = C_1 \times G_{22}(t)_{uniq} + C_2$ in the region $t \geqq 50$ ns. In this formula, $G_{22}(t)_{uniq}$ is the theoretically given perturbation factor as a function of ω_L and ω_Q, on the assumption that a random orientation of microcrystals with a unique static interaction,[7)] and C_1 and C_2 are adjustable parameters. The spectra measured at high temperatures were reproduced considerably well with negligibly small values of C_2 (Fig. 1 (a) and (b)). On the other hand, those measured at low temperatures were only poorly reproduced (Fig. 1 (c)). These results mean that the above assumptions hold well at high temperatures, whereas they do not at low temperatures.

Next, we analyzed the spectra measured at low temperatures assuming a distribution of one of the hyperfine parameters. We define a quantity $G_{22}(t)\Delta\xi$ as the perturbation factor when a hyperfine

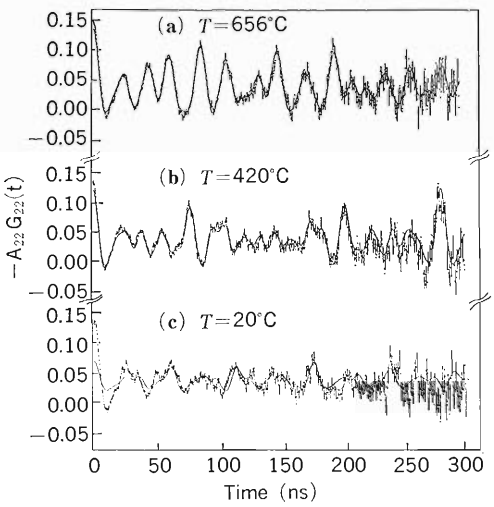

Fig. 1. TDPAC coefficient $A_{22}\cdot G_{22}(t)$ of the ^{111}Cd($\leftarrow{}^{111}$In) γ-γ correlation in α-Fe_2O_3. (a): at 656°C, (b): at 420°C, and (c): at 20°C. The solid curves represent the fitted values of $C_1 \times G_{22}(t)_{uniq} + C_2$.

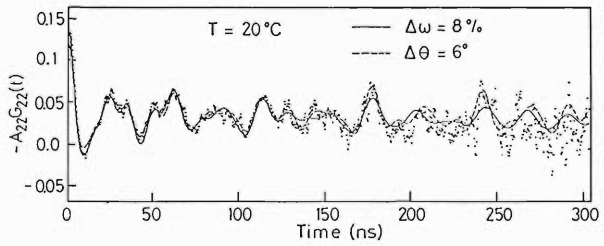

Fig. 2. TDPAC coefficient $A_{22}\cdot G_{22}(t)$ of the ^{111}Cd($\leftarrow{}^{111}$In) γ-γ correlation in α-Fe_2O_3 at 20°C. The solid curve represents the fitted values assuming a distribution of $\Delta\omega_Q/\omega_{Q0}=8\%$, and the dotted line represents the values assuming $\Delta\theta=6°$.

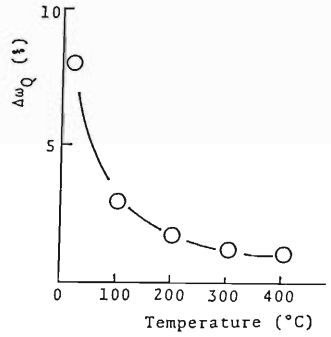

Fig. 3. Temperature dependence of $\Delta\omega_Q$.

parameter ξ in the interaction Hamiltonian has a Gaussian distribution around ξ_0 with a width $\Delta\xi$. We examined the three cases of $\xi=\omega_L$, ω_Q, or θ by applying a least-squares fitting. In the case of $\xi=\omega_L$, the χ^2-factor was not reduced by assigning any finite value to $\Delta\omega_L$. On the contrary, the factor was reduced considerably on assuming 1) a distribution of ω_Q with $\Delta\omega_Q/\omega_{Q0}=8\%$ or 2) that of θ with $\Delta\theta=6°$ around $\theta_0=90°$. The fitted curves for the spectrum at 20°C are shown in Fig. 2. The obtained values of ω_L were the same for these two cases, and that of ω_{Q0} for the case 1) was equal to that of ω_Q for the case 2).

The temperature dependence of $\Delta\omega_Q$ giving the best fit is shown in Fig. 3. The value increases rapidly with the decrease in temperature below 200°C. The temperature dependences of H_{hf} and ω_Q (or ω_{Q0}) are shown in Fig. 4 (a) and (b). These temperature dependences of H_{hf} and ω_Q (or ω_{Q0}) are those expected for the electronic ground state ^{111}Cd ions.

The distribution of the hyperfine parameters observed at low temperatures is ascribed to the after-effects of the preceding EC decay. The plausible mechanism is as follows. The ^{111}Cd ions arising from ^{111}In are in highly excited electronic states as the result of the following Auger effect, and then relax to the stable state through some low-lying electronic excited states which have rather long

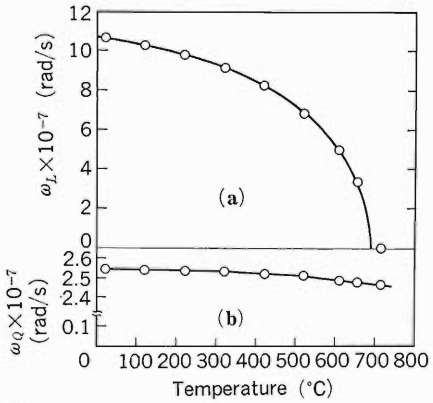

Fig. 4. Temperature dependences of hyperfine frequencies for ^{111}Cd in α-Fe_2O_3. (a): ω_L, (b): ω_Q.

lifetimes; ^{111}Cd nuclei in the ions which are still left in these low-lying excited electronic states also contribute to the perturbation factor along with ^{111}Cd in the ions already relaxed to the stable state. Probably, each ^{111}Cd nucleus in the excited ion feels some extra EFG in addition to the EFG in the stable-state ion because of some electronic defect in its environment. The temperature dependence of the distribution means that the lifetime of the excited ions decreases with the increase in temperature, because of an increase in electron mobility resulting in a high rate of valence rearrangement.

It is revealed by the present work that the after-effects of the preceding EC decay of ^{111}In do not influence the TDPAC spectrum of ^{111}Cd in α-Fe_2O_3 at high temperatures, where the excited ions are annealed out in a short enough time. This finding proves TDPAC of ^{111}Cd ($\leftarrow{}^{111}$In) to be a valuable tool for the study of insulators at high temperatures. The features of the excited ^{111}Cd ions and of their relaxation mechanism are now under consideration. We have a plan to use a nuclide ^{111}Cd ($\leftarrow{}^{111m}$Cd) for the study of insulators at low temperatures, because it is known that the after-effects of isomeric decay on TDPAC spectrum are negligibly small.[2)]

References

1) P. Lehmann and J. Miller: *J. Phys. Radium*, **17**, 526 (1956).
2) H. Haas and D.A. Shirley: *J. Chem. Phys.*, **58**, 3339 (1973).
3) J. P. Adloff: *Radiochim. Acta*, **25**, 57 (1978).
4) P. Boyer and A. Baudry: Hot Atom Chemistry, (ed. by T. Matsuura), Kodansha, Tokyo, p. 315 (1984).
5) M. Salomon: *Nucl. Phys.*, **54**, 171 (1964).
6) K. Asai, F. Ambe, S. Ambe, and H. Sekizawa: *J. Phys. Soc. Jpn.*, **53**, 4109 (1984).
7) H. Frauenfelder and R. M. Steffen: α-, β- and γ-Ray Spectroscopy, Vol. 2, (ed. by K. Siegbahn), North-Holland, Amsterdam, p. 1111 (1964).

RIKEN Accel. Progr. Rep. 18 (1984)

III-2-26. TDPAC of γ-Rays Emitted from ^{111}Cd ($\leftarrow^{111}$In) in Fe_3O_4

K. Asai, T. Okada, and H. Sekizawa

Nuclei of diamagnetic ions in magnetic oxides feel the hyperfine magnetic fields transferred from the neighboring magnetic ions through the intervening oxygen ions. This quantity, the supertransferred hyperfine magnetic field H_{STHF}, has been widely studied because it provides information on the superexchange interactions between the magnetic ions in the oxides.[1] Time differential perturbed angular correlation (TDPAC) of γ-rays emitted from ^{111}Cd ($\leftarrow^{111}$In) is a useful method in this type of studies. In the present report, we present some remarks on the experimental geometry in measuring H_{STHF} in a ferro- or a ferrimagnet, and then show some results in Fe_3O_4 obtained with the newly proposed geometry.

When the specimen is a collinear ferro- or a ferrimagnet polycrystal, coincident counts $N_\perp(\theta, t)$ of the cascade γ-rays are measured usually with an external magnetic field H_{ext} applied perpendicular to the detectors plane in order to polarize the magnetization of the specimen to this direction, where θ is the angle between the cascade γ-rays, and t, the time interval between them. We define the direction of H_{ext} as the z-axis of the system. The direction of H_{STHF} is expected to be parallel or antiparallel to the z-axis in this setup.

One method employed widely for deriving the frequency profile of the Larmor frequency ω_L is to derive it from the frequency spectrum of the normalized difference $R(t)$ between the coincident counts at $\theta=\pi/2$ and π. The definition of $R(t)$ is as follows:

$$R(t)\equiv[N_\perp(\pi/2, t)-N_\perp(\pi, t)]/[N_\perp(\pi/2, t)+N_\perp(\pi, t)]\fallingdotseq-\frac{3}{4}A_{22}\cos(2\omega_L t).$$

We call, hereafter, this method "multiple $\pi/2$-method". This method, however, has some drawbacks in actual experiments:

(1) The sign of ω_L cannot be determined.
(2) The time spectrum $R(t)$ has the Fourier components not only at $\omega=2\omega_L$, but also at ω_L and at 0, if the magnetizations of the microcrystals are not completely aligned to the z-axis. In this situation, the profile of $2\omega_L$ is not obtained directly from the Fourier spectrum of $R(t)$.
(3) The time spectrum $R(t)$ has non-zero value and can oscillate, even when there are no appreciable hyperfine magnetic interactions at the nuclei. Thus, a false value of ω_L can be derived in this case.

Then, we propose another method to derive the frequency profile of ω_L. In this method, the profile is derived from the Fourier spectrum of the normalized difference $R'(t)$ between the coincident counts at $\theta=3/4\pi$, and $+3/4\pi$. The definition of $R'(t)$ is as follows:

$$R'(t)\equiv[N_\perp(-3/4\pi, t)-N_\perp(+3/4\pi, t)]/[N_\perp(-3/4\pi, t)+N_\perp(+3/4\pi, t)]\fallingdotseq\frac{3}{4}A_{22}\sin(2\omega_L t)$$

We call this method "multiple $\pi/4$-method". This method has no drawbacks described above:

(1) The profile of ω_L is determined up to the sign.
(2) The spectrum $R'(t)$ has no Fourier components except at $\omega=2\omega_L$, even if the magnetizations are not completely aligned to the z-axis provided that they are symmetrically distributed around it. In this situation, the amplitude of the frequency component at $\omega=2\omega_L$ is reduced.
(3) The spectrum $R'(t)$ is always equal to zero, when there are no appreciable hyperfine magnetic interactions at the nuclei.

Thus, we consider that the "multiple $\pi/4$-method" is more appropriate than the "multiple $\pi/2$-method" in the study of H_{STHF} of a ferro- or a ferrimagnet below the Curie temperature.

Figure 1 shows the spectra of $R'(t)$ in Fe_3O_4 at various temperatures. The value of ω_L ($=-\gamma H_{STHF}$) is positive, meaning that the direction of H_{STHF} is parallel to that of H_{ext} because the nuclear gyromagnetic ratio γ of the 5/2+ state of ^{111}Cd is negative. The profiles of ω_L derived from $R'(t)$ are shown in Fig. 2. The distribution of ω_L is narrow at temperatures above 131 K, whereas considerably broad at temperatures below 110 K. On the assumption that H_{STHF} ($\propto\omega_L$) has a Gaussian distribution, the center value and the width of the distribution are calculated by a least-squares fitting.[2] The results are shown in Fig. 3. There are stepwise changes both in H_0 and ΔH.

The detailed mechanism of the distribution of H_{STHF} will be presented elsewhere. Only the qualitative explanation is described in the following. In Fe_3O_4, ^{111}Cd nuclei are in the tetrahedral (A) sites

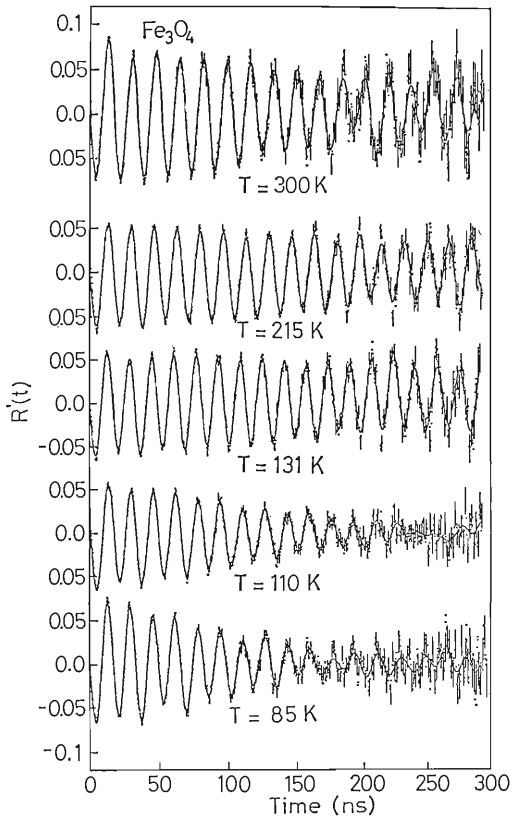

Fig. 1. Normalized anisotropy $R'(t)$ of the coincident counts in Fe_3O_4.

and feel H_{STHF} transferred dominantly from the octahedral (B) site magnetic ions. There are nominally the same number of Fe^{2+} and Fe^{3+} ions in the B sites in this oxide. At high temperatures about the the Verwey temperature (T_V=120 K), 3d electrons of the ions itinerate among them and thus, there are only one kind of Fe ions in the B sites and H_{STHF} felt in the A site is unique. On the other hand, at low temperatures below T_V, Fe^{2+} and Fe^{3+} ions are ionically ordered in the B sites[3] in a way that there are some kind of non-equivalent A sites and thus H_{STHF} felt in the A site is distributed.

In the present report, it is shown that TDPAC of γ-ray is a useful technique in the study of H_{STHF} in the magnetic oxide. The study on various magnetic oxides other than Fe_3O_4 is in progress.

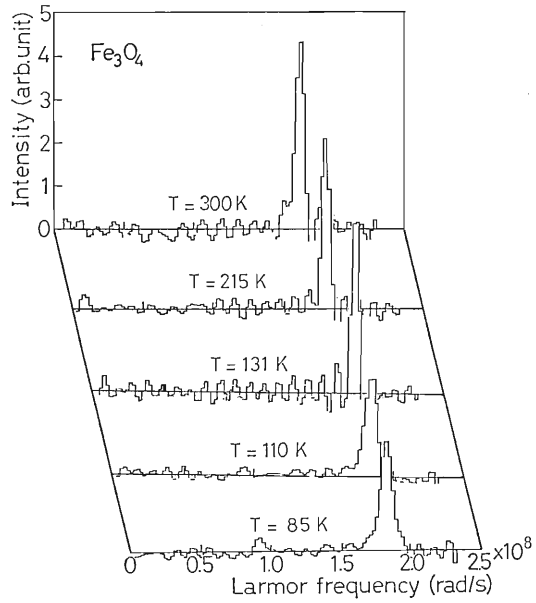

Fig. 2. Profiles of the Larmor frequency ω_L.

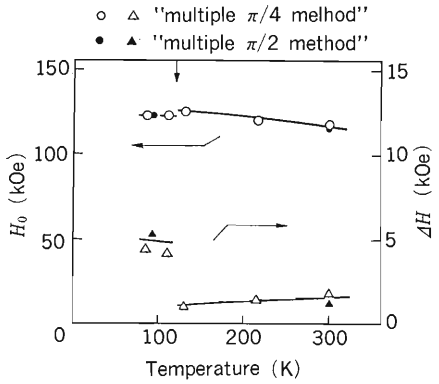

Fig. 3. Temperature dependences of the center value H_0 and the width ΔH of the distribution of H_{STHF}. ○ and △ represent the values obtained by the "multiple π/4-method", and ● and ▲, by the "multiple π/2-method".

References

1) B. J. Evans and L. J. Swartzendruber: *Phys. Rev. B*, **6**, 223 (1972).
2) H. Sekizawa, K. Asai, T. Okada, N. Sakai, N. Shiotani, and E. Yagi: *IPCR Cyclotron Progr. Rep.*, **11**, 106 (1977).
3) G. Shirane, S. Chikazumi, J. Akimitsu, K. Chiba, M. Matsui, and Y. Fujii: *J. Phys. Soc. Jpn.*, **39**, 949 (1975).

RIKEN Accel. Progr. Rep. **18** (1984)

III-2-27. Perturbed Angular Distributions of Gamma-Rays from Dy under Transient Magnetic Field

A. Hashizume, N. Sakai, and K. Asai

When a recoil nucleus produced by the Coulomb excitation process is implanted into a polarized ferromagnetic material, the nucleus receives a strong magnetic field in the deceleration process. The hyperfine interaction between the transient magnetic field and the magnetic moment of the very short-lived excited nuclear level causes precession of angular distribution of the γ-rays emitted from the state.

As reported in Ref. 1, perturbed angular distribution experiments of γ-rays were performed by bombarding natural dysprosium evaporated onto a 6 μm Fe foil by 48 to 51 MeV ^{40}Ar ions accelerated by RILAC. In γ-ray spectra, 168.8 keV ($4^+ \rightarrow 2^+$) γ-ray in ^{164}Dy was well separated. $A_2 = 0.137 \pm 0.012$, $A_4 = -0.07 \pm 0.012$, and $A_2 = 0.122 \pm 0.014$, $A_4 = -0.011 \pm 0.02$ were obtained for the angular distribution of the γ-rays when the external fields of upward and downward direction were applied perpendicular to the plane defined by the incident beam and γ-ray detection directions. An angular shift of 0.39 rad was observed.

Parametrizations of the transient magnetic field have been proposed by many authors. We used the following equation to estimate the transient magnetic field.[2)]

$$B(v, Z) = a \cdot Z(v/v_0) \cdot \exp(-\beta v_0/v),$$

where B is the transient field, v_0 the Bohr velocity, and a and β are parameters. The value of g factor of the 0.242 keV (4^+) state is not known. However from the systematics, it is expected that the value is not so different from that of the 2^+ state. If an equation, $g(I) = g(2)(1+\alpha I^2)/(1+4\alpha)$, is used with a parameter $\alpha = -1.5 \times 10^{-3}$ obtained from ^{160}Dy, and with $g(2) = +0.684$ for ^{164}Dy, an approximately calculated value becomes 0.42.

By using the parameter $a = 11.5$ T and $\beta = 0.1$, the mean precession angle was calculated from

$$\phi(t) = -0.047 g \int_0^t B(t)\, dt \quad (\text{mrad} \cdot T^{-1} \cdot \text{ps}^{-1})$$

and

$$\bar{\phi} = \lambda \int_0^\infty \phi(t) \cdot \exp(-\lambda t)\, dt,$$

where $\phi(t)$ is the precession angle, $\bar{\phi}$ the mean precession angle, and λ the decay constant of the excited state. Using the maximum recoil velocity of Dy caused by ^{40}Ar ions, one obtains 0.62 rad as an upper limit of the precession angle. The obtained experimental value is to within this limit. We are now developing a code following the method of Winther and de Boer to make more precise analysis.

References

1) A. Hashizume, N. Sakai, and K. Asai: *RIKEN Accel. Progr. Rep.*, **17**, 27 (1983).
2) O. Häusser, H. R. Andrews, D. Ward, N. Rud, P. Taras, R. Nicole, J. Keinonen, P. Skensved, and C. V. Stager: *Nucl. Phys. A*, **406**, 339 (1983).

RIKEN Accel. Progr. Rep. **18** (1984)

III-2-28. Plasma Wall Interaction

Y. Sakamoto, Y. Ishibe, S. Ishii, A. Minoh, K. Okazaki,
H. Oyama, K. Yano, and S. Kakinuma

We report the present status of three studies relating to plasma wall interaction: (1) deuterium atom depth profile near a surface of TiC irradiated with an ECR plasma, (2) LIFS (laser induced fluorescence spectroscopy) measurement of physical sputtering of iron bombarded by plasma ions and (3) interaction of hydrogen ions with iron oxide.

(1) Deuterium atom depth profile near a surface of TiC irradiated with an ECR plasma

It is indispensable to know the depth profiles of hydrogen isotopes near the surface in order to understand their recycling in fusion devices or mechanism of discharge cleaning. We have been investigating TiC samples irradiated by an ECR deuterium plasma. TiC is one of the most important first wall materials of fusion devices in the near future. The ECR hydrogen (isotope) plasma produces abundant neutral atoms useful for discharge cleaning. The TiC samples (20 μm in thickness) were prepared by means of CVD coating on poco graphite substrate. The samples contain much hydrogen owing to its manufacturing process (CVD). This is a reason why we use a deuterium plasma.

Figure 1 shows the deuterium plasma irradiation apparatus. The electron density and the temperature of plasma were respectively 9.6×10^{9} cm^{-3} and 4.7 eV at a gas pressure of 2×10^{-2} Pa. The flux densities of ion and neutral atom flowing onto the sample surface becomes about 10^{15}/cm^2·sec respectively.

Deuterium atoms near the surface were detected by ERD[1] (elastic recoil detection) method by using Ar^{4+} beam from the RILAC, whose incidence angle and energy were 30° and 46.92 MeV, respectively. Figure 2 shows the depth profiles of H and D. The arrows indicate the energy of recoiled atoms from the surface. The deuterium density near the surface increases with irradiation time. The hydrogen density decreases with irradiation time; this is because of desorption of hydrogen due to the sample temperature rise during the irradiation (200°C). Deuterium atoms are distributed up to several thousand Å from the surface, but reach saturation near the surface after 5 hr irradiation. Since during the ECR discharge cleaning the wall temperature is kept at about 200°C, we must assume a similar density profile.

(2) LIFS measurement of physical sputtering of iron bombarded by plasma ions

Since the LIFS method gives a useful information for the assessment of materials under the irradiation by plasma particles, we measured physically sputtered Fe atom flux near the target by this method. A preliminary experiment has been carried out to obtain the relative neutral Fe atom density.[2]

Figure 3 shows the experimental arrangement. An ECR plasma was produced in a magnetic mirror field by applying 9 GHz, 2 kW, pulsively modulated (10 ms) microwave. The target was set at the end of a plasma column and insulated from the wall in order to give arbitrary bias voltage. Gases used were Ne (M=20), Ar (40), and Kr (84). Light from a laser (Phase R. Co., dye laser, DL-2100C) was transformed into the second harmonic by an ADP crystal. Output power was 6.2 kW (at 3,020 Å) and a saturation parameter was 0.4. By exciting Fe

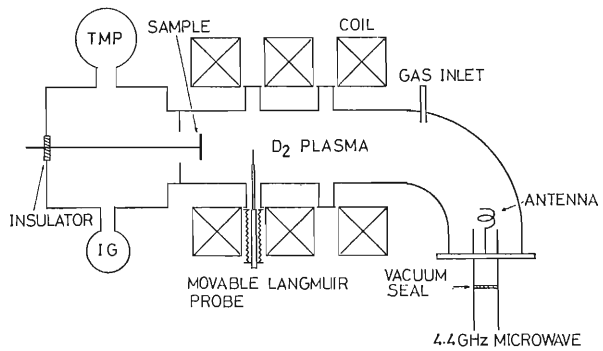

Fig. 1. Schematic arrangement of D_2 plasma irradiation apparatus.

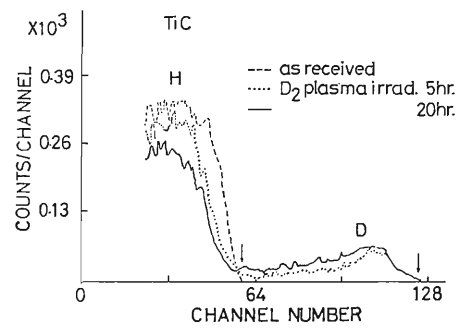

Fig. 2. Deuterium atom depth profiles in the near surface of TiC irradiated with ECR plasma, together with that of hydrogen. Arrows show positions of surface atoms.

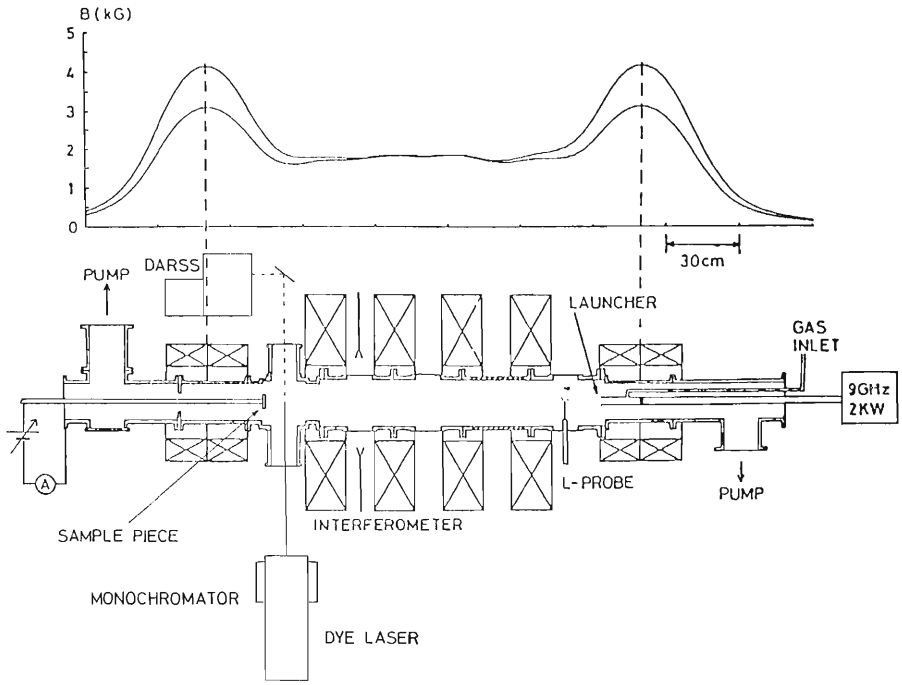

Fig. 3. Apparatus for plasma irradiation of Fe metal sample and the measurement system.

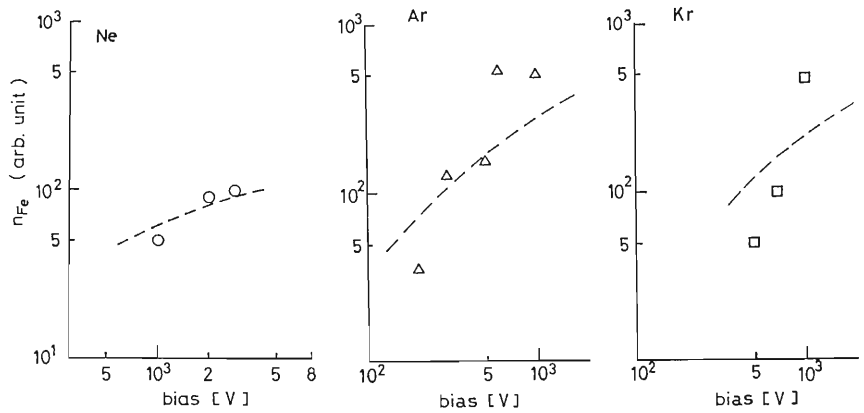

Fig. 4. Variation of iron density with bias voltage. Dotted lines present relative sputtering yields.

atoms by the transition $a^5D_4 \rightarrow y^5D_4^o$ (3,020 Å) or $a^5D_4 \rightarrow y^5D_4^o$ (3,059 Å), we observed fluorescence $y^5D_4^o \rightarrow a^5F_5$ (3,820 Å) using a condenser system (F/10) and a monochromator (25 cm). Figure 4 shows the dependence of the measured atom density on the bias voltage; a dotted line represents the dependence of the relative sputtering yield on the ion energy (calculated by Yamamura's formula and adjusted for the best fit).[3] A good agreement between the yield and the measured value was obtained with Ne, but deviation found was large with large ion masses (Ar and Kr).

In the next experiment we will determine the absolute value of density as well as the velocity distribution in order to determine atom flux.

(3) Study on reduction of metal oxide by hydrogen ion

In the glow discharge cleaning process, ions have energies of several hundred eV. This experiment aims at the elucidation of a reduction mechanism of metal oxide by incident ions, H^+ and H_2^+. An effort has been devoted to realize clean conditions in the Auger electron analysis chamber: 10^{-6} Pa and low H_2O partial pressure.

References

1) Y. Yatsurugi, O. Kuboi, M. Hashimoto, H. Nagai, M. Aratani, I. Kohno, and T. Nozaki: *Appl. Phys. Lett.*, **44** (2), 246 (1984).
2) K. Okazaki, A. Minoh, S. Ishii, Y. Ishibe, H. Oyama, Y. Sakamoto, and K. Yano: 25th Vacuum Symp., 31Ba-5, Oct. 29–31, Osaka (1984).
3) N. Matsunami: IPPJ-AM-32, Nagoya Univ. (1983).

RIKEN Accel. Progr. Rep. 18 (1984)

III-2-29. Origin of Hydrogen in Amorphous Silicon Produced by Glow-Discharge in $Si_2H_6+D_2$ and $Si_2D_6+H_2$

O. Kuboi, M. Hashimoto,* Y. Yatsurugi, H. Nagai, M. Aratani,
M. Yanokura, S. Hayashi, I. Kohno, and T. Nozaki

Recently, more and more investigators have been studying hydrogenated amorphous silicon (a-Si: H) growth from disilane because of the faster growth with disilane than monosilane. We have previously reported amorphous silicon growth from monosilane.[1] It appears that the growth mechanism with disilane is different from that with monosilane.[2)-7)] We employed the identical test set-up for these tests as those reported previously with monosilane. ^1H and D in amorphous silicon were measured by Rutherford recoil measurement technique.[1] Amorphous silicon was deposited by means of RF glow discharge on a high-purity silicon wafer at 250°C and at 1 Torr. The two gas mixtures used in this investigation were $Si_2H_6+D_2$ and $Si_2D_6+H_2$. The following chemical reactions show methods employed to synthesize Si_2H_6 and Si_2D_6.

$$Si+3\,SiCl_4 \rightarrow 2\,Si_2Cl_6 \quad (1)$$

$$2\,Si_2Cl_6+3\,LiAlH_4 \rightarrow 2\,Si_2H_6+3\,LiCl+3\,AlCl_3 \quad (2)$$

$$2\,Si_2Cl_6+3\,LiAlD_4 \rightarrow 2\,Si_2D_6+3\,LiCl+3\,AlCl_3 \quad (3)$$

Si_2H_6 and Si_2D_6 so produced were purified by distilling three times.

Figure 1 shows the relationship between amorphous silicon growth rate and the RF power. It shows that the growth at A and B is almost the same against the RF power. But, at low power, the growth at B is much larger than at A. It was said in general that the amorphous silicon growth rate with disilane is 5 to 20 times faster than with monosilane.[8] However, our tests show that this tendency is apparent only at low power. Let us examine curves B and C. The flow rate of disilane in C is twice that of B. At low power, the growth rate of C is also twice that of B. However, at high power, the difference in the growth rates becomes smaller.

Figure 2 indicates the relationship between ^1H and D in amorphous silicon *vs.* RF power when the gas mixture is $Si_2H_6+D_2$. At low power, an excessive amount of ^1H from Si_2H_6 appears in the amorphous silicon. On the other hand, at high power, an excessive amount of D from the dilution gas D_2 appears in the amorphous silicon.

Figure 3 shows the isotopic fraction of ^1H in amor-

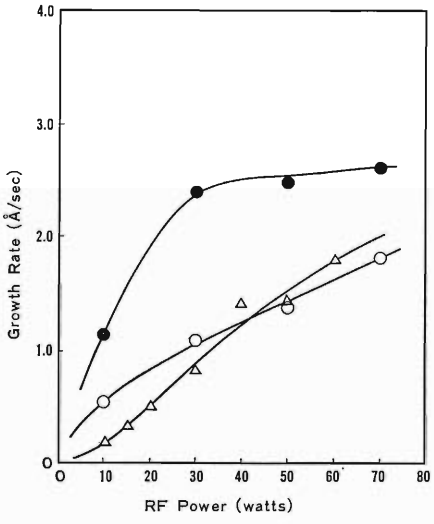

Fig. 1. Growth rate *vs.* RF power. Gas flow rate: △; (A) SiH_4(10 sccm)+D_2(40 sccm), ○; (B) Si_2H_6(5 sccm)+D_2 (40 sccm), ●; (C) Si_2H_6(10 sccm)+D_2(40 sccm).

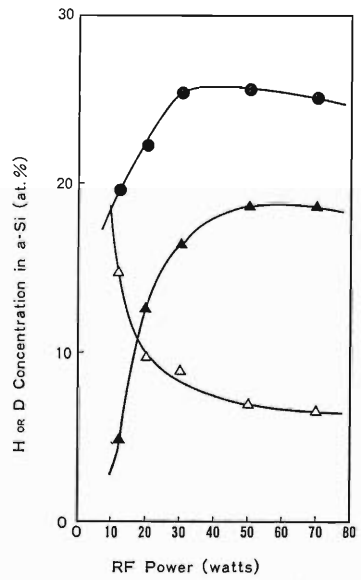

Fig. 2. H, D, and H+D concentrations in a-Si:H:D *vs.* RF power. ●; H+D, △; H, ▲; D. Gas flow rate, Si_2H_6(10 sccm) +D_2(40 sccm).

* Komatsu Electronic Metals Co.

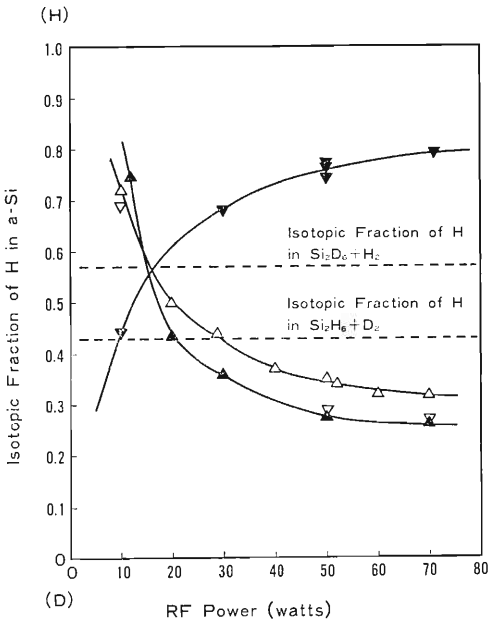

Fig. 3. Isotopic fraction of H in a-S:H:D *vs.* RF power. Gas flow rate: △, ▲, ▽; Si_2H_6(10 sccm)+D_2(40 sccm), ▼; Si_2D_6(10 sccm)+H_2(40 sccm).

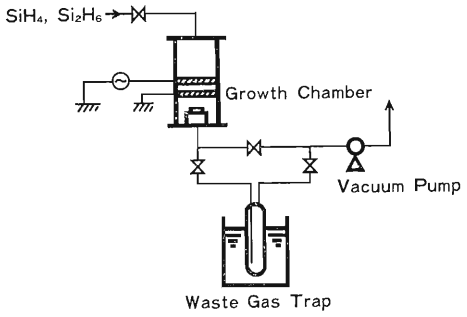

Fig. 4. Trapping system for silanes.

phous silicon *vs.* RF power. It clearly shows that regardless of whether Si_2H_6 or Si_2D_6 is used, an excessive amount of the gas atoms in disilane (^1H: in case of Si_2H_6, D: in case of Si_2D_6) appears in the amorphous silicon at low RF power, while an excessive amount of the gas atoms in the dilution gas appears in the amorphous silicon at high RF power. In contrast with the above data, our previous tests with monosilane showed that, at high power, ^1H in amophous silicon approached the isotopic equilibrium of the gas mixture.[1)]

As shown in Fig. 4, tests were also conducted to trap condensible gases in the exhaust gas stream to detect the presence of Si_nH_{2n+2}. The test results are shown in Fig. 5. At low RF power, a substantial amount of monosilane was captured; this suggests SiH_2 could have been decomposed on the silicon

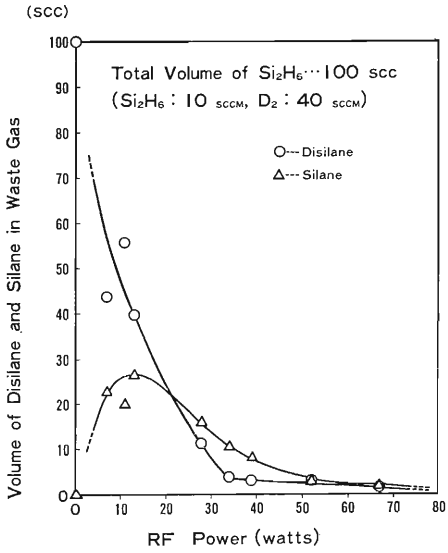

Fig. 5. Volume of silanes in waste gas of glow discharge. Gas flow rate, Si_2H_6(10 sccm)+D_2(40 sccm). Sampling period: 10 min. ○; Disilane, △; Silane.

wafer through the following reaction.

$$Si_2H_6 \rightarrow SiH_2+SiH_4 \quad (4)$$

At high RF power, however, monosilane started to disappear. It could be that silanes, polymer, H_2 and *etc.* were formed and higher silanes, polymer, and *etc.* were deposited on the pipe wall preventing the compound reaching the trap. Judging from the data in Fig. 3, SiH_2 intermediate seems to decompose into silicon and hydrogen. Further tests need to be conducted to confirm the presence of these heavier compounds.

References

1) Y. Yatsurugi, O. Kuboi, M. Hashimoto, H. Nagai, M. Aratani, M. Yanokura, I. Kohno, and T. Nozaki: *Appl. Phys. Lett.*, **44**, 246 (1984).
2) B. A. Scott, R. M. Plecenik, and E. E. Simonyi: *ibid.*, **39**, 73 (1981).
3) Y. Mishima, M. Hirose, Y. Osaka, K. Nagamine, Y. Ashida, N. Kitagawa, and K. Isogaya: *Jpn. J. Appl. Phys.*, **22**, L46 (1983).
4) A. Matsuda, T. Koga, H. Tanaka, L. Malhotra, and K. Tanaka: *ibid.*, p. L115.
5) B. A. Scott, J. A. Reimer, and P. A. Longeway: *J. Appl. Phys.*, **54**, 6853 (1983).
6) P. A. Longeway, R. D. Estes, and H. A. Weakliem: *J. Phys. Chem.*, **88**, 73 (1984).
7) A. Matsuda, T. Koga, H. Tanaka, and K. Tanaka: 10th Int. Conf. on Amorphous and Liquid Semiconductors, Tokyo (1983).
8) B. A. Scott, M. H. Brodsky, D. C. Green, P. B. Kirby, R. M. Plecenik, and E. E. Simonyi: *Appl. Phys. Lett.*, **37**, 725 (1980).

RIKEN Accel. Progr. Rep. 18 (1984)

III-2-30. Application of Heavy-Ion RBS to the Analysis of Silicon Ohmic Contact Systems

K. Ikeda, N. Ito, T. Aimi, S. Hayashi, M. Yanokura,
I. Kohno, H. Nagai, M. Aratani, and T. Nozaki

(1) Introduction

Heavy-ion Rutherford back-scattering (RBS) was used for the depth profiling of gold and antimony in semiconductor silicon. In order to take electrical contact with the bottom side of a silicon power device, some metals are evaporated on the bottom surface and then caused to make alloy by heat treatment. The bottom surface has often been roughened by sand-blasting. As the metals, gold containing a small quantity of antimony is frequently preferred.

(2) Experimental

Description of the samples used in the present study is given in Table 1 along with the results of neutron activation analysis of Au and Sb. The samples were prepared by the following processes, with due considerations towards application to device. Two kinds of metal thin layers were prepared successively on the sand-blasted rough surface of a silicon wafer: the first layer was obtained with electron-beam evaporated Ti and the second Au-Sb layer was obtained by resistance-evaporation of a pellet of Au containing a small quantity of Sb. After deposition, the samples were alloyed in N_2 atmosphere. Total amounts of Au and Sb in the samples were determined by neutron activation analysis. In the RBS, incident ions of $^{40}Ar^{4+}$ (50 MeV; beam current, several nA; beam spot, 1.5 mm; measurement, 10–60 min) were used. The arrangement for RBS measurement is shown in Fig. 1.

(3) Results

The backscattering spectra of samples 3–5 are

Table 1. Samples used in the present study.

No.	Si surface	Treatment	Analytical surface	Contents of Au and Sb*
1.	mirror	as evap.	metal	Au=2500±100 μg/g Sb= 23± 1 μg/g
2.	mirror	alloying	metal	
3.	sand-blasted	as evap.	metal	
4.	sand-blasted	alloying	metal	
5.	sand-blasted	alloying	etched surface	Au=15.5+0.8 μg/g Sb= 2.3+0.1 μg/g

* Values obtained by neutron activation analysis.

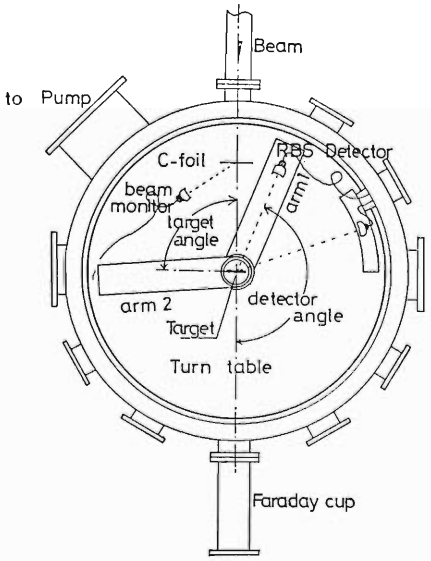

Fig. 1. Experimental arrangement.

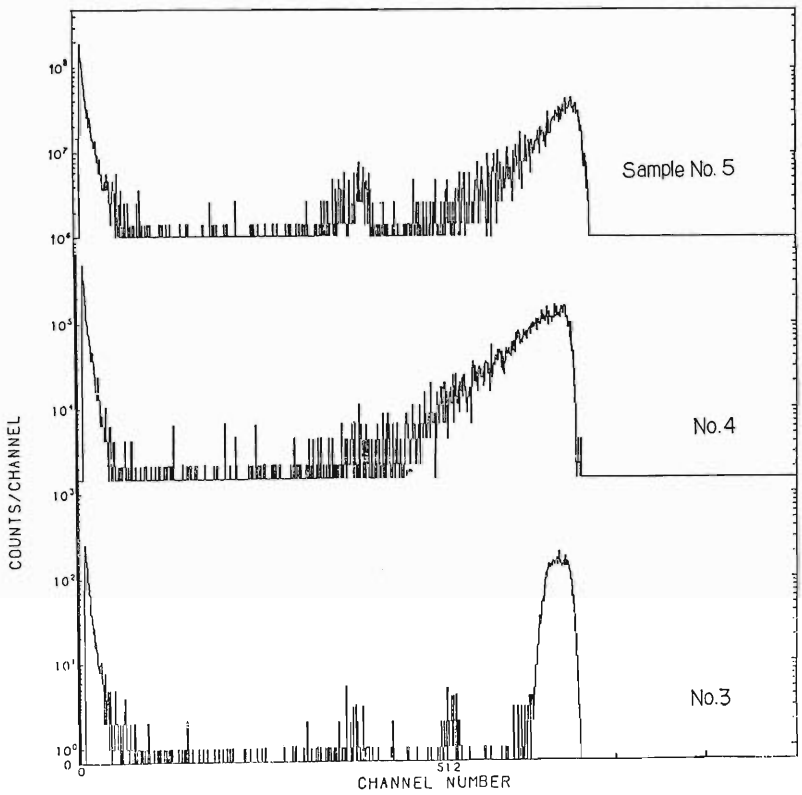

Fig. 2. RBS spectra of Au (Sb) layer.

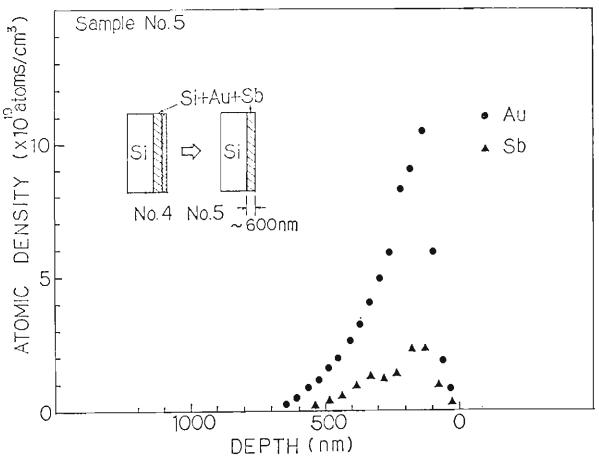

Fig. 3. Au and Sb depth profiles of sample 5. Au-rich layer was etched off with HF and aqua regia.

shown in Fig. 2. The thickness of the Au (Sb) film, estimated from sample 1, is 73 nm, in good agreement with that of 72 nm obtained from neutron activation analysis. As for sample 4, Au was considered to diffuse into silicon to 750 nm as a result of alloying, with a peak Au concentration of 1.2×10^{22} atoms/cm^3. When the Au-rich layer of sample 5 was etched with HF and aqua regia, well-separated spectra of Au and Sb were observed as expected. Figure 3 shows the depth profile of Au and Sb from the surface of the substrate after etching as calculated from the spectra of sample 5. Figure 3 indicates that Au and Sb are spread to a depth of about 600 nm with peak concentrations of 1.2×10^{20} and 2.3×10^{19} atoms/cm^3, respectively. As for Sb, the region with a concentration of more than 10^{18} atoms/cm^3, a value sufficient for forming an ohmic contact, extends to a depth of 430 nm.

It was shown that the depth profile of the heavy metals under a rough surface can be determined by RBS just as under a mirror-flat surface. This is a clear advantage of RBS over SIMS.

RIKEN Accel. Progr. Rep. 18 (1984)

III-2-31. Depth Profiling of Deuterium in Titanium Carbide by Elastic Recoil Detection Analysis

T. Kobayashi, S. Hayashi, H. Sakairi, M. Iwaki,
M. Aratani, M. Yanokura, and S. Oohira

As a part of the study on the behavior of hydrogen in titanium carbide, a depth profile of deuterium implanted into TiC was obtained by the elastic recoil detection analysis (ERD). A TiC foil of about 1 μm thickness was prepared by a reactive ion plating method. The plating was performed by depositing Ti ions on an aluminum substrate at 300°C in C_2H_2 of a partial pressure of about 2×10^{-4} Torr under a background pressure of about 5×10^{-6} Torr. An analysis of the sample composition is now in preparation.

Deuterium implantation was carried out by using the RIKEN 200 kV Low Current Implanter. Instead of D^+ ions, molecular ions D_2^+ were used to avoid mixing of H_2^+ ions. Energy of D_2^+ ions was 50 keV, which corresponds to 25 keV for D^+ ions. The implantation was performed with an ion flux of 1.25×10^{12} $D_2^+/cm^2\cdot s$ to the fluence of 5×10^{16} D/cm^2 at 1×10^{-6} Torr at room temperature. The beam was analyzed magnetically and scanned electrically across the surface for uniform lateral distribution of the implants. A raise in the sample temperature during implantation was not monitored but considered to be negligibly small because the input power density was 10 mW/cm^2.

The D-implanted TiC sample was, after being kept at room temperature for two weeks, analyzed by ERD with 50.45 MeV Ar^{4+} ions from the RILAC.

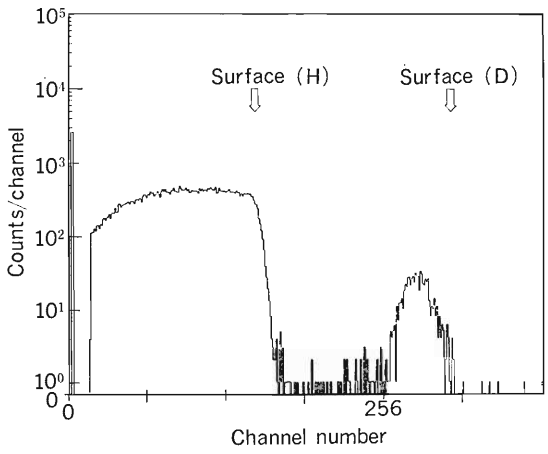

Fig. 1. Energy spectrum of H and D ions elastically recoiled from the D implanted TiC obtained with 50.45 MeV Ar^{4+} ions. Scattered Ar ions and recoiled Ti and C ions were eliminated by an aluminum absorber placed in front of the detector.

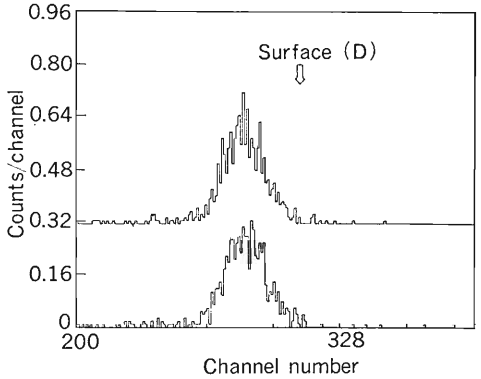

Fig. 2. Deuterium region of the spectra: the lower, first run; the upper, second run.

The experimental arrangement was almost the same as described in a previous report.[1] Since scattered Ar ions and recoiled Ti and C ions were absorbed by a 20 μm thick aluminum foil placed in front of the detector, only recoiled H and D ions were detected.

An energy spectrum of recoiled H and D ions is shown in Fig. 1, from which depth profiles are concluded to be almost Gaussian for deuterium and uniform for hydrogen. It is considered that a large quantity of hydrogen atoms were dissolved in the sample during plating.

Figure 2 shows the spectra for deuterium obtained in the first and the second runs with the same sample. To obtain each spectrum the sample was irradiated with 50. 45 MeV Ar^{4+} ions of 20 nA, which corresponds to 2×10^{12} $Ar^{4+}/cm^2\cdot s$, and of a fluence of 1.6×10^{15} Ar/cm^2. It seems that the distribution of implanted deuterium was hardly affected by such irradiation. By assuming that a deuterium content in the implanted sample was preserved during the experiment, a hydrogen content is estimated from the deuterium content. On the assumption that the TiC sample has a stoichiometric composition, a hydrogen content was found to be 8 at.%.

Further experiments are planned to study a possible use of implanted deuterium as a standard for the quantitative analysis of hydrogen in TiC.

Reference

1) H. Nagai, M. Aratani, S. Hayashi, T. Nozaki, M. Yanokura, I. Kohno, O. Kuboi, and Y. Yatsurugi: *RIKEN Accel. Progr. Rep.*, **17**, 102 (1983).

RIKEN Accel. Progr. Rep. **18** (1984)

III-2-32. Stress-Induced Site Change of H in V Observed by Channeling Experiments

E. Yagi, T. Kobayashi, S. Nakamura, Y. Fukai,* and K. Watanabe*

Recently, Suzuki *et al.*[1] reported that the diffusivity of H in V is enhanced enormously by application of tensile stress along a <1 1 1> direction, and concluded with the help of their Huang scattering experiments that it is a consequence of stress-induced site change T→4T. However, their observation of "superdiffusion of 4T-hydrogen" has since been questioned by Metzger[2] and Schober and Golczewski,[3] and still remains in dispute. The objective of the present paper is to report our first results of channeling experiments on H in V, especially on stress-induced site changes which, we believe, are closely related to the observation of Suzuki *et al.*[1]

The lattice location of hydrogen was determined by utilizing the nuclear reaction $^{1}H(^{11}B, \alpha)\alpha\alpha$. Because of the low sensitivity of this reaction for hydrogen detection, the concentration was chosen to be $VH_{0.1}$ (α-phase). Specimens were cut from a 99.95% pure single crystal into discs of 1.5 mm thick and chemically polished. In order to introduce hydrogen up to the concentration $VH_{0.1}$ without ever forming β precipitates before observation, hydrogen was charged electrolytically into one half of the disc (serving as a reservoir) up to the average concentration of $VH_{0.2}$, and was subsequently diffused into the remaining half (serving as a specimen) by heating the crystal on a target holder up to 150°C, a temperature well above the α-($\alpha+\beta$) phase boundary (~110°C) for the composition $VH_{0.1}$. To ensure homogeneous distribution of hydrogen, channeling experiments were performed at 150°C after holding the specimen at this temperature for 24 hr.

The collimation of the incident $^{11}B^{2+}$ beam (2.02 MeV) was better than 0.057° for a {1 1 1} planar channel, and 0.076° in other cases. The crystal orientation was set to within ±0.004°. The $^{11}B^{2+}$ beam was 1.0 mm in diameter with current of about 1 nA. Both α particles and backscattered ^{11}B were measured as a function of angle between the direction of the beam and axial or planar channel. More detailed results of the experiment were described in our previous paper on H in Ta.[4]

* Faculty of Science and Engineering, Chuo University.

Results of the angular scans for {1 0 0} and {1 1 1} planar channels are shown in Fig. 1. From Fig. 1 it is unambiguously concluded that most of H atoms are located at T (tetrahedral) sites. The results on <1 0 0> and <1 1 0> axial channels were also consitent with this conclusion.

After the measurements at 150°C described above, the specimen was cooled to room temperature at a rate of 0.8 K/min and was kept there for 24 hr. It was then reheated to 150°C at a rate of 0.35 K/min, and kept there for 24 hr before the anglular scan for a {1 0 0} channel was made. The result is shown in Fig. 2. One of the most important findings of the present experiment is that the profile of the α-yield is changed markedly by the heat treatment. After the heat treatment, the profile consists of a wide dip with approximately the same width as that of the ^{11}B dip, and two shoulder peaks located at about ±0.25°. This result indicates that a major proportion of H atoms occupies interstitial sites displaced from normal positions of T sites. We shall here assume, from symmetry considerations, that the observed profile originates from displaced-T (d-T) or 4T configurations, in both of which the position of maximum density of hydrogen is displaced toward the O (octahedral) site. The displacement from the T site was estimated to be 0.44 Å, which, in comparison with the T-O distance of 0.76 Å, means that the position of a maximum density is closer to O sites than T sites.

A recent theoretical calculation[5] has shown that, as the vanadium lattice is elongated along one of its cube axes (z-axis), the most stable self-trapped configuration changes continuously: T → d-T → 4T → O_z. Therefore, it is expected that the presence of tensile stress, either external or internal, may induce transition from T to d-T or 4T configurations.

In the present experiment, precipitation of the β phase on cooling to room temperature is expected to produce internal stress. The effect of internal stress is evident in Fig. 2: The depth of the ^{11}B dip, which recovers to only 75% of its original value after reheating, clearly shows that the internal strain in the β-redissolved state is appreciably larger than in the virgin α state. In order to estimate the

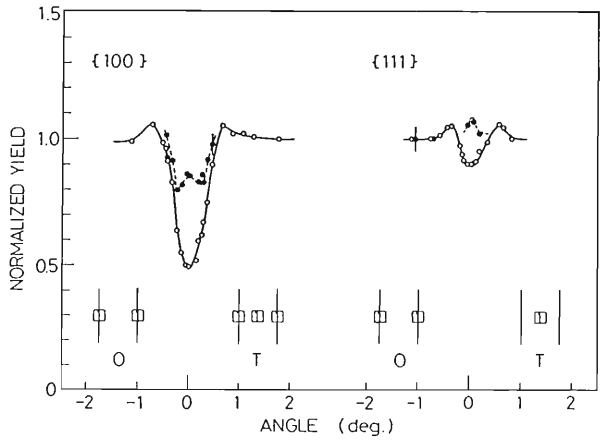

Fig. 1. Angular profiles of α-particle and backscattered ^{11}B yields across {1 0 0} and {1 1 1} planes in $VH_{0.1}$. The full curves and the dashed curves are drawn to guide the eye. The insets indicate the projection of O and T sites (squares) with their relative weights (numbers in the squares) on the plane perpendicular to the planar channel in question. The lines represent the projections of atomic planes.

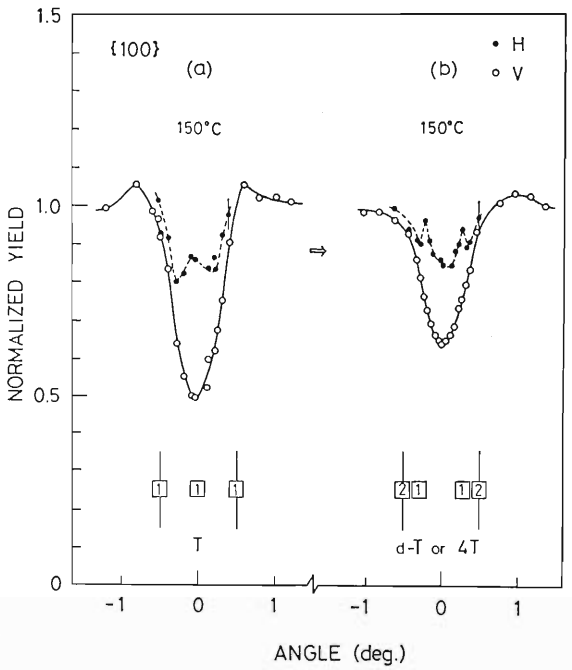

Fig. 2. A change of {1 0 0} angular profiles of β- and ^{11}B-yields in (a) the virgin α state (150°C), and (b) in the β-redissolved α state (150°C). The full curves and the dashed curves are drawn to guide the eye.

magnitude of the internal stress introduced by precipitation of the β-phase, the X-ray diffraction was measured on a single crystal specimen subjected to the same thermal cycling process as in the channeling experiment. The measurement of the rms angular broadening of the (2 0 0) diffraction line caused by precipitation indicates the rms strain of 2.6×10^{-4}, and the internal stress of 1/4 to 1/3 of the elastic limit.

We conclude from these observations that the configuration of H in V is extremely sensitive to the presence of stress: the transition T → d-T or 4T takes place at stress levels much lower than the yield stress. As the internal stress in the β-redissolved α-phase is just comparable to the values of external stress at which the superdiffusion sets in,[1] we may further conclude that the stress-induced configuration presently observed is responsible for the occurrence of superdiffusion. More detailed results are described in Ref. 6.

References

1) T. Suzuki, H. Namazue, S. Koike, and H. Hayakawa: *Phys. Rev. Lett.*, **51**, 798 (1983).
2) T. H. Metzger: *ibid.*, **52**, 476 (1984).
3) T. Schober and J. Golczewski: *ibid.*, p. 478.
4) E. Yagi, T. Kobayashi, S. Nakamura, Y. Fukai, and K. Watanabe: *J. Phys. Soc. Jpn.*, **52**, 3441 (1983).
5) H. Sugimoto: *ibid.*, **53**, 2592 (1984).
6) E. Yagi, T. Kobayashi, S. Nakamura, Y. Fukai, and K. Watanabe: *Phys. Rev. B*, **31**, 1640 (1985).

RIKEN Accel. Progr. Rep. 18 (1984)

III-2-33. Lattice Location of Hydrogen in Nb α-Phase as Observed by Channeling Method

E. Yagi, S. Nakamura, T. Kobayashi, K. Watanabe,* and Y. Fukai*

In a previous study, we have made the first determination of the lattice location of hydrogen in Ta by the channeling method using a nuclear reaction $^{1}H(^{11}B, \alpha)\alpha\alpha$ and demonstrated that this method is useful to locate the hydrogen dissolved in metals[1]; the hydrogen was detected by measuring emitted α-particles. In the present study, this method was applied to locate the hydrogen in Nb α-phase.

Hydrogen was introduced electrolytically into the one half of a Nb single crystal disc in the same way as in the case of V,[2] and was diffused subsequently into the remaining half (serving as a specimen) by heating the disc to 155°C on the target holder for the channeling experiment. The hydrogen concentration was $NbH_{0.13}$ (α-phase). The channeling experiment was performed at 155°C by using a 2.03 MeV $^{11}B^{2+}$ beam. Collimation of the beam was better than 0.076°. Detailed description on the experiment was given in a previous paper on H in Ta.[1] The results of angular scan on <1 1 0> and {1 0 0} channels are shown in Fig. 1. These angular profiles of the α-yields, *i.e.*, hydrogen yields, indicate that most of hydrogen atoms are located at tetrahedral interstitial sites (T-sites). (The positions of two subsidiary peaks observed in the <1 1 0> axial scan, located at $\pm 0.35°$ from the center, are consistent with the position expected from the calculation for the T-site ($\pm 0.34°$).

After the measurement at 155°C, the specimen was cooled to room temperature and kept there for 24 hr. It was reheated to 155°C, kept there for 24 hr, and then angular scan was performed. This heat treatment is similar to that made in the case of V.[2] The results are shown in Fig. 2. Although this thermal cycle made the dip of ^{11}B-yield shallow, angular profiles of the α-yield still exhibit a feature characteristic of T-site occupancy. These results lead to the conclusion that the lattice location of hydrogen in the Nb α-phase was not changed by the thermal cycle. This result is essentially different from that on H in V α-phase; the {1 0 0}

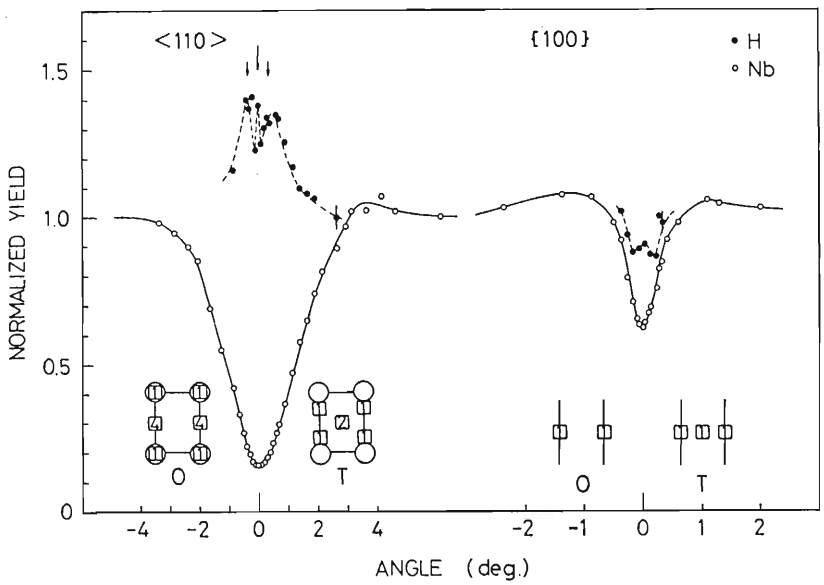

Fig. 1. Angular profiles of α-particle and backscattered ^{11}B yields across <1 1 0> axis and {1 0 0} plane in $NbH_{0.13}$. The full curves and the dashed curves have been drawn to guide the eye. The insets in the figure indicate the projection of O and T sites (squares) with their relative weights (numbers in the squares) on the plane perpendicular to the channel in question. The open circles and the lines represent the projections of atomic rows and planes, respectively.

* Faculty of Science and Engineering, Chuo University.

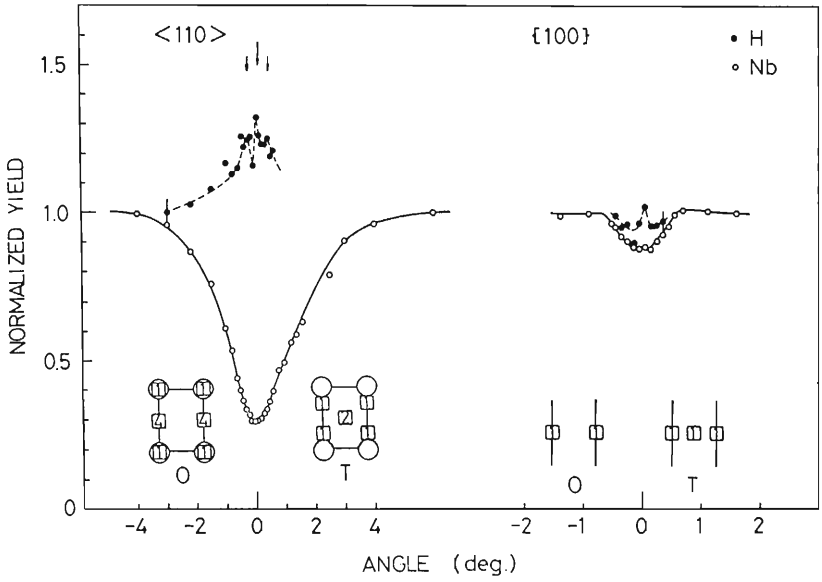

Fig. 2. Angular profiles of α- and ^{11}B-yields in the β-redissolved α state in $NbH_{0.13}$.

α-angular profile was changed markedly by the same thermal cycle.[2] As described in the case of V,[2] most of hydrogen atoms precipitate into the β-phase on cooling and the precipitates are redissolved on reheating, but this process introduces an appreciably large strain into the β-redissolved α-phase. Comparison of the present result with that on H in V which was subjected to the same thermal cycle suggests that hydrogen location in V was changed even when the {1 0 0} ^{11}B-dip recovered to 75% of its original value by redissolution of the β-phase, while in Nb the hydrogen location was not changed despite much smaller recovery of the {1 0 0} ^{11}B-dip, *i.e.*, only 35%. The observed fraction of such recovery may indicate that the thermal cycle introduces a much larger internal strain in Nb than in V. Therefore the present result indicates that the lattice location of hydrogen is less sensitive to the strain in the Nb α-phase than in the V α-phase.

References

1) E. Yagi, T. Kobayashi, S. Nakamura, Y. Fukai, and K. Watanabe: *J. Phys. Soc. Jpn.*, **52**, 3441 (1983).
2) E. Yagi, T. Kobayashi, S. Nakamura, Y. Fukai, and K. Watanabe: *Phys. Rev. B*, **31**, 1640 (1985).

RIKEN Accel. Progr. Rep. 18 (1984)

III-2-34. Compositions of Anodized Aluminum with Europium Implantation

M. Iwaki

Aluminum substrates doped with transition metals or rare-earth metals show an electroluminescence proper to doped particles during formation of an anodically oxidized film in solution. For example, Al-1%Mn alloys show bright yellow electroluminescence during anodization in the ammonium pentaborate solution. On the other hand, luminescence of aluminum implanted with phosphors has not yet been investigated. Recently, we observed the reddish-orange electroluminescence emitted from europium-implanted aluminum surface during anodization in the ammonium pentaborate solution. In the present work, compositions of europium-implanted aluminum sheets after anodization are investigated by means of a He^+ backscattering technique.

All specimens used were 4 N aluminum sheets (Toyo Aluminum Co., Ltd.). Before ion implantation, they were immersed in a 5% NaOH solution for 2 min and rinsed with de-ionized water. Ion implantation was performed to a dose of 5×10^{14} Eu/cm^2 at 100 keV at room temperature. Anodic oxidation of europium-implanted aluminum was carried out in the 0.1 M ammonium pentaborate solution at about 20°C. At a constant current density of 15 mA/cm^2 forming voltage was measured. During anodization, the implanted region of the aluminum surface emitted electroluminescence characterized by Eu^{+3}.

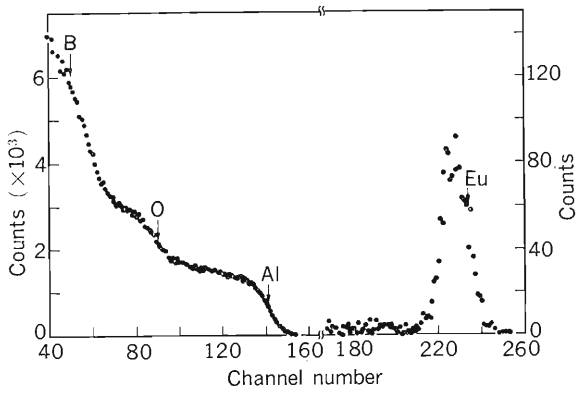

Fig. 1. Backscattering spectrum of europium-implanted aluminum anodized in ammonium pentaborate solution.

The Rutherford backscattering measurement was carried out by using 1 MeV $^4He^+$ with a fluence of 5 μC to estimate the compositions of surface layers of aluminum. Backscattered particles at an angle of 150° were detected and analyzed by using a solid state detecter and conventional electronics. The samples were mounted on a goniometer in a target chamber below 3×10^{-4}Pa.

Figure 1 shows the spectrum obtained for backscattered particles from europium-implanted aluminum anodized in solution. The arrows of channel numbers 50, 90, 141, and 234 correspond to the energy edges of boron, oxygen, aluminum, and europium at the specimen surface, respectively. It was found that implanted europium atoms make a gaussian distribution near the surface layer. The ratio of aluminum to oxygen atoms is about 2: 3, but the amounts of boron atoms are unexpectedly larger than those of aluminum atoms by one order of magnitude. It is considered that the boron atoms were doped into an aluminum sheet during anodization in the ammonium pentaborate solution.

RIKEN Accel. Progr. Rep. 18 (1984)

III-2-35. Surface Compositions of Argon-Implanted Kapton Films

M. Iwaki and K. Yoshida

Ion implantation has been widely employed in modifying materials because of its ability to introduce a controlled amount of particles into a target. However, studies on its application to organic materials were rather few and the effects of ion implantation on organic materials were not known well. Recently, Kapton films have been implanted with a variety of ion species and an electrical conductivity of implanted polymers has been measured as functions of energy and dose. The results showed that polymer films irradiated to high doses at energies of 0.3–2 MeV exhibit metallic luster and low resistivities of about $5\times10^{-4}\Omega\cdot$cm. The ion energies used in these experiments were higher than that utilized normally for ion implantation, *e.g.*, 50–200 keV. Recently we have found that a Kapton film implanted with 150 keV Ar ions forms a highly conductive surface layer with metallic luster. The present report describes a preliminary result of a Rutherford backscattering measurement on the surface compositions of argon-implanted Kapton film.

Argon-implantation in the Kapton film was performed to a dose of 1×10^{17} Ar/cm^2 at an energy of 150 keV. In order to prevent films on a target holder from temperature elevation, the implanted area was reduced less than 10 mm in diameter by masking the film with an aluminum sheet and the ion-beam current density was lowered to less than 1 μA/cm^2.

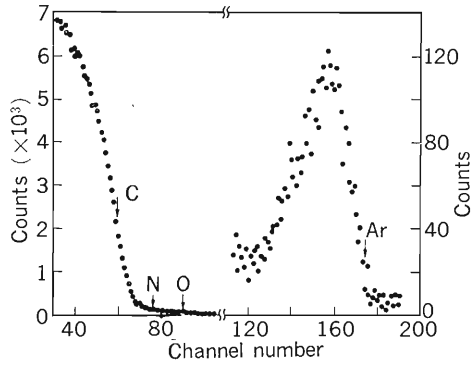

Fig. 1. Backscattering spectrum of argon-implanted Kapton.

The Rutherford backscattering measurement was carried out by using 1 MeV $^4He^+$ with the fluence of 5 μC. Backscattered particles at an angle of 150° were detected and analyzed by means of a solid state detector and coventional electronics. The samples were mounted on a goniometer in a target chamber, the pressure of which was below 3×10^{-4} Pa.

With increasing doses, the surface of the implanted Kapton films was colored and began to show metallic luster at a dose of 1×10^{17} Ar/cm^2. Figure 1 shows a spectrum obtained with backscattered particles from the argon-implanted Kapton with matellic luster. The leading edge of carbon atoms of the Kapton surface is at No. 59 channel and the energy edge of argon atoms at the Kapton surface is at No. 174 channel. The energies at No. 59 and 174 are 0.273 and 0.687 MeV, respectively.

Kapton is an organic polymer containing large amounts of nitrogen and oxygen atoms. If nitrogen and oxygen atoms exist, the energy edges of nitrogen and oxygen atoms at the Kapton surface are 0.333 and 0.385 MeV, respectively, which correspond to No. 76 and 90. The backscattering spectrum indicates the absence of nitrogen and oxygen atoms in the Kapton surface layers. The result suggests that argon-implantation decreases the densities of nitrogen and oxygen atoms in the Kapton surface layers; it is considered that argon-implantation results in decomposition and carbonization in the Kapton surface layers.

Moreover, the spectrum shows that the number of the argon atoms retained in Kapton is smaller than the implanted dose by two orders of magnitude. The phenomenon will be explained as out-diffusion of argon atoms during or/and after argon implantation.

The decomposition and carbonization of Kapton surface layers and out-diffusion of implanted argon is considered to play a significant role for electrical conduction of Kapton.

RIKEN Accel. Progr. Rep. **18** (1984)

III-2-36. Lamp Annealing of Cd-Implanted GaP

K. Aono, M. Iwaki, and S. Namba

Lamp annealing of disordered semiconductors is a relatively new field of semiconductor device physics. It is an extremely rapid and efficient method for recrystalization of ion-implanted semiconductor wafers by transient irradiation with tungsten halogen lamps. In the present work, the effects of lamp annealing on the depth profiles of Cd atoms and radiation damages in Cd-implanted GaP have been investigated by means of 1.5 MeV He^+ channeling technique using the TANDETRON.

Substrates used were 0.1 Ω·cm S-doped (1 1 1) GaP wafers. The Cd implantation in GaP was performed at doses of 10^{13}–10^{16} Cd^+cm^{-2} at 150 keV in the random direction. For annealing, the GaP wafers inserted between two 3-inch Si wafers were held in inert atmosphere, thermally isolated from the wafer cooled base, and separated by quartz plate from the air cooled lamps. Annealing was carried out at the temperature range 350–900°C for 3s. Channeling measurements were carried out by using the 1.5 MeV He^+ ions with a fluence of 2μC cm^{-2}. The specimens were mounted on a 3-axis goniometer in a target chamber, which was kept at pressure below 5×10^{-6} Torr. Backscattered particles at an angle of 150° were detected and analyzed with a solid-state detector and conventional electronics.

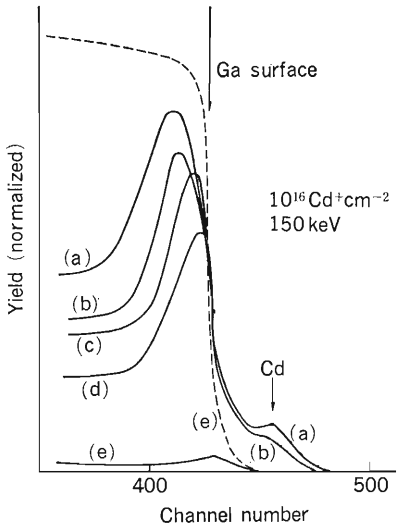

Fig. 1. Random (----) and <1 1 1> aligned (——) spectra of GaP implanted with Cd. (a), as-implanted; (b), annealed 500°C for 3s; (c), annealed 750°C for 3s; (d), annealed 900°C for 3s; (e), un-implanted.

Figure 1 shows the random and the <1 1 1> aligned spectra observed for Cd-implanted GaP with 10^{16} Cd^+cm^{-2} as a function of annealing temperature. The Cd depth profiles in the random and the aligned spectra of as-implanted specimens are Gaussian. However, in the scattering yields from the lamp annealed specimen, the random and the aligned spectra showed that Cd atoms moved inward and/or foward. Radiation damage in Cd-implanted layers was investigated from the spectra obtained from Ga in GaP as shown in Fig. 1. As the annealing temperature becomes high, backscattering yields of the aligned spectra decrease and then the peak was shifted toward the surface. The result shows that recrystallization of Cd-implanted GaP occurs from the deep region toward the surface for the lamp annealed specimen.

RIKEN Accel. Progr. Rep. 18 (1984)

III-2-37. Helium Bubble Formation in Ni

Y. Higashiguchi,* E. Yagi, Y. Suzuki,* and H. Kayano*

In the present study, the relation between the He bubble formation and the grain growth was investigated in a He-injected Ni. Specimens were 99.99% pure Ni sheets of 0.3 to 0.5 mm in thickness. 36 MeV α-particles were injected into the specimens at room temperature by two methods: by setting an edge-shaped graphite degrader in front of the specimens to ensure the uniform depth distribution of helium, and without the degrader. Total helium doses were 4.0×10^{20} He-ions/m^2 in the former and 8.0×10^{19} He-ions/m^2 in the latter.

Both Ni specimens injected with and without the degrader were annealed at 1,073 K for 100 hr in a vacuum. The cross section cut in the plane perpendicular to the beam-incident surface was observed by optical microscopy after polishing and chemical etching. The results on the specimens irradiated with the degrader and without the degrader are shown in Fig. 1 (a) and 1 (b), respectively. In the specimen injected without the degrader, the defect band, which consists of high density of He bubbles and irradiation-induced defects such as loops and dislocations, was observed just at the depth of projected range of 36 MeV α-particles (Fig. 1 (b)). In the specimen injected with the degrader, the He-injected region and the uninjected region, which were bounded at the same depth as

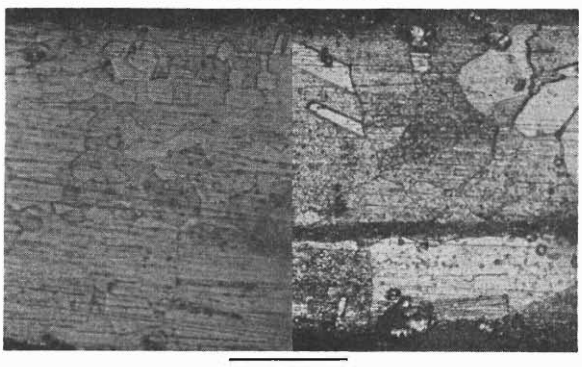

Fig. 1. Opticalmicrographs of the structure observed after annealing at 1,073 K for 100 hr in Ni specimens injected with 36 MeV α-particles with the degrader (a) and without the degrader (b).

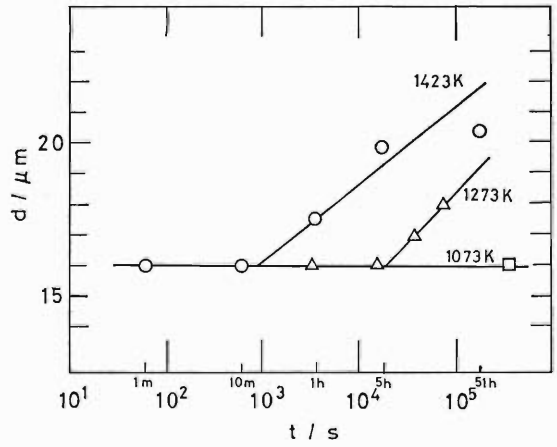

Fig. 2. The change of grain size of a He-injected Ni specimen as a function of annealing time at various temperatures.

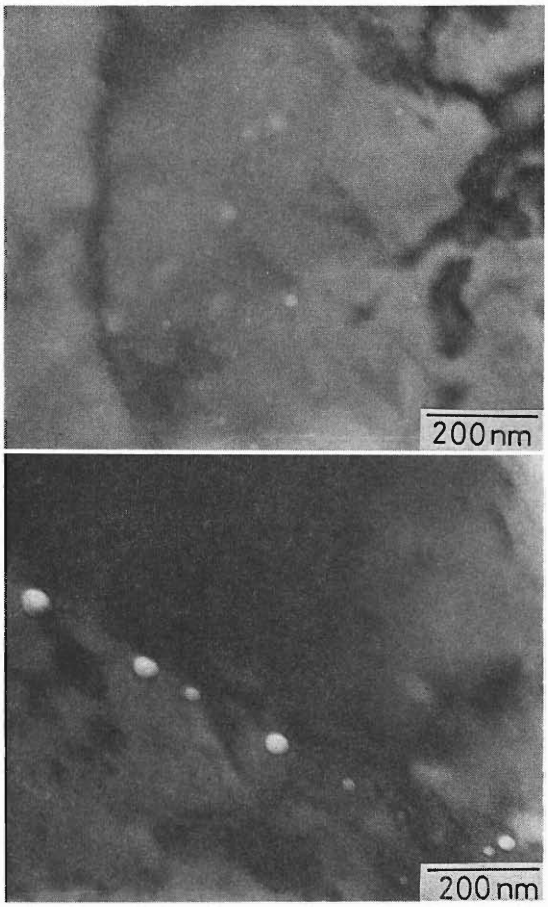

Fig. 3. Transmission electronmicrographs of a He-injected Ni specimen observed after annealing at 1,423 K for 51 hr.

* The Oarai Branch, The Research Institute for Iron, Steel and Other Metals, Tohoku University.

that of the defect band in Fig. 1 (b), exhibit the marked difference in the grain size (Fig. 1 (a)); the grain size is small in the uniformly He-injected region and very large in the uninjected region. The grain size in the He-injected region was nearly equal to that in the virgin state before injection. This result indicates that helium atoms or small bubbles prevent the grain growth during annealing at 1,073 K for 100 hr.

In order to investigate this effect in more detail, similar observation was made after annealing at 1,273 K and 1,423 K in a vacuum. The result is given in Fig. 2. It is clearly shown that the incubation period exists in the grain growth process in the He-injected crystal. Observation of He bubbles was made by transmission electron microscopy. The result obtained after annealing at 1,423 K for 51 hr is shown in Fig. 3. Small bubbles are observed in the matrix and large ones at the boundary.

The observed long incubation period for the grain growth at elevated temperature is explained by considering the flow rate of He atoms and small bubbles to grain boundaries, the flow rate of Ni atoms from one side to another side of grain boundaries, and that the bubble faceting is a rate-determining process for the bubble growth. The detailed discussion will be described elsewhere.

RIKEN Accel. Progr. Rep. 18 (1984)

III-2-38. Creep Property Improvement of Helium Injected JPCA by Thermomechanical Treatments

N. Yamamoto, H. Shiraishi, H. Kamitsubo, I. Kohno, and T. Shikata

It is well known that helium generated by (n, α) reactions causes the deterioration of mechanical properties in the fusion reactor structural materials because it accumulates at the grain boundaries where it has a strong influence on intergranular fracture. Among a number of metallurgical approaches to reduce the deterioration, the method of helium trapping at TiC precipitates in the grain interiors has recently been considered most effective in the case of austenitic stainless steel. The purpose of the present work is to clarify the effect of TiC distribution on the suppression of harmful helium effects and to seek the best pre-irradiation thermal-mechanical treatment in the Ti-modified austenitic stainless steel.

The alloy used was Japanese Prime Candidate Alloy (JPCA: Fe–0.06%C–16%Ni–15%Cr–2.4% Mo–1.8%Mn–0.53%Si–0.24%Ti–0.027%P–0.0035 %B), which is considered to be the first wall material in the Japanese program for an experimental fusion reactor. Three different pre-injection thermal-mechanical treatments were adopted for different TiC distributions; [A] SA (1,050°C, 1 hr); [B] SA (1,050°C, 1 hr)+A (800°C, 10 hr); [C] SA (1,050°C, 1 hr)+CW (20%)+A (750°C, 1 hr). The average size and number density of TiC in each treatment were 50–100 nm; 10^{18} n/m^3 [A], 37 nm; 3×10^{20} n/m^3 [B], 5 nm; 1×10^{22} n/m^3 [C], respectively. Helium was uniformly injected all over the specimen depth at 650°C by α-particle irradiation. The injected helium content was about 50 at. ppm. The creep rupture tests were carried out on the uninjected and injected specimens at 650°C in flowing argon gas of 99.998% up purity. The fractography by a scanning electron microscope (SEM) and microstructure observation by a transmission electron microscope (TEM) were made on the fractured specimens.

Figure 1 shows creep rupture curves of helium injected and uninjected specimens. Helium caused a reduction in creep rupture strength, although the extent of the reduction varied in three treatments. The reduction in treatment A amounted to about 15% of the uninjected values, while there was almost no change in treatments B and C. These results indicate that the presence of intragranular TiC precipitates before helium introduction appreciably improved the creep rupture strength of the helium-containing material.

The creep rupture elongation is shown in Fig. 2 as a function of the creep rupture time. The values of the rupture elongation were considerably spoiled by helium in all three treatments. The extent of the deterioration was almost the same and amounted to about 50% of the uninjected values. Fractographs by SEM revealed that in helium free controls the fracture occured perfectly in transgranular ductile mode, while the helium injected specimens partially

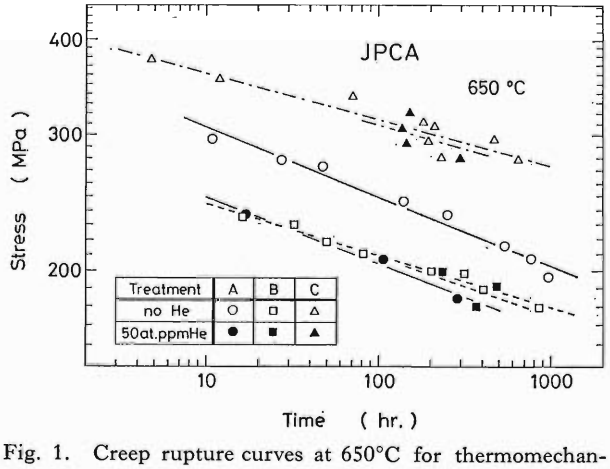

Fig. 1. Creep rupture curves at 650°C for thermomechanically treated JPCA in which helium was uninjected and injected to 50 at. ppm.

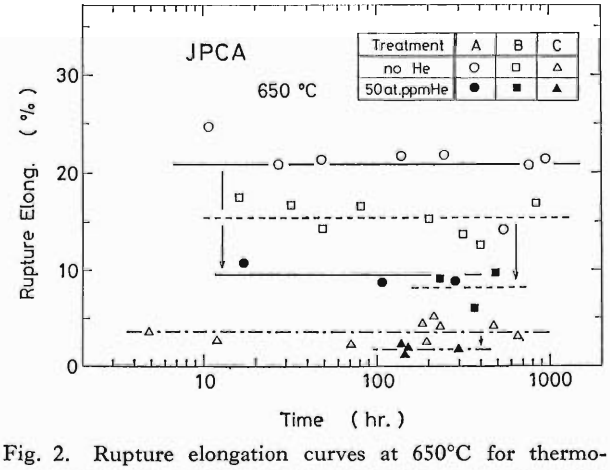

Fig. 2. Rupture elongation curves at 650°C for thermomechanically treated JPCA in which helium was uninjected and injected to 50 at. ppm.

Table 1. Microstructural data from helium injected and creep ruptured specimens tested at 650°C (σ: applied stress, t_r: creep rupture time, and F: percentage of helium bubbles trapped in the matrix).

Preinjection treatment	Creep data		Helium bubble					TiC (in the matrix)	
			Matrix		G. B.		F*		
	σ (MPa)	t_r (hr)	Average size (nm)	Number density (m^{-3})	Average size (nm)	Number density (m^{-2})	(%)	Average size (nm)	Number density (m^{-3})
A	237	17.2	15.8	1.2×10^{20}	18.4	1.1×10^{14}	79 (72)	29.5	3.7×10^{20}
	207	106.7	23.6	1.4×10^{20}	14.8	1.4×10^{14}	77 (91)	40.5	2.1×10^{20}
B	200	234.9	23.8	1.7×10^{20}	18.1	1.7×10^{14}	77 (87)	67.1	4.3×10^{19}
	191	491.3	15.3	2.9×10^{20}	11.2	2.1×10^{14}	82 (91)	73.1	5.9×10^{19}
C	306	137.1	10.5	1.6×10^{20}	12.4	4.9×10^{13}	92 (88)	7.5	1.1×10^{22}
	293	146.8	10.2	2.1×10^{20}	10.5	6.2×10^{13}	92 (92)	6.1	9.7×10^{21}

* The values in the parentheses indicate calculated percentages of helium atoms trapped in the matrix.

showed intergranular brittle fracture in all treatments. These observations provide direct evidence for helium embrittlement.

The TEM examination was made mainly to study the morphology of helium bubbles. There existed a few bubbles larger than 100 nm on $M_{23}C_6$ and/or Laves phase at grain boundaries, which should be the crack nuclei of intergranular fracture. Smaller bubbles were also distributed at the grain boundaries and in the grain interiors. Plenty of smaller ones were trapped at the interfaces of the precipitates. Especially, almost all bubbles in the matrix were trapped at TiC precipitates. The results of quantitative observations are presented in Table 1. It is noteworthy that in spite of the wide variety of dispersion of intragranular TiC precipitates there was not much difference in helium bubble distribution under all conditions both at the grain boundaries and in the matrix. The percentages of intragranularly trapped helium bubbles were quite high and intragranular helium trapping by TiC precipitates was almost achieved. But the creep rupture elongation was considerably reduced by helium. These results indicate that there seem to be some difficulties in suppressing the helium embrittlement only by TiC precipitates and that structural strengthening of grain boundaries themselves should be necessary for further suppression of helium embrittlement.

RIKEN Accel. Progr. Rep. **18** (1984)

III-2-39. Irradiation Creep of 316 Stainless Steel

J. Nagakawa, H. Shiraishi, H. Kamitsubo, I. Kohno, and T. Shikata

Type 316 stainless steel is one of the most useful alloys for use in core structure of fusion and fast-breeder reactors. However, metals including stainless steels are responsible for acceleration of creep deformation on bombardment with energetic particles like fast neutrons or high energy ions (creep is slow, steady plastic deformation under relatively low stress). This phenomenon termed irradiation creep is a serious problem to the nuclear reactors, for it limits the planned operation through a significant dimensional change on one hand, and it increases the reactor life time by enhancing stress relaxation and consequently increases the fatigue life on the other. It is, therefore, essential for the reactor design to assess the irradiation creep behavior of the reactor structural materials.

In the present investigation irradiation creep was measured *in situ* under 16 MeV proton bombardment by using the cyclotron in a torsional creep apparatus. Torsional creep measurement is not affected by the fluctuation of thermal strain associated with that of specimen temperature, which is a serious problem in the ordinary tensile creep measurement. Thus, this creep apparatus is capable of having very high strain resolution, and the measurement of creep strain with a low irradiation effect due to the low beam current of the cyclotron was made possible. Figure 1 shows the mechanism of the apparatus schematically. Stress is applied on the wire specimen by a controlled DC current through the torque coil. Strain is measured by monitoring rotation of the small mirror by using a non-contact optical tracking device. Emphasis was placed on the study of microstructure effects on the irradiation creep, and both cold worked (high dislocation density) and annealed (low dislocation density) specimens were examined.

Figure 2 shows stress dependence of the irradiation creep rate. The slope of near unity indicates proportionality of the creep rate to the applied stress. The data with number "1" were obtained at the first irradiation run of each specimen and they deviate from a line extrapolated from other data. Figure 3 shows temperature dependence of the irradiation creep rate along with that of the thermal creep rate (creep rate without irradiation).[1] Very weak temperature dependence of the irradiation creep is noticed in comparison with that of the thermal creep.

Linear stress dependence at relatively low stress levels and temperatures as observed in the present case is generally considered to favor the SIPA

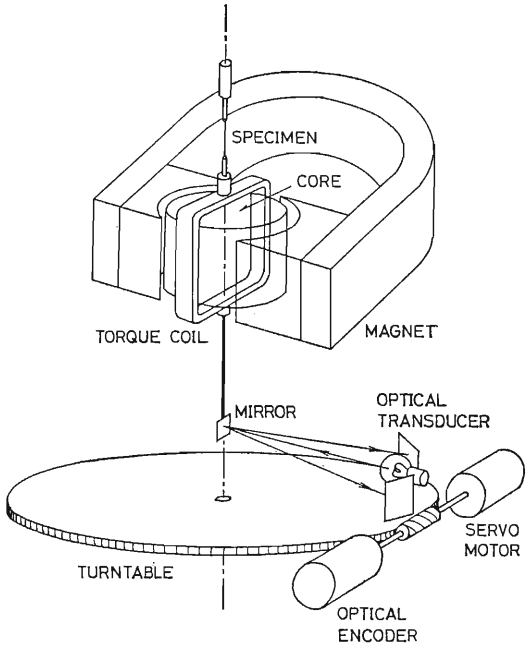

Fig. 1. Schematic diagram of torsional creep apparatus.

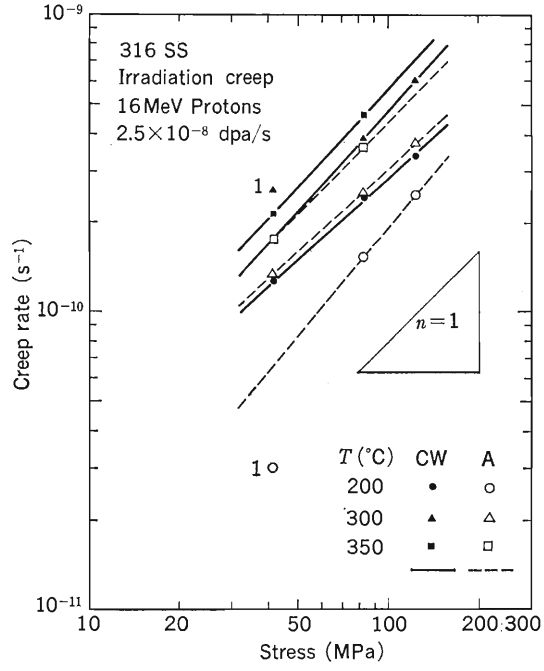

Fig. 2. Stress dependence of irradiation creep rate for cold worked (CW) and annealed (A) specimens.

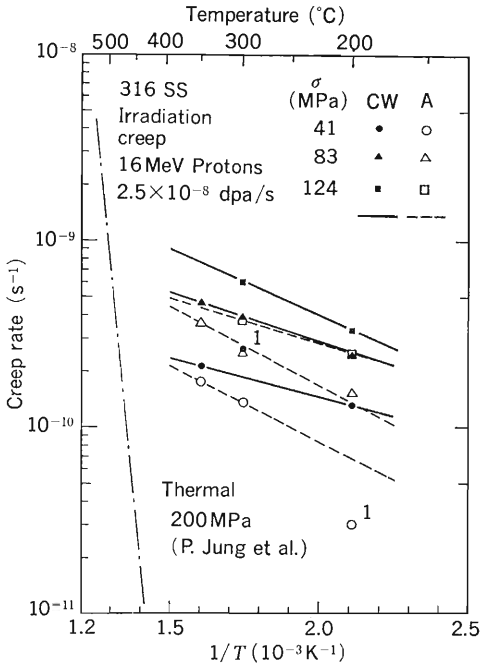

Fig. 3. Temperature dependence of irradiation creep rate with that of thermal creep rate.

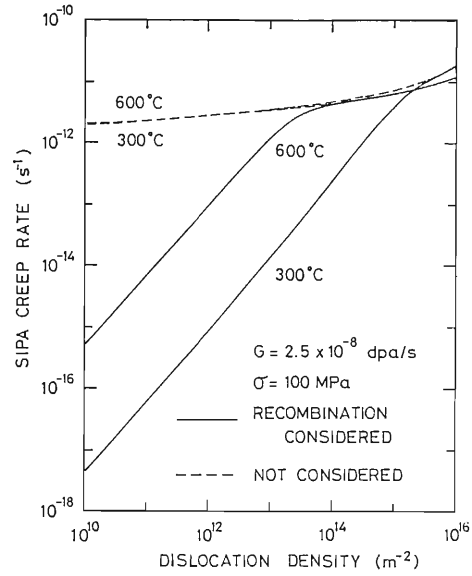

Fig. 4. Calculated dependence of SIPA creep rate on dislocation density.

(Stress-Induced Preferential Absorption of interstitials by dislocations) mechanism.[2] This model is based on a climb motion of specific dislocations of which stress field enhances interstitial absorption through interaction with the strain field of interstitial atom and with the applied stress. The SIPA creep rates were evaluated for 316 stainless steel and their dependence on dislocation density is shown in Fig. 4. Strong dependence is predicted only when the recombination of interstitials and vacancies is the dominant mode of defect loss. A rather small difference in the irradiation creep rate observed between the cold worked (dislocation density: $\sim 3\times 10^{15}$ m^{-2}) and the annealed ($\sim 1\times 10^{12}$ m^{-2}) specimens apparently rules out recombination. Calculated temperature dependence of the SIPA creep rate (not shown) does not agree with the present result either, when the recombination is taken into account. However, the magnitude of the calculated SIPA creep rate is in the order of the in-reactor creep rates measured at high accumulated damages (>1 dpa: displacement per atom) but two orders of magnitude smaller than the observed creep rates at the present low total damage ($<2\times 10^{-3}$ dpa). An unrealistically large stress effect on the preferential interstitial absorption by dislocations must be considered instead of the effect estimated on the basis of the elastic theory in order to explain the present creep rate results. Even in the in-reactor creep cases, there is a region at the onset of irradiation (primary in-reactor creep) that shows a creep rate one to two orders of magnitude higher than the steady-state creep rate at higher accumulated damage. Thus, it seems that not the recombination but the SIPA mechanism should be re-examined in the first place.

In conclusion, the SIPA mechanism can hardly explain the irradiation creep rates of 316 stainless steel under proton bombardment and also in the in-reactor neutron irradiation when the total accumulated damage is still very low. The present results indicate that a new irradiation creep model is necessary at an early stage of the irradiation where accumulated damages is still low.

References

1) P. Jung, C. Schwaiger, and H. Ullmaier: *J. Nucl. Mater.*, **85/86**, 867 (1979).
2) P. T. Heald and M. V. Speight: *Philos. Mag.*, **30**, 869 (1974).

RIKEN Accel. Progr. Rep. **18** (1984)

III-2-40. Depth-Dependent Damage Profile in Stainless Steels Irradiated with Ar- and N-ions

K. Shiraishi,* K. Fukai,* E. Yagi, T. Sawai,* and S. Hamada*

The heavy-ion irradiation experiments have been performed to simulate the neutron irradiation damage for fusion reactor materials. In the simulation study, precise estimation of the mean projected range is required for microstructural observation of the radiation damage. This experiment is carried out following the study on depth dependent damage profile in stainless steel irradiated with He-ions accelerated by the cyclotron.[1)]

Samples of Type 316 stainless steel and steel modified with titanium of 0.25 wt% were solution-annealed in a vacuum for 1 hr at 1,373 K and 1,473 K, respectively. After electropolishing, the 316 stainless steel samples were irradiated at ambient temperature with monoenergetic Ar-ions of 40.5 to 50.1 MeV to a total dose of 1.4×10^{20} ions/m^2 by using the heavy-ion linac. Monoenergetic N-ions of 57.0 to 86.7 MeV were irradiated to the 316 and Ti-modified steels to a total dose of 1.6×10^{20} ions/m^2 by using the cyclotron. The irradiated samples were electroplated with nickel on both irradiated and back surfaces, and then sliced in a plane normal to the ion-incident surface. The sectioned sample was mechanically polished and subsequently etched with a saturated solution of CuCl in aqua regia. The specimen for transmission electron microscopy was prepared by electropolishing to perforation after punching the sectioned sample. The cross-sectional microstructure was observed with an electron microscope operating at 200 kV. Post-irradiation annealing of the sectioned sample was carried out for 1 hr at 1,023 K in a vacuum.

An etched line parallel to the ion-incident surface is revealed with optical microscopy at the surface of the sectioned sample as shown in Fig. 1 for the 316 steel irradiated with 45.7 MeV Ar-ions and 86.2 MeV N-ions. The distance of the etched line from the ion-incident surface measured on the photograph are 6 and 40 μm for Ar- and N-ion irradiated specimens, respectively. In the calculation for 86.2 MeV N-ions injected into amorphous iron, peaks of the distribution curves for the damage rate and the injected ions occur at depths of 39.6 and 39.8 μm, respectively; the peak positions agree closely in both distribution curves. Thus, the center of the etched line shown in Fig. 1a approximates the mean projected range for 86.2 MeV N-ions injected into the 316 stainless steel, and the measured value of 40 μm is in good agreement with the calculated value of 39.8 μm.

In the measurement of the mean projected range by optical microscopy, uncertainty arises from identification of the ion-incident surface and an error in the measurement is estimated to be about 0.5 μm. This error corresponds to the uncertainty of 1.3% for the range of around 40 μm for 86.2 MeV N-ions injected into the 316 steel. However, this error of 0.5 μm is not so small compared with the range of about 6 μm for 45.7 MeV Ar-ions injected into the 316 steel. Furthermore, the stopping power for Ar in the steel has not been evaluated

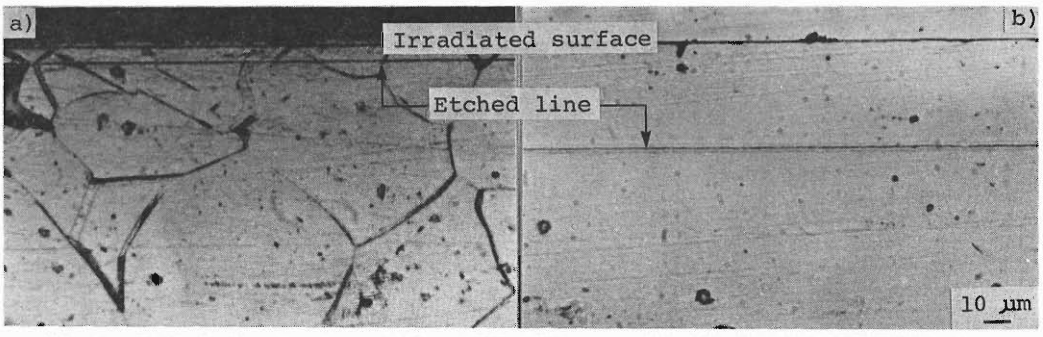

Fig. 1. Optical microstructures of Type 316 stainless steel irradiated with 45.7 MeV Ar-ions a) and 86.2 MeV N-ions b).

* Japan Atomic Energy Research Institute.

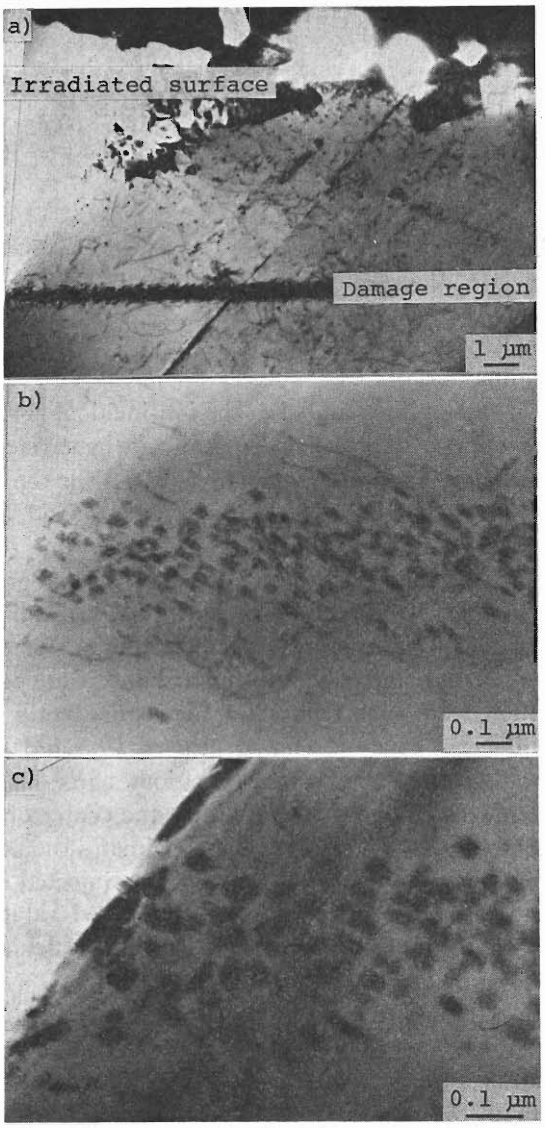

Fig. 2. Microstructures in Type 316 stainless steel irradiated with 45.7 MeV Ar-ions and annealed for 1 hr at 1,023K. Full-range electron microstructure a), details of the damaged region showing carbide precipitation b), and argon bubbles c).

correctly in the vicinity of 50 MeV. Then, the agreement between the measurement and the calculation for the Ar-ions injected into the 316 steel is not so well as that for N-ions injected into the 316 steel.

When the irradiated specimens are annealed for 1 hr at 1,023 K, the etched line appears distinctly at the identical position with the as-irradiated specimens. Figure 2 shows the microstructure relevant to the etched line in the 316 steel irradiated with 45.7 MeV Ar-ions to 6.3×10^{19} ions/m^2 and annealed for 1 hr at 1,023 K. The etched line observed by optical microscopy is correlated definitely to the electron micrograph (Fig. 2a). It is evident in the photographs of high magnifications presented as Figs. 2b and 2c that the damaged region indicated in Fig. 2a contains rectangular plate-like precipitates and argon bubbles. The precipitates elongated along the $<1\,1\,0>$ direction in the matrix were identified to be $M_{23}C_6$ type carbide from a selected area electron diffraction pattern. The distributions of number density and average diameter of the bubbles have peaks of 4.3×10^{22}/m^3 and 7 nm, respectively, at the center of the damaged region. This fact indicates that the argon injected into the 316 steel at ambient temprature stabilized Frank loops to induce the nucleation of the carbide at the loop during the post-irradiation annealing, as in case of helium in the steel.[2] The carbide is observed in the region where contains argon of exceeding 200 appm to form bubbles during the annealing.

References

1) K. Shiraishi and K. Fukai: *J. Nucl. Mater.*, **117**, 134 (1983).
2) K. Shiraishi, K. Fukaya, and K. Fukai: *ibid.*, **119**, 268 (1983).

RIKEN Accel. Progr. Rep. **18** (1984)

III-2-41. Effects of Fast Neutron Irradiation on Insulating Materials

M. Yatsuhashi,* T. Suematsu,* H. Kobayashi,* I. Kohno,
M. Yanokura, S. Motonaga, and H. Kamitsubo

It has become indispensable to elucidate the effects of fast neutron irradiation on insulating materials, because development of fast breeder reactors, controlled thermonuclear reactors, and high energy particle accelerators is being hurried on.

Several kinds of insulating materials, such as poly (vinyl chloride), cross-linked polyethylene, ethylene-propylene rubber and silicone rubber, were irradiated by fast neutron from the 160 cm cyclotron as reported previously.[1] The size of the irradiated samples was 5 cm × 5 cm in area and 1mm in thickness; the maximum neutron fluence was 2.6×10^{16} n/cm^2. The effects of fast neutron irradiation were compared with those of γ-ray irradiation by using a conversion factor of 1 rad $=1.3\times10^8$ neutrons, which was obtained from the value of absorbing coefficient of fast neutron in polyethylene[2),3)].

After irradiation, changes in volume resistivity, dielectric constant, and dielectric loss (tan δ) of the samples were measured at first. Then, three tensile test specimens, JIS K6301 No. 4 dumbbell shape, were stamped out from the sample, and the changes in tensile strength and elongation of the specimens were measured.

Figure 1 shows absorbing dose dependence of the tensile strength and elongation of cross-linked polyethylene (XLPE); results of ^{60}Co γ irradiation are also shown. Up to a maximum dose of 2×10^8 rad (2.6×10^{16} n/cm^2), the change in tensile strength is small and, although elongation is lowered, a value of about 120% is retained.

In this report elongation is defined as $\{(l-l_0)/l_0\}\times100$ (%). l_0 is original length between marked points on the specimen and l is length when it is broken.

Figure 2 shows the absorbing dose dependence of volume resistivity and tan δ of XLPE sample.

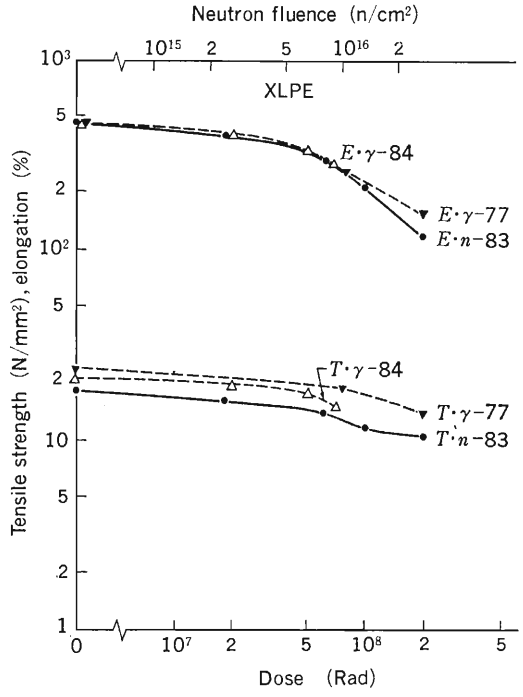

Fig. 1. Mechanical properties of XLPE. $E\cdot\gamma$-84 indicates change of elongation by γ-ray irradiation measured in 1984 and $T\cdot n$-83, change of tensile strength by neutron irradiation measured in 1983.

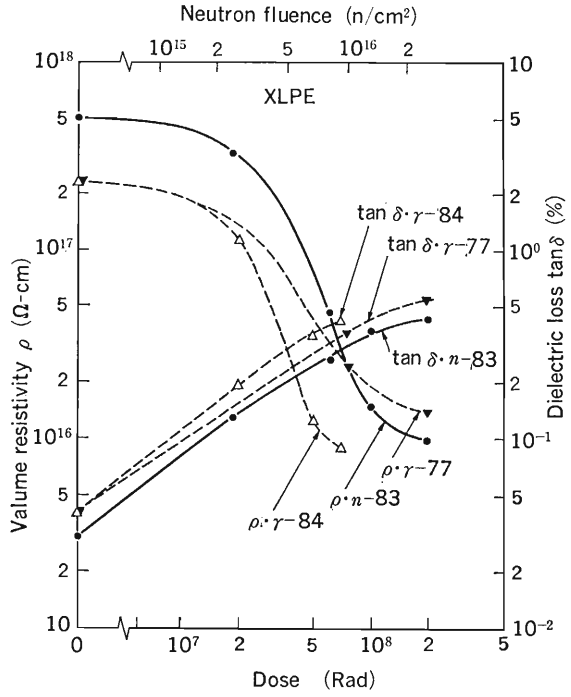

Fig. 2. Electrical properties of XLPE. tan $\delta\cdot\gamma$-77 indicates change of tan δ by γ-ray irradiation measured in 1977 and $\rho\cdot n$-83, change of volume resistivity (ρ) by neutron irradiation measured in 1983.

* Fujikura Ltd.

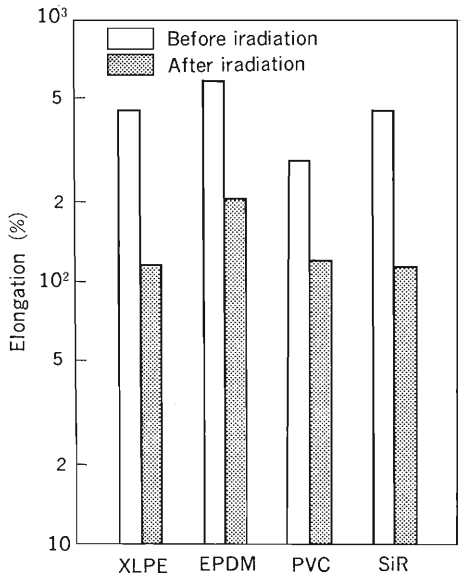

Fig. 3. Degradation of elongation properties.

Value of tan δ is increased by 0.5% and volume resistivity is decreased to 10^{16} Ω cm. The dielectric constant was almost invariant by fast neutron irradiation to 2×10^{8} rad.

In Fig. 3 degradations of elongation property for four insulating materials are shown. Degradation of electrical characteristics of poly (vinyl chloride) (PVC) was large, but those of ethylene-propylene rubber (EPDM) and silicone rubber (SIR) were similar to those of XLPE.

The results of changes in the electrical and mechanical properties caused by fast neutron irradiation are similar to those obtained by ^{60}Co γ ray irradiation. In conclusion, the irradiation effects on the electrical and mechanical properties of the insulating materials for electrical cables may not be different appreciably between fast neutrons and γ rays if absorbing doses are the same.

References

1) H. Kamitsubo, I. Kohno, S. Motonaga, M. Yanokura, T. Shikata, M. Yatsuhashi, T. Suematsu, and H. Kobayashi: *RIKEN Accel. Progr. Rep.*, **16**, 118 (1982).
2) A. E. Profio: Radiation Shielding and Dosimetry, Wiley-Interscience, New York (1931).
3) A. Charlesby: Atomic Radiation and Polymers, Pergamon Press, London (1960).

RIKEN Accel. Progr. Rep. 18 (1984)

III-3. Radiochemistry and Nuclear Chemistry

1. Isotope Production and Labelled Compound Synthesis

T. Nozaki, S. Ambe, M. Iwamoto, Y. Minai, M. K. Kubo, E. Tsuchida,
M. Yuasa, Y. Ogata, H. Nishide, M. Suehiro, and F. Yokoi

In this period, the following studies have been undertaken: (1) adsorption of ^{29}Al by soils, (2) determination of oxygen chemically bound to hemoglobin and synthetic heme by ^{15}O tracer method, (3) synthesis and *in vivo* behavior studies of ^{77}Br-bromoperidol, and (4) preliminary study of the labelling by the malonic acid ester synthesis. Also, an automatic synthesizer of ^{11}C-methyl iodide was fabricated in the Technology Division of our institute.

We previously reported on the production of ^{29}Al and its distribution in animal organs.[1] We tried some utilization of ^{29}Al, but its too short life did not allow us to obtain any satisfactory result. Recently, we have measured the adsorption of ^{29}Al by soils. Soils of different origins are suspended in water, and no-carrier-added ^{29}Al is added to the suspension with various amounts of HCl. The resultant suspension is shaken, and an aliquot of it is taken at 4 to 5 min intervals and centrifuged rapidly. The supernatant liquid is withdrawn and its ^{29}Al activity is measured. Relative rate and equilibrium of the adsorption are thus shown to be different according to the origin of the soil. Further study is in progress.

A liposomal heme was synthesized as an artificial oxygen carrier by some of the present authors,[2] and embedded in a bilayer of liposome with a radius of 400 Å. In order to study the oxygen transfer mechanism for this compound, the ^{15}O tracer technique is regarded as highly useful. Hence, the uptake of $^{15}O_2$ by this compound was first studied. The $^{15}O_2$ was supplied from a steady flow gas line. A mixture of O_2 (100 Torr) and N_2 (660 Torr) was conducted to a target cell and bombarded with deuterons (8 MeV, 2 μA) to induce the reaction of ^{14}N(d, n)^{15}O. The crude $^{15}O_2$-O_2-N_2 mixture was passed through columns of copper powder and soda lime (100 mm dia., 10 cm length) for removal of NO_x and ^{17}F formed by the radiation effect and by the ^{16}O(d, n)^{17}F reaction, respectively. The gas mixture was supplied with a steady flow (200 ml/min) and a steady radioactivity intensity (1 μC/ml).

Before the measurement of the $^{15}O_2$ absorption by the sample, it was ascertained that: (1) the ^{15}O was in sufficient radiochemical purity, (2) the absorption saturation was attained in a few min when the gas was bubbled into the sample solution, and (3) no notable isotopic exchange took place between the ^{15}O and water. Oxygen uptake by the samples of hemoglobin and the synthetic heme was measured from the ^{15}O radioactivity at the absorption equilibrium. The results are shown in Table 1. Each value was obtained as an average over 10 samples. The heme-bound oxygen was also determined spectrophotometrically; the results are shown in Table 1 together with those by an O_2 probe method,

Table 1. Oxygen uptake by red blood cell and liposomal heme.

Sample (Heme concn.)	Annihilation radiation intensity (t=0, cpm/ml)	Standard deviation (%)	Oxygen uptake volume (ml O_2/100 ml)			
			Present method	O_2-probe	Spectroscopy	Relative (%) $\frac{\text{Present method}}{\text{Spectroscopy}} \times 100$
Red blood cell						
(0.5 mM)	2,970	4.0	1.57	0.415	1.64	96
(1.0 mM)	5,560	4.8	2.94	0.417	2.86	103
Liposomal heme						
(1.0 mM)	3,540	4.2	1.87	0.423	2.04	92
Aqueous media[a]	795	1.8	0.421	—	—	—
$^{15}O_2$-N_2 gas	24,900	—	—	—	—	—

At 30°C, 760 Torr and p(O_2)=100 Torr

[a] Aqueous media; distilled water, phosphate buffer solution, and phospholipid liposome solution.

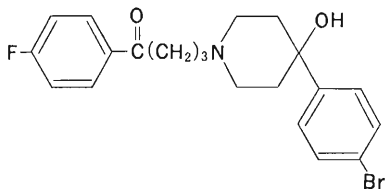

Fig. 1. Bromoperidol.

which gives only dissolved oxygen quantity. More detailed results of this study are described in Ref. 3.

Bromoperidol (Fig. 1), is thought to be one of the compounds which bind specifically with dopamine receptors *in vivo*. This compound was labelled with ^{77}Br by way of Sandmeyer reaction. Aminoperidol was diazotized, and no-carrier-added ^{77}Br was added to the diazonium solution together with copper powder. The mixture was heated gradually to 75°C in 15 min. After addition of a sufficient quantity of ammonia to the mixture, the product was extracted with chloroform and separated from the major by-products chromatographically. Finally, the ^{77}Br bromoperidol was purified by inverse phase, liquid chromatography and its purity was ascertained by thin layer chromatography. The ^{77}Br bromoperiodol was administered intravenously to rats and mice, and the biodistribution was studied together with a carrier effect on tissue uptake. The distribution of this labelled neuroleptic in the brain was examined by radioautography.

These biomedical assessments have revealed the following facts.

(1) Brain uptake 10–240 min after injection was 4–2.5% dose/whole brain, 9–6% dose/g of the tissue, which was 27–63 times higher than the blood radioactivity level. The brain uptake was affected considerably by the specific activity and chemical purity of the compound.

(2) In the brain, the radioactivity was localized in striatum, where a dopamine receptor density is thought to be high, and cerebral cortex. The distribution of the ^{77}Br was also affected by the specific activity and purity of the labelled bromoperidol; low specific activity and low chemical purity result in non-specific and uniform distribution in the brain.

(3) The distribution of ^{77}Br-bromoperidol in tissues other than brain reproduced similar trend to that of low specific activity ^{82}Br-bromoperidol reported by Vincent *et al.*[4] The addition of unlabelled compound to the labelled bromoperidol suggested that about 50 nmol, *i.e.*, 1 mg/kg of body weight, is the maximum torelable dose for normal metabolism. More detailed results of this study are published elsewhere.[5]

References

1) T. Nozaki, S. Ambe, M. Iwamoto, and Y. Minai: *RIKEN Accel. Progr. Rep.*, **15**, 95 (1983).
2) E. Tsuchida, H. Nishide, M. Yuasa, E. Hasegawa, Y. Matsushita, and K. Eshima: *J. Chem. Soc., Dalton Trans.*, 1149 (1984).
3) M. Yuasa, Y. Ogata, H. Nishide, E. Tsuchida, M. Iwamoto, and T. Nozaki: *Chem. Lett.*, **11**, 1889 (1984).
4) S. H. Vincent, M. B. Sambhu, and A. G. Digens: *J. Med. Chem.*, **23**, 75 (1980).
5) M. Suehiro, F. Yokoi, M. K. Kubo, M. Iwamoto, and T. Nozaki: Proc. IAEA Conf. Labelled Comp. Radiopharm. (1984), in press.

RIKEN Accel. Progr. Rep. 18 (1984)

III-3-2. Charged Particle Activation Analysis

T. Nozaki, Y. Itoh, Y. Ohkubo, T. Kimura,
H. Fukushima, T. Abe, and T. Masui

Since the end of last year, charged particle activation analysis of carbon, nitrogen, and oxygen in several matrices has been undertaken by Japan Analytical Chemistry Center by the use of the cyclotron.[1] We have aided this semi-commercial trust analysis, and about 200 samples in all have been analyzed this year. For the analyses of carbon and nitrogen by the reactions of $^{12}C(^{3}He,\alpha)^{11}C$ and $^{14}N(p,\alpha)^{11}C$, respectively, an improved method was devised for the chemical separation of the ^{11}C last year. This method consists of (1) matrix dissolution in an alkali solution containing a carbonate carrier, (2) the addition of $KMnO_4$ to the solution and its heating in a microwave oven until the dried mass becomes dull red, and (3) the evolution of $^{11}CO_2$ from the resultant mass and its conversion into Li_2CO_3 precipitate.

Silicon containing ^{11}C without other radioactivity was used to check on this chemical separation, because some uncertainty still existed in whether any correction was necessary in the measured carrier recovery due to contamination from non-radioactive CO_2 and whether the ^{11}C in the sample silicon was totally mixed with the carrier. Silicon doped with boron was bombarded to give ^{11}C by the $^{11}B(p,n)^{11}C$ reaction, and induced positron activities were measured nondestructively. After the decay of ^{30}P (2.5 min half-life) formed by the $^{30}Si(p,n)^{30}P$ reaction, the sample was subjected to the chemical separation. From the radioactivities of ^{11}C in the sample just before the separation and in the separated Li_2CO_3 together with the weight of the Li_2CO_3, correction factor for this chemical separation was found to be 1.15 ± 0.07. This method is now used routinely.

The fabrication of a new apparatus for surface oxygen analysis considerably delayed, and our plan also delayed. The apparatus has recently been completed, and the study has become in progress again.

We reported on the escape of oxygen from melt of antimony-doped silicon in the last volume of this report. We wrote there that oxygen probably escaped as antimony oxide. By thermochemical calculation, however, this has been shown to be wrong. Now we think with fair confidence that the evaporation of antimony accelerates the evaporation of oxygen as SiO just like in the steam distillation in which steam flow accelerates the distillation of less volatile organic compounds.

A reliable method is now urgently needed for the analysis of carbon in gallium arsenide. Charged particle activation analysis with the $^{12}C(^{3}He,\alpha)^{11}C$ reaction cannot be used for Czochralski GaAs crystals, because they are crystallized under B_2O_3 melt and thus contains some boron. (Helium-3 bombardment of boron also gives ^{11}C by the $^{10}B(^{3}He,pn)^{11}C$ reaction.) Hence, the use of $^{12}C(d,n)^{13}N$ reaction is necessary for this purpose together with a proper devise of the separation of the ^{13}N.

We intend to undertake the following study scheme for the establishment of the process of analysis: (1) preparation of ^{13}N-doped GaAs for use in the study of the chemical separation of ^{13}N, (2) study for quantitative separation of the ^{13}N from the matrix by dry fusion and its purification by passing through successive columns, (3) ascertainment of the quantitative absorption of the ^{13}N in a column, in a suitable state for activity measurement, and (4) check on the reliability of the process and, if necessary, determination of the correction factor due to non-quantitative recovery of the ^{13}N.

For the preparation of ^{13}N-doped GaAs sample by recoil implantation, two GaAs plates were placed in parallel with a small aperture in which an oxygen stream was bombarded with a proton beam as shown in Fig. 1. Atoms of ^{13}N formed by the $^{16}O(p,\alpha)^{13}N$ reaction are provided with recoil energies, by which a part of the atoms are

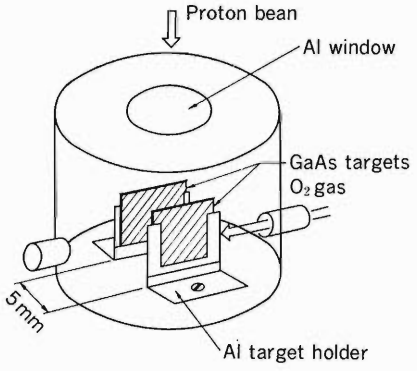

Fig. 1. Apparatus for recoil implantation.

implanted into the GaAs plates. The plates were found to contain also some other radioactivities, such as those produced from matrix Ga and As by the bombardment with scattered protons and ^{18}F formed by the $^{18}O(p,n)^{18}F$ reaction.

After bombardment with protons (1 μA, 10 min) of 11 MeV incident energy, at which this reaction has a maximum cross section, a few times 10^5 Bq of ^{13}N was in the GaAs together with activities of other radionuclides. This GaAs plate is very useful for the succeeding studies.

The ^{13}N was found to be separated quantitatively by fusion of the matrix with copper grains in a helium stream. An RF generator of 2 kW maximum power was used for heating. By passing the helium stream carrying ^{13}N through a column of Molecular Sieve 5A cooled with liquid nitrogen, the ^{13}N proved to be adsorbed quantitatively in a very narrow inlet portion of the column, indicating the ease of the measurement of ^{13}N activity by the coincidence counting of positron annihilation.

For the purification of the ^{13}N in the helium stream, a column of Molecular Sieve 4A was inserted in the stream pass at the room temperature. Although this column proved to be very effective for the removal of radioactive impurities, it also caught a considerable portion of ^{13}N. Various columns are now under test for satisfactory purification of ^{13}N.

Determination of implanted oxygen in silicon and its oxide is reported independently in this volume.

Reference

1) T. Nozaki, Y. Itoh, M. Iwamoto, H. Shinyashiki, K. Nomura, T. Kimura, and H. Fukushima: *RIKEN Accel. Progr. Rep.*, **17**, 96 (1983).

RIKEN Accel. Progr. Rep. 18 (1984)

III-3-3. Charged Particle Activation Analysis of Ion-Implanted Oxygen

T. Nozaki, Y. Itoh, Y. Misawa, and T. Saito

Oxygen ion implantation for the formation of an oxide film in a solid has been studied for being applied, for example, to an SiO_2 layer formation in semiconductor silicon to separate its device elements. Many papers have been published dealing with the depth profile of implanted oxygen in silicon, without any exact information about the quantitative amount of oxygen incorporated in silicon or other substrates.[1] By the same experimental charged particle activation analysis as was used for the determination of oxygen in SIPOS film,[2] we measured quantitatively the amount of oxygen implanted into films in order to obtain a relationship between the integrated ion flux impinging on the sample and the quantitative amount of oxygen incorporated in it.

Substrate plates used were of CZ silicon, <1 0 0> orientation, and n-type with resistivity of 10 Ω·cm. Oxygen ions or carbon monoxide ions of $(1\text{–}10)\times 10^{17}$ at·cm^{-2} integrated flux were impinged into these plates by the implantation technique. Also, SiO_2 film made on the plate by thermal oxidation

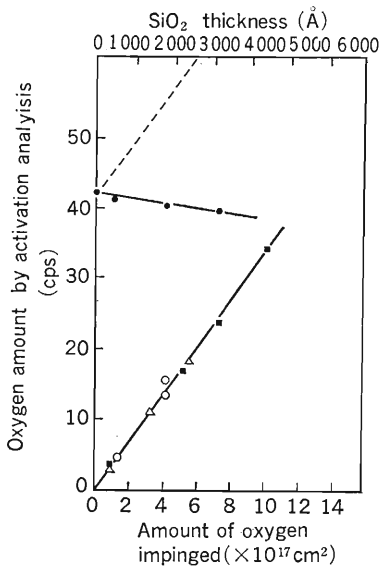

Fig. 1. Oxygen concentration detected by activation analyses *vs.* amount of oxygen having impinged. ○, SiO_2 without implantation; ■, oxygen-implanted Si; △, carbon monoxide-implanted Si; ●, SiO_2 film after oxygen ion impingement.

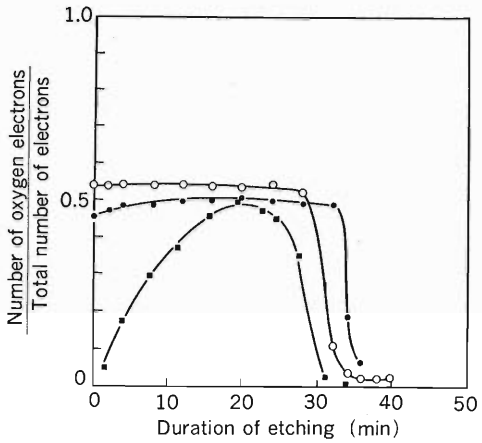

Fig. 2. Depth profiles of oxygen in Si and SiO_2 films observed by Auger electron spectroscopy. ○, Thermal oxidation film (500 nm in thickness); ■, 7×10^{17} O^+ cm^{-2} implantation in Si; ●, 7×10^{17} O^+ cm^{-2} implantation in SiO_2.

was treated similarly. The total quantity and distribution of oxygen in these samples were measured by charged particle activation analysis with the $^{16}O(^3He,p)^{18}F$ reaction and by Auger electron spectroscopy, respectively.

As shown in Fig. 1, all oxygen ions having impinged to the silicon plates were found to be incorporated into the silicon. Silicon plates after thermal oxidation to various thicknesses were used as the activation standard. Carbon monoxide ions were also shown to be incorporated quantitatively into silicon. To the SiO_2 substrate, however, no oxygen was found to be incorporated, only the quantity of oxygen in the SiO_2 before the implantation being detected. As shown in Fig. 2, the depth profiles of oxygen also indicate that oxygen was incorporated quantitatively into silicon but almost no additional oxygen was present in SiO_2.

References

1) K. Izumi, M. Doken, and H. Ariyoshi: *Jpn. J. Appl. Phys.*, **19** (1) (suppl.), 151 (1980).
2) T. Matsushita, T. Aoki, T. Otsu, H. Yamamoto, H. Hayashi, M. Okayama, and Y. Kawana: *Jpn. J. Appl. Phys.*, **15** (suppl.), 35 (1975).

RIKEN Accel. Progr. Rep. 18 (1984)

III-3-4. Application of PIXE to Environmental Science

K. Maeda, Y. Sasa, M. Maeda,* S. Noriki,** and M. Uda

A rapid, sensitive, multielemental analytical method is required for investigating the material balance problems in environmental science. The PIXE (Particle Induced X-ray Emission) spectroscopy is one of the advanced tools which meet such a requirement. We report here the application of the PIXE to settling particles in marine water, together with some new aspects of the experimental technique.

The experimental procedures and setups were described elsewhere[1),2)] except that a tungsten electron gun was newly set in front of the target to eliminate the charging effect. When the target composed of insulating materials is irradiated by ions, it often happens that positive charges are stored in the target during irradiation. As a result, strong continuous X-rays are generated and hence the sensitivity and the accuracy of measurements become low. The efficacy of the electron gun is demonstrated in Fig. 1. The K_α peaks of S, Cr, and Mn are hindered by the superposition of continuous X-ray background in the spectrum without the electron gun. These peaks are detected clearly when the target is flooded with electrons.

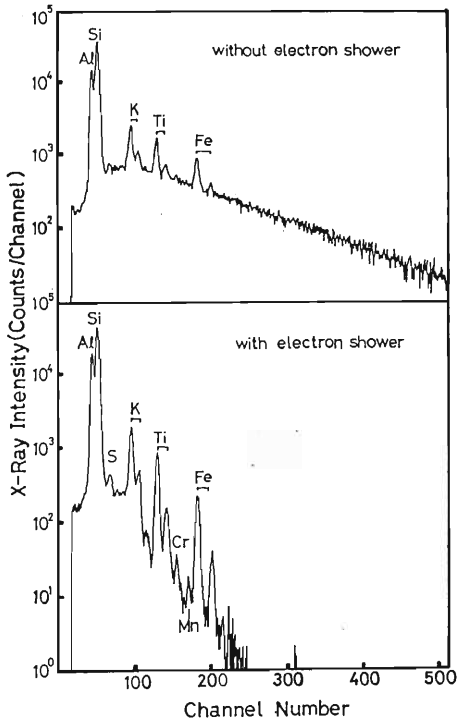

Fig. 1. PIXE spectra from clay (NBS standard 98a) induced by 5 MeV He^+ ions with and without electron shower.

Generally, light ions such as p and α particles are used for excitation in the PIXE analysis. Few studies on the PIXE by means of heavy ion impacts have been reported in the literature. Then it is interesting to compare the X-ray spectra induced by light ions and heavy ions. We previously reported the analysis of the suspended particulates in water of the Tama River.[3)] For this purpose 15 MeV N^{2+} ions alone were available to use for the excitation. From the end of the last year, He^+ and He^{2+} ions as well as N^{2+} have been accelerated by RILAC. Now the direct comparison of the light-ion and heavy-ion induced PIXE spectra becomes possible. Figure 2 shows the concentrations of titanium and iron in the suspended particulates determined by use of $\sim$ 1 MeV/amu N^{2+} and He^+ ions, where the same targets were used. The analytical results agreed well with each other. The resolutions of the X-ray peaks were somewhat better in He^+ induced spectra than in N^{2+} induced ones. The X-ray yields were, however, much higher in N^{2+} impact than in He^+ impact. This suggests that heavy ions are rather preferable when the amounts of samples are extremely small.

The study on transportation of elements by marine water is important to solve the mechanisms of geochemical material cycling. We have attempted to apply the PIXE to the analysis of settling particles in water of the Antarctic Ocean. Samplings were

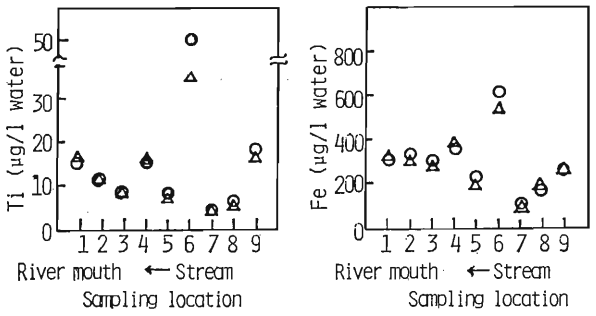

Fig. 2. Variations of concentrations of particulate titanium and iron along the Tama River. ○: 5 MeV He^+ impact, △: 15 MeV N^{2+} impact. See Ref. 3 as for the sampling conditions and the locations.

* Tokyo University of Fisheries.
** Faculty of Fisheries, Hokkaido University.

Table 1. Total flux and elemental concentrations relative to Si in settling particles in water of the Antarctic Ocean.

Sampling period	Depth (m)	Total flux ($mg/m^2/day$)	Concentration ratio (by weight)				
			K/Si	Ca/Si	Fe/Si	Zn/Si	Sr/Si
12/25–1/4	1,565	900	0.0034	0.0125	0.0003	0.0002	0.0001
1/4–1/14		2,540	0.0028	0.0157	0.0002	0.0002	0.0003
1/14–1/24		460	0.0027	0.0117	0.0001	0.0003	0.0015
1/24–2/3		320	0.0010	0.0080	0.0003	0.0003	0.0001
12/25–1/4	3,770	600	0.0021	0.0121	0.0039	0.0006	0.0002
1/4–1/14		2,230	0.0033	0.0101	0.0004	0.0001	0.0001
1/14–1/24		760	0.0034	0.0222	0.0016	0.0002	0.0002
1/24–2/3		480	0.0032	0.0189	0.0029	0.0003	0.0001

made four times between December 1983 and February 1984 at the station located at 61°30′S and 150°02′E. The depth of the sea at this point is 3,920 m. Two samplers were arranged at the depths of 1,565 m and 3,770 m, respectively. Settling particles were accumulated over a period of ten days at each depth. A part of each sample was dispersed in a small amount of pure water and deposited on a Nuclepore filter of 1 mg/cm^2 by filtering, and then served as the target. The thickness of sample itself was controlled to be 0.7 mg/cm^2. Homogeneous thin targets with controlled thickness were prepared by this method, but there is a possibility of underestimating water-soluble elements. Improvement of the target preparation is in progress. Chemical analysis of the same samples is to be carried out in Hokkaido University.

The main component of the particles in the Antarctic Ocean is, in general, considered to be silica from biogenic origin. Then we chose Si as a reference element. The concentrations of some elements relative to Si estimated from the PIXE spectra are summarized in Table 1 together with the total flux of settling particles. Here 5 MeV protons were used for the excitation. The total flux was very large in the second sampling period. This must be caused by a temporary blooming of planktons such as phytoplanktons. In all the sampling periods, iron was enriched in the particles collected at the deeper region. This indicates that, during the sedimentation, Fe ions resolved in water or contained in suspended particulates were caught by the settling particles which had been generated at the surface layer by biogenic reactions. The high concentration of Sr at the upper region in the third period is also noteworthy though the reason has not yet been solved.

References

1) K. Maeda and M. Uda: *Reports I. P. C. R.* (in Japanese), **58**, 96 (1982).
2) K. Maeda, Y. Sasa, and M. Uda: *RIKEN Accel. Progr. Rep.*, **17**, 123 (1983).
3) K. Maeda, Y. Sasa, M. Maeda, M. Kobayashi, and M. Uda: *ibid.*, p. 132.

RIKEN Accel. Progr. Rep. 18 (1984)

III-3-5. Application of PIXE to Medical Science (II)

K. Maeda, H. Kusuyama, Y. Yokode, Y. Sasa,
S. El. Nasr,* M. Kobayashi, and M. Uda

The PIXE (Particle Induced X-ray Emission) is an advanced, extremely sensitive, multielemental analytical method. It is especially valuable for analysis of small amounts of heavy elements in matrixes composed of light elements such as organic materials. In biological organs injured by diseases, elemental compositions of affected parts might differ from those of normal tissues. In some cases, elemental compositions of blood, urine, and hair reveal the indications of diseases; the PIXE is useful for diagnosis. We have continued a study on the application of this method to medical science.[1] We present here some examples of the PIXE analysis of human tissues. We also report a preliminary experiment using a new Si(Li) detector designed for analysis of light elements.

The details of the experimental procedures and setups are described elsewhere.[1),2)] This year the magnet system for incident ion beams has been improved. Now the scanning of ion beams of 0.5 × 0.5 mm^2 spot size is possible. Tissue samples were freeze-dried and sectioned with a microtome to about 10 μm slices. Then they were placed on 1 μm thick polypropylene film and used as targets without any pre-treatments. For blood and blood serum samples, we have examined several target preparation techniques. Homogeneous thin targets could be prepared by the following treatment: liquid samples homogenized with an ultrasonic generator are painted on polypropylene backing film and dried in a vacuum desiccator.

Human tissues taken from patients of various kinds of diseases have been analyzed. Deficiency of iodine in diseased thyroid grands was reported previously.[1] The results of the PIXE analysis of the additional samples has ascertained such a feature.

The most impressive is the case of renal adenocarcinoma. As Fig. 1 shows, the iron content in the active cancer tissue is extremely high as compared to the normal one. The Fe content in the necrosed tissue in the cancer is between these two. On the other hand, the zinc content in the cancer tissue is much lower than in the normal one. Table 1 shows the elemental concentrations estimated from the individual X-ray intensities in the PIXE spectra. The enrichment factor of Fe in cancer tissues is of the order of 10 to 100.

The change in elemental composition was also recognized for the bladder cancer though it is not so striking as the above case. Table 2 represents the K_α peak intensities relative to the potassium K_α obtained from the PIXE spectra of cancer and

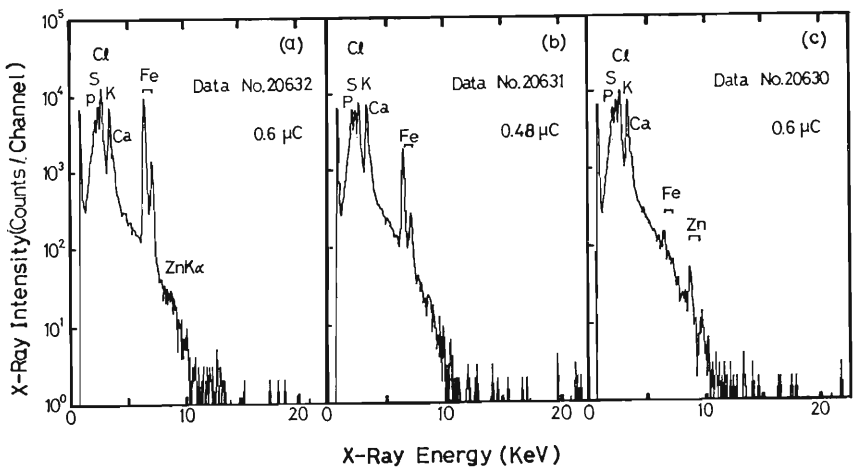

Fig. 1. PIXE spectra obtained from (a) active cancer, (b) necrosed, and (c) normal tissues in a kidney taken from a patient of renal adenocarcinoma. 5 MeV protons were used for excitation.

* Teacher's College for Women, Kuwait.

Table 1. Elemental concentrations in tissues of kidneys taken from patients of renal adenocarcinoma.

		Elemental concentrations (μg/cm^3)				
		P	Cl	K	Fe	Zn
Case 1	Cancer tissue	3,000	2,600	3,200	8,500	49
	Necrosis tissue	5,000	2,000	4,100	2,100	70
	Normal tissue	4,000	2,100	3,500	73	110
Case 2	Cancer tissue	3,700	1,700	3,900	660	41
	Normal tissue	3,100	1,700	2,800	64	100

Table 2. PIXE K_α peak intensities relative to $K\,K_\alpha$ obtained from tissues in bladders. σ: standard deviation.

Element	Cancer tissue	(σ)	Normal tissue	(σ)
P	0.44	(0.05)	0.40	(0.02)
S	0.48	(0.11)	0.70	(0.18)
Cl	0.80	(0.28)	2.13	(1.18)
Fe	0.0068	(0.0012)	0.0081	(0.0025)
Zn	0.0016	(0.0006)	0.0026	(0.0006)

normal tissues in bladders taken from five patients. Potassium was chosen as a reference element because its concentration is constant in all the samples. Chlorine and sulfur seem to decrease in the cancer tissues while the concentrations of P, K, Fe, and Zn are almost the same in both of cancer and normal tissues.

Recently a new Si(Li) detector system has been constructed. The detector has three windows: open, a thin Parylene film, and a 7.5 μm thick beryllium foil. These windows are exchangeable in vacuum from the outside. The K_α X-rays of the elements lighter than $Z=13$ can not be detected by an ordinary detector with a Be window because of the absorption of X-rays in Be. By using the open or thin window, all the elements except $Z=1$–3 can be analyzed. Figure 2 shows the examples of the PIXE spectra measured through the thin window.

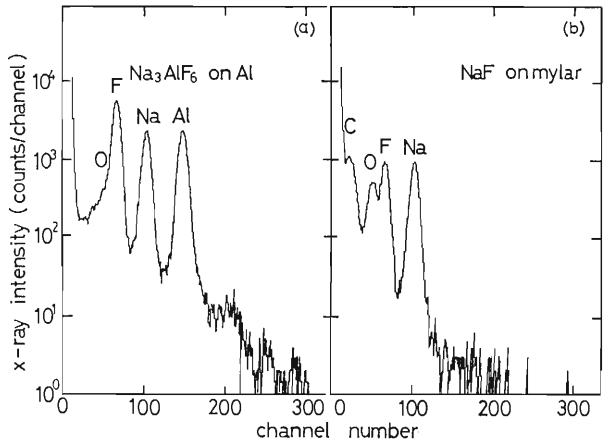

Fig. 2. PIXE spectra of (a) Na_3AlF_6 on Al backing film and (b) NaF on Mylar backing film measured through the thin window. 5 MeV He^+ ions were used for excitation.

References

1) M. Uda, K. Maeda, Y. Yokode, and Y. Sasa: *RIKEN Accel. Progr. Rep.*, **17**, 134 (1983).
2) K. Maeda and M. Uda: *Reports I. P. C. R.* (in Japanese), **58**, 96 (1982).

RIKEN Accel. Progr. Rep. 18 (1984)

III-3-6. Reliability and Detection Limit for the Elastic Recoil Measurement of Hydrogen

H. Nagai, M. Aratani, S. Hayashi, T. Nozaki, M. Yanokura,
I. Kohno, O. Kuboi, and Y. Yatsurugi

Elastic recoil measurement is usefull in the analysis of hydrogen on or near the surface of solid.[1)-4)] The reliability of this method was checked by comparing its results with those of other methods, and the detection limit of hydrogen was investigated.

Experimental procedures are the same as in our previous studies.[1),2)] We used Ar-ions accelerated up to 50 MeV, the beam current being 30–50 nA.

Nine amorphous silicon (a-Si: H) samples were prepared by glow discharge of a monosilane-hydrogen gas mixture, for the reliability measurement. Thickness of these samples ranged from 2,700 to 10,650 Å. The hydrogen contents of these samples were measured by the following three methods: elastic recoil (ER), vacuum extraction (VE), and heat conductivity (HC) measurements. The results are shown in Table 1. Hydrogen contents of a-Si: H samples were about 14 at. %. The values determined by the ER method were in agreement with those obtained by the VE and HC methods to within 20%. Average ratios of hydrogen content obtained by VE and HC to that by ER were 1.02 ± 0.13 and 1.10 ± 0.08, respectively. Thus these results indicate that the absolute hydrogen content can be determined fairly correctly by the ER method.

Table 1. Hydrogen contents in amorphous silicon samples measured by three methods: elastic recoil (ER), vacuum extraction (VE), and heat conductivity (HC).

Sample No.	Thickness (Å)	ER (at. %)	ER ($\times10^{17}$ atoms/cm^2)	VE* (at. %)	VE* ($\times10^{17}$ atoms/cm^2)	HC (at. %)	HC ($\times10^{17}$ atoms/cm^2)	VE/ER	HC/ER
59-1-18-2	10,650	14.7	7.48	13.0	6.50	14.5	7.38	0.87	0.99
58-9-19-2	8,950	16.9	7.42	16.2	7.06			0.95	
59-1-18-1	8,300	14.1	5.59	13.7	5.38	14.8	5.90	0.96	1.06
59-1-19-2	6,720	13.4	4.24	14.4	4.62	15.7	5.11	1.09	1.21
59-1-19-1	6,500	12.4	3.75	14.0	4.32	14.2	4.40	1.15	1.17
58-9-19-2	5,260	15.7	4.00	17.4	4.52			1.13	
58-9-09-1	5,100	14.4	3.50	11.7	2.76			0.79	
59-1-19-3	3,100	15.8	2.37	16.7	2.54	17.4	2.67	1.07	1.13
59-1-19-4	2,700	14.1	1.82	15.9	2.08	14.6	1.89	1.14	1.04
							Average	1.02 $\pm$0.13	1.10 $\pm$0.08

* Measured by Dr. Ogawara (Science University of Tokyo)

Table 2. Bulk and surface hydrogen contents in quartz, Si-wafer, and oxidized Si-wafer by elastic recoil measurement.

Sample	Bulk Hydrogen (at. ppm)	Bulk Hydrogen (wt. ppm)	Surface hydrogen ($\times10^{15}$ atoms/cm^2)	Ref. Bulk Hydrogen (Content) S. A. (wt. ppm)
ES*	1870$\pm$70	94 $\pm$3	—	90 –130
IR*	78$\pm$ 6	3.9$\pm$0.3	3.2$\pm$0.2	0.2– 0.6
OX*#	289$\pm$22	14.5$\pm$1.1	5.0$\pm$0.3	10 – 30
	276$\pm$37	13.8$\pm$1.8	10.0$\pm$0.7	
Art.*#	70$\pm$19	3.5$\pm$0.9	4.6$\pm$0.5	—
	51$\pm$ 6	2.6$\pm$0.3	10.3$\pm$0.3	
Nat.*#	56$\pm$28	2.8$\pm$1.4	3.1$\pm$0.7	—
	61$\pm$ 7	3.0$\pm$0.3	9.6$\pm$0.3	
Si-SiO_2**	22$\pm$ 4	0.8$\pm$0.2	5.9$\pm$0.2	—
Si***	73$\pm$10	2.6$\pm$0.4	13.7$\pm$0.5	—

* Quartz, ** Si-wafer+SiO_2 (340 Å), *** Si-wafer,

upper row, first measurement; lower row, second measurement

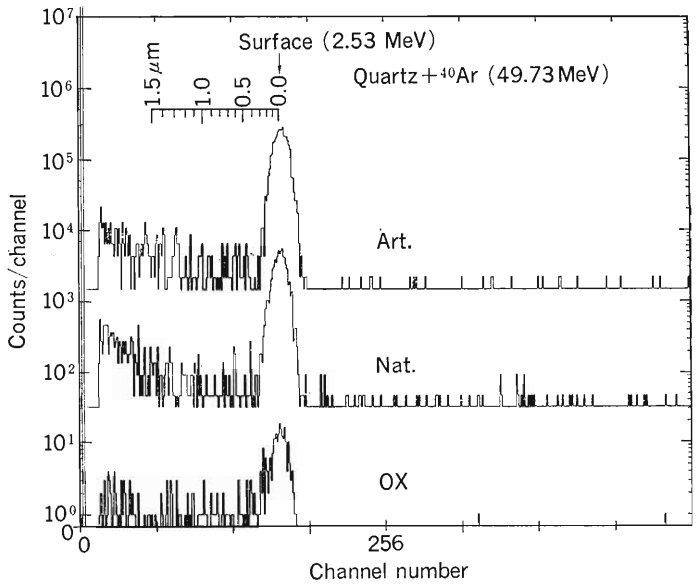

Fig. 1. The energy spectra of the hydrogen atoms recoiled by 49.73 MeV Ar-ions in the quartz samples (Art., Nat., and OX). The spectra were devided into three regions. Large peaks of the recoil surface hydrogen atoms are observed in the higher energy region. High energy edges of recoil oxygen atoms are observed in the lower energy region (deeper than 1.5 μm). Bulk hydrogen recoil spectra are observed in the 0.3–1.5 μm region without interference.

For the determination of a detection limit, natural and artificial high purity quartz samples (Nihon Sekiei Garasu Co.) were used. The results are shown in Table 2. The bulk hydrogen contents of the samples ES and OX were in good agreement with the literature values, but the value of the sample IR was about 10 times greater than the literature value. In addition, the apparent hydrogen contents in the bulk of low hydrogen samples, IR, Art., and Nat., were correlated with the quantity of hydrogen on the surface. It is probable that measured events in the energy spectra corresponding to interior of samples (Fig. 1) are derived from surface hydrogen atoms which were recoiled and then scattered into the detector with decreased energies. To ascertain this, we made measurements with a Si-wafer and Si-wafer oxidized by water vapor (Hitachi Manufacturing Co.) as well as the three quartz samples. The surface hydrogen contents of these samples were expected to be different from one another. Results are shown in Table 2. Though we expected to find a correlation or non-correlation between the bulk and the surface hydrogen contents, we get a conflicting results. For the quartz samples, while surface hydrogen amounts vary by a factor of 2 to 3, the bulk values of second measurements were in good agreement with the previous values. On the contrary, the Si-wafer data indicate that the bulk contents correlated with the surface amounts. We have not yet determined the effect of surface amount on the bulk content precisely; further studies are in progress. At present, the detection limit of this method is estimated to be less than about 200 at. ppm.

References

1) H. Nagai, M. Aratani, T. Nozaki, M. Yanokura, I. Kohno, O. Kuboi, and Y. Yatsurugi: *RIKEN Accel. Progr. Rep.*, **16**, 125 (1982).
2) H. Nagai, M. Aratani, S. Hayashi, T. Nozaki, M. Yanokura, I. Kohno, O. Kuboi, and Y. Yatsurugi: *ibid.*, **17**, 102 (1983).
3) M. Aratani, H. Nagai, S. Hayashi, M. Yanokura, O. Kuboi, Y. Yatsurugi, I. Kohno, and T. Nozaki: *ibid.*, p. 104.
4) Y. Yatsurugi, O. Kuboi, M. Hashimoto, H. Nagai, M. Aratani, M. Yanokura, I. Kohno, and T. Nozaki: *Appl. Phys. Lett.*, **44**, 246 (1984).

RIKEN Accel. Progr. Rep. **18** (1984)

III-3-7. Measurement of the Impurity Hydrogen Concentrations on the Surfaces of the Neutron Bottle

Y. Kawabata, M. Utsuro, S. Okamoto,* S. Hayashi, and T. Nozaki

Neutrons having energies below about 100 neV are called "ultracold neutrons (UCN)." Owing to such low energies, their motion is affected easily by the gravity, magnetic fields, or nuclear potentials in condensed materials. Therefore UCN provide much unique information.[1)-6)]

UCN having energies lower than the sum of nuclear and magnetic potentials are reflected at any incident angle. Nickel and beryllium, which have the total potential of 2.7 or 2.0×10^{-7} and 2.5×10^{-7} eV, respectively, are regarded as being useful materials for long-time confinement of UCN. Although many neutron bottle experiments have been carried out, all of the results show the confinement times far shorter than the theoretical values. The reason for this is supposed to be the presence of surface hydrogens. Despite the successful measurements of the quantity of the hydrogen on some neutron bottle surfaces,[7)] all trials to remove the hydrogen have failed.[8)] In the present study, therefore, we repeated the measurement of the surface hydrogen with some neutron bottle materials and tried another approach to remove it from the evaporated Ni layer.

The Rutherford Forward Scattering (RFS) was used for the measurement of light elements on the surfaces. ^{40}Ar ions were accelerated to about 50 MeV by the RIKEN linac. The experimental arrangement was similar to that described in a preceding report. As an another method hydrogen concentration profile can also be measured by the resonance reactions of ^{15}N and H. Lanford *et al.*[7)] have used this method for some neutron bottle materials. In the present study, deuterium should also be measured in some case, and the RFS method was used instead of the nuclear reaction method. The RFS method employed has the spatial resolution of about 500 Å and the accuracy in measuring total hydrogen amount is better than the resonance method.

The spectra obtained with 1,500 Å Ni deposited on Cu and Al substrates at 1×10^{-6} Torr are shown in Fig. 1. Hydrogen peaks are seen on the Ni surface and the Ni-substrate interface. For Ni-Cu mirror numbers of hydrogen of 1.5×10^{16} and 2.9×10^{16} atoms/cm^2 were found on the surface and the interface, respectively; for Ni-Al, 1.7×10^{16} atoms/cm^2 and 1.2×10^{16} atoms/cm^2 on the surface and the interface, respectively. These values are in good agreement with the results obtained with the ^{15}N resonance method. For other neutron bottle materials also, similar values were reported.[7)] The

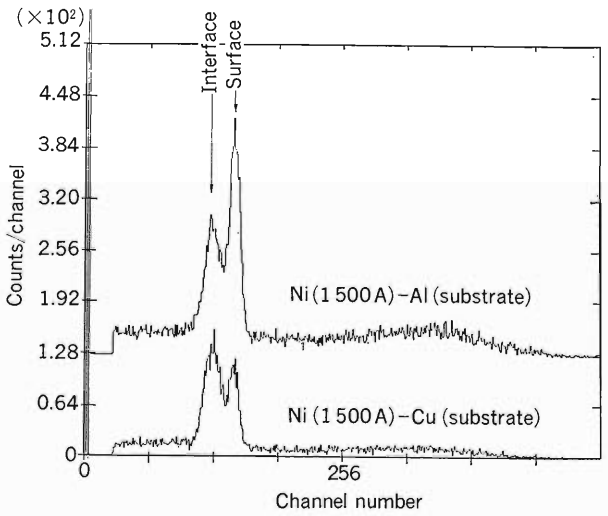

Fig. 1 Rutherford forward spectra for hydrogen distribution profiles. Right peak shows the surface hydrogen and left the interface.

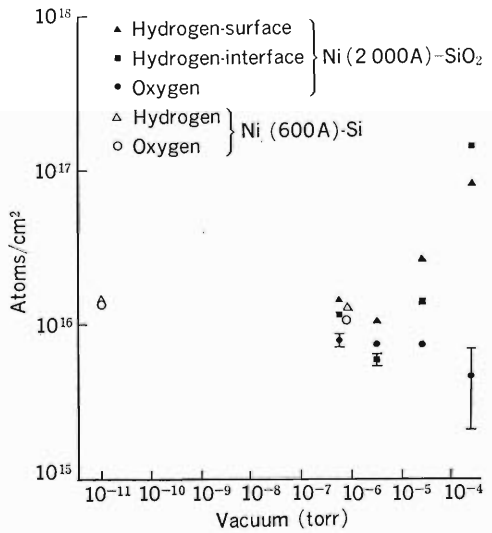

Fig. 2. Hydrogen and oxygen concentrations at various evaporating pressure.

* Research Reactor Institute, Kyoto University.

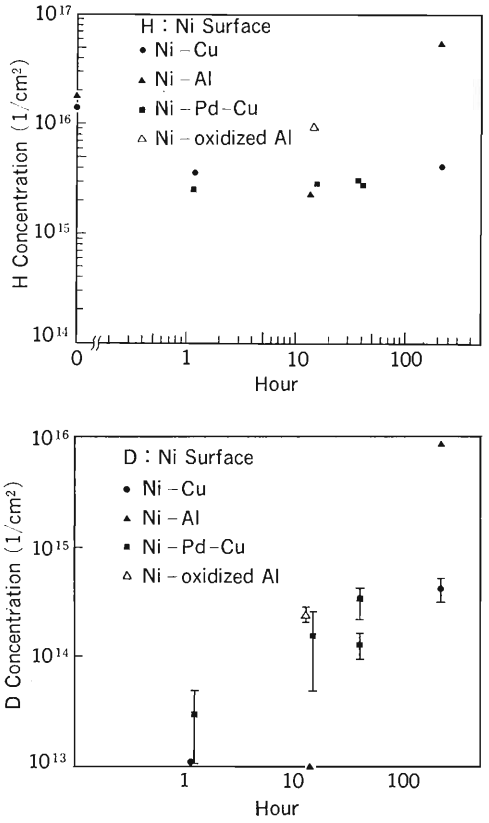

Fig. 3. Relation between the surface hydrogen (upper) and deuterium (lower) concentration and the elapsed time in liquid D_2O.

hydrogen profiles in deposited Ni layer at various vacuum pressures are shown in Fig. 2. The amount of hydrogen in the Ni surface layer is hardly affected by the pressure in the region lower than 1×10^{-6} Torr. When the pressure increases further, the region containing hydrogen extends to deeper. Although the total hydrogen concentration increases in this way, the surface hydrogen concentration is hardly affected. This fact indicates that the surface hydrogen comes from the residual gas after the deposit of the layer.

In order to examine the effects of the substrates on the quantity of the surface hydrogen, Cu, Al and quartz substrates deposited with Ni are compared. As the inner surfaces of neutron bottle must be a high-quality mirror for multiple reflections of UCN, they were polished optical-flatly. Their surface roughness for depth was less than 200 Å. The quantity of hydrogen on the interface was affected considerably by the surface condition of the substrate. For instance, the presence of oxygen layer on the Al substrate causes the increase of hydrogen. Palladium, as a hydrogen reservoir, was deposited between the substrate and the Ni layer. Quartz was also used for the substrate and assured to be clean for hydrogen. However, the quantity of the surface hydrogen with 2,000 Å Ni layer was independent of hydrogen concentrations in the substrates.

The Ni-deposited samples were immersed in liquid D_2O to examine the possibility of the replacement of H with D. The quantities of H and D were measured as a function of the immersion time. Results shown in Fig. 3 indicate that permeation of D obviously takes place from the surface, though the surface hydrogen concentration seems to be invariant. Thus, it is expected that the replaced D on a very thin surface layer may be reexchanged with H in the atmosphere within a very short time. As an another explanation, the presence of D on the surface cannot prevent possible hydrogen absorption. Therefore, these results indicate the difficulty of removing the hydrogen by the exchange with D.

One of the attractive materials for a neutron bottle is Be, since it has a high nuclear potential. The surface hydrogen in Be was also measured and found to be 2.1×10^{16} atoms/cm^2. It is the same order as the other materials.

References

1) A. Steyerl: in Springer Tracts in Modern Physics, vol. 80, Springer, Berlin p. 57 (1977).
2) R. Golub and J. M. Pendleburg: *Rep. Prog. Phys. Lett.*, **42**, 439 (1979).
3) M. Utsuro and Y. Kawabata: *Physica*, **120B**, 118 (1983).
4) A. Steyerl, B. Gmal, K.-A. Steinhauser, N. Achiwa, and D. Richter: *Z. Phys.*, **255**, 146 (1972).
5) M. Utsuro: *J. Phys.*, **C3**, 277 (1984).
6) R. Golub and J. M. Pendleberg: *Phys. Lett.*, **50A**, 177 (1974).
7) W. A. Lanford and R. Golub: *Phys. Rev. Lett.*, **39**, 1509 (1977).
8) P. H. La Marche, W. A. Lanford, and R. Golub: *Nucl. Instrum. Methods*, **189**, 533 (1981).

RIKEN Accel. Progr. Rep. 18 (1984)

III-3-8. High Sensitivity Analysis of Deuterium in Solids by ^{15}N-Induced Nuclear Reactions

S. Hayashi, H. Nagai, M. Aratani, T. Nozaki, M. Yanokura,
I. Kohno, O. Kuboi, and Y. Yatsurugi

We have already reported[1] on not only a method for measuring the depth profile of hydrogen but a new method for determining the contents of deuterium with such a high sensitivity as 10^{18} at·cm^{-3} in solids by means of ^{15}N-induced nuclear reactions. Further, we have developed and applied this new method to measure deuterium contents in various materials. Surfaces of most materials, however, are always covered with hydrogen, which is derived by adsorbing water or hydrocarbons in an atmosphere. The adsorbed hydrogen often interferes with precise measurement of hydrogen in the bulk. In order to study hydrogen in solids, the use of deuterium as an activable tracer is regarded as widely profitable. This method of high sensitivity quantitative analysis of deuterium by ^{15}N-induced nuclear reactions was discovered during the study of depth profiling of hydrogen in some materials by using the resonance nuclear reaction, ^{1}H(^{15}N, $\alpha\gamma$)^{12}C ($E\gamma$=4.44 MeV). The method of determining deuterium is based on other nuclear reactions, ^{2}H(^{15}N, pγ)^{16}N and ^{2}H(^{15}N, nγ)^{16}O. No precise cross sections of the nuclear reactions have been reported by now. They must not be resonance reactions, and therefore they can be applied not to depth profiling but to quantitative analysis of deuterium.

Incident beam of ^{15}N^{2+} ions was supplied from the RIKEN heavy-ion linac, and led to the A1 course. Experimental arrangement is almost the same as was shown in the previous report.[1] A pair of BGO ($Bi_4Ge_3O_{12}$) scintillators has been used for

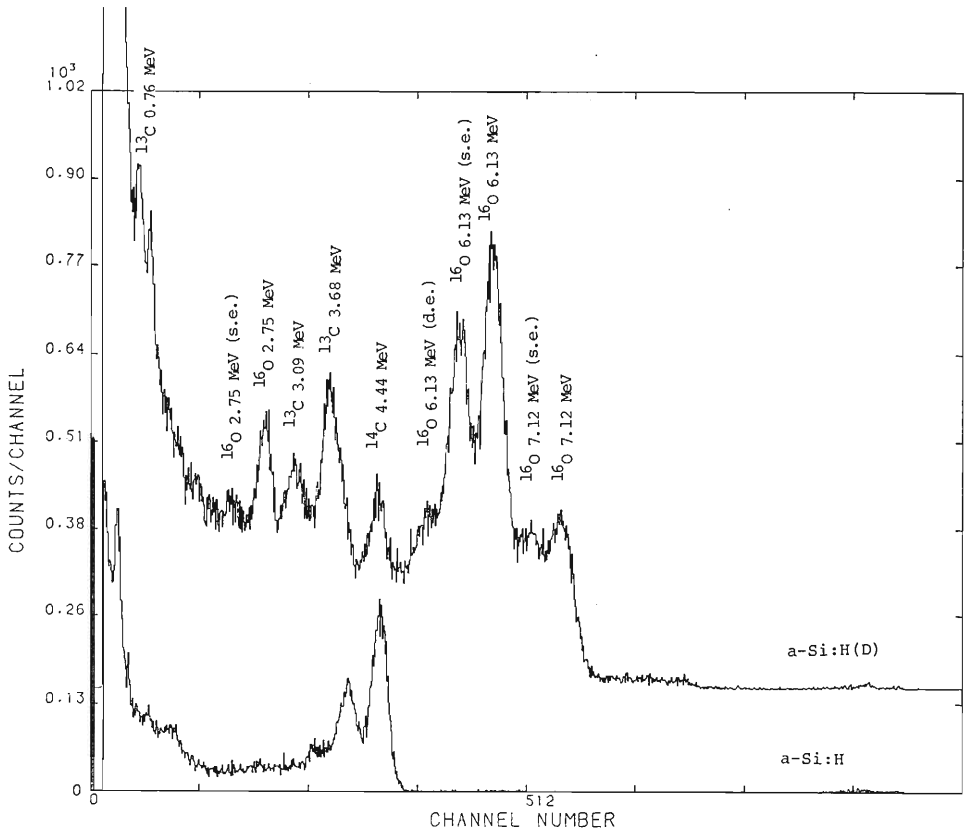

Fig. 1. Typical energy spectra for gamma-rays in amorphous silicons induced by ^{1}H(^{15}N, $\alpha\gamma$)^{12}C, ^{2}H(^{15}N, pγ)^{16}N (β^--decay, $T_{1/2}$=7.13 s), ^{2}H(^{15}N, nγ)^{16}O, and ^{2}H(^{15}N, $\alpha\gamma$)^{13}C. upper, a-Si: H(D); lower, a-Si: H, (s.e.), single escape peak; (d.e.), double escape peak.

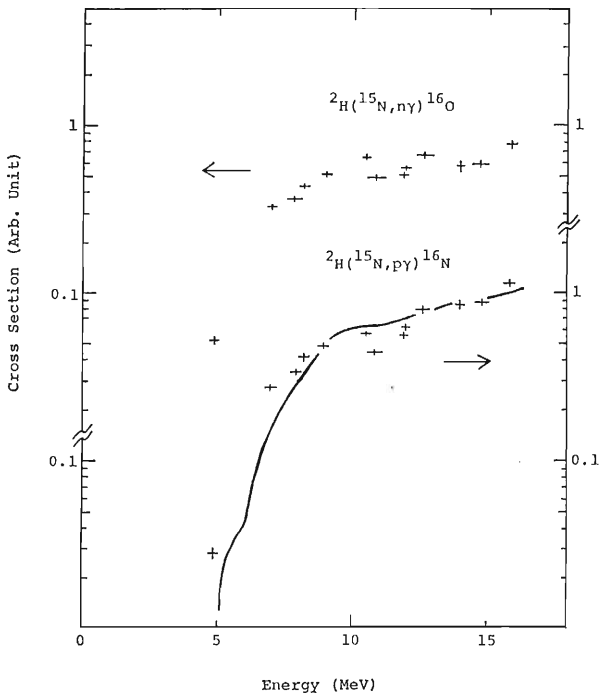

Fig. 2. Excitation functions of $^2H(^{15}N, n\gamma)^{16}O$ (upper) and $^2H(^{15}N, p\gamma)^{16}N$(lower). Solid curve was derived from the reaction of $^{15}N(d, p)^{16}N$ reported by Bostron *et al.*[2]

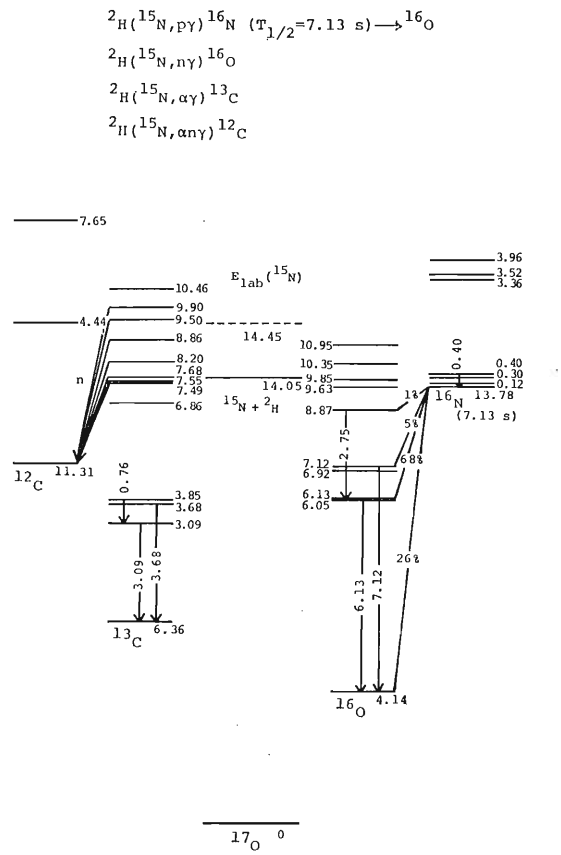

Fig. 3. Energy levels of the ^{12}C, ^{13}C, ^{16}O, and ^{16}N nuclei for reference to identify the origins of the gamma-rays emitted from four nuclear reactions: $^2H(^{15}N, p\gamma)^{16}N$, $^2H(^{15}N, n\gamma)^{16}O$, $^2H(^{15}N, \alpha\gamma)^{13}C$, and $^2H(^{15}N, \alpha n\gamma)^{12}C$.

gamma-ray detection. We have partially improved the gamma-ray detection system. The total cross sections of these two reactions have tendencies to increase with the ^{15}N energy over a wide range. However, neutrons with continuous energies are emitted by the process of $^{15}N \rightarrow {}^{14}N+n$, when the energy of ^{15}N exceeds $\sim$11 MeV. These fast neutrons, which also give scintillation in the BGO crystal, interfere seriously with gamma-ray detection. We successfully adopted an ordinary pulse-shape discrimination technique for n-γ separation. In order to monitor the incident beam, a thin carbon foil ($\sim$10 $\mu g/cm^2$) was used, and scattered particles from the foil were detected by using silicon surface barrier detector (SSD).

First, we measured the excitation functions of total cross sections for two nuclear reactions, $^2H(^{15}N, p\gamma)^{16}N$ and $^2H(^{15}N, n\gamma)^{16}O$. In the first step, we obtained the sum of the two total cross sections by measuring the intensities of high energy gamma-rays ($E\gamma$=6.13 and 7.12 MeV) emitted from the two processes in a thin target of deuterium-enriched amorphous silicon a-Si:H(D) (2,280 A). Figure 1 shows typical energy spectra of gamma-rays induced by ^{15}N ions (upper, a-Si:H(D); lower, a-Si:H). In the second step, only the cross section of $^2H(^{15}N, p\gamma)^{16}N$ reaction was evaluated by measuring the intensities of such gamma-rays using least-squares analysis of the decay curve in the multi-channel scaling measurement of ^{16}N ($T_{1/2}$=7.13s) during beam off. The excitation functions from 5 to 16 MeV are shown in Fig. 2. A solid curve overlapping our experimental data of the cross section for $^2H(^{15}N, p\gamma)^{16}N$ reaction is derived from other experimental results of $^{15}N(d, p)^{16}N$ reaction reported by Bostron *et al.*[2] for reference, in which a projectile and target were interchanged. An ordinate in Fig. 2 is a total cross section in arbitrary units. Further experiments for determining absolute values of the total cross sections are now in progress.

Secondly, we applied this method to the determination of deuterium contents in various materials. As is shown in Fig. 1, several other gamma-ray peaks are observed in addition to 4.44, 6.13, and 7.12 MeV peaks. All these peaks are shown to originate from following three nuclear reactions, $^2H(^{15}N, p\gamma)^{16}N$, $^2H(^{15}N, n\gamma)^{16}O$, and $^2H(^{15}N, \alpha\gamma)^{13}C$. To identify the origin of gamma-rays, we illustrate the energy levels of the ^{12}C, ^{13}C, ^{16}O, and ^{16}N nuclei in Fig. 3. Among these peaks, 6.13 and 7.12 MeV peaks are very suitable for quantitative analysis of deuterium, because there are no interference peaks in the energy region higher than the hydrogen-originated 4.44 MeV peak. Total amount of deuterium in various materials was determined

Table 1. Deuterium contents measured by ^{15}N-NRA and Rutherford recoil methods.

(at·cm^{-3} unit)

Sample	^{15}N-NRA	Rutherford
a-Si: H (D) (730A)	$(2.23\pm0.13)\times10^{21}$	2.16×10^{21}
a-Si: H (D) (1330A)	$(1.35\pm0.07)\times10^{21}$	1.35×10^{21}
SIPOS	$(4.97\pm0.02)\times10^{20}$	
SiN_x (in D_2O, 127°C)	$(2.17\pm0.04)\times10^{19}$	
c-Si (in D_2, 800°C)	$(7.32\pm0.22)\times10^{18}$	
c-Si (in D_2, 1100°C)	$(2.43\pm0.13)\times10^{18}$	

with reference to a standard material of deuterium-enriched amorphous silicon a-Si: H(D) (1,000 A). Deuterium contents in some kinds of materials are summarized in Table 1; in this calculation, relative cross sections of these reactions were used. Table 1 also shows experimental data for a-Si: H(D) by the Rutherford recoil method for reference.[3] We can ensure that by using the present method deuterium is analyzed down to a concentration of a few times 10^{18} at·cm^{-3}, the most sensitive one in determining deuterium in solids. Furthermore, two isotopes, ^{1}H and ^{2}H, can be measured simultaneously without mutual interference below 14.45 MeV of incident ^{15}N ions. Another reaction channel, ^{2}H(^{15}N, $\alpha n\gamma$)^{12}C, can be opened at that energy, and produced the same energy gamma-ray ($E\gamma=$ 4.44 MeV) as hydrogen originates; see Fig. 3.

References

1) S. Hayashi, H. Nagai, M. Aratani, T. Nozaki, M. Yanokura, I. Kohno, O. Kuboi, and Y. Yatsurugi: *RIKEN Accel. Progr. Rep.*, **17**, 106 (1983).
2) N. A. Bostron, E. L. Hudspeth, and I. L. Morgan: *Phys. Rev.*, **105**, 1545 (1957).
3) H. Nagai, M. Aratani, S. Hayashi, T. Nozaki, M. Yanokura, I. Kohno, O. Kuboi, and Y. Yatsurugi: *RIKEN Accel. Progr. Rep.*, **17**, 102 (1983).

RIKEN Accel. Progr. Rep. 18 (1984)

III-3-9. Thermoluminescence from the Ar-bombarded Silica

M. Aratani, T. Hashimoto, S. Hayashi, M. Yanokura,
H. Nagai, I. Kohno, and T. Nozaki

Observation has been made on the thermoluminescence from Ar-bombarded silica. Silica samples used were quartz plates and silicon oxide films (SiO_x, x=2, 0·26 μm) prepared by thermal oxidation. Bombardment was performed by using a 1 m scattering chamber installed in a course, A-1, of the Linac under the various conditions listed in Table 1. The samples were set slant by an angle of 30° to an incident beam. Si ions forward recoiled by Ar ions were used for monitoring the incident Ar-ion beam. Si ions were detected with a silicon-surface-barrier detector situated at the angle of 37° to the indident Ar beam. Detailed experimental arrangement was previously reported.[1]

The samples (9 mm × 19 mm) Ar-bombarded in the dark vacuum chamber were taken out without exposure to light, and transferred to a photon-counting thermoluminescence detector.[2] The thermoluminescence of the samples was observed by raising temperature at a rate of 1°/s. A temperature-thermoluminescence curve (glow curve) was recorded from 50° to 400°C. Some of the samples were examined in the photographic observation system using extremely high-sensitive color films.

Some results are shown in Figs. 1 to 3. In each case, the glow curve is shown with a background curve. Dominant peaks are seen in the vicinity of 200°C in Figs. 1 and 3. In every case, continuum with ten waves is observed. These glow curves have never been reported in the literatures published on the thermoluminescence from geological samples exposed to the natural-origin radiations, main part which is due to the α-particles emitted from the natural α-emitters. These glow curves are not seen in the thermoluminescence from the silicate samples bombarded with a He-ion beam, either.[3] Silica is regarded as a main component of natural samples. Thus, the peak in the vicinity of 200°C and waved

Table 1. Bombardment conditions in A-1 course of the Linac.

Sample No.	Material	Thickness	Ar (MeV)	Beam intensity (nA)	Time	Forward recoil Si	Light output
1	SiO_2	0.5 mm	50.7	50	5 min	2,004	
2	SiO_2	0.5 mm	50.7	15	1 hr	22,798	overscale
3	SiO_2	0.5 mm	50.7	1	1 hr	8,135	
4	c-Si	0.3 mm	49.6	15	1 hr	147,048	not observed
5	SiO_2	0.26 μm	49.6			8,078	
			52.2			19,041	
			52.2			3,023	

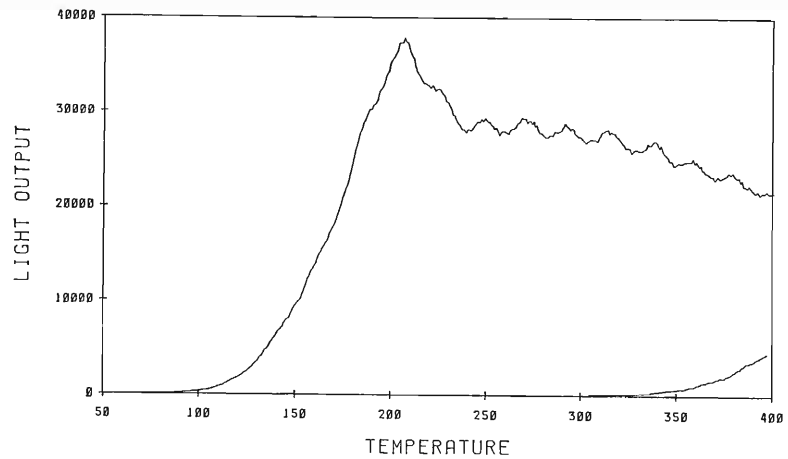

Fig. 1. Thermoluminescence of the quartz plate bombarded with Ar ion (15 nA) for 5 min.

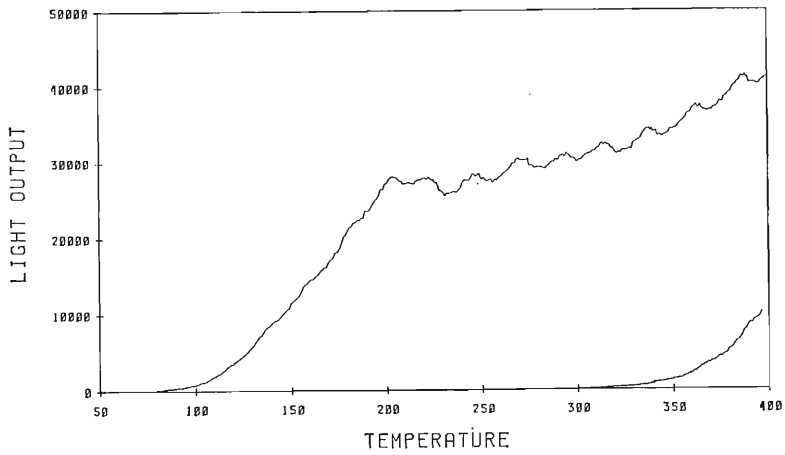

Fig. 2. Thermoluminescence of the quartz plate bombarded with Ar ion (1 nA) for 1 hr.

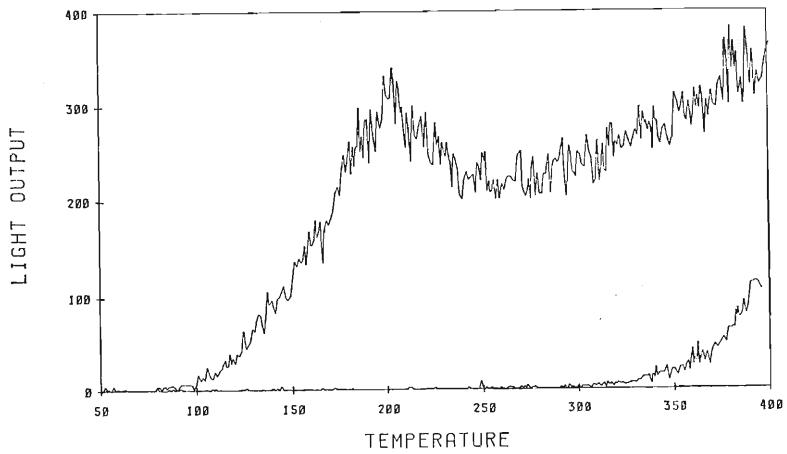

Fig. 3. Thermoluminescence of the SiO_2 film on a Si wafer bombarded with Ar ion.

continuum are regarded as characteristic of the Ar-bombarded silica. The silica samples employed in the present study were high-purity artificially prepared SiO_2, and a color image of the plate sample taken between 50°C and 400°C showed blue luminescence.

Present results suggest that the thermoluminescence study of high-purity material bombarded with heavy ions will be an unexplored field of the opto-electronic application. For example, high-purity silica and that containing controlled impurities are subjected to research aiming at heavy-ion dosimeters and standard materials, especially for geological and archaeological samples.

References

1) H. Nagai, M. Aratani, S. Hayashi, T. Nozaki, M. Yanokura, I. Kohno, O. Kuboi, and T. Yatsurugi: *RIKEN Accel. Progr. Rep*, **17**, 102 (1983).
2) T. Hashimoto, K. Kimura, A. Koyanagi, K. Takahashi, and T. Sotobayashi: *Radioisotopes*, **32**, 525 (1983).
3) J. Kalef-Ezra and Y. S. Horowitz: *Int. J. Appl. Radiat. Isot.*, **33**, 1085 (1982).

RIKEN Accel. Progr. Rep. 18 (1984)

III-3-10. Adsorption Kinetics of ^{119}Sb(V) Ions onto α-Fe_2O_3 Surfaces

S. Ambe, T. Okada, and F. Ambe

We are studying the adsorption kinetics of ^{119}Sb-(V) onto α-Fe_2O_3 surfaces[1] in relation to the study on chemical states of the adsorbed ^{119}Sb(V) ions by Mössbauer emission spectroscopy.[2)-4)] In this period, we carried out kinetic studies using an ^{119}Sb(V) solution of known Sb concentration and obtained an adsorption rate equation related not only to the antimony concentration but also to the surface area of α-Fe_2O_3.

Adsorption of hydrolyzable metal ions on the surfaces of metal oxides from aqueous solutions have been extensively studied from equilibrium measurement of the ionic adsorption density and surface charge density. However, little attention has been paid to adsorption kinetics yet, because the adsorption of metal ions usually proceeds too fast to be observed by ordinary methods and is often accompanied with simultaneous precipitation of hydroxides after neutralization of solutions. We found that the adsorption of no-carrier-added ^{119}Sb(V) ions on α-Fe_2O_3 proceeds at a rate measurable by a conventional tracer method.

When no-carrier-added ^{119}Sb (half-life: 38.0 hr) was employed as a tracer, it was separated from ^{119m}Te (half-life: 4.68 days) produced by α-particle irradiation of tin. The procedures of the separation of ^{119}Sb and the final purification of the solution using activated carbon to remove trace impurities, Sn(IV) and Te(IV), were described elsewhere.[5)] The resulting 0.25 mol dm^{-3} LiCl solution containing ^{119}Sb(V) was used for the adsorption experiments after adjusting pH to 4.0. Concentration of antimony in the solution was found to be 1.1×10^{-8} mol dm^{-3} by neutron activation analysis after preconcentration of Sb(V) on α-Fe_2O_3. Forty five mg of α-Fe_2O_3 was added to 60 cm^3 of the ^{119}Sb(V) solutions at 30, 40, 50, and 60°C. Adsorption experiments were also carried out with various amounts of α-Fe_2O_3 at 50°C. The suspension was shaken in an 8-shape mode with a shaker. An aliquot of the suspension was taken every one minute for determination of the fraction of ^{119}Sb adsorbed. After removal of α-Fe_2O_3 particles in the aliquot by filtration using a glass fiber paper, 23.8 keV γ-rays and Sn K X-rays of ^{119}Sb in each filtrate were counted with an NaI scintillation counter.

Let us suppose that the rate of the adsorption reaction

$$\underset{(a-x)}{\text{Sb (V)}}+\underset{(b-y)}{(\alpha\text{-Fe}_2\text{O}_3\text{ surface})}\xrightarrow{k}\text{product}$$

is experessed by

$$dx/dt=k(a-x)^n(b-y)^m \qquad (1)$$

where a is the initial concentration of antimony (V) ions in the solutions, and b is that of the free surface area of α-Fe_2O_3. The reverse reaction, that is, the desorption of ^{119}Sb(V) from the ^{119}Sb-α-Fe_2O_3 was found to be negligible. The surface area of α-Fe_2O_3 employed (45 mg) is considered to be in large excess for the adsorption of Sb(V) ions, because the BET surface area of 45 mg of the sample used in the present study is 1.2 m^2 and monolyer adsorption of 6.6×10^{-10} mol of Sb (Sb in 60 ml of the tracer solution) requires 5.6×10^{-5} m^2. Thus, y can be neglected against b and Eqn. (1) can be simplified as

$$dx/dt=k'(a-x)^n \qquad (2)$$

$$k'=kb^m,\ i.e.,\ \log k'=m\log b+\log k \qquad (3)$$

The free surface area b is proportional to the quantity of α-Fe_2O_3 and can be expressed in the unit of mol dm^{-3} for convenience. By analyzing the adsorption data obtained at 30, 40, 50, and 60°C according to Eqn. (2) in a differential and integral forms, the order of the reaction n was found to be 2. Figure 1 shows the results of analysis by the integration method. The relation between $1/(a-x)$ and t exhibited a good linearity, giving the apparent rate constant k' from the slope.

The value of m can be obtained from the slope of a

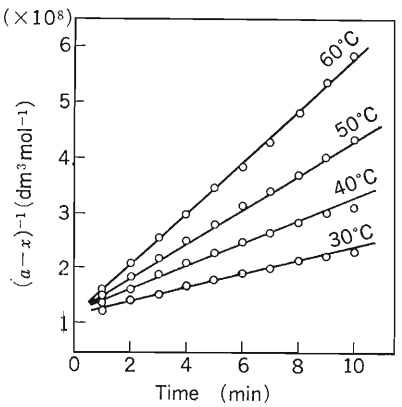

Fig. 1. Relation of $1/(a-x)$ *vs.* time.

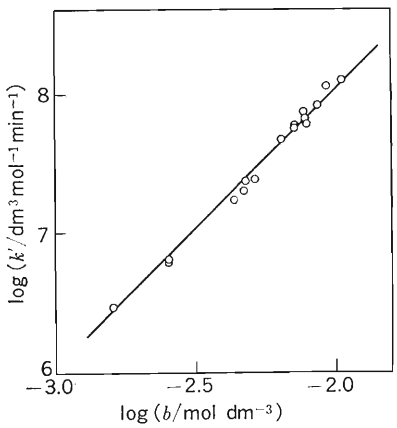

Fig. 2. Relation of log k' *vs.* log b.

log k' *vs.* log b plot and the intercept of log k' gives the rate constant k. From the rate constants k' obtained at 50°C with various quantities of α-Fe_2O_3, m was found to be 2 as shown in Fig. 2. The rate of adsorption is, therefore, expressed as:

$$dx/dt = k(a-x)^2 b^2$$

$$k = 1.1 \times 10^{12}\ \mathrm{dm^9 mol^{-3} min^{-1}}\ \text{at } 50°\mathrm{C}$$

From the finding that n is equal to 2, it is likely that two Sb(V) ions or dimers are involved in the adsorption reaction. Similar experiments on other oxides having the corundum- and spinel-type crystal structures are also being carried out.

References

1) S. Ambe, F. Ambe, and T. Okada: *RIKEN Accel. Progr. Rep.*, **15**, 114 (1981).
2) T. Okada, S. Ambe, F. Ambe, and H. Sekizawa: *J. Phys. Chem.*, **86**, 4726 (1982).
3) F. Ambe, S. Ambe, T. Okada, and H. Sekizawa: *RIKEN Accel. Progr. Rep.*, **17**, 109 (1983).
4) F. Ambe, S. Ambe, T. Okada, and H. Sekizawa: p.141 in this report.
5) S. Ambe: *J. Radioanal. Nucl. Chem., Articles*, **81**, 77 (1984).

RIKEN Accel. Progr. Rep. 18 (1984)

III-3-11. *In Situ* Emission Mössbauer Study of $^{119}Sb^{5+}$ ($\rightarrow ^{119}Sn^{4+}$) Ions at α-Fe_2O_3-Aqueous Solution Interfaces

F. Ambe, S. Ambe, T. Okada, and H. Sekizawa

We have been studying the chemical states of cyclotron-produced $^{119}Sb^{5+}$ ions adsorbed on magnetic oxide-surfaces by emission Mössbauer measurement of supertransferred hyperfine (STHF) fields on $^{119}Sn^{4+}$ nuclei arising from $^{119}Sb^{5+}$.[1] In the last report,[2] we showed that *in situ* Mössbauer observation is feasible with $^{119}Sb^{5+}$ ($\rightarrow ^{119}Sn^{4+}$) at the interfaces between oxide particles and an aqueous solution. Here, the effects of heating on the suspension of α-Fe_2O_3 particles with adsorbed $^{119}Sb^{5+}$ ions are reported. Results on a dried $CoFe_2O_4$-$^{119}Sb^{5+}$ sample are described in a separate report of this volume.[3]

The procedure of separating no-carrier-added ^{119}Sb from α-irradiated tin target was described elsewhere.[4] The experimental setup of the *in situ* Mössbauer measurement was given in Fig. 1 of Ref. 2. The α-Fe_2O_3-$^{119}Sb^{5+}$-aqueous solution system was heated in a water bath with a glass reflux

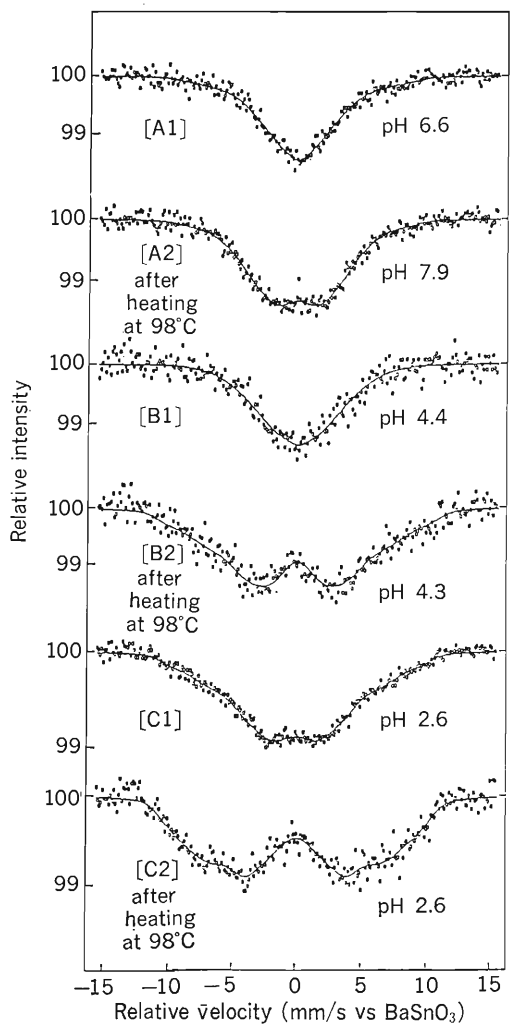

Fig. 1. Preheating effects of the sample suspensions at 98°C for 30 min upon the *in situ* emission Mössbauer spectra of ^{119}Sn arising from $^{119}Sb^{5+}$ at the α-Fe_2O_3-0.25 mol dm^{-3} LiCl solution interfaces (measurement at room temperature). The curves are composed from the results of Hesse-Rübartsch analysis given in Fig. 2.

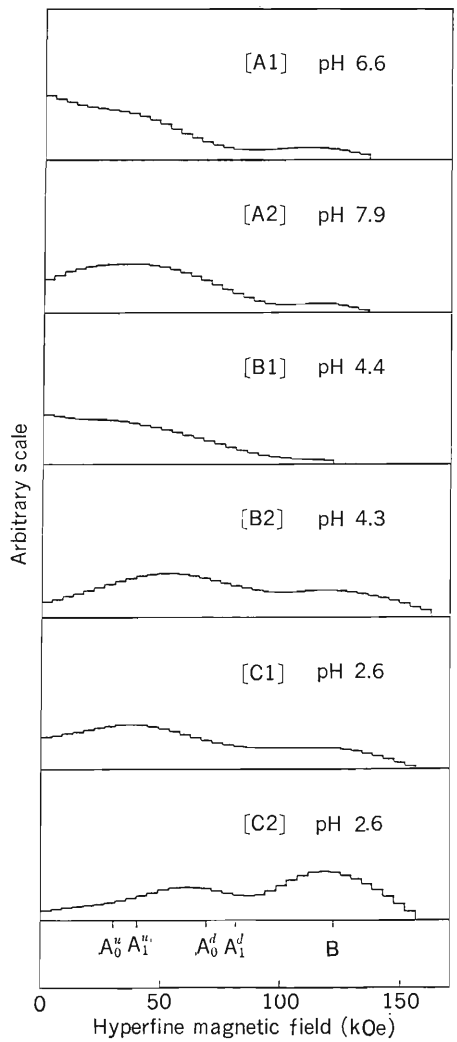

Fig. 2. Distribution of the STHF fields on $^{119}Sn^{4+}$ nuclei obtained by the Hesse-Rübartsch analysis of the spectra shown in Fig. 1.

cooler connected to the top of the Teflon sample vessel.

Figure 1 compares the Mössbauer emission spectra of the α-Fe_2O_3-$^{119}Sb^{5+}$-0.25 mol dm^{-3} LiCl solution system at three different pH before ((A1)–(C1)) or after heating at 98°C for 30 min ((A2)–(C2)). The experiment was made on the α-Fe_2O_3 sample prefired at 900°C. As in the "as obtained" α-Fe_2O_3 sample reported previously,[2] ^{119}Sn ions arising from $^{119}Sb^{5+}$ at the interfaces are exclusively of the tetravalent state and the line width of their emission increases with decrease in pH of the aqueous phase. A large change in pH was observed after heating the system of pH 6.6, since no buffer was employed in the aqueous phase. At every pH value studied, the emission spectra show considerable broadening or even immature splitting to a sextet after heating. The observation suggests incorporation of more $^{119}Sb^{5+}$ ions by heating into the surface metal-ion sites having significant STHF interaction with the antiferromagnetically ordered $^{57}Fe^{3+}$ ions of the substrate. Further heating up to 100 min brought about no further appreciable change in the spectra.

The STHF field distributions obtained by the Hesse-Rübartsch analysis[5] of the spectra in Fig. 1 are given in Fig. 2. At the bottom of Fig. 2 is shown the STHF magnetic field on $^{119}Sn^{4+}$ nuclei in the bulk of α-Fe_2O_3 at room temperature (122 kOe)[6] as well as the fields for $^{119}Sn^{4+}$ at the surface metal sites, A^u_0, A^d_0, A^u_1, and A^d_1 (see Fig. 10 of Ref. 1), calculated on the assumption that the STHF field is proportional to the algebraic sum of the reduced magnetization of the Fe^{3+} ions interacting with them. The values of the reduced magnetization for surface Fe^{3+} ions of α-Fe_2O_3 were taken from our previous work.[7]

As can be seen from Fig. 2, a considerable amount of $^{119}Sb^{5+}$ ions are present in the bulk (the second and deeper layers) after heating at pH 4.3 (B2) and 2.6 (C2). In the dried α-Fe_2O_3-$^{119}Sb^{5+}$ sample reported previously, no appreciable diffusion of the surface $^{119}Sb^{5+}$ ions into the second or deeper layers was observed on heating the sample at 200°C for 2 hr (Fig. 3 of Ref. 1). Therefore, the change of the field distribution observed in the present *in situ* experiment is not likely due to diffusion of surface $^{119}Sb^{5+}$ ions into the second or deeper layers. Moreover, the finding that the change saturates on 30 min heating suggests a different mechanism. We consider that a certain chemical rearrangement of the surfaces occurs when the α-Fe_2O_3 particles are in contact with the aqueous phase at 98°C. Namely, some Fe^{3+} ions are released from the surfaces of α-Fe_2O_3 particles and are again attached to them so as to incorporate a part of the $^{119}Sb^{5+}$ ions into the second or deeper layers. Since the change does not proceed further after 30 min, it is concluded that the rearrangement is limited only to a few layers of the surfaces and the $^{119}Sb^{5+}$ ions are distributed among them.

References

1) T. Okada, S. Ambe, F. Ambe, and H. Sekizawa: *J. Phys. Chem.*, **86**, 4726 (1982).
2) F. Ambe, S. Ambe, T. Okada, and H. Sekizawa: *RIKEN Accel. Progr. Rep.*, **17**, 109 (1983).
3) T. Okada, F. Ambe, S. Ambe, and H. Sekizawa: p. 90 in this report.
4) S. Ambe: *J. Radioanal. Nucl. Chem., Articles*, **81**, 77 (1984).
5) J. Hesse and A. Rübartsch: *J. Phys. E*, **7**, 526 (1974).
6) Unpublished data.
7) F. Ambe, T. Okada, S. Ambe, and H. Sekizawa: *J. Phys. Chem.*, **88**, 3015 (1984).

RIKEN Accel. Progr. Rep. **18** (1984)

III-3-12. Correlation between Angular Anisotropy of Fission Fragment and Its Mass in System of p+^{232}Th

Y. Hamajima,* K. Sueki, M. Magara,** H. Nakahara, and I. Kohno

Möller and Nilsson[1] suggested that there might be two kinds of saddle configurations, one with reflection symmetry with respect to the axis perpendicular to the nuclear symmetry axis and the other with reflection asymmetry, and that the fission barrier height for the symmetric saddle would be a few MeV higher than the one for the asymmetric saddle. They also suggested that the final mass division mode could be related closely to these two kinds of saddle point configurations. It there truly exist two kinds of saddles and if they control the final mass division mode, fragment mass dependence of angular anisotropies should be observable in a fission system where an appreciable difference in anisotropies is expected from Bohr's channel theory[2] for the fragments that have passed through different kinds of saddles. In 1982, Kudo *et al.*[3] reported for the 15 MeV p+^{232}Th system that correlation between the angular anisotropy and the fragment mass could well be reproduced on the above assumption.

In the present study energy dependence of the correlation between the angular distribution of fission fragments and its mass is examined further with the system of 13 and 15 MeV p+^{232}Th.

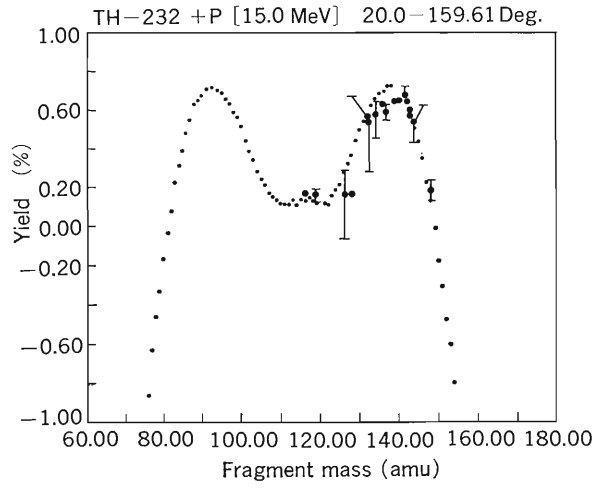

Fig. 1. Mass-yield curve of the proton induced fission of ^{232}Th. Small dots for 15 MeV p (this work) and closed circles for 14.8 MeV p (Kudo *et al.*).

* Faculty of Science, Kanazawa University.
** Faculty of Science, Tokyo Metropolitan University.

The Th target (about 0.1 mg/cm^2 in thickness) prepared by vacuume evaporation onto a carbon film was bombarded with 13 MeV and 15 MeV proton beams from the cyclotron. The coincident complementary fragments were detected with two surface barrier detectors. Details of experimental setup and the analysis have been given previously.[4]

The mass yield curve (small dots) observed for the 15 MeV p+^{232}Th system at 20° is compared with that for the 14.8 MeV p+^{232}Th system reported by Kudo *et al.*[5] (closed circles) in Fig. 1. The curve obtained in the present study is in good agreement with the result by Kudo *et al.* who used a radiochemical technique. Mass dependent angular anisotropies ($W(0°)/W(90°)$) for the 13 MeV (open circles) and 15 MeV (closed circles) p+^{232}Th system are shown in Fig. 2. In the 15 MeV p+^{232}Th system the angular anisotropies of symmetrically divided fission fragments were found different from those of asymmetrically divided ones. Theroretically predicted angular anisotropies in the 15 MeV p+^{232}Th are 1.06 for symmetric fission and 1.3 for asymmetric one. They have been calculated from the expression given by Vandenbosch and Huizenga[6] by taking into account the contribution of multiple change fissions predicted from the statistical model that assumes the existence of two different saddle points. Experimental data are in good agreement with theoretical values.

For the 13 MeV p+^{232}Th system, theoretically

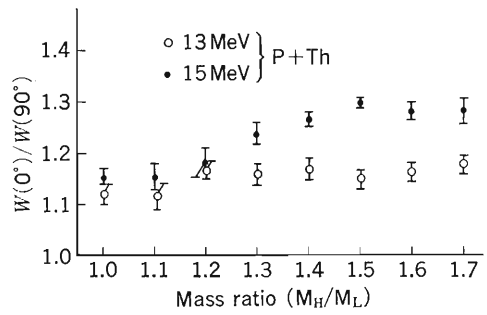

Fig. 2. Mass dependent angular anisotropies for the 13 MeV (open circles) and 15 MeV (closed circles) p+^{232}Th systems. Theoretically predicted angular anisotropies for symmetric fission are 1.06 for both 13 and 15 MeV and those for asymmetric fission are 1.06 and 1.30 for 13 and 15 MeV, respectively.

predicted anisotropies are 1.06 for both symmetric and asymmetric fission. Although the anisotropies of this study are somewhat higher than the theoretical ones, they are consistent with the theory which predicts that the anisotropy for symmetric products would not be much different from that for asymmetric ones.

The agreement between the theoretical prediction and the observed anisotropies suggests that there are two kinds of saddle points with different barrier heights and that the final mode of mass division is determined essentially at the saddle points in the process of nuclear deformation toward fission.

References

1) P. Möller and S. G. Nilsson: *Phys. Lett. B*, **31**, 283 (1970).
2) A. Bohr: Proc. 1st UN Conf. on the Peaceful Uses of Atomic Energy (II), 911 and 151 (1955).
3) H. Kudo, Y. Nagame, H. Nakahara, K. Miyano, and I. Kohno: *Phys. Rev. C*, **25**, 909 (1982).
4) Y. Hamajima, K. Sueki, H. Nakahara, and I. Kohno: *RIKEN Accel. Prog. Rep.*, **17**, 29 (1983).
5) H. Kudo, H. Muramatsu, H. Nakahara, K. Miyano, and I. Kohno: *Phys. Rev. C*, **25**, 3011 (1982).
6) R. Vandenbosch and J. R. Huizenga: "Nuclear Fission," Academic, New York (1973).

RIKEN Accel. Progr. Rep. 18 (1984)

III-4. Radiation Chemistry and Radiation Biology

1. Electron Scavenger Effects on the Fluorescence Induced by Single High-LET Particle

Y. Ito,* Y. Aoki,* T. Azuma,* Y. Katsumura,* Y. Tabata,* and K. Kimura

The present study on fluorescence induced by high-LET ions is an extension of our previous comparative studies for electron scavenger effects on positronium formation, muonium formation, and γ-induced fluorescence. A single-particle hitting and single-photon counting technique, whose block diagram is shown in Fig. 1, was used for measurement of fast fluorescence decay. The 24 MeV α-particles, after passing through a thin film of plastic scintillator and a thin window of titanium, was stopped in the cell which contained a solution of cyclohexane with both scintillator (PPO: 2, 5-diphenyloxazole) and electron scavenger. Two photomultipliers (PM, HTV 1828–01) were provided: PM 1 gave a start pulse by counting a photon from the scintillator film; PM 2 attached to the window of the sample cell gave a stop pulse by counting of fluorescence of the sample. The time between the start and the stop signal was analyzed by a time-to-amplitude converter and a 1K channel pulse height analyzer.

In order to satisfy the conditions of a single-particle hitting radiolysis, the current of α-particles was extremely reduced so that the rate of the start pulse was less than 10^{-3} times of the cycrotron RF-frequency (7 MHz). This may be supported by the observed excellent time resolution, ca. 1.5 ns at FWHM, which was estimated from the rise time of the fluorescence time profile. This resolution time may, however, be shortened somewhat, probably by improvement of such as efficient photon collection by PM 1, since that for γ-induced fluorescence obtained using by the same electronic circuits was 1.0 ns.

A sample solution containing PPO as a scintillator (10 mM) and C_2H_5Br as electron scavenger (10^{-4} to 1 mM), was bubbled with He gas and pumped into the cell by using a continuous flow-system. Benzene was also used as the solvent for comparison.

Figure 2 compares the time profiles of the γ- and α-induced fluorescence in 10 mM PPO solutions in cyclohexane and benzene. The fast components of the lifetimes of excited PPO* on both irradiations were estimated from Fig. 2 (a) and 2 (b) by using a convolution technique. The obtained lifetime for γ-irradiation was close to an intrinsic one of excited PPO* (1.6 ns), while the lifetime for α-irradiation was much shorter, 1.2 ns. For the fluorescence in benzene, on the other hand, the lifetime of the fast component was not much different between γ- and α-irradiation.

The fluorescence intensity was more intense in benzene than in cyclohexane: the intensity ratio,

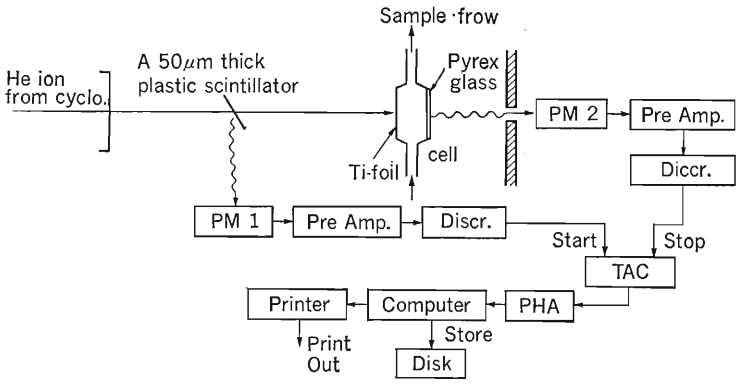

Fig. 1. Block diagram for fluorescence measurement using the single-particle and single-photon counting technique.

* Faculty of Engineering, The University of Tokyo.

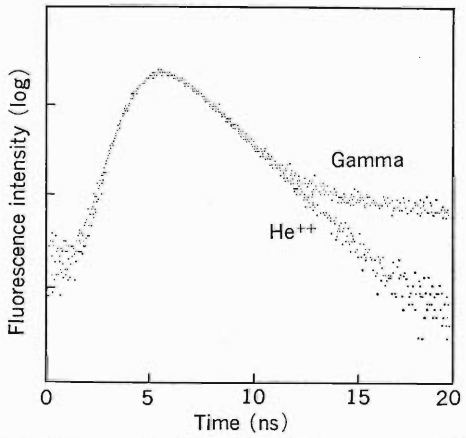

Fig. 2 (a) Time resolved profile of fluorescence of PPO in C-hexane.

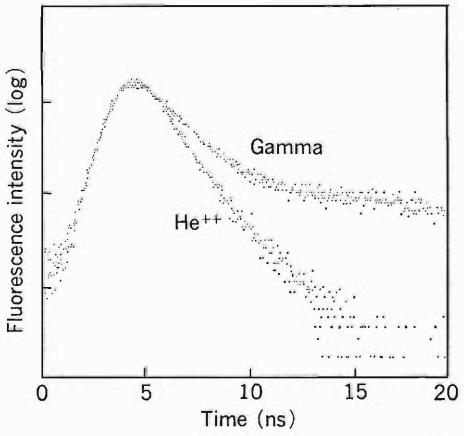

Fig. 2 (b) Time resolved profile of fluorescence of PPO in benzene.

I_F(10 mM PPO in benzene)/I_F(10 mM PPO in cyclohexane), was 30 for α-irradiation in contrast to the ratio of 2 for γ-irradiation.

The effect of the electron scavenger, C_2H_5Br, on the intensity of the α-induced fluorescence was measured and compared with the results of γ-induced fluorescence. As in γ-induced fluorescence,[1] C_2H_5Br did not influence the lifetime of the emission but simply reduced the intensity. A plot of fluorescence intensity vs. scavenger concentration is shown in Fig. 3. In the case of the γ-induced fluorescence in cyclohexane solution, the effect of C_2H_5Br can be explained in terms of competition in electron

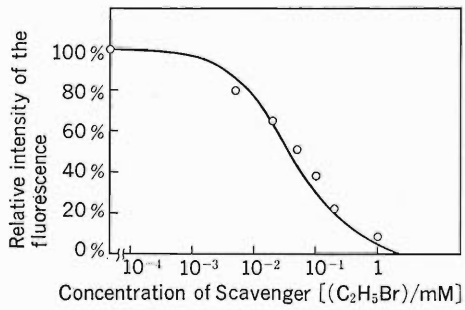

Fig. 3. Relative intensity of fluorescence as a function of scavenger (C_2H_5Br) concentration.
——, γ-irradiation; ○, α-irradiation.

scavenging reactions between PPO and C_2H_5Br. A modified experimental Warman-Asmus-Schuler (WAS) equation (Eqn. (1)) was found to express the experimental results fairly well[1]:

$$\frac{I_F}{I_F^0}=\frac{\sqrt{\alpha_0 C_0}}{\sqrt{\alpha_0 C_0+\alpha C_3}}\,\frac{1+\sqrt{\alpha_0 C_0}}{1+\sqrt{\alpha_0 C_0+\alpha C}} \quad (1)$$

where I_F^0 and I_F are the fluorescence intensities in 10 mM PPO solution in cyclohexane without and with the scavenger, respectively; α_1(=15 M^{-1}) and α_2 (=7.2 M^{-1}) are the reactivity parameters of PPO and C_2H_5Br: c_1 and c_2 are their concentrations. The solid line in Fig. 3 represents the results for γ-ray induced fluorescence (or Eqn. (1)). The experimental plot for the α-induced fluorescence deviates from this line only slightly.

The WAS-type equation is believed to be related to the inhomogeneous nature of the distribution between geminate ion pairs in γ-irradiated cyclohexane. The similarity in the electron scavenger effects between γ- and α-induced fluorescence might mean that the local structure of the spur which is responsible for the formation of the excited PPO* is not much different for both γ-ray and α-particle.

Further experiments using heavy ions with much larger LET are under way.

Reference

1) Y. Ito, Y. Katsumura, T. Azuma, and Y. Tabata: *J. Phys. Chem.*, **84**, 1921 (1984).

RIKEN Accel. Progr. Rep. 18 (1984)

III-4-2. Inactivation of Bacterial Spores by a Single Heavy Ion (II)

T. Takahashi, F. Yatagai, T. Katayama, A. Yunoki,
Y. H. Kang, D. S. Kim, I. Kaneko, and S. Okada

Experiments have been carried out for a better understanding of the mechanism of inactivation of *B. subtilis* spores by heavy-ion and alpha-particle irradiation. Measurements were made on the fractions of dead spores hit by ions whose paths were within about 0.5 μm from the center of the spore. The spores were fixed with 10% aqueous polyvinyl alcohol solution on a CR-39 plastic detector and the outgrowth for each spore was photographed after irradiation.[1] The plastic detector was etched for 120–140 min in case of alpha-particle irradiation. The etching condition for heavy ions was the same as previously reported.[1] Preliminary results show that the fraction of dead spores hit by a single alpha-particle of 0.8–1.7 MeV is 20–30%, by an Ar-ion of energy ~35 MeV is about 30%, and by a Xe ion of energy 20–60 MeV is about 50%. In Fig. 1 is shown the fraction of dead spores as a function of radial distance from the track of an Ar-ion. The result obtained for Ar is in accordance qualitatively with those obtained by Facius *et al.*[2] and Schäfer *et al.*[3] who claimed "a low inactivation probability at small impact parameters." As for the "long range effect" of heavy ions,[1)–4)] our preliminary results are favorable (Fig. 1), but the number of spores tested is not sufficient to obtain a decisive conclusion. Further improvement of viability of the spores and more precise marking on the plastic detector are necessary.

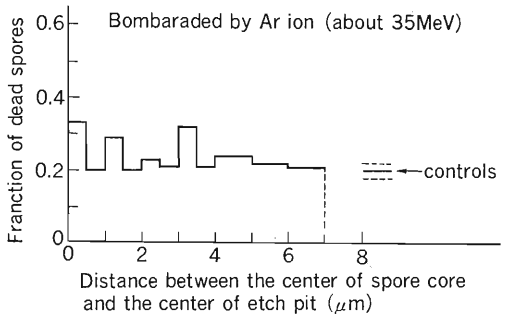

Fig. 1. Fraction of dead spores as a function of distance from the center of the spore core to the center of the etch pit.

Table 1. Relative yield of luminescence from CR-39 and cellulose nitrate (CN) as compared with BaF_2 scintillator for UV photons and Pilot U scintillator for photons of visible wave lengths.

	Visible	Ultraviolet
CR-39	10^{-3}	10^{-4}
CN	10^{-3}	10^{-4}
BaF_2		1
Pilot U	1	

A possibility of UV emission by impinging ions upon a plastic detector (CR-39 or cellulose nitrate) has been examined by using ^{210}Po alpha-source, because UV photons may inactivate spores. Figure 2 shows a device which is capable of measuring light yields, and Table 1 gives present results. Since the yields of ultraviolet light emitted from the plastic detectors by an alpha-particle are less than 10^{-4} to those from BaF_2 scintillator, the possibility of inactivation of the spores due to UV photons is ruled out.

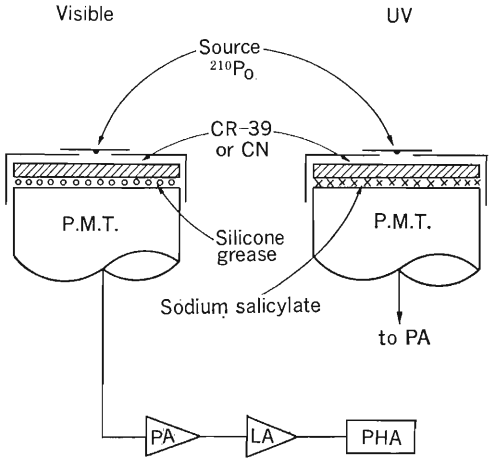

Fig. 2. A device for the measurement of light yield.

References

1) T. Takahashi, F. Yatagai, T. Katayama, Y. H. Kang, S. Tamada, I. Kaneko, and S. Okada: *RIKEN Accel. Progr. Rep.*, **17**, 116 (1983).
2) R. Facius, M. Schäfer, and H. Bücker: *Adv. Space Res.*, **3**, 85 (1983).
3) M. Schäfer, R. Facius, and H. Bücker: Proc. 8th Symp. Microdosimetry, p. 755 (1983).
4) T. Takahashi, F. Yatagai, and A. Matsuyama: *Sci. Papers I. P. C. R.*, **74**, 51 (1980).

RIKEN Accel. Progr. Rep. **18** (1984)

III-4-3. DNA Damage in Cultured Human Tumor Cells after Nitrogen-Ion Irradiation

I. Kaneko, K. Eguchi, T. Takahashi, T. Inada, and K. Nakano

Heavy-ion irradiation shows marked biological effect compared to that of γ- or X-rays. In order to elucidate the cause of this enhanced cell inactivation and characterize the effect of δ-rays on DNA lesions, induction and repair kinetics of DNA lesions after exposure to N-ions were studied in comparison to those after irradiations with 180 kVp X-rays and ^{60}Co γ-rays.

Throughout the work, we used HMV-I cultured cells derived from human melanoma. Cells were cultured in an F12 medium supplemented with 10% fetal calf serum. Cells in the exponential phase of growth were irradiated with 95 MeV N-ions ($LET_D \times 932$ keV/μm) as described previously.[1] Two weeks after irradiation, the number of colonies containing more than 50 cells was counted. This cell line is characterized by a large shoulder on its dose-survival curves after X-ray or γ-ray irradiation as shown in Fig. 1; however, the survival curve after N-ion irradiation shows small or no shoulder. A value of the relative biological effectiveness (RBE) for N-ions to 180 kVp X-rays at 1% survival was 1.9.

For detection of DNA damage, we used the alkaline elution technique developed by Kohn and his co-workers.[2] This technique is sensitive enough to detect DNA damage induced by radiation at the doses as small as those used for cancer therapy. Irradiated cells were lysed on the membrane filter with 10 ml of Sarkosyl solution consisting of 0.2% sodium lauroylasarcosine (Sarkosyl), 2 M-NaCl and 0.02 M-EDTA (pH 10.1), and then eluted with an alkaline solution (pH 12.1). The DNA fraction remaining on the filter after the elution (FR) was calculated by subtracting the amount of DNA in eluted fraction from total DNA initially poured onto the filter measured microfluorometrically. A dose-response curve for the production of DNA lesions by X-rays, γ-rays, and N-ions is shown in Fig. 2. The FR which was assayed immediately after X-irradiation decreased exponentially with dose up to 9 Gy. The decrease in log (FR) reflects an increase in the number of DNA lesions such as single strand breaks and alkali-labile sites. Therefore, Fig. 2 shows that the amount of initial DNA lesions, assayed immediately after X-irradiation, increased

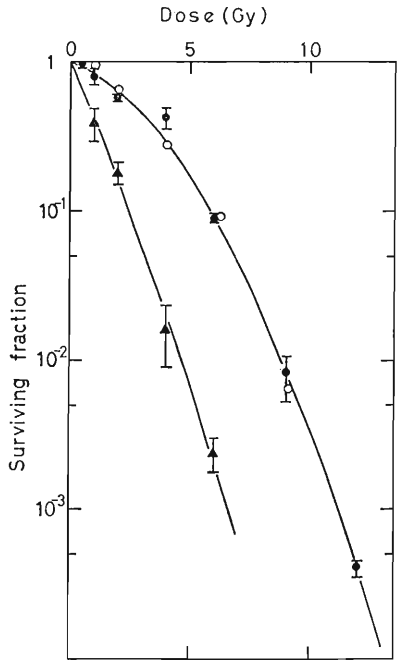

Fig. 1. Survival curves of HMV-I cells after irradiation with N-ions, ^{60}Co γ-rays, and X-rays.
The symbols and error bars represent the means of 3 or 4 samples and standard errors. The curves were drawn by least-square fitting. ●, X-rays; ○, ^{60}Co γ-rays; ▲, N-ions.

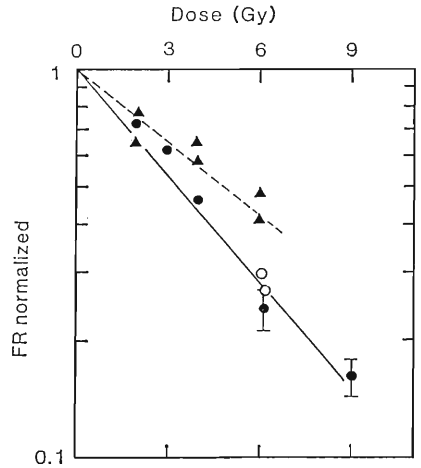

Fig. 2. Initials DNA lesions in HMV-I cells after irradiation with N-ions, ^{60}Co γ-rays, and X-rays.
Vertical bars represent standard errors for means of 3 or 8 experiments. FR was the fraction of DNA remaining on filter after elution. Meanings of the symbols are the same as those in Fig. 1.

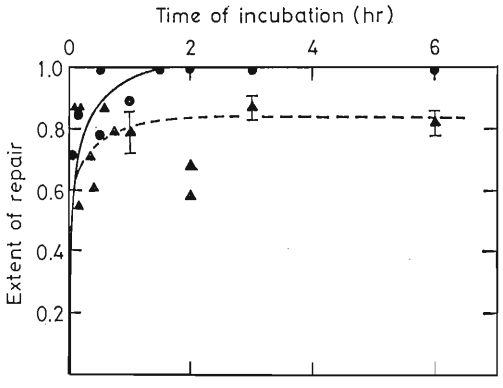

Fig. 3. Repair kinetics of DNA lesions induced by N-ions (6 Gy) and X-rays (6 Gy).
The symbols and vertical bars represent the mean of 3 to 5 experiments and standard errors, respectively. Symbols without error bars are a single experiment. ●, X-rays; ▲, N-ions.

with the dose. The amount of DNA lesions produced by γ-rays was almost the same level as that by X-rays. The initial DNA lesions induced by N-ions also increased with dose up to 6 Gy. The yield of DNA lesions per unit dose was lower for N-ions than that for X-rays and γ-rays, and the RBE for production of DNA lesions was less than unity (about 0.7). This observation at these low doses is in agreement with the results of other investigators.[3,4] Figure 3 shows the repair kinetics of DNA lesions induced by 6 Gy of X-rays or 5 Gy of N-ions. Extents of repair were calculated by

$$\log (FR_{ro}/FR_{rt})/\log (FR_{ro}/FR_{c}),$$

where subscripts *ro*, *rt*, and *c* stand for FR's for cells just irradiated, for cells irradiated and then incubated at 37°C, and for control cells, respectively. It was shown that the repair kinetics for N-ions is similar to that for X-rays in an early incubation period, but residual DNA lesions remained at a higher level after a 6 hr incubation for N-ions than for X-rays.

These results suggest that N-ions induce at least 2 types of DNA lesions, repairable and non-repairable; these are presumably caused by low and high LET components, respectively. It is known that the energy deposition of N-ions includes a high LET component in the track core, and the low LET component by δ-ray penumbra along the track. Takahashi *et al.* have concluded that δ-rays cause essentially the same effect as that of γ-rays.[5] On the other hand, the lesions induced by the high LET component have been considered to be non-repairable.[5,6] The DNA lesions caused by the low LET component appear to be rapidly repaired within about 1 hr after irradiation, similar to those caused by X-rays. We calculate that about 85% of DNA strand breaks induced by N-ions was easily rejoined (see Fig. 3). The small RBE value of the DNA lesion production may be explained in terms that when cells are irradiated with N-ions DNA strand breaks are mainly produced by δ-rays and fraction of δ-rays in absorbed dose is about 50% or less.[5] On the other hand, the high RBE value of N-ions for cell inactivation must be due to higher yield of non-repairable DNA lesions than those by X- or γ-rays.

References

1) I. Kaneko, T. Ohno, K. Nakano, and F. Yatagai: *IPCR Cyclotron Progr. Rep.*, **14**, 102 (1980).
2) K. W. Kohn, L. C. Erickson, R. A. G. Ewig, and C. A. Friedman: *Biochemistry*, **15**, 4629 (1976).
3) M. A. Ritter, J. E. Cleaver, and C. A. Tobias: *Nature*, **266**, 653 (1977).
4) R. Roots, T. C. Yang, L. Craise, E. A. Blakely, and C. A. Tobias: *Radiat. Res.*, **78**, 38 (1979).
5) T. Takahashi, F. Yatagai, and S. Kitayama: *Adv. Space Res.*, **3**, 95 (1983).
6) A. C. Nelson and C. A. Tobias: *ibid.*, p. 195.

RIKEN Accel. Progr. Rep. 18 (1984)

III-4-4. New Broad Emission Bands from Pressurized Liquid He Impinged by N Ions

K. Kimura, K. Akasu, T. Kuriyama, T. Azuma, and Y. Aoki

At first, the scintillation response of low-temperature, high-density helium gas to N-ion impingement is summarized, based on detailed analysis of the dependence of scintillation efficiency, dL/dE, specific scintillation, dL/dX, and their decay curves on the stopping power along the path of N ions.[1] Dense helium gas impinged by ions at 5.2 K and 420 Torr (average interatomic distance is about 10 Å) gives emission bands most of which are assignable to excimer emissions. An unknown triplet centered at 4,585 Å, the decay of which consists of a fast (an apparent lifetime, 32 ns) and a slow (aftergrow) components, was found and explained as due to an excimer dimer associated with vibrational sidebands which consist of the lowest triplet excimer a^3 and some of long-lived excimers. In addition, helium presented good scintillation response to low-energy ions, that is, the yield of excited states increases rapidly with increasing stopping power, dE/dX, toward its maximum value, 12 MeV mg^{-1} cm^2 as shown in Fig. 1. This shows not only little quenching of excited states of helium (atoms, excimers, and excimer dimers) produced densely in the "primary column" of the ions, but also suggests an enhanced yield of excited states at dE/dX larger than 6 MeV mg^{-1} cm^2. Such scintillation response cannot be observed in usual scintillators (See Fig. 1) and is contrary to what the scintillation theory predicts.[2]

N-ion impinged liquid helium at 3.9 K shows emission bands quite different from those obtained by electron irradiation except for several emission peaks. Broad bands at 5,600, 5,220, 4,980, 4,790, and 4,490 Å are new bands which have not been reported for electron irradiation (Fig. 2). Of this spectrum, the bands at 7,280, 7,050, 6,570, and 6,390 Å can be ascribed to excimer emissions due to the transition, $H^1 \rightarrow C^1$, $J^1 \rightarrow C^1$, $D^1 \rightarrow B^1$, and $d^3 \rightarrow b^3$, respectively, although they are broadened compared with those obtained in gas phase (see Fig. 2). The new broad bands are evidently due neither to superposition nor to broadening of many sharp emission peaks ovserved in gas phase, since there are no gas-phase emission peaks within the wavelength region covering the broad bands, especially for those centered at 5,600 and 5,220 Å, as shown in Fig. 2. These new broad bands decreased in their intensities with decreasing pressure: the intensity of the 5,600 Å band decreased to 1/20 with decreasing pressure from 5 to 1 atm. By contrast, the excimer emissions as those observed in gas phase increase in their intensities by decreasing pressure: the intensity for the $d^3 \rightarrow b^3$ transition increased to 100 times by decreasing pressure from 5 to 1 atm. Also, many of the known excimer emissions which cannot be observed in pressurized liquid helium became distinct with decreasing pressure to less than about 1 atm as shown in Fig. 2.

The new broad emission bands are most likely due to cluster states of helium excimers, since the bands appeared only under the conditions of high-density excitation, condensed phase, and impingement of ions of large stopping-power. The broadness of the bands may be caused by loose binding

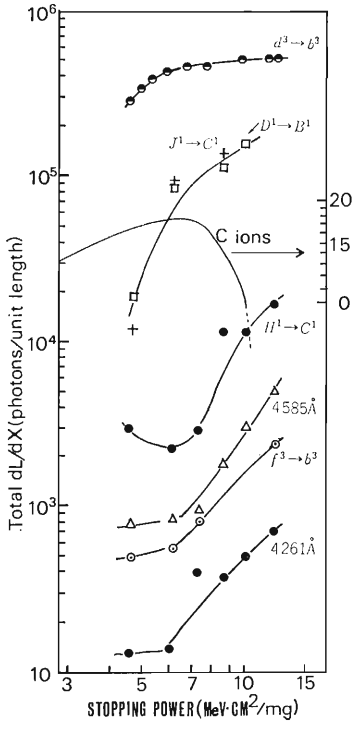

Fig. 1. Total specific scintillation, dL/dX vs. dE/dX for several excimers produced in helium gas impinged by 4 MeV/amu N ions at 5.2 K and 420 Torr. Notations of excimers were according to Herzberg's. A curve denoted as C ions is data with a plastic scintillator obtained by Becchetti *et al.*: *Nucl. Instrum. Methods*, **138**, 93 (1976).

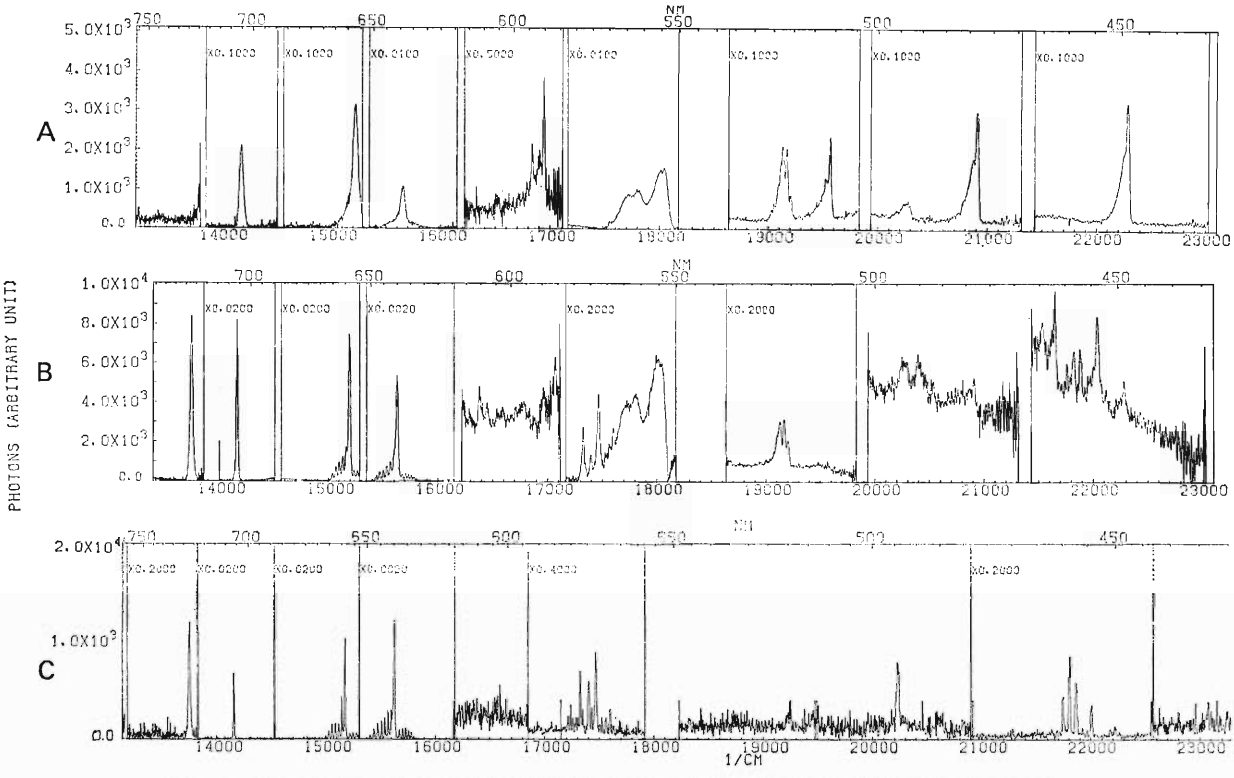

Fig. 2. Emission spectra of pressurized liquid helium impinged by 5 MeV/amu N ions. A, spectrum at 5 atm and 3.9 K; B, at 1 atm and 3.9 K; C, gas-phase spectrum at 5.2 K and 420 Torr. Real spectral intensities are obtained by dividing those read from the spectrum by scale factors, if they are given in the upper area of each band.

of excimers which undergo frequent exchange reactions with neighbor excimers in bulks. Lifetimes of the 5,600 and 5,220 Å bands were found to be so long that no decay was observed within a pulse interval of N ions (129 ns). These results clearly indicate that the long-lived metastable a^3 (1 ms) is a constitutent of the cluster.

The pressure dependense is considered to be correlated with the density of excimers produced. Liquid helium is known to present large pressure dependence of density: the density at 4.0 K increases from 0.129 to 0.142 g cm^3 with increasing pressure from 1 to 5 atm. The fact that emission intensities of these new bands level off at 2 atm for α impingement seems to support the above explanation for the pressure dependence.

References

1) K. Kimura, Y. Toda, and M. Imamura: Proc. 7th Int. Congr. Radiat. Res., (1983), Al-28; K. Kimura, T. Kato, N. Yamazaki, S. Kubota, and M. Imamura: *RIKEN Accel. Progr. Rep.*, **17**, 113 (1983).
2) R. Voltz, J. Lopes da Silva, G. Laustriat, and A. Coche: *J. Chem. Phys.*, **45**, 3306 (1966); S. P. Ahlen: *Rev. Mcd. Phys.*, **52**, 121 (1980); F. D. Becchetti, C. E. Thorn, and M. J. Levine: *Nucl. Instrum. Methods*, **138**, 93 (1976).

RIKEN Accel. Progr. Rep. **18** (1984)

III-5. Instrumentation

1. RIKEN BGOACS System

M. Fukuda, Y. Gono, Y. Ishikawa, M. Sugawara, T. Inamura, M. Ishihara, T. Nomura, I. Kohno, H. Kamitsubo, J. Kasagi, and T. Murakami

Today, a Ge-detector is most widely used in nuclear spectroscopy for its excellent energy resolution. But its relatively small peak-to-total ratio is unfavourable to detect weak γ-rays when there is a large background. The improvement of this ratio can be achieved by using the Anti-Compton Shield (ACS).

Six sets of ACS system which uses BGO ($Bi_4Ge_3O_{12}$; Bismuth Germanate) crystals are now under construction. The advantages to use BGO instead of NaI(Tl) are as follows: (1) A high absorption coefficient ($\sim$2.5 times of that of NaI(Tl)) which reduces the volume of ACS, (2) Manageability owing to its non-hygroscopic property.

The cross-sectional view of RIKEN BGOACS is shown in Fig. 1. This system consists of 13 segments of BGO crystals (six thin trapezoidal- (T-type), six long trapezoidal- (L-type) and one hexagonal-type (H-type)) and seven photomultiplier tubes (PMT's). Six pairs of T- and L-type crystals and one H-type crystal are connected to the PMT's independently by light guides so that this system can accept high counting rates.

Performance of the system was tested with γ-rays from a ^{60}Co source. Figure 2(A) shows γ-ray spectra taken with and without Compton suppression. The suppression factor, the ratio between the counts in the unsuppressed and suppressed spectra, is given in Fig. 2 (B) as a function of energy. The average suppression factor below 1,130 keV is about 4. Broad unsuppressed peak at the Compton edge in the suppressed spectrum is due to the entrance hole of the ACS through which the back scattered γ-rays can escape. The effectiveness of T-type crystals could be proved comparing the width of these peaks in the suppressed spectra taken with and without them.

These results were well reproduced by the Monte-Carlo calculation as shown in Fig. 3 (A), (B). The size of the Ge detector and the solid angle considered in this calculation are the same as those of the test measurement mentioned above. The assumed materials between the Ge detector and BGO crystals are as follows: (1) 4 mm radius Ge P-type core, (2) 0.7 mm Ge dead layer, (3) 3 mm Al

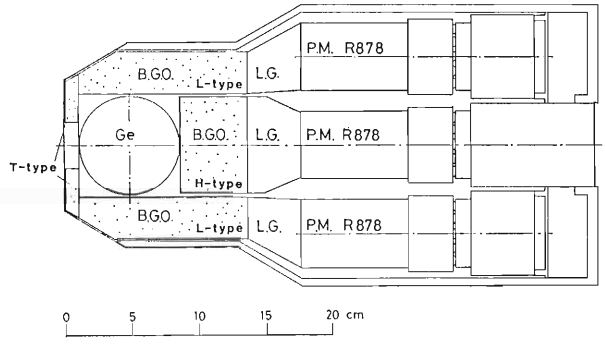

Fig. 1. Crosssectional view of BGOACS. The system consists of three types of crystals, thin trapezoidal-(T-type), long trapezoidal-(L-type) and hexagonal-type (H-type).

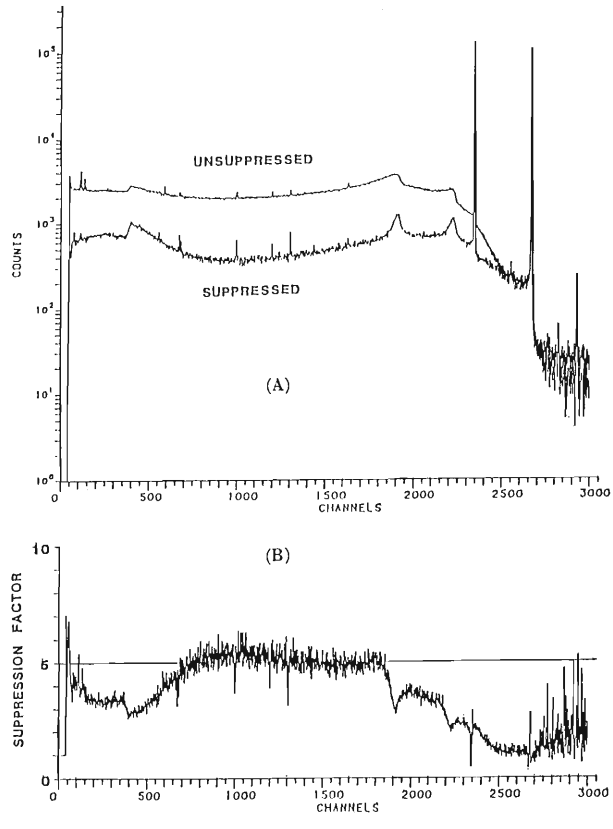

Fig. 2. Measured γ-ray spectra of ^{60}Co with and without Compton suppression.

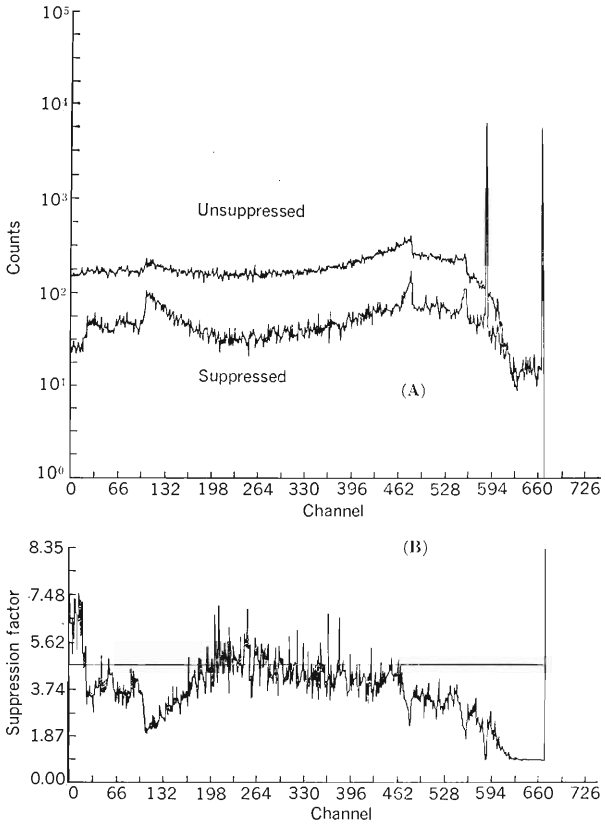

Fig. 3. Calculated spectra as same as those of Fig. 2.

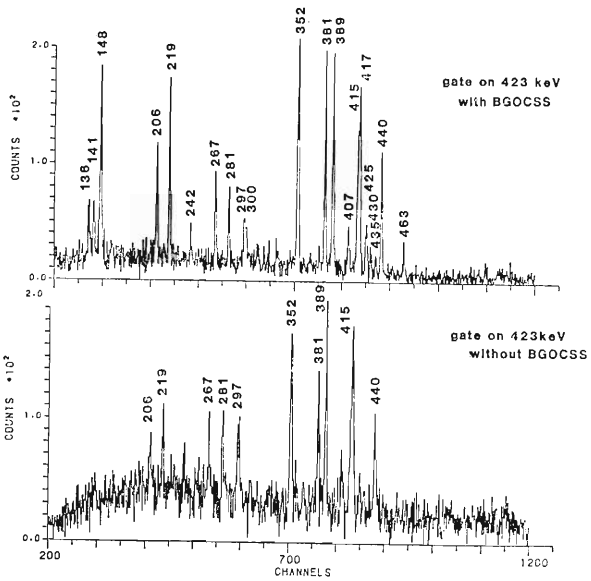

Fig. 4. Gamma-ray coincidence spectra of ^{218}Ra gated on the 423 keV γ-ray taken with (upper) and without (below) BGOACS.

housing and (4) 0.5 mm $BaSO_4$ reflector. The calculations were carried out with various thicknesses of these materials, which produce the bump of the back scattering, affect the suppression factor significantly. According to the calculation, this factor could be improved to be about seven without the P-type core, dead layer, alminum housing and

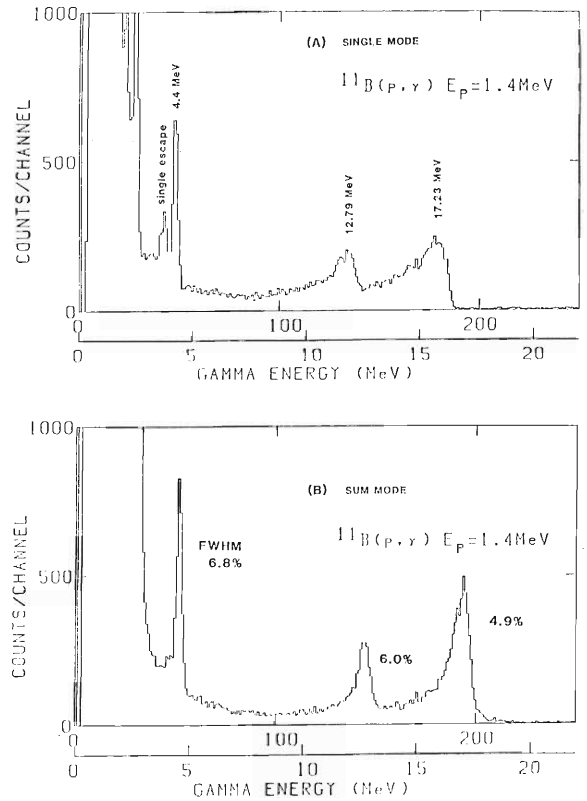

Fig. 5. The spectra of high energy γ-rays from the reaction ^{11}B(p, γ)^{12}C, A, taken by the center BGO; B, taken by summing the signals from all the BGO.

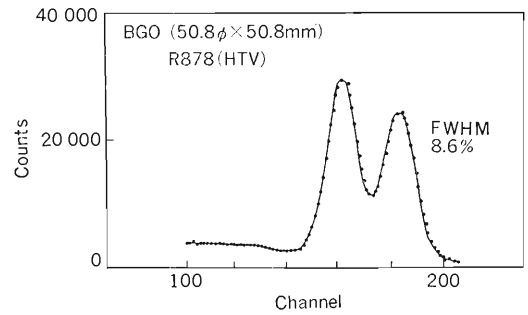

Fig. 6. Gamma-ray spectrum of ^{60}Co taken by the center BGO.

$BaSO_4$ reflector.

Four sets of BGOACS were used for the γ-γ coincidence experiment with the ^{208}Pb(^{13}C, 3n)-^{218}Ra reaction at E=75 MeV. A background was reduced by factors of two and four for the singles and coincidence spectra, respectively. Four million coincidence events were collected in 60 hours. This result is compared in Fig. 4 with that obtained from 64 million events run with two Ge(Li) detectors without BGOACS.

The BGO shield can also be used to detect high enegy γ-rays by replacing the Ge detector by a BGO crystal. This set-up is useful because (1) a better resolution is easily obtained by using a small crystal and (2) the smaller size of this system com-

paring with a similar set-up of other kind of scintillators having the same efficiency reduces a background such as cosmic rays. The system was tested by using the $^{11}B(p, \gamma)^{12}C$ reaction. Proton beams of 1.4 MeV were derivered from a Van de Graaff accelerator of Tokyo Institute of Technology. The energy spectra are shown in Fig. 5. Spectrum A was taken by using only the center detector ($2''\phi \times 2''$ BGO). Spectrum B was taken by summing the signals from all BGO crystals. The energy resolutions of 6 and 5% were obtained for 12.79 and 17.23 MeV γ-rays, respectively. The characteristics of the center BGO may be seen in Fig. 6.

RIKEN Accel. Progr. Rep. 18 (1984)

III-5-2. A Compound Counter System for High-Energy Gamma-Ray Detection

S. Kubono,* M. Tanaka,* M. Ishihara, K. Morita,
S. Kato,** H. Kawakami,* and C. Konno***

We have constructed a counter assembly for detection of high-energy gamma rays of several tens MeV. Figure 1 shows the configuration of the detectors composing the assembly. The central piece of NaI crystal with a hexagonal shape is dosely packed with 6 pieces of trapezoid NaI crystal. Plastic counters are placed further to cover these detectors. The non-cylindrical shapes for NaI were adopted for ease of fabrication and packing. The length of the central detector is 6″ and other dimensions of the detectors may be inferred from Fig. 1. The seven NaI crystals are lapped with stainless steel walls of 0.5 mm in thickness. Light signals from each crystal are collected through a light guide onto a separate photomultiplier.

Gamma rays are incident on the central detector through a Pb collimator. Energy deposition of gamma rays via the photo-electron, Compton scattering, and pair creation processes will occur primarily in this detector. The surrounding NaI crystals will serve to detect partially-slowed secondary electrons or Compton-scattered and annihilation photons, which have escaped from the central detector. The plastic counters will serve to detect cosmic rays and other radiations from outside.

The detector assembly can be operated in several modes such as (A) coincidence mode, in which coincidence signals between the central and surrounding NaI detectors are summed up to produce a total-energy singnal, and (B) veto mode, in which signals from the central detector are registered only when no signals are present on the surrounding detectors. In any modes, signals from the plastic

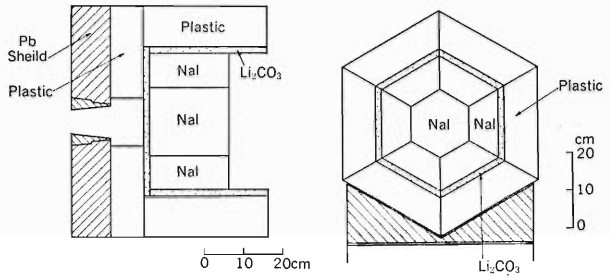

Fig. 1. Schematic view of the counter assembly for high-energy gamma-ray detection.

counters are used to veto registering data.

The performance of the setup was tested by measuring gamma rays from the (p, γ) reaction on a BN target using 6.95 MeV protons from the INS cyclotron. For the 22.93 MeV transition corresponding to $^{11}B(p, \gamma_0)^{12}C_{g.s.}$, detection efficiency in terms of total-energy peak was about two times larger in mode A than in mode B. On the oher hand, better energy-resolution of 4.5% was obtained in mode B than that of 6.0% in mode A. The reduced resolution for coincidence mode operation may be related partly to use of crystal of poor quality for surrounding detectors and partly to the thickness of the stainless-steel wall, which may absorb energy of transmitting electrons.

The system has been proved useful for detection of high-energy gamma rays and being used for the study of the radiative capture reaction $^{12}C+^{12}C$. Meanwhile, improvement of the performance is being pursued through re-fabrication of NaI crystal with better quality.

* Institute for Nuclear Study, University of Tokyo.
** Department of Education, Yamagata University.
*** Department of Science, Kyoto University.

RIKEN Accel. Progr. Rep. **18** (1984)

III-5-3. Liquid Ionization Chamber

S. Konno, T. Takahashi, and K. Masuda

Liquid ionization chambers have been used as nuclear radiation detectors. The mediums used in these chambers include liquid rare gases, such as argon and xenon, which have relatively large electron mobilities and high ionization yields. In spite of suitable properties, liquid rare gases have not been used widely because of inconvenient low-temperature techniques.

Since 1968, we have studied ionization in liquid rare gases.[1)-3)] Now we are looking for what is called "warm liquids" which are usable at room temperature. Tetramethylsilane and tetramethylgermane seem to be such liquids; their physical properties are summarized in Table 1.

One of the serious problems is due to difficulty in removing electronegative impurities which capture electrons produced by ionization and decrease output signals from detectors. We thus contrived purification system shown in Fig. 1. In the first step of the purification, liquid in a lower vessel is evaporated and condensed into an upper vessel. Then a part of vapor is cautiously pumped through a glass cold trap. After distillation, the condensed liquid was admitted into a lower vessel. These procedures are repeated. In the second step, the vapor of the liquid was passed through a spiral tube filled with Molecular Sieves.

The ionization chamber, shown in Fig. 2, has a thin window (zero potential) and a collector electrode (positive potential). Incident radiation through the window produces electron-ion pairs in the liquid. Most of them are separated by the applied electric

Table 1. Physical properties of liquids.

Liquid	ρ (g·cm^{-3})	T_b (K)	T_m (K)	μ (cm^{2}V^{-1}s^{-1})	G
Tetramethylsilane	0.648 (293 K)	299.7	171.0	90[4)]	—
Tetramethylgermane	1.006 (293 K)	316.6	185.2	90[4)]	—
Liquid argon	1.41 (83.8 K)	87.3	83.8	475[5)]	4.3
Liquid xenon	2.96 (161.4 K)	165.1	161.4	2,200[5)]	6.4

ρ, density; T_b, boiling point; T_m, melting point; μ, low-field electron mobility; G, ionization yield (number of electrons per 100 eV).

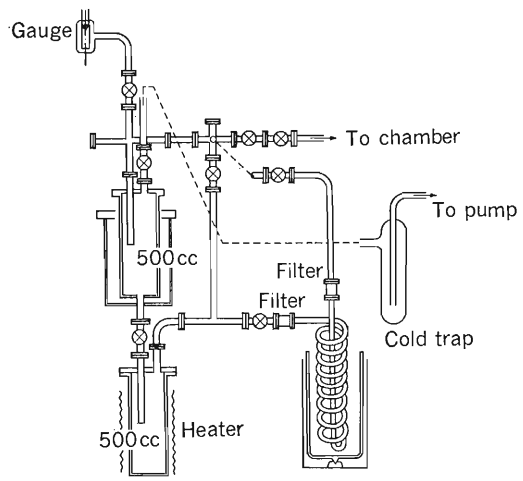

Fig. 1. Liquid purification system.

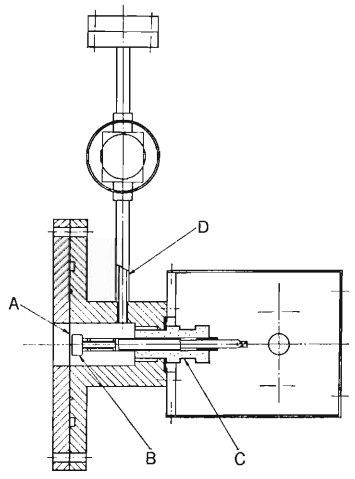

Fig. 2. Liquid ionization chamber.
A, window; B, collector electrode; C, insulator; D, liquid inlet pipe.

field and the signal charge would be induced on the collector electrode by the drift of electrons.

The construction of the purifier and the ionization chamber are now under way.

References

1) S. Konno and S. Kobayashi: *Sci. Papers I. P. C. R.*, **67**, 57 (1973).
2) T. Takahashi, S. Konno, T. Hamada, M. Miyajima, S. Kubota, A. Nakamoto, A. Hitachi, E. Shibamura, and T. Doke: *Phys. Rev. A*, **12**, 1771 (1975).
3) K. Masuda, T. Doke, and T. Takahashi: *Nucl. Instrum. Methods*, **188**, 629 (1981).
4) W. F. Schmidt: *Can. J. Chem.*, **55**, 2197 (1977).
5) L. S. Miller, S. Howe, and W. E. Spear: *Phys. Rev.*, **166**, 871 (1968).

RIKEN Accel. Progr. Rep. 18 (1984)

III-5-4. Use of Charge Integrating ADC's with Pulse Shape Discriminators for Neutron-Gamma Discrimination

J. Kasagi, T. Murakami, and T. Inamura

A neutron-gamma discrimination method using a CANBERRA 2160 pulse shape discriminator (PSD)[1] is a simple and convenient one to suppress gamma rays in neutron detection system since only anode output of a photomultiplier is required by the PSD. In our neutron multiplicity filter system at the cyclotron laboratory,[2] which was constructed for in-beam gamma-ray spectroscopy for neutron deficient nuclei, anode output pulses of photomultipliers of six neutron detectors (NE213) are fed directly into the PSD's. When only the neutron event information is required, output pulses of the PSD's in n mode can be used as neutron event pulses after adjusting the strobe delay. In practice, however, the pulse shape information of each event is required for the later off-line analysis, since the quality of the n-γ discrimination depends on the pulse height of the detector output. In this case, output pulses of the PSD's in n+γ mode are used as stop pulses of CAMAC TDC's. The detection system becomes complicated because output pulses of the constant fraction discriminator (CFD) must be delayed to be accepted within a time interval of the TDC (typically 250 ns). Furthermore, the computer busy time increases because unwanted gamma-ray events cannot be reduced by adjusting the strobe delay.

We have found a simple method to obtain pulse shape spectra without TDC's, realizing to reduce unwanted events easily. The method is an application of the time measurement by charge integrating ADC's recently reported.[3] We have measured total charge of the output pulse of the PSD in n mode instead of measuring the time difference between output pulses of the CFD and the PSD in n+γ mode.

The pulse shapes at various points of the PSD circuit for n and n+γ mode are shown in Fig. 1 according to the notation in Ref. 1. In n+γ mode, the leading-edge of the output pulse is defined by the zero-crossing time of the RC-shaped input signal when the strobe pulse is covering the right time region. Thus, the time difference between output pulses of the CFD and the PSD gives the pulse shape information of the input pulse. On the other hand the leading-edge of the output of the PSD in n mode is defined by the leading-edge of the strobe pulse triggered by delayed CFD output, and no pulse shape information is available. However, the time of the tailing-edge is defined by the zero-crossing time of the RC-shaped input signal. Therefore the width of the output pulse gives the pulse shape information. This information can be digitized easily by using the charge integrating ADC since the output of the PSD is provided by a stable current source of 16 mA. The fact that the pulse width of the gamma-ray event is always smaller than that of the neutron events makes the reduction of unwanted gamma-ray events possible without losing the pulse shape information. It can be done by adjusting the strobe delay. The output of the PSD in n+γ mode might be also used to obtain the pulse shape information by the charge integrating ADC. In this case, the output pulse width of the gamma-ray event is larger than that of the neutron event because the tailing-edge of the output pulse is defined by the tailing-edge of the strobe pulse. Thus, the neutron events can be eliminated without losing the pulse shape information.

Pulse shape spectra obtained from a 5″×3″ neutron detector with a 2 mCi Am-Be source are compared in Fig. 2. The spectrum measured by the conventional time difference method is shown in

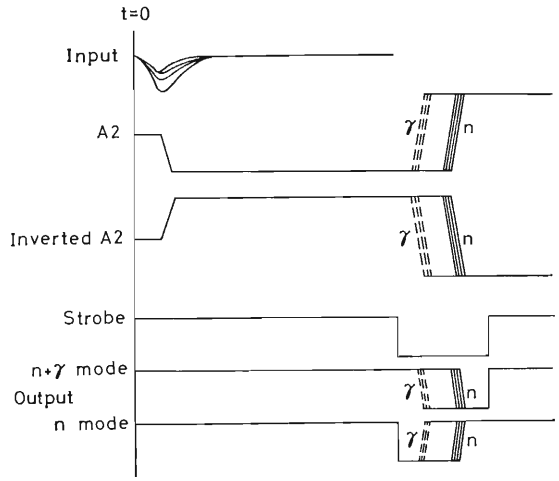

Fig. 1. Pulse shapes and time relationship between the pulses at various points of the SPD circuit. A2 is the output of a high-gain limiting amplifier.

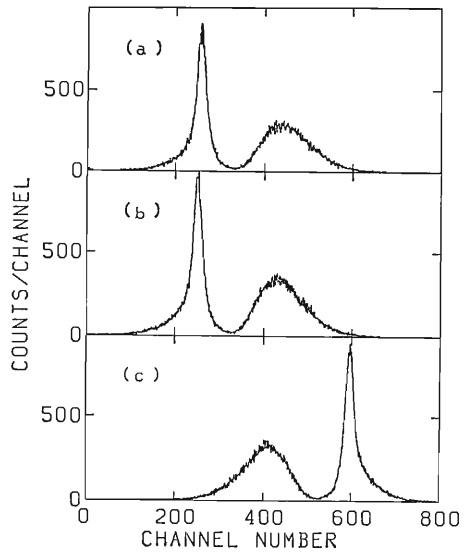

Fig. 2. Pulse shape spectra for an NE213 detector.
(a) Measured by the conventional time difference method with the TDC (125 ps/ch), (b) measured with the charge integrating ADC for the PSD in n mode, (c) for the PSD in n+γ mode.

Fig. 2 (a), while in Fig. 2 (b) is the spectrum obtained by the charge integrating ADC for the PSD in n mode and in Fig. 2 (c) for the SPD in n+γ mode. The output pulse of the PSD was attenuated by 16 dB in order to obtain the charge-time ratio of 2 pC/ns. As can be seen in Fig. 2, the spectra obtained by the present method give the same quality of the n-γ separation as that of the conventional method.

The present method has been employed for n-γ discrimination of our neutron multiplicity filter system with simpler cable connection and data taking program. The main advantages of this method are as follows:

(1) The pulse shape information from neutron detector can be obtained only from the PSD output, independently from the CFD output.

(2) The reduction of unwanted events can be realized easily without losing the pulse shape information.

References

1) P. Sperr, H. Spieler, M. R. Maier, and D. Evers: *Nucl. Instrum. Methods*, **116**, 55 (1974).
2) T. Murakami, J. Kasagi, H. Harada, and T. Inamura: *RIKEN Accel. Progr. Rep.*, **17**, 125 (1983).
3) W. Z. Venema: *Nucl. Instrum. Methods*, **219**, 257 (1984).

RIKEN Accel. Progr. Rep. 18 (1984)

III-5-5. Particle Identification with a BaF_2 Scintillator

T. Murakami, J. Kasagi, T. Inamura, and M. Ishihara

We have tested a BaF_2 scintillator as a charged particle detector since the BaF_2 scintillator is considered to be a modular detector of a multi-detector system for experiments on the SSC to detect charged particles together with γ-rays.

Attractive features of the BaF_2 scintillator as a γ-ray and particle detector with moderate energy resolution are the following.

(1) Time resolution of about 150 ps has been obtained because of the existence of the fast decay component in the scintillation light.[1]
(2) Stopping power for charged particles is much larger than that of the plastic scintillator, so that 200 MeV proton can be detected with BaF_2 crystal of 10 cm in thickness.
(3) Gamma-ray efficiency is about 30% higher than that of NaI.
(4) Energy resolution for charged particles is better than that of a plastic scintillator.[2]

In addition, pulse shape difference between γ-rays and particles has been observed.[2),3)] Thus, our immediate interest is to investigate the possibility of particle identification by a pulse-shape-discrimination technique.

The BaF_2 crystal used in the present work was a high purity one made by Ohyo Koken Kogyo Co., Ltd. It was rectangular in shape with dimensions of 2 cm × 4 cm × 1 cm. In order to detect the fast component of the scintillation efficiently, *p*-terphenyl was evaporated on the crystal surface as wavelength shifter, and the crystal was wrapped with a conical mirror with a 1 cm diameter hole. The crystal was optically coupled to a photomultiplier (Hamamatsu R329) with usual silicone grease. Figure 1 shows a schematic diagram used for the pulse shape discrimination. The fast component of the scintillation light was measured by a charge-sensitive ADC shown as QDC in the figure. A CAMAC data taking system[4] was used to collect and analyze data.

The particle identification was tested for the

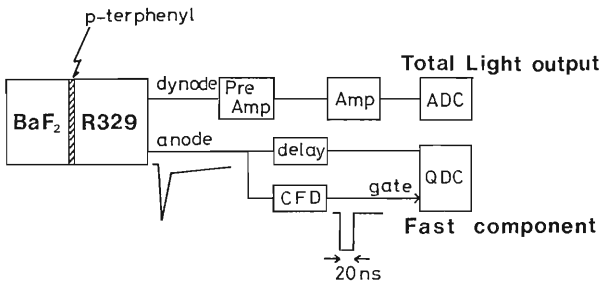

Fig. 1. Electronics diagram used for particle identification.

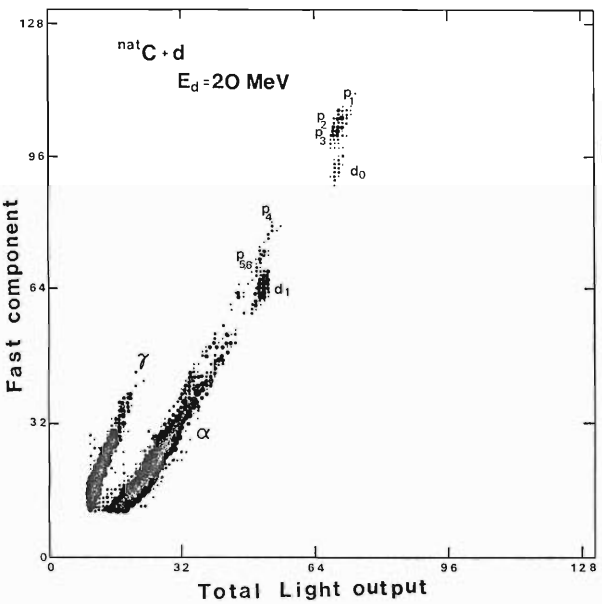

Fig. 2. Contour plot of total light output *vs.* fast component of light from the BaF_2 scintillator.

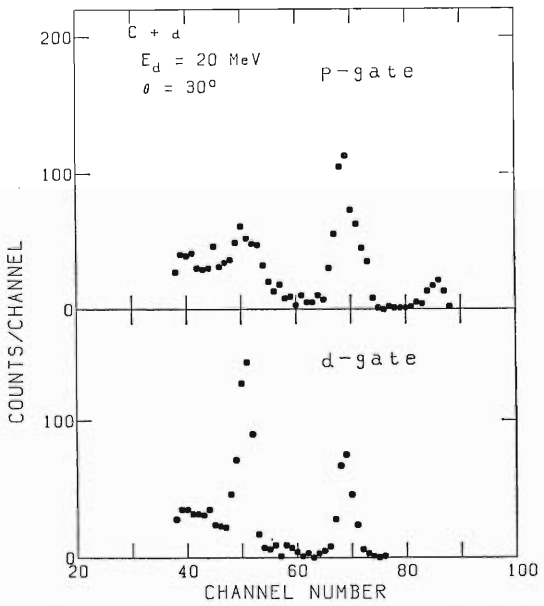

Fig. 3. Pulse height spectra for protons (upper) and deuterons (lower).

C+d reaction. A 20-MeV deuteron beam from the cyclotron was used to bombard C-foil of 5 mg/cm^2 in thickness. The BaF_2 detector was placed at 30° to the beam axis.

Obtained two-dimensional spectrum is shown in Fig. 2. As expected from the observation for γ-rays and α particles,[2),3)] the light output of the fast component decreases for heavier particles. Clearly separated loci are observed in the spectrum, namely one corresponding to protons and the other to deutrons. Gamma rays (electrons) are well separated from the charged particles. However, the separation is not so good for the region of $E_p \leq 10$ MeV where α particles are also observed. Two-dimensional measurement with time of flight vs. total light output is necessary for such low energy particles. The excellent time resolution of the BaF_2 detector would make the particle identification possible by measuring flight time.

In Fig. 3 are shown projected spectra for protons and deuterons. Several peaks from the $^{12}C(d, p)^{13}C$ and $^{12}C(d, d)^{12}C$ reactions are clearly seen in the spectra. The energy resolution of about 450 keV for E_d=20 MeV was obtained.

References

1) M. Laval, M. Moszynski, R. Allemand, E. Cormoreche, P. Guinet, R. Odru, and J. Vacher: *Nucl. Instrum. Methods*, **206**, 169 (1983).
2) T. Murakami and J. Kasagi: unpublished.
3) K. Wisshak and F. Kapeler: *Nucl. Instrum. Methods*, **227**, 91 (1984).
4) T. Inamura, T. Murakami, J. Kasagi, H. Kumagai, and H. Gono: *RIKEN Accel. Progr. Rep.*, **17**, 124 (1983).

RIKEN Accel. Progr. Rep. **18** (1984)

III-5-6. Test of MCP and PSD Using X-Rays and Electrons

H. Kumagai, Y. Itoh, T. Koizumi, H. Shibata, and Y. Awaya

A position-sensitive electron-spectrometer, in which a tandem micro-channel-plate (MCP: Hamamatsu Photonics) and a Si-position-sensitive detector (PSD: Hamamatsu Photonics) are used, was constructed and a performance of the spectrometer was tested. The spectrometer was used to measure the energy of scattered and ejected electrons in electron-atom collisions, and spectra of elastically scattered electrons and Auger electrons were obtained. During the test, it was noticed that a detection efficiency is not always the same on every position of the MCP-PSD assembly. Therefore we tested a uniformity of the detection efficiency of the assembly itself using X-ray and electron sources.

An experimental setup is shown in Fig. 1. The X-ray (13–16 keV) is emitted from a point source of a diameter of 1 mm, passes through a thin Al-window, and then hits the MCP surface uniformly. An applied voltage for each MCP was 1 kV and a potential difference between MCP and PSD was about 20 V; under these conditions, an output pulse height distribution is optimized.

A position signal was processed by means of analog devices and then fed to a pulse height analyzer (see Fig. 2).

An observed spectrum is shown in Fig. 3. As the X-rays hit the MCP surface uniformly, this spectrum reflects the position dependence of the detection efficiency of MCP and PSD assembly. The detection efficiency on the studied area was fairly

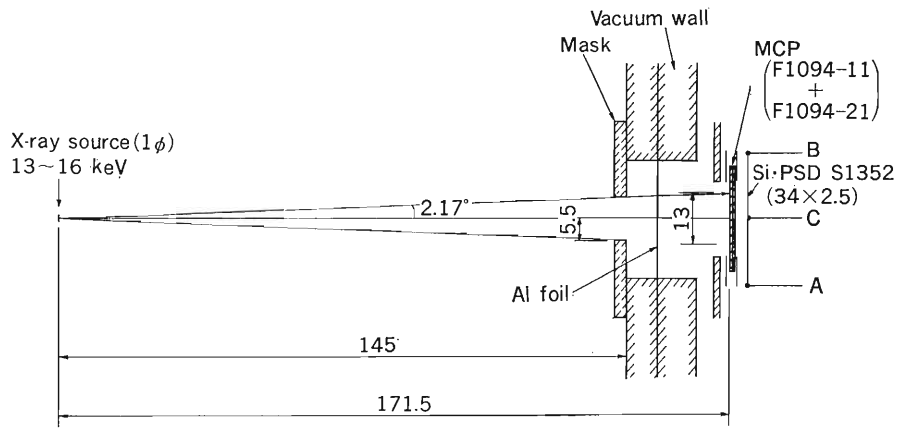

Fig. 1. Experimental setup to measure the uniformity of the detection efficiency.

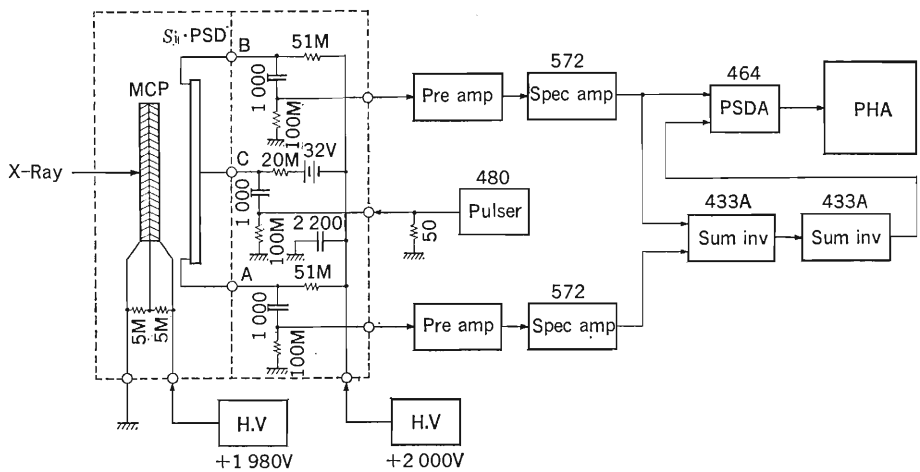

Fig. 2. Circuit diagram for a position sigal processing.

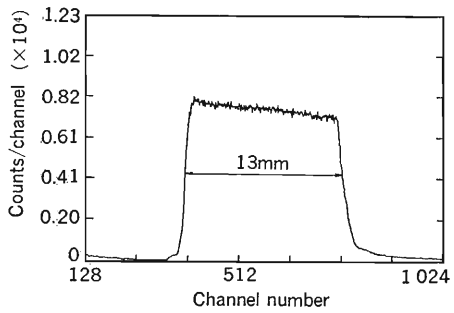

Fig. 3. Observed detection efficiency of the MCP-PSD assembly tested.

flat but not constant; the deviation from the unity is about ±5% when the efficiency is normalized at the center of the MCP. This deviation may be caused by the MCP or PSD, or both. When the test was repeated after the PSD was turned by 180°, the same position dependence remains on a spectrum. Therefore, the observed position dependence is considered to be caused by a different gain of the MCP at a different position.

This tendency of the position dependence was also observed when the assembly was exposed to stray thermal-electrons, which hit MCP surface fully randomly, from an ion-gauge.

Conclusions of these tests are: (1) the uniformity of the PSD is good enough and (2) the detection efficiency of the MCP has some position dependence of about ±5% deviation from unity.

RIKEN Accel. Progr. Rep. **18** (1984)

III-5-7. One Dimensional Position Sensitive Parallel Plate Avalanche Counter

H. Kumagai, S. H. Be, M. Ishihara, Y. Ikegami,
M. Fuse, and E. Gotoh

A parallel plate avalanche counter (PPAC) is a well-known heavy-ion detector widely used for nuclear physics and atomic physics. The PPAC has an excellent timing property and a high counting rate capability. It is useful for a large area position sensitive detector. Furthermore, there are little problems with radiation damage.

We have constructed a prototype PPAC to study fundamental characteristic of the counter and to develop improved electronic circuits for fast timing measurement. Through this work, we aim to establish basic production techniques of larger area PPAC detectors required for future use at the RIKEN SSC.

Figure 1 shows the cross sectional view of the detector. The detector consists of two different PPACs.

(1) A position sensitive PPAC which consists of an anode, grid, and cathode. The anode and cathode are made of 2.5 μm Hostaphan foil evaporated with a gold layer (60 μg/cm^2) which has an active area of 30×105 mm^2. The grid consists of 40 μm-diameter tungsten wires strung 2 mm apart, and is gilded with gold. All wires are connected to each other by a resister of 200 Ω. The respective distance between the anode and grid or the grid and cathode is 1.5 mm for either case.

(2) A timing PPAC. This PPAC consists of an anode and cathode of the same kind as in former case but without a grid. Two PPACs are set up in parallel 10 mm apart from each other as shown in Fig. 1.

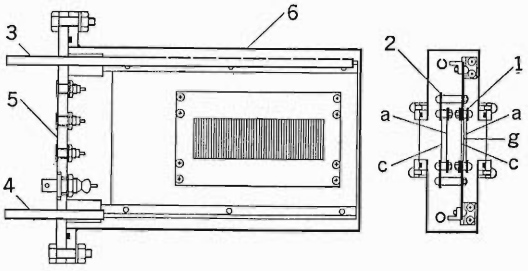

Fig. 1. Cross sectional view of the detector.
1: Position sensitive PPAC, 2: Timing PPAC, 3: Gas inlet, 4: Gas outlet, 5: Flange, 6: Stainless box, a: Anode, g: Grid, c: Cathode.

The detector housing consists of a flange, on which two counters and seven coaxial connectors are mounted, and a box having two windows (30×110 mm^2) covered with 2.5 μm Hostaphan foil. In addition, two extremly small fast-preamplifiers (diameter 4 mm, thickness 2.5 mm, gain 10, and bandwidth 1.2 GHz) are mounted directly on the counters and operated in the gas atmosphere.

We have chosen isobutylene as a counting gas which seems best for a fast timing signal (Ref. 1); further, it is cheap and easy to handle. A gas-feed system is shown in Fig. 2. The gas pressure is kept constant at about 10 Torr by adjusting a flow rate

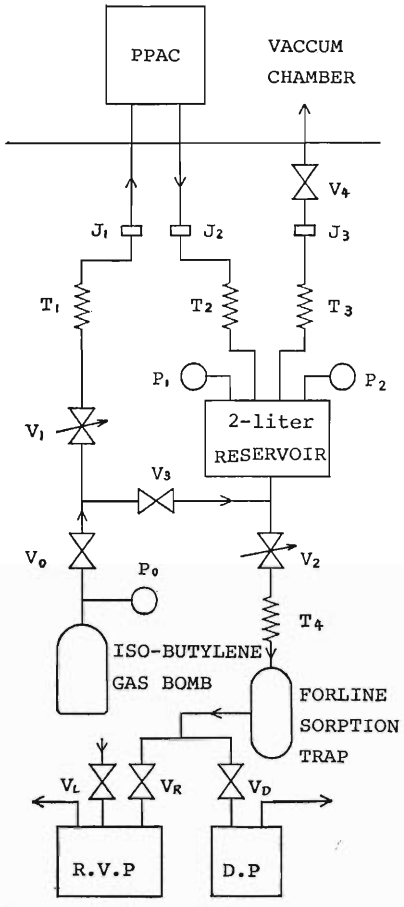

Fig. 2. Diagram of the gas-feed system.
V_1, V_2: Needle valves, V_0, V_3, V_L, V_R, V_D: Shut-off valves, V_4: Bellows valve, T_1–T_4: Flexible tubes, J_1–J_3: Tube joints, P_0–P_2: Vacuum gauge ports, R. V. P: Rotary vane pump, D. P: Diaphragm pump.

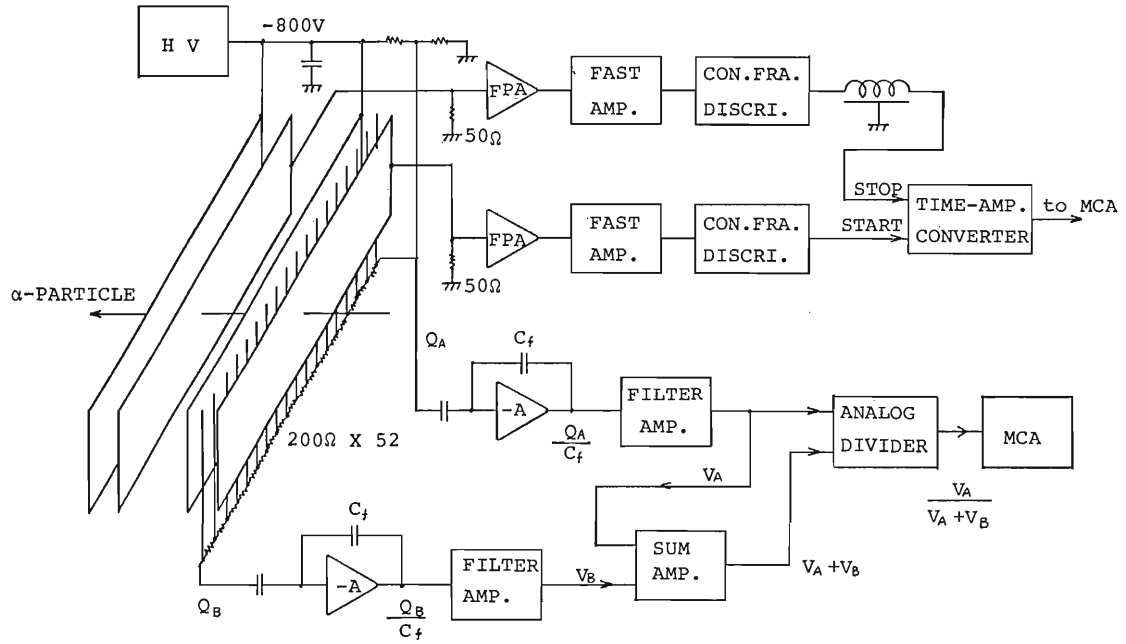

Fig. 3. Block diagram of the electronic system.
FPA: Fast-preamplifier.

of the gas with needle valves V_1 and V_2.

In order to avoid backstreaming of oil- and water-vapor from a rotary vane pump to the system, and to prevent deterioration of the oil caused by the gas, a foreline sorption trap is mounted on the inlet of the pump. A diaphram pump is used to exhaust the absorbed gas evolved from the sorption trap, when the trap is regenerated by heating.

Figure 3 shows a diagram of the electronic system for measurement of position resolution of the detector and time resolution. The charge division method is used for position measurement. The signals from both ends of the grid are received with charge sensitive amplifiers and then amplified with improved S/N through filter amplifiers. The position signal is obtained by dividing one-side signal by total signal which is obtained by summing up two signals from both ends of the grid.

The timing property is observed from measurement of the flight time of an α-particle between the two transmission PPACs. The fast timing signals, taken off at the anodes of the PPACs, are fed via fast-preamplifiers mounted on the counters into fast timing amplifiers and processed by constant fraction discriminators, and then sent to a time-to-pulse amplitude converter. By using the above fast-preamplifiers, an improved time resolution is expected in this system. The above position data and timing data are stored in a multichannel pulse-hight analyzer.

Reference

1) H. Stelzer: *Nucl. Instrum. Methods*, **133**, 409 (1976).

RIKEN Accel. Progr. Rep. **18** (1984)

III-5-8. Test Machine for Ion Guide Isotope Separator On-Line

K. Morita, T. Nomura, T. Inamura, H. Kudo, and K. Sueki

The ISOL (Isotope Separator On-line) technique was developed for the study of very short-lived and rare radioisotopes. In recent years the Ion Guide Isotope Separator On-Line (IGISOL) has been developed[1] as a new type of ISOL which does not require an ion source. In the case of IGISOL, reaction products emitted from a target are slowed down and stopped in helium gas. Although most of ionic reaction products are neutralized in the gas, some amounts of them (1–10%) hold a charge state of +1. And then by using an electrostatic field, these ions are extracted and accelerated for mass analysis. Because an IGISOL system have no ion source, this system will enable us to study more kinds of elements than those by an ordinary type ISOL with an ion source.

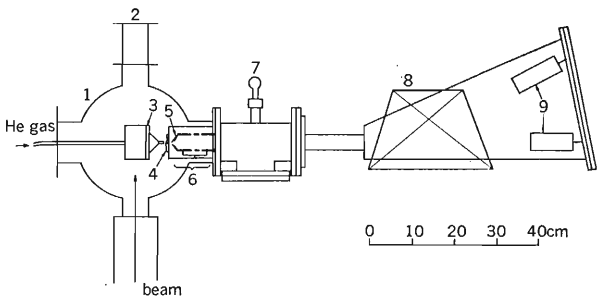

Fig. 1. Schematic diagram of the test machine system for IGISOL.
1, Vacuum chamebr; 2, Faraday cup; 3, Target box; 4, Skimmer; 5, Extraction electrode; 6, Einzel lense; 7, Vacuum guage (B-A guage); 8, Analyzer magnet; 9, Electron multiplier.

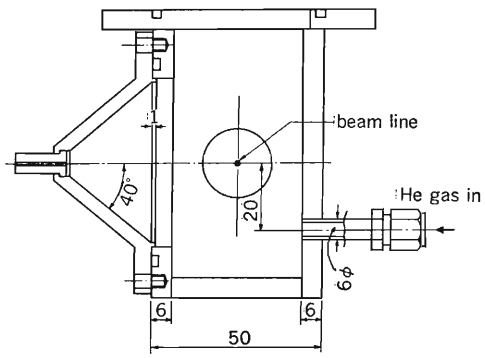

Fig. 2. Cross sectional view of the target box.

In order to develop the IGISOL system we have constructed a test machine. This test machine is composed of four parts: (1) a target box, (2) an extraction and acceleration system, (3) a mass analysing system, and (4) a detection system, Fig. 1 shows a schematic diagram of the total system. We use the dipole magnet as a mass analyzer and an electron multiplier for detecting ions. Accelerating voltage can be set 3–4 kV, and voltage between target box and skimmer can be set 150–200 V.

The vacuum chamber outside the target box is evacuated by a mechanical booster pump, and the acceleration part is evacuated by a diffusion pump. These two parts are separated by a skimmer with a hole of 1 mmϕ. While the pressure in the target box is kept 10–30 Torr by flowing helium gas, that of outside the target box is kept $\sim 10^{-2}$ Torr, and that of the acceleration part $\sim 2\times 10^{-5}$ Torr. A cross sectional view of the target box is shown in Fig. 2.

A test experiment was done by using 30 MeV α-beam from the cyclotron with a natural titanium target. Although there are many peakes seen in the mass spectrum, they correspond to ions of the gases ionized by the beam. From the yield of a $^4He^+$ peak in the spectrum, the total efficiency of this test machine is estimated to be less than 10^{-8}. Modification of the target box and other parts to enlarge the efficiency will be required.

Reference

1) J. Ärje and K. Valli: *Nucl. Instrum. Methods*, **179**, 533 (1981).

RIKEN Accel. Progr. Rep. **18** (1984)

III-5-9. A Coulomb-Excitation Mössbauer Spectrometer

N. Sakai, F. Ambe, and K. Asai

A Mössbauer spectrometer for γ-rays from Coulomb-excited states has been designed and constructed. Since most of Mössbauer γ-rays created by Coulomb excitation have relatively high energy, it is required that both a source and an absorber are held near liquid-N_2 temperature to increase the recoilless fraction.

The side view of the spectromater is shown in Fig. 1. It is divided into two parts: (1) a transducer and its attachment to an absorber holder, (2) a target chamber with a liquid-N_2 cryostat.

The heavy-ion beam comes in along the upward direction normal to the plane of the paper, and strikes a target which makes an angle of 45° to the beam line. Then, Coulomb-excited Mössbauer nuclei recoil out of the target and are implanted into a fixed stopper. This sotpper, which acts as a Mössbauer source, is cooled by a cold rod suspended from a liquid-N_2 bath having a capacity of 1.5 litre. Liquid N_2 is supplied automatically from another liquid-N_2 container. The Doppler-modulated absorber is also cooled through springs connected to a cold box of the cryostate. The target and stopper holder can be pulled up, and the position of the beam can be adjusted by observing fluorescence emitted from an inclined quartz plate which is joined to the target holder. The fluorescence is detected through a viewing window at the bottom of the target chamber.

In order to keep the vacuum of the linac clean, the transducer is placed in a separate chamber so as to avoid the problem of gas desorption from the transducer. The transducer chamber is separated from the target chamber by a soft bellows. It is sufficient to evacuate the transducer chamber by a rotary pump so that there in no severe pressure difference between the transducer chamber and the target chamber. The rod of the transducer can be released at the positions A, B, and C denoted in Fig. 1.

The γ-rays penetrating through a Be window, which is placed at a right angle to the direction of the ion beam, are counted by a Ge detector.

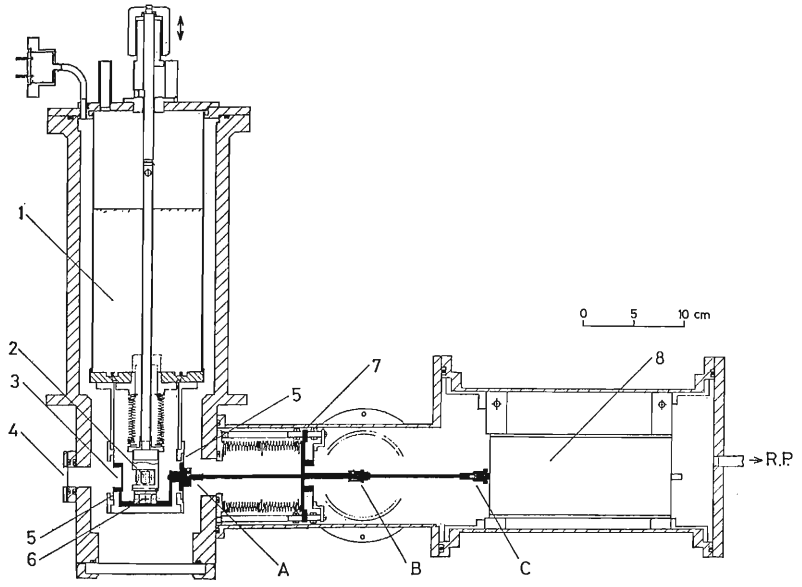

Fig. 1. In-beam Mössbauer spectrometer for γ-rays from Coulomb-excited nuclei. 1, Liquid-N_2 bath; 2, target and stopper; 3, absorber; 4, Be window; 5, springs; 6, quartz plate; 7, safety stopper; 8, transducer.

RIKEN Accel. Progr. Rep. 18 (1984)

IV. NUCLEAR DATA

1. Status Report of the Nuclear Data Group

A. Hashizume, Y. Tendow, and T. Nozaki

Since the last Meeting of the Nuclear Data Centers in October, 1983, in Obninsk and Moscow,[1] RIKEN Nuclear Data Group has recognized the importance of compilation of Data of charged-particle induced reactions useful for production of radioactive isotopes in biomedical use.

The compilation of data has been started this year by keeping contact with the Nuclear Data Section (NSD) in IAEA and other data centers.

Our primary interest is in the reaction cross sections which are concerned with production of the following isotopes: ^{11}C, ^{13}N, ^{15}O, ^{18}F, ^{28}Mg, ^{52}Fe, ^{67}Ga, ^{74}As, ^{77}Br, ^{82}Br, ^{77}Kr, ^{81}Rb, ^{82m}Rb, ^{111}In, ^{123}Xe, ^{127}Xe, ^{123}I, ^{124}I, and ^{125}I.

Because this period is the time of foundation and consolidation of the Group, efforts were made for two directions, policy,[1] and technics. The activity of the Group has formally been approved as one of the projects in the accelerator division. A nation-wide advisory group consisted of 4 physicians, 5 physicists, and 4 chemists has been organized to keep close relation with other data groups and with experts in various fields in Japan. The first meeting was held in February and the second in November, 1984.

Technical activities

(1) We use the center computer (FACOM M 380) of RIKEN as a host computer for compilation of data. The majority of data are registered in the EXFOR format. Curve reading techniques for data compilation have been established by using a curve digitizer and a mini-computer. The mini-computer can be connected on-line to the host computer. Several programs were developed to support the compilation.

(2) Implementation of some programs of the EXFOR and Dictionary system obtained from NDS are now going on. Check New Entry Run and Generate Dictionary Run are now under investigation. The book-keeping programs are in operation and the second trans-tape data are treated by these programs.

(3) Two data tapes (R001, R002) have been transmitted to NDS. The contents of the first tape were consisted of 10 entries (37 subentries) and those of the second tape consisted of 6 entries (140 subentries) and corrected entries of the first. The first trans-tape contained the data of excitation function in the region of about A=130 and the second contained those of about A=11. The latter consisted of the differential cross section data, because in the region relatively few total production cross section data are available. We consider that this preliminary data compilation is a case study because whole Check Run program is not yet in operation.

(4) Bibliography: Lists of references which are concerned with our subject are being accumulated continuously and checked on the coverage of the existing EXFOR files.

(5) Other activities are concerned with the mass chain evaluations of nuclear structure data. In cooperation with JEARI group, we have finished the evaluation of experimental data pertaining to mass number A=129 nuclei.[2] Evaluation of A=120 chain has been almost finished and is under inspection of other data groups in Japan.

References

1) "Report on the 7th IAEA consultants" Meeting of Nuclear Reaction Data Centers, INDC (NDS)-154 (1984).
2) A. Hashizume, Y. Tendow, and M. Ohshima: *Nucl. Data Sheets*, for A=129, NDS **39**, 551 (1983).

RIKEN Accel. Progr. Rep. 18 (1984)

V. ACCELERATOR DEVELOPMENT

1. Present Status of the RIKEN Ring Cyclotron Project

H. Kamitsubo

The project for construction of the $K=540$ MeV separated sector cyclotron (Ring Cyclotron) at RIKEN has progressed as intended in 1984. The cyclotron vault was almost completed in March and assembling of the sector magnets in the vaults was carried out from April through June. As described previously, each sector magnet can be separated into thirty pieces, that is, two poles and twenty eight slabs of the yoke, for the convenience of transportation from the factory to RIKEN. The slabs of the yokes were transported by land whereas the poles were brought by ship to Tokyo and then by land to the institute. Four sector magnets were assembled at the same time on the base in the cyclotron vault by adjusting their relative positions to each other precisely. Six invar bars were set connecting the fixed points on the upper faces of four sector magnets to measure their displacements to each other. Change in the relative positions has thus been monitored continuously since then.

Power supplies for the main and trim coils were brought into the cyclotron vault in August and their tuning up and inspections of the current stability have been carried out. The stability better than 2×10^{-6} was realized for the main coil currents. Measurements of excitation characteristics and magnetic field distributions will start in January, 1985.

The components of the Ring Cyclotron other than the sector magnets were ordered to SUMITOMO Heavy Industries, Ltd. and the final design for their fabrication have been performed. Design of the valley chambers was almost finished and vacuum pumps other than cryopumps and vacuum elements such as valves, vacuum gauges, and Q-mass analyzers were on order. Development of the cryopumps having a pumping speed of 10,000 l/s is in progress.

As described in a previous report, we decided to adopt a new type resonator having two vertical straight stems on the upper and lower sides of the accelerating electrode (dee) and also two moving boxes as a frequency changing device. The resonator is made of copper clad stainless steel fabricated by a diffusion-welding technique. In order to realize better cooling efficiency there are channels for cooling water on the copper clad side of the stainless steel.

Basic design of the RF system was finished and the system was ordered to Denki Kogyo Co.,Ltd. It consisits of a master oscillator, wide band amplifiers, and a final power amplifier for which a Siemens RS2042SK tetrode is used.

A computer-aided control system is introduced for the present accelerator system. The main system composed of three MELCOM 350-60/500 computers, disks and I/O devices, and networks of the CAMAC as well as GP-IB will be used for control of the Ring Cyclotron and two injectors. New CAMAC interfaces, named CIM (Communication Interface Module) and DIM (Device Interface Module), were developed. The first system of MELCOM 350-60/500 and several sets of the CIM and DIM were delivered and are being used for developing the control program. They will be used for the field mapping of the sector magnets.

Design of the injection elements such as bending magnets, magnetic, and electric inflection channels were finished. The magnetic elements will be completed in next spring and will be attached to the sector magnets to measure their effects on the field distributions of the main magnets. The beam transport line between the injector linac and the Ring Cyclotron was designed to realize the better matching of two accelerators extensively carrying out the beam dynamical calculations with the computer program TRANSPORT. Prototypes of beam diagnostic elements such as emittance and profile monitors and a phase probe were fabricated and tested.

Discussions on the experimental facilities to be constructed at the early stage of beam acceleration started in this period by both inside and outside users. Experiments on nuclear physics and biological studies are expected to be pursued with the first beams from the Ring Cyclotron.

Construction of the experimental halls as well as control and counting rooms started in December, 1984. Design of the radiation monitoring system is in progress.

RIKEN Accel. Progr. Rep. **18** (1984)

V-2. Sector Magnets for the RIKEN SSC

S. Motonaga, H. Takebe, T. Wada, A. Goto, I. Takeshita,
J. Fujita, H. Kamitsubo, J. Abe,* H. Saito,* and T. Mita*

All four sector magnets for the SSC have been assembled in the cyclotron vault. Characteristics of the sector magnets and preliminary measurements of the magnetic field made at the factory were described in previous reports.[1] The four sector magnets were installed during a period of March–May, 1984. Work on the electrical wiring as well as cooling water connection was completed in July, 1984. Figure 1 shows a photograph of the sector magnets in the cyclotron vault.

Power supplies for main and trim coils have been installed and are now being tested. Table 1 lists the specifications of the power supplies. A total of 67 power supplies are required to energize main and trim coils for formation of the magnetic field distribution. These power supplies are grouped into six types according to the way of connection between four sectors. All power supplies are housed in eleven cubicles. Two types of power supplies (M1 and M2) are used for main coils and four types of power supplies (TA, TB, TC, and TD) are for trim coils to form various isochronous field and harmonic fields.[2),3)] Strict current stability is required for M1 and M2 power supplies to obtain a high quality beam. The current sensing to achieve such high stability is performed with a precision shunt resistance made of germanium-manganese-copper alloy (ZERAMIN) with a temperature coefficient less than 3 ppm/°C between 15°C and 33°C. The shunt resistance is cooled by temperature-controlled water kept at 25°C±0.5°C. Both power supplies have been inspected and tested. Current stability of 5×10^{-6} for 24 hr was achieved at currents of 1,050 A and 600 A. Test of four types of power supplies for trim coils has almost been accomplished. Power supplies of TD type are now being adjusted to attain the specified current stability.

All the power supplies are controlled by the computer through the CAMAC modules named CIM

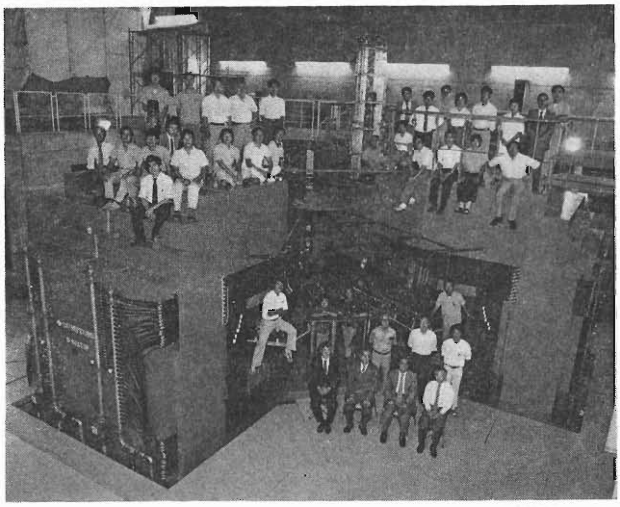

Fig. 1. Photograph of the sector magnets assembled in the cyclotron vault.

Table 1. Specifications of the power supplies for the main and trim coils.

Type	Max current (A)	Bypass current (A)	Power (kW)	Current stability
Main coil				
M 1	1050		370	$5\times10^{-6}/24^{H}$
M 2-O	1050		140	$5\times10^{-6}/24^{H}$
1~4		−100		
Trim coil				
TA 1	330		4.7	$1.5\times10^{-5}/8^{H}$
TA 2	410		7.8	
TA 3	490		24.7	
TA 4	530		17.9	
TA 5	560		18.3	
TB1-O	230		2.2	$1.5\times10^{-5}/8^{H}$
1~4		−55		
TB2-O	420		5.7	
1~4		−50		
TB3-O	530		32.3	
1~8		−50		
TB4-O	550		18.6	
1~4		−40		
TB5-O	590		10.9	
1~4		−50		
TC 1	450		4.3	$2.5\times10^{-5}/8^{H}$
TC 2-1, 2	500		5.6	
*TD 1-1, 2	250		1.58	$5.0\times10^{-5}/8^{H}$
*TD 2-11, 12, 13 14, 21, 22, 31, 32, 33, 4.	400		18.6	
*TD 3-11, 12, 21, 22, 23, 24, 31, 32, 33, 34, 35, 36	550		42.7	

* polarity of these power supplies can be changed.

* Sumitomo Heavy Industries, Ltd.

and DIM (M60: M350–60/500).[4] Figure 2 shows a schematic diagram of control system of the power supplies for the sector magnet. Information between CIM and DIM is transmitted through optical fiber and Receiver/Transmitter provided for CIM and DIM. DIM is set in each cubicle of the power supply. Figure 3 shows a block diagram of a control sequence of the power supplies and DIM. Four input and output ports of DIM are connected through optical elements to devices to be controlled. Each power supply is provided with a 16 bits D/A converter.

A field measuring system was already constructed and used before for the field measurements.[5] This system was controlled by DEC LSI-11 micro computer with a CAMAC system. In October 1984, an M60 super minicomputer has replaced the LSI-11 micro computer for control of the measuring system and processing of the field data. An NMR gaussmeter (SENTEC) equipped with four NMR probes and a multiplexer is introduced to this system. Selection of the NMR probes and the search out of an NMR signal are done by the CAMAC system. NMR signal is also read out by the CAMAC system.

Calibration of the Hall elements is now being made. Detailed measurements of the magnetic field distribution are scheduled to start at the end of 1984 and will be carried out until fall of 1985.

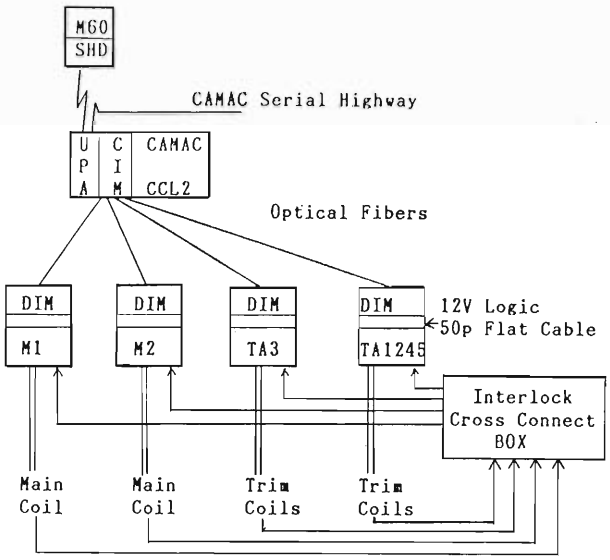

Fig. 2. Schematic diagram of the computer-assisted control system of power supplies.

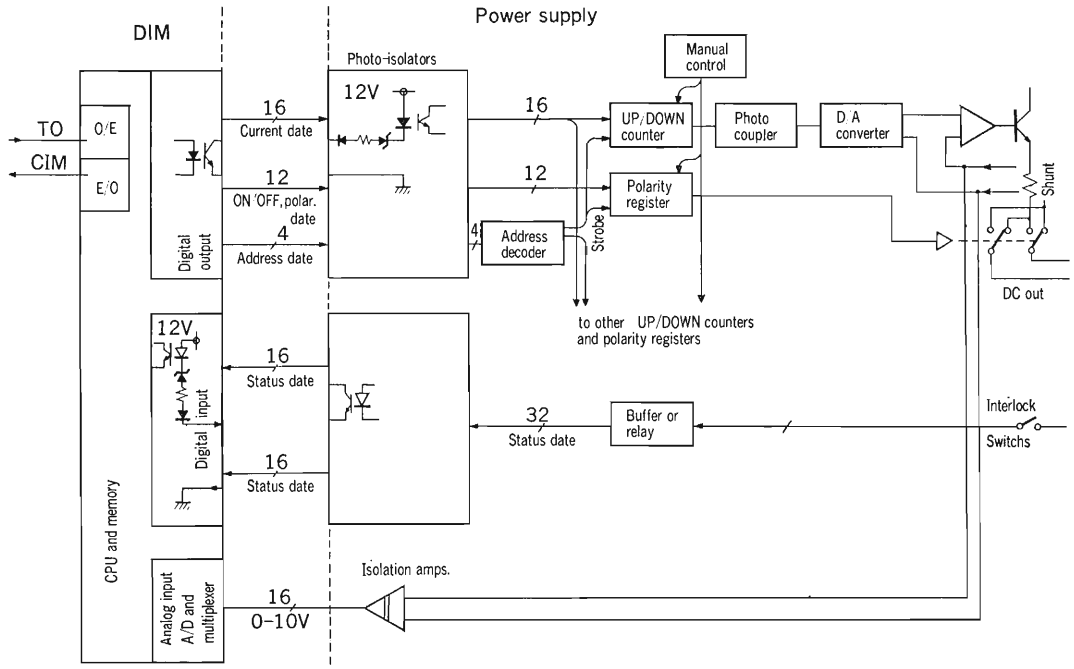

Fig. 3. Block diagram of a control sequence of power supplies and DIM.

References

1) S. Motonaga, H. Takebe, A. Goto, T. Wada, Y. Oikawa, I. Takeshita, Y. Ikegami, J. Abe, T. Tsukumo, H. Saito, and T. Sato: *RIKEN Accel. Progr. Rep.*, **16**, 183 (1982); *Sci. Papers I. P. C. R.*, **77**, 8 (1983).
2) S. Motonaga, H. Takebe, A. Goto, Y. Yano, T. Wada, and H. Kamitsubo: *J. de Physique.*, Cl 213 (1984).
3) A. Goto, H. Takebe, S. Motonaga, Y. Yano, N. Nakanishi, and T. Wada: *Sci. Papers I. P. C. R.*, **77**, 54 (1983).
4) T. Wada, J. Fujita, K. Shimizu, I. Yokoyama, and T. Kambara: *RIKEN Accel. Progr. Rep.*, **17**, 138 (1983); K. Shimizu, J. Fujita, T. Wada, and I. Yokoyama: *ibid.*, p. 141.
5) H. Takebe, I. Takeshita, J. Fujita, T. Wada, I. Yokoyama, N. Nakanishi, S. Motonaga, and T. Sato: *RIKEN Accel. Progr. Rep.*, **16**, 188 (1982); *Sci. Papers I. P. C. R.*, **77**, 20 (1983).

RIKEN Accel. Progr. Rep. 18 (1984)

V-3. Model Study of the RF Resonator for the RIKEN SSC

K. Ogiwara, T. Fujisawa, Y. Oikawa, and S. Kohara

Design study of a RF resonator for the RIKEN SSC was previously reported.[1),2)] It proved practicability of the movable box structure tuning scheme in the frequency range from 17 to 45 MHz, but the voltage distribution along the dee gap was found minimum at around 1/4 way of the dee radius and the value at frequency 43 MHz was 80% of the voltage at the injection radius (see Fig. 1 a); such voltage distribution was unsatisfactory for beam quality.[3)] This distribution resulted from the resonator structure employing slanting stems toward outer radius to reduce power consumption in the vicinity of the lowest frequency. A radially increasing voltage distribution desirable for good beam quality is realized in a movable box resonator using straight stemps positioned at an inner radius (see Fig. 1 b). Such modification, however brings unacceptable power loss at frequencies below 20 MHz. As a compromise, we decided to employ a straight stem resonator and to discard a part of the frequency range below 20 MHz. In this case, the same range of energy and nuclide is realized by extending the harmonic number of acceleration in the SSC to 10 or 11.[4)]

The new resonator was designed and its performance was studied on a 1/4 scale model. Figure 2 shows a photograph of the new 1/4 scale model resonator. In Fig. 3, Q values and positions of the movable box deduced from the experimental results are shown against the resonant frequency together with the values calculated by the transmission line approximation. The Q values are estimated by multiplying the measured Q values by a scale factor

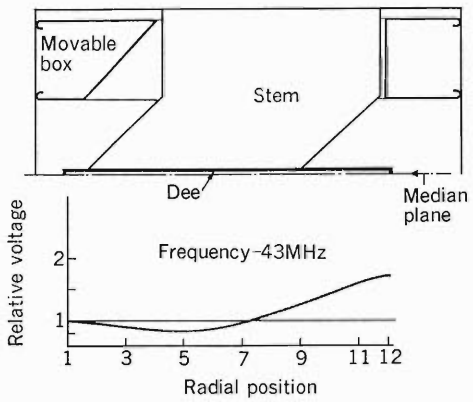

Fig. 1 a. Example of relative dee voltage for the resonator with slanting stems.

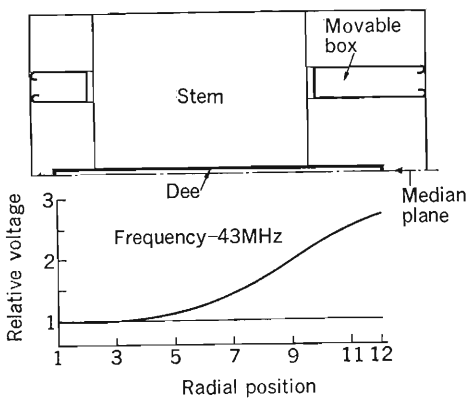

Fig. 1 b. Example of relative dee voltage for the resonator with straight stems.

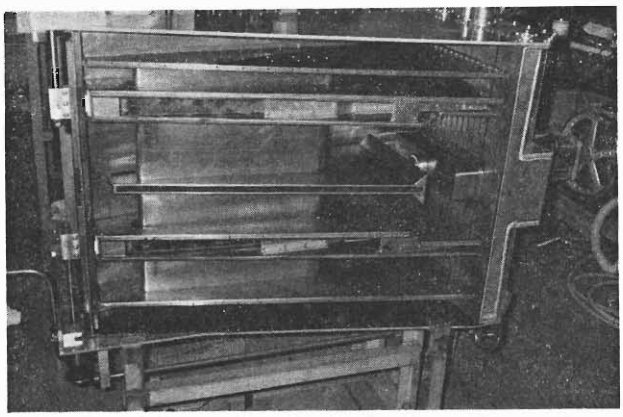

Fig. 2. A photograph of the 1/4 scale model resonator.

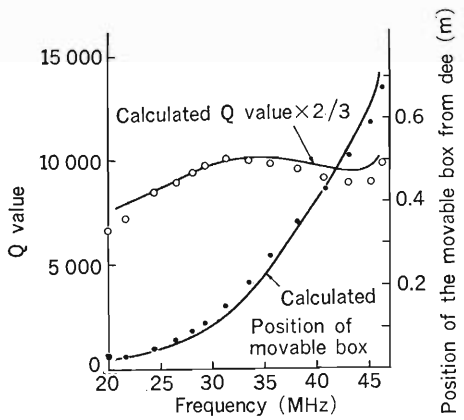

Fig. 3. Q values and position of the movable boxes for the actual resonator estimated by the experimental results. Solid lines show the calculated values by transmission line approximation.

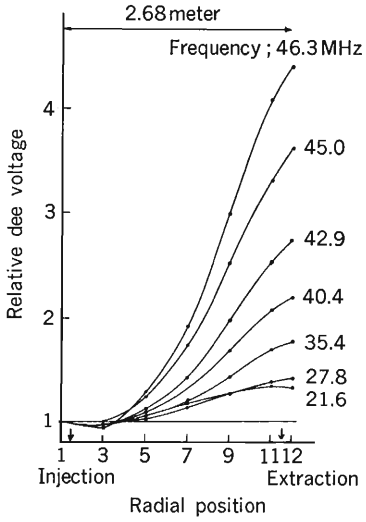

Fig. 4. Relative distributions of RF electric field along the dee gap. The frequency shown is 1/4 times of the measured one.

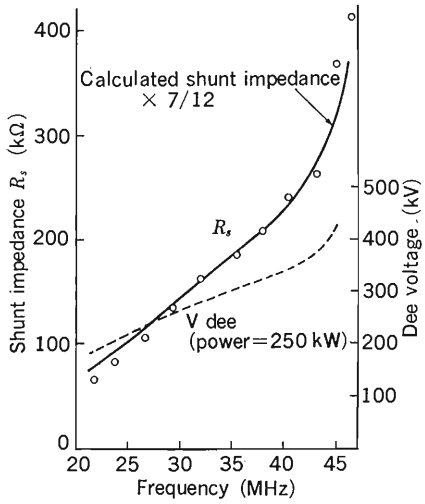

Fig. 5. Shunt impedance (R_S) and estimated dee voltage (V dee) for the actual resonator estimated by the experimental results. Open circles show the shunt impedance at extraction radius.

of $\sqrt{4}$ and resonant frequencies by 1/4. The resonant frequencies measured are reproduced fairly well by calculations. The measured Q values are 2/3 of the calculated ones. Relative distributions of RF electric field along the dee gap were measured by a perturbation method.[5] The results are shown in Fig. 4, where the dee voltages are normalized at a beam injection radius. The distributions are desirable more than those measured on the previous model.

The shunt impedance was deduced from measurements of the dee voltage and the power loss. The

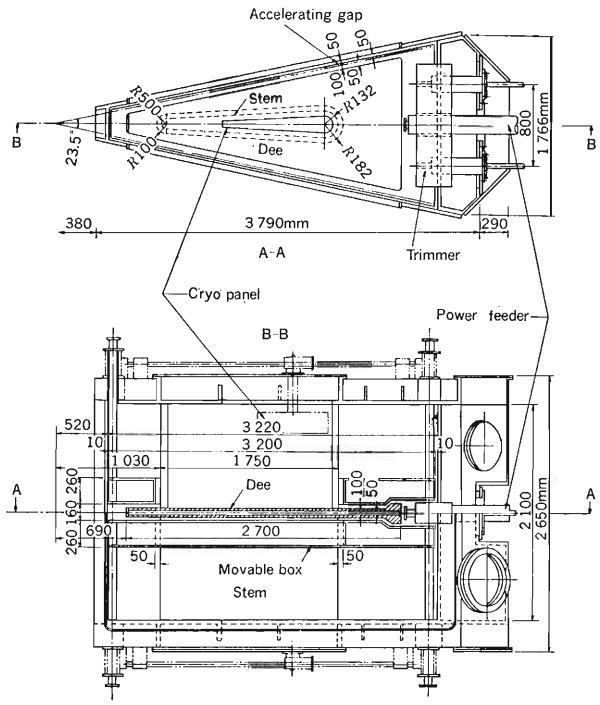

Fig. 6. Cross-sectional view of the actual resonator.

dee voltage was measured with a calibrated voltage pick-up which gave little effect on the resonator characteristics. The power loss was obtained by measuring input RF current, voltage, and their phase on the feeder. The shunt impedance of the actual resonator was estimated by multiplying the model's value by the scale factor of $\sqrt{4}$. Figure 5 shows the shunt impedances and the dee voltage estimated for input power of 250 kW.

The difference between the calculations and measurements in shunt impedance and Q value are not small. However, we consider such disagreements are inevitable in the one-dimensional transmission line approximation because the resonator has complex structure and resistances of many contacts are neglected.

From the satisfactory results of the present model test, we designed a new resonator shown in Fig. 6.

References

1) K. Ogiwara, T. Fujisawa, and Y. Oikawa: *RIKEN Accel. Progr. Rep.*, **17**, 145 (1983).
2) T. Fujisawa: *ibid.*, **15**, 196 (1981).
3) A. Goto, N. Nakanishi, and Y. Yano: 10th Int. Conf. on Cyclotrons, p. 36 (1984).
4) H. Kamitsubo: *ibid.*, p. 257 (1984).
5) L. C. Maier, Jr. and J. C. Slater: *J. Appl. Phys.*, **23**, 68 (1952).

RIKEN Accel. Progr. Rep. 18 (1984)

V-4. RF Power Amplifier for the RIKEN SSC

T. Fujisawa, S. Kohara, K. Ogiwara, and Y. Kumata*

The power amplifier for the RIKEN SSC using an RCA 4648 tetrode has been already designed.[1] The amplifier will satisfy the required performance. However, the amplifier was redesigned with following reasons. Recently we can obtain a new tube RS2042SK whose maximum plate disipation is 300 kW. This tube is inexpensive and is quickly obtainable compared with the 4648. Furthermore, engineers of the factory which is to fabricate the amplifier prefer to use the RS2042SK because it is more convenient to use in a grounded grid configuration than the 4648 which is designed as a grounded cathode tube. The RS2042SK is lately developed by SIEMENS. It has been used for a 300 kW middle wave broadcast transmitter and also used as the last stage of the amplifier of the RFQ linac of GSI. Some pieces of RS2074SK which is a bigger sister tube of RS2042SK are working well as amplifiers for the accelerators at GSI and SIN.[2] The final amplifier was studied on a full-sized model with a real RS2042SK.

Interelectrode capacitances of the RS2042SK were measured and the results are listed in Table 1 together with those given in a catalog. The amplifier is designed based on the measured ones. Figure 1 shows a schematic drawing of the amplifier system. The RS2042SK is used in a grounded grid configuration. The plate circuit is the same as that designed for the 4648.[1] The cathode circuit is a quarter wave length coaxial line having a variable tuning capacitor

Table 1. Interelectrode capacitances of RS2042SK tetrode (pF). $C_{A,G1}$, and $C_{A,K}$ were obtained by measuring voltage transmission ratios from the plate to the grid and cathode. The others were measured with a conventional LCR meter. The information was given by Siemens.

	Measured	Catalogue	Information
$C_{A,G2}$	113.5	75.	100.
$C_{A,G1}$	5.7	5.	4.5
$C_{A,K}$	1.1	1.	1.1
$C_{G1,G2}$	451.	450.	442.
$C_{G2,K}$	37.5	40.	34.
$C_{G1,K}$	315.	280.	318.

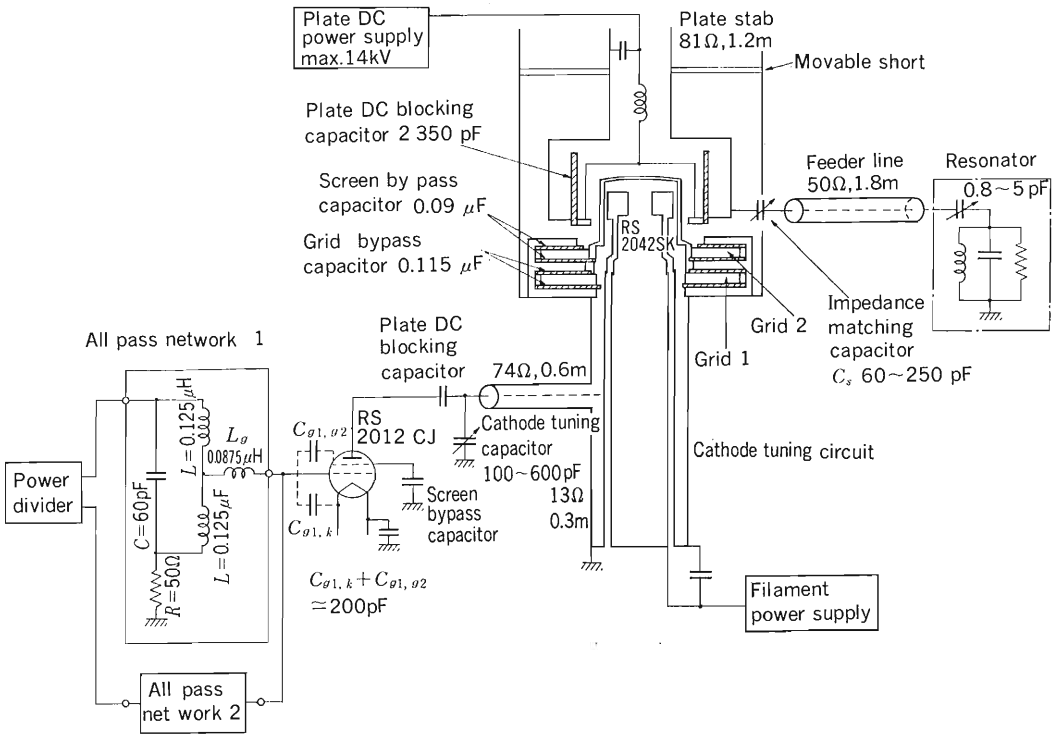

Fig. 1. Schematic drawing of the amplifier for the RIKEN SSC.

* Sumitomo Heavy Industries, Ltd.

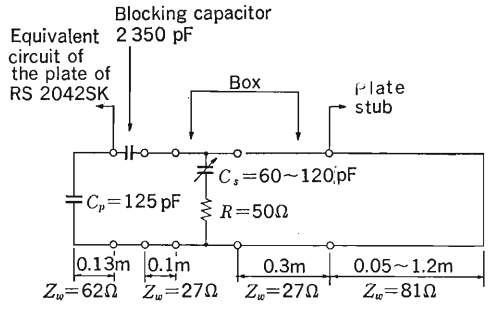

Fig. 2. Equivalent circuit for the plate circuit.

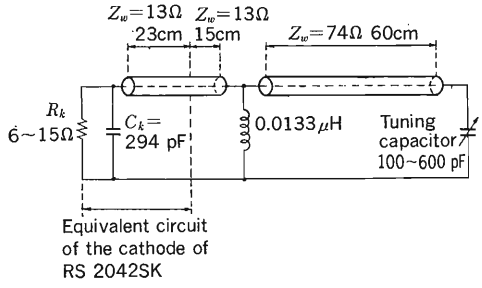

Fig. 3. Equivalent circuit for the cathode circuit.

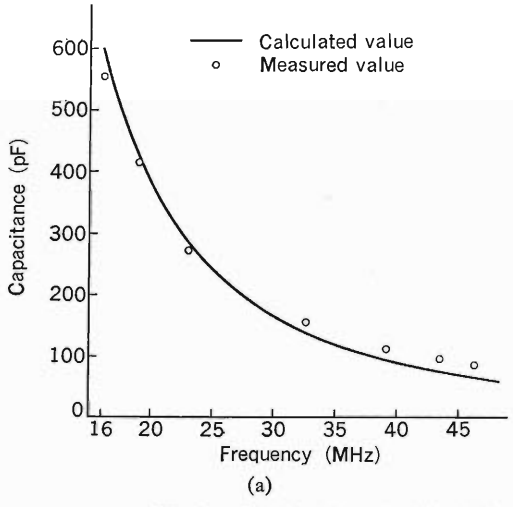

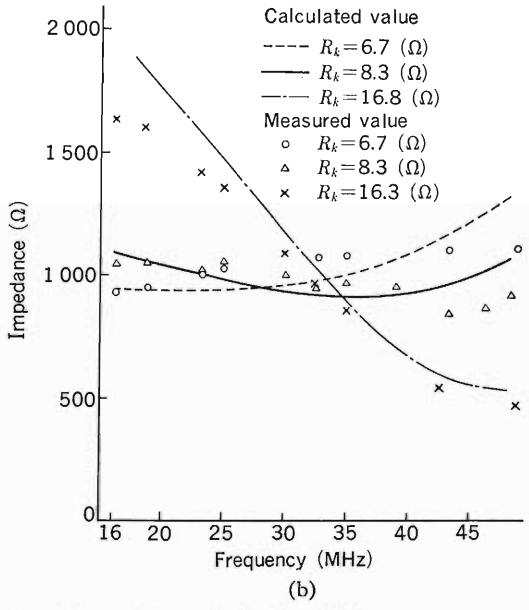

Fig. 4. Tuning characteristics (a) and input impedance of the cathode circuit (b).

(20 to 500 pF). This coaxial line also functions as a filament choke coil. The RS2042SK is driven by a 15 kW driver amplifier. The input circuit of the driver consists of a pair of all pass networks similar to the one developed by Mosko.[3)]

An equivalent circuit of the plate tuning circuit is shown in Fig. 2. The performance of the same circuit for the 4648 has been already presented.[1)] The tuning and matching characteristics were measured on the full-sized model with the real tube. They are in good agreements with the calculations with the equivalent circuit shown in Fig. 2. The stroke of the movable shorting plate is estimated to be 1.2 m to cover a frequency range of 17 to 45 MHz and the range of capacitance of the impedance matching capacitor (C_s) is from 60 to 120 pF to make the load resistance 200 Ω.

The plate DC blocker is a cylindrical capacitor (35 cm height × 35 cm diameter: 2,350 pF) whose insulator is made of Kapton film (125 μm × 16 turns). It was also installed on the model amplifier and its frequency characteristic was measured at frequencies from 17 to 150 MHz. No resonance caused by the blocking capacitor was detected.

The cathode driving voltage was estimated to be about 450 V to deliver the power of 300 kW and the cathode input impedance about 8 Ω. Consequently, driving power of 12 kW is required. The driver tube RS2012CJ can deliver the power of 15 kW for load resistances from 500 to 1,500 Ω, and its optimum load resistance is about 1,000 Ω. The cathode equivalent circuit is shown in Fig. 3. Tuning and impedance matching conditions are investigated on a full sized model mounted on a model tube which is a coaxial line as large as the real tube and has a resistance as a dummy of the cathode resistance. The results are shown in Fig. 4. The lines in Fig. 4 show the calculations with the equivalent circuit shown in Fig. 3. The calculations and measurements are in fairly good agreements. The cathode input resistance varies from about 6 to 15 Ω depending on the cathode RF and grid DC voltages. As you can see in Fig. 4 (b), the input impedance of the cathode circuit is between 500 and 1,600 Ω for frequency range of 17 to 45 MHz even if the cathode resistance changes.

The control and screen grid bypass capacitors have the same structure as shown in a previous

report by the authors.[1] The full sized models were fabricated and installed on the model amplifier with the real tube. The capacitance of the control grid bypass is 115,000 pF and that of the screen 90,000 pF. The voltage transmission ratios from the plate to the grids and cathode were measured in a frequency range of 30 to 48 MHz. They showed almost flat frequency dependence and are about 6×10^{-5} for the control grid, 1.2×10^{-3} for the screen grid and 3×10^{-3} for the cathode. These values are consistent with the interelectrode capacitances.

It was made sure on a model that the all pass network for the input of the driver amplifier worked well in a frequency range of 17 to 45 MHz.

References

1) T. Fujisawa, S. Kohara, T. Ogiwara, Y. Oikawa, and Y. Kumata: *RIKEN Accel. Progr. Rep.*, **17**, 148, 149 (1983); S. Kohara, T. Fujisawa, and Y. Chiba: *ibid.*, p. 152; T. Fujisawa, K. Ogiwara, S. Kohara, Y. Oikawa, I. Yokoyama, M. Hara, I. Takeshita, and Y. Chiba: Proc. 10th Int. Conf. Cyclotron and their Appl. East Lansing, Michigan, U.S.A., p. 311 (1984).
2) G. Hutter: Contribution Paper to Particle Accel. Conf. Santa Fe, New Mexico, U.S.A. (1983); Private communication by A. Nickel at Siemens.
3) S. W. Mosko: *IEEE Trans. Nucl. Sci.*, **NS-24** (3), 1786 (1977).

RIKEN Accel. Progr. Rep. **18** (1984)

V-5. A Method of Measuring Two-Dimensional Motion of the Orbit Center Using Three Radial Differential Probes

Y. Yano and A. Goto

In the SSC, radial differential probes are arranged at three azimuths of sector-edge lines as shown in Fig. 1. A method of measuring the position of the orbit center using these probes has been studied.

We define the valley mid-line and the dee mid-line as x- and y-axes, respectively. The condition for the acceleration equilibrium orbit (AEO) was described in a previous paper[1]; this orbit is depicted in Fig. 2. The radial gain Δr is the difference in radii between the successive AEO's in one turn. The angle a derived from the above condition is given by

$$a=\frac{\Delta r}{4\sin(\pi\nu_r/2)}\left(\frac{rr_o'}{r_o}\right) \tag{1}$$

where r_o (radial displacement) and r_o' (angle) represent the principal axes of the eigen-ellipse at the radius of r on the x-axis and ν_r the corresponding radial focusing frequency. From Fig. 2 the radii of the AEO at each azimuth of probe, P_{e1}–P_{e6}, are given by

$$P_{e1}=\frac{1}{c}(1+zt)\left(r-\frac{1}{4}\Delta r\right)$$

$$\fallingdotseq\frac{1}{c}\left(r-\frac{1}{4}\Delta r\right) \tag{2}$$

$$P_{e2}=\frac{1}{c}(1+zt)\left(r+\frac{3}{4}\Delta r\right)$$

$$\fallingdotseq\frac{1}{c}\left(r+\frac{3}{4}\Delta r\right) \tag{3}$$

$$P_{e3}=\frac{1}{c}(1+at)r\fallingdotseq\frac{1}{c}\left(r+\frac{1}{4}tf\Delta r\right) \tag{4}$$

$$P_{e4}=\frac{1}{c}(1+at)(r+\Delta r)$$

$$\fallingdotseq\frac{1}{c}\left\{r+\left(1+\frac{1}{4}tf\right)\Delta r\right\} \tag{5}$$

$$P_{e5}=\frac{1}{c}(1-at)\left(r+\frac{1}{2}\Delta r\right)$$

$$\fallingdotseq\frac{1}{c}\left\{r+\left(\frac{1}{2}-\frac{1}{4}tf\right)\Delta r\right\} \tag{6}$$

$$P_{e6}=\frac{1}{c}(1-at)\left(r+\frac{3}{2}\Delta r\right)$$

$$\fallingdotseq\frac{1}{c}\left\{r+\left(\frac{3}{2}-\frac{1}{4}tf\right)\Delta r\right\} \tag{7}$$

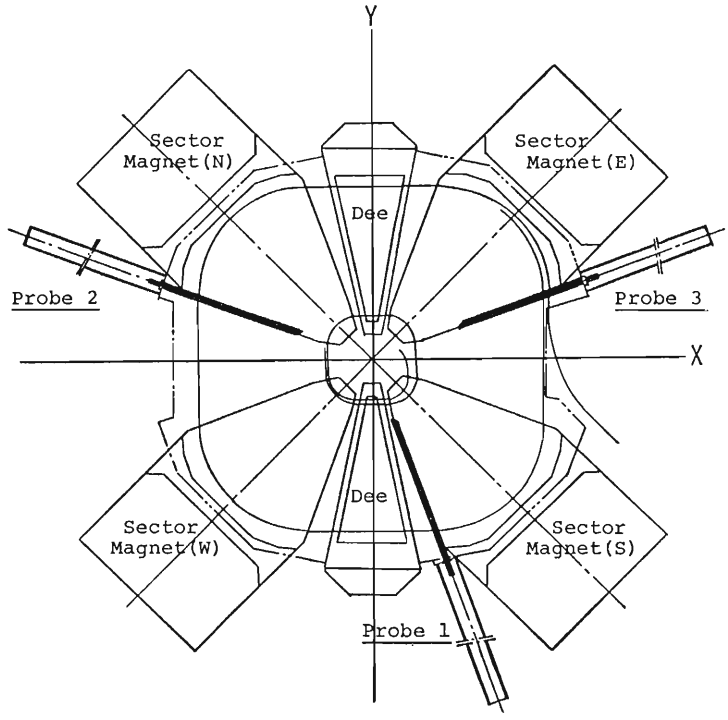

Fig. 1. Arrangement of radial differential probes in the SSC.

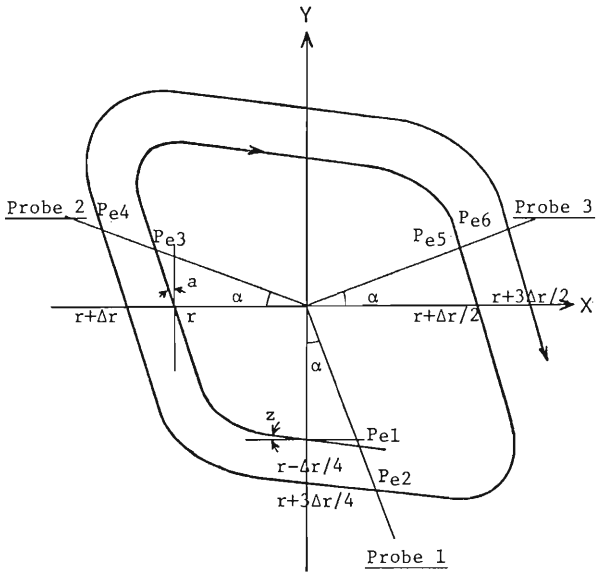

Fig. 2. Acceleration equilibrium orbit (AEO) and configuration of three radial differential probes. In case of our SSC, $\alpha=20°$.

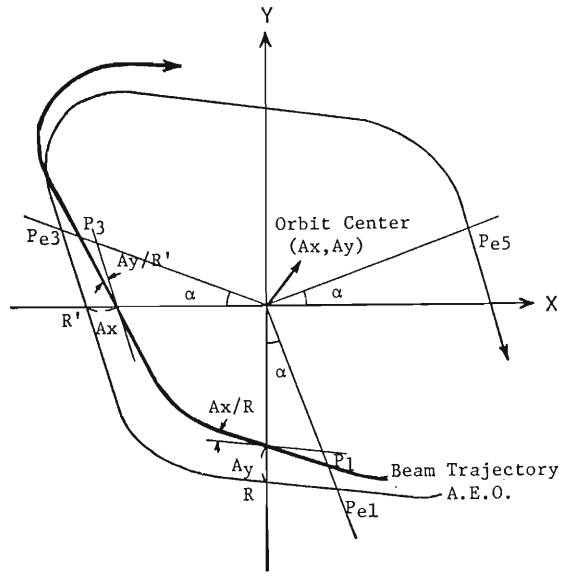

Fig. 3. Beam trajectory with respect to the AEO. The orbit center exists at the coordinate of (A_x, A_y).

where $c=\cos\alpha$, $t=\tan\alpha$,

$$z=a\cdot\cos\left(\frac{\pi}{2}\nu_r\right) \tag{8}$$

and $$f=\frac{1}{\sin(\pi\nu_r/2)}\left(\frac{rr_o'}{r_o}\right) \tag{9}$$

Because the value of z is negligible, it is taken to be null in Eqns. (2) and (3). The term, $(\Delta r)^2$, is also neglected in Eqns. (4)–(7).

The beam trajectory with respect to the AEO is shown in Fig. 3 when the orbit center exists at the coordinate of (A_x, A_y). We neglect the rotation of the orbit center during about $1\frac{1}{2}$ turns. From Fig. 3 the radius (P_1) of the position where the probe 1 catches the beam is given by

$$P_1=P_{e1}+\frac{1}{c}(tA_x-A_y) \tag{10}$$

In the same way,

$$P_2=P_{e2}+\frac{1}{c}(tA_x-A_y) \tag{11}$$

$$P_3=P_{e3}-\frac{1}{c}(A_x-tA_y) \tag{12}$$

$$P_4=P_{e4}-\frac{1}{c}(A_x-tA_y) \tag{13}$$

$$P_5=P_{e5}+\frac{1}{c}(A_x+tA_y) \tag{14}$$

$$P_6=P_{e6}+\frac{1}{c}(A_x+tA_y) \tag{15}$$

From Eqns. (2)–(15) the following relations are obtained.

$$A_x=\frac{1}{8}\cos\alpha\,(P_6+3P_5-3P_4-P_3)+\frac{1}{8}\sin\alpha f\,(P_6-P_5+P_4-P_3) \tag{16}$$

$$A_y=\frac{1}{2}\cdot\frac{1}{1+\tan\alpha}\{2A_x\tan\alpha-\cos\alpha(P_1+P_2-P_3-P_5)\} \tag{17}$$

Reference

1) Y. Yano, A. Goto, and N. Nakanishi: *RIKEN Accel. Progr. Rep.*, **15**, 155 (1981).

RIKEN Accel. Progr. Rep. 18 (1984)

V-6. Acceleration of Off-Centered Beam in the RIKEN SSC

N. Nakanishi, A. Goto, and Y. Yano

For a beam which does not have enough turn spacing in the extraction region, we have some ways to achieve single turn extraction. As one of them, acceleration of an off-centered beam has been examined. The turn separation of the off-centered beam shows an oscillatory pattern because of rotation of the orbit center around the machine center. The radial position of an off-centered particle is given by[1)]

$$R_n = R_c(n, \varphi_{cp}) + A\cos\left\{\Psi_0 - 2\pi\int_0^n (\nu_r(R)-1)dn\right\}$$

where R_c is the radial position at a turn number n of a well-centered particle with a central position phase, φ_{cp}, and A the oscillation amplitude, Ψ_0 is the betatron oscillation phase at an injection point, and ν_r the radial focusing frequency.

In the above equation, the amplitude A is a function of the radial displacement and the angle of the off-centered orbit with respect to the well-centered orbit at the injection point. The integration term depends on the acceleration voltage. Firstly, the values of the radial displacement and the angle were searched to give as large oscillation amplitude as possible under the restriction that the off-centered beam clears all of obstacles like injection elements. Secondly, the acceleration voltage was adjusted so that the maximum turn separation and the optimum angle of the beam can be obtained at the extraction point.

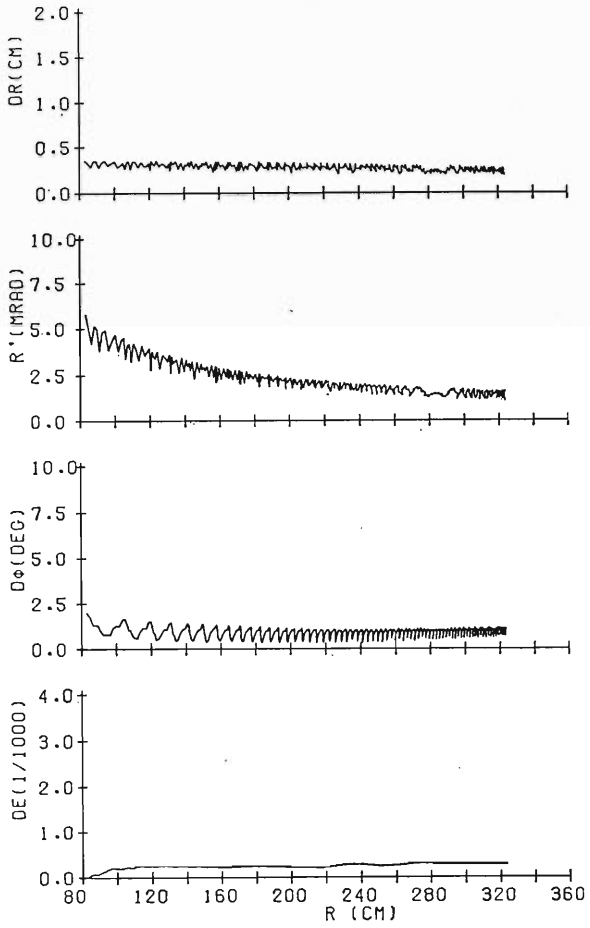

Fig. 1. Variation of beam properties in radial and longitudinal phase spaces for a 9 MeV off-centered proton beam.

Calculation was made for a proton beam of an injection emmitance of 20 mm·mrad. Initial energy spread and central position phase were set to be zero. The vertical component of the rf magnetic

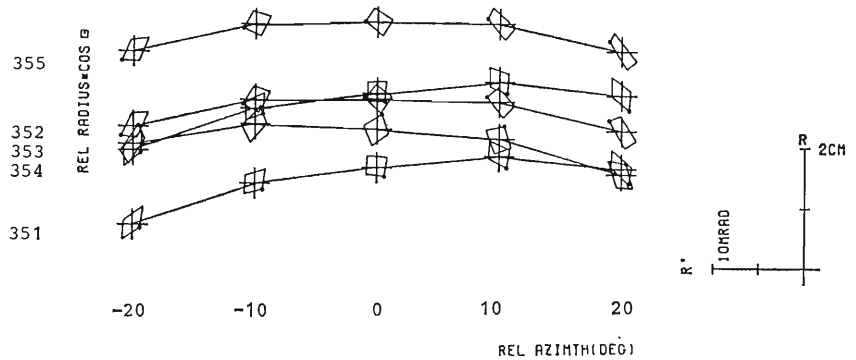

Fig. 2. Radial phase space ellipses in the last five turns. Abscissa is a relative azimuth. The 0 deg. corresponds to a valley center. Ordinate is the product of radius and cosine of a relative azimuth. Numerals at the left show turn numbers.

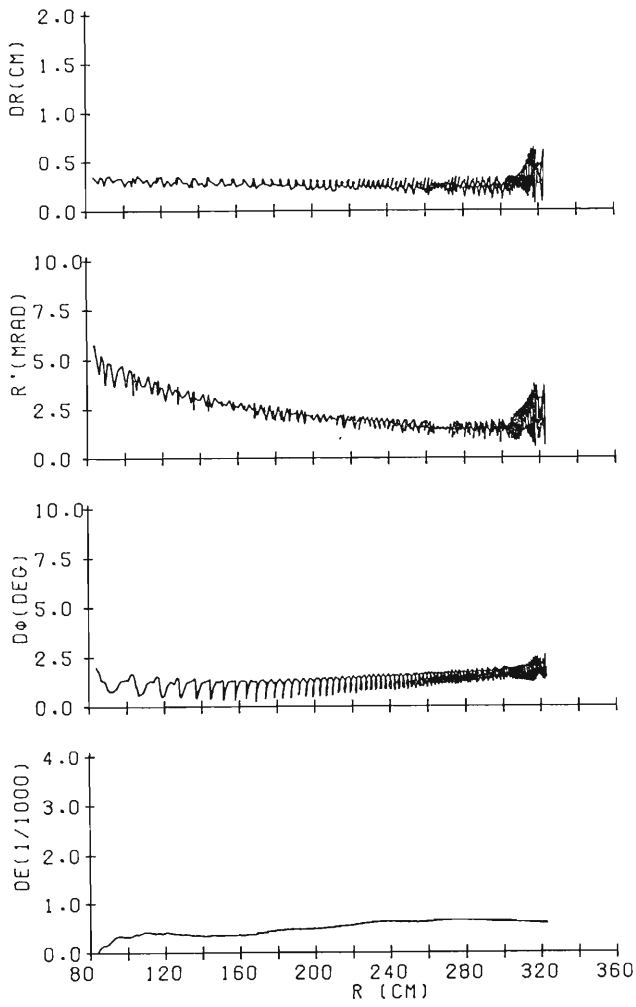

Fig. 3. Variation of beam property in radial and longitudinal phase spaces for a 10 MeV off-centered proton beam. The effect induced by a resonance $\nu_r=4/3$ is observed.

field caused by voltage distribution along accelerating gap was taken into account using distribution measured in a model cavity. Behavior of four parameters in the radial and longitudinal phase spaces is shown in Fig. 1 for the off-centered 9 MeV proton beam. The difference between the well- and off-centered beams was found to be very small except that energy resolution degrades slightly in the off-centered case. In Fig. 2 are shown radial phase ellipses in the last five turns at several azimuthal positions at the extraction region.

The 10 MeV proton beam encounters a resonance of radial focusing frequency $\nu_r=4/3$ at the energy of 188 MeV. It is known that this is a quadratic, nonlinear, and intrinsic resonance. We confirmed that its influence is negligibly small for the well-centered beam. As seen in Fig. 3, on the other hand, it is not so small for the off-centered beam. This is due to the effective extension of a radial beam size. Therefore, this method is not always suitable for the 10 MeV proton beam.

There are many parameter sets to make extraction of the off-centered beam possible. We have to employ the parameter set which does not make beam quality bad.

Reference

1) W. M. Schulte: The Theory of Accelerated Particles in AVF Cyclotrons, thesis, Eindhoven University of Technology (1978).

RIKEN Accel. Progr. Rep. 18 (1984)

V-7. Beam Sharing System for RIKEN SSC

K. Hatanaka, T. Inamura, Y. Yano, K. Yamaguchi, and H. Kamitsubo

The RIKEN heavy-ion linac (RILAC), which is to be used as an injector to the separated-sector cyclotron (SSC), will also supply beams for the experiments using RILAC itself at the same time when SSC is in operation. For such beam sharing between SSC and the experiments using RILAC, a pulsed deflection magnet with a fast rise- and fall-time is designed.

Figure 1 shows the plan view of the beam transport system from RILAC to SSC. A pulsed deflection magnet (DALO) is introduced to deflect beams by an angle of 5.73°. The bending radius is 3 m and the maximum field is 0.26 T. The pole gap is 4 cm, which is sufficiently large compared with the vertical beam size in the magnet. The coil is wound of copper hollow conductor having a cross section of 8.5×8.5 mm^2 with a hole of 4 mm in diameter; the total number of windings is 16. The magnet will be excited with a pulse mode of a rise- and fall-time of 1 ms and a flat-top of longer than 10 ms. Designed values of electrical characteristics are listed in Table 1.

The system consisting of two dipole magnets (DML1 and DML2) and quadrupole magnets (QDL11, QSL12, and QDL13) is a beam shifting section. Beams are achromatized after passing through this system. Four quadrupole magnets (QSJ24–QSJ27) are introduced for matching beam emittance to a succeeding system.

A beam pulsing system by a sinusoidal wave, a pulsed beam chopper, and a mechanical beam chopper are planned to be installed on the beam line as shown in Fig. 1 (SPX22, SPX23, and MCX23). They are useful in obtaining a pulsed beam for TOF or life-time measurements.

An ion-optical calculation of the beam transport system was performed on the basis of the following specifications: (1) maximum magnetic rigidity, $B\rho$, is 0.785 T·m for $^{238}U^{40+}$ at 0.84 MeV/u after passing through a charge stripper; (2) emittance in the transverse phase space is 6π mm·mrad at maximum; (3) energy resolution, $\Delta E/E$, is better than 0.15% at FWHM; and (4) the RF phase width of the beam phase is less than 6°. Beam envelopes throughout the system in the on- and off-midplanes are shown in Fig. 2.

The plan view of the beam handling system leading beams to the experimental areas from SSC is shown in Fig. 3. A numerical calculation of ion optics was reported previously. The system provides the following beam preparation modes: (1) achromatic, double-telescopic transport to every target

Table 1. Designed values of electrical characteristics of a pulsed magnet to share the beam from RILAC.

Maximum current	520 A
Resistance	5.9 mΩ
Inductance	0.48 mH
Direct voltage	3.1 V
$L\frac{dI}{dt}$	250 V
Power	1.6 kW

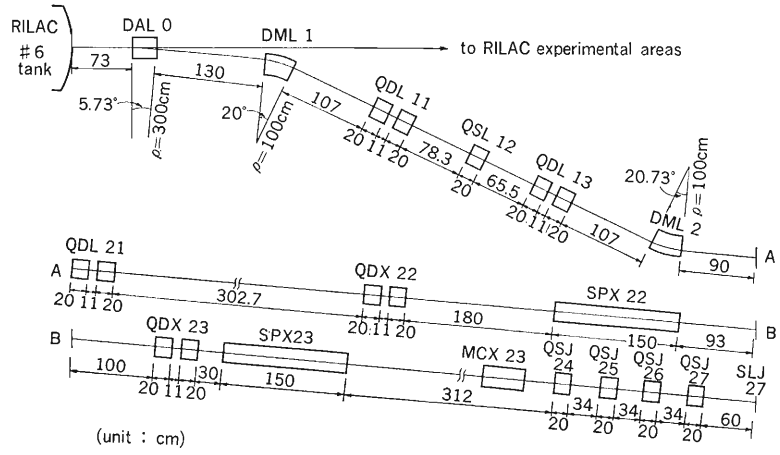

Fig. 1. Plan view of the beam transport system from RILAC to the slit SLJ27.

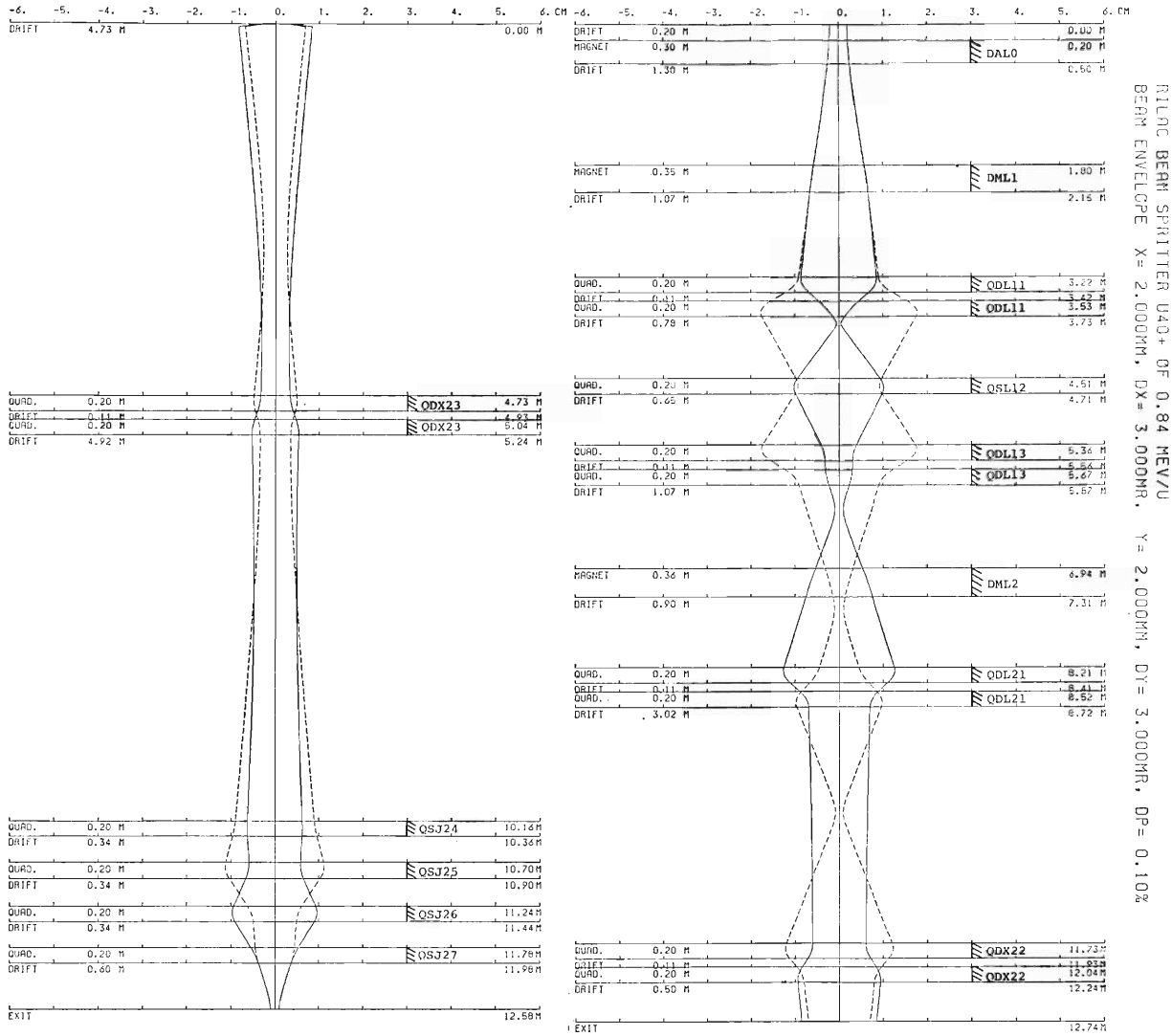

Fig. 2. Beam envelopes through the system from RILAC to the slit SLJ27. Solid and dashed curves show beam envelopes in the on- and off-midplanes, respectively.

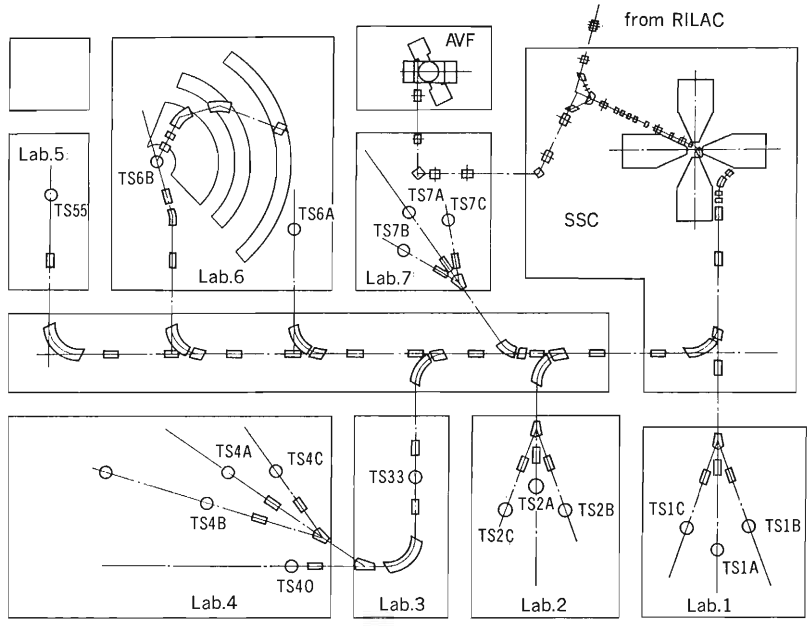

Fig. 3. Plan view of the beam handling system for SSC experimental area.

Table 2. Designed values of electrical characteristics of a 26.5° bending magnet.

Maximum current	500 A
Resistance	60 mΩ
Inductance	160 mH
Direct voltage	30 V
$L\frac{dI}{dt}$	160 V
Power	15 kW

area except for Lab 1; (2) double-dispersive, double-telescopic transport with a momentum resolution up to 25,000 in Labs 2, 3, and 6; and (3) isochronous transport to Labs 4 and 6. A crossed-beam experiment can be performed at the target station TS7A.

Sometimes it will be beneficial for two experimental groups to share the beam. For this purpose, every 90° bending magnet is divided into two pieces as shown in Fig. 3, one of which deflects the beam by 26.5° and the other by 63.5°. It has been confirmed by an ion-optical calculation that the beam conditions obtained from the previous analysis[1] with 90° bending magnets is reproduced satisfactorily by this modified configuration. The dipole magnet which deflects the beam by 26.5° will be operated in a pulse mode, and more than two experimental groups can share the beam. The pole gap is 6 cm. The coil is wound of copper hollow conductor having a cross section of 13×13 mm^2 with a hole of 6 mm in diameter. The total number of windings is 128. It takes 1 s to reach the flat-top and also 1 s to fall down to zero field. The beam is shut off during these transient periods. The flat-top duration will be adjusted according to requirements from experiments. The designed electrical characteristics are listed in Table 2.

Reference

1) T. Inamura, N. Kishida, Y. Hata, and H. Kamitsubo: *Sci. Papers I. P. C. R.*, **77**, 96 (1983).

RIKEN Accel. Progr. Rep. **18** (1984)

V-8. Design of Beam Buncher in the SSC Injection Beam Transport Line

A. Goto, T. Fujisawa, and I. Takeshita

The beam transport line from the RILAC to the SSC has a length of as long as 65 m. Therefore, a beam buncher is indispensable to make beam time-focused at the injection point of the SSC. It was decided from ion-optical calculations that the buncher is placed 37 m downstream from the RILAC. The buncher reduces the pulse width of a beam, for example, from $\pm 6°$ in rf phase at the exit of the RILAC to $\pm 3.6°$ at the injection point of the SSC. Calculations showed that a total voltage required for bunching is 160 kV at the maximum.

The buncher was designed to work with as low power losses as possible and have as small a size as possible. For that purpose, a second harmonic mode with respect to the frequency of RILAC/SSC rf system (20–45 MHz) was adopted. Maximum peak voltage per gap and the separation of gaps can be reduced by a factor of two by this adoption. Furthermore, multi-gap system was taken for further reduction of required voltage. Characteristics of the buncher thus determined are as follows:

Frequency range	40–90 MHz
Harmonics	2
Number of gaps	4
Maximum peak voltage per gap	20 kV
Width of each gap	20 mm
Separation of gaps	156 mm
Aperture of beam transmission	30 mm

Figure 1 shows the schematic drawing of the designed resonator. The resonator is of a $\lambda/4$ coaxial type with a movable shorting plate. In Fig. 2 are shown the tuning characteristics, current density at the movable shorting plate, and total power losses that were calculated by using the transmission line approximation. The maximum power loss was estimated to be smaller than 500 W. Current density is kept less than 20 A/cm. A sliding contact for the shorting plate will necessitate no special technique. Stroke of the shorting plate is about 1 m.

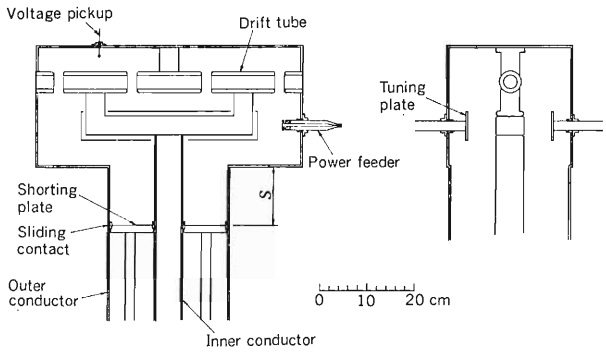

Fig. 1. Schematic drawing of a model buncher.

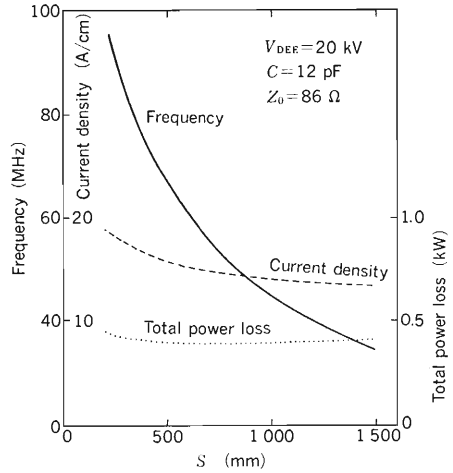

Fig. 2. Calculation of electrical characteristics of a model buncher. Parameter S is a distance between the shorting plate and the neck of the outer conductor as shown in Fig. 1.

A model of the buncher is now under fabrication to verify the calculation. Detailed design of the buncher and the selection of a wide-band power amplifier will be made after the measurement of electrical characteristics of the model.

RIKEN Accel. Progr. Rep. **18** (1984)

V-9. Control System of the RIKEN SSC

T. Wada, J. Fujita, K. Shimizu, I. Yokoyama,
T. Kambara, and H. Kamitsubo

RIKEN SSC is controlled with a computer system. The control system consists of a computer network and a CAMAC serial loop. Micro processors are used for the interface between devices and the CAMAC system.

Figure 1 shows the network system. Three minicomputers are linked by using duplex optical fiber cables at a transmission rate of 15.36 Mbps. Each computer is of the same type, and is MELCOM 350-60/500 (M 60). The characteristics of this computer and the configuration of peripheral devices were reported previously.[1] One of the three computers was installed in the SSC vault in August, 1984. A CAMAC serial highway driver (SHD) was installed in November. Figure 2 is the photograph of this computer and Fig. 3 shows the configuration.

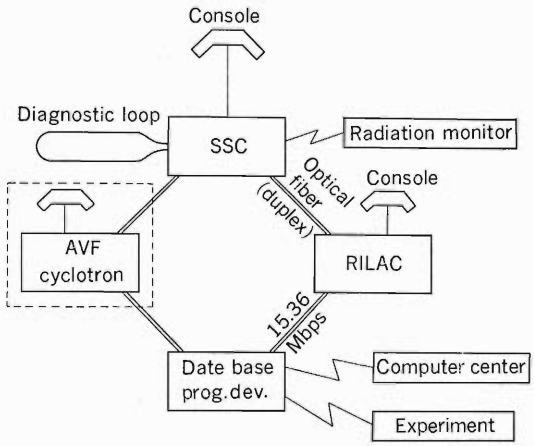

Fig. 1. Network system.

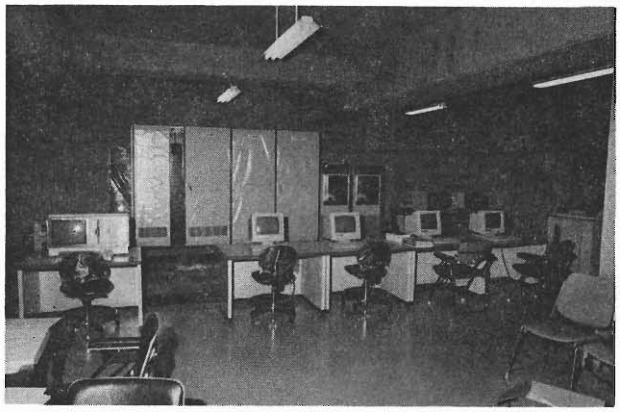

Fig. 2. Photograph of the present MELCOM 350-60/500 computer.

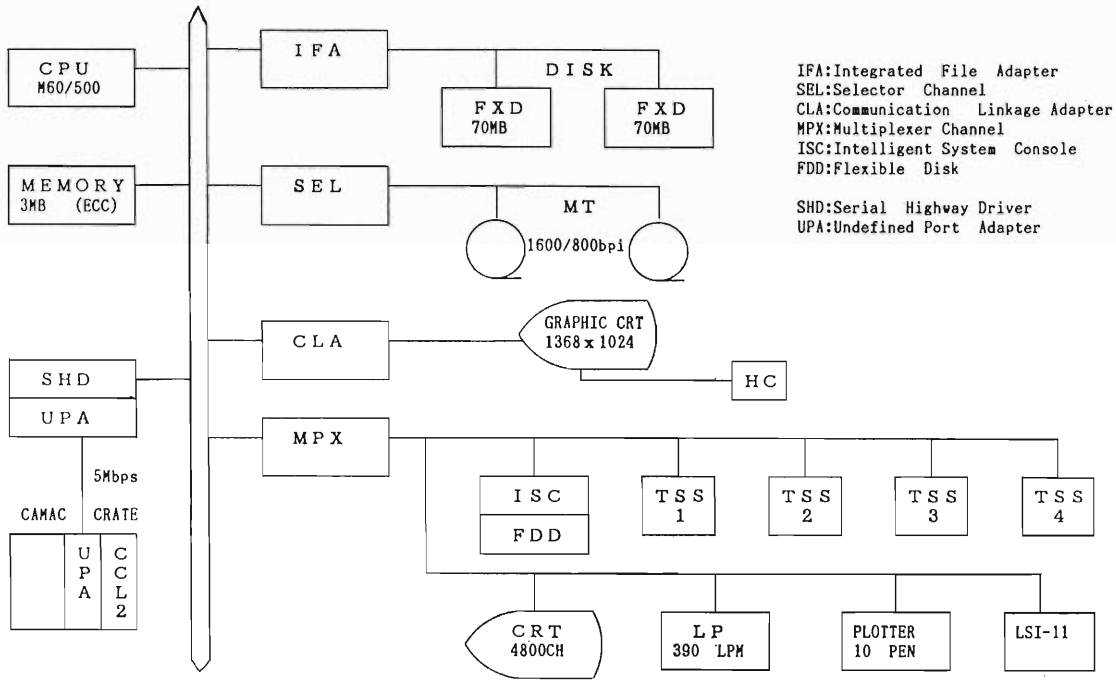

Fig. 3. Configuration of the present computer system.

Two disk units are supplied, which are of a fixed head type because of reliability. As was mentioned previously,[1] the operating system OS60/UMX is a combination of real time and UNIX systems. One of the two disk units stores OS60 files and the other UNIX files. The color graphic CRT is used for the display of magnetic field distribution, beam profiles, *etc.* The color character CRT is used for the display of synoptic diagrams of various systems. Four TSS terminals can be used in a UNIX system for program development. One of them (#1) can also be used in an OS60 system. The line printer can print out capital and small letters because the small letters are frequently used in the UNIX system. A micro computer LSI-11/02 is linked to the M60 computer by an RS-232C cable at a transmission rate of 9,600 bps. The programs and data are transmitted using this link. Five CIM's and fifteen DIM's is fabricated[2] in October, 1984. Each DIM are installed in each box of the power supply for the main and trim coils.

This computer system has been working well without trouble during four months. The development of many application programs and data base for the control are in progress in the UNIX system. The UNIX system is very convenient for the program development. The developed programs are transfered to OS60 files and are tested in real time operation. A disadvantage of this dual operating system may be the fact that we must remember two kinds of operational commands. The programs of micro processors in CIM and DIM are developed using a micro processor developing system.

The magnetic field measurement will start in December, 1984. The programs for the measurement in the LSI-11 computer which were used in 1982[3] are converted to the M60 computer. Almost all devices are controlled through the CAMAC system. A digital volt meter and a scanner which measure the voltages of HALL probes have to be linked to a computer by GP-IB. A GP-IB module of CAMAC is developed[4] because the installation of GP-IB interface of M60 is scheduled in October, 1985.

References

1) T. Wada, J. Fujita, K. Shimizu, I. Yokoyama, and T. Kambara: 5th Symposium on Accelerator Science and Technology, Tsukuba, Japan (1984).
2) K. Shimizu, M. Nagase, and I. Takeshita: *ibid.*
3) H. Takebe, I. Takeshita, J. Fujita, I. Yokoyama, T. Wada, S. Motonaga, and T. Sato: *RIKEN Accel. Progr. Rep.*, **16**, 188 (1982).
4) J. Fujita: p. 187 in this report.

RIKEN Accel. Progr. Rep. 18 (1984)

V-10. An Intelligent CAMAC GP-IB Controller Module

J. Fujita

A CAMAC module with intelligence and GP-IB function is developed and its outlines are described.

(1) Purpose

The main purpose is to decrease overhead of a host computer on short protocols repeated frequently during message and data communication from GP-IB devices. The module is designed based on the following requisites. A large quantity of data can be transfered rapidly at a time. The module receives messages or character strings from the host, translates them, executes a sereis of GP-IB functions and stores data generated by devices on a GP-IB bus without intervention of the host.

(2) Hardware

A block diagram of the module is shown in Fig. 1. The circuit consists of three portions. The first is a basic and intelligent portion which forms a single microcomputer board. It consists of a MC6800 microprocessor, two PROMs (4 KB+4 KB), two RAMs (2 KB +8 KB), a MC6850 serial port, and a MC6821 parallel port. One of PROMs is for a monitor software and another is dedicated for GP-IB functions. A small RAM is used as a working area of the monitor and a large one for temporary storage of collected data on the GP-IB bus and at the same time for loading test programs. The MC6850 port is connected to a cassette tape recorder and used for loading and saving test programs. The MC6821 port is used for a console of the microcomputer.

The second is a portion of the GP-IB interface which consists of a TEXAS INSTRUMENTS TMS9914A GP-IB adapter chip supported by the greater part of IEEE488 GP-IB standard and two GP-IB bus interface IC chips. The TMS9914A chip selected by an address decoder circuit on the microprocessor bus behaves as a bus controller on the instrument bus.

The third is a portion of the interface with a CAMAC dataway and storage of data collected on the instrument bus. Here are two memories of 768 and 12 K bytes both of which are composed of six IC chips. They are accessed in an 8 bits byte mode from the microcomputer and in a 24 bits word mode from the CAMAC dataway side. They are continuously addressed in the dataway, but not in the microcomputer since there is no memory range corresponding to its addressed signals (address lines A1=1, A0=1). A routine of software solves periodical absence of the address and can virtually continue address manipulation on sacrifice of their access time.

(3) Software

The host computer can check the states of two memories by reading half-byte status information through READ lines on the dataway. The last three bytes of the 12 KB memory give error conditions occuring at statement syntax or handshake on the GP-IB bus and count number of collected data in

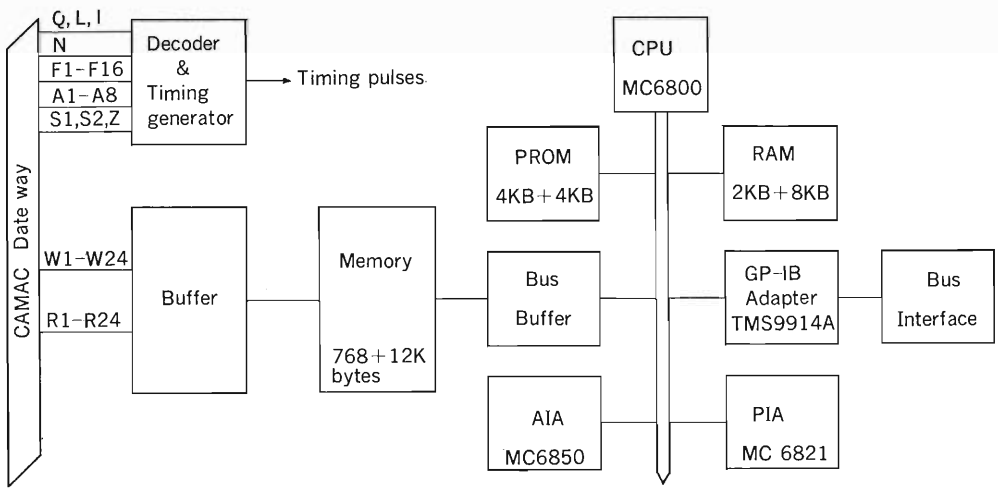

Fig. 1. Block diagram of an intelligent CAMAC GP-IB controller.

sixteen bits binary number.

The host computer writes a message of an ASCII string with hexadecimal codes into a 768 bytes memory. The message is a chain of statements which begin with one of the following six alphabets, T, I, D, W, R, and B, accompanied by definite codes and ASCII data after them and end with a colon. These alphabets show abbreviated commands in the microcomputer.

Statements have the following formats and meanings. A small letter *n* is an integer value from 1 to 255.

T*n* (. . .):	shows *n* times repetition of the statement within brackets.
D*n*:	delay time intervals of $n \times 0.1$ sec.
I:	resets the TMS9914A chip and the GP-IB bus.
W*n* ". . .":	writes ASCII data enclosed by quotation marks to a device number *n* on the bus.
R*n*:	reads data from the device number *n* into the module.
B*n* ". . .":	is a concatenation of W and R or equivalent to a statement W*n* ". . .": R*n*:.

A message from CAMAC dataway is executed while being resolved into any of above statements in the same manner as a BASIC interpreter. If a statement begins with a character other than above six ones or is told in a false format, error flag is set at bit-0 of error status byte mentioned above. Time out error on the GP-IB handshake is also indicated by bit-1 or bit-2 of the same byte. When a R or B statement is executed, collected data count number is set in binary number at two bytes succeeding to the error status byte.

(4) Test results

Tests are performed by using a DEC LSI-11 microcomputer and a Perkin Elmer 3220 minicomputer. The GP-IB module is connected to two GP-IB instruments, a 2204A scanner and a 8502A digital voltmeter of FLUKE. Messages and data are delivered correctly between the 3220 minicomputer and the module in a Stop or Repeat mode of block transfer modes described in the IEEE standard 583.

For example, following messages are transmitted from the LSI-11 to the module where decimal numbers after T, B, D, and W are given in hexadecimal codes. Device addresses of the scanner and the digital voltmeter are 3 and 1, respectively.

1) I: B1 "VR": W3 "0,":
2) T20 (B1 "?": W3 "+": D 10:):

The first statement sets the digital voltmeter to the measurement of DC voltage in an auto-range mode and the scanner at a channel number 0. The next one causes the voltmeter to measure a voltage of an object and transmit the reading data of a fourteen byte size into the module through the GP-IB adapter, and then the scanner to advance one channel and the module to wait for a second. The sequence is repeated twenty times and data of total 280 bytes are stored in the 8 KB memory.

The module works properly, but the following points should be improved in hardware and software. They are (1) to add a LAM circuit to the CAMAC interface portion in order to report Message Accepted or Data Ready states of the memories to the host computer and (2) to use an interrupt line of the MC6800 microprocessor and make known Message Ready or Data Accepted states of the memories, and (3) to develop a software extended by those processes.

RIKEN Accel. Progr. Rep. **18** (1984)

V-11. Method of Sealing Vacuum Chambers and Pumping Control System for the SSC

K. Ikegami, S. Nakajima, Y. Oikawa, and S. H. Be

The final design of the vacuum chamber[1] was fixed and the chambers are now under fabrication in a factory. A vacuum test for four magnet chambers will be done in September, 1985. Design of the pumping control system for the SSC is in progress.

In January, 1984, a method of sealing by using a pneumatic expansion seal[2] for the chambers was changed to that by using a side flange with a welded bellows. The welded bellows is shaped like a race-track and its size is about $3{,}000 \times 30$ mm. Figure 1 shows a cross sectional view of the side flange with welded bellows between the magnet chamber and the RF chamber. The side flange with the welded bellows is fixed to the magnet chamber and is pressed with bolts tightly to the RF chamber. A similar method is also employed between the magnet chamber and the valley chamber.

The magent chamber is surrounded with additional chambers in which pole pieces made of mild steel and trim coils flash-coated with a thin alumina layer are placed, because of a high outgassing rate expected from them. The additional chamber is partitioned by a thin stainless-steel plate of 4 mm in thickness from the high vacuum chamber and is evacuated to a pressure below 10^{-1} Torr. This partition wall may be deformed when the pressure difference between the additional chamber and the high vacuum chamber becomes higher than one tenth of atmospheric pressure and collapsed perfectly under atmospheric pressure. To prevent the partition wall from collapse a safety valve to be mounted between two chambers was developed. Figure 2 shows a model of the safety valve. The characteristics of this valve are shown in Fig. 3. A moving plate of the valve is pressed to a valve seat by a weight in the moving housing. An operating pressure difference is determined by a number of the weights put in the moving housing. Thus, the valve begins to operate above the pressure difference in the range of 8–50 Torr.

Control of pumping system

The pumping system described in a previous RIKEN Accel. Report[3] is operated automatically with a programable controller which is made by SUMITOMO SCC-1000 having an I/O port of max. 1,024 points according to a predetermined

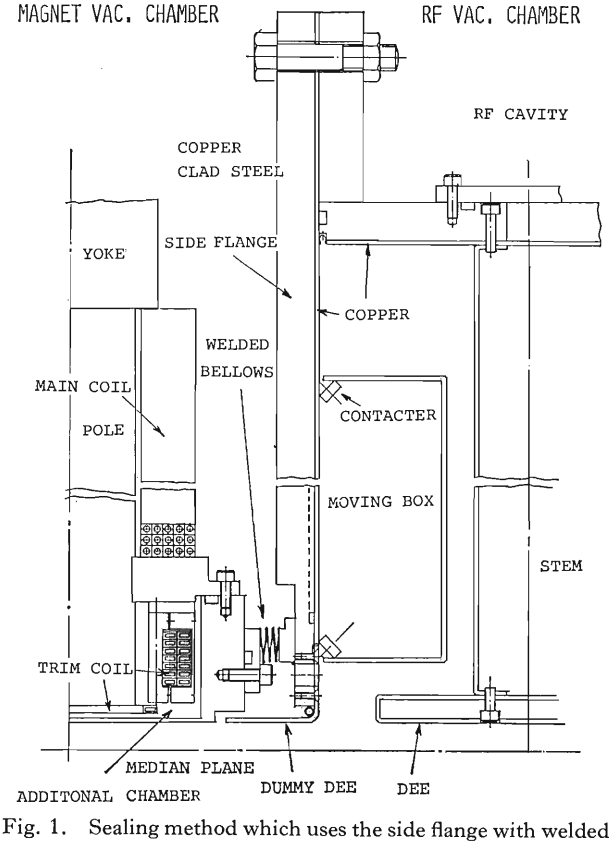

Fig. 1. Sealing method which uses the side flange with welded bellows between magnet and RF chamber.

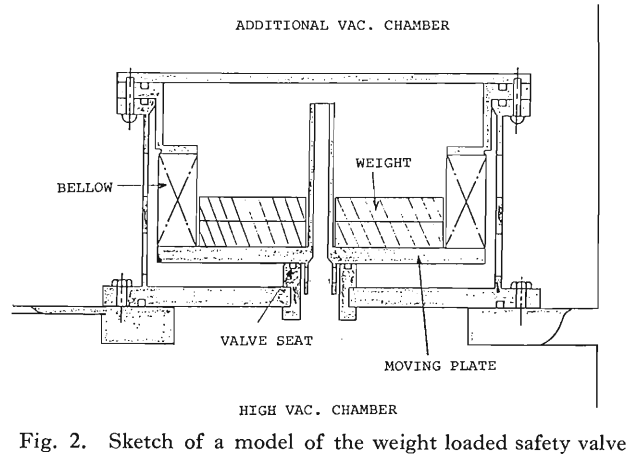

Fig. 2. Sketch of a model of the weight loaded safety valve equipped between high vacuum chamber and the additional chamber. The valve seat is pressed by the weight in the moving housing; elasticity of the welded bellows does not play an essential role, because the elastic strength is usually decreased slightly with time.

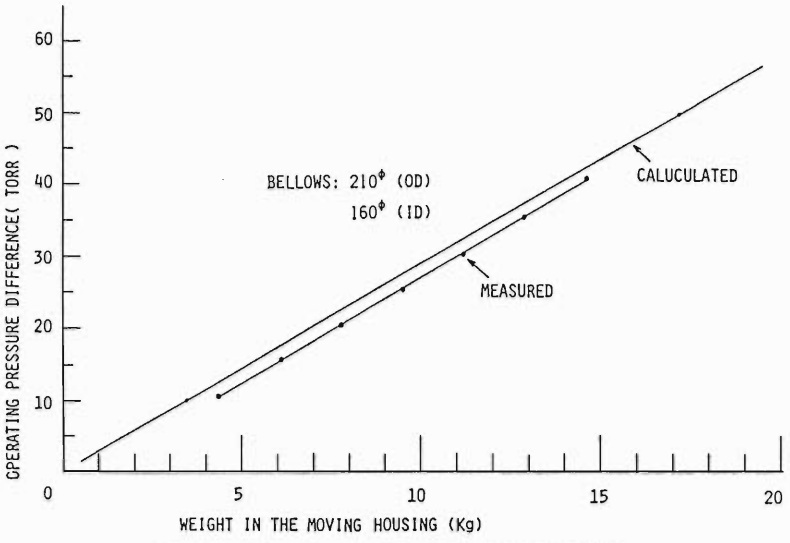

Fig. 3. The characteristics of the safety valve.

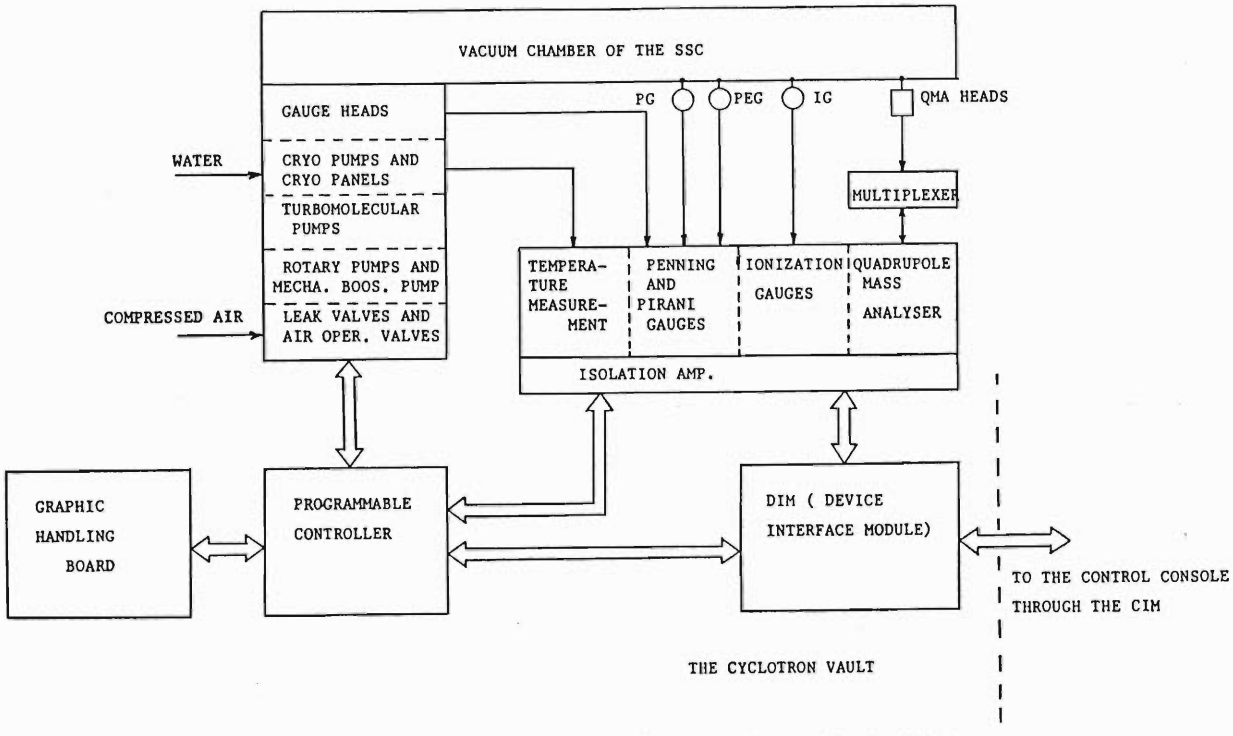

Fig. 4. Block diagram of the pumping control system for the SSC.

sequence. The following conditions are included in programing of the controller.

(1) Evacuation from atmospheric pressure to (pressures of the order of) 10^{-8} Torr.
(2) Protection of the chamber and pumps from vacuum failure and electrical failure.
(3) Stopping the pumping system and admitting dry N_2 gas into the chamber from (pressures of the order of) 10^{-8} Torr to the atmospheric pressure.
(4) Regeneration of cryopumps and cryopanels.

Figure 4 shows a block diagram of the pumping control system. On the graphic handling board which is placed in the cyclotron vault, both mannual and automatic operation is possible.

For the automatic operation of the pumping system, vacuum gauges such as Pirani gauges (32 gauge heads), Penning gauges (8 gauge heads), and ionization gauges (4 gauge heads) are planned to be used for the system. In addition, for observation of residual gases in the vacuum chamber and detection of leaks from gasket seals, and welded parts, and so on of the chamber, a quadrupole mass analyzer having four heads through multiplexer is equipped to each RF and valley chamber. Information of the pumping system is sent through DIM (Device

Interface Module)[4] and CIM (CAMAC Interface Module) to the central control console.

References

1) K. Ikegami, S. Nakajima, Y. Oikawa, and I. Takeshita: *RIKEN Accel. Progr. Rep.*, **15**, 200 (1981).
2) K. Ikegami, S. Nakajima, Y. Oikawa, S. Motonaga, and H. Kamitsubo: *Sci. Papers I. P. C. R.*, **77**, 87 (1982).
3) K. Ikegami, S. Nakajima, S. H. Be, I. Takeshita, Y. Oikawa, and S. Motonaga: *RIKEN Accel. Progr. Rep.*, **17**, 156 (1983).
4) K. Shimizu, T. Wada, J. Fujita, and I. Yokoyama: Proc. Int. Conf. Cyclotron and Their Application, Michigan (1984).

RIKEN Accel. Progr. Rep. 18 (1984)

V-12. Performance Test in Cryopump

S. Nakajima, K. Ikegami, Y. Oikawa, and S. H. Be

As a main vacuum pump for the SSC vacuum chamber, a cryopump with a large pumping speed and large refrigeration capacity may be useful. The cryopump which functions by condensation and adsorption of gas on the cold panel cooled at about 10 K can evacuate virtually all kinds of gas to the ultra high vacuum region. We plan to use ten cryopumps with a pumping speed of 10^4 1/sec (N_2) and four cryopanels of 5×10^3 1/sec (N_2) for obtaining ultimate pressure of 10^{-8} Torr in the SSC vacuum chamber. In this report, we present preliminary experimental results on the characteristics of the cryopump with a special emphasis on regeneration of low temperature cryopanel coated with activated charcoal. The regeneration interval depends on the pumping capacity for hydrogen molecules and decides the operational interval of the SSC.

Tests were carried out with a 4×10^3 1/sec (N_2) ANELVA cryopump. Figure 1 shows time-dependent variation of temperature and pressure for the cryopump. Temperature was measured on the second stage cryopanel with a platinum resistance thermometer and pressure was measured at an inlet of the cryopump with an ionization gauge. The panel temperature reaches 70 K for 65 min and 10 K for 80 min. Final pressure in each test run seems to vary owing to the previous history of the vacuum system. Generally, the time required to reach 10^{-6} Torr is about 100 min, namely after about 20 min the cryopanel was completely cooled down. Figure 2 shows temperature rise of the cryopanel and pressure rise in the chamber as a function of time. As seen from Fig. 2, the temperature rises rapidly at first and then slowly to reach room temperature. As the temperature of the cryopanel rises, the pressure begins to rise at first and then drops. Soon it rises again but drops after a while. It rises once more and finally reaches an almost saturated value after about 15 hr. A partial pressure was measured at the same time with a quadrupole mass analyzer (Q.M.A.). The result is shown in Fig. 3. From these two results, we conclude that the first peak is due to hydrogen and the second due to nitrogen. The peak above 160 K is due mainly to water.

A comparative study was made on regeneration of the cryopump by admitting dry nitrogen gas into the pump; the results are shown in Fig. 4. The purge of the chamber was done after shut down of the pump. As seen from Fig. 4, the time required for regeneration of the cryopump is shortened by gas purge. The quantity of absorbed water on the inner wall of the chamber is also reduced by purging. Thus, it makes evacuation easier.

Pumping speeds for hydrogen and nitrogen were also measured. The results are shown in Fig. 5. The obtained value is about 2.3×10^3 1/sec for

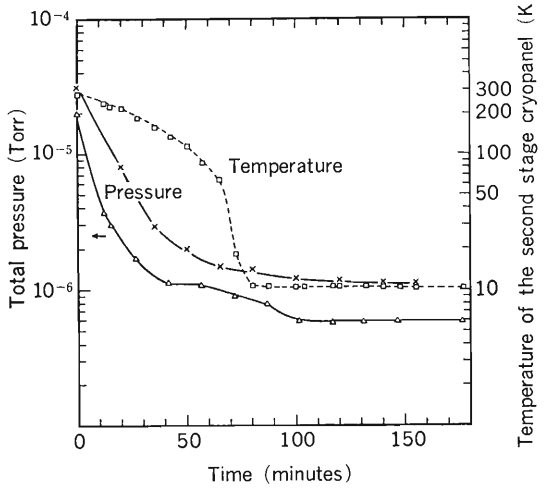

Fig. 1. Time dependent variation of temperature and pressure for the cryopump.

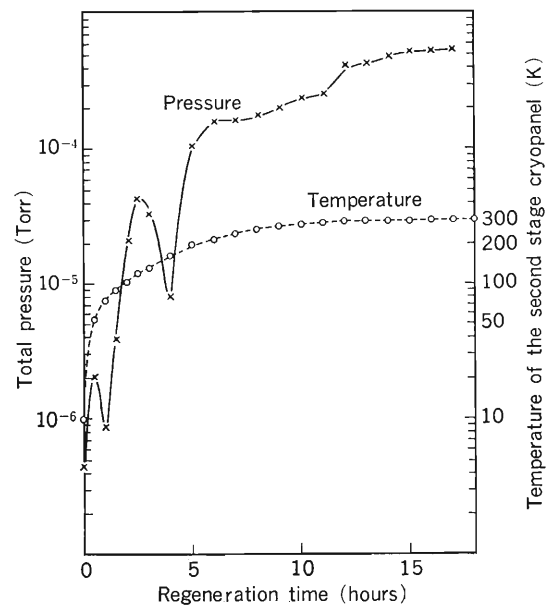

Fig. 2. Temperature rise of the cryopanel as a function of time and a pressure rise in the chamber after the refrigerator was switched off.

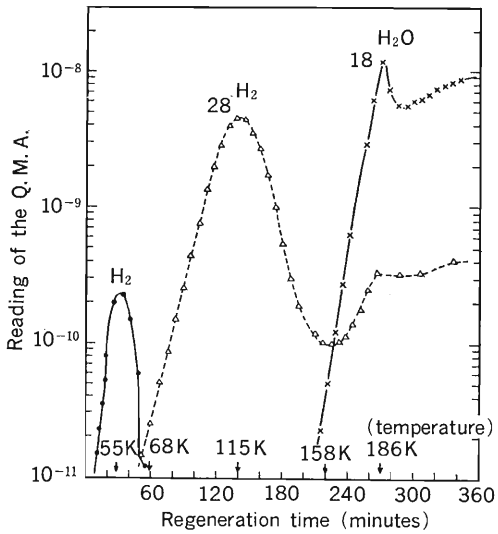

Fig. 3. Partial pressure curves during regeneration.

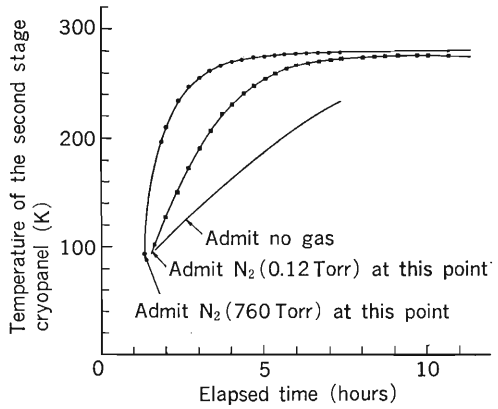

Fig. 4. Comparison between the experiments for regeneration of the cryopump with and without admitting dry nitrogen gas into the pump.

either case. Since a cryosorption capacity of charcoal for hydrogen is considered to affect the regeneration of the cryopump, hydrogen gas was admitted into the pump at a constant flow rate and the variation of pumping speed was observed. This result is shown in Fig. 6, which indicates that the pumping speed began to decrease and the pressure began to increase after about 66 hr. The total hydrogen admitted for 66 hr is estimated to be 2.7×10^3 Torr·*l*, which means that a pumping capacity for hydrogen gas is

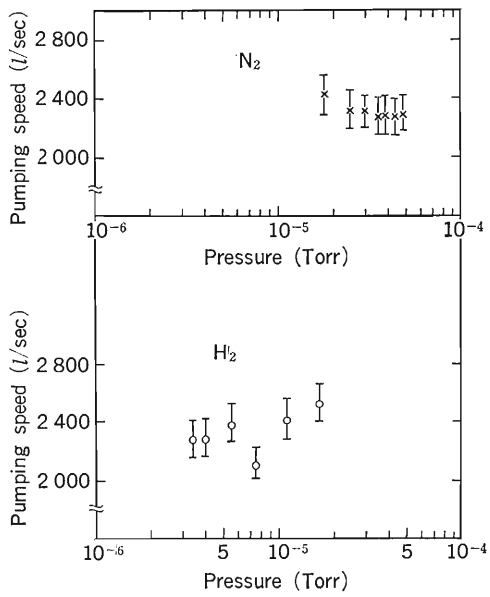

Fig. 5. Pumping speeds for hydrogen gas and nitrogen gas measured at several equilibrium pressures.

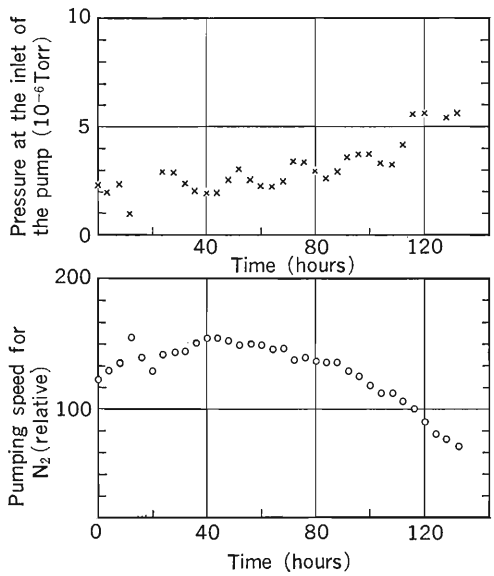

Fig. 6. Variation of pumping speed and pressure with time when hydrogen gas was admitted at a constant flow rate.

40 Torr·*l* per 1 g charcoal. No trouble was observed in the cryopump during 4,000 hr operation at 10^{-8} Torr.

RIKEN Accel. Progr. Rep. 18 (1984)

V-13. Calculation for the Design of a Beam Dump

N. Nakanishi, T. Shikata, S. Fujita, and T. Kosako*

In a previous report,[1] the design of a beam dump was made rather roughly, because cross section data were not available in the energy range appropriate to the RIKEN SSC at that time. Recently the neutron-photon multigroup cross section in an ANISN format for neutron energies from thermal to 400 MeV has become available, and the calculation using the ANISN code has been made to obtain diagrams which are used for determination of the configuration of beam dumps.

Neutrons to be shielded are assumed to be generated by reactions of (1) 200 MeV protons with a thick aluminum target and (2) 135 MeV/u carbon ions with a thick iron target. In both cases the beam intensity is assumed to be 6×10^{12} ions/sec as before.[2] These reactions are abbreviated as (p+Al) and (C+Fe), respectively.

To begin with, we calculated the dose attenuation and the energy spectra of neutrons for several shielding materials. Considering these results, we took several kinds of beam dumps composed of different materials and carried out the transport calculation. The most desirable structure has been proved to be a shell structure of iron surrounded by a heavy concrete layer.

The design calculation of the beam dump in a forward direction relative to ion beams was performed using the (p+Al) source and those for other directions were carried out using the (C+Fe) source, because the (p+Al) source has more pronounced forward-peaking characteristics than the (C+Fe) source. An essential part of the cyclotron building and allowable dose rates around the beam dump are shown in Fig. 1.

Geometries employed in the calculation and the results are shown in Figs. 2–5. For the forward direction, if the beam dump is designed so as to

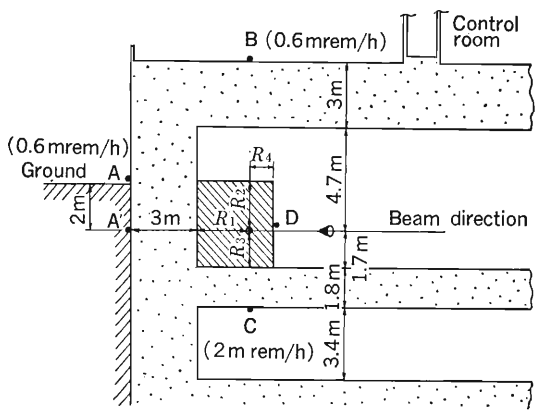

Fig. 1. A longitudinal sectional view of the building around a beam dump and allowable dose rates at several points.

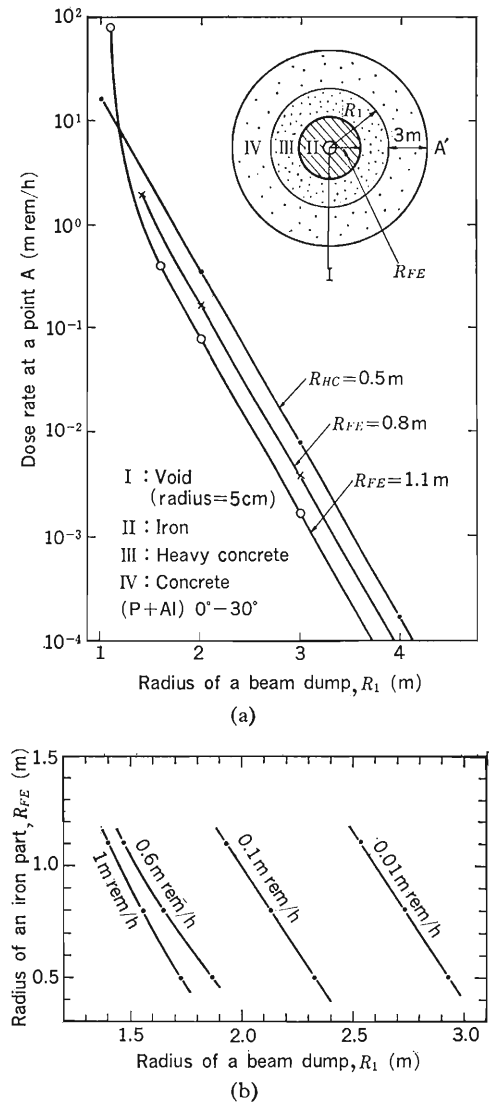

Fig. 2. Result of the design calculation for the forward direction: (a) Geometry employed in the calculation using ANISN code, and the dose rate at a point A′ as a function of the radius of the beam dump (sum of radial thickness of iron and heavy concrete parts). (b) Effect of thickness of each component of the iron-heavy concrete beam dump.

* Research Center for Nuclear Science and Technology, The University of Tokyo.

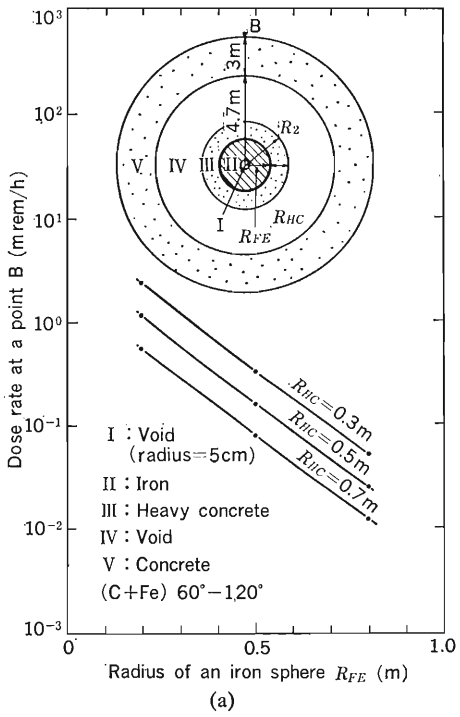

(a)

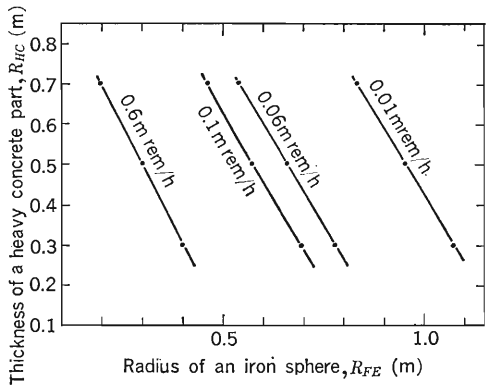

(b)

Fig. 3. Result for the upward direction. (a) Geometry and dose rate at a point B. (b) Effect of thickness.

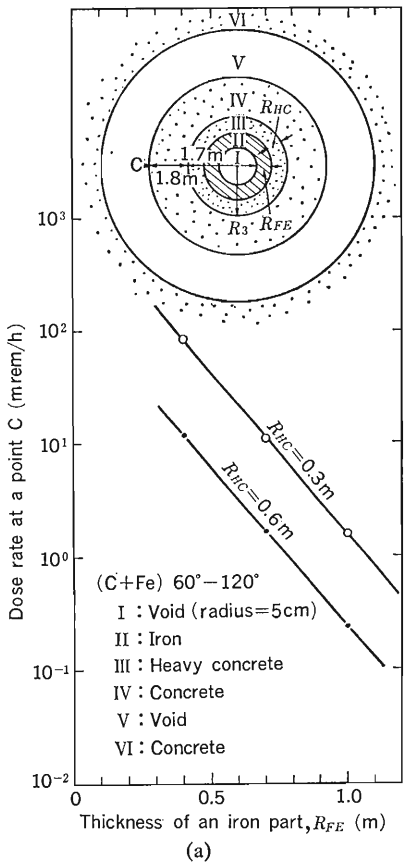

(a)

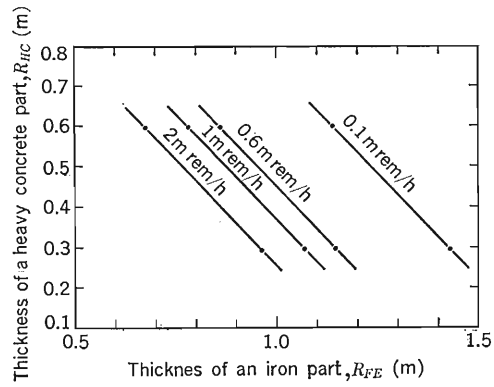

(b)

Fig. 4. Result for the downward direction. (a) Geometry and dose rate at a point C. (b) Effect of thickness.

suppress the dose rate at A′ below the allowable level, the dose rate at A will be safely below the tolerance level. The calculated result is shown in Fig. 2 (a). The dose rate at the surface of the outermost concrete shell is given as a function of the radius of the beam dump (sum of radial thicknesses of iron and heavy concrete parts). Figure 2 (a) is also expressed like Fig. 2 (b). One can choose an arbitrary combination of each thickness of iron and heavy-concrete parts at a given dose rate. Similarly, geometries employed in the calculation and the results for different directions are shown in Figs. 3–5. The relation shown in Fig. 4 is also useful for the design of sideward shielding. In the design for the backward direction, if the dose at the surface of the beam dump is less than about 3 rem/h, neutron doses in neighboring rooms will be safely below the tolerance level. There exists, however, a problem to minimize the leakage neutrons through the entrance of the beam dump not only for health hazard but also for radiation background in experimental equipments. This problem is to be solved in the near future together with those of the activation and the heat generation in the beam dump.

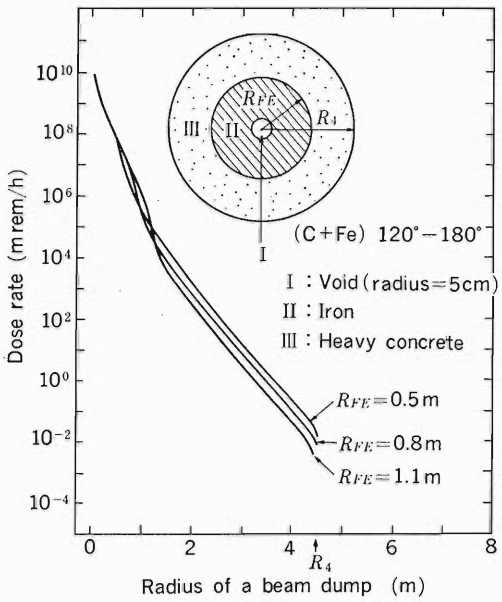

Fig. 5. Dose attenuation by transport calculation of neutrons upon passage through an iron-heavy concrete beam dump in the backward direction.

References

1) T. Shikata, T. Kosako, S. Fujita, S. Yamaji, and H. Kamitsubo: *Sci. Papers I. P. C. R.*, **77**, 99 (1982).
2) S. Fujita, S. Yamaji, and T. Shikata: *IPCR Cyclotron Progr. Rep.*, **14**, 203 (1980).

RIKEN Accel. Progr. Rep. **18** (1984)

V-14. Beam Attenuation Device

Y. Miyazawa, M. Hemmi, T. Chiba, and M. Kase

The new beam attenuation device, installed in a beam line between the linac and injector, is capable of controlling beam intensity onto a target over a wide range by a ratio between 1 to10^{-4}. Figure 1 shows inside structure of the device. Three attenuation plates (attenuator) are mounted on three of four holes in a disk made of chrome-copper alloy. Since the disk itself is made to form a gear wheel, the attenuation plates can be correctly positioned by a motor via a rack and pinion. Two such disks are used in tandem to obtain large change in attenuation ratio specified above. The size of device was reduced by use of a magnetic fluid vacuum seal between the disks in a vacuum and the motor in atomosphere. The disk rotates at about 1/3 rps. As shown in Fig. 2, the attenuator plate has a lot of small holes perforated by chemical etching. In the table below Fig. 2, ϕ is a diameter of small hole, p is a distance between small holes in mm, and n is the ratio of the area of the plate to the perforated area which defines the attenuation power of the plate. Table 1 shows the beam attenuation ratios for various combinations of the two attenuators. Heat generated by beam loss in the attenuator is removed into air by conduction through the disk and vacuum flange made of crome-copper alloy having a good heat conductivity. The disk driving circuit[1] is shown in Fig. 3. The angular position of the disk is converted into electric signal voltage by use of a multi-turn potentiometer, and its signal is fed to a window comparator (I_{C102}) through a buffer-amplifier with a low-pass filter. The position signal is compared with the reference signal by the comparator. Four reference voltages

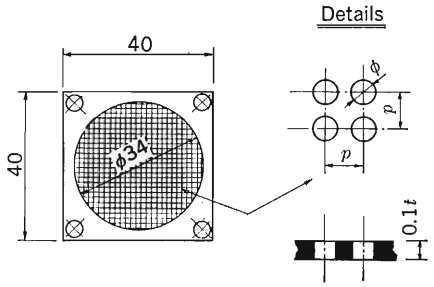

Type	ϕ	p	n
A	0.5	0.66	2.2
B	0.1	0.19	4.6
C	0.1	0.42	22
D	0.1	0.61	47
E	0.1	0.89	100

Fig. 2. Parameters of the attenuator.

Table 1. Beam attenuation ratio for various combination of the positions of the two disks.

		Position of disk **I**			
		0	**1**(D)	**2**(C)	**3**(E)
Position of disk **II**	**0**	0	4.7	22	100
	1(A)	2.2	10	48	220
	2(D)	47	220	1,000	4,700
	3(E)	100	470	2,200	10,000

The words in the brackets present a type of attenuator.

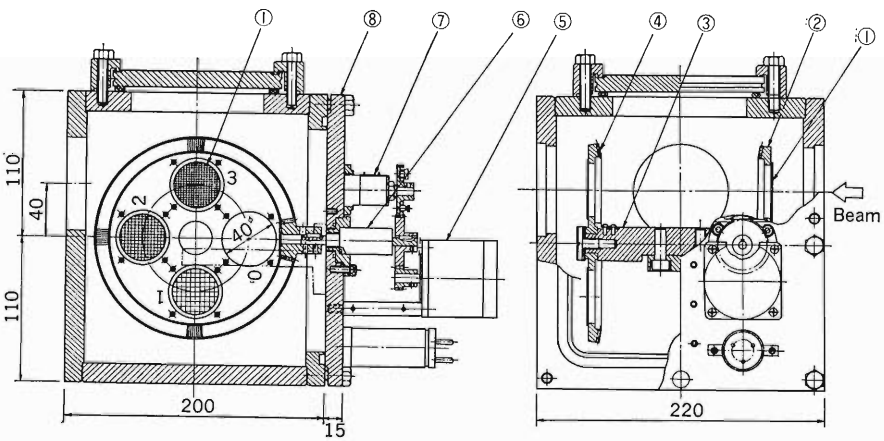

Fig. 1. A beam attenuation device. 1, Attenuation plate; 2, First disk; 3, Disk shaft (copper); 4, Second disk; 5, Synchronous motor (60 rpm); 6, Magnetic fluid vacuum seal; 7, Multi-turn potentiometer; 8, Vacuum flange (chrome-copper alloy).

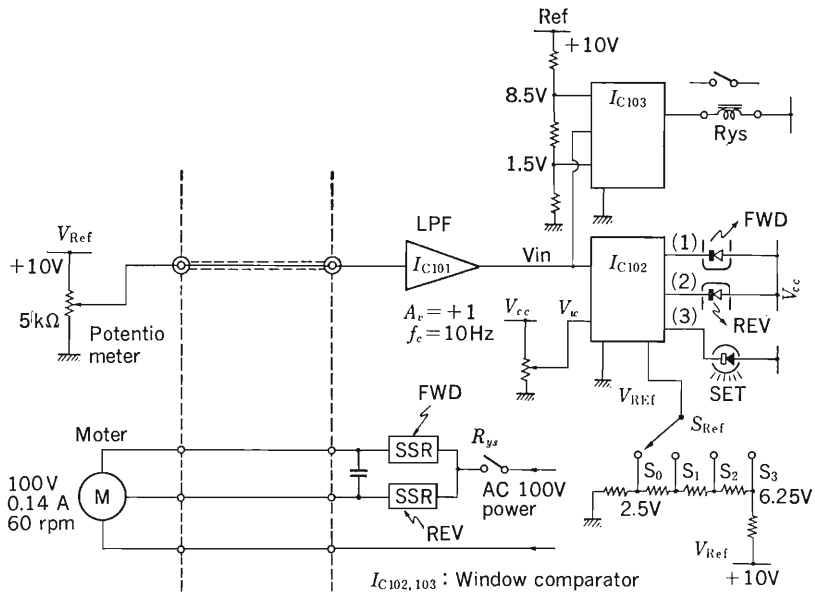

Fig. 3. Disk driving circuit.

given by S_{ref} correspond to the four angular position of the disk. When the switch is turned on, the synchronous motor drives the disks automatically and stops when the voltage of the potentiometer coincides with the reference voltage. The accuracy in setting the disk can be made higher by choosing a narrower voltage window for comparison. But if the window voltage is made too small, the disk runs over the narrow width of the reference position because of its mechanical inertia, and begins to oscillate back and forth around the specified position. Therefore, the synchronous motor having a small inertia was used in order to reduce the overshooting of the disk. At present, the setting accuracy of the disks at four reference points is less than $\pm$ 1 mm giving a large margin to make the beam go through the two successive holes without hitting the attenuator holders.

Reference

1) M. Hemmi: Wheel driving circuit, private communication.

RIKEN Accel. Progr. Rep. 18 (1984)

V-15. Emittance Monitor

M. Kase, I. Takeshita, and I. Yokoyama

A prototype of the emittance measuring device, which will be used in the SSC injection beam transport line, has been built and installed in the RILAC beam line.

The measurement method is the same as that described in Ref. 1. The device is composed of two main sections: the detector and the actuator.

The detector has a slit and a multi-wire profile monitor. The specifications of the detector is listed in Table 1. The thirty-two gold-plated tungsten wires of the profile monitor are fixed on the Macor mount with melted glass. Figure 1 shows a photograph of the profile monitor.

The actuator supports the detector and moves it by a stroke of 100 mm with a 1.8° stepping motor and ball screw. The position of an origin is detected by a photo-switch. The relative position from the origin is measured by counting the signals from a rotary pulse encoder. The resolution of position is 0.02 mm and the position reproducibility is less than 0.1 mm.

A pair of emittance measuring devices are installed in a vacuum chamber, one is set horizontally and used for the measurement of horizontal emittance and the other is set vertically and used for that of vertical emittance. Figures 2 and 3 show the photo-

Table 1. The technical specifications of the detecting system.

Slit	Width	0.1 mm
	Length	30 mm
	Material	molybdenum
Profile monitor	Material of wire	gold-plated tungsten
	Material of insulator	Macor
	Number of wires	32
	Diameter of wire	0.1 mm
	Length of sensitive region	35 mm
	Pitch of wires	0.35 mm
Distance between slit and detector		300 mm
Angular range		±18 mrad
Angular resolution		±1.2 mrad

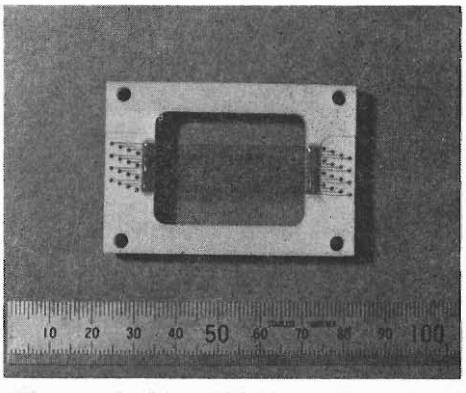

Fig. 1. Photograph of the multi-wire profile monitor. Thirty-two tungsten wires are strung on the insulator mount.

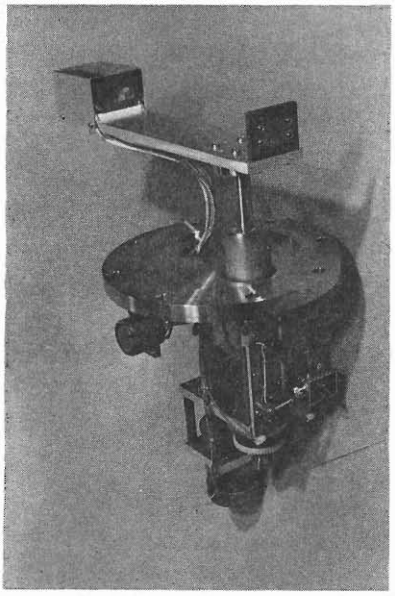

Fig. 2. Photograph of the emittance measuring device.

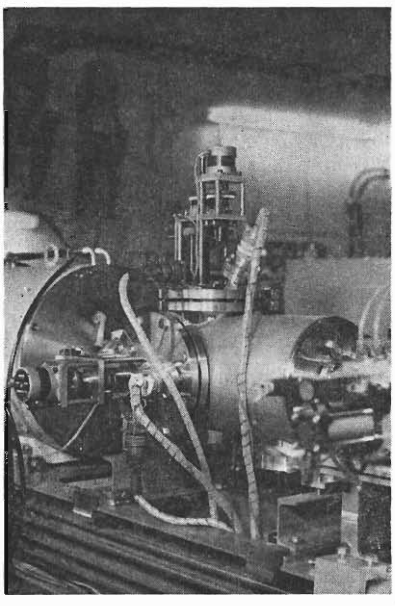

Fig. 3. Full view of the emittance monitor installed at the RILAC beam line.

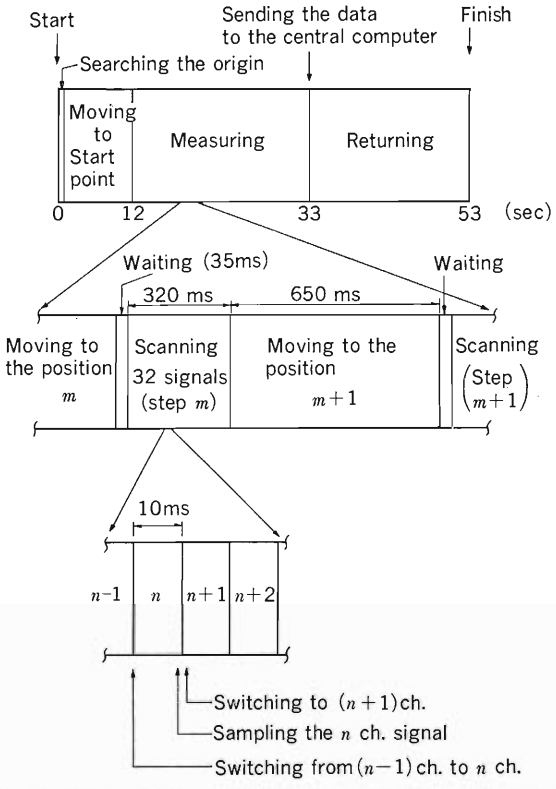

Fig. 4. Time chart of the emittance measuring processes.

graphs of the device.

The electronic control circuit is fundamentally the same as that in Ref. 1. Unlike the previous circuit two 16-ch multiplexers with MOS analogue switches are used for scanning the 32 input signals directly from wires. The leak current of the switch is less than 0.1 nA. The sampling time has to be delayed by 10 ms after switching to a new channel in order to damp a switching noise current. Therefore the time required for scanning the whole channels is 320 ms. It takes 33 s to obtain the one-axis emittance data after making a "start" command at the console in the control desk. Further 20 s is needed for the detector to return to the stand-by position. The time chart of all the processes of the emittance measurement is shown in Fig. 4.

When the dc amplifier is inserted in the input stage of the multiplexer for each channel and the low current signals are converted to voltage signals, the scanning time of the multiplexer for the 32 ch signals can be reduced to 30 ms. Furthermore if the position setting within 0.05 mm is allowed, the speed of the actuator can be set at a higher rate. Finally the time required to get the emittance data for one axis after the start command is expected to be as short as 15 s.

Reference

1) I. Yokoyama, M. Kase, and T. Kambara: *RIKEN Accel. Progr. Rep.*, **15**, 141 (1981).

RIKEN Accel. Progr. Rep. **18** (1984)

V-16. Charge Exchange Technique in the Linac

M. Yanokura

It is well known that the charge states of high energy heavy ions are varied by passing the ions through thin foil or gas stripper. By use of this phenomenon, we can obtain ions in various charge states; this is an useful technique in atomic physics.[1] We plan to apply the technique to the linac operation in order to obtain ions of higher charge states and to save power consumption of the linac as well.

The linac functions as a velocity filter. At a fixed acceleration frequency, the velocity of an accelerated ion is not dependent on its charge state, but the accelerating voltage is in inverse ratio to the charge state when an ion is specified. It means that, if we accelerate ions in the higher charge states, we can use lower voltage and save RF power for acceleration.

The linac composed of six resonators has many beam diagnosis boxes which are set at every inter-resonator position and downstream of the No. 6 resonator. By use of those boxes a stripper can be set at any position and ions are stripped at various energies. We choose thin carbon-foil of 10 $\mu g/cm^2$ as a stripping material. A simple foil changer which fit in the beam diagnosis box was fabricated at the machine shop of the institute; a sketch of the foil changer is shown in Fig. 1. A maximum foil diameter is 20 mm and 3 foils can be set on it. The position of the foil is adjustable by using a bellow and a screw mechanism. Results of the test operation using this device are shown below.

Ar^{4+} ions were accelerated to 42 MeV by using No. 1–4 resonators and were passed through carbon-foil. A lower part of Fig. 2 shows charge distribution of Ar ions thus obtained. Analysis was made by using a switching (SW) magnet. The most probable charge state of Ar ions measured is 12+ at 42 MeV. An upper part of Fig. 2 shows the same charge distribution, when the RF power was fed into the No. 5 resonator and tuned for acceleration of 12+. Ar^{12+} ions were accelerated to 50.6 MeV. This energy was measured by the analyzing magnet which is set downstream of the SW magnet. Acceleration voltage of No. 5 resonator was nearly 1/3 of that for Ar^{4+} acceleration. Some of other charge state ions were also accelerated by No. 5 resonator, but the energy gain per charge for those ions was less than that of Ar^{12+} ions.

Figure 3 shows another charge distribution spectrum of Ar ions measured under following conditions. RF power was fed into all resonators except No. 6, and the stripper was set between No. 2 and No. 3 resonators. Energy of Ar beam at the stripper was about 22 MeV, and the most probable charge state of the outcoming ions is Ar^{10+}.[2] In subsequent acceleration, only 10+ ion was accelerated efficiently, because a long accelerating path functions as a velocity selector. We obtained a 51 MeV Ar^{10+} beam of 20 neA, when Ar^{4+} ions of 200 neA were injected into the linac. About 4% of the injected Ar particles were accelerated in this operation. On the other hand, total electric power consumption was about 20% of that for Ar^{4+} acceleration without stripping. The charge stripping technique is useful to save electric power though tuning of the linac becomes complex little bit.

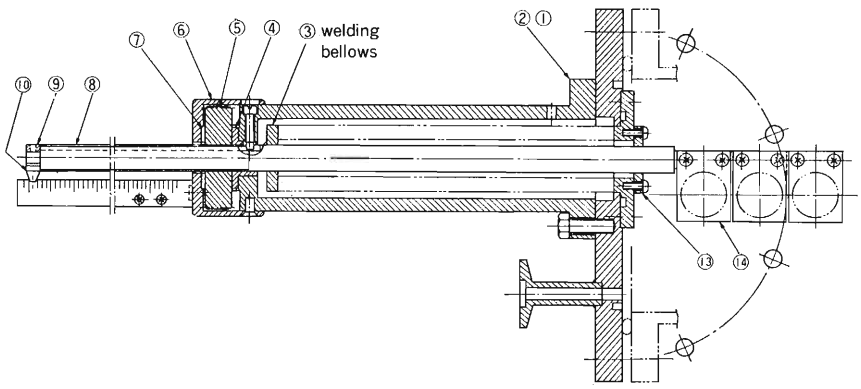

Fig. 1. Simple foil changer.

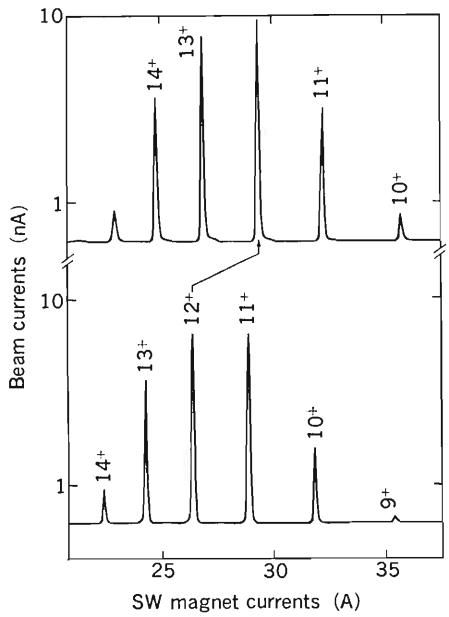

Fig. 2. Acceleration of Ar^{12+} to 50.6 MeV by the linac. 40 MeV Ar^{4+} passed through carbon-foil and changed its charge state from 4+ to 12+. The abscissa is excitation current of the SW magnet.

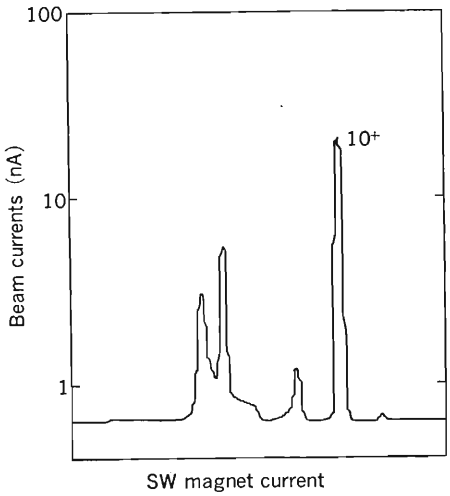

Fig. 3. Acceleration of Ar^{10+} to 51 MeV. 20 MeV Ar^{4+} changed its charge state to 10+ by a foil stripper.

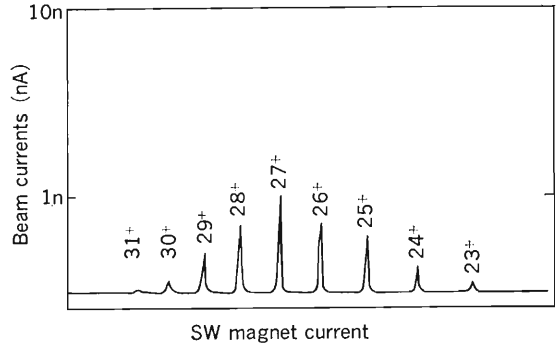

Fig. 4. Charge distribution of 108 MeV Xe ions.

Finally, Fig. 4 shows charge distribution of Xe ions, when 108 MeV Xe^{9+} ions were passed through a carbon foil; many charge states from 23+ to 31+ were formed. The stripper was set between No. 6 resonator and the SW magnet. Xe ions were not accelerated after stripping.

Charge stripping at the upstream positions is more favorable than at the downstream positions for saving power. However, subsequent tuning of the linac takes more time when the stripper is set upstream position. A best position must be determined by weighing those factors. Continuous use for about 20 days did not cause radiation damage of the foil. The longevity of the foil may be due to following two reasons. One is that energy of ions are rather high and, therefore, its energy loss in the foil is very small, 0.5 MeV for 40 MeV Ar. The other is that the beam shape of the linac is adjusted to about 10 mm square at the stripper; therefore the energy loss is spread in a wider area than for the strippers in the terminal of a tandem Van de Graaff accelerator. The resulting little energy transfer provides little damage for the foil.

References

1) Y. Baudinet-Robinet: *Phys. Rev. A*, **26**, 62 (1982).
2) T. Tonuma: *J. Phys. B: Atomic Molecular Physics*, **17**, 317 (1984).

RIKEN Accel. Progr. Rep. **18** (1984)

V-17. Design of a Rebuncher in RILAC

M. Kase and M. Odera

Figure 1 shows the calculations of longitudinal phase oscillation at RILAC from the buncher in the injection beam line to the final resonator tank (cavity #6). All the parameters affecting these oscillations are set according to the synchronous condition around −25 deg. The buncher rf voltage is

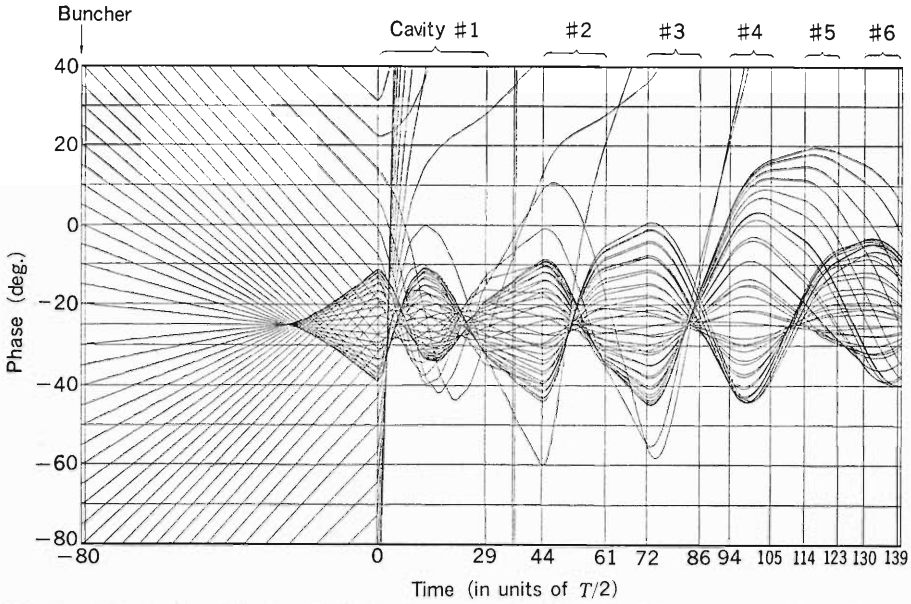

Fig. 1. Calculation of the longitudinal phase traces in RILAC. The vertical axis is a phase on rf voltage and horizontal one is time expressed in units of $T/2$ (T is period of rf) and $t=0$ when beam reaches at the first gap of the first resonator tank. The curves represent the phase history of particles injected at phases from −130 to 130 with 5 deg. steps into the buncher.

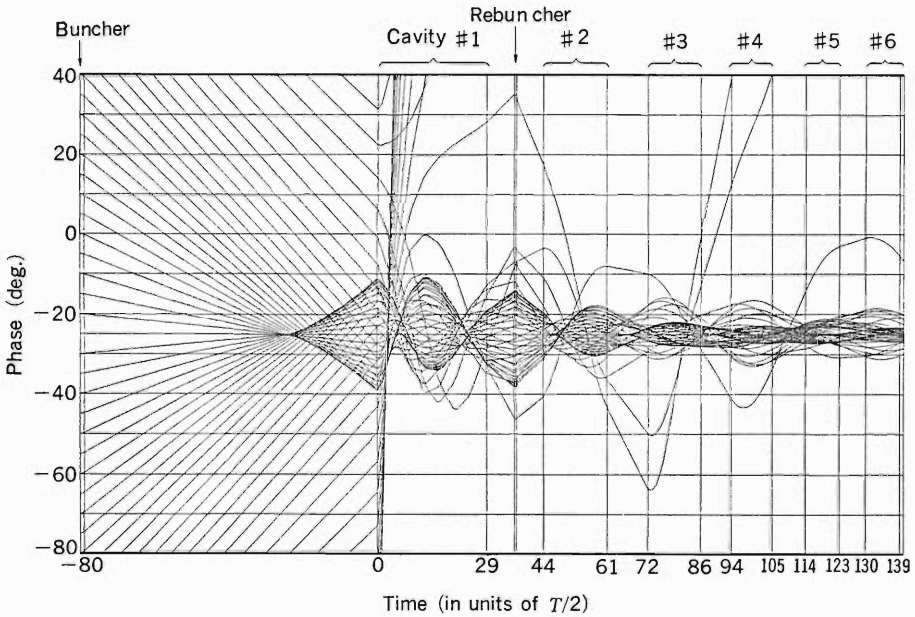

Fig. 2. Calculation of the longitudinal phase trace when a rebuncher is used between the cavities #1 and #2. Other conditions are the same as in Fig. 1.

Table 1. Comparison of calculated beam qualities between cases in Fig. 1 (case I) and Fig. 2 (case II).

	Case I	Case II
Energy spread (fwhm)	1.9%	0.7%
Phase spread (fwhm) (at the exit of cavity #6)	25 deg.	5 deg.
Phase acceptance	57%	61%

selected so that the phase acceptance is maximized. As seen in Fig. 1, the phase oscillation becomes larger and larger in the later portion of the linac and no phase compression can be seen. These results are attributed to the effects of phase divergence in the drift spaces between the cavities, especially between cavities #1 and #2 and between cavities #3 and #4. The beam quality will be bad at the exit of the final cavity.

One method to damp the phase oscillation is to use a rebuncher in a proper section. Figure 2 shows the longitudinal phase oscillation when the second harmonic buncher is inserted between cavities #1 and #2. The rf voltage of the rebuncher is selected so that the energy spread at the exit of the final tank is minimized. Other conditions are the same as in Fig. 1. Obviously the phase compression can be seen compared with the case in Fig. 1. Table 1 shows that some improvements in beam qualities can be expected by using the rebuncher.

Table 2. Specifications of the rebuncher.

Type	2-gap buncher
Frequency range	34–90 MHz
Maximum peak voltage per gap	70 kV

Since the space between the cavities #1 and #2 has been occupied fully by a couple of quadrupole magnets, two gate valves, and a universal beam diagnosis vacuum box, the rebuncher should be compact enough to be installed in the beam diagnosis box.

As a resonant element of the rebuncher, we chose a quarter-wave coaxial type cavity with a drift tube attached at the open end of its center conductor. Second harmonic frequency of the rf used in the linac was chosen as its resonant frequency to make its drift tube length as short as a port of the vacuum box (10 cm). The use of high frequency is also effective to reduce the rf voltage.

The specifications of the rebuncher are listed in Table 2. It is being fabricated and its characteristics will be measured soon.

RIKEN Accel. Progr. Rep. 18 (1984)

V-18. Production of Highly Charged Ions by Whistler Heating of Plasmas

S. Ishii, H. Amemiya, Y. Sakamoto, and M. Yanokura

In a previous report[1] we presented a design of a hexapole plasma source for studying the production of highly charged ions. Plasma heating is indispensable for obtaining them. We had proposed the plasma heating by whistler wave because it can penetrate dense plasmas without being cut off. The whistler frequency was chosen 2.45 GHz and the target plasma was produced by ECR discharge at a frequency of 9 GHz.

Construction of the hexapole plasma source was completed this year. The hexapole coil consists of six straight bars parallel to the magnetic axis of the mirror field. Each bar is a bundle of six conductors arranged in wedge shape and their effective center is 0.103 m apart from the magnetic axis. We measured a magnetic configuration. The direction and strength of the hexapole field are dependent on the radial and azimuthal coordinates. Near the axis ($R\sim0$), however, the absolute value is almost independent of the azimuth angle and rises quadratic with R. Figure 1 shows the radial distribution of the absolute values of the hexapole field. The measured values are in excellent agreement with the calculated ones. At a hexapole coil current I_h of 4,800 A the ECR field for a frequency of 2.45 GHz exists within the plasma vessel, the diameter of which is 0.106 m.

When the mirror field is superposed on the hexa-

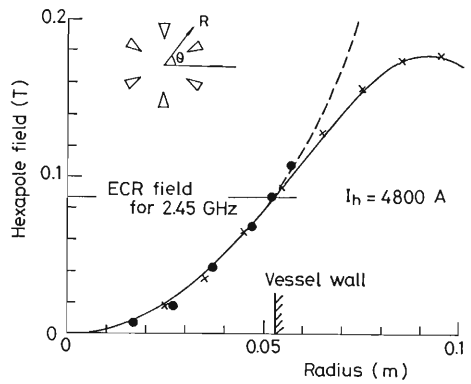

Fig. 1. Radial distributions of the hexapole field at a coil current of 4,800 A. The inserted sketch illustrates the end view of the hexapole coil and describes the related polar coordinate (R, θ). The solid and dashed curves show the hexapole fields calculated at $\theta=0°$ and 30°, respectively. The measured values are plotted by × at $\theta=0°$ and ● at $\theta=30°$.

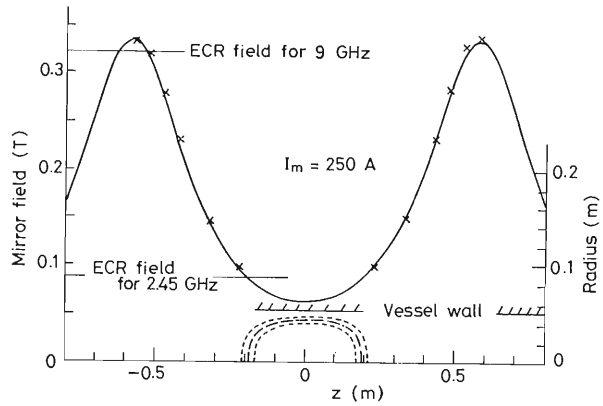

Fig. 2. Axial distribution of the mirror field at a coil current of 250 A and the ECR zone for a frequency of 2.45 GHz when the hexapole field shown in Fig. 1 is superposed. The solid curve shows the calculated mirror field and × represents plots of the measured values. The dashed curve shows a geometrical shape of the ECR zone for zero electron temperature. The dotted curves show the Doppler shifted zone for $T_e=10$ eV and $n_e=1\times10^{18}$ m^{-3}.

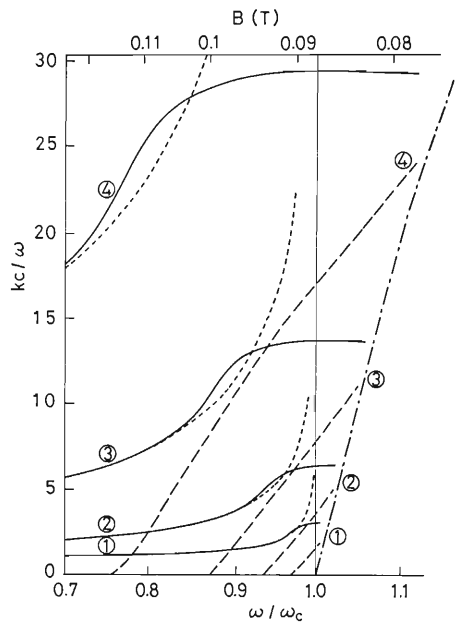

Fig. 3. Dispersion relations of the whistler wave. The solid and dashed curves show, respectively, real and imaginary parts of the wave numbers at various electron densities: ① $n_e=10^{16}$ m^{-3}, ② 10^{17}, ③ 10^{18}, ④ 10^{19}. The electron temperature T_e is fixed at 10 eV. The dotted curves denote the wave numbers for zero temperature. $\omega/2\pi$ is fixed at 2.45 GHz and the magnetic field is varied. The abscissa indicates the normalized frequency which is inversely proportional to the magnetic field B. The ordinate means the wave number normalized with the wave number in vacuum.

pole field, the resonance zone forms an oval surface. In Fig. 2 is shown the calculated resonance zone (dashed curve) together with the axial distribution of the mirror field. Its dimension is 0.38 m in length and 0.08 m in diameter. This can be varied by changing the coil currents and the mirror spacing.

This resonance zone, however is valid for zero electron temperature. Taking into account finite temperature we calculated the dispersion relations for the whistler. The space-time variation is taken as $\exp[i(kz-\omega t)]$. The relevant design parameters suffice the regime of spatial growth,[2] in which ω is real. The imaginary part of the wave number k gives the spatial growth rate. The calculated wave numbers for various electron densities n_e are shown in Fig. 3 as a function of the magnetic field B near ECR. The wave frequency $\omega/2\pi$ is fixed throughout at 2.45 GHz. For the cold plasmas the resonance ($k \to \infty$) takes place at $\omega=\omega_c$ and k_i (the imaginary part of k) is non-zero, where ω_c is the electron cyclotron angular frequency. When $\omega<\omega_c$, however, k_i is equal to 0. This means that the wave energy is absorbed only on the infinitesimally thin surface shown in Fig. 2 (dashed curve). For the warm plasmas, on the other hand, k_r (the real part of k) is deformed (solid curves in Fig. 3) and k_i is substantially large over a broad range of B (dashed curves in Fig. 3). This arises from the Doppler broadening due to the finite temperature. The chain curve in Fig. 3 denotes the Doppler shift. It is noteworthy that this shift becomes large with increasing n_e. Thus the wave energy can be absorbed in the thickened zone indicated by dotted curves in Fig. 2.

The critical density beyond which the ordinary wave is cut off is equal to 7×10^{16} m^{-3} in the present case. It is clear from Fig. 3 that the whistler has no such a limit and in addition the absorption of the wave energy increases as n_e rises.

Thus we are confident that the whistler is in favor of heating the overdense plasmas.

References

1) S. Ishii, Y. Sakamoto, and M. Yanokura: *RIKEN Accel. Progr. Rep.*, **17**, 177 (1983).
2) L. S. Hall and J. E. Scharer: *Phys. Fluids*, **16**, 2352 (1973).

RIKEN Accel. Progr. Rep. 18 (1984)

V-19. Construction of ECR2

M. Yanokura, S. Ishii, Y. Sakamoto, and M. Odera

We reported outlines of two stage ECR ion source (ECR2)[1] which has two cavities. In the first cavity, dense plasma of low charge state ions is formed by the Whistler mode heating. The plasma then diffuses into the second cavity through a narrow orifice. Highly charged ions are expected to be formed by further heating under a high vacuum by microwave at the second cavity. This year, we have added some modification in design of the ECR2. Most of the components were completed and construction of ECR2 was started.

In the previous design[1] the use of aluminum was planned as construction material of the second cavity, however, some problems were found in the use of aluminum. In the second cavity, it was designed to set six pieces of permanent magnets around an axis of the cavity to form hexapole magnetic field. Although positions of the magnets must be adjustable to obtain desirable field distribution, it was found difficult to build such a position adjustment mechanism in an aluminum vessel. We changed material for the second cavity from aluminum to stainless steel. By this change, cooling of the second cavity became much more difficult, because heat conductivity of stainless steel is smaller than that of aluminum. Therefore we set longer cooling pipe around the second cavity to improve heat removal.

Magnetic field distribution produced by three solenoid coils is shown in Fig. 1. This magnetic field distribution satisfies conditions for ECR and also Whistler mode heating. For the Whistler mode excitation, microwave power is injected axially through a helix antenna into the first cavity from the position where the magnetic field strength is higher than that of the ECR resonance. A mirror ratio for the second cavity is about 1.69, which is nearly equal to that of an old single stage ECR source (ECR 1).[2] Hexapole magnetic field, formed by a samarium-cobalt permanent magnet, is added only to the mirror field of the second cavity. Further microwave power is injected radially into the second cavity at the valley of the mirror field.

On completion, the ECR 2 will be set on the high-voltage terminal of the linac injector. Therefore, power consumption for the ECR 2 must conform to limitation of electric power supply for the terminal. The ECR 2 requires extraction high voltage, 2.45 GHz microwave, and magnet power supplies. A PIG ion source installed on the terminal has a magnet power supply of 50 V and 150 A. We decided to use this power supply for the ECR 2 either and designed three solenoid coils. Each solenoid coil consists of a pair of tape-coils and a stainless steel disk which was set between the tape-coils. These coils are cooled with the disk which has coolant channels and is pressed tightly to an end surface of the tape-coils. A size of copper conductor is 65 mm in width and 0.8 mm in thickness. No. 1, No. 2, and No. 3 solenoid coils consist of a pair of 110, 110, and 140 turn coils, respectively. Total impedance of the three solenoid coils is about 200 mΩ as shown in Fig. 1. Positions of the first and second cavities in the mirror field are also shown in Fig. 1. A magnet excitation current of 120 A forms an ECR zone inside each cavity. This year, we could construct only a No. 3 coil and, therefore, we had to use the solenoid coils of the ECR 1 for the No. 1 and No. 2 coils tentatively though the inner diameter of the coils is smaller than an outer diameter of a metal-seal flange which is to be used for the second cavity. Therefore we use tentatively an elastomer-sealed flange of which diameter is smaller than that of a metal-seal flange. After construction of the new No. 1 and No. 2 solenoid coils, we shall change the flange to the metal-seal one.

A new type 2.45 GHz oscillator using a magnetron-tube was manufactured. Its maximum output power is 1.3 kW (CW); a block diagram of its electric circuit is shown in Fig. 2. This oscillator has two features different from commercial oscillator using a magnetron-tube. One is that the oscillator works in a complete CW mode by using a three phase rectification and smoothing circuit and a ripple in the output is less than 30%, whereas most oscillators using a magnetron-tube, which are called CW, work really intermittently. In order to obtain highly charged ions, the CW mode of heating is essential, because tightly bound electrons are stripped off from the ions in the step by step process which takes time. Secondly, this oscillator has an amplitude modulation circuit and the modulation frequency is adjustable in a range from 50 to 120 kHz. The 2.45 GHz oscillator with amplitude modulation was chosen because some instabilities which are produced in the over dense plasma

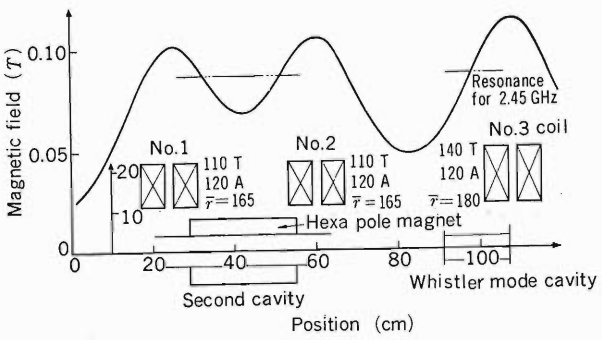

Fig. 1. Magnetic field distribution of ECR2 formed by three solenoid coils. Dots and dashes lines indicate an ECR zone for 2.45 GHz.

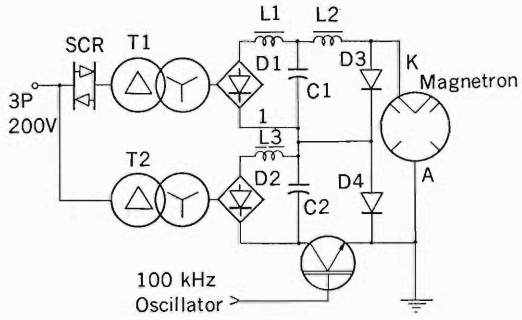

Fig. 2. Block diagram of the 100 kHz modulated 2.45 GHz oscillator using a magnetron-tube.

formed by the Whistler mode excitation and cause trouble are suppressed by modulation of the microwave at a suitable frequency.[3] Such a modulation technique is difficult to be applied to usual high-frequency oscillator using a magnetron-tube. A special design was tried, however, to take advantage of the high efficiency and low cost of magnetron-tubes.

A new type vacuum window made for 2.45 GHz microwave is used at a port of the second cavity. However, we had to solve some problems. One was power loss due to window materials. If the power loss becomes excessive, the window will be eventually broken. The other was a reflection on the window. Thus, we choose ceramic for window material. A 4 mm thick ceramic disk metallized at its edge was set inside a short cylindrical wave guide by welding. Heat expansion of the ceramic window is absorbed by deformation of the thin wall of cylindrical wave guide made of copper. This window is cooled by air blow. Reflection of microwave power on the window was minimized by adjusting the position of the ceramic window and varying a length of the cylindrical wave guide. After optimization, the voltage standing wave ratio (VSWR) was found to be 1.045 for 2.45 GHz, which is a very good VSWR value for a vacuum tight window.

Main components of the ECR 2 were completed at the end of October, 1984. Assembling and tuning of the magnetic field distribution of the ECR 2 were started in November.

References

1) M. Yanokura, S. Ishii, Y. Sakamoto, and M. Odera: *RIKEN Accel. Prog. Rep.*, **17**, 175 (1983).
2) M. Yanokura and M. Odera: *ibid.*, **15**, 137 (1981).
3) Y. Sakamoto: *Jpn. J. Appl. Phys.*, **16**, 1011 (1977).

RIKEN Accel. Progr. Rep. **18** (1984)

V-20. Automatic Control of a Gas Circulation and Gas-Feed System for the Ion Source

K. Ikegami, T. Noda, N. Kamiyama, T. Watanabe, and I. Kohno

The gas circulation system and gas-feed system for the ion source of the 160 cm cyclotron were newly developed and installed in the control room in January, 1984. These systems are operated automatically according to the sequence predetermined by a programmable controller which consists of an OMRON SYSMAC M5R having an I/O port of max. 256 points.

1) Gas Circulation System

The high priced gases, such as ^{3}He, enriched $^{13}CO_2$, and $^{15}N_2$, necessitate the use of a circulation system to recover a part of gases not accelerated or trapped in the cyclotron. The system purifies the gases for reuse in the ion source. Figure 1 shows a block diagram of the gas circulation and the gas-feed system for the ion source. The system consists of a vacuum-tight intake and exhaust rotary pump (RP2) for circulation, a first charcoal trap (T1), second two charcoal traps (T2 and T3), two reservoirs (one is for the ^{3}He gas and another is for other gases such as $^{13}CO_2$ and $^{15}N_2$), several Pirani and absolute gauges, a rotary pump for evacuation, many air-operated and electromagnetic valves, and a programable controller. For connection of all pipes the Swagelok tube fitting is used. For second traps a metal seal called Helico Flex is used. The operating status is graphically displayed on the handling board.

The gas flow rate to the ion source is adjusted by a pressure controller (PC). Two mechanical booster pumps are connected to an exhaust of a diffusion pump to compress gases instead of a rotary pump (MRP) used in the normal operation of cyclotron evacuation. Gases collected are passed through

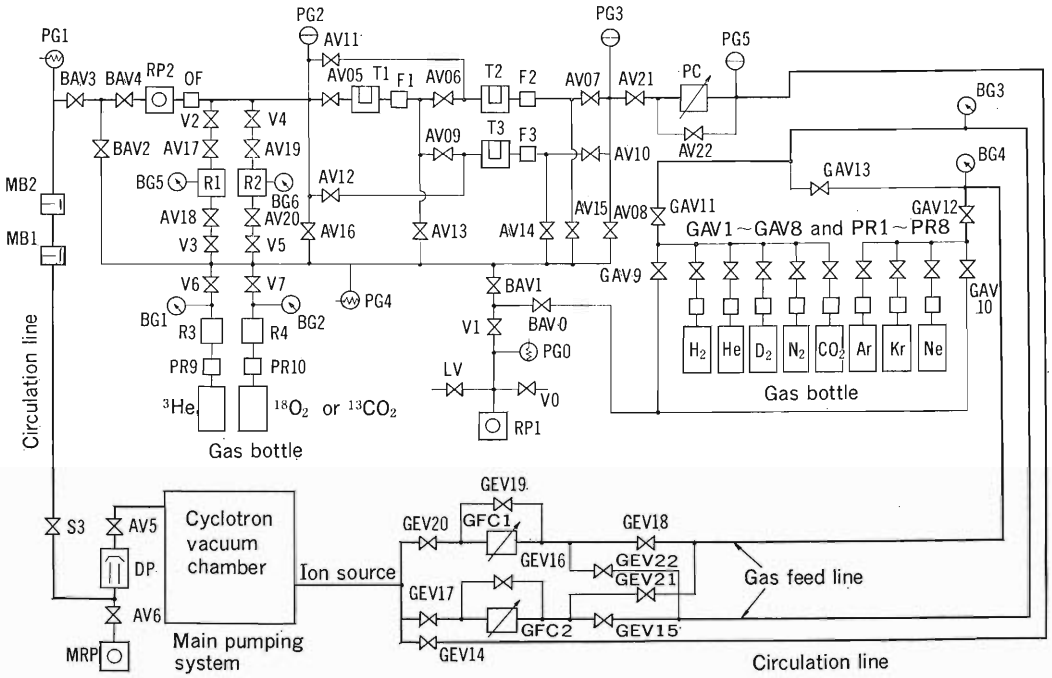

Fig. 1. Block diagram of the gas circulation and gas-feed system for the ion source. RP1 and MRP, rotary pumps; RP2, circulation pump; MB, mechanical booster pump; DP, diffusion pumps of 32″ and 14″ connected in series; OF, oil filter; F, filter; BAV, GAV, AV and S3, air-operated valves; V, hand valve; GEV, electromagnetic valve; R1 and R2, reservoirs of 15 *l*; R3 and R4, reservoirs of 0.1 *l*; T1, thermoelectrically cooled charcoal trap; T2 and T3, liquid nitrogen cooled charcoal traps with baking heater wound (these traps are set in a thermos with a lifter moved by a motor); PR, pressure regulator; PG and BG, Pirani and absolute gauges; PC, pressure controller (100–10^{-1} Torr); GFC1 and GFC2, gas flow controllers (GFC1: max 5 cc/min, GFC2: max 10 cc/min).

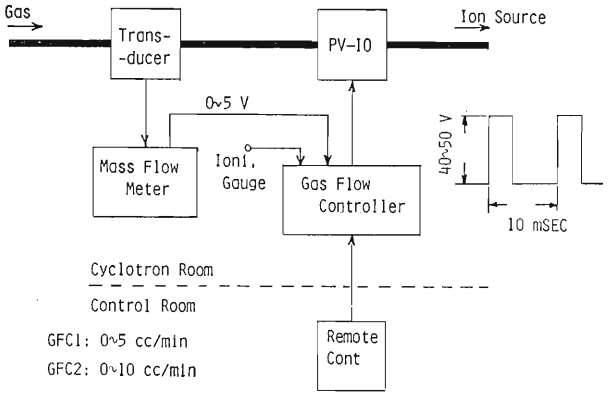

Fig. 2. Block diagram of the gas flow controller.

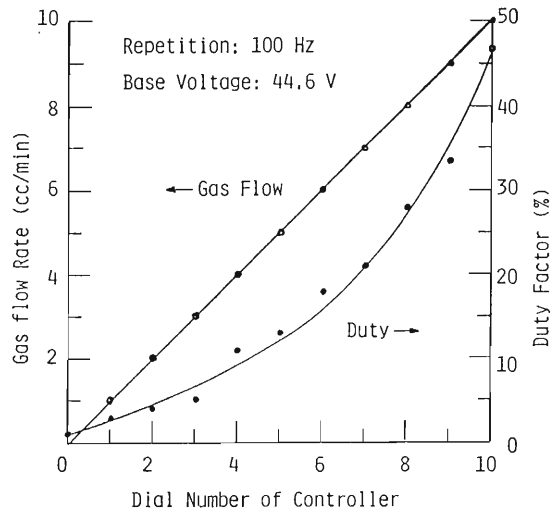

Fig. 3. Gas flow rate and corresponding duty factor of the electric pulse applied to the valve according to a dial number of the controller.

first and second traps. The first charcoal trap is cooled at temperatures below −20°C by four thermoelectric cooling units. Water vapor in the residual gases is almost trapped by charcoal. Other residual gases except ^{3}He are adsorbed in the second trap cooled by liquid nitrogen.

The system is automatically operated by simply starting the programable controller after we select a reservoir to be filled with gas and traps. After evacuating the system and cooling the traps, gas is supplied from the reservoir into the system by using the circulation pump and circulated to be purified through traps in the system. After purification, the gas is sent through a pressure controller to the ion source and recovered from the cyclotron chamber back to the system. When the circulation is stopped, the gas used is recovered into the reservoir by the circulation pump after purification. To remove gas adsorbed in the traps, the traps are evacuated with the rotary pump (RP1) for several hours while the traps are heated to around 70°C and 150°C at the first and second trap, respectively.

2) Gas-feed System

This system consists of eight gas bottles each having a pressure regulator, several air-operated and electromagnetic valves, and two gas-feed lines for mixing gases with a gas flow controller. A gas flow controller is composed of a piezoelectric valve (PV-10) and a mass flow meter. Figure 2 shows a block diagram of the gas flow controller. The valve PV-10 is operated by an electric pulse with a repetition rate of 100 Hz and an amplitude of 40–100 V. By varying the pulse duration from 0 to 50%, one gas flow controller (GFC 1) can control the flow rates over the range of 0–5 cc/min and the other controller (GFC 2) from 0–10 cc/min. Figure 3 shows a gas flow rate for nitrogen gas *vs.* the duty factor of the electric pulse applied to the PV-10. In the case of mixed gas,[1] the main gas is supplied to the ion source through one gas-feed line and the supporting gas is supplied through the other line to produce highly-charged heavy ions and to allow stable operation of the ion source.

The system is operated by simple button push after the required gas is selected. When the switch "START" is pushed on the graphic panel, the system is evacuated and gas is fed in the ion source.

Reference

1) K. Ikegami, K. Ogiwara, T. Kageyama, and I. Kohno: Proc. 6th Symp. Ion Source and Ion-Assisted Tec., p. 155 (1982).

RIKEN Accel. Progr. Rep. **18** (1984)

V-21. Low-β RFQ Structure-II: High Frequency Model Measurement

M. Odera and M. Hemmi

Design of a model of the four-vane type low-β RFQ structure was described in the previous report.[1] It has a rectangular cross section for its outer shell and has different heights for the horizontal and vertical vanes to try separation of the unwanted H-11 dipole mode from the H-21 quadrupole acceleration mode. It is also fitted with current shorting ring between the vertical vanes to reduce number of resonant modes near the wanted mode.[1] Its cross sectional view is shown in Fig. 1. The vertical height of the fabricated model is 300 mm, the horizontal width is 150 mm, and the axial length is 600 mm. An aperture for beam, initially 5 mm, was expanded to 10 mm for convenience of bead pulling perturbation measurements.

Table 1 shows resonant frequencies measured for the two apertures. Large separation intended for the unwanted modes from the wanted one has been realized and the separation remains substantially constant against the change in the aperture. Other resonant frequencies were not observed below 400 MHz. Two current shorting rings connecting vertical vanes reduced the number of the resonant modes.

Figure 2 shows a field distribution for the H-21 mode along the beam axis. The reproducible and sharp field change reflects roughness of the vane tip surface. The small asymmetry of the bead position due to the surface roughness with respect to the gap distance between vane tips is amplified by a steep change of electric field strength generated by shift of the central axis of the quadrupolar field. The distribution shown in the Fig. 2 actually represents a resonant frequency deviation proportional to square of field strength at the bead position. Therefore, the change in the quadrupolar field symmetry caused by the irregularity of the vane tip surface generates a sharp change as shown in Fig. 2. On the other hand, the dipole mode H-11 does not show such high sensitivity to the surface finish as seen from Fig. 3, and therefore, its field strength does not change so drastically with position as in the H-21 mode.

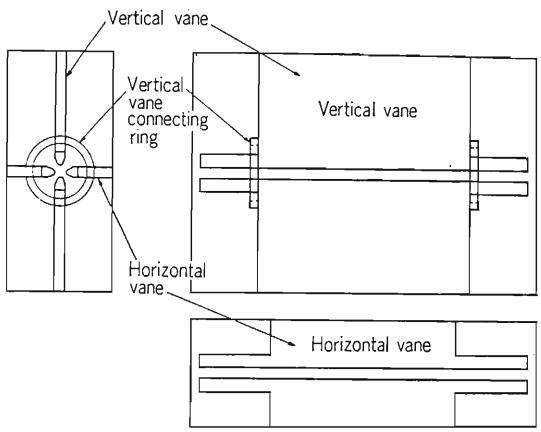

Fig. 1. Cross sections of the rectangular RFQ structure.

Table 1. Resonant frequencies measured below 400 MHz.

Aperture	H-21 mode	H-11 mode
5 mm	189.261	204.474
10 mm	207.986	223.026

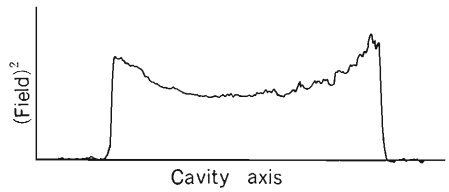

Fig. 2. Field intensity distribution along the beam axis for H-21 acceleration mode, 207.986 MHz.

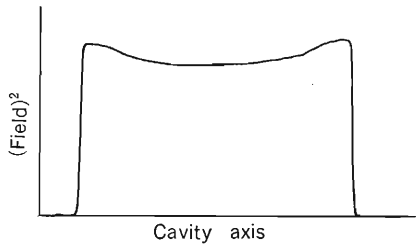

Fig. 3. Field intensity distribution along the beam axis for H-11 dipole deflecting mode, 223.026 MHz.

According to these results, the rectangular RFQ structure seems to have satisfactory characteristics aimed at first.[1] There is no problem in mode discrimination which sometime presents trouble in the case of the symmetrical four-vane structure because of too close frequency separation. Tolerance in fabrication is not so tight as in the case of the conventional symmetrical type without a current shorting ring. Uniformity of the field strength along the beam axis can be improved by selecting a length of vane arms and their separation from the end plate. That is the subject for further study.

Reference

1) M. Odera: *RIKEN Accel. Progr. Rep.*, **17**, 185 (1983).

RIKEN Accel. Progr. Rep. **18** (1984)

V-22. Development of the Medium-β RFQ Structure-III: Study by High Frequency Model

M. Odera and M. Hemmi

A previously reported two-cell chain structure[1] was modified and a new model was fabricated to give a larger beam aperture and an ample distance between the neighboring electrodes to simulate an actual accelerator. Because the former structure was developed only to test feasibility of the chain scheme, no realistic consideration was given in its geometry and the new model had to be constructed. However, it is still a constant velocity version, having 10 cells of the same length. Figure 1 is a photograph of the new resonator showing an array of chain electrodes inside. The tank diameter is 500 mm, the axial length is 600 mm, and the length of 2π cell is 60 mm. A gap to cell ratio is taken as 1/4. Figure 2 shows an electrode assembly which corresponds to the length of 4π. A train of such electrodes in a horizontal plane is interlaced with another train of similar assemblies in the vertical plane displaced longitudinally by a length of 2π. The combination results in the chain-like accelerating structure in which acceleration and focusing regions alternate along the beam axis.

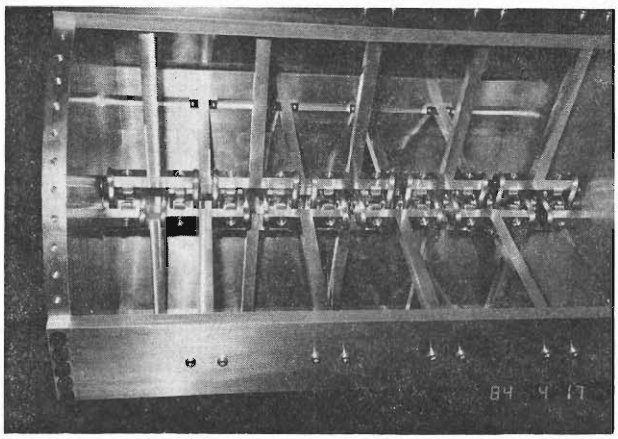

Fig. 1. Photograph of the type-2 resonator model.

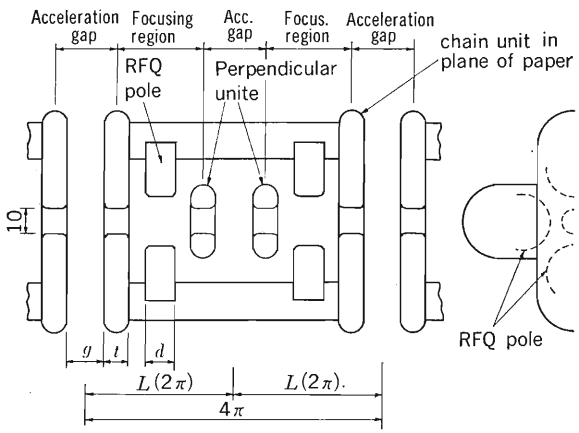

Fig. 2. Sectional view of a chain electrode array.

Resonant frequency spectra are shown in Fig. 3. No unwanted mode is present below 460 MHz for (a) and the nearest unwanted mode is separated from the wanted acceleration mode at 264 MHz by

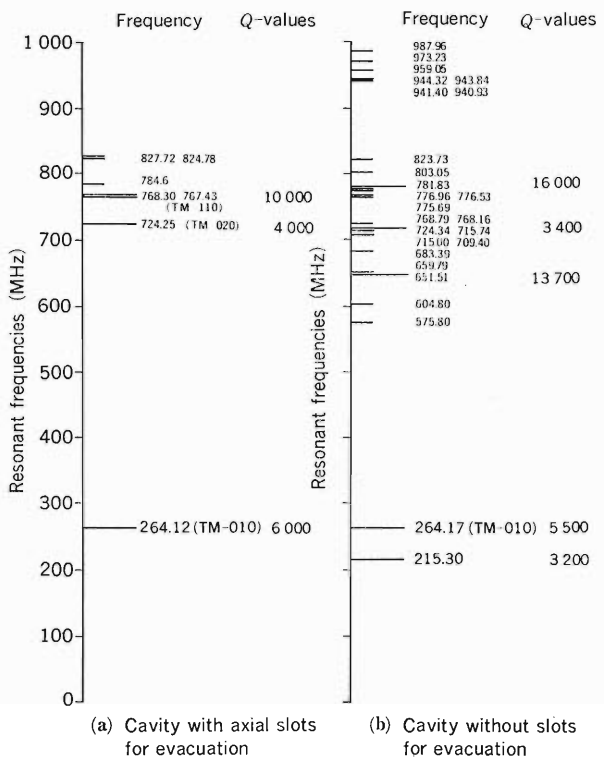

Fig. 3. Resonant frequency spectra. (a) With axial slots in the cavity wall, (b) slots closed.

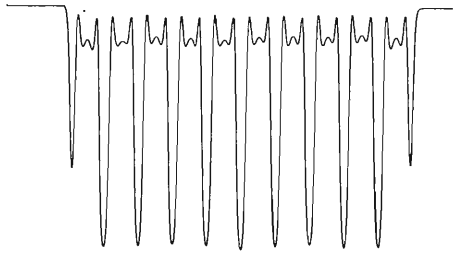

Fig. 4. Distribution of the accelerating voltage in gaps at 264.12 MHz for the TM-010 acceleration mode.

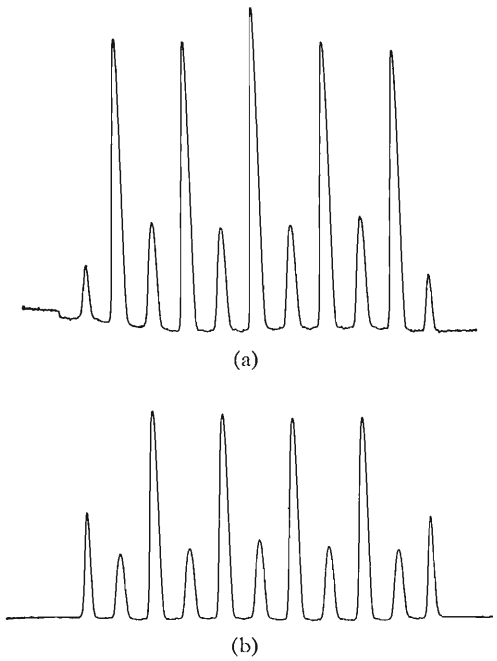

Fig. 5. TM-110 modes. (a) At 767.43 MHz, (b) at 768.30 MHz.

49 MHz for (b). An Alvarez linac having 10 cells usually presents a closely spaced frequency spectrum called a dispersion curve, when plotted as a function of a phase difference between adjacent cells. In the case of (a), axial slots in the outer conductor of the cylinder simulating evacuation port were somewhat effective to suppress the resonant mode in which current flows azimuthally. As seen in (b), however, the closure of the slots had not influence on the frequency spectrum essentially. Of course the number of modes which have azimuthal current components increased. But the increase is seen in the frequency higher than 575 MHz except one at 215.3 MHz, 49 MHz lower than TM-010. The nature of the lowest frequency mode has not been clarified yet. The reason of the scarcity of the resonant modes near the TM-010 mode in the chain structure is interesting for further study. The large separation of the nearest modes simplifies resonator fabrication and tuning.

Field distribution was studied by using a usual perturbation technique. Figure 4 shows a plot of

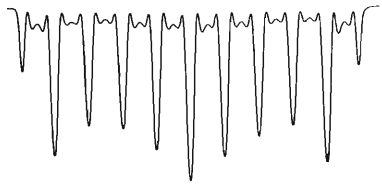

Fig. 6. TM-020 mode at 724.25 MHz.

frequency deviation which is proportional to square of the field strength at the position of the perturbing metallic bead for the TM-010 mode. Peaks at the left and right ends correspond to voltage for half cells and are lower than those for normal cell. This distribution is suitable for beam acceleration. Other significant modes are also described below.

Figure 5 gives the distributions for the two TM-110 modes. For these modes, the magnetic field is concentrated in the acceleration gaps whereas the strong electric field exists there for the TM-010. Therefore, the direction of frequency deviation by perturbation in Fig. 5 is contrary to that in Fig. 4. Shifts of the large and small peaks by 2π are seen between the two TM-110 modes. The change corresponds to rotation by 90 of the position of the nodal plane of the TE-110 mode. A distribution for TM-020 is also shown in Fig. 6.

The highest quality factor was observed for the TM-110 modes for which no electric field is present in the acceleration gaps and in the focusing quadrupoles. The gaps and the poles do not capacitively load the cavity in that mode and give the high Q-values. By pulling a metal bead perpendicular to the beam axis, the electric field by the TM-110 mode was found to be concentrated somewhere between the beam axis and the cavity wall.

The obtained distribution confirms the possibility of use of this structure as a linear accelerator. The obtained field distribution reproduces the previously reported distribution measured by a two cell magnetic analog model when the latter is squared.

Reference

1) M. Odera, M. Hemmi, T. Chiba, and E. Ikegami: *RIKEN Accel. Progr. Rep.*, **17**, 183 (1983).

RIKEN Accel. Progr. Rep. 18 (1984)

V-23. Development of the Medium-β RFQ Structure IV: Effect of Change of Cell Length, Measurements by Magnetic Analog Models

M. Odera and M. Hemmi

Transit time factor of an RFQ structure with a chain-like electrode configuration which we call type-1 was calculated using the field distribution measured by a magnetic model and reported in Ref. 1. An effective shunt impedance obtained is rather high showing possibility to realize a linac economical in power consumption.[1] Another model which we call type-2 having more realistic dimensions was fabricated and the field distribution in it was measured and reported elsewhere.[2] The transit time factor obtained for the new model was 83% at the acceleration gaps and a little smaller than the value of 90% of the type-1 reported[1] in spite of use of the same gap to cell ratio. The cell length was 48.9 mm and the beam aperture was 6 mm for the first type, whereas 60 mm and 14 mm, respectively for the second type. This shows sensitivity of the transit time factor on the geometry of the electrode.

In order to study the geometry effect further, four magnetic models with different cell length were fabricated.[3] In those models, longitudinal dimen-

Table 1. Parameters of the magnetic models.*

		Model number			
		#1	#2	#3	#4
Cell length	L (mm)	60	90	120	150
Gap length	g (mm)	15	22.5	30	37.5
Plate thickness	t (mm)	10	15	20	25
Pole length	d (mm)	12	18	24	30

* g/L is 1/4, beam aperture is 10 mm, aperture of quadrupoles is 20 mm, and other transversal dimensions are kept constant. Letters representing parameters are the same as those of Fig. 1.

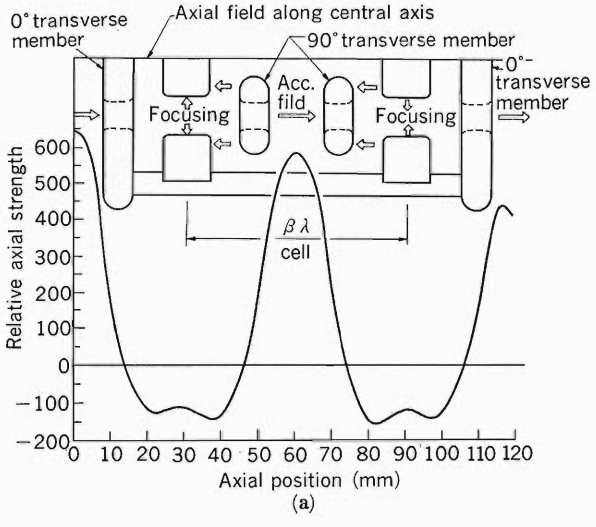

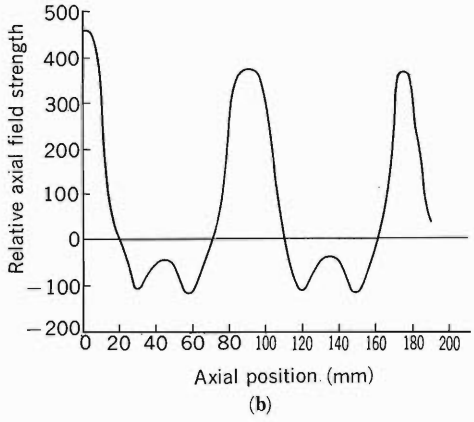

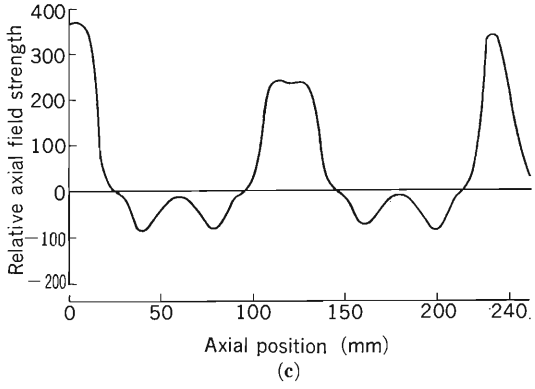

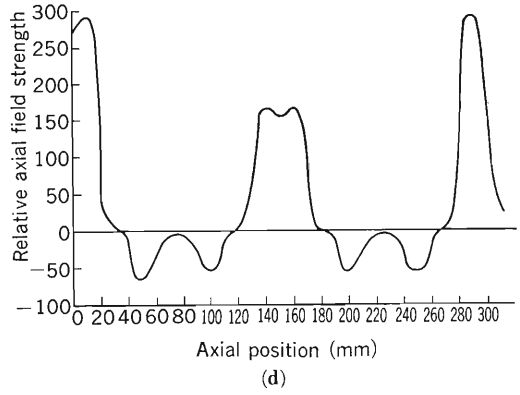

Fig. 1. Distribution of axial field measured by Hall probes. (a) For number 1 geometry, (b) For number 2, (c) For number 3, (d) For number 4.

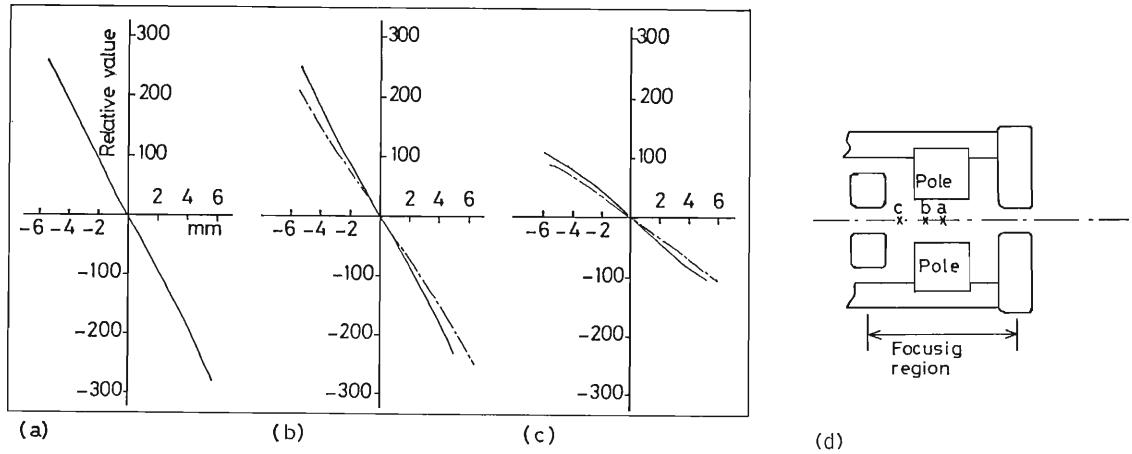

Fig. 2. Focusing field in the quadrupole gaps. Pole to pole distance is 20 mm. (a) At the center of quadrupoles. ——, Probe moves in the plane of paper; —·—, probe perpendicular to paper. (b) Axial position 4 mm from the center. (c) Axial position 10.2 mm from the center or 3.7 mm from the pole edge. (d) Longitudinal cross section of the chain structure showing the axial position of measurement of the focusing field.

sions were taken proportional to the cell length whereas transversal parameters were kept constant. Table 1 gives the parameter values. Letters denoting parameters correspond to those in Fig. 2 of a preceding paper.[4]

The four curves in Fig. 1 are values measured for the two-cell magnetic models. In the measurements, the left-hand side beam aperture was filled with plugs made of soft iron in order to see effect of beam aperture on the field distribution. Hall probes were inserted from the right-hand side. The effect of beam aperture is clearly seen in the change of field amplitude which is the largest at the left end where the plug fills the aperture and then decreases toward right direction. Figure 2 shows transversal focusing fields in the quadrupole region. A little difference is seen among field gradients in the directions perpendicular with each other as expressed by dash and dot, and a solid lines when position of measurement is displaced axially from the center of the focusing region. However, larger asymmetry is always present in the usual RFQ structure and is not harmful for orbit stability. Calculation of the transit time factor by using the obtained results is in progress.

References

1) M. Odera, M. Hemmi, T. Chiba, and E. Ikezawa: *RIKEN Accel. Progr. Rep.*, **17**, 183 (1983).
2) M. Odera: Proc. 1984 Linear Accel. Conf., Seeheim, GSI-84-11, p. 36 (1984).
3) As to a photograph of the magnetic model, see Fig. 4 of the paper; M. Odera, M. Hemmi, A. Goto, M. Hara, and M. Kase: Proc. 5th Symp. Accel. Sci. Technol., Sept. 1984, KEK Tsukuba, p. 56 (1984).
4) M. Odera and M. Hemmi: p. 212 in this report.

RIKEN Accel. Progr. Rep. 18 (1984)

V-24. Application of the Medium-β RFQ Structure

M. Odera, M. Hemmi, A. Goto, and M. Hara

According to a previous model study, a new RFQ structure of the Alvarez type with a chain-like accelerating electrode configuration was found likely to have a moderate effective shunt impedance.[1] Since exact evaluation of the effective shunt impedance for such a complex construction is difficult, rough estimation was made according to a following procedure. The dimension of drift tubes of a two-cell Alvarez cavity which has an outer conductor of the same diameter as that for the chain model were calculated by the "Super Fish" code to give the same resonant frequency. Drift tubes thus determined were fabricated and installed inside the cavity shell in place of the chain electrodes and the quality factor was measured. Assuming that the shunt impedance is proportional to the Q-value, we have obtained a value larger than 100 MΩ/m.

On the other hand, the chain model fabricated for the comparison with the Alvarez type had a few defects; edges of the electrodes were not rounded and the distance between quadrupoles was so small that it is not likely to hold acceleration voltage. The aperture in the accelerating electrodes for beam transmission was also too small. Field distribution and the Q-value may be changed if these defects are modified. A second high-frequency model was fabricated taking account of these considerations. The new model has 10 cells but is still a constant velocity version having the same length for every cell. Its characteristics measured are described separately in this report.[2] The effect of change in cell length by increase of velocity on the field distribution has been studied by the magnetic analog models and the result was also given separately.[3] However, comparison with the Alvarez type as made for the two-cell model of the first type has not been made yet. Instead, we are planning to fabricate an acceleration model which has a different cell length for every cell reflecting increase in velocity of ions by acceleration. Field distribution and the Q-value may be different from those for the constant velocity model. We intend to measure the effect of uneven cell length on the effective shunt impedance by the third model.

If the high effective shunt impedance is confirmed for the realistic third model again, this structure will find several applications not only because of power economy but also of its simplicity of operation. Once the best geometry of the chain electrodes is established, fine tuning of the focusing elements, as is often necessary in the ordinary drift tube linacs, will not be required. Since the strength ratio of the accelerating to the focusing fields is automatically maintained constant, the beam trajectory becomes invariant against the change in the mass to charge ratio of the ions under acceleration. On the other hand, exact determination of the field configuration along the beam trajectory must be made by using models to allow prediction of the orbit characteristics by numerical integration.

A few examples of use of the structure are mentioned here.

Case 1: Increase in energy of ions of heavy elements accelerated by the RILAC.

At present, ions having a mass to charge ratio (A/q) of 20 are being accelerated up to 0.8 MeV/n at 20 MHz. This ratio can be decreased by charge stripping at the exit of the RILAC and the ions are further accelerated by the chain structure operated at a frequency of integer multiple of 20 MHz. The linac of 3.6 m long operated at 200 MHz is capable of accelerating ions of A/q smaller than 7 up to 1.8 MeV/n and the maximum power consumption will be 140 kW for an axial field gradient of 1.5 MV/m, on the assumption that the effective shunt impedance is 100 MΩ/m.

Case 2: Increase in intensity of light heavy ions.

Singly or doubly charged ions of which mass is lighter than that of Ne can be accelerated at a reduced power level by the RILAC at 20 MHz and similarly by the structure of Case 1. For these ions charge stripping at 0.8 MeV/n by gaseous media between the RILAC and the booster to make A/q ratio smaller than 5 is feasible and the high intensity will cause no problem of lifetime of the strippers. After the ions are accelerated up to 1.8 MeV/n, a foil stripper is used to reduce the A/q value to 2 and further acceleration by another 8 m section can increase energy up to 7 MeV/n. A necessary RF power is 140 kW for a field gradient of 1 MV/m, neglecting a probable change in the effective shunt impedance due to change in velocity.

Case 3: Increase in energy of light ions accelerated by the RILAC at 40 MHz and charge stripped to $A/q=2$.

The RILAC energy operating at 40 MHz can be

Table 1. Examples of the possible applications of the new Alvarez type linac with the chain-like accelerating electrodes.

Case No.	E_{in} MeV/n	E_{out} MeV/n	A/q	Cavity length (Acc. Grad.) m at (MV/m)	Freq. (RILAC) MHz	Freq. (Chain) MHz
1	0.8	1.8	7	3.63 (1.5)	20	200
2	0.8	7.0	2	3.63+7.98 (1.0)	20	200
3	3.2	7.1	2	5.07 (1.2)	40	200
4*	0.8	10.6	1	6.29 (1.2)		200

* Injected from a rectangular low-β RFQ linac.[4]

increased from 3.2 MeV/n up to 7 MeV/n by use of a 5 m long section operated at 200 MHz. Power consumption is 130 kW for the field gradient of 1.2 MV/m. For acceleration of protons the power loss becomes 1/4.

Case 4: Acceleration of intense protons.

Combined with the rectangular four-vane type low-β RFQ linanc,[4] the structure can be used as an economical high intensity proton accelerator. For instance, by receiving protons at 800 keV from the low-β section, the linac of 6.3 m long is sufficient to boost energy up to 10 MeV/n. Power consumption is around 160 kW for the shunt impedance of 100 MΩ/m and the field gradient of 1.2 MV/m. Such a proton linac is useful as a prototype high intensity accelerator. It is desired for study of heavy radiation damage of fusion materials or as an injector of a high energy and high intensity linac for a pion generation or for a spallation neutron source, as well as for the RIKEN separated sector cyclotron under construction.

Power consumptions in the above examples are given only for rough estimation of the RF equipments and should be examined by further study. The axial field gradients were chosen so that the power consumption per resonator remains less than 200 kW. The gradients and other parameters are summarized in Table 1. For accelerating frequency of the chain structure, 200 MHz has been used throughout for the sake of simplicity of presentation. Higher or lower frequency is also possible and will be chosen by considering availability of the high power-high frequency tubes in the market, ease of structure construction, and so forth. The end energy was arbitrarily chosen and should be modified according to acceleration conditions in the post stripper part. For instance, if it is used as an injector to the separated sector cyclotron, velocity of the ions must satisfy conditions of the subharmonic acceleration in the circular orbit of the cyclotron.

The maximum surface field sustainable for the structure must also be studied carefully, though use of the extremely high field is frequently reported in the recent RFQ linac papers.

References

1) M. Odera, M. Hemmi, T. Chiba, and E. Ikezawa: *RIKEN Accel. Progr. Rep.*, **17**, 183 (1983); M. Odera: Proc. 1984 Linear Accel. Conf., Seeheim, GSI-84-11, p. 36 (1984).
2) M. Odera and M. Hemmi: p. 212 in this report.
3) M. Odera and M. Hemmi: p. 214 in this report.
4) M. Odera and M. Hemmi: p. 211 in this report.

RIKEN Accel. Progr. Rep. **18** (1984)

VI. RADIATION MONITORING

1. Leakage-Radiation Measurement in the Underground Passage of the Cyclotron Building

S. Fujita, I. Sakamoto, H. Takebe, and I. Kohno

1) Measurement with a film badge

Leakage doses measured from April, 1983, to March, 1984, with γ-ray and neutron film badges which were placed at two positions of the underground passage (points A and B in Fig. 1) are shown in Table 1. In this period, the beam times allotted to deuteron acceleration were 63 hr in July, 72 hr in December, and 72 hr in March. Fast neutrons were generated at the end of the beam course No. 2 by bombarding a thick beryllium target with 20 MeV deuterons in December. The average beam current was 15 μA. The average energy and the flux of the fast neutrons were estimated using data in Ref. 1 and 2 to be 5 MeV and 4×10^{12} n·cm^{-2}·sec^{-1}, respectively, in the direction of a 0-degree angle at the center of the target.

2) Measurement with a radiation detector

Leakage-radiation in the underground passage was measured when the cyclotron was operating on 12 MeV proton (target silicon), 24 MeV deuteron (target beryllium), 18 MeV helium-3 (target silicon), and 28 MeV alpha (target argon). All targets were set on the end of the beam course No. 2. As shown in Figure 1 the measuring points of radiations are marked at intervals of 2 m from point C in the underground passage and the measuring points on the stair have a distance of 14 m (J), 16.5 m (K), and 19 m (L) from point C. The measurements were carried out from October to December, 1983.

The neutron radiation was measured with a rem meter* using a pulse counter.** The value of pulse counts obtained during 10 min at 0.5 m above the floor was converted into the dose equivalent rate by using the conversion factor, 3.6 cps per mrem/hr given in the instruction manual. The minimum detectable level of neutron dose rate in this mea-

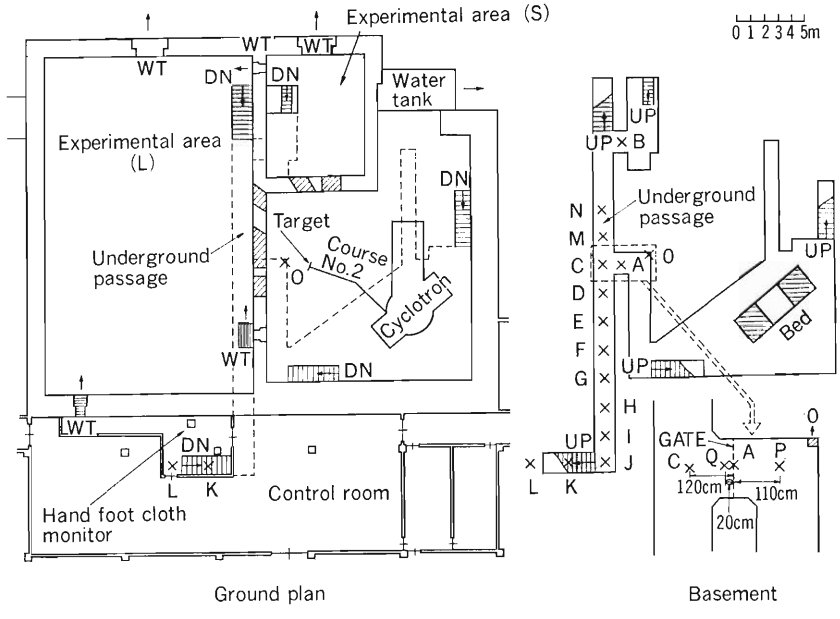

Fig. 1. Measuring positions of neutron and γ-ray dose rates in the cyclotron building.

* Neutron Dose Rate Meter 2202D, manufactured by AB Atomenergi, Sweden.

** UP/DOWN Counter MH-712A, manufactured by Honda KIT, Japan.

Table 1. Leakage-radiation dose (in mrem) in the underground passage of the cyclotron building from April, 1983 to March, 1984.

Radiation	Position*					
	A					B
	Deuteron			Other ions	Total	
	July**	December	March			
γ-Rays (mrem)	2,530	9,790	20	2,200	14,540	70
Thermal neutrons (mrem)	780	2,610	0	590	3,980	30
Fast neutrons (mrem)	10	17,550	0	170	17,730	20
Total (mrem)	3,320	29,950	20	2,960	36,250	120

* Positions indicated in Fig. 1.

** The beam times allotted to deuteron acceleration in July were 63 hr, but the values were obtained by measuring for 27 hr.

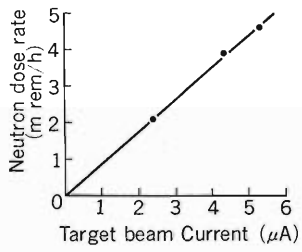

Fig. 2. Neutron dose rates at point C *vs.* the target beam current when the cyclotron was operating on 28 MeV alpha.

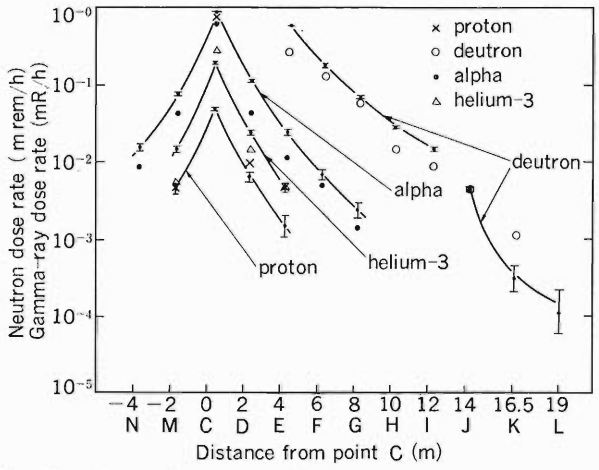

Fig. 3. Attenuation curves of neutron dose rates and γ-ray dose rates. The solid line shows neutron dose rates and the points indicated by ×, ○, •, and △ show γ-ray dose rates.

surement was about 1×10^{-4} mrem/hr. The neutron radiation was also measured with a rate meter equipped with the rem meter. The range of measurement with the rate meter was 0.1 to 10,000 mrem/hr The ratio of neutron dose rates with the pulse counter of the rem meter to those by the rate meter was about 1.4 at point C. The γ-ray dose rate was measured with a GM survey meter,* and the value of the target beam current was recorded by using an electronic recorder.**

* Geiger-Muller Counter Tube Type Radiation Survey Meter SUM-BG6, manufactured by IPCR.

** Multi-pen Recorder KA-62-32L, manufactured by Rikadenki, Japan.

Table 2. Neutron dose rates (mrem/hr) at points P and Q.

Position	Height above the floor	
	0.5 m	1.4 m
P	0.28	0.35
Q	0.19	0.10

Figure 2 shows the neutron dose rates at point C as a function of the target beam current when the cyclotron was operating on 28 MeV alpha. Since the dose rate is proportional linearly to the beam current, the dose rates measured at given target beam currents were normalized to the dose rates per unit target beam current.

The attenuation curves of neutron dose rate and γ-ray dose rate are shown in Fig. 3. These attenuation curves indicate that:

(1) Attenuation of the neutron dose rate was observed clearly in the low dose rate range, because the neutron was measured by the rem meter with pulse counter.

(2) The neutron dose rates rapidly decreased at distances larger than 14 m from point C, because the passage is curved to the right angle and the area at the end of the underground passage is open.

(3) In Fig. 3 the γ-ray dose rates are compared with neutron dose rates. The ratios of γ-ray dose rate to neutron dose rate were about 0.5–1.0 on acceleration of deuteron, helium-3, and alpha. When the proton was accelerated, the ratio became larger as the measuring points approach the cyclotron vault. The ratios measured at points A, C, D, and E were >17, 14, 1.5, and 3, respectively.

There is a hole (point O) through which many cables run between the cyclotron vault and the underground passage. In order to know the streaming effect through this hole we measured neutron dose rates at 1.4 m and 0.5 m above the floor at

points P and Q. The results are listed in Table 2.

The neutron dose rate at 1.4 m of point P was higher than that at 0.5 m, and that at 0.5 m of point Q was higher than the dose rate at 1.4 m, because the leakage neutrons from the hole were added to those from the cyclotron vault.

References

1) M. A. Lone, C. B. Bigham, J. S. Fraser, H. R. Schneider, T. K. Alexander, A. J. Ferguson, and A. B. Mcdonald: *Nucl. Instrum. Methods*, **143**, 331 (1977).
2) H. Kamitsubo, I. Kohno, S. Motonaga, M. Yanokura, T. Shikata, M. Yatsuhashi, T. Suematsu, and H. Kobayashi: *RIKEN Accel. Progr. Rep.*, **16**, 118 (1982).

RIKEN Accel. Progr. Rep. 18 (1984)

VI-2. Routine Monitoring of RIKEN Accelerators

I. Sakamoto, S. Fujita, M. Yanokura, T. Kobayashi, and K. Igarashi

Results of routine radiation monitoring carried out on the cyclotron, RILAC, and TANDETRON from April, 1983, to March, 1984, are described.

Some aspects of the leakage radiation from the cyclotron are described in the succeeding report.

1) Residual Radiation of the Cyclotron

In December, 1983, the cyclotron had been operated for about 70 hr with 20 MeV deuteron and with target beam current of 10–20 μA. The dose rates due to residual activities of the machine were measured 17 days after machine shutdown. The result is shown in Table 1.

The external exposure doses of two workers during replacement of septum were 20 and 30 mrem.

2) Surface and Air Contamination in the Cyclotron Building

The surface contamination has been kept below 10^{-5} μCi/cm^2 on the floor of the cyclotron vault and below 10^{-6} μCi/cm^2 on the floors of the experimental areas, underground passage, hot laboratory, and chemical laboratories. The radioactive nuclides found by γ-ray spectrometry were ^{65}Zn, ^{185}Os, ^{183}Re, and ^{184}Re. The contamination was wiped off twice a year, and immediately after this decontamination, the contamination on the floor of the above places was reduced to a value below 10^{-7} μCi/cm^2.

Table 1. Dose rates of residual activities.

Location	Dose rate (mR/hr)
ca. 70 cm apart from septum (before replacement of septum)	100
ca. 20 cm apart from septum holder (after replacement of septum)	100
at top of dee	100
Baffle box before BE magnet	30

When the radioactive substances were handled in the hot laboratory and chemical laboratories, the air in the draft chamber was contaminated by radioactivity. The air in the draft chamber was discharged through an exhaust, and the radioactivity in the exit was below 10^{-12} μCi/cm^3.

3) Drainage

The radioactivities in the drain water from the cyclotron and linac buildings were found to be of the order of 10^{-8}–10^{-4} μCi/cm^3. The total activities in aqueous effluents in this period was about 100 mCi, and the main radioactive nuclide was tritium, and the other nuclides could not be detected by the γ-ray spectrometry.

4) Radiation Monitoring of RILAC and TANDETRON

Leakage radiation during operation of RILAC was measured at the circumference of the linac building every month. No leakage γ-rays and neutrons from the linac building were detected.

The surface and air contamination due to residual activities could not be found in the radiation control area in the linac building.

X-ray monitoring was carried out on TANDETRON when boron ions were accelerated. When a vanadium target was bombarded by 2 MeV B^{2+} ions at 0.82 nA, the maximum dose rates

Table 2. Annual exposure doses received by RIKEN accelerator workers from April, 1983 to March, 1984.

Workers	Number of persons				Collective dose (man-mrem)
	Dose undetectable	10–100 (mrem)	>100 (mrem)	Total	
Cyclotron operation and maintenance group	2	6		8	230
Linac operation and maintenance group	8	2		10	20
Nuclear physicists	4	4		8	100
Accelerator physicists	11	3		14	40
Physicists in other fields	22	3	1	26	190
Nuclear chemists	3	7	1	11	380
Radiation chemists	4			4	
Biological chemists	10			10	
TANDETRON workers	12			12	
Health physicists	8			8	
Total	84	25	2	111	960

Average annual dose per person: 8.6 mrem; Maximum individual annual dose: 140 mrem.

measured around TANDETRON and at the outside of the TANDETRON room were 3.9 and 0.12 mR/hr, respectively. No leakage X-rays could be detected around the target chamber.

5) Personnel Monitoring

The external exposure doses to personnel were measured by using γ-ray and neutron film badges. The doses received during the present period by all RIKEN accelerator workers are shown in Table 2. The collective γ-ray dose to all workers was 960 man-mrem, while the collective dose owing to thermal and fast neutron exposures was too small to be detected. The collective dose to the workers was equal to that in the preceding period.

In this period the average annual dose per person was 8.6 mrem, and the maximum individual annual dose was 140 mrem.

VII. LIST OF PUBLICATIONS

1. Accelerator development and accelerator physics
   1) M. Odera: "Operation of the Riken Variable Frequency Heavy-Ion Linac, RILAC," Proc. China-Japan Joint Symp. on Accelerators for Nuclear Science and Their Applications, Ed. Yang Chenzhong and Wei Bowen, Lanzhou, p. 103 (1983).
   2) M. Odera: "Recent Progress of RIKEN Linac, RILAC," Proc. Int. Symp. on Heavy Ion Inertial Fusion, Ed. T. Katayama, INS, Tokyo, p. 425 (1984).
   3) M. Odera: "Report on Frequency Tunable Linac," Proc. 1984 Linear Accelerator Conf., Seeheim 1984, Ed. N. Angert, GSI-84-11, p. 36 (1984).
   4) M. Kase, T. Kambara, T. Tonuma, and M. Odera: "Beam Quality of the Variable-Frequency Linac, RILAC," Proc. 1984 Linear Accelerator Conf., Seeheim 1984, Ed. N. Angert, GSI-84-11, p. 145 (1984).
   5) M. Odera and M. Hemmi: "Accelerating Structure with Chain-Like Electrode Structure," Proc. 1984 Linear Accelerator Conf., Seeheim 1984, Ed. N. Angert, GSI-84-11, p. 346 (1984).
   6) I. Kohno: "Current Status on Confinement Ion Sources for Multiply Charged Heavy Ions," *J. Accel. Sci. and Tech.* (in Japanese), **2**, 53 (1984).
   7) Y. Yano: "RIKEN Accelerator Facility," *Genshikaku Kenkyu* (in Japanese), **28**, 341 (1984).
   8) M. Odera, Y. Chiba, T. Tonuma, M. Hemmi, Y. Miyazawa, T. Inoue, T. Kambara, M. Kase, T. Kubo, and F. Yoshida: "Variable Frequency Heavy-Ion Linac, RILAC. I. Design, Construction and Operation of Its Accelerating Structure," *Nucl. Instrum. Methods*, **227**, 187 (1984).

2. Nuclear physics and nuclear instrumentation
   1) T. Fukuda, T. Nomura, T. Shimoda, K. Katori, S. Shimoura, K. Sueki, and H. Ogata: "Linear Momentum Transfer in the Reaction ^{232}Th(^{14}N, Light Particles) at 208 MeV," *Nucl. Phys. A*, **429**, 193 (1984).
   2) J. Kasagi, K. Itoh, T. Kishimoto, M. Sasaki, and H. Ohnuma: "Gamma Decay of Positive-Parity Levels in ^{45}Ti from the ^{42}Ca(α, nγ) ^{45}Ti Reaction," *Nucl. Phys. A*, **414**, 206 (1984).
   3) K. Hatanaka, N. Matsuoka, T. Saito, K. Hosono, M. Kondo, S. Kato, T. Higo, S. Matsuki, Y. Kadota, and K. Ogino: "Systematic Study of the (d, p) Reaction with 56 MeV Polarized Deuterons," *Nucl. Phys. A*, **419**, 530 (1984).
   4) K. Hatanaka, N. Matsuoka, H. Sakai, T. Saito, K. Hosono, Y. Koike, M. Kondo, K. Imai, H. Shimizu, T. Ichihara, K. Nisimura, and A. Okihana: "Measurements of Analyzing Powers A_y, A_{xx}, A_{yy} and A_{xz} in dp Elastic Scattering at E_d=56 MeV," *Nucl. Phys. A*, **426**, 77 (1984).
   5) S. Yamaji and M. Tohyama: "Effects of Two Particle-Two Hole Excitations of the Mass Distribution in the ^{16}O+^{40}Ca Reaction at E_{Lab}=157.3 MeV," *Phys. Lett. B*, **147**, 399 (1984).
   6) Y. Ishibe, S. Ishii, K. Okazaki, H. Oyama, Y. Sakamoto, K. Yano, N. Noda, K. Toi, S. Tanahashi, and K. Okubo: "An Attempt to Improve the Electron Cyclotron Resonance Discharge Cleaning of a Tokamak Devices," *J. Nucl. Mater.*, **128** & **129**, 889 (1984).
   7) T. Kawabe, H. Hirata, M. Ichimura, H. Kanda, N. Yamaguchi, K. Yatsu, and Y. Sakamoto: "Wall Conditioning of Gamma 10 Tandem Mirror Device," *J. Nucl. Mater.*, **128** & **129**, 893 (1984).
   8) M. Sugawara, Y. Gono, and Y. Itoh: "In-Beam γ-Ray Study of ^{217}Ra," *J. Phys. Soc. Jpn.*, **53**, 2956 (1984).
   9) K. Hatanaka, M. Fujiwara, K. Hosono, N. Matsuoka, T. Saito, and H. Sakai: "^{24}Mg (p, d) ^{23}Mg Reaction at 65 and 80 MeV," *Phys. Rev. C*, **29**, 13 (1984).
   10) H. Kudo, K. J. Moody, and G. T. Seaborg: "Mass Distributions in the Reaction of 240 MeV ^{12}C with ^{197}Au," *Phys. Rev. C*, **30**, 1561 (1984).
   11) Y. Nagame, H. Nakahara, K. Sueki, H. Kudo, M. Yanokura, and I. Kohno: "Studies on Strongly Damped Components in Relatively Light Heavy Ion Reaction Systems," *Z. Phys. A-Atoms Nuclei*, **317**, 31 (1984).
   12) A. Hashiba, K. Masuda, T. Doke, T. Takahashi, and Y. Fujita: "Fano Factor in Gaseous Argon Measured by the Proportional Scintillation Method," *Nucl. Instrum. Methods*, **227**, 305 (1984).
   13) K. Asahi, M. Ishihara, H. Kamitsubo, N. Takahashi, Y. Nojiri, T. Minamisono, A. Mizobuchi, and K. Sugimoto: "Measurement

of Ejectile Spin Polarization in Heavy Ion Reactions via β Decay Asymmetry," *Nucl. Instrum. Methods*, **220**, 389 (1984).
14) Y. Ishibe, S. Ishii, K. Okazaki, H. Oyama, Y. Sakamoto, K. Yano, T. Nozaki, M. Aratani, S. Hayashi, I. Kohno, N. Noda, K. Toi, S. Tanahashi, K. Akaishi, and K. Okubo: "ECR Discharge Cleaning in the JIPPT-II U Torus Device," *Shinku* (in Japanese), **27**, 376 (1984).
15) Y. Sakamoto, S. Ishii, K. Okazaki, K. Yano, N. Noda, and R. E. Clausing: "ECR Discharge Cleaning for the TEXTOR Device II," *Shinku* (in Japanese), **27**, 380 (1984).
16) H. Ohsumi, H. Ejiri, T. Shibata, Y. Nagai, K. Okada, T. Motobayashi, N. Noumachi, A. Shimizu, and K. Maeda: "Neutron Spectroscopy for Giant Resonance," Proc. Int. Symp. on Nuclear Spectroscopy and Nuclear Interactions; World Scientific Publishing Co., Singapore, p. 317 (1984).
17) T. Nomura and T. Sugitate: "Energetic Light-Particle Emission and Its Polarization in Heavy-Ion Reactions," *Butsuri* (in Japanese), **39**, 261 (1984).
18) T. Nomura: "Evidence for Lower Angular-Momentum Cutoff in Heavy-Ion Fusion Reactions," JAERI-M 84-085, p. 104 (1984).

3. Atomic and solid-state physics
1) M. Uda, H. Endo, K. Maeda, Y. Sasa, K. Fujima, and K. Fuwa: "Application of Ion Induced X-Ray Emission Spectroscopy to Chemistry," Proc. 2nd Symp. on Ion Beam Technology, Hosei Univ., p. 129 (1983).
2) K. Maeda, Y. Sasa, Y. Yokode, M. Maeda, M. Kobayashi, K. Fujima, and M. Uda: "Several Applications of PIXE Analysis," Proc. 2nd Symp. on Ion Beam Technology, Hosei Univ., p. 157 (1983).
3) K. Fujima and T. Watanabe: "Electronic Structure of Cold Neon Plasma," Proc. of 1984 Int. Symp. on Heavy Ion Accelerators and Their Applications to Inertial Fusion (Inst. Nucl. Study, Univ. of Tokyo), p. 571 (1983).
4) I. Shimamura and A. C. Roy: "Transitions of Molecules between High-Angular-Momentum States," Atomic Collision Res. in Japan-Prog. Rep., No. 10, p. 1 (1984).
5) A. Ohsaki, T. Watanabe, K. Nakanishi, and K. Iguchi: "Classical Trajectory Monte Carlo Calculation for $\mu^+ + (\mu^- p) \rightarrow (\mu^+ \mu^-) + p$ and $e^+ + (e^- p) \rightarrow (e^+ e^-) + p$," Atomic Collision Res. in Japan-Prog. Rep., No. 10, p. 3 (1984).
6) Q. Ma, X. Chang, Z. Liu, Y. Liu, and T. Watanabe: "Distorted Wave Born Cross Section for $\mu^+ + (\mu^- p) \rightarrow (\mu^+ \mu^-) + p$," Atomic Collision Res. in Japan-Prog. Rep., No. 10, p. 6 (1984).
7) S. Karashima, T. Watanabe, X. Chang, Z. Liu, Q. Ma, and Y. Liu: "Electron Stripping Cross Section of Multiply Charged Ions by Collision with Neutral Atoms," Atomic Collision Res. in Japan-Prog. Rep., No. 10, p. 52 (1984).
8) K. Ando, T. Tonuma, S. Kohmoto, H. Kumagai, Y. Awaya, S. Tsurubuchi, and K. Sato: "Spectra of Highly Ionized Aluminum Atoms in Beam-Foil Experiment," Atomic Collision Res. in Japan-Prog. Rep., No. 10, p. 73 (1984).
9) T. Kambara, Y. Awaya, M. Kase, H. Kumagai, H. Shibata, and S. M. Shafroth: "Kβ X-rays from Ar-Ions Passing through Foils," Atomic Collision Res. in Japan-Prog. Rep., No. 10, p. 75 (1984).
10) S. M. Shafroth, Y. Awaya, T. Kambara, M. Kase, H. Kumagai, M. Nishida, and H. Shibata: "Angular Distribution of REC for Ar^{4+} on C at 1 MeV/u," Atomic Collision Res. in Japan-Prog. Rep., No. 10, p. 78 (1984).
11) J. Mizuno, T. Ishihara, and T. Watanabe: "Classical and Quantal Auger Profiles Due to Inner-Shell Photoionization near Threshold," *J. Phys. B: At. Mol. Phys.*, **17**, L85 (1984).
12) T. Tonuma, M. Kase, T. Kambara, H. Kumagai, T. Matsuo, J. Urakawa, H. Shibata, J. Takahashi, S. Özkök, S. H. Be, I. Kohno, and H. Tawara: "Projectile Charge-State Dependence of Recoil-Ion Charge-State Distribution Produced in Heavy-Ion Impact," *J. Phys. B: At. Mol. Phys.*, **17**, L317 (1984).
13) H. Shibata, K. Kuroki, F. Nishimura, and N. Oda: "Partial Generalized Oscillator Strengths for Ionization of the Nitrogen Molecule by 1 keV Electron Impact," *J. Phys. B: At. Mol. Phys.*, **17**, L739 (1984).
14) T. Kambara: "Collisional Quenching of np States of 110 MeV H-Like Ne Ions in Gaseous Targets," *J. Phys. B: At. Mol. Phys.*, **17**, 1599 (1984).
15) N. Shimakura and T. Watanabe: "Differential Cross Sections for $Li^+ + Li$ Collisions Using Molecular Bases: Quantum Effect," *J. Phys. B: At. Mol. Phys.*, **17**, 2638 (1984).
16) S. Hara and H. Sato: "Theoretical Study of Autoionizing States of Molecules: H_2 and He_2^{2+}," *J. Phys. B: At. Mol. Phys.*, **17**, 4301 (1984).

17) H. Suzuki, Y. Kajikawa, N. Toshima, H. Ryufuku, and T. Watanabe: "Electron-Capture Cross Sections from He in Collision with Bare Nuclear Ions," *Phys. Rev. A*, **29**, 525 (1984).
18) H. Suzuki, N. Toshima, T. Watanabe, and H. Ryufuku: "Exponential Distorted-Wave Approximation for Charge Transfer in Collisions of Multicharged Ions with Atomic Hydrogen," *Phys. Rev. A*, **29**, 529 (1984).
19) M. Uda, K. Maeda, A. Koyama, and Y. Sasa: "Chemical Effects on F KVV Auger Spectra Induced by Photon Impact," *Phys. Rev. A*, **29**, 1258 (1984).
20) E. Yagi, G. Flik, K. Fürderer, N. Haas, D. Herlach, J. Major, A. Seeger, W. Jacobs, M. Krause, M. Krauth, H. -J. Mundinger, and H. Orth: "Quantum Diffusion of Positive Muons in Iron," *Phys. Rev. B*, **30**, 441 (1984).
21) Y. Yatsurugi, O. Kuboi, M. Hashimoto, H. Nagai, M. Aratani, M. Yanokura, I. Kohno, and T. Nozaki: "Studies of a-Si: H Growth Mechanism by Rutherford Recoil Measurement of H and D in Films Prepared from SiH4-D2 and SiD4-H2, *Appl. Phys. Lett.*, **44**, 246 (1984).
22) O. Kuboi, M. Hashimoto, Y. Yatsurugi, H. Nagai, M. Aratani, M. Yanokura, S. Hayashi, I. Kohno, and T. Nozaki: "Origin of Hydrogen in Amorphous Silicon Produced by Glow Discharge in Si2H6+D2 and Si2D6+H2," *Appl. Phys. Lett.*, **45**, 543 (1984).
23) T. Tonuma, S. H. Be, H. Kumagai, H. Shibata, M. Kase, T. Kambara, I. Kohno, and H. Tawara: "Multiple Ionization of Atoms by Highly Ionized Heavy Ion Impact," Abstracts of International Conference on the Physics of Highly Ionized Atoms, Oxford Univ., p. 59 (1984).
24) K. Asai, F. Ambe, S. Ambe, and H. Sekizawa: "TDPAC of γ-Rays Emitted from ^{111}Cd ($\leftarrow$ ^{111}In) in α-Fe_2O_3," *J. Phys. Soc. Jpn.*, **53**, 4109 (1984).
25) K. Nishiyama, E. Yagi, K. Ishida, T. Matsuzaki, K. Nagamine, and T. Yamazaki: "New Approach in μ^+SR Study on Critical Phenomena in Ni," *Hyperfine Interact.*, **17–19**, 473 (1984).
26) K. Fukai, K. Shiraishi, E. Yagi, S. Hamada, and T. Sawai: "Measurement of Mean Projected Range for Argon- and Nitrogen-ions Irradiated in Stainless Steels," *J. At. Energy Soc. Jpn.* (in Japanese), **26**, 974 (1984).
27) E. Yagi: "Diffusion of Positive Muons in Metals," JAERI-M83 (in Japanese), p. 19 (1984).
28) Y. Sakamoto, O. Nomura, and H. Oyama: "Plasma Chemical Reactions on Solid Surface," *J. Chem. Soc. Jpn.* (in Japanese), No. 10, p. 1617 (1984).
29) T. Watanabe: "Electron Capture and Loss Cross Sections by Atomic Collisions," Proc. of 1984 INS Int. Symp. on Heavy Ion Accelerators and Their Applications to Inertial Fusion (Inst. Nucl. Study, Univ. of Tokyo), p. 495 (1984).
30) S. Karashima and T. Watanabe: "Charge Equilibrium of Fast Ions Traversing through Gaseous Media," Proc. of 1984 INS Int. Symp. on Heavy Ion Accelerators and Their Applications to Inertial Fusion (Inst. Nucl. Study, Univ. of Tokyo), p. 561 (1984).
31) S. Karashima and T. Watanabe: "Charge Equilibrium of Energetic Heavy Ions in Gaseous Media (Ideal Atomic Hydrogen Gas)," *Jpn. J. Appl. Phys.*, **22**, 895 (1984).
32) I. Shimamura: "Rotational Excitation of Molecules by Slow Electrons," Electron-Molecule Collisions, Eds. I. Shimamura and K. Takayanagi, Plenum Press, New York, Chap. 2, p. 89 (1984).
33) T. Watanabe, T. Arikawa, I. Shimamura, and A. Yagishita: "Report on the 13th International Conference on the Physics of Electronic and Atomic Collisions and Related Satellite Meetings," *Bull. Phys. Soc. Jpn.*, **39**, 203 (1984).
34) M. Sekiya, T. Noro, F. Sasaki, and K. Ohno: "The Calculation of L_{23}-M_1M_1 Auger Energy and Relative Auger Rates for Ar^{6+} and Ar^{7+}," Contribution from the Research Group on Atoms and Molecules, **14**, 4 (1984).
35) I. Shimamura: "Line-Shape Analysis of Energy-Loss Spectra and Photoelectron Spectra," Wavefunctions and Mechanisms from Electron Scattering Processes, Springer, Berlin, p. 210 (1984).
36) S. Karashima and T. Watanabe: "Equilibrium Charge and LET of Incident Heavy Ions (Ne and Ar) in Hydrogen Gas," *Radiat. Res.*, **99**, 476 (1984).
37) N. Sakai, O. Terashima, and H. Sekizawa: "Magnetic Compton Profile Measurement Using Circularly Polarized Gamma-Rays from Oriented ^{191m}Ir Nuclei," *Nucl. Instrum. Methods*, **221**, 419 (1984).
38) Y. Sakamoto, H. Oyama, and S. Kakinuma: "Simulation Experiment on Chemical Sputtering of Carbides for the ECR and Glow Discharge Cleaning," *J. Nucl. Mater.*, **128**

& **129**, 867 (1984).
39) S. H. Be and K. Yano: "Production of Negative Ions by Bombarding a Cesiated Metal Surface with Cluster Ions and Post-Acceleration," *Rev. Sci. Instrum.*, **55**, 1928 (1984).
40) Y. Sakamoto and H. Oyama: "Interaction of TiC with Hydrogen Plasma," *Shinku* (in Japanese), **27**, 383 (1984).

4. Radiochemistry, radiation chemistry and radiation biology
1) T. Ohno, T. Nishimura, K. Nakano, and I. Kaneko: "Differential Recovery from Potentially Lethal Damage in Normal Human Lung Fibroblasts after Irradiation with ^{60}Co γ-Rays and Accelerated N-Ion Beam," *Int. J. Radiat. Biol.*, **45**, 21 (1984).
2) T. Takahashi, F. Yatagai, T. Katayama, M. Inada, and S. Konno: "Track Structure Theories and Their Application for Inactivation Cross Sections of Bacterial Cells," *J. Radiat. Res.*, **25**, 21 (1984).
3) M. Nakamura, Y. Mochizuki, K. Usami, Y. Itoh, and T. Nozaki: "Infrared Absorption Spectra and Compositions of Evaporated Silicon Oxides (SiO_x)," *Solid State Comm.*, **50**, 1079 (1984).
4) M. Yuasa, Y. Ogata, H. Nishide, E. Tsuchida, M. Iwamoto, and T. Nozaki: "Determination of Chemically Bound Oxygen by ^{15}O-O Tracer Method. Application to Hemoglobin- and Synthetic Heme-Bound Oxygen," *Chem. Lett.*, **1984**, 1889.
5) S. Ambe: "Separation of Trace Elements, In(III), Sn(IV), Sb(V) and Te(IV) by Adsorption on Activated Carbon and Graphite," *J. Radioanal. Nucl. Chem. Articles*, **81**, 77 (1984).

(Papers Presented at Meetings)

1. Accelerator development and accelerator physics
1) Y. Yano: "RIKEN Accelerator Facility," INS-Kikuchi Winter School on Accelerators for Nuclear Physics, Fujiyoshida, Jan. (1984).
2) T. Kambara: "Variable Frequency Heavy Ion Linear Accelerator," INS-Kikuchi Winter School on Accelerators for Nuclear Physics, Fujiyoshida, Jan. (1984).
3) K. Ikegami, S. Nakajima, Y. Oikawa, S. Motonaga, and S. H. Be: "Vacuum System of the RIKEN SSC," Proc. 5th Meeting Ultra High Vacuum Techniques for Accelerator and Storage Rings, Tsukuba, Mar., p. 135 (1984).
4) K. Ikegami, K. Nakajima, Y. Oikawa, S. Motonaga, and S. H. Be: "Status of the Design of the SSC Vacuum System at RIKEN," Proc. 5th Meeting Ultra High Vacuum Techniques for Accelerators and Storage Rings," Tsukuba, Mar., p. 139 (1984).
5) N. Nakanishi, A. Goto, and Y. Yano: "Orbit Analysis for Off-Centered Beams in the RIKEN SSC," 39th Ann. Meeting Phys. Soc. Jpn., Fukuoka, Apr. (1984).
6) M. Kase, A. Goto, T. Kambara, and M. Odera: "Acceleration Characteristics of Variable Frequency Heavy-Ion Linac," 39th Ann. Meeting Phys. Soc. Jpn., Fukuoka, Apr. (1984).
7) M. Kase and M. Odera: "Variable Frequency Linac, RILAC, as an Injector of a Separated Sector Cyclotron," 10th Int. Conf. Cyclotrons and Their Applications, East Lansing, U.S.A., Apr. (1984).
8) A. Goto, N. Nakanishi, and Y. Yano: "Computer Simulations of Accelerated Particles in the RIKEN SSC," 10th Int. Conf. Cyclotrons and Their Applications, East Lansing, U.S.A., May (1984).
9) T. Fujisawa, K. Ogiwara, S. Kohara, Y. Oikawa, I. Yokoyama, M. Hara, I. Takeshita, and Y. Chiba: "Design of the RF System of the RIKEN SSC," 10th Int. Conf. Cyclotrons and Their Applications, East Lansing, U.S.A., May (1984).
10) M. Kase, T. Kambara, T. Tonuma, and M. Odera: "Beam Quality of Variable Frequency Linac, RILAC," 1984 Linear Accelerator Conf., Seeheim, W. Germany, May (1984).
11) K. Ikegami, T. Noda, N. Kamiyama, and I. Kohno: "Automatic Operation of Gas Circulation and Gas-Feed System for the Ion Source of the 160 cm Cyclotron," Proc. 8th Symp. on Ion Sources and Ion-Assisted Technology, Tokyo, June, p. 115 (1984).
12) Y. Yano: "RIKEN Accelerator Facility," Proc. 8th Symp. on Ion Sources and Ion-Assisted Technology, Tokyo, June, p. 157 (1984).
13) M. Yanokura: "Design Study of the RIKEN ECR II," Proc. 8th Symp. Ion Sources and Ion-Assisted Technology, Tokyo, June (1984).
14) S. Motonaga and SSC Group: "Status of the RIKEN SSC," Proc. 5th Symp. on Accelerator Science and Technology, Tsukuba, Sept., p. 21 (1984).
15) K. Ikegami, T. Noda, N. Kamiyama, and I. Kohno: "Automatic Operation of Gas Circulation and Gas-Feed System for the Ion

Source of the 160 cm Cyclotron," Proc. 5th Symp. on Accelerator Science and Technology, Tsukuba, Sept., p. 36 (1984).
16) M. Odera, M. Hemmi, A. Goto, and M. Hara: "New Alvarez-Type Linac Structure with Chain-Like Electrodes," Proc. 5th Symp. Accelerator Science and Technology, Tsukuba, Sept., p. 56 (1984).
17) Y. Yano and A. Goto: "A Method to Measure Two-Dimensional Motion of Orbit Center with Three Radial Differential Probes," Proc. 5th Symp. Accelerator Science and Technology, Tsukuba, Sept., p. 133 (1984).
18) K. Hatanaka, T. Inamura, Y. Yano, K. Yamaguchi, and H. Kamitsubo: "The RIKEN SSC Beam Handling System," Proc. 5th Symp. Accelerator Science and Technology, Tsukuba, Sept., p. 184 (1984).
19) S. Nakajima, K. Ikegami, Y. Oikawa, S. H. Be, and S. Motonaga: "Design of the Vacuum System of the RIKEN SSC," Proc. 5th Symp. Accelerator Science and Technology, Tsukuba, Sept., p. 229 (1984).
20) T. Wada, J. Fujita, K. Shimizu, I. Yokoyama, and T. Kambara: "Control System of the RIKEN SSC (I)," Proc. 5th Symp. Accelerator Science and Technology, Tsukuba, Sept., p. 358 (1984).
21) T. Kambara and M. Odera: "Control System of IPCR Heavy Ion Linac," Proc. 5th Symp. Accelerator Science and Technology, Tsukuba, Sept., p. 364 (1984).
22) T. Shikata, N. Nakanishi, T. Kosako, and S. Fujita: "Radiation Shielding for the RIKEN SSC," Proc. 5th Symp. Accelerator Science and Technology, Tsukuba, Sept., p. 391 (1984).

2. Nuclear physics and nuclear instrumentation
1) T. Nomura: "Evidence for Lower Angular-Momentum Cutoff in Heavy-Ion Fusion Reactions," JAERI-Symp. Heavy Ion Reactions, Tokai, Jan. (1984).
2) S. Yamaji: "Present Status of the Application of TDHF Theory to Heavy Ion Collisions," JAERI-Symp. Heavy Ion Reactions, Tokai, Jan. (1984).
3) S. Yamaji: "Effect of Two-Body Collisions in TDHF," RIFP-Symp. Collective Motions, Kyoto, Jan. (1984).
4) H. Ohsumi, K. Okada, T. Shibata, Y. Nagai, T. Motobayashi, and H. Ejiri: "Neutron Decay Properties of Giant Quadrupole Resonance Region in ^{92}Zr," Int. Symp. Nuclear Spectroscopy and Nuclear Interactions, Osaka, Mar. (1984).
5) Y. Gono, M. Fukuda, M. Ishihara, T. Inamura, T. Nomura, and H. Kamitsubo: "BGO Anti-Compton Spectrometer," 39th Ann. Meeting Phys. Soc. Jpn., Fukuoka, Apr. (1984).
6) N. Yoshida, A. Arima, and T. Otsuka: "Description of High-Spin States in the Interacting Boson Model," 39th Ann. Meeting Phys. Soc. Jpn., Fukuoka, Apr. (1984).
7) K. Takeyama, K. Matsuta, K. Asahi, Y. Nojiri, and T. Minamisono: "Nuclear Spin Polarization of Short-Lived β-Emitting Nucleus Using Tilted Foil Technique," 39th Ann. Meeting Phys. Soc. Jpn., Fukuoka, Apr. (1984).
8) K. Matsuta, T. Minamisono, Y. Nojiri, and K. Asahi: "Energy Dependence of Anisotropy in β-decays of the A=12 System," 39th Ann. Meeting Phys. Soc. Jpn., Fukuoka, Apr. (1984).
9) S. Yamaji and M. Tohyama: "Effects of Two Particle-Two Hole Excitations on the Variances of Mass Distribution in the ^{16}O+^{40}Ca Reaction," 39th Ann. Meeting Phys. Soc. Jpn., Fukuoka, Apr. (1984).
10) M. Sugawara, Y. Gono, T. Kubo, and M. Fukuda: "In-Beam γ-Ray Study of ^{212}Po," 39th Ann. Meeting Phys. Soc. Jpn., Fukuoka, Apr. (1984).
11) A. Hashizume, M. Ohshima, T. Inamura, E. Minehara, S. Kikuchi, and H. Kumahora: "Ground State Rotational Band Excited by (^{58}Ni, ^{58}Ni')," 39th Ann. Meeting Phys. Soc. Jpn., Fukuoka, Apr. (1984).
12) S. Yamaji and M. Tohyama: "Effects of Two Particle-Two Hole Excitations on the Variances of Mass Distribution in the ^{16}O+^{40}Ca Reaction at E_{Lab}=157.3 MeV," 1984 INS-RIKEN Int. Symp. Heavy Ion Physics, Yamanashi, Aug. (1984).
13) T. Nomura: "Low Angular-Momentum Cutoff in Heavy-Ion Fusion Reactions," 1984 INS-RIKEN Int. Symp. Heavy Ion Physics, Yamanashi, Aug. (1984).
14) T. Nomura, K. Sueki, S. Kohmoto, H. Kudo, K. Morita, T. Kubo, and M. Adachi: "Possible Existence of Low-Spin Cutoff in Heavy-Ion Fusion Reactions," 1984 INS-RIKEN Int. Symp. Heavy Ion Physics, Yamanashi, Aug. (1984).
15) T. Nomura: "Sensitivity of Product Cross Sections to Low Angular-Momentum Cutoff in Fusion Reactions," 1984 INS-RIKEN Int. Symp. Heavy Ion Physics, Yamanashi, Aug. (1984).
16) T. Inamura: "Massive Transfer in Heavy

Ion Reactions," Invited Lecture at the 16th Masurian Summer School on Nuclear Physics "Heavy Ions in Nuclear Physics," Mikolajki, Poland, Aug. (1984).

17) T. Murakami, J. Kasagi, H. Harada, H. Tachibanaki, Y. Gono, and M. Fukuda: "BGO Crystal-as a High Energy γ-Ray Detector," 1984 Fall Meeting Phys. Soc. Jpn., Mito, Sept. (1984).
18) H. Harada, T. Murakami, J. Kasagi, and T. Inamura: "Excited States in ^{110}Sn Studied with the ^{98}Mo(^{16}O, 4nγ)^{110}Sn Reaction," 1984 Fall Meeting Phys. Soc. Jpn., Mito, Sept. (1984).
19) Y. Gono, Y. Ishikawa, M. Sugawara, M. Fukuda, and Y. Yoshikawa: "Spectroscopy of ^{218}Ra Studied with BGOACS," 1984 Fall Meeting Phys. Soc. Jpn., Mito, Sept. (1984).
20) T. Murakami, J. Kasagi, H. Harada, H. Tachibanaki, Y. Gono, and M. Fukuda: "High-Energy γ-Ray Detector of BGO," 1984 Fall Meeting Phys. Soc. Jpn., Mito, Sept. (1984).
21) K. Sato: "Backward Angular Distribution in the Generalized Exciton Model," 1984 Fall Meeting Phys. Soc. Jpn., Mito, Sept. (1984).
22) K. Sueki, M. Magara, H. Nakahara, Y. Hamajima, and I. Kohno: "Heavy Particle Emitting Reaction from ^{16}O+^{54}Fe and ^{20}Ne+^{50}Cr Systems," 1984 Fall Meeting Phys. Soc. Jpn., Mito, Sept. (1984).
23) H. Harada, M. Murakami, J. Kasagi, and T. Inamura: "Study of Level Structure of ^{110}Sn by the ^{98}Mo(^{16}O, 4nγ)^{110}Sn Reaction," 1984 Fall Meeting Phys. Soc. Jpn., Mito, Sept. (1984).
24) S. Kohmoto: "Tilted Foil Method by Thin Foils," 1984 Fall Meeting Phys. Soc. Jpn., Mito, Oct. (1984).
25) Y. Hamajima, K. Sueki, M. Magara, H. Nakahara, and I. Kohno: "Mass Splitting of Lower Energy Fission," 28th Symp. Radiochemistry, Kobe, Oct. (1984).
26) T. Nomura, S. Kohmoto, K. Morita, H. Kudo, K. Sueki, M. Magara, and M. Adachi: "Search of Lower Critical Angular Momentum for Heavy-Ion Fusion Reaction," 28th Symp. Radiochemistry, Kobe, Oct. (1984).
27) K. Sueki, M. Magara, H. Yoshikawa, Y. Hatsukawa, H. Nakahara, Y. Hamajima, and I. Kohno: "Search of Fusion-Fission from Compound Nucleus ^{70}Se," 28th Symp. Radiochemistry, Kobe, Oct. (1984).
28) M. Magara, K. Sueki, H. Nakahara, I. Kohno, H. Kudo, and Y. Hamajima: "Heavy-Ion Reaction between ^{14}N+^{238}U," 28th Symp. Radiochemistry, Kobe, Oct. (1984).
29) T. Aoki, H. Garna, D. Price, Y. Sakamoto, and RFC Group: "Characterization of RF Pulse Discharge Cleaning," Proc. 1st Fall Meeting Jpn. Soc. Plasma Physics and Nuclear Fusion, Kanagawa, Oct., p. 96 (1984).
30) Y. Gono, M. Fukuda, Y. Ishikawa, M. Sugawara, T. Inamura, M. Ishihara, T. Nomura, I. Kohno, H. Kamitsubo, J. Kasagi, and T. Murakami: "RIKEN BGOACS System," Conf. Inst. Heavy-Ion Nuclear Research, Oak Ridge, U.S.A., Oct. (1984).

3. Atomic and solid-state physics

1) T. Watanabe: "Electronic Structure of High Density Plasma III," Discussion Meeting Theoretical Foundation for Pelet Design, Katada, Jan. (1984).
2) K. Fujima and T. Watanabe: "Electronic Structure of Cold Ne Dense Plasma," 1984 INS Int. Symp. Heavy Ion Accelerators and Their Applications to Inertial Fusion, Tanashi, Jan. (1984).
3) T. Watanabe: "Electron Capture and Loss Cross Sections in Atomic Collisions," 1984 INS Int. Symp. Heavy Ion Accelerators and Their Applications to Inertial Fusion, Tanashi, Jan. (1984).
4) S. Karashima and T. Watanabe: "Charge Equilibrium of Fast Heavy Ions Traversing Gaseous Media," 1984 INS Int. Symp. Heavy Ion Accelerators and Their Applications to Inertial Fusion, Tanashi, Jan. (1984).
5) T. Watanabe and K. Hino: "Theory of Ion-Atom Collisions at High Energy (I); Non-Radiative and Radiative Electron Capture," Joint Seminar Atomic Physics, Solid State Physics and Material Sciences in High Energy Region of Tandem Accelerators, Tokai-mura, Jan. (1985).
6) S. Karashima and T. Watanabe: "Theory of Ion-Atom Collisions at High Energy (II); Charge Equilibrium Processes," Joint Seminar Atomic Physics, Solid State Physics and Material Sciences in High Energy Region of Tandem Accelerators, Tokai-mura, Jan. (1985).
7) O. Kuboi, Y. Yatsurugi, H. Nagai, M. Aratani, M. Yanokura, S. Hayashi, I. Kohno, and T. Nozaki: "Studies of a-Si: H Growth Mechanism by Distilling Exhaust Gas of Glow Discharge Plasma," 31th Spring Meeting Jpn. Soc. Appl. Phys. and Related Societies, Kawasaki, Mar. (1984).
8) A. Yunoki, S. Tamada, K. Masuda, A. Hitachi, J. Kikuchi, T. Doke, and T. Taka-

hashi: "LET Dependence of Scintillation Light Yield from Liquid Argon and Xenon," 31th Spring Meeting Jpn. Soc. Appl. Phys. and Related Societies, Kawasaki, Mar. (1984).
9) K. Fukai, K. Shiraishi, S. Hamada, T. Sawai, and E. Yagi: "Measurement of Mean Projected Range for Ar- and N-Ions Injected into Stainless Steels," 1984 Ann. Meeting At. Energy Soc. Jpn., Osaka, Mar. (1984).
10) Y. Kawabata, M. Utsuro, S. Okamoto, H. Yoshiki, S. Hayashi, and T. Nozaki: "Elimination and Deuteration of Impurity Hydrogens on the Surface of Neutron Bottle Materials," 1984 Ann. Meeting At. Energy Soc., Osaka, Mar. (1984).
11) T. Tonuma, H. Shibata, S. H. Be, H. Kumagai, M. Kase, T. Kambara, I. Kohno, and H. Tawara: "Production of Secondary Ions by Heavy Ion Impact," 39th Ann. Meeting Phys. Soc. Jpn., Fukuoka, Mar. (1984).
12) K. Hino: "Radiative Electron Capture II," 39th Ann. Meeting Phys. Soc. Jpn., Fukuoka, Mar. (1984).
13) I. Shimamura and A. C. Roy: "Rotational Transitions between High Angular Momentum States of a Molecule—In the Case of Symmetric Top Molecule," 39th Ann. Meeting Phys. Soc. Jpn., Fukuoka, Apr. (1984).
14) K. Nakanishi, K. Iguchi, A. Ohsaki, and T. Watanabe: "The Calculation for $(\mu^+\mu^-)$ Production by Classical Trajectory Monte Carlo Method," 39th Ann. Meeting Phys. Soc. Jpn., Fukuoka, Apr. (1984).
15) K. Hino, T. Watanabe, and I. Shimamura: "The Theory of Radiative Electron Capture (REC)," 39th Ann. Meeting Phys. Soc. Jpn., Fukuoka, Apr. (1984).
16) S. Karashima and T. Watanabe: "Charge State and Ranges of Incident Heavy Ions in Matter," 39th Ann. Meeting Phys. Soc. Jpn., Fukuoka, Apr. (1984).
17) E. Yagi, T. Kobayashi, S. Nakamura, Y. Fukai, and K. Watanabe: "Lattice Location of Hydrogen in V," 39th Ann. Meeting Phys. Soc. Jpn., Fukuoka, Apr. (1984).
18) E. Yagi, G. Flik, K. Fürderer, N. Haas, D. Herlach, J. Major, A. Seeger, W. Jacobs, M. Krause, M. Krauth, H.-J. Mundinger, and H. Orth: "Muon Diffusion in Iron," 39th Ann. Meeting Phys. Soc. Jpn., Fukuoka, Apr. (1984).
19) N. Sakai and H. Sekizawa: "Magnetic Compton Profiles of Fe Metal, Fe_3O_4 and $MnFe_2O_4$," 39th Ann. Meeting Phys. Soc. Jpn., Fukuoka, Apr. (1984).
20) K. Asai, T. Okada, and H. Sekizawa: "A Study of MFe_2O_4 (M=Mn, Fe, Co, and Mg) by TDPAC of γ-Rays of $^{111}Cd(\leftarrow {}^{111}In)$," 39th Ann. Meeting Phys. Soc. Jpn., Fukuoka, Apr. (1984).
21) K. Asai, F. Ambe, S. Ambe, T. Okada, and H. Sekizawa: "Perturbed Angular Correlation of γ-Rays Emitted from ^{111}Cd ($\leftarrow {}^{111}In$) in α-Fe_2O_3," 39th Ann. Meeting Phys. Soc. Jpn., Fukuoka, Apr. (1984).
22) T. Tonuma, S. H. Be, H. Kumagai, M. Kase, H. Shibata, T. Kambara, H. Tawara, and I. Kohno: "Measurements of Cross Sections for Production of Secondary Ions by Heavy Ion Impact," 39th Ann. Meeting Phys. Soc. Jpn., Fukuoka, Apr. (1984).
23) H. Shibata, T. Matsuo, J. Urakawa, A. Yagishita, Y. Awaya, T. Kambara, M. Kase, H. Kumagai, and J. Takahashi: "Measurements of Ar L-MM Auger Electrons in Ar^{4+}+Ar Collisions," 39th Ann. Meeting Phys. Soc. Jpn., Fukuoka, Apr. (1984).
24) T. Kambara, Y. Awaya, M. Kase, H. Kumagai, H. Shibata, and S. M. Shafroth: "Kβ X-Ray Spectra of Ar-Ions Passing through Solid Targets," 39th Ann. Meeting Phys. Soc. Jpn., Fukuoka, Apr. (1984).
25) S. Sato, S. Tsurubuchi, K. Ando, H. Kumagai, S. Kohmoto, T. Tonuma, and Y. Awaya: "The Measurement of Sensitivity of Spectrometer Used for Beam-Foil Spectroscopy," 39th Ann. Meeting Phys. Soc. Jpn., Fukuoka, Apr. (1984).
26) H. Shibata, T. Matsuo, J. Urakawa, A. Yagishita, Y. Awaya, T. Kambara, M. Kase, H. Kumagai, and J. Takahashi: "Measurements of Ar L-MM Auger Electrons in Ar^{4+}+Ar Collisions," 39th Ann. Meeting Phys. Soc. Jpn., Fukuoka, Apr. (1984).
27) T. Doke, T. Takahashi, and E. Shibamura: "Measurement of eD_L/μ in Liquid Xe (III)," 39th Ann. Meeting Phys. Soc. Jpn., Fukuoka, Apr. (1984).
28) T. Takahashi, K. Masuda, Y. Awaya, T. Tonuma, K. Izumo, A. Hashizume, A. Hitachi, S. Uchiyama, and T. Doke: "Stopping Power of 5–7 MeV/amu He and C Ions, Z_1^3 Deviation from the Bethe Formula," 31th Spring Meeting Jpn. Soc. Appl. Phys. and Related Societies, Kawasaki, Apr. (1984).
29) K. Aono, M. Iwaki, and S. Namba: Annealing of Ion-Implanted GaP (IV)," 31th Spring Meeting Jpn. Soc. Appl. Phys. and Related Societies, Kawasaki, Apr. (1984).
30) K. Masuda, T. Takahashi, Y. Awaya, T. Tonuma, K. Izumo, A. Hashizume, A. Hitachi, S. Uchiyama, and T. Doke: "Z_1^3-

Dependence of Stopping Power for 5–7 MeV/amu He- and C-Ions," 31th Spring Meeting Jpn. Soc. Appl. Phys. and Related Societies, Kawasaki, Apr. (1984).
31) S. M. Shafroth, Y. Awaya, T. Kambara, M. Kase, S. Shibata, and H. Tawara: "Angular Distribution of REC for Ar^{4+} on C at 47.5 and 51.9 MeV," Washington Meeting Am. Phys. Soc., Washington, U.S.A., Apr. (1984).
32) J. Nagakawa, H. Shiraishi, M. Okada, H. Kamitsubo, I. Kohno, and T. Shikata: "Irradiation Creep of 316 Stainless Steel and Effect of Initial Microstructure," 94th Meeting Jpn. Inst. Metals, Narashino, Apr. (1984).
33) O. Kuboi, M. Hashimoto, Y. Yatsurugi, H. Nagai, M. Aratani, S. Hayashi, M. Yanokura, I. Kohno, and T. Nozaki: "Studies of a-Si: H Growth Mechanism, Using Deuterium, by Rutherford Recoil Measurement," 17th IEEE Photovoltaic Specialists Conf., Orland (Florida), U.S.A., May (1984).
34) T. Watanabe: "Atomic Structure of High Density Plasma," Meeting of Working Group on Atomic Structure of High Density Plasma, Nagoya, May (1984).
35) E. Yagi: "Diffusion of Positive Muons in Iron," Res. Inst. Fundamental Phys. Kyoto Univ. Symp. Charged Particle Motion in Metals, Kyoto, June (1984).
36) Y. Fukai, K. Watanabe, E. Yagi, S. Nakamura, and T. Kobayashi: "4T State of Hydrogen in V," Symp. Refractory Metals, Kawato, June (1984).
37) A. Ohsaki, T. Watanabe, K. Nakanishi, and K. Iguchi: "Classical Trajectory Monte Carlo Calculation for $\mu^+ + (\mu^- p) \rightarrow (\mu^+ \mu^-) + p$ and $e^+ + (e^- p) - (e^+ e^-) + p$," 9th Int. Conf. Atomic Physics, Seattle, U.S.A., July (1984)
38) Q. Ma, X. Chang, Z. Liu, Y. Liu, and T. Watanabe: "Distorted Wave Born Cross Section for $\mu^+ + (\mu^- p) \rightarrow (\mu^+ \mu^-) + p$," 9th Int. Conf. Atomic Physics, Seattle, U.S.A., July (1984).
39) S. Karashima, T. Watanabe, X. Chang, Z. Liu, Q. Ma, and Y. Liu: "Electron Stripping Cross Section on Multiply Charged Ions by Collision with Neutral Atoms," 9th Int. Conf. Atomic Physics, Seattle, U.S.A., July (1984).
40) A. C. Roy and I. Shimamura: "Transitions of Molecules between High Rotational States," 9th Research Meeting Soc. for Atomic Collision Research (Japan), Wako, July (1984).
41) A. Ohsaki and T. Watanabe: "Where is Difficult for the Calculation of Positronium Formation," 9th Research Meeting Soc. for Atomic Collision Research (Japan), Wako, July (1984).
42) T. Tonuma, S. H. Be, H. Kumagai, H. Shibata, M. Kase, T. Kambara, I. Kohno, and H. Tawara: "Ionization of He, Ne and Ar Atoms by 1.05 MeV/amu C^{q+} (q=2–6) and Ar^{q+} (q=4–14) Ion Impact," Int. Conf. Physics of Highly Ionized Atoms, Oxford, England, July (1984).
43) T. Tonuma, S. H. Be, H. Kumagai, H. Shibata, M. Kase, T. Kambara, I. Kohno, and H. Tawara: "Multiple Ionization of Atoms by Highly Ionized Heavy Ion Impact," Int. Conf. Physics of Highly Ionized Atoms, Oxford, England, July (1984).
44) K. Maeda, Y. Hayashi, and M. Uda: "Oxygen K Emission Spectrum Free from Multiple-Vacancy Satellite," Int. Conf. X-Ray and Inner-Shell Processes in Atoms, Molecules and Solids, Leipzig, E. Germany, Aug. (1984).
45) Y. Awaya, T. Kambara, M. Kase, H. Kumagai, H. Shibata, and S. M. Shafroth: "Multiple Inner-Shell Ionization of Ar Ions Passing through Foils," Int. Conf. X-Ray and Inner-Shell Processes in Atoms, Molecules and Solids, Leipzig, E. Germany, Aug. (1984).
46) M. Uda, A. Koyama, K. Maeda, and Y. Sasa: "Valence Electron Rearrangement Prior to X-Ray or Auger Electron Emission," Int. Conf. X-Ray and Inner-Shell Processes in Atoms, Molecules and Solids, Leipzig, E. Germany, Aug. (1984).
47) Y. Awaya: "Multiple Inner-Shell Ionization of Heavy Ions Passing through Foils," Brasov Int. School, Atomic and Nuclear Heavy Ion Interactions, Brasov, Rumania, Aug. (1984).
48) M. Uda: "Chemical Effects in Characteristic X-Ray Emitted from Multiply Ionized States," Brasov Int. School, Atomic and Nuclear Heavy Ion Interactions, Brasov, Rumania, Sept. (1984).
49) Y. Sakamoto, H. Oyama, and S. Kakinuma: "ECR Discharge Cleaning Device with Permanent Magnet," Proc. 25th Vacuum Symp., Osaka, Oct., p. 127 (1984).
50) K. Okazaki, A. Minoh, S. Ishii, Y. Ishibe, H. Oyama, Y. Sakamoto, and K. Yano: "LIFS Measurements of Sputtering Particle Densities by Plasma Irradiation," Proc. 25th Vacuum Symp., Osaka, Oct., p. 129 (1984).
51) H. Oyama, S. Kakinuma, and Y. Sakamoto:

"Interaction of Titanium Oxide with Hydrogen Plasma," Proc. 25th Vacuum Symp., Osaka, Oct., p. 135 (1984).
52) Q. Ma, X. Chang, Z. Liu, Y. Liu, and T. Watanabe: "The Distorted Wave Born Calculation for $\mu^+ + (\mu^- p) \rightarrow (\mu^+ \mu^-) + p$," 1984 Fall Meeting Phys. Soc. Jpn., Toyama, Oct. (1984).
53) S. Karashima, H. Kawagoshi, and T. Watanabe: "The Electron Stripping Cross Section of Incident Multiply Charged Ion by Many-Electron Target Atom," 1984 Fall Meeting Phys. Soc. Jpn., Toyama, Oct. (1984).
54) S. Karashima, H. Kawagoshi, T. Watanabe, Y. Liu, X. Chang, Z. Liu, and Q. Ma: "The Electron Stripping Cross Section of Multiply Charged Ion by BEA," 1984 Fall Meeting Phys. Soc. Jpn., Toyama, Oct. (1984).
55) M. Sekiya, T. Noro, F. Sasaki, and K. Ohno: "Auger Energies of Ar^{6+} L_{23}-M_1M_1 and Their Relative Transition Probabilities," 1984 Fall Meeting Phys. Soc. Jpn., Toyama, Oct. (1984).
56) M. Uda and A. Koyama: "Chemical Effects on AES Induced by Ions," 1984 Fall Meeting Phys. Soc. Jpn., Toyama, Oct. (1984).
57) K. Ando, S. Komoto, T. Tonuma, H. Kumagai, Y. Awaya, S. Tsurubuchi, and K. Sato: "Analysis of Beam-Foil Spectra of Highly Ionized Aluminum," 1984 Fall Meeting Phys. Soc. Jpn., Toyama, Oct. (1984).
58) Y. Kawabata, M. Utsuro, S. Okamoto, H. Yoshiki, S. Hayashi, and T. Nozaki: "Measurements of the Impurity Hydrogen Concentration on the Surface of the Materials for Neutron Bottle," 1984 Fall Meeting Atomic Energy Soc., Tokai, Oct. (1984).
59) K. Ando, T. Tonuma, S. Kohmoto, H. Kumagai, Y. Awaya, S. Tsurubuchi, and K. Sato: "Analysis of Spectra of Highly Ionized Aluminum Atoms Obtained by Beam-Foil Spectroscopy," 1984 Fall Meeting Phys. Soc. Jpn., Toyama, Oct. (1984).
60) E. Yagi, S. Nakamura, T. Kobayashi, K. Watanabe, Y. Fukai, F. Kano, S. Seguchi, and K. Watanabe: "Lattice Location of H in Nb," 1984 Fall Meeting Phys. Soc. Jpn., Toyama, Oct. (1984).
61) N. Sakai and H. Sekizawa: "Computer Simulation of the Energy Spectrum of Spin-Dependent Doubly Compton Scattered Gamma-Rays," 1984 Fall Meeting Phys. Soc. Jpn., Toyama, Oct. (1984).
62) T. Okada, K. Asai, and H. Sekizawa: "A Study of MFe_2O_4 (M=Mn, Fe, Co, and Mg) by TDPAC of γ-Rays of ^{111}Cd ($\leftarrow$ ^{111}In) (II)," 1984 Fall Meeting Phys. Soc. Jpn., Toyama, Oct. (1984).
63) K. Asai, F. Ambe, S. Ambe, T. Okada, and H. Sekizawa: "Perturbed Angular Correlation of γ-Rays Emitted from ^{111}Cd ($\leftarrow$ ^{111}In) in α-Fe_2O_3 (II)," 1984 Fall Meeting Phys. Soc. Jpn., Toyama, Oct. (1984).
64) T. Okada, K. Asai, F. Ambe, and H. Sekizawa: "^{111}In TDPAC in Ferrite," 1984 Fall Meeting Phys. Soc. Jpn., Toyama, Oct. (1984).
65) M. Fujinaga, K. Asahi, Y. Nojiri, and T. Minamisono: "NMR of the Short-lived β-emitter ^{12}B in Single Crystal Ta," 1984 Fall Meeting Phys. Soc. Jpn., Toyama, Oct. (1984).
66) T. Iwayama, Y. Nojiri, K. Asahi, and T. Minamisono: "Hyperfine Interactions of Short-Lived β-Emitter ^{12}N in Single Crystal Fe," 1984 Fall Meeting Phys. Soc. Jpn., Toyama, Oct. (1984).
67) K. Asahi, F. Ambe, S. Ambe, T. Okada, and H. Sekizawa: "TDPAC of ^{111}In in Fe_2O_3," 28th Symp. Radiochemistry, Kobe, Oct. (1984).
68) K. Ikeda, N. Ito, T. Aimi, S. Hayashi, M. Yanokura, I. Kohno, T. Nagai, M. Aratani, and T. Nozaki: "Application of Heavy-Ion Probe RBS to the Analysis of Si Ohmic Contact Systems," 28th Symp. Radiochemistry, Kobe, Oct. (1984).
69) S. Kakinuma, H. Oyama, and Y. Sakamoto: "Ti Surface Control by Hydrogen Plasma," Proc. 1st Fall Meeting Jpn. Soc. Plasma Phys. and Controlled Fusion, Tokai Univ., Kanagawa, Oct., p. 115 (1984).
70) K. Maeda, Y. Yokode, H. Kusuyama, Y. Sasa, and M. Uda: "Application of PIXE to Medical Science," 20th Tokyo Symp. Applied Spectrometry, Tokyo, Nov. (1984).
71) K. Maeda, Y. Sasa, M. Maeda, and M. Uda: "Diagnosis of Environment by PIXE," 20th Tokyo Symp. Applied Spectrometry, Tokyo, Nov. (1984).
72) K. Ando, S. Kohmoto, T. Tonuma, H. Kumagai, Y. Awaya, S. Tsurubuchi, and K. Sato: "Beam-Foil Spectroscopy of Highly Ionized Aluminum Atoms," US-Japan Workshop on Tokamak Diagnostics by X-Ray, VUV, and Optical Radiation, Nagoya, Nov. (1984).
73) Y. Awaya: "Target Atomic Number Dependence of Simultaneous K-Shell and L-Shell Ionization of Projectile Heavy Ions," 8th Conf. on the Application of Accelerator in Research and Industry, Denton (Texas), U.S.A., Nov. (1984).

74) Y. Awaya, S. Karashima, T. Watanabe, and Y. Liu: "Electron Stripping Cross Section from Multiply Charged Ions by Neutral Atoms," 2nd Int. Workshop on Cross Sections for Fusion and Other Applications, College Station (Texas), U.S.A., Nov. (1984).
75) K. Shiraishi, K. Fukai, E. Yagi, T. Sawai, and S. Hamada: "Depth-Dependent Damage Profile in Stainless Steels Irradiated with Ar- and N-Ions," 1st Int. Conf. on Fusion Reactor Materials, Tokyo, Dec. (1984).
76) J. Nagakawa, H. Shiraishi, M. Okada, H. Kamitsubo, I. Kohno, and T. Shikata: "Irradiation Creep Simulation under Low Proton Flux," 1st Int. Conf. on Fusion Reactor Materials, Tokyo, Dec. (1984).
77) N. Yamamoto, H. Shiraishi, H. Kamitsubo, I. Kohno, T. Shikata, and A. Hishinuma: "Effects of TiC Distribution on the Creep Properties of Helium Injected JPCA," 1st Int. Conf. Fusion Reactor Materials, Tokyo, Dec. (1984).
78) T. Takahashi and T. Doke: "Comment on the Track Formation and Scintillation Light Yield in Liquid Rare Gases," Workshop on the Interaction of Ion Beam with Solids, Nagoya, Dec. (1984).
79) T. Watanabe: "Theory for Characteristic Radiation Interaction by Heavy Ion Impact," Riken Symp. Interaction of Heavy Ions with Matter, Wako, Dec. (1984).

4. Radiochemistry, radiation chemistry and radiation biology
1) T. Takahashi, F. Yatagai, I. Kaneko, T. Katayama, Y. H. Kang, A. Yunoki, S. Konno, and S. Okada: "Detection of Argon Ions by a Plastic Detector and Fraction of Dead Spores as a Function of Impact Parameter," 31th Spring Meeting Jpn. Soc. Appl. Phys. and Related Societies, Kawasaki, Apr. (1984).
2) Y. Itoh, T. Nozaki, T. Masui, and T. Abe: "Oxygen Concentration in Heavily Doped Silicon," 31th Spring Meeting Jpn. Soc. Appl. Phys. and Related Societies, Tokyo, Apr. (1984).
3) F. Ambe, S. Ambe, T. Okada, and H. Sekizawa: "*In situ* Emission Mössbauer Spectroscopy of $^{119}Sb^{5+}$ at the α-Fe_2O_3-Aqueous Solution Interfaces," 49th National Meeting Chem. Soc. Jpn. (Spring), Tokyo, Apr. (1984).
4) S. Hayashi, H. Nagai, M. Aratani, T. Nozaki, M. Yanokura, I. Kohno, O. Kuboi, and Y. Yatsurugi: "High Sensitivity Analysis of Deuterium in Solids by 15N-Induced Nuclear Reactions," 8th Symp. Ion Sources and Ion-Assisted Technology, Tokyo, June (1984).
5) M. Yanokura, M. Aratani, H. Nagai, S. Hayashi, I. Kohno, T. Nozaki, O. Kuboi, and Y. Yatsurugi: "The Heavy-Ion Probe Rutherford Scattering Analysis Applied to the Study of Electronic Materials," 8th Symp. Ion Sources and Ion-Assisted Technology, Tokyo, June (1984).
6) K. Fukushi, T. Irie, O. Inoue, T. Yamasaki, and T. Nozaki: "6-Halo-9-Benzylpurines as Carriers of Various Radiohalogen Ions into Brain," 5th Int. Symp. Radiopharmaceutical Chemistry, Tokyo, July (1984).
7) T. Hara, T. Nozaki, T. Karasawa, M. Iio, and R. Izuchi: "(^{11}C)-1-Glucose and Mannose as Specific Tumor Markers," 5th Int. Symp. Radiopharmaceutical Chemistry, Tokyo, July (1984).
8) K. Eguchi, I. Kaneko, and T. Inada: "DNA Damage and Its Repair in Human Tumor Cells by Heavy Ions," Riken Symp. DNA Lesion, Tokyo, July (1984).
9) T. Takahashi, F. Yatagai, I. Kaneko, T. Katayama, and K. Matsuda: "Dosimetry of Heavy Ions and Inactivation of *B. subtilis* Spore by a Single Heavy Ion," 27th Ann. Meeting Jpn. Radiat. Res. Soc., Chiba, Sept. (1984).
10) I. Kohno, M. Yanokura, S. Motonaga, H. Kamitsubo, T. Suematsu, H. Kobayashi, and M. Yatsuhashi: "Irradiation of Insulating Materials for Cable by Fast Neutron (I)," 1984 Fall Meeting Atomic Energy Soc. Jpn., Tokai, Oct. (1984).
11) T. Suematsu, H. Kobayashi, M. Yatsuhashi, I. Kohno, M. Yanokura, S. Motonaga, and H. Kamitsubo: "Irradiation of Insulating Materials for Cable by Fast Neutron (II)," 1984 Fall Meeting Atomic Energy Soc. Jpn., Tokai, Oct. (1984).
12) K. Kimura: "Unusual Emission Spectra of Liquid Helium Impinged by Heavy Ions I," 1984 Spring Meeting Phys. Soc. Jpn., Fukui, Oct. (1984).
13) K. Kimura: "Unusual Emission Spectra of Liquid Helium Impinged by Heavy Ions II," 1984 Fall Meeting Phys. Soc. Jpn., Toyama, Oct. (1984).
14) H. Nagai, M. Aratani, S. Hayashi, T. Nozaki, M. Yanokura, I. Kohno, O. Kuboi, and Y. Yatsurugi: "Rutherford Forward Scattering Applied to the Analysis of Hydrogen (III)," 28th Symp. Radiochemistry, Kobe, Oct. (1984).
15) S. Hayashi, H. Nagai, M. Aratani, T. Nozaki,

M. Yanokura, I. Kohno, O. Kuboi, and Y. Yatsurugi: "High Sensitivity Analysis of Deuterium in Solids by 15N-induced Nuclear Reactions," 28th Symp. Radiochemistry, Kobe, Oct. (1984).

16) F. Ambe, S. Ambe, T. Okada, and H. Sekizawa: "*In situ* Emission Mössbauer Spectra of ^{119}Sb Adsorbed on the Surfaces of α-Fe_2O_3 and γ-Fe_2O_3," 28th Symp. Radiochemistry, Kobe, Oct. (1984).
17) K. Kimura, T. Azuma, Y. Aoki, and Y. Ito: "Unusual Emission Spectra of Liquid Helium Impinged by Heavy Ions," 27th Conf. Radiation Chemistry, Tokyo, Oct. (1984).
18) Y. Aoki, T. Azuma, Y. Katsumura, Y. Tabata, Y. Ito, and K. Kimura: "Single-Photon Counting of Fluorescence Induced by Heavy Ions," 27th Conf. Radiation Chemistry, Tokyo, Oct. (1984).
19) F. Ambe: "Mössbauer Spectroscopy of Metal Ions Adsorbed on Surfaces of Magnetic Material and Its Applications," 1984 Int. Chem. Congr. Pacific Basin Soc., Honolulu (Hawaii), U.S.A., Dec. (1984).
20) H. Kudo, T. Nomura, K. Sueki, and M. Magara: "Isomeric Transitions of ^{211m}Po and ^{212m}Po," 1984 Int. Chem. Congr. Pacific Basin Soc., Honolulu (Hawaii), U.S.A., Dec. (1984).
21) T. Takahashi, K. Eguchi, T. Katayama, and I. Kaneko: "Track Structure Theories and Biological Effect of Heavy Ions," Symp. of Interaction of Heavy Ion with Matter, Wako, Dec. (1984).

VIII. LIST OF OUTSIDE USERS AND THEIR THEMES

(Jan.–Dec. 1984)

1)	T. Kimura "Radiochemical Analysis of ^{16}O, ^{14}N and ^{11}C in Si Crystal and GaSb"	Japan Chemical Analysis Center
2)	H. Ueyama "Study of Effect by Bombarding High Energy Proton on a Si Solar Cell"	Sharp Co., Ltd.
3)	H. Nakahara "Production of ^{125}I and ^{131}Xe"	Faculty of Science, Tokyo Metropolitan Univ.
4)	S. Orito and S. Nakamura "Test of Sensibility of CR39 Track Detector for High Energy Proton"	Faculty of Science, Univ. of Tokyo
5)	H. Homareda "Production of ^{43}K"	Faculty of Medicine, Kyorin Univ.
6)	S. Suzuki "Study of Effect by Bombarding High Energy Proton on a Solid Fuel for a Rocket"	Space Development Div., Nissan Automobile Co., Ltd.
7)	H. Shinyashiki and M. Takeya "Radiochemical Analysis of ^{16}O in GaAs"	Central Res. Lab., Mitsubishi Metal Co., Ltd.
8)	H. Yamamoto "Radiation Damage of Cover Glass for a Solar Cell"	R & D Div., Asahi Glass Co., Ltd.
9)	M. Yatsuhashi and T. Suematsu "Study of Effect by Irradiating Fast Neutron on a Insulator Covering a Cable"	Fujikura Cable Works, Ltd.

IX. LIST OF SEMINARS

(Jan.–Dec. 1984)

1) D. Böhne, GSI (West Germany), 2 February
"Present Situation and Future Plans of UNILAC (GSI)"

2) P. Lapostolle, GANIL (France), 3 February
"Present Situation at GANIL"

3) H. Sakamoto, Univ. of Tsukuba (Ibaraki), 21 February
"Present Status and Future Image of Data Processing System for Nuclear Experiments"

4) T. A. N. Miller, Indiana Univ. (USA), 23 February
i) "Current Studies at IUCF"
ii) "Facility Developments at IUCF"

5) K. Tanabe, Saitama Univ. (Saitama), 29 February
"Nuclear Structure of High-Excited High-Spin States"

6) G. Bruge, Saclay (France), 27 March
"$\bar{p}$-Nucleus Experiments"

7) A. Gelberg, Univ. zu Köln (West Germany), 28 March
"Two-Quasiparticle States in Xe, Ba, and Ce Nuclei"

8) B. Herskind, Niels Bohr Inst. (Denmark), 28 March
"Anti-Compton Ge-Detector Array and Study of High-Spin States"

9) F. Touchard, Orsay (France), 29 March
"Laser Spectroscopy of Radioactive Atomic Nuclei"

10) O. Hashimoto, INS (Tokyo), 11 April
"Experiments and Data Processing System at BEVALAC"

11) J. Kasagi, Tokyo Inst. Tech. (Tokyo), 11 April
"Experiments and Data Processing System at MSU"

12) A. Ikeda, Tokyo Inst. Tech. (Tokyo), 17 April
"Effects of γ-Vibration on High-j Rotational Bands"

13) H. Morinaga, Tech. Univ. München (West Germany), 24 April
"Energy Transfer in Heavy Ion Transfer Reactions"

14) J. Chiba, Univ. of Tokyo (Tokyo), 1 May
"On-Line Data Processing System at KEK"

15) K. Nagamine, Univ. of Tokyo (Tokyo), 22 May
"μ-Production by Heavy Ion Beam and Its Many-Fields Application"

16) H. P. Blok, Vrigh Univ. Amsterdam (Holland), 29 May
"Recent (e, e′) and (e, e′p) Results at the Amsterdam Electron Accelerator"

17) T. Motobayashi, St. Paul Univ. (Tokyo), 17 July
"d-^{2}He Reaction on Light Nuclei"

18) H. Tanabe, Univ. of Tokyo (Tokyo), 31 July
"Role of Δ in Pion Photoproduction"

19) T. Tamura, Univ. of Texas (USA), 20 August
"Heavy-Ion Fusion (Subthreshold, above Threshold)"

20) J. D. Garrett, Niels Bohr Inst. (Denmark), 1 September
"Pair Phase Transitions"

21) V. Metag, Univ. Giessen (West Germany), 1 September
"Crystal Ball"

22) G. Münzenberg, GSI (West Germany), 1 September
"Heaviest Elements"

23) S. Chojnacki, Warsaw Univ./Dubna (Poland), 13 November
"Mechanism of α-Particle Emission in the $^{16}O+^{232}Th$ Reactions"

X. LIST OF PERSONNEL

Members of the Board

AWAYA Yohko 粟屋容子
HASHIZUME Akira 橋爪 朗
ISHIHARA Masayasu 石原正泰
KIRA Akira 吉良 爽
NOZAKI Tadashi 野崎 正
OKADA Shigefumi 岡田重文
SAKAMOTO Yuichi 坂本雄一
SHIMA Makoto 島 誠*
UDA Masayuki 宇田応之
YOSHIDA Kiyota 吉田清太
CHIBA Yoshiaki 千葉好明
IMAMURA Masashi 今村 昌*
KAMITSUBO Hiromichi 上坪宏道
KOHNO Isao 河野 功
ODERA Masatoshi 小寺正俊
SAKAIRI Hideo 坂入英雄
SEKIZAWA Hisashi 関沢 尚
SHIOTANI Nobuhiro 塩谷亘弘
WATANABE Tsutomu 渡部 力**

* through March 31, 1984

** chairman

Cyclotron Operation and Maintenance Group

FUJITA Shin 藤田 新
KAGEYAMA Tadashi 影山 正
KOHNO Isao 河野 功
TAKEBE Hideki 武部英樹
IKEGAMI Kumio 池上九三男
KOHARA Shigeo 小原重夫
OGIWARA Kiyoshi 荻原 清

Linac Operation and Maintenance Group

CHIBA Yoshiaki 千葉好明
IKEZAWA Eiji 池沢英二
KAMBARA Tadashi 神原 正
KUBO Toshiyuki 久保敏幸
YANOKURA Minoru 矢野倉 実
HEMMI Masatake 逸見政武
INOUE Toshihiko 井上敏彦
KASE Masayuki 加瀬昌之
MIYAZAWA Yoshitoshi 宮沢佳敏

Scientific and Engineering Personnel

Cyclotron Laboratory

BE Suck Hee 裵 碩喜
FUJITA Jiro 藤田二郎
HARA Masahiro 原 雅弘
INAMURA Takashi 稲村 卓
KARASAWA Takashi 唐沢 孝
MORITA Kohsuke 森田浩介
NAGASE Makoto 長瀬 誠
NAKANISHI Noriyoshi 中西紀喜
FUJISAWA Takashi 藤沢高志
GOTO Akira 後藤 彰
HATANAKA Kichiji 畑中吉治
KAMITSUBO Hiromichi 上坪宏道
KOHNO Isao 河野 功
MOTONAGA Shoshichi 元永昭七
NAKAJIMA Shunji 中島諄二
NOMURA Toru 野村 亨

OIKAWA Yoshifumi 老川嘉郁
SHIKATA Takashi 四方隆史
TAKESHITA Isao 竹下勇夫
YAMAJI Shuhei 山路修平
YOKOYAMA Ichiro 横山一郎
SAKAMOTO Ichiro 坂本一郎
SHIMIZU Kazuo 清水和男
WADA Takeshi 和田 雄
YANO Yasushige 矢野安重
YOSHIDA Nobuaki 吉田宣章

(Visitors)
AUGER Pierre (CSNSM, Orsay)
FURUNO Kohei 古野興平 (Inst. Phys., Univ. of Tsukuba)
IEKI Kazuo 家城和夫 (Dept. Phys., Tokyo Inst. Tech.)
INOUE Makoto 井上 信 (RCNP, Osaka Univ.)
KAMIMURA Masayasu 上村正泰 (Dept. Phys., Kyushu Univ.)
KASAGI Jirota 笠木治郎太 (Dept. Phys., Tokyo Inst. Tech.)
KATORI Kenji 鹿取謙二 (Dept. Phys., Osaka Univ.)
KIKUCHI Fumio 菊地文男 (Dept. Math., College of General Education, Univ. of Tokyo)
KOHMOTO Susumu 河本 進
KUDO Hisaaki 工藤久昭 (Dept. Chem., Niigata Univ.)
MORINAGA Haruhiko 森永晴彦 (Dept. Phys., Technische Universität Munchen)
MOTOBAYASHI Toru 本林 透 (Dept. Phys., Rikkyo Univ.)
MURAKAMI Takeshi 村上 健 (Dept. Phys., Tokyo Inst. Tech.)
NAGAKAWA Johsei 永川城正 (Nat. Res. Inst. for Metals)
NAGAMIYA Shoji 永宮正治 (Dept. Phys., Univ. of Tokyo)
NAKAHARA Hiromichi 中原弘道 (Dept. Chem., Tokyo Metropolitan Univ.)
ONISHI Naoki 大西直毅 (Phys. Inst., College of General Education, Univ. of Tokyo)
ROMMEL G. (GANIL, France)
ROY Amulya C. (Dept. Phys., Univ. of Kalayani)
SATO Kenichi 佐藤憲一 (Division Phys., Tohoku College of Pharmacy)
SHIRAISHI Haruki 白石春樹 (Nat. Res. Inst. for Metals)
TAKADA Eiichi 高田栄一 (Dept. Phys., Kyoto Univ.)
TAKEMASA Tadashi 武政尹士 (Dept. Phys., Saga Univ.)
WHITTEN C. A. Jr. (Dept. Phys., Univ. of California)
YAMAMOTO Norikazu 山本徳和 (Nat. Res. Inst. for Metals)
YOSHIDA Shiro 吉田思郎 (Dept. Phys., Tohoku Univ.)

(Students)
ENOMOTO Masato 榎本雅人 (Fac. Sci. and Eng., Chuo Univ.)
HARADA Hideo 原田秀郎 (Dept. Phys., Tokyo Inst. Tech.)
NAKAMURA Masami 中村正美 (Fac. Sci. and Eng., Chuo Univ.)
SHIMOMURA Hideo 下村英雄 (College of Hum. and Sci., Nihon Univ.)
SUEKI Keisuke 末木啓介 (Dept. Chem., Tokyo Metropolitan Univ.)
TACHIBANAKI Hiroshi 橘木 寛 (Dept. Phys., Tokyo Inst. Tech.)
YAMAGUCHI Kazuya 山口和也 (College of Hum. and Sci., Nihon Univ.)

Linac Laboratory
CHIBA Toshiya 千葉利哉
CHIBA Yoshiaki 千葉好明

GONO Yasuyuki 郷農靖之
HOSHINO Kiichi 星野紀一
ISHIKAWA Yoshiharu 石川美晴
KASE Masayuki 加瀬昌之
MIYAZAWA Yoshitoshi 宮沢佳敏
ODERA Masatoshi 小寺正俊
TONUMA Tadao 戸沼正雄
HEMMI Masatake 逸見政武
INOUE Toshihiko 井上敏彦
KAMBARA Tadashi 神原 正
KUBO Toshiyuki 久保敏幸
MIZOGAWA Tatsumi 溝川辰己
SHIBATA Hiromi 柴田裕実
YANOKURA Minoru 矢野倉 実

(Visitors)
FUJIWARA Ichiro 藤原一郎 (Inst. Atomic Energy, Kyoto Univ.)
HAYASHIBE Shogo 林部昭吾 (Dept. Phys., Tohoku Univ.)
ITO Noriaki 伊藤憲昭 (Dept. Crystalline Materials, Nagoya Univ.)
MATSUO Takashi 松尾 崇 (Tokyo Medical and Dental Univ.)
MORITA Susumu 森田 右 (College of Eng., Hosei Univ.)
ODA Nobuo 織田暢夫 (Res. Lab. for Nucl. Reactors, Tokyo Inst. Tech.)
OTANI Shunsuke 大谷俊介 (Inst. Plasma Phys., Nagoya Univ.)
SUGAWARA Masahiko 菅原昌彦 (Fund. Sci., Chiba Inst. Tech.)
SUZUKI Hiroshi 鈴木 洋 (Dept. Phys., Sophia Univ.)
TAWARA Hiroyuki 俵 博之 (Inst. Plasma Phys., Nagoya Univ.)
URAKAWA Junji 浦川順治 (Nat. Lab. High Energy Phys.)
YAGISHITA Akira 柳下 明 (Nat. Lab. High Energy Phys.)

(Student)
FUKUDA Mitsunori 福田光順 (Fac. Sci., Tokyo Inst. Technol.)

Radiation Laboratory

ASAHI Koichiro 旭 耕一郎
ISHIHARA Masayasu 石原正泰
KONNO Satoshi 金野 智
OHSUMI Hideaki 大隅秀晃
TAKAHASHI Tan 高橋 旦
HASHIZUME Akira 橋爪 朗
IZUMO Koichi 出雲光一
KUMAGAI Hidekazu 熊谷秀和
OKANO Masaharu 岡野真治
TENDOW Yoshihiko 天道芳彦

(Visitors)
DOKE Tadayoshi 道家忠義 (Sci. and Eng. Res. Lab., Waseda Univ.)
FUJIOKA Manabu 藤岡 学 (Dept. Phys., Tohoku Univ.)
HASEGAWA Takeo 長谷川武夫 (Inst. Nucl. Study, Univ. of Tokyo)
HITACHI Akira 月出 章 (Sci. & Eng. Res. Lab., Waseda Univ.)
IIO Masahiro 飯尾正広 (Fac. Med., Univ. of Tokyo)
KANG Yung-Ho 姜 栄浩 (Dept. Natural Sci., Kyung-Pook Univ.)
KIM Do Sung 金 道聖 (Dept. Natural Sci., Kyung-Pook Univ.)
KOBAYASHI Hisanobu 小林久信 (Fac. Eng., Saitama Univ.)
KUBOTA Shinzou 窪田信三 (Fac. Sci., Rikkyo Univ.)
LEE Sang Mu 李 相茂 (Univ. Tsukuba)
MASUDA Kimiaki 増田公明 (School Sci. Eng., Waseda Univ.)
MIURA Taichi 三浦太一 (Dept. Chem., Tokyo Metropolitan Univ.)

MOTOBAYASHI Toru 本林 透 (Fac. Sci., Rikkyo Univ.)
MURAMATSU Hisakazu 村松久和 (Nat. Lab. High Energy Phys.)
NAGAHARA Teruaki 永原照明 (Inst. Atomic Energy, Rikkyo Univ.)
OHTSUKA Hideko 大塚秀子
OHTSUKA Rikuro 大塚陸郎 (Nagoya Inst. Technol.)
ONAI Yoshio 尾内能夫 (Dept. Phys., Cancer Inst.)
SHIBAMURA Eido 柴村英道 (Saitama College of Health)

(Students)
HATSUKAWA Yuichi 初川雄一 (Dept. Chem., Tokyo Metropolitan Univ.)
SUZUKI Satoshi 鈴木 聡 (School Sci. Eng., Waseda Univ.)
YANAGA Makoto 矢永誠人 (Dept. Chem., Tokyo Metropolitan Univ.)
YUNOKI Akira 柚木 彰 (School Sci. Eng., Waseda Univ.)

Atomic Processes Laboratory

ANDO Kozo 安藤剛三
NISHIDA Masami 西田雅美
SHIMAMURA Isao 島村 勲
AWAYA Yohko 粟屋容子
OHSAKI Akihiko 大崎明彦
WATANABE Tsutomu 渡部 力

(Visitors)
FUJIMA Kazumi 藤間一美 (Dept. Phys., Chuo Univ.)
HARA Shunsuke 原 俊介 (Dept. Phys., Univ. of Tsukuba)
ISHII Keishi 石井慶之 (Dept. Eng. Sci., Kyoto Univ.)
ITOH Yoh 伊藤 陽 (Fac. Sci., Josai Univ.)
KARASHIMA Shosuke 唐島照介 (Dept. Electr. Eng., Tokyo Univ. of Sci.)
KOIKE Fumihiro 小池文博 (School Med., Kitasato Univ.)
KOIZUMI Tetsuo 小泉哲夫 (Dept. Phys., Rikkyo Univ.)
KOYAMA Naoto 小山直人 (Dept. Eng. Phys., Univ. of Electrocommunications)
MATSUMOTO Atsushi 松本 淳 (Inst. Plasma Phys., Nagoya Univ.)
MATSUO Takashi 松尾 崇 (Dept. Pathology, Tokyo Med. and Dent. Univ.)
MATSUZAWA Michio 松澤通生 (Dept. Eng. Phys., Univ. of Electrocommunications)
OHTANI Shunsuke 大谷俊介 (Inst. Plasma Phys., Nagoya Univ.)
ROY Amulya C. (Dept. Phys., Univ. of Kalayani)
SATO Hiroshi 佐藤浩史 (Dept. Phys., Ochanomizu Univ.)
SATO Kuninori 佐藤国憲 (Inst. Plasma Phys., Nagoya Univ.)
SHIMA Kunihiro 島 邦博 (Inst. Appl. Phys., Univ. of Tsukuba)
SHIMAKURA Noriyuki 島倉紀之 (General Educ. Dept., Niigata Univ.)
TAWARA Hiroyuki 俵 博之 (Inst. Plasma Phys., Nagoya Univ.)
TOKORO Nobuhiro 所 伸宏 (Res. Lab. Nucl. Reactors, Tokyo Inst. Tech.)
TOSHIMA Nobuyuki 戸嶋信幸 (Inst. Appl. Phys., Univ. of Tsukuba)
TSURUBUCHI Seiji 鶴淵誠二 (Fac. Technol., Tokyo Univ. Agric. Tech.)

(Students)
HINO Kenichi 日野健一 (Dept. Appl. Phys., Univ. of Tokyo)
KAWAGOSHI Hiroshi 川越 浩 (Fac. Eng. Sci., Univ. of Tokyo)

SEKIYA Masahiro 関谷雅弘 (Dept. Chem., Hokkaido Univ.)
NAKANISHI Kiyotaka 中西清隆 (Dept. Chem., Waseda Univ.)

Metal Physics Laboratory
KOYAMA Akio 小山昭雄
SHIOTANI Nobuhiro 塩谷亘弘
NAGAMINE Kanetada 永嶺謙忠
YAGI Eiichi 八木栄一

(Student)
NAKAMURA Shiho 中村志保 (School Sci. Eng., Waseda Univ.)

Magnetic Materials Laboratory
ASAI Kichizo 浅井吉蔵
SAKAI Nobuhiko 坂井信彦
OKADA Takuya 岡田卓也
SEKIZAWA Hisashi 関沢 尚

Plasma Physics Laboratory
ISHIBE Yukio 石部行雄
OKAZAKI Kiyohiko 岡崎清比古
SAKAMOTO Yuichi 坂本雄一
ISHII Shigeyuki 石井成行
OYAMA Hitoshi 大山 等
YANO Katsuki 矢野勝喜

(Student)
KAKINUMA Sadanori 柿沼貞徳 (Fac. Sci. and Eng., Chuo Univ.)

Semiconductors Laboratory
(Visitor)
AONO Keiko 青野桂子 (College of Liberal Arts, Kitasato Univ.)

Solid-State Chemistry Laboratory
KOBAYASHI Masayoshi 小林雅義
SASA Yoshihiko 佐々嘉彦
MAEDA Kuniko 前田邦子
UDA Masayuki 宇田応之

(Visitors)
KUSUYAMA Hiroyuki 楠山弘之 (Cancer Institute Hospital Tokyo)
YOKODE Yutaka 横出 裕 (School of Medicine, Nihon Univ.)
NASR Samir Ahmed Hassan Seif El (Teacher's College for Women, Kuwait)

Radiochemistry Laboratory
AMBE Fumitoshi 安部文敏
ARATANI Michi 荒谷美智
ITOH Yoshiko 伊東芳子
NOZAKI Tadashi 野崎 正
AMBE Shizuko 安部静子
HAYASHI Shigeki 林 茂樹
IWAMOTO Masako 岩本正子
OHKUBO Yoshitaka 大久保嘉高

TERAI Yoshiro 寺井善郎

(Visitors)
ABE Takao 阿部孝夫 (Shin-Etsu Handotai Co.)
AIMI Toshihiko 相見俊彦 (NEC Corporation)
FUKUSHIMA Hiroto 福島浩人 (Japan Chemical Analysis Center)
HASHIMOTO Tetsuo 橋本哲夫 (Fac. Sci., Niigata Univ.)
IKEDA Kazuko 池田和子 (NEC Co.)
ITOH Nobuyuki 伊藤信之 (NEC Co.)
KAWABATA Yuji 川端祐司 (Res. Reac. Inst., Kyoto Univ.)
KIMURA Toshimasa 木村敏正 (Japan Chemical Analysis Center)
KUBOI Osamu 久保井 收 (Komatsu Electronic Metal Co., Ltd.)
MASUI Tsumoru 桝井 積 (Shin-Etsu Handotai Co.)
MINAI Yoshitaka 薬袋佳孝 (Fac. Sci., Univ. of Tokyo)
NAGAI Hisao 永井尚生 (College Hum. and Sci., Nihon Univ.)
NISHIDE Hiroyuki 西出宏之 (School Sci. and Eng., Waseda Univ.)
OOHIRA Shigeo 大平重男 (Nikkei Techno Res. Co., Ltd.)
SUEHIRO MAKIKO 末広牧子 (Tokyo Metropolitan Geriatric Hospital)
TSUCHIDA Eishun 土田英俊 (School Sci. and Eng., Waseda Univ.)
UTSURO Masahiko 宇津呂雄彦 (Res. Reac. Inst., Kyoto Univ.)
YATSURUGI Yoshifumi 八剱吉文 (Komatsu Electronic Metals Co., Ltd.)
YOKOI Fuji 横井風児 (Mental and Muscular Disorders, National Center for Nervous)

(Students)
KUBO Kenya 久保謙哉 (Fac. Sci., Univ. of Tokyo)
OGATA Yoshitaka 尾形嘉貴 (School Sci. and Eng., Waseda Univ.)
YUASA Makoto 湯浅 真 (School Sci. and Eng., Waseda Univ.)

Radiation Chemistry Laboratory
KIMURA Kazuie 木村一宇

(Visitor)
ITO Yasuo 伊藤泰男 (Res. Center Nucl. Sci. and Tech., Univ. of Tokyo)

(Students)
AKASU Keiri 赤須計理 (Dept. Phys., Chuo Univ.)
AOKI Yasushi 青木 康 (Fac. Eng., Univ. of Tokyo)
AZUMA Toshiyuki 東 俊行 (Fac. Eng., Univ. of Tokyo)
KURIYAMA Tatsuto 栗山龍人 (Dept. Phys., Chuo Univ.)

Radiobiology Laboratory
EGUCHI Kiyomi 江口清美
KANEKO Ichiro 金子一郎
NAKANO Kazushiro 中野和城
OKADA Shigefumi 岡田重文
YATAGAI Fumio 谷田貝文夫

(Visitors)
INADA Tetsuo 稲田哲雄 (Inst. of Basic Medical Sci., Univ. of Tsukuba)
MAJIMA Hideyuki 馬嶋秀行 (Fac. Med., Univ. of Tokyo)
OHNO Tadao 大野忠夫 (Nat. Inst. Radiological Sciences)
OKADA Gensaku 岡田源作 (Tokyo-Toritsu-Itabashi-Kango-Senmon-Gakko)

Safety Control Affairs Office
IGARASHI Kazui 五十嵐一戍
KAGAYA Satoru 加賀屋 悟
KATOU Takeo 加藤武雄
KURIHARA Osamu 栗原 修
MIYAGAWA Makoto 宮川真言
SAKAMOTO Ichiro 坂本一郎
TAKI Kenro 滝 剣朗
USUBA Isao 薄葉 勲

Beam Analysis Center
IWAKI Masaya 岩木正哉
KOBAYASHI Takane 小林 峰
SAKAIRI Hideo 坂入英雄
URAI Teruo 浦井輝夫

(Visitor)
YOSHIDA Kazuo 吉田和夫 (Toray Ind., Inc.)

AUTHOR INDEX

ABE Takao 阿部孝夫 123
ABE Junya 阿部準也 170
ADACHI Minoru 足立 実 15
AIMI Toshihiko 相見俊彦 101
AKASU Keiri 赤須計理 150
AMBE Fumitoshi 安部文敏 90, 92, 139, 141, 167
AMBE Shizuko 安部静子 90, 92, 121, 139, 141
AMEMIYA Hiroshi 雨宮 宏 205
ANDO Kozo 安藤剛三 69, 71
AOKI Yasushi 青木 康 145, 150
AONO Keiko 青野桂子 110
ARATANI Michi 荒谷美智 99, 101, 103, 130, 134, 137
ARIMA Akito 有馬朗人 26
ASAHI Kenichi 旭 健一 41
ASAI Kichizo 浅井吉蔵 92, 94, 96, 167
AWAYA Yohko 粟屋容子 59, 71, 73, 75, 77, 84, 162
AZUMA Toshiyuki 東 俊行 145, 150
BE Suck Hee 裵 碩喜 78, 80, 82, 164, 189, 192
CHENG Xixiang 張 錫祥 45, 57
CHIBA Toshiya 千葉利哉 197
CHIBA Yoshiaki 千葉好明 4
EGUCHI Kiyomi 江口清美 148
EL Nasr S.S. 128
FUJIMA Kazumi 藤間一美 55, 59
FUJISAWA Takashi 藤沢高志 172, 174, 184
FUJITA Jiro 藤田二郎 170, 185, 187
FUJITA Shin 藤田 新 2, 194, 218, 221
FUKAI Katsumaro 深井勝麿 117
FUKAI Yuh 深井 有 104, 106
FUKUDA Mitsunori 福田光順 30, 32, 152
FUKUDA Tomokazu 福田共和 41
FUKUSHIMA Hiroto 福嶋浩人 123
FUSE Masaharu 布施雅治 164
GONO Yasuyuki 郷農靖之 30, 32, 152
GOTO Akira 後藤 彰 170, 177, 179, 184, 216
GOTOH Eiichiro 後藤栄一郎 164
HAMADA Shozo 浜田省三 117
HAMAGAKI Hideki 浜垣秀樹 10
HAMAJIMA Yasunori 浜島靖典 12, 37, 143
HARA Masahiro 原 雅弘 216
HARA Shunsuke 原 俊介 49
HARADA Hideo 原田秀郎 22, 24
HASHIMOTO Masanori 橋本正則 99
HASHIMOTO Tetsuo 橋本哲夫 137
HASHIZUME Akira 橋爪 朗 28, 96, 168
HATANAKA Kichiji 畑中吉治 181
HATSUKAWA Yuichi 初川雄一 12
HAYASHI Shigeki 林 茂樹 99, 101, 103, 130, 132, 134, 137
HEMMI Masatake 逸見政武 4, 197, 211, 212, 214, 216
HIGASHIGUCHI Yasuhiro 東口安宏 111
HINO Kenichi 日野健一 62, 64
IGARASHI Kazui 五十嵐一成 221
IGUCHI Kaoru 井口 馨 43
IKEDA Kazuko 池田和子 101
IKEDA Nobuo 池田伸夫 41
IKEGAMI Kumio 池上九三男 2, 189, 192, 209
IKEGAMI Yuji 池上祐司 164
IKEZAWA Eiji 池沢英二 4
INADA Tetsuo 稲田哲雄 148
INAMURA Takashi 稲村 卓 20, 22, 24, 28, 152, 158, 160, 166, 181
INOUE Toshihiko 井上敏彦 4
ISHIBE Yukio 石部行雄 97
ISHIHARA Masayasu 石原正泰 8, 10, 39, 41, 69, 152, 155, 160, 164
ISHII Shigeyuki 石井成行 97, 205, 207
ISHIKAWA Yoshiharu 石川美晴 30, 32, 152
ITO Yasuo 伊藤泰男 145
ITO Yoh 伊藤 陽 162
ITO Nobuyuki 伊藤信之 101
ITOH Yoshiko 伊東芳子 123, 125
IWAKI Masaya 岩木正哉 7, 103, 108, 109, 110
IWAMOTO Masako 岩本正子 121
KAGEYAMA Tadashi 影山 正 2
KAKINUMA Sadanori 柿沼貞徳 97
KAMBARA Tadashi 神原 正 4, 73, 75, 77, 78, 80, 82, 84, 185
KAMITSUBO Hiromichi 上坪宏道 113, 115, 119, 152, 169, 170, 181, 185
KAMIYAMA Norio 上山憲雄 209
KANEKO Ichiro 金子一郎 147, 148
KANG Yuno-Ho 姜 栄浩 147
KARASHIMA Shosuke 唐島照介 57
KASAGI Jirota 笠木治郎太 22, 24, 152, 158, 160
KASE Masayuki 加瀬昌之 4, 73, 75, 77, 78, 80, 82, 84, 197, 199, 203
KATAYAMA Toshiko 片山敏子 147
KATO Seigo 加藤静吾 155

KATORI Kenji 鹿取謙二 41
KATSUMURA Yousuke 勝村庸介 145
KAWABATA Yuji 川端祐司 132
KAWAGOSHI Hiroshi 川越 浩 57
KAWAKAMI Hirokane 川上宏金 15, 155
KAYANO Hideo 茅野秀夫 111
KIHARA Kiyotaka 木原清隆 4
KIKUCHI Shiro 菊地士郎 28
KIM Do-Sung 金 道聖 147
KIMURA Kazuie 木村一宇 145, 150
KIMURA Mineo 季村峯夫 53
KIMURA Toshimasa 木村敏正 123
KOBAYASHI Hirotada 小林弘忠 119
KOBAYASHI Masayoshi 小林雅義 128
KOBAYASHI Takane 小林 峰 6, 103, 104, 106, 221
KOHARA Shigeo 小原重夫 2, 172, 174
KOHMOTO Susumu 河本 進 8, 10, 15, 69, 71
KOHNO Isao 河野 功 2, 12, 37, 78, 80, 82, 99, 101, 113, 115, 119, 130, 134, 137, 143, 152, 209, 218
KOIZUMI Tetsuo 小泉哲夫 162
KONNO Chikara 今野 力 41, 155
KONNO Satoshi 金野 智 156
KOSAKO Toshiso 小佐古敏荘 194
KOYAMA Akio 小山昭雄 86, 88
KUBO M. Kenya 久保謙哉 121
KUBO Toshiyuki 久保敏幸 4, 8, 15
KUBOI Osamu 久保井 収 99, 130, 134
KUBONO Shigeru 久保野 茂 155
KUDO Hisaaki 工藤久昭 15, 35, 37, 166
KUMAGAI Hidekazu 熊谷秀和 71, 73, 75, 77, 78, 80, 82, 84, 162, 164
KUMAHORA Hiroki 熊洞宏樹 28
KUMATA Yukio 熊田幸生 174
KURIYAMA Tatsuto 栗山龍人 150
KUSUYAMA Hiroyuki 楠山弘之 128
LIU Yaoyang 劉 耀陽 45, 57
LIU Zhijing 劉 之景 45, 57
MA Quaching 馬 千乘 45, 57
MAEDA Kuniko 前田邦子 126, 128
MAEDA Masaru 前田 勝 126
MAGARA Masaaki 間柄正明 12, 35, 37, 143
MASUDA Kimiaki 増田公明 156
MASUI Tsumoru 桝井 積 123
MATSUO Takashi 松尾 崇 84
MINAI Yoshitaka 薬袋佳孝 121
MINAMISONO Tadanori 南園忠則 41
MINEHARA Eisuke 峰原英介 28
MINOH Arimichi 箕曲在道 97
MISAWA Yutaka 三沢 豊 125
MITA Takeshi 三田 武 170
MIYAZAWA Yoshitoshi 宮沢佳敏 4, 197
MORITA Kosuke 森田浩介 15, 155, 166
MOTOBAYASHI Toru 本林 透 39
MOTONAGA Shoshichi 元永昭七 119, 170
MURAKAMI Takeshi 村上 健 22, 24, 152, 158, 160
NAGAI Hisao 永井尚生 99, 101, 130, 134, 137
NAGAI Yasuki 永井泰樹 39
NAGAKAWA Johsei 永川城正 115
NAKAHARA Hiromichi 中原弘道 12, 37, 143
NAKAJIMA Shunji 中島諄二 189, 192
NAKAMURA Shiho 中村志保 104, 106
NAKANISHI Kiyotaka 中西清隆 43
NAKANISHI Noriyoshi 中西紀喜 179, 194
NAKANO Kazushiro 中野和城 148
NAMBA Susumu 難波 進 110
NISHIDA Masami 西田雅美 75
NISHIDE Hiroyuki 西出宏之 121
NODA Takashi 野田 隆 209
NOJIRI Yoichi 野尻洋一 41
NOMURA Toru 野村 亨 15, 35, 69, 152, 166
NORIKI Shinichiro 乗木新一郎 126
NORO Takeshi 野呂武司 67
NOZAKI Tadashi 野崎 正 99, 101, 121, 123, 125, 130, 132, 134, 137, 168
ODERA Masatoshi 小寺正俊 4, 203, 207, 211, 212, 214, 216
OGATA Yoshitaka 尾形嘉貴 121
OGIWARA Kiyoshi 荻原 清 2, 172, 174
OHKUBO Yoshitaka 大久保嘉高 123
OHNO Kimio 大野公男 67
OHSAKI Akihiko 大崎明彦 43
OHSHIMA Masumi 大島真澄 28
OHSUMI Hideaki 大隅秀晃 10, 39
OIKAWA Yoshifumi 老川嘉郁 172, 189, 192
OKADA Shigefumi 岡田重文 147
OKADA Takuya 岡田卓也 90, 92, 94, 139, 141
OKAMOTO Sunao 岡本 朴 132
OKAZAKI Kiyohiko 岡崎清比古 97
OLSON R. E. 53
OOHIRA Shigeo 大平重男 103
OYAMA Hitoshi 大山 等 97
ROY A. C. 47, 51
SAITO Hajime 斉藤 肇 170
SAITO Takaichi 斉藤隆一 125

SAKAI Nobuhiko 坂井信彦 96, 167
SAKAIRI Hideo 坂入英雄 6, 103
SAKAMOTO Ichiro 坂本一郎 218, 221
SAKAMOTO Yuichi 坂本雄一 97, 205, 207
SASA Yoshihiko 佐々嘉彦 86, 88, 126, 128
SASAKI Fukashi 佐々木不可止 67
SATO Hiroshi 佐藤浩史 53
SATO Kenichi 佐藤憲一 18
SATO Kuninori 佐藤国憲 71
SAWAI Tomotsugu 沢井友次 117
SEKIYA Masahiro 関谷雅弘 67
SEKIZAWA Hisashi 関沢 尚 90, 92, 94, 141
SHIBATA Hiromi 柴田裕実 73, 75, 77, 78, 80, 82, 84, 162
SHIKATA Takashi 四方隆史 113, 115, 194
SHIMA Kunihiro 島 邦博 75
SHIMAMURA Isao 島村 勲 47, 62, 64
SHIMIZU Kazuo 清水和男 185
SHIMODA Tadashi 下田 正 39, 41
SHIMOURA Susumu 下浦 享 41
SHIRAISHI Haruki 白石春樹 113, 115
SHIRAISHI Kensuke 白石健介 117
SUEHIRO Makiko 末広牧子 121
SUEKI Keisuke 末木啓介 12, 15, 35, 37, 143, 166
SUEMATSU Tatsuya 末松達也 119
SUGAWARA Masahiko 菅原昌彦 30, 32, 152
SUGIMOTO Kenzo 杉本健三 10
SUZUKI Yoshimitsu 鈴木吉光 111
TABATA Yoneho 田畑米穂 145
TACHIBANAKI Hiroshi 橘木 寛 22, 24
TAKAHASHI Tan 高橋 旦 147, 148, 156
TAKEBE Hideki 武部英樹 2, 170, 218
TAKESHITA Isao 竹下勇夫 170, 184, 199
TANABE Tetsumi 田辺徹美 10
TANAKA Masahiko 田中雅彦 155
TAWARA Hiroyuki 俵 博之 78, 80, 82
TENDOW Yoshihiko 天道芳彦 168
TOHYAMA Mitsuru 遠山 満 14
TOKORO Nobuhiro 所 伸宏 84
TONUMA Tadao 戸沼正雄 71, 77, 78, 80, 82
TOSHIMA Nobuyuki 戸嶋信幸 62
TSUCHIDA Eishun 土田英俊 121
TSURUBUCHI Seiji 鶴淵誠二 71
UDA Masayuki 宇田応之 86, 88, 126, 128
URAI Teruo 浦井輝夫 6
UTSURO Masahiko 宇津呂雄彦 132
WADA Takeshi 和田 雄 170, 185
WATANABE Kenji 渡辺健次 104, 106
WATANABE Tsutomu 渡部 力 43, 45, 51, 55, 57, 59, 62, 64, 67
WATANABE Tokuji 渡辺徳治 209
YAGI Eiichi 八木栄一 6, 104, 106, 111, 117
YAMAGUCHI Kazuya 山口和也 181
YAMAMOTO Norikazu 山本徳和 113
YAMAJI Shuhei 山路修平 14
YANO Katsuki 矢野勝喜 97
YANO Yasushige 矢野安重 177, 179, 181
YANOKURA Minoru 矢野倉 実 4, 99, 101, 103, 119, 130, 134, 137, 201, 205, 207, 221
YATAGAI Fumio 谷田貝文夫 147
YATSUHASHI Motoharu 八橋元治 119
YATSURUGI Yoshifumi 八剣吉文 99, 130, 134
YOKODE Yutaka 横出 裕 128
YOKOI Fūji 横井風児 121
YOKOYAMA Ichiro 横山一郎 185, 199
YOSHIDA Kazuo 吉田和夫 22, 24, 109
YOSHIDA Nobuaki 吉田宣章 26
YUASA Makoto 湯浅 真 121
YUNOKI Akira 柚木 彰 147

RIKEN Accelerator Progress Report

理化学研究所加速器年次報告　第18巻（1984）

印　刷　昭和60年（1985）6月25日
発　行　昭和60年（1985）6月30日
発行者　理化学研究所
代表者　宮　島　龍　興
〒351-01　埼玉県和光市広沢2番1号
電話（0484）62-1111
編集者　理化学研究所加速器運営委員会
製　作　財団法人　学会誌刊行センター
〒113　東京都文京区弥生2丁目4番16号
印刷所　研究社印刷株式会社
〒352　埼玉県新座市野火止7丁目14番8号

定価 5,000円

理化学研究所

埼玉県　和光市　広沢